博士論文

Cyclic simple shear tests using stacked-rings on multiple liquefaction properties of sands
（砂の複数回液状化特性に関する積層リングを用いた繰返し単純せん断試験）

Wahyudi Seto

(ワヒュディ セト)

A thesis submitted in partial fulfillment
of the requirements for the degree of

Doctor of Philosophy

Department of Civil Engineering
University of Tokyo
Tokyo, Japan
September, 2014

ABSTRACT

This thesis is aimed to investigate the behaviors of sand subjected with multiple liquefactions and factors that have significant influence in determining its behaviors.

Liquefaction is a phenomenon in which the soil loses its strength and stiffnessand becomes more like a liquid. Liquefaction usually occurs whensaturated sand is subjected to rapid cyclic shear loading such as earthquake. Similar to the liquefaction phenomenon, multiple-liquefactionphenomenon means liquefaction that occurred repeatedly overtime at the same site.

Multiple-liquefaction phenomenon re-gained much attention after the recent Great East Japan Earthquake in Japan and Christchurch Earthquake in New Zealand. Both of these earthquakes happened almost at the same period in 2011. In Japan, the occurrence of multiple liquefactions have been studied and recorded by several researchers. Recently, it was reported that at least90 cases of repeated liquefaction happened during the Great East Japan Earthquake alone.

Interestingly, the majority of the cases mentioned before happened in the three typical types of area, which are former/abandoned river channel, artificial fills, and lower slopes of sand dunes. Based on these recent cases, it is clear that not just liquefaction certainly is able to re-occur at the same site, but also the damage caused by re-liquefaction could be more severe than the previous liquefaction. Therefore, this factis raisinggreat concern among engineers and researchers on the potential danger of future earthquakes.It is also very clear that the areas that once had liquefied before are the same areas wherepotentially another liquefactionmay take place in the future.

Several pioneer works have been conducted by investigating the behaviors of sand during 2-stage of liquefaction (re-liquefaction). It was found that the liquefaction resistance of soil is very much affected by at least two major factors,which are the effects of strain amplitude and anisotropy.

Most of the previous studies done by previous researchers were only capable to simulate at most 2-stage of liquefaction test. This was due to the limitation of the apparatuses itself (e.g.triaxial and torsional shear apparatuses). These types of apparatus are not suitablefor performing multi-stage liquefaction test, since the flexible membrane is not capable of maintaining the geometry of the specimen after full liquefaction or under extremely large shear deformation. To overcome

theseproblems, Institute of Industrial Science – The University of Tokyohas developed a new apparatus, so called stacked-ring shear apparatus. This apparatus was purposely designed to be able to maintain the geometry of the specimen to remain constant under multiple liquefactions or large shear deformation.

Despite its advantage, the stacked-ring shear apparatus has a major drawback. Large excessive friction is generated between the soil particles and the ring itself. The development of the apparatus is needed to reduce the amount of excessive friction. In general, two attempts were conducted: first was to reduce the contact surface of the specimen by reducing the number of rings composing stacked rings, second was to layer the surface of the rings using frictionless material (Diamond-Like-Coating). The results showedthat reducing number of rings is much more effective than the use of frictionless coating. However, both attempts were finally combined in the final setting of the apparatus.

In general, there are two types of test that were conducted in the current study. Type-I test is conducted to perform multi-stage liquefaction test where no residual deformation is allowed during each liquefaction stage ($\gamma = 0$), while the type-II test is conducted to performmulti-stage liquefaction test, where some form of residual deformation is allowed ($\gamma \neq 0$). The former test is aimed to investigate the effects of shear strain amplitude, while the latter test is aimed to investigate the effect of stress-induced anisotropy caused by residual strain.

The procedures to conduct both types of test in the stacked-ring shear apparatus are almost similar. First, the specimen needs to be consolidated up to the pre-determined initial confining stress. Then, each specimen is sheared cyclically under constant volume condition up to the maximum pre-fixed value on each liquefaction stage (e.g. γ_{DA}= 2.0%, 5.0%, 10.0%, and etc.). For the type-I test, another half-cycle of cyclic shear loading needs to be appliedafter reaching its maximum pre-fixedvalueto the origin (γ= 0%). This is done in order to avoid/minimize the effects of induced-anisotropy on the liquefied specimen. For the type-II test, the shear loading is stopped at zero shear stress (τ= 0 kPa) after it reach the maximum pre-fixed shear strain amplitude value. To conduct the second stage of liquefaction, the liquefied specimen needs to be re-consolidated again up to same initial confining stressas the previous liquefaction. Then, another cyclic shear loading was applied until second

liquefaction state achieved. The next liquefaction stages are done by following the same procedures as has been described earlier in the first and second stages.

The results on the both types of test revealed that the effects of increase in the specimen's density during re-consolidation in post liquefaction arenot significant in determining the soil resistance against multiple liquefactions. The specimen which had undergone large shear deformation showed larger increase in its density, but smaller liquefaction resistance in the following liquefactions. In the other hand, the specimen which had undergone smaller shear deformation showedsmaller increase in its density, butlarger increase in its liquefaction resistance in the following liquefactions.

The results of the type-I test revealed that the soil behaviors during multiple liquefactions are very much affected with the history of strain amplitudes. The specimens sheared with larger strain amplitude showedsmaller resistance against multiple liquefactions. In the other hand, the specimens sheared with smaller strain amplitude showed larger resistance against multiple liquefactions. However, these may not show the complete impact of the strain amplitude to the soil behaviors during multiple liquefactions. In another set of test, which the specimens sheared up to 0.5% shear strain double amplitude, the effects of strain amplitude showed different impact. In this set, the specimens sheared with larger strain amplitudes showed larger resistances against multiple liquefactions, and the specimens sheared with smaller shear strain amplitude showed smaller resistances against multiple liquefactions.Later, these two different behaviors were found to be related with the amount of energy dissipated on each liquefaction stage.

The experimental results on the type-I tests above only describe the global soil behaviors during multiple liquefactions. These experimental data may not enough to understand the impact of different stain amplitude to the soil behaviors subjected with multiple liquefactions. An additional observation is conducted with the aim to investigate the local deformation behaviors of the specimen during multiple liquefactions by using image analysis method.

To conduct the image analysis, a digital camera was installed to capture the movement of each ring with certain interval of time. Then, the series of picture were analyzed to obtain the deformation of each ring.

Image analysis results found that the specimens which hadundergone large shear deformation havelarger variations on their local shear deformations. Some sections

ofthe specimen showed larger shear deformations, while other sections showed smaller shear deformations as compare to their global one. The sections that were sheared larger than others may create localization within the specimen itself.Consequently, the localized specimen would have lower resistance in the future liquefactions. In the other hand, the specimens which had undergone smaller shear deformation showedless variation in their local deformations. This could mean better re-arrangement between soil particles inside the specimen. Thus, the resistance of the future liquefaction becomes higher.

Both results from experimental data and image analysis are very important to understand the mechanism that is taking place during multiple liquefactions. One of the methods to identify this mechanism is using energy approach. The energy approach is based on Newtonian energy concept. This concept says that energy is eternal, thus neither can be created or destroyed. However, energy can change its form. In soil mechanics, the energy is mainly consumed through the rolling and sliding mechanisms. These two modes of mechanism directly related to the increase or the decrease of soil's effective stress (σ') during liquefaction. The energy approach shows relation between the dissipated energy in a stage of liquefaction ($\Sigma\Delta W$) to the soil resistance in the future liquefaction.

The results found that there is a virtual boundary in which the amount of dissipated energy will result on increasing or decreasing the liquefaction resistances of the future liquefaction. The amount of energy dissipated in a stage of liquefaction will have a positive impact ($\Sigma\Delta W^{(+)}$) when the stress path of the sheared specimendoes not passing the phase transformation line (PTL). Within this boundary, the larger the dissipated energy is, the higher the liquefaction resistance will be in the future liquefaction. If the applied energy of the sheared specimen exceeds the PTL, a negative impact is started to take place ($\Sigma\Delta W^{(-)}$). In this region, the larger the dissipated energy is, the lower the liquefaction resistanceswill be in the future liquefaction.

As important to the effects of strain amplitude, the effects of anisotropy (type-II test) also showed significant impact in determining the soil behaviors during multiple liquefactions.

The effects of stress-induced anisotropy are investigated by analyzing the dilatancy characteristics of the specimen that had experienced a single or multiple liquefactions before.Then, the liquefied specimen is re-consolidated to its original effective stress and subjected with drained cyclic shear constant stress test to obtain their dilatancy characteristics. In an isotropic specimen, the dilatancy characteristics are symmetric in each direction of loading.

The results found that the specimen affected by anisotropy has unsymmetrical dilatancy characteristics on different loading directions (e.g. clockwise and anticlockwise). Moreover, the specimen that affected by anisotropy shows higher contraction than the specimen that does not. These behaviors mean thatthe specimen affected by stress-induced anisotropy would have smaller liquefaction resistance than the specimen that does not affected by anisotropy.

ACKNOWLEDGEMENT

TABLE OF CONTENTS

Chapter 1 : INTRODUCTION

Chapter 2 : TEST MATERIAL, APPARATUS, AND PROCEDURES

Chapter 3 : FORMULATION OF STRESSES AND STRAINS

Chapter 4 : DEVELOPMENT OF STACKED-RING SHEAR APPARATUS

Chapter 5 : EFFECTS OF STRAIN AMPLITUDES ON THE BEHAVIOR OF SAND SUBJECTED WITH MULTIPLE LIQUEFACTIONS

Chapter 6 : EFFECTS OF INDUCED ANISOTROPY TO THE BEHAVIORS OF SAND SUBJECTED WITH MULTIPLE LIQUEFACTIONS

Chapter 7 : SOIL CHARACTERISTICS UNDER MULTIPLE LIQUEFACTIONS BASED ON ENERGY APPROACH

Chapter 8 : CONCLUSIONS AND RECOMMENDATIONS

Appendix A: PHOTOS OF PROTOTYPE COATING DURABILITY TEST

LIST OF TABLE

Chapter 6

LIST OF FIGURES

Chapter 3

Chapter 4

Chapter 5

Chapter 6

Chapter 7

SYMBOLS AND ABREVIATIONS

τ	shear stress
τ_{Top}	shear stress measured by the top load cell
τ_{Bo}	shear stress measured by the bottom load cell
τ_{Avg}	average shear stress applied to the specimen
σ_v	vertical stress
$\sigma_{v.Top}$	vertical stress measured by the top load cell
$\sigma_{v.Bo}$	vertical stress measured by the bottom load cell
$\sigma_{v.avg}$	average vertical stress applied to the specimen
σ_g	overburden stress
σ_r	radial stress
σ_θ	circumferential stress
σ_1	major principal stress
σ_2	intermediate stress
σ_3	minor principal stress
σ_{mem}	membrane stress
Po	axial stress applied to the outer surface of the specimen
Pi	the axial stress applied to the inner surface of the specimen
A	surface area of the specimen
R_o	outer radii of the specimen
R_i	inner radii of the specimen
Ko	lateral soil pressure's coefficient at rest
t_{mem}	membrane thickness
γ	global shear strain
$\gamma_{Loc.}$	local shear strain
γ_{DA}	double amplitude of shear strain
$\gamma_{DA.max}$	maximum double amplitude of shear strain
γ_{SA}	single amplitude of shear strain
$\gamma_{SA.max}$	maximum single amplitude of shear strain
$\gamma_{SA.max(CW)}$	maximum single amplitude of shear strain in the clockwise direction
$\gamma_{SA.max(ACW)}$	maximum single amplitude of shear strain in the anticlockwise direction
γ_{res}	residual shear deformation
γ_s	unit weight of sand material
γ_w	unit weight of water
V_s	volume of soil/solid

V_v	volume of void
V_w	volume of water
G_s	material's specific gravity
E	Young's modulus
G	shear modulus
G_{max}	maximum shear modulus
G_{sec}	secant shear modulus
e	void ratio
e_0	initial void ratio
e_{max}	maximum void ratio
e_{min}	minimum void ratio
D_{50}	particle's mean diameter
Dr	specimen's relative density
Dr_{ini}	specimen's initial relative density
Dr_0	specimen's relative density after 1st consolidation
F_c	fines content
T	torque force
F_z	axial force in the vertical direction
$f_{z\theta}$	soil-ring frictional force generated in the vertical direction
$f_{\theta\theta}$	soil-ring frictional force generated in the circumferential direction
$\delta_{z\theta}$	soil-ring friction angle in the vertical direction
$\delta_{\theta\theta}$	soil-ring friction angle in the circumferential direction
δ_{max}	maximum deviation between the local and global soil's deformation
δ_{res}	residual deviation between the local and global soil's deformation
$\Sigma\Delta W$	dissipated energy in a stage of liquefaction
$\Sigma\gamma$	accumulated shear strain in a stage of liquefaction
$\Sigma\Delta W^{(+)}$	amount of dissipated energy that have positive impact
$\Sigma\Delta W^{(-)}$	amount of dissipated energy that have negative impact
$N\gamma_{DA(2.0\%)}$	number of cycle to cause shear strain double amplitude of 2.0%
ε_z	vertical strain
$\varepsilon_{Vol.}$	volumetric strain
ε_r	radial strain
ε_θ	circumferential strain
$d\varepsilon_{Vol}$	volumetric strain increment
$d\varepsilon_{Vol}^{p}$	plastic volumetric strain increment
$d\gamma$	strain increment
$d\gamma^{p}$	plastic strain increment

p'	soil's effective stress	
LC	Load Cell	
GS	Gap Sensor	
EDT	External Displacement Transducer	
H	specimen's height	

1 INTRODUCTION

1.1 Background

This thesis is aimed to investigate the behaviors of sand during multiple liquefactions and the mechanisms that are taking place in this phenomenon. Liquefaction is a phenomenon in which the soil losses its strength and stiffness due to rapid shear loading. It generally appears in the highly saturated soil subjected with rapid earthquake motions. The earthquake motions increase the pore water pressure in the soil and reduce the contact forces between the soil particles. In the full liquefaction state, there is virtually no contact between the soil particles. As a result, the soil behaves much more like a liquid than solid. Massive damages on structures and lifelines can happen due to the loss of soil bearing capacity during liquefactions.

Similar to the liquefaction phenomenon, multiple liquefactions phenomenon mean liquefaction that occurred repeatedly over time in the same site. Need to be mentioned that the multiple liquefactions do not occur due to the aftershocks of an earthquake. Instead, each liquefaction in the series of multiple liquefactions happens at different period of time, where the pore water pressure on the previous liquefaction had been fully dissipated.

Japan is considerably the frontier on the earthquake related research and studies. There has been countless number of studies conducted by various researchers in investigating the soil behaviors during liquefaction. The investigations include all forms of experimental tests and field investigations. These extensive numbers of study are happen due to the fact that Japan is one of the countries that most frequently struck and devastated by earthquake. Geologically, Japan is located in three major plates, which are Eurasian Plate in the west, Pacific Plate in the east, and Philippine's Plate in the south. Both Pacific Plate and Philippine's plate are moving to the west-ward direction and sub-ducted into the Eurasian Plate around the East Coast of Japan. The sub-ducted zone of these three plates is called Japan Trench. This trench is the location where most of the history of major earthquakes happened, such as the recent Great East Japan Earthquake (Mw 8.9) in March 2011.

The multiple liquefactions phenomenon re-gained much attention after two recent major earthquakes event that happened almost in the same period of time, which are Christchurch Earthquake in New Zealand (2010 - 2011) and Great East Japan Earthquake (2011). In Christchurch Earthquake, multiple liquefactions phenomenon happened during the period of September 2010 to the end of 2011. During this period, the Christchurch city and its surrounding were struck by series of strong earthquakes. At least, six of these series caused multiple liquefactions on 4 September 2010 (Mw 7.1), 22 February 2011 (Mw 6.2), 13 June (Mw 5.3 and Mw 6.0), and 23 December 2011 (Mw 5.8 and Mw 5.9). Cubranovski et al. (2012) reported that 22 February 2011 earthquake caused the most severe liquefaction-

induced damage as compare to other earthquakes. Series of multiple liquefactions left serious damages on thousands of homes, buildings, and lifelines (Cubranovski and Taylor, 2011; Cubranovski and Hughes, 2011; and Yamada et al., 2011). These investigation reports are very important, because it shows not just the liquefaction can appear twice, but it can appear repeatedly over time at the same site.

In Japan, Kuribayashi and Tatsuoka (1975) pioneered the data collection of the liquefaction history in Japan from 44 earthquakes in the last 100 years. Among these earthquake events, it was found that the liquefaction sites seem to be concentrated only in some areas. Those areas are the area around Tone River (Chiba Prefecture), Nobi plain (Nagoya prefecture), and Hokuriku region (west coast of Japan) as can be seen in Fig. 1. Detail investigations revealed that all of these areas have similar geomorphologic conditions, which all of them are located in the surrounding area of downstream rivers or former/abandoned river channel. Yasuda and Tohno (1988) conducted another study where they found approximately 16,800 potentially liquefied sites during the period 745 to 2008 by using GIS satellite data analysis. In recent years, Wakamatsu (2011) also made comprehensive data collection of earthquake events from period of 416 - 1997 based on the documentary reports, post-earthquake reconnaissance surveys, and interviews to the local residents. Wakamatsu (2011) found that at least 140 cases of liquefaction had re-occurred at the same sites, where some of these areas had been previously suspected by Yasuda and Tohno (1988). He also found that the liquefaction sites were concentrated in the areas not just in former/abandoned river channel (36 sites), but also in the areas of artificial fills (35 sites), and lower slopes of sand dunes (26 sites).

The recent multiple liquefaction events that happened in the area around Tone River (Northern part of Capital Tokyo) drew big attention among researchers. Historically, liquefaction had re-occurred in this area at least four times in four successive earthquakes in 1894 (M 7.5), 1895 (7.3), 1923 (M 7.5), and 1931 (M 7.0). The recent field investigation studies done by Wakamatsu (2012) and Koseki et al. (2012) showed that this area was once again severely damaged during the last great earthquake.
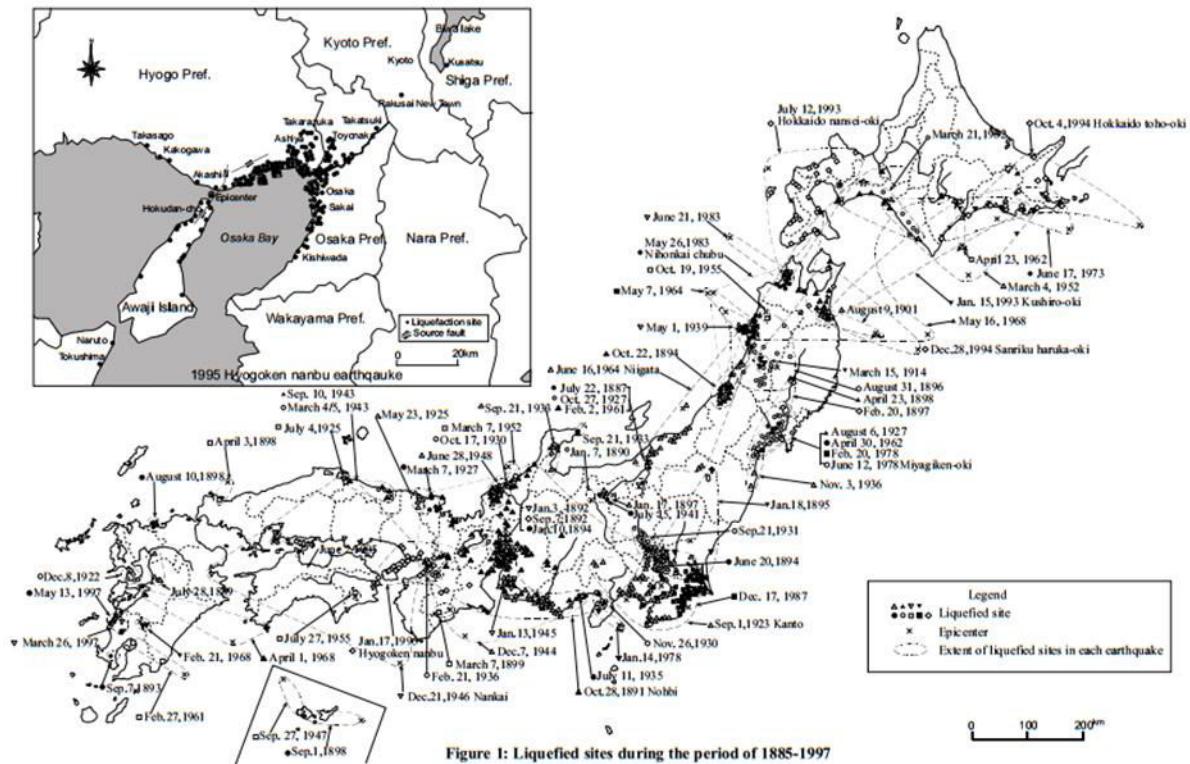
Fig. 1: Liquefaction sites during the period of 1885-1997 (Wakamatsu, 2011)

Multiple liquefactions do not only being reported in Japan or New Zealand. Other countries such as United States, Greece (Youd and Hoose, 1978; Youd and Wieczorek, 1982; and Papathanssiou et al., 2005) had reported the occurrence of multiple liquefactions, In United States, liquefaction have re-occurred at several areas in the State of California during Hayward Earthquakes on 1868 (M 6.5 – 7) and 1931 (M 7.0). Similar to the case in Christchurch Earthquake, the damage caused by the second liquefaction was much more severe than the first one.

On the several examples that have been described earlier, it is clear that not just liquefaction certainly able to re-occur at the same site, but also the damage caused by re-liquefaction could be worse than previous liquefaction. Therefore, this fact is raising great concern among engineers and researchers on the potential danger of future earthquakes. Based on these data collections, it can be also assumed that some particular geomorphologic conditions are susceptible to liquefy repeatedly. Therefore, the multiple-liquefaction susceptible areas/map can be made.

As an engineer, we tend to assume that once soil liquefied, than it might become harder for the same soil to re-liquefy again at another time. That is due to the densification and re-consolidation processes took place in post liquefaction. Therefore, it is expected that the soil resistance in the future liquefactions becomes stronger. However, it was found that the soil resistance in the future liquefaction could be smaller than previous liquefaction. Researchers

have found that the resistances of the future liquefaction are very much affected to the stresses and strains history of the previous liquefactions. This effect is called the effect of pre-shearing history. Finn eta al. 1970, Seed et al. 1977, Ishihara and Okada (1978 and 1982), Oda (1972a and 1972b), Suzuki and Toki (1984), Suzuki and Suzuki (1988), and Towhata and Ishihara (1985) were among the first researchers to investigate the effects of pre-shearing history on the soil behaviors in 2 stages liquefaction tests. In general, it was found that the histories of strain amplitude as well as the induced anisotropy were among the parameters that have significant impact in determining the soil resistance in the future liquefactions.

Since all of the previous studies were conducted using triaxial and torsional shear apparatuses, therefore, the number of liquefaction stage that can be conducted is limited to approximately 2 stages of successive liquefaction. This happens due to the limitation of these apparatuses itself as will be explained later. In reality, liquefaction can appear more than two times. To investigate the soil behaviors during series of multiple liquefactions, a new type of apparatus will be introduced. The apparatus is called stacked-ring shear apparatus and purposely designed to be able to simulate the soil subjected with multiple liquefactions. The development of this new apparatus becomes one of the major objectives in this study.

1.1.1 Development of stacked-ring shear apparatus

There are few to almost no experimental studies, as far as the author understands, have been conducted to investigate the soil behaviors under multiple liquefactions. This happens due to the nature of the testing apparatuses itself (e.g. triaxial and torsional shear apparatus). The triaxial and torsional shear apparatus are not capable to simulate multiple liquefactions due to the use of flexible membrane. The flexible membrane will deform along with the sheared specimen. In full liquefaction state, the specimen's effective stress is significantly reduced up to the point where the contact forces between the soil particles are very small. In this state, a flow type shear deformation is taking place. Chiaro (2011) conducted series of single liquefaction tests in the hollow cylinder torsional shear apparatus. The study was aimed to investigate the effects of initial static stress during liquefaction, in which the specimens were sheared under very large shear deformation. He found that the specimen's geometry was no longer constant up to certain amplitude of shear deformation.

In simulating the multiple liquefactions test, it is essential to keep the geometry of the specimen to remain constant on each stage of successive liquefactions. Therefore, the multiple liquefactions test needs to be conducted with the type of apparatus that capable to maintain the specimen's geometry under series of liquefaction and large shear deformation. In June

2011, Institute of Industrial Science – The University of Tokyo developed a different variant of the ring shear apparatus, so called stacked-ring shear apparatus. Instead of using flexible membrane, the specimen in the stacked-ring shear apparatus is constrained in between inner and outer vertically stacked rings.

The original ring shear apparatus was first introduced by Hvorslev (1939). The Hvorslev's ring shear apparatus consists of two rings (so called split ring shear apparatus), which are fixed ring and rotating ring. Then, this type of apparatus was developed by Bishop et al. (1971). The Bishop's ring shear apparatus is capable to measure the generated friction in the specimen by installing a pair of load cell on each fixed and rotating parts of the rings. Later, this type of ring shear apparatus was used and further developed by various researchers such as Broomhead (1979), Hungr and Morgenstern (1984), Tika (1989), Garga and Sendano (2002), Sassa (1984), Sassa et al. (2004), Sadrekarimi and Olsen (2007) among others.

The stacked-ring shear apparatus has different design and characteristics than the common split ring shear apparatus. Instead of using fixed and rotating rings, the stacked-ring shear apparatus is composed by 5mm vertically stacked individual rings. Each of these rings is capable to move independently in circumferential directions, but constrained in the vertical directions. This feature makes the stacked-ring shear apparatus has several advantages than the common split ring shear apparatus. However, like other types of ring shear apparatus, the stacked-ring shear apparatus also has similar problems. Some of these problems are:

Excessive friction - in all types of ring shear apparatus, the excessive friction cannot be avoided due to the nature of the apparatuses itself. The excessive friction will be generated due to the contact between the soil particles and the metal rings itself. The friction induces non-uniform distribution of stresses and strains along the height of the specimen. These effects become very predominant in the general split ring shear apparatus than the stacked-ring shear apparatus as shown in Fig. 2 and Fig. 3. Since, the split ring shear is composed by only fixed and rotating ring, the stresses and strains distribution are concentrated in the shearing plane as can be seen in Fig. 2. Therefore, this type of apparatus commonly has very short height. However, the shorter height of the specimen enhances the effect of end restrain. Due to this problem, the split ring shear apparatus cannot be used to conduct multiple liquefactions test. In the other hand, the design of the stacked-ring shear apparatus is capable to significantly reduce the non-uniform stresses and strains distribution along the height of the specimen in the circumferential direction as can be seen in Fig. 3.

Soil extrusion – the extruded soil is also one of the chronic problems in the all types of ring shear apparatuses. Bishop (1971), Tika et al. (1996), and Iverson et al. (1998) were confronted to this problem. The soil particles may extrude in the shearing plane located in between two

split rings. The extruded sand particles will induce additional frictions that create higher apparent shear stress. In the stacked-ring shear apparatus, this problem is significantly reduced due to the 0.1mm fix gap between the individual rings. This 0.1mm gap is small enough to ensure the sand particles that has mean particle diameter larger than 0.1mm will not extrude during shearing.
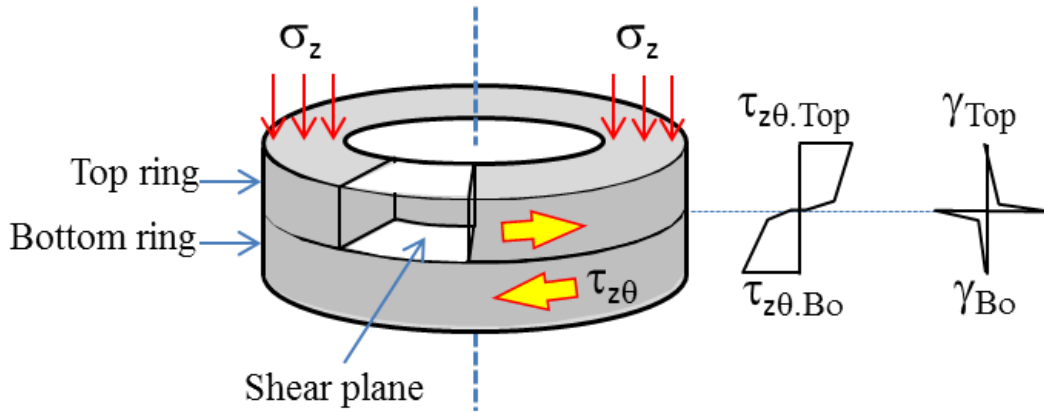
Fig. 2: Common split ring shear apparatus
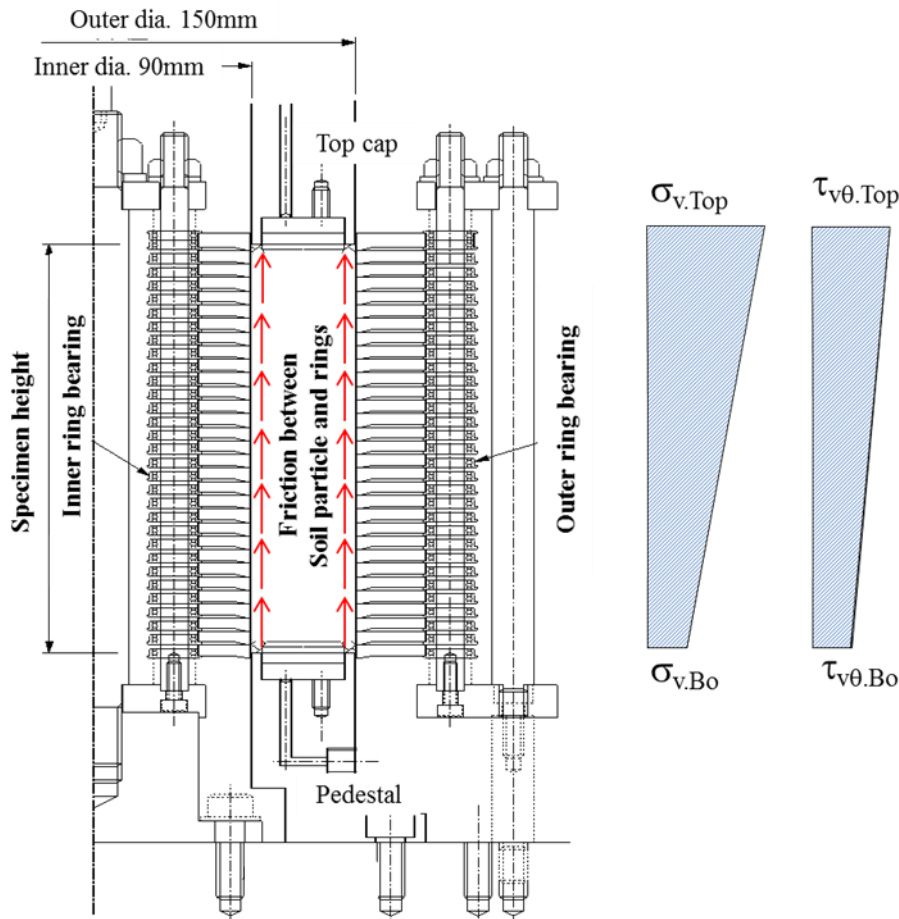
Fig. 3: Configuration of stacked-ring shear apparatus

Need to be noted that none of the soil testing apparatuses (e.g. triaxial, hollow cylinder torsional shear apparatus and ring shear apparatuses among others) are perfect. Each of this apparatuses is designed with specific purpose with its own advantages and disadvantages. However, the stacked-ring shear apparatus is considered as the optimum tool to simulate multiple liquefactions phenomenon.

1.1.2 Effects of shear strain amplitudes in the soil behaviors during multiple liquefactions

As mentioned in the beginning, the history of strain amplitudes was found to be one of the major factors that influence the soil behaviors during multiple liquefactions. This effect was originally investigated by two frontier experiments conducted by Finn et al. (1970) and Seed et al. (1977). Finn et al. (1970) conducted two stages liquefaction test in triaxial apparatus. They found that the soil resistance on the 2nd liquefaction was lower than the one in 1st liquefaction. In the other hand, Seed et al. (1977) conducted two stages of liquefaction test in model test using shaking table. They found completely opposite than the one found by Finn et al. (1970). Seed et al. (1977) found that the soil resistance in the 2nd liquefaction was much higher than 1st liquefaction. Later, it was found that the specimens in the two studies had undergone with different level of stain amplitudes. The two stages liquefaction tests by Finn et al. (1970) was undergone with larger shear deformation as compare to the two stages liquefaction tests by Seed et al. (1977). These two frontier studies began to reveal the nature of multiple liquefactions phenomenon.

The effects of shear strain amplitude on 2 stages of liquefaction test were first thoroughly investigated by Ishihara and Okada (1978 and 1982). In their study, the amplitudes of the shear strain history were divided into two part, which are large pre-shearing and small pre-shearing. Large pre-shearing is applied to the specimen when the stress path of the previous liquefaction passes the so-called Phase Transformation line (PT), while small pre-shearing history is applied to the specimen when the stress path of the previous liquefaction does not passes the Phase Transformation line. Phase Transformation line itself is a line that marks the change of soil behavior from contraction to dilation and vice-versa. Their results showed that the behaviors of the two types of test were completely different. The specimen that was sheared beyond the phase transformation line should expect a decrease in its resistance in the next liquefaction. In the opposite side, the specimen that was sheared within the boundary of phase transformation line should expect an increase in its resistance in the future liquefaction.

Later, these findings were confirmed again by the 2 stages liquefaction tests conducted by Towhata and Ishihara (1985), Suzuki and Toki, (1984) and Oda et al. (2001) among others.

It has been well understood that the application of small cyclic loading prior to the liquefaction tests will significantly increase the soil resistance against liquefaction. This phenomenon has been studied by various researchers (Wichtmann et al., 2005; Niemunis, 2003; Withcman and Triantafyllidis, 2004; Seed et al., 1988; and Suzuki and Toki, 1984 among others). Niemunis (2003) tracked the movements of the soil particles using particle image velocimetry to observe the impact of small cyclic loading in the fabric of the specimen, while Withcman and Triantafyllidis (2004) measured the stiffness of the pre sheared specimens by P and S waves measurements using resonant column. In both of these studies, the impacts of small cyclic loading to the change of soil fabric were not conclusive. In the opposite side, the study conducted by Roscoe et al. (1970) found that the pre-dilated specimens require less number of cycles to reach liquefaction than the original soil without dilation. Furthermore, they found that the level of the decreases in soil liquefaction resistance depends on the level of dilation in pre-dilated specimen. The larger the dilation, the lesser the number of cycles required to liquefy the specimen. Suzuki and Toki (1984) also found a strain limit, so-called threshold strain, in which the specimen would show smaller liquefaction resistance if it is sheared beyond this limit.

As mentioned earlier, the other impact of multiple liquefactions are excessive soil settlement. In fact, most of the damages during liquefaction such as the tilting of the house, the excessive bending of lifelines among others are created due to the excessive or un-even soil settlement. Some of the state –of-the-art studies has been published to link the relation between shear strain amplitudes and the soil settlement in post liquefaction (Tokimatsu and Seed, 1987; Nagase and Ishihara, 1988; Ishihara and Yoshimine, 1992). Tokimatsu and Seed (1987) conducted direct site investigation to evaluate the amount of settlement that was created in post liquefactions, while Ishihara and Yoshimine (1992) found that the soil settlement increased linearly with the applied shear strain amplitude up to some limit as shown in Fig. 4. At some point, the amount of soil settlement would remain constant even under very large shear strain amplitudes.

It is fair to assume that denser the soil will show larger resistance in the future liquefaction. However, based on previous cases and studies, it seems that the increase of soil's density in post liquefaction has little impact in determining the resistance of the future liquefaction.
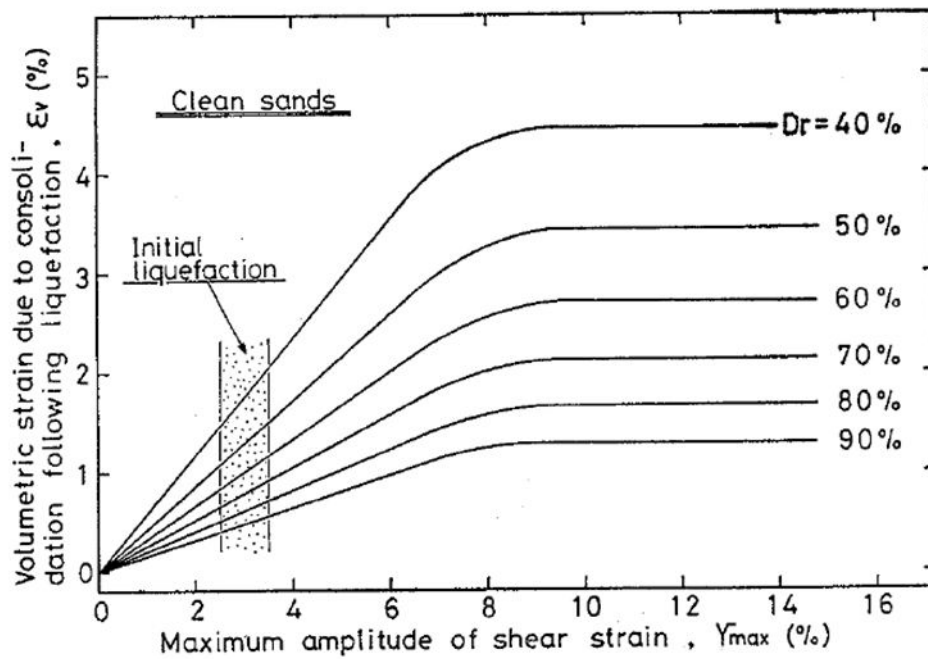
Fig. 4: Relationship between maximum amplitude of shear strain and volumetric strain during reconsolidation of liquefied specimen in Toyoura sand (Ishihara and Yoshimine, 1992)

In the current study, the effects of strain amplitudes on the behaviors of sand during multiple-liquefaction tests are conducted by shearing the specimen with different shear strain amplitudes. In addition, the experimental results of this effect are being re-analyzed using image analysis and energy approach. The image analysis aims to investigate the local behaviors of the specimen as compare to their global ones during multiple-liquefaction test, while the application of energy approach is aimed to understand the mechanism that is taking place in the soil subjected to the multiple liquefactions.

1.1.3 Local deformation measurement by image analysis

The output from the experimental studies on multiple-liquefaction tests in the stacked-ring shear apparatus only shows the global behaviors of the specimen. These results may not enough to understand the whole impacts of pre-shearing history in the multiple liquefactions. Therefore, additional analysis is needed to investigate the local deformation behaviors of soil during multiple liquefactions. In the current study, the local deformation of soil is obtained by using image analysis technique. In geotechnical engineering field, image analysis is commonly used to observe the behaviors of strain localization and the evolution of void distributions on the sheared specimen. Various means of image analysis technique have been developed for different purposes. Scarpelly and Wood (1982) and Han and Vardoulakis

(1991) used X-ray radiograph method to investigate the void distributions in the sheared specimen. Tatsuoka et al. (1990) and Mokni (1992) used laser technique. Stereo photogrammetry was used by Desrues et al. (1985), Yoshida et al. (1994), and Harris et al. (1995) to investigate the shear band evolution. Niemunis (2003) conducted image analysis on the liquefaction test with pre-sheared specimen with the aim to investigate the change in particle re-arrangement due to small cyclic loading prior to the liquefaction tests. The movements of the soil particles were tracked by using particle image velocimetry (PIV) technique.

In the stacked-ring shear apparatus, the local shear deformations of the specimen can be obtained by tracking the movement of each individual stacked ring. It is assumed that the movements of individual stacked rings represent the deformation of each section of the specimen. Need to be noted that this assumption may not be always true, particularly at the time when the specimen reaches full liquefaction state. At this state, the contact forces between the soil particles and the metal rings become very small. As a result, the deformations of the individual ring would be very likely to underestimate the real deformations of the specimen.

For the practical reason, the experiments on most of the image analysis related studies were conducted using prismatic specimen such as plane strain compression test. In the plane strain compression test, each section of the specimen is moving in two-dimensional plane (2D). In the stacked-ring shear apparatus, the movement of each individual ring is moving in the three-dimensional space (3D). As a result, the apparent deformations that are captured by the camera are not the real one. This happens because the camera works by converting the three-dimensional objects into two-dimensional images. Wahyudi (2012) proposed a simple mathematical solution to obtain the real deformation of the sheared specimen in the hollow cylinder torsional shear apparatus in the application of image analysis for shear band observation.

1.1.4 Mechanisms of multiple liquefactions by energy approach

The current study attempts to understand the mechanisms that are taking place during multiple liquefactions using energy approach. Energy approach is derived from the basic principal of Energy Conservation's Law. This law says that the total amount of energy is constant. However, energy can change its form from one another. A frontier study conducted by Nemat-Nasser and Shookoh, (1979) found a simple mathematical formulation to the relation between the amount of dissipated energy and the change in relative density during drained

constant stress test. The dissipated energy mostly consumed due to friction between the soil particles in the rolling and sliding motions. By understanding the mechanisms in the drained constant stress test, the same principal can be applied in the undrained constant volume tests. The contraction and dilation in the undrained liquefaction test changes the generation of pore water pressure (u). The contracted specimen increases the generation of pore water pressure, hence, decreases the soil's effective stress (σ'). Based on these correlations, the liquefaction potential of soil can be evaluated. Davis and Berril (1982) and Berril and Davis (1985) developed similar methods to quantify the soil liquefaction potential. Other researchers proposed much simpler relation between the dissipated energy and the generation of pore water pressure (Figueroa, 1990; Figueroa and Dahisaria, 1991; Figueroa et al., 1994; and Towhata and Ishihara, 1985; Kokusho, 2013 among others). Their methods evaluate the amount of dissipated energy per unit volume by calculating the area within the hysteretic loop of stress-strain relationship.

All of these studies were obtained from the experimental tests conducted with uniform sand specimen under specific conditions. In the real situation, the initial properties of soil are far more complex. To consider this complexity, other researchers proposed simple empirical equations to evaluate the soil liquefaction potential based on in situ test SPT data. Seed et al. (1983), Bieganuosky et al. (1976), Tatsuoka, et al. (1980), Douglas et al. (1981), Tokimatsu and Yoshimi, (1981) among others.

Need to be noted that all of these proposed methods were conducted in the sample that did not have any history of previous liquefaction. In the current multiple-liquefaction study, the liquefaction potential for the future liquefactions are very much affected to the history of previous liquefactions.

1.1.5 Effects of induced anisotropy in the soil behaviors during multiple liquefactions

Besides the effects of strain amplitudes as have been lengthy discussed earlier, there is another factor that plays major role in determine the behaviors of sand in the multiple liquefactions test, so called anisotropy. In the geotechnical engineering field, anisotropy can be divided into two categories, which are the inherent anisotropy and induced anisotropy. Inherent anisotropy is a type of anisotropy that appears because of the initial re-arrangement of soil particles during sedimentation process. In the nature, the sedimentation of soil particles follows the direction of the gravitational force. Similar analogy happens in pouring the soil particles during specimen preparation of experiment test. The direction of particles

sedimentation will cause the specimen to have different shear resistance on different loading directions. Oda et al. (2001) conducted several series of test using triaxial apparatus to investigate the impacts of inherent anisotropy to the soil's liquefaction resistance. In their study, two types of specimen were prepared. One type of specimens was prepared by pouring the soil particles in parallel to the gravitational force while the other was prepared with 45 degree angle to the gravitational force. The result showed that the specimen prepared with 45 degree angle than the one prepared with parallel direction to the gravitational force. This happens due to the fact that the specimen prepared with 45° angle is in parallel to the direction of major principal stress during shearing. In the current study, the effect of inherent anisotropy in the tests conducted with stacked-ring shear apparatus is negligible. Therefore, the observation of this effect will be neglected.

Another type of anisotropy, so-called induced anisotropy, plays more significant role in determining the resistance of soil under multiple liquefactions. Induced anisotropy is caused by the unequal properties, deformations, and stress conditions within the specimen that has undergone shear deformation. Towhata and Ishihara (1985), Suzuki and Suzuki (1988), and Oda et al. (2001) among others had conducted specific tests to investigate the effects of induced anisotropy on the behaviors of soil during 2 stages liquefaction tests. Recently, Yamada et al. (2010) conducted similar tests in the triaxial test apparatus. Their studies found that the resistance of the future liquefactions can be different in different loading directions due to the effects of induced anisotropy. The resistance of the future liquefaction would likely to increase, if the liquefied specimen is sheared in the same direction to the residual direction in previous liquefaction. In the similar way, the resistance of the future liquefaction would likely to decrease, if the liquefied specimen is sheared in the opposite to the direction to the residual deformation in past liquefaction. This is a significant finding in revealing another characteristic of multiple-liquefied soil. In the real situation, the liquefied soil is very likely to always have some degree of residual deformation. As a result, the resistance of future liquefactions may always be affected by some degree of induced anisotropy.

The effects of induced anisotropy can be evaluated by various means such as initial soil's stiffness by static and dynamic measurements as well as using stress-dilatancy relationship. Both static and dynamic measurement usually applied in the triaxial apparatus. In the rings shear apparatus.

1. The static measurement evaluates the soil stiffness during the application of small cyclic loading within the quasi-elastic range ($\gamma \leq 0.001\%$). To do so, a high resolution of probing tools is needed. Researchers have been developing several types of probes that can evaluate such a small deformation, which some of them are the proximity transducers

(Hird and Yung, 1987 and 1989), inclinometer (Burland, 1989), LVDT (Cuccovillo and Coop, 1997), LDT (Goto et al. 1991), pin type LDT for hollow cylinder specimen (Hong Nam, 2005; De Silva et al., 2005) among others. To evaluate the effects of induced anisotropy on the liquefied soil, several pairs of probe need to be attached on different side of the specimen.

2. The dynamic measurement is widely used recently because it capable to provide better results in evaluating the initial stiffness of soil. This method works by measuring the travel time of the propagated waves (P and S waves) from the trigger to the receiver, where the travel time of the propagated waves has direct relation to the stiffness of soil. Several dynamic measurement methods have been developed recently are bender element (Schultheiss, 1981; Dyvik and Madshus, 1985; Viggiani and Atkinson, 1995, Chaudary et al. 2004; Wicaksono et al., 2007), Triggers and accelerometers (AhnDan and Koseki, 2007; Maqbool, 2005; Kiyota, 2007, Wicaksono et al., 2007; Suwal, 2013). Similar to the static measurement, the evaluation of induced anisotropy can be done by attaching several pairs of sensor on different sides of the specimen.

3. Stress-dilatancy relationship measures the impact of induced anisotropy by analyzing the specimen dilatancy characteristics in different loading directions. Stress-dilatancy shows the relation between the plastic volumetric strain increment over plastic shear strain increment ($=d\varepsilon_{Vol}^{p}/d\gamma^{p}$) and shear stress ratio ($=\tau/p'$). Rowe (1962, 1964, and 1969) first derived the stress-dilatancy relation in the series of test conducted in triaxial compression, triaxial extension, and plane strain tests. This relation assumes the granular material can be represented as a regular packing of spheres, where the ratio between the input energy to the output energy is constant (K). Since then, other researchers proposed several modifications of the original Rowe's stress-dilatancy for different apparatuses, and testing conditions (Pradhan and Tatsuoka, 1989; Balakhrisnaiyer, 2000; Shahnazari, 2001, De Silva. 2008 among others).

1.2   Objectives of the study

Primarily there two major objectives in this study, which are to investigate the behaviors of sand under multiple liquefactions as well as to develop the stacked-ring shear apparatus itself. The details of the scope of study are:

1. Development of the new stacked-ring shear apparatus

   This new apparatus was assembled at 2011 with the aims to simulate multi stages liquefaction test. The apparatus is capable to maintain the geometry of the specimen that

undergoes very large deformation. The development of the apparatus includes the modifications on the several components of the apparatus itself and the installment of additional sensors for specific purpose, among others.

2. Overcoming the excessive friction in the stacked-ring shear apparatus

   In its original version, the stacked-ring shear apparatus generated extraordinarily large friction between the soil particles and the metal rings. The excessive friction causes the extensive loss of vertical stress applied to the specimen. As a result the vertical stress distribution within the specimen is not uniform. This study is attempted to reduce the excessive friction in the stacked-ring shear apparatus.

3. Investigation on the effects of strain amplitudes.

   The first attempt to understand the impact of the pre-shearing history to the soil behaviors under multiple liquefactions was done by understanding the effects of shear strain amplitudes. It is expected that different shear strain amplitude history would show different resistance in the future liquefaction. Several studies have been investigated this effect on the 2 stages of liquefaction test, while the current study is aimed to investigate the effects of shear strain amplitudes in the multiple liquefactions test.

4. Investigation on the density increase in multiple liquefactions

   In general, denser specimens will give higher resistance against liquefaction. This behavior is true to specimen without history of previous liquefaction. However, this may not be the case in the specimen that has the history of previous liquefaction. Therefore, this study is also aimed to investigate the increase of soil's density to the soil resistance in the multiple-liquefaction test.

5. Investigation on the local behavior of specimen using image analysis

   The experimental results on the effects of strain amplitudes in the multiple liquefaction tests only show us the global soil behaviors. These results may not enough to fully understand their true nature. Therefore, additional investigation needs to be conducted with the aims to observe the local deformation behaviors of the specimen using image analysis method.

6. Understanding the mechanism in the multiple-liquefaction test using energy approach

   From the experimental results, the current study attempts to explain the mechanism that is taking place during multiple liquefactions. By understanding their mechanisms, researcher will be able to mitigate the disaster induced by multiple liquefactions.

7. Investigation on the soil stiffness during multiple liquefactions

   In the pre-sheared specimen, the stiffness of soil could become one of the indicators to the increase or the decrease of soil resistance during liquefaction. Higher stiffness means

higher resistance against liquefaction and vice-versa. However, this only true to the specimen that does not have any history of previous liquefaction. The current study aims to find the relation between the soil's stiffness and their resistance in the multiple liquefactions.

8. Investigation on the effect of induced anisotropy in the multiple-liquefaction test

   Several studies had concluded that the effects of induced anisotropy play significant role in determining the soil behaviors in the 2 stages of liquefaction tests. Most of these studies were conducted using triaxial apparatus. As a result, the numbers of liquefaction stage that can be performed were limited mostly up to two stages. The current study is attempted to investigate the effects of induced anisotropy on the multiple-liquefaction tests using stacked-ring shear apparatus.

1.3   Organization of the thesis

Chapter 1	**<u>INTRODUCTION</u>** This chapter contains background of this study, literature reviews, objectives, and the organization of thesis itself.
Chapter 2	**<u>TEST MATERIALS, APPARATUS, AND TESTING PROCEDURES</u>** This chapter contains several parts, which are: - Test material - The detail of the stacked-ring shear apparatus - Testing procedures to conduct multiple-liquefaction test using stacked-ring shear apparatus - Testing procedures to conduct image analysis
Chapter 3	**<u>FORMULATION OF STRESSES AND STRAINS</u>** This chapter contains several formulations of : - Void ratio - Stresses and strains in the stacked ring shear apparatus - Evaluation of friction in the vertical and circumferential directions - Correction method in the image analysis results - Formulation to evaluate local shear strain
Chapter 4	**<u>THE DEVELOPMENTS OF THE STACKED-RING SHEAR APPARATUS</u>** This chapter explains the detail of the stacked-ring shear apparatus and its

	development
	- The friction measurement in the stacked-ring shear apparatus
	- Effects of different specimen's height
	- Effects of coating
Chapter 5	<u>**THE EFFECTS OF SHEAR STRAIN AMPLITUDES ON THE BEHAVIOR OF MULTIPLE-LIQUEFIED SAND**</u> This chapter presented the test results on the impact of different shear strain amplitudes on the behaviors of multiple-liquefied soil in 31, 11 non-coated stacked rings shear, and 11 coated stacked-ring shear

Chapter 6	<u>**THE EFFECTS OF INDUCED ANISOTROPY ON THE BEHAVIORS OF MULTIPLE-LIQUEFIED SAND**</u>
	
	This chapter explains the effects of the induced anisotropy in the behavior of multiple-liquefied soil by two means, which are:
	
	1. Soil stiffness measurement using static measurement on the previous results of multiple-liquefaction tests
	2. Stress-dilatancy relations on the liquefied soil with several loading combinations:
	    - Different loading directions: clockwise or anti-clockwise
	    - With and without residual strain

Chapter 7	<u>**BEHAVIORS OF MULTIPLE LIQUEFIED SAND BASED ON ENERGY PRINCIPALS**</u> This chapter introduces and describes the characteristics of soil behavior on the typical liquefaction test, two stages of liquefaction tests, and multiple-liquefaction tests based on energy concept
Chapter 8	<u>**CONCLUSIONS**</u> This chapter summarizes all the findings and observations in the current study as well as recommendations for the future studies.

1.4   References

1. AnhDan, L., Koseki, J. and Sato, T. (2002). "Comparison of Young's moduli of dense sand and gravel measured by dynamic and static methods", *Geotechnical Testing Journal*, ASTM, Vol. 25, No. 4, pp. 349-368.

2. Balakrishnayer, K. (2000). "Modelling of deformation characteristics of gravel subjected to large cyclic loading", *Ph.D. thesis*, Department of civil engineering, The University of Tokyo, Japan.

3. Berril, J. B. and Davis, R. O. (1985) "Energy dissipation and seismic liquefaction of sands: revised model." *Soils and Foundations*, 25(2), pp. 106-118.

4. Bieganuosky, W. A. and Marcuson, W. F. (1976) "Liquefaction potential of dams and foundations-Report 1: Laboratory Standard Pene4tration tests on Reid Bedford Model and Ottawa Sand." Report S-76-2, Water ways experimental station.

5. Bishop, A. W., Green, G. E., Garga, V. K., Andersen, A., and Browns J. D. (1971) "A new ring shear apparatus and its application to the measurement of residual strength," *Geotechnique*, 21, 4, pp. 273-328.

6. Bromhead, E. N. (1979) "A simple ring shear apparatus," *Ground Eng.*, Vol. 12, No. 5, pp. 40-44.

7. Burland, J. B. (1989). "Small is beautiful- the stiffness of soil at small strains", Ninth Laurits Bjerrum memorial lecture, *Canadian Geotechnical Journal*, Vol. 26, pp. 499-516.

8. Chaudhary, S. K., Kuwano, J. and Hayano, Y. (2004). "Measurement of Quasi-elastic Stiffness Parameters of Dense Toyoura Sand in Hollow Cylinder Apparatus and Triaxial Apparatus with Bender Elements", *Geotechnical Testing Journal*, ASTM, Vol. 27, No. 1, pp. 23-35.

9. Chiaro, G. (2010) "Deformation properties of sand with initial static shear in undrained cyclic torsional shear tests and their modelling," *Doctor of Engineering Dissertation*, Department of Civil Engineering, The University of Tokyo, Japan.

10. Cubrinovski, M., Henderson, D., and Bradley, B. (2012) "Liquefaction impacts in residenstial area in the 2010-2011 Christchurch Earthquake." *Proc. of Int'l Symp. On Engrg. Lesson Learned from 2011 great East Japan Earthquake.*

11. Cubrinovski, M., Hughes, M., Bradley, B., McCahon, I., McDonald, Y., Simpson, H., Cameron, R., Christison, M., Hendeson, B., Orense, R., and O'Rourke, T. (2011) "Liquefaction impacts on pipe networks." *Recovery Project No. 6, Natural Hazards Research Platform*, University of Canterbury, pp. 149.

12. Cubrinovski, M. and Taylor, M. (2011) "Liquefaction map of Christchurch based on Drive-through reconnaissance after 22 February 2011 Earthquake." University of Canterbury.

13. Cubrinovski, M. and Hughes, M. (2011) "Liquefaction map of Christchurch based on Drive-through reconnaissance after 13 June 2011 Earthquake." University of Canterbury.

14. Cuccovillo, T. and Coop, M. R. (1997). "The measurement of local axial strain in triaxial tests using LVDT's", *Geotechnique*, Vol. 47, No. 1, pp. 167-171.

15. Davis, R. O. and Berril, J. B. (1982) "Energy dissipation and seismic liquefaction of sands." *Earthq. Engrg. Struct. Dyn.*, 10, pp. 59-68.

16. De Silva, L. I. N. (2008). "Deformation characteristics of sand subjected to cyclic drained and undrained torsional loadings and their modelling", *Doctor of Engineering Dissertation*, Department of civil engineering, The University of Tokyo, Japan.

17. De Silva, L. I. N., Koseki, J., Sato, T. and Wang, L. (2005). "High capacity hollow cylinder apparatus with local strain measurements", *Proc. of the Second Japan-U.S. Workshop on Testing, Modeling and Simulation*, Geotechnical Special Publication, ASCE, Vol. 156, pp. 16-28.

18. Desrues, J., Lanier, J., and Stutz, P. (1985) "Localization of the deformation in tests on sand sample." *Engrg. Fracture Mech.*, 21(4), pp. 909-921.

19. Douglas, B. J., Olsen, R. S. Richard, S., and Martin, G. R. (1981) "Evaluation on cone penetration tests for SPT liquefaction assessment." *In Situ Testing to Evaluate Liquefaction Susceptibility, ASCE.*

20. Dyvik, R. and Madshus, S. (1985). "Laboratory measurement of G_{max} using bender elements", *Proceedings of ASCE convention*, Detroit, pp. 186-196.

21. Figueroa, J. L. (1990) "A method for evaluating soil liquefaction by energy principles." *Proc. 4th Nat'l. Conf. on Earthquake Engrg.*, Earthquake Engineering Research Institute.

22. Figueroa, J. L. and Dahisaria, M. N. (1991) "An energy approach in defining soil liquefaction." *Proc. 2nd Int'l. Conf. on Recent Advances in Geotech. Earthquake Engrg. and Soil Dyn.*, University of Missouri, Mo.

23. Figueroa, J. L., Saada, A. S., Liang, L., and Dahisaria, N. M. (1994) "Evaluation of soil liquefaction by energy principles." *J. of Geotech. Engrg.*, ASCE, 120(9), pp. 1554-1569.

24. Finn, W. D. L., Bransby, P. L., and Pickering, D. J. (1970) "Effects of strain history on liquefaction of sand." *J. Soil Mech. and Found. Div.,* ASCE, 96(6), pp. 1917-1934.

25. Finn, W. D. L. and Vaid, Y. P. (1977): "Liquefaction potential from drained constant volume cyclic simple shear test." *Proc. Of the 6th World Conference on Earthquake Engineering, New Delhi, India.*

26. Garga, V. K. and Sendano, J. I. (2002) "Steady state strength of sands in constant volume ring shear apparatus," *Geotech Testing Journal*, 25(4), pp. 414-421.

27. Goto, S., Tatsuoka, F., Shibuya, S., Kim, Y. S. and Sato, T. (1991). "A simple gauge for local small strain measurements in the laboratory", *Soils and Foundations*, Vol. 31, No. 1, pp. 169-180.

28. Han, C. and Vardoulakis, I. G. (1991) "Plane strain compression experiments on water-saturated fine-grained sand." *Geotechnique*, 41(1), pp. 49-78.

29. Harris, W. W., Viggiani, G., Mooney, M. A., and Finno, R. J. (1995) "Use of stereophotogrammetry to analyze the development of shear bands in sand." *Geotech. Testing J.*, 18(4), pp. 405-420.

30. Hird, C. C. and Yung, P.C.Y. (1989): The use of proximity transducers for local strain measurements in triaxial tests, *Geotechnical Testing journal*, 12(4), 292-296.

31. Hong Nam, N. and Koseki, J. (2005). "Quasi-elastic Deformation Properties of Toyoura Sand in Cyclic Triaxial and Torsional Loadings", *Soils and Foundations*, Vol. 45, No. 5, pp. 19-38.

32. Hungr, O. and Morgenstern, N. R. (1984) "High velocity ring shear tests on sand," Vol. 34, No. 3, pp. 415-421.

33. Hvorslev, M. J. (1939) "Torsion shear tests and their place in the determination of shearing resistance of soils," *Proc. of the American Society of Testing and Materials*, 39, pp. 999 – 1022.

34. Ishihara, K. and Okada, S. (1978) "Effects of stress history on cyclic behavior of sand." *Soils and Foundations*, Tokyo, 18(4), pp. 31-35.

35. Ishihara, K. and Okada, S. (1982) "Effects of large preshearing on cyclic behavior of sand." *Soils and Foundations*, Tokyo, 22(3), pp. 109-125.

36. Ishihara, K. and Yoshimine, M. (1992) "Evaluation of settlements in sand deposits following liquefaction during earthquakes." *Soils and Foundations*, 32(1), pp. 172-188.

37. Iverson, N. R., Hooyer, T. S., and Baker R. W. (1998) "Ring shear studies of till deformation: Coulomb-plastic behavior and distributed strain in glacier beds," *Journal of Glaciology*, 22, pp. 167 – 175.

38. Kiyota, T. (2007) "Liquefaction strength and small strain properties of in-situ frozen and reconstituted sandy soils," *Doctor of Engineering Dissertation*, Department of Civil Engineering, The University of Tokyo, Japan.

39. Kokusho, T. (2013) "Applicability of energy-based liquefaction potential evaluation method compared with FL-method." *Proc. Japanese Geotech. Society Conf.* 8(3), pp. 463-475

40. Koseki, J., Miyashita, Y., Deng, J., and Araki, H. (2012) "Liquefaction along Tone River basin in Japan caused by the 2011 Off the Pacific Coast of Tohoku Earthquake." *Proc. 2nd Intl. Conf. on Performance-based Design in Earthquake Geotechnical Engineering*, Taormina. (in press)

41. Kramer, S. L., Bennet, B. A., and Wang, C. H. (2002) "Sand behavior at large strain in ring simple shear," US-Japan Seminar on Seismic Disaster Mitigationin Urban Area by Geotechnical engineering, pp. 291 – 303.

42. Kuribayashi, E. and Tatsuoka, F. (1975) "Brief review of soil liquefaction during earthquakes in Japan." *Soils and Foundations*, 15(4), pp. 81-92.

43. La Gatta, D. P. (1970) "Residual strength of clay and clay-shales by rotation of shear stress," Harvard Soil Mechanics Series, Cambridge, Massachussets, 86.

44. Maqbool, S. (2005). "Effects of compaction on strength and deformation properties of gravel in triaxial and plain strain compression tests", *PhD thesis*, Dept. of Civil Engineering, The University of Tokyo, Japan.

45. Mokni, M. (1992) "Relations entre deformations en masse et deformations localisees dans les materiaux granulaires." *PhD Thesis*, Universite J. Fourier de Grenoble, France.

46. Nagase, H. and Ishihara, K. (1988) "Liquefaction-induced compaction and settlement of sand during earthquakes." *Soils and Foundations*, 28(1), pp. 65-76.

47. Nemat-Nasser, S. and Shookoh, A. (1979) "A unified approach to densification and liquefaction of cohesionless sand in cyclic shearing." *Can. Geotech. J.*, 16, pp. 659-678.

48. Niemunis, A. (2003) "Extended hypoplastic models for soils" *Institute of Found. Engrg. and Soil Mech.*, Ruhr-university Bochum, Issue No. 34.

49. Oda, M. (1972a) "Initial fabrics and their relations to mechanical properties of granular material." *Soils and Foundations*, Tokyo, 12(1), pp. 17-36.

50. Oda, M. (1972b) "A mechanism of fabric changes during compressional deformation of sand." *Soils and Foundations*, Tokyo, 12(2), pp. 1-18.

51. Oda, M., Kawamoto, K., Suzuki, K, Fujimori, H., and Sato, M. (2001) "Microstructural interpretation on reliquefaction of saturated granular soils under cyclic loading." *J. Geotech. and Geoenvironmental Engrg*, 127(5), pp. 416-423.

52. Papathanssiou, G., Pavides, S., Christras, B., Pitilakis, K. (2005) "Liquefaction case histories and empirical relations of earthquake magnitude versus distance from the broader Aegean Region." *J. of Geodynamics*, 40, pp. 257-278.

53. Pradhan, T.B.S., and Tatsuoka, F (1989). "On stress-dilatancy equations of sand subjected to cyclic loading", *Soils and Foundations*, Vol.29, No.1, pp.65-81.

54. Pradhan, T.B.S., and Tatsuoka, F. and Sato, Y. (1989). "Experimental stress-dilatancy relations of sand subjected to cyclic loading", *Soils and Foundations*, Vol.29, No.1, pp.45-64.

55. Roscoe, K. H. (1970): "The influence of strains in the soil mechanics," *Geotechnique*, 20(2), pp.129-170.

56. Rowe, P. W. (1969). "The relation between the shear strength of sands in triaxial compression, plane strain and direct shear", *Geotechnique*, Vol. 19, No. 1, pp. 75-86.

57. Rowe, P. W. Barden, L. and Lee, I.K. (1964). "Energy components during the triaxial tests and direct shear tests", *Geotechnique*, Vol. 14, No. 3, pp. 247-261.

58. Rowe, P.W. (1962). "The stress-dilatancy relation for static equilibrium of an assembly of particles in contact", *Proceedings of the Royal Society of London*, series A, Vol.269, pp. 500-527.

59. Sadrekarimi, A. and Olsen, S. M. (2007) "Development of an improved ring shear device to measure liquefied shear strength of sandy soils," *4th Int'l Conf. on Earthquake Geotech. Engrg. 1330.*

60. Sassa, K. (1984) "The mechanism starting liquefied landslides and debris flows," Proc. of 4th Int'l Symp. On Landslides, Toronto, 2, pp. 349-354.

61. Sassa, K., Fukuoka, H., Wang, G., and Ishikawa, N. (2004) "Undrained dynamic loading ring shear apparatus and its application to landslides dynamics,"

62. Scarpelli, G. and Wood, D. M. (1982) "Experimental observations of shear band patterns in direct shear tests." *Proc., IUTAM Conf. on Deformation and Failure of Granular Materials*, Balkema, Rotterdam, Netherland, pp. 473-484.

63. Schultheiss, P. J. (1981). "Simultaneous measurement of P and S wave velocities during conventional soil testing procedures", *Marine Geotechnology*, Vol. 4, No. 4, pp. 343-367.

64. Seed, H. B., Chan, C. K., and Mori, K. (1977) "Influence of seismic history of liquefactions of sands," *J. Geotech. Engrg. Div., ASCE*, 103(4), pp. 257 – 270.

65. Seed, R. B., Lee, S. R., and Jong, H. L. (1988) "Penetration and liquefaction resistance:

66. Seed, H. B., Idriss, I. M., and Arango, I. (1983) "Evaluation of liquefaction potential using field performance data." *J. of Geotech. Engrg.,* 114(6), pp. 691-697.

67. Shahnazari, H. (2001). "Experimental investigation on volume change and shear deformation characteristics of sand undergoing cyclic loading", *Ph.D. Thesis*, Department of civil engineering, The University of Tokyo, Japan.

68. Suwal, L. P. (2013) "Disk transducer for elastic wave measurement and its application to unsaturated sandy soils." *PhD thesis*, Dept. of Civil Engineering, The University of Tokyo, Japan.

69. Suzuki, T. and Suzuki, T. (1988) "Effects of density and fabric change on re-liquefaction resistance of saturated sand." *J. Japanese Geotech. Soc.*, Tokyo, 28(2), pp. 187 - 195. (in Japanese)

70. Suzuki, T. and Toki, S. (1984) "Effect of preshearing on liquefaction characteristics of saturated sand subjected to cyclic loading." *Soils and Foundations*, Tokyo 24(2), pp. 16-28.

71. Tatsuoka, F., Ishihara, M., Uchimura, T. and Gomes Correia, A. (1999). "Non-linear resilient behavior of unbound granular materials predicted by the cross-anisotropic hypo-quasi-elasticity model", *Unbound Granular Materials*, Gomes Correia (ed.), Balkema, pp. 197-204.

72. Tatsuoka, F., Iwasaki, T., Tokida, K., Yasuda, S., Hirose, M., Imai, M., and Kon-no, M. (1980) "Standard penetration tests and soil liquefaction potential evaluation." *Soils and Foundations*, 20(4).

73. Tatsuoka, F. and Silver, M. L. (1981) "Undrained stress-strains behavior of sand under irregular loading," *Soils and Foundations*, 21(1), pp. 51-66.

74. Tika, T. E., Vaughan, P. R., and Lemos, L. J. (1996) "Fast shearing of pre-existing shear zones in soil," *Geotechnique*, 46(2), pp. 197 – 233.

75. Tokimatsu, K. and Seed, H. B. (1987) "Evaluation of settlements in sands due to earthquake shaking," *J. of Geotech. Engrg.*, 113(8), pp. 861-878.

76. Tokimatsu, K. and Yoshimi, H. (1981) "Field correlation of soil liquefaction with SPT and grain size." *Proc. of the Int'l. Conf. on Recent Advances in Geotech. Eartquake Engrg and Soil Dynamics*.

77. Tokue, T. (1978). "A consideration about Rowe's minimum energy ratio principal and a new concept of shear mechanism", *Soils and Foundations*, Vol.18, No.1, pp.1-10.

78. Towhata, I. and Ishihara, K. (1985) "Undrained strength of sand undergoing cyclic rotation of principal stress axes." *Soils and Foundations*, 25(2), pp. 135-147.

79. Viggiani, G. and Atkinson, J. (1995) "Interpretation of bender element tests." *Geotechnique*, 45(1), pp. 149-154.

80. Wahyudi, S., Miyashita, Y. and Koseki, J. (2012) "Shear band behavior of sand in torsional shear tests by means of image analysis." *Proc. ISSMGE Conf. of Advances in Multiphisical Tesing of Soils and Shale*s, Lausanne, Switzerland.

81. Wicaksono, R. I., Tsutsumi, Y., Sato, T., Koseki, J. and Kuwano, R. (2007). "Small strain stiffness of clean sand and gravel based on dynamic and static measurements", *Proc. Of the 9th International Summer Symposium*, Yokohama, Japan.

82. Wakamatsu, K. (2011) "Maps of historic liquefaction sites in Japan, 745 – 2008." *University of Tokyo Press* (In Japanese with English manual).

83. Wakamatsu, K. (2012) "Recurrence of liquefaction at the same site induced by 2011 Great East Japan Earthquake Compared with Previous Earthquakes." *Proc. of 15th Int'l World Conf. of Earthquake. Engrg.*

84. Wichtmann, T., Niemunis, A., Triantafyllidis, T., and Poblete, M. (2005) "Correlation of cyclic preloading with liquefaction resistance." *J. of Soil Dyn. And Earthquake Engrg.*

85. Yamada, S., Kiyota, T., and Hosono, Y. (2011) "3rd big earthquake in Christchurch, New Zealand." *ISSMGE Bulletin*, 5(3), pp. 25-29.

86. Yamada, S., Takamori, T., and Sato, K. (2010) "Effects on reliquefaction resistance produced by changes in isotropy during liquefaction." *Soils and Foundations*, 50(1), pp. 19-25.

87. Yasuda, S. and Tohno, I (1988) "Sites of reliquefaction caused by the 1983 Nihonkai-Chubu earthquake." *Soils and Foundations*, Tokyo, 28(2), 1-34, 61-72.

88. Yoshida, T., Tatsuoka, F., Siddique, M. S. A., Kamegai, Y. and Park, C. S. (1994) "Shear banding in sands observed in plane strain compression," *Proc. Symp. On Localization and Bifurcation Theory for Soils and Rocks*, R. cambou, J. Desrues, and I. Vardoulakis, eds., Balkema, Rotterdam, The Netherlands, pp. 165-179.

89. Yoshida, T. and Tatsuoka, F. (1997) "Deformation property of shear band subjected to the plane strain compression and its relation to particle characteristics." *Proc. of 14th Intl. Conf. on Soil Mech. and Found. Engrg.*, 1, pp. 237-240.

90. Youd, T. L. and Hoose, S. N. (1978) "Historic ground failure in Northern California triggered by earthquakes." *U.S. Geol. Surv. Profess*. Pap. 993.

91. Youd, T. L. and Weiczorek (1982) "Liquefaction and ground failure, in the Imperial Valley, California, Earthquake of October 15, 1979." *U.S. Geol. Surv. Profess. Pap. 1254*, pp. 223-246.

2 TEST MATERIAL, APPARATUS, AND PROCEDURES

2.1 Introduction

In Chapter 1, it has been discussed the comparison (advantages and disadvantages) among different types of soil testing apparatuses (e.g. triaxial, torsional shear apparatus, and ring shear apparatus and etc). Each of these apparatuses is used based on different test purposes, preferred boundary conditions among others. However, none of these apparatuses are capable to simulate multiple liquefactions phenomenon. Therefore, in the current study, the stacked-ring shear apparatus was used to investigate soil behaviors during multiple liquefactions.

The details of the apparatus, material, and testing procedures to conduct multiple-liquefaction tests in the current study, will be discussed as follows.

2.2 Stacked-ring shear apparatus

2.2.1 Characteristics of stacked rings

The stacked-ring shear apparatus has been developed since June 2011 in the Institute of Industrial Science (IIS), The University of Tokyo. The full picture of the stacked-ring shear apparatus is shown in Fig. 2.1, while technical details are presented through Fig. 2.2 to Fig. 2.8. Originally, the height of the stacked-ring was 155 mm, which consists of a series of 31 vertically stacked donut-shape metal rings (Fig. 2.9). Nevertheless, during the development process of this apparatus, the height of the specimen was varied in order to find the optimum test setting and to reduce the excessive friction generated between the soil particles and the stacked-ring itself (for more detail refer to Chapter 4). Throughout the laboratory activity, four types of specimen height were tested: 155mm (31 stacked rings), 55mm (11 stacked rings), 40mm (8 stacked rings), and 25mm (5 stacked rings). Note that, the original size of inner and outer diameters (90mm and 150mm, respectively) of the specimen was kept unchanged.

Eventually, it was found later that the optimum height of the stacked ring shear was 55mm (11 stacked rings), which is the setting currently in use. Yet, the improvement of the stacked-ring shear continued by coating the 11 stacked-rings shear with a frictionless material so called Diamond-Like-Coating (DLC) as shown in Fig. 2.10. The DLC material has the frictional coefficient of about 0.15 - 0.20, while the original stainless steel material has the frictional coefficient of about 0.6 - 0.8.

The details of these developments of the stacked-ring shear apparatus will be discussed again later.

2.2.2 Assembling procedure

Each ring in the stacked-ring shear apparatus is made from hardened stainless-steel and has a thickness of 5mm (Fig. 2.11). It is placed within the steel frame/guider which is composed of two flat donut-shape metal rings on the base and on the top of the frame, six metal cylinder guider columns for the outer rings, and four guider columns for inner rings (Fig. 2.1). The assembling sequence of the stacked-ring is briefly described hereafter:

1. The six guider columns are screwed on the bottom metal frame for outer rings, as well as the four guider columns are installed on the bottom frame for inner rings (Fig. 2.1).

2. A bearing (Fig. 2.12) is inserted on each of the inner and outer guider columns. Importantly, these bearings are used as frictionless rollers enabling the inner and outer rings to move freely in the circumferential direction.

3. A 0.1 mm thick donut-shape spacer (Fig. 2.12) is inserted on each guider column on the top of the bearings. The 0.1 mm thickness of the spacer is large enough to avoid any contact between neighborhood rings, but small enough to prevent the extrusion of the Toyoura sand particles ($D_{50} \approx 0.16$ mm). However, due to this 0.1 mm gap in between the stacked rings, materials such as clay, silt, among others cannot be tested.

4. Next, donut-shape inner and outer rings (Fig. 2.11) are placed on the top of the spacers.

5. The procedure described at points 1-3 is repeated until reaching the desired specimen height.

6. Lastly, the plate cap is placed on top of the stacked-ring and tightened with bolts to lock the position of each stacked rings.

2.2.3 Vertical and torsional loading systems

In the original version of the stacked-ring shear apparatus, a single bi-component of load cell was installed at the top of the specimen as shown schematically in Fig. 2.4. Its axial and torque capacities are 15 kN and 3 kN.m, respectively. Later, a second bi-component load cell was installed at the bottom of the specimen (Fig. 2.5) during the development of the stacked-ring shear apparatus. The bottom load cell has identical capacity as the top load cell.

The top load cell is able to move freely along with the loading shaft, while the bottom load cell is fixed to the pedestal and has similar axial and torque capacities as the top load cell. The bottom load cell was installed with the aim to measure the stress level at the bottom of the specimen, which due to friction effect, is different from that applied from the top. The difference in the measured stresses were used later to calculate the amount of friction generated in axial and circumferential directions between the stacked-ring and the soil particles.

In the stacked-ring shear apparatus, a pneumatic system consisting of a pair of bellofram cylinders (Fig. 2.3) with the dimension of 20 cm in diameter and 5 cm in height is used to apply the axial loading. Basically, a bellofram cylinder is divided into two chambers, namely the lower and the upper chambers. The force applied to the specimen depends on the pressure difference inside the two chambers. Larger positive pressure applied into the upper chamber means that loading shaft will move in downward direction, thus a positive axial loading will be applied to the specimen. Alternatively, larger positive pressure applied into the bottom chamber means loading shaft will move in upward direction, thus negative axial loading will be applied to the specimen. The pressures in both chambers are controlled by electro-pneumatic transducers (E/P) with the capacity of 1000 kPa (1.0 MPa), which are connected to a computer via D/A converter.

On the other hand, the torsional loading is applied by using a Direct-Drive Motor system (DD System), which is mainly composed by two parts, one fixed and other rotating. In each fixed and rotating part of the motor, 3,600,000 pieces of magnet coils are placed. The rotation of the motor comes from alternating currents that generate strong magnetism forces between the coils in the fixed and rotating part of the motor. The motor is controlled by the servo motor (manufactured by Nippon Denso Co.), which is connected to a computer via 12 bit D/A converter. The minimum and maximum speeds produced by this system are 0.015 deg./min and 64.8 deg./min, respectively. Unlike the gear systems commonly used in the hollow cylinder torsional shear apparatus (De Silva, 2008 and Chiaro, 2010), the DD System is capable of producing limitless rotation in both clockwise and anti-clockwise directions. Therefore, the simulation of the soil specimen response undergoing extremely large shear deformation can be done.

2.2.4 Measurement of stresses, axial and shear strains

In total, the developed stacked-ring shear apparatus employs a system of 12 channels to measure stresses and strains components. Two pairs of channels are used for the axial load

and torque measurements obtained by both top and bottom load cells, respectively. Two channels are used for the external displacement transducers (EDT-1 and EDT-2). Two channels are dedicated to the potentiometers, one for the wire-type potentiometer (POT-1), and the other one for the roller-type potentiometer (POT-2). Finally, four channels are reserved to the proximity transducers/gap sensors (GS-1, GS-2, GS-3, and GS-4).

The features of each measuring device are described below:

Load cell - the two bi-component load cells have a negligible coupling effect (i.e. no effect of axial load on torque load measurement and vise-versa). They have an identical load capacity of 15 kN for the axial loading and 3 kN.m for the torsional loading.

EDT - the External Differential Transducer measures the axial strain deformation of the specimen. The two EDTs are installed outside the cell on the opposite direction to one another. The maximum displacement capacity of employed EDT is 20 mm. Note that, since the specimen lateral deformation is constrained in this apparatus, the EDT is also used for measuring specimen volume change.

Potentiometers - Two types of potentiometer are used: the wire-type potentiometer and roller-type potentiometer. The wire-type potentiometer can measure very large deformation of the specimen up to 1000% shear strain, while the roller-type potentiometer aims to measure smaller deformation with the capacity up to 20% shear strain. The wire-type potentiometer has less accuracy than the roller-type potentiometer. It was found that the error of the wire-type potentiometer is about 0.5% while the error of the roller-type potentiometer is about 0.01%. Nevertheless, considering the maximum shear strain applied in this study of about 10%, only the roller-type potentiometer is used in the current setting of the testing apparatus.

Gap sensors - Four gap sensors with the range of measurement about 4 mm are located inside the chamber. A pair of gap sensors was installed around the top cap to measure the rotation of top cap, while another pair of gap sensors was installed to measure the vertical movement of the top cap. All the gap sensors were manufactured by Showa Electronic Company.

2.3 Test Material, specimen preparation, and installation of sensors

2.3.1 Test material

In this study, Toyoura sand from "Batch-J" was used as testing material. It has a mean diameter (D_{50}) of 0.200 mm, specific gravity (G_s) of 2.635, maximum void ratio (e_{max}) of 0.992, minimum void ratio (e_{min}) of 0.632 and fines content less than 75μm (F_c) of 0.1%. Its particles have angular/sub-angular shape. Typical particle size distribution curve obtained for Toyoura sand from batch-J is shown in Fig. 2.13.

Similarly to the experiments conducted by Chiaro (2010), specimens were prepared by the air-dried pluviation method. To minimize the degree of inherent anisotropy in the radial direction of the hollow cylindrical sand specimens, the sample preparation was carried out carefully by pouring the sand particle into the mold (i.e. between inner and outer stacked rings) while moving the nozzle of pluviator radially and circumferentially at the same time in alternative directions, i.e. first clockwise and then anticlockwise directions (De Silva et al., 2006). In addition to obtain specimens with highly uniform density, the falling height was kept constant throughout the pouring process. Note that, the pouring height was changed from 20 cm to 200 cm to prepare specimens with initial dry density (Dr_{ini}) varying from 40.0% and 90.0%. More details regarding the specimen preparation are descried henceforward.

2.3.2 Specimen preparation

Unlike triaxial and hollow cylinder torsional shear apparatus, the stacked-ring shear apparatus does not required mould during the specimen preparation. The inner and outer stacked-ring itself serve as mould. About 1.5 kg of dry Toyoura sand is needed to prepare a 155 mm (31 pieces of stacked rings) height specimen with an initial relative density of about 50–53%. For the other types of specimen, the weight of sand required to make a specimen of 55 mm (11 rings), 40 mm (8 rings), and 25 mm (5 rings) are 1.0 kg, 0.8 kg, and 0.6 kg, respectively. The sequence of sand specimen preparation using the stacked-ring shear apparatus is briefly described hereafter:

1. Before pluviating the sand, a plastic bag is attached to the stacked-ring shear frame, with the aim of collecting the sand particles that do not fall in the space between the inner and outer rings during the pluviation process. To pour the sand, a pluviator having a nozzle at

the bottom end is used. The opening of the nozzle should be about 20 times of the mean diameter of the particles (i.e. for Toyoura sand about 3.2 mm). A thin rope is attached at the bottom end of the pluviator to define the falling height of the sand particles during pluviation (the higher the falling height is, the denser the specimen is). In this study, the range of the falling height varied between 20 cm to 200 cm corresponding to an initial relative density of the specimen of 40% to 90%.

2. To pluviate the sand, first, the sand particles are poured in clockwise or anti-clockwise circumferential direction. After completing one loop (360 degrees), the pouring direction is reversed. While pouring the sand particles into circumferential direction, the pluviator is also moved in the radial direction in a zig-zag pattern (Fig. 2.14). During this process, the falling height of the pluviation is kept somehow constant in order to obtain specimen with highly uniform density.

3. Finally, when the pouring process ends, the sand particles in excess on top of the specimen are removed and the top surface of the specimen is carefully flattened.

2.3.3 Pre-loading procedures

Using the new testing apparatus, liquefaction tests were mostly simulated using dry sand specimens. This is due to the technical nature of the stacked-ring shear itself. In fact, due to the 0.1 mm gap existing between the rings, water cannot be retained and thus excess pore water pressure could not be generated. However, the liquefaction behavior of sand evaluated on dry specimens is expected to be similarly to that evaluated on fully water-saturated specimens (Bjerrum and Landva, 1966; Finn and Vaid, 1977; among others). This assumption is based on the fact that in fully water-saturated specimens, water does not have shear resistance, so that reduction of effective stress is essentially caused by the generation of excess pore water pressure induced by the contraction of soil particles. By using dry specimens, the reduction of effective stress (vertical stress in case of stacked-ring shear apparatus) is caused by the densification (rotation and packing) of sand particles during contraction, which reduces the contact forces between the specimen and the fixed top cap. Bjerrum and Landva (1966) conducted liquefaction test in direct simple shear test (DSS) by using dry and fully saturated sand and observed similar behaviors between the two conditions. Later, their findings were confirmed again by Finn and Vaid (1977) in both direct simple shear test and triaxial test.

After the specimen is ready, a test in stacked-ring shear (SRS) apparatus is conducted following the procedures as described below:

1. The controlling and sampling software called Digit Show Basic is open. The software is written in C++ language program and customized for the SRS apparatus.

2. Input the calibration factors of each measuring device are uploaded from a file.

3. Next the top cap is connected to the specimen. Before attaching the top cap, the axial load and torque reading from both load cells need to be adjusted to 0 value. Then, the loading shaft is lowered by reducing the amount of positive pressure in the lower chamber of cell bellofram cylinders (not to be confused with apparatus bellofram cylinders) until it slightly touches the upper surface of the specimen. At the time when the loading shaft touches the surface of the specimen, the amplifier would show an increase in their voltage values. An axial stress of about 3-5 kPa needs to be applied at this stage to make the specimen stable during entire preparation.

4. Since most of the tests were conducted in dry condition, the acrylic glass of the cell chamber does not need to be placed.

5. Next the stacked-ring shear cell is aligned to the center line below the motor shaft and finally locked using two metal clips at the bottom plate of the cell.

6. The motor shaft is carefully lowered by reducing the amount of positive pressure on the lower chamber of the machine bellofram cylinder (not to be confused with the cell bellofram cylinder) and carefully attached to the cell loading shaft and then secured

7. Two EDTs to measure the vertical deformation of the cell's loading shaft are attached to the two small guider column located outside the cell. The EDTs are installed in the upward position to have a contact with a circular plate attached to the loading shaft as shown in Fig. 2.15. To measure the upward and downward movements of the loading shaft, the EDTs are set at certain initial strain.

8. The roller-type potentiometer is then attached to the loading shaft for the tests to be conducted under medium range strain deformation ($\gamma_{DA} < 20\%$). Yet, in the case of the specimen tested up to large strain deformation $\gamma_{DA} > 20\%$, both roller-type and wire-type potentiometers were used and attached at the loading shaft.

9. Two gap sensors (GS-1 and GS-2), measuring the rotation of the top cap, are positioned in perpendicular direction to the vertical flat metal plates attached at the top cap inside the cell as shown in Fig. 2.16.

10. In addition, another two gap sensors (GS-3 and GS-4) measuring the vertical displacement of the top cap is positioned in perpendicular direction to the horizontally-flat metal plates attached at the top cap inside the cell (Fig. 2.17).

2.4   Timeline of the stacked-ring shear apparatus development

The stacked-ring shear apparatus arrived and was assembled in the Institute of Industrial Science, The University of Tokyo since June 2011. Since then, various changes and modifications have been made to improve the workability of the stacked-ring shear itself. These are timeline on the development of the stacked-ring shear apparatus.

- June 2011 – The assembly of the stacked-ring shear apparatus started. In its original version, the height of the stacked rings was 155 cm (31 metal rings). The apparatus had only one bi-component load cell located at the top cap. One EDT was used to measure the axial strain, while two potentiometers (i.e. the roller-type and wire-type potentiometers) were used to measure the shear strain.

- September 2011 – First calibration of the apparatus devices (bi–component load cell, EDT, roller-type and wire-type potentiometers) was completed. A series of monotonic constant stress tests was conducted to verify the workability of the new apparatus and the soil behaviors in the stacked-ring shear apparatus. Then, a series of single stage constant volume cyclic shear tests were conducted to simulate liquefaction phenomenon.

- Early 2012 – Multiple-liquefaction tests were performed using the 31 stacked-ring type.

- May 2013 – An additional load cell was installed at the bottom pedestal to measure the reduction of axial stress applied to the specimen due to friction between soil particles and the metal rings.

- June 2013 – The height of the stacked rings was reduced using 11 rings type (55 mm height), 8 rings type (40 mm height), and 5 rings type (25 mm height). The reduction on the number of rings was necessary to reduce the loss of axial stress due to excessive friction.

- July 2013 – Another attempt was done to further reduce the excessive friction by coating the contact surface of the stacked rings using Diamond-Like Coating (DLC). Along with the coating of the rings, the outer surface of each ring was punched to create 18 small holes for conducting image analysis during the test. Each hole was evenly distributed every 30° (33.3 mm) along the circumferential direction.

- October 2013 – Among several types of stacked rings that had been tested, the 11 stacked rings type was finally chosen as the optimum setting of the apparatus and it is still currently used (Fig. 2.18).

- February 2014 – Two gap sensors were installed to measure small rotation of the specimen and consequently to evaluate the sand shear modulus (G) during multiple-liquefaction tests. Moreover, two additional gap sensors (GS-3 and GS-4) were installed to measure more accurately the vertical displacement of the specimen and thus to evaluate the stress-dilatancy characteristics of soil during multiple liquefactions.

2.5   Experiment program

2.5.1 Constant normal stress test (Cyclic and monotonic shear loading)

Before conducting multiple-liquefaction tests, a series of constant stress tests were conducted in order to evaluate the workability of the newly developed stacked-ring shear apparatus. The procedures to conduct these two different types of test are similar, except for the application of loading.

To conduct constant stress tests on stacked-ring shear apparatus, first, the specimen is consolidated one dimensionally up to a predetermined vertical stress of 200 kPa ($\sigma_{v.Top}$= 200 kPa). Note that the vertical stress on the stacked-ring shear apparatus was controlled solely based on the measurement of top load cell. The consolidation rate applied in these tests was 5 kPa/min. After reaching the target value of vertical stress, the consolidation process continued for additional 20 minutes or more until the change in volume was nearly zero ($d\varepsilon_{vol}/dt=0$). After consolidation, each specimen was subjected to a monotonic shear loading under constant vertical stress. Each specimen was sheared up to 100 – 1000% shear strain deformation. Finally, the results were compared to the monotonic drained constant stress test on hollow cylinder torsional shear apparatus conducted by Chiaro (2010).

The monotonic constant stress tests conducted in this study are listed in Table 2.1, while the stress path employed is also described in the this table.

2.5.2 Single stage liquefaction test

In the stacked-ring shear apparatus, the liquefaction phenomenon is simulated by subjecting the soil to cyclic shear loading under constant volume condition. The testing procedures are similar to those of the tests conducted under constant stress condition up to consolidation process. After one-dimensionally consolidating the specimen up to 200 kPa of vertical stress

($\sigma_{v.Top}$= 200 kPa), the position of the loading shaft needs to be locked by using two pairs of nuts located just below the bellofram cylinder. It is important to note that the value of the vertical stress can easily change due to any movement of the loading shaft. Therefore, it is very important to maintain the initial vertical stress constant by adjusting the tightness of the loading shaft nuts.

The amplitude of cyclic shear stress applied to the specimen is varied depending on the number of the stacked rings or the height of the specimen. Using the 31 stacked-rings, cyclic shear stress of ±10 kPa was applied for loose sand specimens, while cyclic shear stress of ±20 kPa was applied for dense sand specimens. Alternatively, using the 11 stacked-rings, cyclic shear stress of ±20 kPa was applied for loose sand specimens and cyclic shear stress of ±25 kPa was applied for dense sand specimens. This was done due to the different amount of generated frictions on different types of apparatus. The higher the specimen is, the larger the friction generated in the stacked-ring shear apparatus is. Therefore, the cyclic stress amplitude on each type of stacked-ring was chosen in order to obtain about 10 − 15 cycles of cyclic shear loading in a single stage liquefaction test.

Beside multiple-liquefaction tests, single stage liquefaction test was also conducted to evaluate soil liquefaction behavior under different density states. Then, the results of this test are going to be compared with the results of multiple-liquefaction tests, where soil density is likely to change in each subsequent liquefaction stage.

The list of single-liquefaction tests conducted in this study as well as their stress path is given in Table 2.3, 2.6, and 2.11.

2.5.3 Multiple-liquefaction test

In the multiple-liquefaction test, each specimen is sheared with different maximum shear strain double amplitudes. The procedures used to perform multiple-liquefaction test is illustrated in Fig. 2.19. First, prior to the application of cyclic shear loading, each specimen was one-dimensionally consolidated up to a vertical stress of 200 kPa ($\sigma_{v.Top}$=200 kPa) as schematically shown by state B. Then, the specimen was subjected to the cyclic shear stress under constant volume condition (i.e. no change in void ratio). The cyclic shear stress amplitudes employed were similar to those applied in the single stage liquefaction tests.

In this study, the onset of full liquefaction was defined as the state when the double amplitude of shear strain reached 2% (N$\gamma_{DA(2\%)}$), while the cyclic loading continued to achieve the pre-fixed $\gamma_{DA.Max}$ value (state C). A stage of liquefaction was completed by adding

another quarter-cycle of cyclic shear loading from state C to state C', with the intention of having shear strain (γ) equal to zero (Fig. 2.19c and Fig. 2.19d) at the end of each liquefaction. States C' and D in this study were set as the ending and the starting states of each stage during re-liquefaction test, respectively. The reason to end each liquefaction stage at the zero shear strain (γ= 0%) was to prevent an additional effect of soil anisotropy induced by residual deformation in post liquefaction, which will be discussed in detail in Chapter 6. The next liquefaction stage is started by re-consolidating the liquefied specimen to their original effective vertical stress ($\sigma_{v.top}$') of 200 kPa at state D. This procedure was adopted also for the subsequent liquefaction stages.

The list of multiple-liquefaction tests conducted in this study as well as their stress path is described in Table 2.2, 2.4, 2.5, 2.8, and 2.12.

2.5.4 Use of image analysis in multiple-liquefaction tests

As mentioned earlier, the current study employed image analysis to observe the local deformation behaviors of soil as compare to their global ones during multiple liquefactions.

In conducting image analysis, a digital camera is employed to capture the movement of the outer rings by using the configuration shown in Fig. 2.20. The digital camera should be able at least to take 1 picture/sec. The camera is set aligned with the center height of the specimen. Then, the camera is remotely connected to the relay switch box, which is connected to the computer via D/A board converter. The relay box consists of a resistor, transistor and the relay switch itself. The computer controlled the shutter of the camera by sending electric current to the relay box with 0 or 5 volts. The 5 volt means the camera will open the shutter and take the picture, while 0 volt means the camera will close the shutter.

The focus, aperture, ISO, white balance and shutter speed of the camera were set manually in each test depending on the testing condition. The meanings of each of these parameters are:

- Aperture – it controls the depth of the field of image taken by camera;
- ISO – it is the level of sensitivity of the camera towards available light;
- Shutter speed – it is the length of time that camera shutter open.
- White balance – it controls the setting of natural lighting mode of the present situation such as daylight, tungsten, fluorescent among others

In most of the tests, the camera was set to take a picture at the increment of 0.2% of shear strain. The deformation of the each part of the specimen was obtained by analyzing the movements of the colored dots (target) marked in the outer surface of the outer rings. It is

assumed that the circumferential deformation of the specimen is equal to the rotation of the rings. Each ring is marked by 18 dots and the distance between the neighboring dots is 33.3 mm or 30° in circumferential direction. To improve the accuracy of the measurement through image analysis process, the dots were marked with a color that well contrast with the color of their surroundings as shown in Fig. 2.21a and Fig. 2.21b.

To obtain the deformation of the specimen, a series of image taken during the test were analyzed using the commercially-available Tr-2D image analysis software. The software works by identifying a moving object that has contrast color as compare to their surroundings in the image. The sequence of the objects tracking by this software can be described as follows:

1. Before the tracking process takes place, the tracking objects and the distance between the objects need to be calibrated. It is important to note that the calibration of the image is conducted on the image before any deformation takes place. Then, the distance of the object is calibrated by their corresponding number of pixels (i.e. in the image analysis, the number of pixels represent the distance between any objects).

2. A single fix point needs to be assigned as a base reference, so that all the deformations in vertical and horizontal directions of moving objects will be calculated with respect to this reference.

3. Next process is the deformation tracking. As mentioned earlier, the software tracks the movements of the objects by identifying their color contrast compared to their surroundings. The stronger the contrast between colors, the better the tracking results. Tr-2D software provides three modes for distinguishing the moving target from its surrounding, which are RGB, mono-chrome (black and white), and HSV. The mono-chrome is the simplest mode among all and it is recommended to use if there are only two different colors contrasting in the image (bright and dark). The RGB (Red-Green-Blue) is recommended to use if there is more than two colors in the image. The RGB type can be used in various combinations of colors in one image. Since the images in the current studies mostly contain bright and dark colors, the monochrome mode is used during tracking process. Prior to the tracking process, the contrast between the darker and lighter areas in the image needs to be adjusted, so that the software can recognize the target objects from their surroundings.

The Tr-2D software can only track the movement of an object in a two-dimensional space (horizontal and vertical axes). However, it is known that the deformation of the specimen in the stacked-ring shear apparatus happens in a three-dimensional space (horizontal, vertical and depth directions) as schematically shown in Fig. 2.22. Therefore, the results obtained

from the image analysis software contain some degree of distortion. The distortion of the image naturally appears because the camera works by transforming the three-dimensional object into two-dimensional image as illustrated in Fig. 2.23. In the imaging research field, this kind of distortion is called barrel distortion. To solve this problem, a mathematical formulation is needed to transform the distorted/apparent coordinates into their real ones. The transformation of the coordinates will be discussed in detail in Chapter 3.

2.6   Calibration of transducers

The calibration results of each transducer are provided through Fig. 2.24 to Fig. 2.35.

2.7   References

1. Bjerrum, L. and Landva, A. (1966): "Direct simple shear tests on a Norwegian quick clay." *Geotechnique*, 16(1), pp. 1-20.

2. Chiaro, G. (2010) "Deformation properties of sand with initial static shear in undrained cyclic torsional shear tests and their modeling," *Doctor of Engineering Dissertation*, Department of Civil Engineering, The University of Tokyo, Japan.

3. De Silva, L. I. N. (2008). "Deformation characteristics of sand subjected to cyclic drained and undrained torsional loadings and their modeling", *Doctor of Engineering Dissertation*, Department of civil engineering, The University of Tokyo, Japan.

4. Finn, W. D. L. and Vaid, Y. P. (1977): "Liquefaction potential from drained constant volume cyclic simple shear test." *Proc. Of the 6th World Conference on Earthquake Engineering, New Delhi, India.*

5. De Silva, L. I. N., Sato, T., and Koseki, J. (2006) "Variations of shear strain along height and perimeter of hollow cylinder specimen during cyclic torsional shear loadings." Proc. of 8th Int'l. Symp. JSCE, Nagoya, Japan, pp. 143-146.

Table 2.1: Monotonic constant stress test (σ_v= 200 kPa) on 31 non-coated stacked-ring type

Test	Specimen condition	Specimen height (mm)	Number of rings	Ring type	$D_{r.ini}$ (%)
MCS1	Dry	155	31 rings	Non-coated	52.3
MCS2	Dry	155	31 rings	Non-coated	75.2
MCS3	Dry	155	31 rings	Non-coated	85.0

Table 2.2: Multiple liquefaction tests of loose sand using 31 non-coated stacked-ring type ($CSR_{(Top)}$= 0.05)

Test	Shear strain amplitude (%)	Specimen condition	Specimen height (mm)	Number of rings	Ring type	$D_{r.ini}$ (%)
ML1	2	Dry	155	31 rings	Non-coated	55.5
ML2	4	Dry	155	31 rings	Non-coated	52.9
ML3	7	Dry	155	31 rings	Non-coated	55.6
ML4	10	Dry	155	31 rings	Non-coated	53.5

Table 2.3: Single liquefaction test using 31 non- coated stacked-ring shear type ($CSR_{(Top)}$= 0.05)

Test	Specimen condition	Specimen height (mm)	Number of rings	Ring type	$D_{r.ini}$ (%)
SL1	Dry	155	31 rings	Non-coated	55.3
SL2	Dry	155	31 rings	Non-coated	49.9
SL3	Dry	155	31 rings	Non-coated	40.7
SL4	Dry	155	31 rings	Non-coated	38.9
SL5	Dry	155	31 rings	Non-coated	70.0
SL6	Dry	155	31 rings	Non-coated	60.6
SL7	Dry	155	31 rings	Non-coated	75.2
SL8	Dry	155	31 rings	Non-coated	83.8
SL9	Dry	155	31 rings	Non-coated	69.9
SL10	Dry	155	31 rings	Non-coated	64.6
SL11	Dry	155	31 rings	Non-coated	63.8
SL12	Dry	155	31 rings	Non-coated	55.5
SL13	Dry	155	31 rings	Non-coated	55.7
SL14	Dry	155	31 rings	Non-coated	58.9
SL15	Dry	155	31 rings	Non-coated	68.3
SL16	Dry	155	31 rings	Non-coated	59.1
SL17	Dry	155	31 rings	Non-coated	59.1
SL18	Dry	155	31 rings	Non-coated	64.9
SL19	Dry	155	31 rings	Non-coated	60.8

SL20	Dry	155	31 rings	Non-coated	69.9
SL21	Dry	155	31 rings	Non-coated	73.0
SL22	Dry	155	31 rings	Non-coated	75.4
SL23	Dry	155	31 rings	Non-coated	80.5
SL24	Dry	155	31 rings	Non-coated	83.4
SL25	Dry	155	31 rings	Non-coated	88.8
SL26	Dry	155	31 rings	Non-coated	55.2
SL27	Dry	155	31 rings	Non-coated	51.3
SL28	Dry	155	31 rings	Non-coated	41.4
SL29	Dry	155	31 rings	Non-coated	46.5
SL30	Dry	155	31 rings	Non-coated	86.5

Table 2.4: Multiple liquefaction tests of loose sand using 31 non-coated stacked-ring type (CSR$_{(Top)}$= 0.05) with residual strain

Test	Shear strain amplitude (%)	Specimen condition	Specimen height (mm)	Number of rings	Ring type	$D_{r.ini}$ (%)
MLRes1	2	Dry	155	31 rings	Non-coated	54.3
MLRes2	4	Dry	155	31 rings	Non-coated	52.5

Table 2.5: Multiple-liquefaction test of dense sand using 31 non-coated stacked-ring type (CSR$_{(Top)}$= 0.10)

Test	Shear strain amplitude (%)	Specimen condition	Specimen height (mm)	Number of rings	Ring type	$D_{r.ini}$ (%)
ML5	2	Dry	155	31 rings	Non-coated	78.3
ML6	4	Dry	155	31 rings	Non-coated	80.0
ML7	5	Dry	155	31 rings	Non-coated	80.0
ML8	5	Dry	155	31 rings	Non-coated	80.3
ML9	10	Dry	155	31 rings	Non-coated	78.9

Table 2.6: Single liquefaction tests using 31 non-coated stacked-rings (CSR$_{(Top)}$= 0.10)

Test	Specimen condition	Specimen height (mm)	Number of rings	Ring type	$D_{r.ini}$ (%)
SL31	Dry	155	31 rings	Non-coated	52.8
SL32	Dry	155	31 rings	Non-coated	56.5
SL33	Dry	155	31 rings	Non-coated	62.8
SL34	Dry	155	31 rings	Non-coated	67.4
SL35	Dry	155	31 rings	Non-coated	73.2
SL36	Dry	155	31 rings	Non-coated	80.0
SL37	Dry	155	31 rings	Non-coated	85.9
SL38	Dry	155	31 rings	Non-coated	88.9
SL39	Dry	155	31 rings	Non-coated	94.0

Table 2.7: Multiple-liquefaction tests of saturated loose sand using 31 non-coated stacked-ring type (CSR$_{(Top)}$=0.10)

Test	Shear strain amplitude (%)	Specimen condition	Specimen height (mm)	Number of rings	Ring type	D$_{r.ini}$ (%)
MLSat1	10	Saturated	155	31 rings	Non-coated	80.2

Table 2.8: Monotonic constant stress test of using 31 non-coated stacked-ring type with top and bottom load cells (CSR$_{(Top)}$=0.10)

Test	Specimen condition	Specimen height (mm)	Number of rings	Ring type	D$_{r.ini}$ (%)
MCS4	Dry	155	31 rings	Non-coated	55.1

Table 2.9: Cyclic constant stress test of using 31 non-coated stacked-ring type with top and bottom load cells (CSR$_{(Top)}$=0.10)

Test	Shear strain amplitude (%)	Specimen condition	Specimen height (mm)	Number of rings	Ring type	D$_{r.ini}$ (%)
SL40	5	Dry	155	31 rings	Non-coated	54.9

Table 2.10: Multiple-liquefaction tests of loose sand using 11 non-coated stacked-ring type (CSR$_{(Top)}$= 0.10)

Test	Shear strain amplitude (%)	Specimen condition	Specimen height (mm)	Number of rings	Ring type	D$_{r.ini}$ (%)
ML10	2	Dry	55	11 rings	Non-coated	52.9
ML11	5	Dry	55	11 rings	Non-coated	51.1
ML12	10	Dry	55	11 rings	Non-coated	53.8

Table 2.11: Single liquefaction tests of loose sand using 11 non-coated stacked-ring type (CSR$_{(Top)}$= 0.10)

Test	Specimen condition	Specimen height (mm)	Number of rings	Ring type	D$_{r.ini}$ (%)
SL41	Dry	55	11 rings	Non-coated	43.9
SL42	Dry	55	11 rings	Non-coated	54.0
SL43	Dry	55	11 rings	Non-coated	83.1
SL44	Dry	55	11 rings	Non-coated	90.4
SL45	Dry	55	11 rings	Non-coated	59.2
SL46	Dry	55	11 rings	Non-coated	70.7

Table 2.12: Constant stress tests for checking the coating material

Test	Specimen condition	Specimen height (mm)	Number of rings	Ring type	D$_{r.ini}$ (%)
CP1	Dry	55	11 rings	Non-coated	79.7
CP2	Dry	55	11 rings	Non-coated	82.2
CP3	Dry	55	11 rings	Non-coated	85.9
CP4	Dry	55	11 rings	Non-coated	80.8
CP5	Dry	55	11 rings	Non-coated	80.7
CP6	Dry	55	11 rings	Non-coated	81.6
CP7	Dry	55	11 rings	Non-coated	81.4
CP8	Dry	55	11 rings	Non-coated	81.7
CP9	Dry	55	11 rings	Non-coated	83.6

Table 2.13: Multiple-liquefaction tests in the 5 and 8 stacked rings shear

Test	Shear stress amplitude (kPa)	Specimen condition	Specimen height (mm)	Number of rings	Ring type	D$_{r.ini}$ (%)
MLRing5	30	Dry	25	5 rings	Coated	49.1
MLRing8	40	Dry	40	8 rings	Coated	59.2

Table 2.14: Multiple-liquefaction tests of loose sand using 11 coated stacked-ring type (CSR$_{(Top)}$= 0.125)

Test	Shear stress amplitude (kPa)	Specimen condition	Specimen height (mm)	Number of rings	Ring type	D$_{r.ini}$ (%)
ML13	0.2	Dry	55	11 rings	Coated	53.1
ML14	0.25	Dry	55	11 rings	Coated	53.0
ML15	0.3	Dry	55	11 rings	Coated	51.9
ML16	0.4	Dry	55	11 rings	Coated	52.0
ML17	0.5	Dry	55	11 rings	Coated	53.6
ML18	1	Dry	55	11 rings	Coated	53.2
ML19	2	Dry	55	11 rings	Coated	51.9
ML20	5	Dry	55	11 rings	Coated	51.2
ML21	7	Dry	55	11 rings	Coated	50.4
ML22	10	Dry	55	11 rings	Coated	49.1

Table 2.15: Two stages liquefaction tests of loose sand using 11 non-coated stacked-ring type (CSR$_{(Top)}$= 0.125)

Test	Shear strain amplitude (%)	Specimen condition	Specimen height (mm)	Number of rings	Ring type	D$_{r.ini}$ (%)
RL1	10	Dry	55	11 rings	Coated	64.6
RL2	10	Dry	55	11 rings	Coated	70.9
RL3	10	Dry	55	11 rings	Coated	58.3

Table 2.16: Stress-dilatancy investigations on multiple-liquefied soil (CSR$_{(Top)}$= 0.125)

Test	Specimen condition	Specimen height (mm)	Number of rings	Ring type	D$_{r.ini}$ (%)
SDRL1	Dry	55	11 rings	Coated	51.6
SDRL2	Dry	55	11 rings	Coated	51.7
SDRL3	Dry	55	11 rings	Coated	50.0
SDRL4	Dry	55	11 rings	Coated	51.8
SDRL5	Dry	55	11 rings	Coated	50.5
SDRL6	Dry	55	11 rings	Coated	51.2
SDRL7	Dry	55	11 rings	Coated	52.3
SDRL8	Dry	55	11 rings	Coated	51.1

Table 2.17: Stress-dilatancy investigations on constant stress test (CSR$_{(Top)}$= 0.125)

Test	Strain amplitude (%)	Specimen condition	Specimen height (mm)	Number of rings	Ring type	$D_{r.ini}$ (%)
SDCS1	2.5	Dry	55	11 rings	Coated	56.0

Table 2.18: Liquefaction resistance with pre-loading (CSR$_{(Top)}$= 0.125)

Test	Specimen condition	Specimen height (mm)	Number of rings	Ring type	$D_{r.ini}$ (%)
SLPre1	Dry	55	11 rings	Coated	51.5
SLPre2	Dry	55	11 rings	Coated	52.7
SLPre3	Dry	55	11 rings	Coated	52.7
SLPre4	Dry	55	11 rings	Coated	53.8

Abbreviations:

MCS: Monotonic Constant Stress test.

ML: Multiple-Liquefaction test.

SL: Single Liquefaction test.

SLPre: Single Liquefaction test with Pre-loading.

RL: Repeated liquefaction (2 stages of liquefaction).

MLRes: Multiple-Liquefaction test with Residual Strain.

MLSat: Multiple-Liquefaction on Saturated Sand test.

CP: Test for Coating Prototypes.

MLRing: Multiple-liquefaction test with 5 and 8 stacked rings

SDRL: Stress-Dilatancy on Repeated-Liquefaction test (2 stages of liquefaction).

SDCS: Stress-Dilatancy on Constant Stress test.

Table 2.19: Stress paths in MCS1 to MCS3, and MCS4
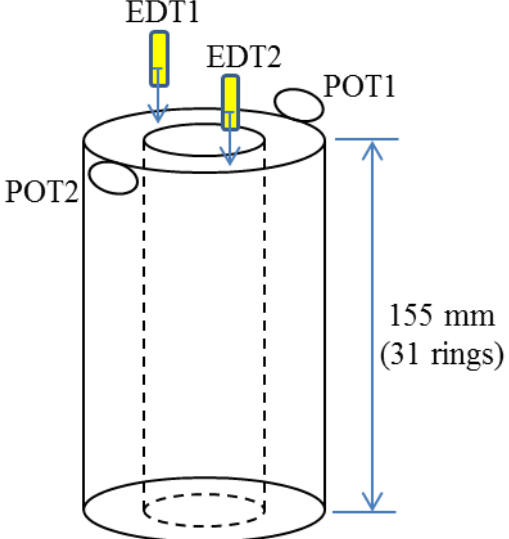
Step	Stress path	Deformation measurement transducers
1	1. Consolidation ($\sigma_{v.Top}$= 5 → 200 kPa) for 45 minutes. 2. Monotonic torsional shear loading under constant stress condition of $\sigma_{v.Top}$= 200 kPa.	 POT1: Wire type potentiometer. POT2: Roller type potentiometer. EDT1: 1st External Displacement Transducer. EDT2: 2nd External Displacement Transducer.
	note: • Bottom axial stress, circumferential and radial stresses ($\sigma_{v.bot}$, σ_θ and σ_r) were unknown, since no sensors were installed in the current setting. Thus, σ_1 and σ_2 were also unknown. • All the specimens were tested under dry condition.	

Table 2.20: Stress paths in ML1 to ML4

Step	Stress path	Deformation measurement transducers
1	1. Consolidation ($\sigma_{v.Top}$= 5 → 200 kPa) for 45 minutes. 2. Cyclic torsional shear loading ($10 \leq \tau_{cy.} \leq 10$ kPa) under constant volume condition up to its pre-determined maximum shear strain double amplitude of 2.0%, 4.0%, 7.0%, and 10.0%. 3. The loading was stopped by adding another quarter cycle of cyclic shear loading to the origin (γ= 0%).	

2 to n^{th}	4. Re-consolidation of vertical stress up to 200 kPa ($\sigma_{v.Top}$= 200 kPa) for 45 minutes. 5. Repeating previous step 2 and 3 on the 1st stage.	 POT2: Roller type potentiometer. EDT1: 1st External Displacement Transducer. EDT2: 2nd External Displacement Transducer.
	note: • Bottom axial stress, circumferential and radial stresses ($\sigma_{v.bot}$, σ_θ and σ_r) were unknown, since no sensors were installed in the current setting. Thus, σ_1 and σ_2 were also unknown. • Process no. 4 and 5 were repeating until the specimen liquefied for the nth times. • All the specimens were tested under dry condition.	

Table 2.21: Stress paths in SL1 to SL30

Step	Stress path	Deformation measurement transducers
1	1. Consolidation ($\sigma_{v.Top}$= 5 → 200 kPa) for 45 minutes. 2. Cyclic torsional shear loading ($10 \leq \tau_{cy.} \leq 10$ kPa) under constant volume condition.	*Similar configuration as those with previous tests.
	note: • Bottom axial stress, circumferential and radial stresses ($\sigma_{v.bot}$, σ_θ and σ_r) were unknown, since no sensors were installed in the current setting. Thus, σ_1 and σ_2 were also unknown. • Process no. 5, 6, 7, and 8 were repeating until the specimen liquefied for the nth times. • All the specimens were tested under dry condition.	

Table 2.22: Stress paths in MLRes1 to MLRes2

Step	Stress path	Deformation measurement transducers
1	1. Consolidation ($\sigma_{v.Top}$= 5 → 200 kPa) for 45 minutes. 2. Cyclic torsional shear loading ($10 \leq \tau_{cy.} \leq 10$ kPa) under constant volume condition up to its pre-determined maximum shear strain double amplitudes of 2.0%, 4.0%, respectively. 3. The loading was stopped by adding another quarter cycle of cyclic shear loading to the origin (γ= 0%).	*Similar configuration as those with previous tests.
2 to n^{th}	4. Re-consolidation of vertical stress up to 200 kPa ($\sigma_{v.Top}$= 200 kPa) for 45 minutes. 5. Repeating previous step 2 and 3 on the 1st stage.	
	note: • Bottom axial stress, circumferential and radial stresses ($\sigma_{v.bot}$, σ_θ and σ_r) were unknown, since no sensors were installed in the current setting. Thus, σ_1 and σ_2 were also unknown. • Step no. 4 and 5 were repeating until the specimen liquefied for the nth times. • All the specimens were tested under dry condition.	

Table 2.23: Stress paths in ML5 to ML9

Step	Stress path	Deformation measurement transducers
1	6. Consolidation ($\sigma_{v.Top}$= 5 → 200 kPa) for 45 minutes. 7. Cyclic torsional shear loading ($20 \leq \tau_{cy.} \leq 20$ kPa) under constant volume condition up to its pre-determined maximum shear strain double amplitudes of 2.0%, 4.0%, 5.0%, 5.0%, and 10.0%, respectively. 8. The loading was stopped by adding another quarter cycle of cyclic shear loading to the origin (γ= 0%).	*Similar configuration as those with previous tests.
2 to n^{th}	9. Re-consolidation of vertical stress up to 200 kPa ($\sigma_{v.Top}$= 200 kPa) for 45 minutes. 10. Repeating previous step 2 and 3 on the 1st stage.	

	note:
	• Bottom axial stress, circumferential and radial stresses ($\sigma_{v.bot}$, σ_θ and σ_r) were unknown, since no sensors were installed in the current setting. Thus, σ_1 and σ_2 were also unknown. • Step no. 4 and 5 were repeating until the specimen liquefied for the nth times. • All the specimens were tested under dry condition.

Table 2.24: Stress paths in SL31 to SL39, and SL40

Step	Stress path	Deformation measurement transducers
1	**1.** Consolidation ($\sigma_{v.Top}= 5 \to 200$ kPa). **2.** Cyclic torsional shear loading ($20 \leq \tau_{cy.} \leq 20$ kPa) under constant stress condition of $\sigma_{v.Top}= 200$ kPa.	*Similar configuration as those with previous tests.
	note: • Bottom axial stress, circumferential and radial stresses ($\sigma_{v.bot}$, σ_θ and σ_r) were unknown, since no sensors were installed in the current setting. Thus, σ_1 and σ_2 were also unknown. • Process no. 5, 6, 7, and 8 were repeating until the specimen liquefied for the nth times. • All the specimens were tested under dry condition.	

Table 2.25: Stress paths in MLsat1

Step	Stress path	Deformation measurement transducers
1	**1.** Consolidation ($\sigma_{v.Top}= 5 \to 200$ kPa) for 45 minutes. **2.** Cyclic torsional shear loading ($20 \leq \tau_{cy.} \leq 20$ kPa) under constant volume condition up to its pre-determined maximum shear strain double amplitude of 5.0%. **3.** The loading was stopped by adding another quarter cycle of cyclic shear loading to the origin ($\gamma= 0\%$).	*Similar configuration as those with previous tests.
2 to n^{th}	**4.** Re-consolidation of vertical stress up to 200 kPa ($\sigma_{v.Top}= 200$ kPa) for 45 minutes. **5.** Repeating previous step 2 and 3 on the 1st stage.	
	note: • Bottom axial stress, circumferential and radial stresses ($\sigma_{v.bot}$, σ_θ and σ_r) were unknown, since no sensors were installed in the current setting. Thus, σ_1 and σ_2 were also unknown. • Process no. 4 and 5 were repeating until the specimen liquefied for the nth times. • The specimen was tested under water saturated condition.	

Table 2.26: Stress paths in ML10 to ML12
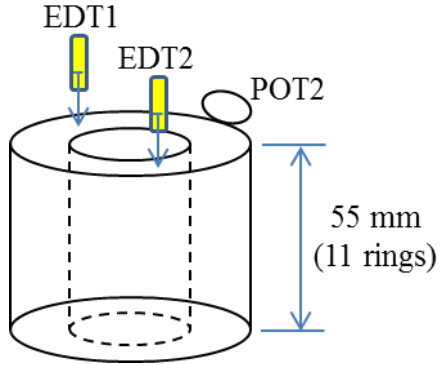
Step	Stress path	Deformation measurement transducers
1	1. Consolidation ($\sigma_{v.Top}$= 5 → 200 kPa) for 45 minutes. 2. Cyclic torsional shear loading (20 ≤ $\tau_{cy.}$ ≤ 20 kPa) under constant volume condition up to its pre-determined maximum shear strain double amplitudes of 2.0%, 5.0%, and 10.0%. 3. The loading was stopped by adding another quarter cycle of cyclic shear loading to the origin (γ= 0%).	
2 to n^{th}	4. Re-consolidation of vertical stress up to 200 kPa ($\sigma_{v.Top}$= 200 kPa) for 45 minutes. 5. Repeating previous step 2 and 3 on the 1st stage.	POT2: Roller type potentiometer. EDT1: 1st External Displacement Transducer. EDT2: 2nd External Displacement Transducer.
	note: • Circumferential and radial (σ_θ and σ_r) were unknown, since no sensors were installed in the current setting. Thus, σ_1 and σ_2 were also unknown. • Axial stress at the bottom of the specimen ($\sigma_{v.bot}$) was measured by bottom load cell. • Process no. 2 and 3 were repeating until the specimen liquefied for the nth times. • All the specimens were tested under dry condition.		

Table 2.27: Stress paths in SL41 to SL46

Step	Stress path	Deformation measurement transducers
1	1. Consolidation ($\sigma_{v.Top}$= 5 → 200 kPa) for 45 minutes. 2. Cyclic torsional shear loading (20 ≤ $\tau_{cy.}$ ≤ 20 kPa) under constant volume condition.	*Similar configuration as those with previous tests.
	note: • Circumferential and radial (σ_θ and σ_r) were unknown, since no sensors were installed in the current setting. Thus, σ_1 and σ_2 were also unknown. • Axial stress at the bottom of the specimen ($\sigma_{v.bot}$) was measured by bottom load cell. • All the specimens were tested under dry condition.		

Table 2.28: Stress paths in CP1 test

Step	Stress path	Deformation measurement transducers
1	1. Consolidation ($\sigma_{v.Top}$= 5 → 100 kPa) for 45 minutes. 2. Cyclic axial loading ($10 \leq \sigma_{v.Top} \leq$ 100 kPa) for 10 cycles.	*Similar configuration as those with previous tests.
	note: • Circumferential and redial stresses (σ_θ and σ_r) were unknown, since no sensors were installed in the current setting. Thus, σ_1 and σ_2 were also unknown. • Axial stress at the bottom of the specimen ($\sigma_{v.bot}$) was measured by bottom load cell. • The specimen was tested under dry condition.	

Table 2.29: Stress paths in CP2 test

Step	Stress path	Deformation measurement transducers
1	1. Consolidation ($\sigma_{v.Top}$= 5 → 150 kPa) for 45 minutes. 2. Cyclic axial loading ($20 \leq \sigma_{v.Top} \leq$ 150 kPa) for 10 cycles.	*Similar configuration as those with previous tests.
	note: • Circumferential and redial stresses (σ_θ and σ_r) were unknown, since no sensors were installed in the current setting. Thus, σ_1 and σ_2 were also unknown. • Axial stress at the bottom of the specimen ($\sigma_{v.bot}$) was measured by bottom load cell. • The specimen was tested under dry condition.	

Table 2.30: Stress paths in CP3 test

Step	Stress path	Deformation measurement transducers
1	1. Consolidation ($\sigma_{v.Top}$= 5 → 200 kPa) for 45 minutes. 2. Cyclic axial loading ($20 \leq \sigma_{v.Top} \leq$ 200 kPa) for 10 cycles.	*Similar configuration as those with previous tests.
	note: • Circumferential and redial stresses (σ_θ and σ_r) were unknown, since no sensors were installed in the current setting. Thus, σ_1 and σ_2 were also unknown. • Axial stress at the bottom of the specimen ($\sigma_{v.bot}$) was measured by bottom load cell. • The specimen was tested under dry condition.	

Table 2.31: Stress paths in CP4 test

Step	Stress path	Deformation measurement transducers
1	1. Consolidation ($\sigma_{v.Top}$= 5 → 200 kPa) for 45 minutes. 2. Monotonic torsional shear loading up to 90 kPa. (τ= 0 → 90kPa).	*Similar configuration as those with previous tests.
	note: • Circumferential and redial stresses (σ_θ and σ_r) were unknown, since no sensors were installed in the current setting. Thus, σ_1 and σ_2 were also unknown. • Axial stress at the bottom of the specimen ($\sigma_{v.bot}$) was measured by bottom load cell. • The specimen was tested under dry condition.	

Table 2.32: Stress paths in CP5 test

Step	Stress path	Deformation measurement transducers
1	1. Consolidation ($\sigma_{v.Top}$= 5 → 200 kPa) for 45 minutes. 2. Cyclic axial loading ($20 \leq \sigma_{v.Top} \leq 300$ kPa) for 10 cycles.	*Similar configuration as those with previous tests.
	note: • Circumferential and redial stresses (σ_θ and σ_r) were unknown, since no sensors were installed in the current setting. Thus, σ_1 and σ_2 were also unknown. • Axial stress at the bottom of the specimen ($\sigma_{v.bot}$) was measured by bottom load cell. • The specimen was tested under dry condition.	

Table 2.33: Stress paths in CP6 test

Step	Stress path	Deformation measurement transducers
1	1. Consolidation ($\sigma_{v.Top}$= 5 → 200 kPa) for 45 minutes. 2. Monotonic torsional shear loading up to 50% global shear strain deformation (γ= 0 → 50%).	*Similar configuration as those with previous tests.
	note: • Circumferential and redial stresses (σ_θ and σ_r) were unknown, since no sensors were installed in the current setting. Thus, σ_1 and σ_2 were also unknown. • Axial stress at the bottom of the specimen ($\sigma_{v.bot}$) was measured by bottom load cell. • The specimen was tested under dry condition.	

Table 2.34: Stress paths in CP7 test

Step	Stress path	Deformation measurement transducers
1	**1.** Consolidation ($\sigma_{v.Top}$= 5 $\rightarrow$ 300 kPa) for 60 minutes. 2. Monotonic torsional shear loading up to 85% global shear strain deformation (γ= 0 $\rightarrow$ 85%).	*Similar configuration as those with previous tests.
	note: • Circumferential and redial stresses (σ_θ and σ_r) were unknown, since no sensors were installed in the current setting. Thus, σ_1 and σ_2 were also unknown. • Axial stress at the bottom of the specimen ($\sigma_{v.bot}$) was measured by bottom load cell. • The specimen was tested under dry condition.	

Table 2.35: Stress paths in CP8 test

Step	Stress path	Deformation measurement transducers
1	**1.** Consolidation ($\sigma_{v.Top}$= 5 $\rightarrow$ 300 kPa) for 60 minutes. **2.** Cyclic torsional shear loading with -200 $\leq \tau_{cy} \leq$ 200 kPa under constant stress test condition at $\sigma_{v.Top}$= 300 kPa.	*Similar configuration as those with previous tests.
	note: • Circumferential and redial stresses (σ_θ and σ_r) were unknown, since no sensors were installed in the current setting. Thus, σ_1 and σ_2 were also unknown. • Axial stress at the bottom of the specimen ($\sigma_{v.bot}$) was measured by bottom load cell. • The specimen was tested under dry condition.	

Table 2.36: Stress paths in CP9 test

Step	Stress path	Deformation measurement transducers
1	**1.** Consolidation ($\sigma_{v.Top}$= 5 $\rightarrow$ 400 kPa) for 90 minutes. **2.** Cyclic torsional shear loading with -250 $\leq \tau_{cy} \leq$ 250 kPa under constant stress test condition at $\sigma_{v.Top}$= 400 kPa.	*Similar configuration as those with previous tests.
	note: • Circumferential and redial stresses (σ_θ and σ_r) were unknown, since no sensors were installed in the current setting. Thus, σ_1 and σ_2 were also unknown. • Axial stress at the bottom of the specimen ($\sigma_{v.bot}$) was measured by bottom load cell. • The specimen was tested under dry condition.	

Table 2.37: Stress paths in MLring1

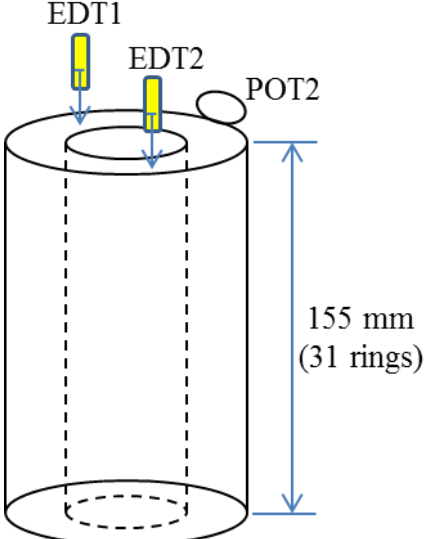| Step	Stress path	Deformation measurement transducers
1	1. Consolidation ($\sigma_{v.Top}$= 5 → 200 kPa) for 45 minutes. 2. Cyclic torsional shear loading ($40 \leq \tau_{cy.} \leq 40$ kPa) under constant volume condition up to its pre-determined maximum shear strain double amplitude of 10.0%. 3. The loading was stopped by adding another quarter cycle of cyclic shear loading to the origin (γ= 0%).	EDT1 EDT2 POT2 25 mm (5 rings)
2 to n^{th}	4. Re-consolidation of vertical stress up to 200 kPa ($\sigma_{v.Top}$= 200 kPa) for 45 minutes. 5. Repeating previous step 2 and 3 on the 1st stage.	POT2: Roller type potentiometer. EDT1: 1st External Displacement Transducer. EDT2: 2nd External Displacement Transducer.
	note: • Circumferential and radial (σ_θ and σ_r) were unknown, since no sensors were installed in the current setting. Thus, σ_1 and σ_2 were also unknown. • Axial stress at the bottom of the specimen ($\sigma_{v.bot}$) was measured by bottom load cell. • Process no. 4 and 5 were repeating until the specimen liquefied for the nth times. • The specimen was tested under dry condition.	

Table 2.38: Stress paths in MLring2

Step	Stress path	Deformation measurement transducers
1	1. Consolidation ($\sigma_{v.Top}$= 5 → 200 kPa) for 45 minutes. 2. Cyclic torsional shear loading ($30 \leq \tau_{cy.} \leq 30$ kPa) under constant volume condition up to its pre-determined maximum shear strain double amplitude of 10.0%. 3. The loading was stopped by adding another quarter cycle of cyclic shear loading to the origin (γ= 0%).	EDT1 EDT2 POT2 40 mm (8 rings)
2 to n^{th}	4. Re-consolidation of vertical stress up to 200 kPa ($\sigma_{v.Top}$= 200 kPa) for 45 minutes. 5. Repeating previous step 2 and 3 on the 1st stage.	POT2: Roller type potentiometer. EDT1: 1st External Displacement Transducer. EDT2: 2nd External Displacement Transducer.
	note: • Circumferential and radial (σ_θ and σ_r) were unknown, since no sensors were installed in the current setting. Thus, σ_1 and σ_2 were also unknown.	

	• Axial stress at the bottom of the specimen ($\sigma_{v.bot}$) was measured by bottom load cell. • Process no. 4 and 5 were repeating until the specimen liquefied for the nth times. • The specimen was tested under dry condition.

Table 2.39: Stress paths in ML13 to ML19

Step	Stress path	Deformation measurement transducers
1	**1.** Consolidation ($\sigma_{v.Top}= 5 \rightarrow 200$ kPa) for 45 minutes. **2.** Cyclic torsional shear loading ($25 \leq \tau_{cy.} \leq 25$ kPa) under constant volume condition up to its pre-determined maximum shear strain double amplitude of 0.20%, 0.25%, 0.30%, 0.40%, 0.50%, and 1.0%, respectively. **3.** The loading was stopped by adding another quarter cycle of cyclic shear loading to the origin ($\gamma= 0\%$).	
2	**4.** Re-consolidation of vertical stress up to 200 kPa ($\sigma_{v.Top}= 200$ kPa) for 45 minutes. **5.** Cyclic torsional shear loading ($25 \leq \tau_{cy.} \leq 25$ kPa) under constant volume condition up to its pre-determined maximum shear strain double amplitude of 2.0%. **6.** The loading was stopped by adding another quarter cycle of cyclic shear loading to the origin ($\gamma= 0\%$).	*Similar configuration as those with previous tests.
3	**7.** Re-consolidation of vertical stress up to 200 kPa ($\sigma_{v.Top}= 200$ kPa) for 45 minutes. **8.** Cyclic torsional shear loading ($25 \leq \tau_{cy.} \leq 25$ kPa) under constant volume condition.	
	note: • Circumferential and radial (σ_θ and σ_r) were unknown, since no sensors were installed in the current setting. Thus, σ_1 and σ_2 were also unknown. • Axial stress at the bottom of the specimen ($\sigma_{v.bot}$) was measured by bottom load cell. • All the specimens were tested under dry condition.	

Table 2.40: Stress paths in ML19 to ML22

Step	Stress path	Deformation measurement transducers
1	1. Consolidation ($\sigma_{v.Top}$= 5 → 200 kPa) for 45 minutes. 2. Cyclic torsional shear loading (25 ≤ $\tau_{cy.}$ ≤ 25 kPa) under constant volume condition up to its pre-determined maximum shear strain double amplitude of 2.0%, 5.0%, 7.0%, and 10.0%, respectively. 3. The loading was stopped by adding another quarter cycle of cyclic shear loading to the origin (γ= 0%).	
2 to n^{th}	4. Re-consolidation of vertical stress up to 200 kPa ($\sigma_{v.Top}$= 200 kPa) for 45 minutes. 5. Repeating previous step 2 and 3 on the 1st stage.	POT2: Roller type potentiometer. EDT1: 1st External Displacement Transducer. EDT2: 2nd External Displacement Transducer. GS1 and GS2: 1st and 2nd Gap sensors for the horizontal displacement measurement.
	note: • Circumferential and radial (σ_θ and σ_r) were unknown, since no sensors were installed in the current setting. Thus, σ_1 and σ_2 were also unknown. • Axial stress at the bottom of the specimen ($\sigma_{v.bot}$) was measured by bottom load cell. • Process no. 4 and 5 were repeating until the specimen liquefied for the nth times. • All the specimens were tested under dry condition.	

Table 2.41: Stress paths in RL1 to RL3

Step	Stress path	Deformation measurement transducers
1	1. Consolidation ($\sigma_{v.Top}$= 5 → 200 kPa) for 45 minutes. 2. Cyclic torsional shear loading (25 ≤ $\tau_{cy.}$ ≤ 25 kPa) under constant volume condition up to its pre-determined maximum shear strain double amplitude of 10%. 3. The loading was stopped by adding another quarter cycle of cyclic shear loading to the origin (γ= 0%).	*Similar configuration as those with previous tests.
2	5. Re-consolidation of vertical stress up to 200 kPa ($\sigma_{v.Top}$= 200 kPa) for 45 minutes. 6. Cyclic torsional shear loading (25 ≤ $\tau_{cy.}$ ≤ 25 kPa) under constant volume condition.	

note: - Circumferential and radial (σ_θ and σ_r) were unknown, since no sensors were installed in the current setting. Thus, σ_1 and σ_2 were also unknown. - Axial stress at the bottom of the specimen ($\sigma_{v.bot}$) was measured by bottom load cell. - All the specimens were tested under dry condition.		

Table 2.42: Stress paths in SDRL1

Step	Stress path	Deformation measurement transducers
1	1. Consolidation ($\sigma_{v.Top}$= 5 → 200 kPa) for 45 minutes. 2. Cyclic torsional shear loading (25 ≤ $\tau_{cy.}$ ≤ 25 kPa) in the clockwise direction under constant volume condition sheared up to maximum shear strain double amplitude of 5% ($\gamma_{DA.max}$= 5.0%). 3. The loading was stopped by adding another quarter cycle of cyclic shear loading to the origin (γ= 0%).	*Similar configuration as those with previous tests.
2	4. Re-consolidation of vertical stress up to 200 kPa ($\sigma_{v.Top}$= 200 kPa) for 45 minutes. 5. Monotonic torsional shear loading in the anti-clockwise direction under constant volume condition.	
	note: - Circumferential and radial (σ_θ and σ_r) were unknown, since no sensors were installed in the current setting. Thus, σ_1 and σ_2 were also unknown. - Axial stress at the bottom of the specimen ($\sigma_{v.bot}$) was measured by bottom load cell. - All the specimens were tested under dry condition.	

Table 2.43: Stress paths in SDRL2

Step	Stress path	Deformation measurement transducers
1	1. Consolidation ($\sigma_{v.Top}$= 5 → 200 kPa) for 45 minutes. 2. Cyclic torsional shear loading ($25 \leq \tau_{cy.} \leq 25$ kPa) in the clockwise direction under constant volume condition sheared up to maximum shear strain double amplitude of 5% ($\gamma_{DA.max}$= 5.0%). 3. The loading was stopped by adding another quarter cycle of cyclic shear loading to the origin (γ= 0%).	*Similar configuration as those with previous tests.
2	4. Re-consolidation of vertical stress up to 200 kPa ($\sigma_{v.Top}$= 200 kPa) for 45 minutes. 5. Cyclic torsional shear loading in the clockwise direction with global shear strain deformation of ±2.5% ($2.5 \leq \gamma \leq 2.5\%$) under constant stress condition of $\sigma_{v.Top}$= 200 kPa.	
	note: • Circumferential and radial (σ_θ and σ_r) were unknown, since no sensors were installed in the current setting. Thus, σ_1 and σ_2 were also unknown. • Axial stress at the bottom of the specimen ($\sigma_{v.bot}$) was measured by bottom load cell. • All the specimens were tested under dry condition.	

Table 2.44: Stress paths in SDRL3

Step	Stress path	Deformation measurement transducers
1	1. Consolidation ($\sigma_{v.Top}$= 5 → 200 kPa) for 45 minutes. 2. Cyclic torsional shear loading ($25 \leq \tau_{cy.} \leq 25$ kPa) in the clockwise direction under constant volume condition sheared up to maximum shear strain double amplitude of 2% ($\gamma_{DA.max}$= 2.0%). 3. The loading was stopped by adding another quarter cycle of cyclic shear loading to the origin (γ= 0%).	*Similar configuration as those with previous tests.

2	**4.** Re-consolidation ($\sigma_{v.Top}= 5 \rightarrow 200$ kPa) for 45 minutes. **5.** Cyclic torsional shear loading ($25 \leq \tau_{cy.} \leq 25$ kPa) in clockwise direction under constant volume condition sheared up to maximum shear strain double amplitude of 2% ($\gamma_{DA.max}= 2.0\%$). **6.** The loading was stopped by adding another quarter cycle of cyclic shear loading to the origin ($\gamma= 0\%$).	
3	**7.** Re-consolidation of vertical stress up to 200 kPa ($\sigma_{v.Top}= 200$ kPa) for 45 minutes. **8.** Cyclic torsional shear loading in the clockwise direction with global shear strain deformation of $\pm2.5\%$ ($2.5 \leq \gamma \leq 2.5\%$) under constant stress condition of $\sigma_{v.Top}= 200$ kPa.	
	note: • Circumferential and radial (σ_θ and σ_r) were unknown, since no sensors were installed in the current setting. Thus, σ_1 and σ_2 were also unknown. • Axial stress at the bottom of the specimen ($\sigma_{v.bot}$) was measured by bottom load cell. • The specimen was tested under dry condition.	

Table 2.45: Stress paths in SDRL4

Step	Stress path	Deformation measurement transducers
1	**1.** Consolidation ($\sigma_{v.Top}= 5 \rightarrow 200$ kPa) for 45 minutes. **2.** Cyclic torsional shear loading ($25 \leq \tau_{cy.} \leq 25$ kPa) in the clockwise direction under constant volume condition sheared until the last cycle of global shear stain accumulated in the clockwise direction. **3.** The loading was stopped by adding another quarter cycle of cyclic shear loading to the zero shear stress ($\tau= 0$ kPa).	 POT2: Roller type potentiometer.

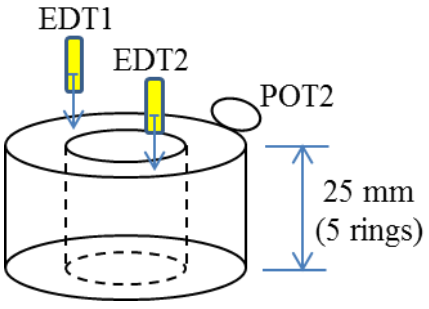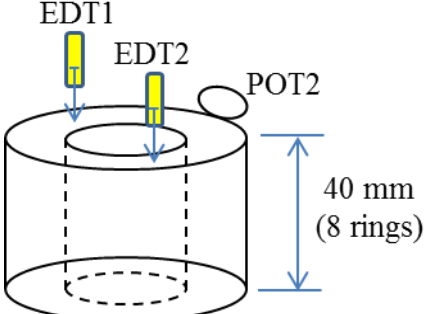|			
2	4. Re-consolidation of vertical stress up to 200 kPa ($\sigma_{v.Top}$= 200 kPa) for 45 minutes. 5. Cyclic torsional shear loading in the <u>anti-clockwise</u> direction with global shear strain deformation of ±2.5% (2.5 ≤ γ ≤ 2.5%) under constant stress condition of $\sigma_{v.Top}$= 200 kPa.	EDT1: 1st External Displacement Transducer. EDT2: 2nd External Displacement Transducer. GS1 and GS2: 1st and 2nd Gap Sensors for horizontal displacement measurement. GS3 and GS4: 1st and 2nd Gap Sensors for vertical displacement measurement.	
	note: • Circumferential and radial (σ_θ and σ_r) were unknown, since no sensors were installed in the current setting. Thus, σ_1 and σ_2 were also unknown. • Axial stress at the bottom of the specimen ($\sigma_{v.bot}$) was measured by bottom load cell. • The specimen was tested under dry condition.		

Table 2.46: Stress paths in SDRL5

Step	Stress path	Deformation measurement transducers
1	1. Consolidation ($\sigma_{v.Top}$= 5 → 200 kPa) for 45 minutes. 2. Cyclic torsional shear loading (25 ≤ $\tau_{cy.}$ ≤ 25 kPa) in the <u>clockwise direction</u> under constant volume condition sheared until the last cycle of global shear stain <u>accumulated in the anti-clockwise direction</u>. 3. The loading was stopped by adding another quarter cycle of cyclic shear loading to the <u>zero shear stress</u> (τ= 0 kPa).	*Similar configuration as those with previous tests.
2	4. Re-consolidation of vertical stress up to 200 kPa ($\sigma_{v.Top}$= 200 kPa) for 45 minutes. 5. Cyclic torsional shear loading in the <u>clockwise</u> direction with global shear strain deformation of ±2.5% (2.5 ≤ γ ≤ 2.5%) under constant stress condition of $\sigma_{v.Top}$= 200 kPa.	
	note: • Circumferential and radial (σ_θ and σ_r) were unknown, since no sensors were installed in the current setting. Thus, σ_1 and σ_2 were also unknown. • Axial stress at the bottom of the specimen ($\sigma_{v.bot}$) was measured by bottom load cell. • The specimen was tested under dry condition.	

Table 2.47: Stress paths in SDRL6

Step	Stress path	Deformation measurement transducers
1	1. Consolidation ($\sigma_{v.Top}$= 5 → 200 kPa) for 45 minutes. 2. Cyclic torsional shear loading (25 ≤ $\tau_{cy.}$ ≤ 25 kPa) in the <u>clockwise direction</u> under constant volume condition sheared up to maximum shear strain double amplitude of 10.0% ($\gamma_{DA.max}$= 10.0%). 3. The loading was stopped by adding another quarter cycle of cyclic shear loading to the <u>origin</u> (γ= 0%).	*Similar configuration as those with previous tests.
2	4. Re-consolidation of vertical stress up to 200 kPa ($\sigma_{v.Top}$= 200 kPa) for 45 minutes. 5. Cyclic torsional shear loading in the <u>anti-clockwise</u> direction with global shear strain deformation of ±2.5% (2.5 ≤ γ ≤ 2.5%) under constant stress condition of $\sigma_{v.Top}$= 200 kPa.	
	note: • Circumferential and radial (σ_{θ} and σ_r) were unknown, since no sensors were installed in the current setting. Thus, σ_1 and σ_2 were also unknown. • Axial stress at the bottom of the specimen ($\sigma_{v.bot}$) was measured by bottom load cell. • All the specimens were tested under dry condition.	

Table 2.48: Stress paths in SDRL7

Step	Stress path	Deformation measurement transducers
1	1. Consolidation ($\sigma_{v.Top}$= 5 → 200 kPa) for 45 minutes. 2. Cyclic torsional shear loading (25 ≤ $\tau_{cy.}$ ≤ 25 kPa) in the <u>clockwise direction</u> under constant volume condition sheared up to maximum shear strain double amplitude of 10.0% ($\gamma_{DA.max}$= 10.0%). 3. The loading was stopped by adding another quarter cycle of cyclic shear loading to the <u>origin</u> (γ= 0%).	*Similar configuration as those with previous tests.

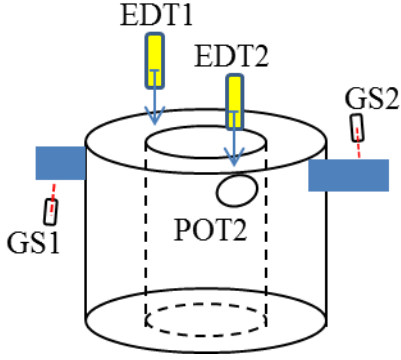|		
2	4. Re-consolidation of vertical stress up to 200 kPa ($\sigma_{v.Top}$= 200 kPa) for 45 minutes. 5. Cyclic torsional shear loading in the <u>clockwise</u> direction with global shear strain deformation of ±2.5% ($2.5 \le \gamma \le 2.5\%$) under constant stress condition of $\sigma_{v.Top}$= 200 kPa.	
	note: • Circumferential and radial (σ_θ and σ_r) were unknown, since no sensors were installed in the current setting. Thus, σ_1 and σ_2 were also unknown. • Axial stress at the bottom of the specimen ($\sigma_{v.bot}$) was measured by bottom load cell. • All the specimens were tested under dry condition.	

Table 2.49: Stress paths in SDRL8

Step	Stress path	Deformation measurement transducers
1	1. Consolidation ($\sigma_{v.Top}$= 5 → 200 kPa) for 45 minutes. 2. Cyclic torsional shear loading ($25 \le \tau_{cy.} \le 25$ kPa) in the <u>clockwise direction</u> under constant volume condition sheared until the maximum shear strain single amplitude was in anti-clockwise direction. 3. The loading continued until the shear strain went to clockwise direction without passing the maximum single strain amplitude on the previous liquefaction. 4. The loading was stopped by adding another quarter cycle of cyclic shear loading to the <u>origin</u> (γ=0%).	*Similar configuration as those with previous tests.
2	5. Re-consolidation of vertical stress up to 200 kPa ($\sigma_{v.Top}$= 200 kPa) for 45 minutes. 6. Cyclic torsional shear loading in the <u>clockwise</u> direction with global shear strain deformation of ±2.5% ($2.5 \le \gamma \le 2.5\%$) under constant stress condition of $\sigma_{v.Top}$= 200 kPa.	
	note: • Circumferential and radial (σ_θ and σ_r) were unknown, since no sensors were installed in the current setting. Thus, σ_1 and σ_2 were also unknown. • Axial stress at the bottom of the specimen ($\sigma_{v.bot}$) was measured by bottom load cell.	

	• All the specimens were tested under dry condition.

Table 2.50: Stress paths in SDCS1

Step	Stress path	Deformation measurement transducers
1	1. Consolidation ($\sigma_{v.Top}= 5 \rightarrow 200$ kPa) for 45 minutes. 2. Cyclic torsional shear loading in the <u>clockwise</u> direction under constant stress condition of $\sigma_{v.Top}= 200$ kPa and sheared with global shear strain deformation of ±2.5% ($2.5 \leq \gamma \leq 2.5\%$)	*Similar configuration as those with previous tests.
	note: • Circumferential and radial (σ_θ and σ_r) were unknown, since no sensors were installed in the current setting. Thus, σ_1 and σ_2 were also unknown. • Axial stress at the bottom of the specimen ($\sigma_{v.bot}$) was measured by bottom load cell. • All the specimens were tested under dry condition.	

Table 2.51: Stress paths in SLPre1 to SLPre4

Step	Stress path	Deformation measurement transducers
1	1. Consolidation ($\sigma_{v.Top}= 5 \rightarrow 200$ kPa) for 45 minutes. 2. Cyclic shear loading under constant stress condition sheared with strain single amplitude of ±0.1% ($-0.1 \leq \gamma_{SA} \leq 0.1\%$). Each specimen was sheared up to 5, 10, 100, 1000 cycles, respectively. 3. Cyclic torsional shear loading started in the <u>clockwise</u> direction under constant volume condition and sheared with global shear strain deformation of ±2.5% ($2.5 \leq \gamma \leq 2.5\%$).	*Similar configuration as those with previous tests.
	note: • Circumferential and radial (σ_θ and σ_r) were unknown, since no sensors were installed in the current setting. Thus, σ_1 and σ_2 were also unknown. • Axial stress at the bottom of the specimen ($\sigma_{v.bot}$) was measured by bottom load cell. • All the specimens were tested under dry condition.	

Fig. 2.1: Stacked-ring shear apparatus developed by Institute of Industrial Science – The University of Tokyo

LOADING EQUIPMENT OVERALL VIEW
Scale : 1/2
Unit : mm

(1) Bottom plate
(2) Intermediate plate
(3) Upper plate
(4) Die plate
(5) Interval fixed plate (bottom)
(6) Interval fixed plate (top)
(7) Cylinder output connection
(8) Cylinder input connection
(9) Spline shaft fitting
(10) Loading bolt fitting
(11) Spline shaft washer
(12) Spline shaft loading guide plate
(13) Loading guide plate supporter
(14) Bearing guide shaft
(15) Loading shaft fixing rod
(16) Donut diaphragm

Fig. 2.2: Systematic figure of loading shaft and direct-motor system for torsional shear loading

Bellofram Cylinder
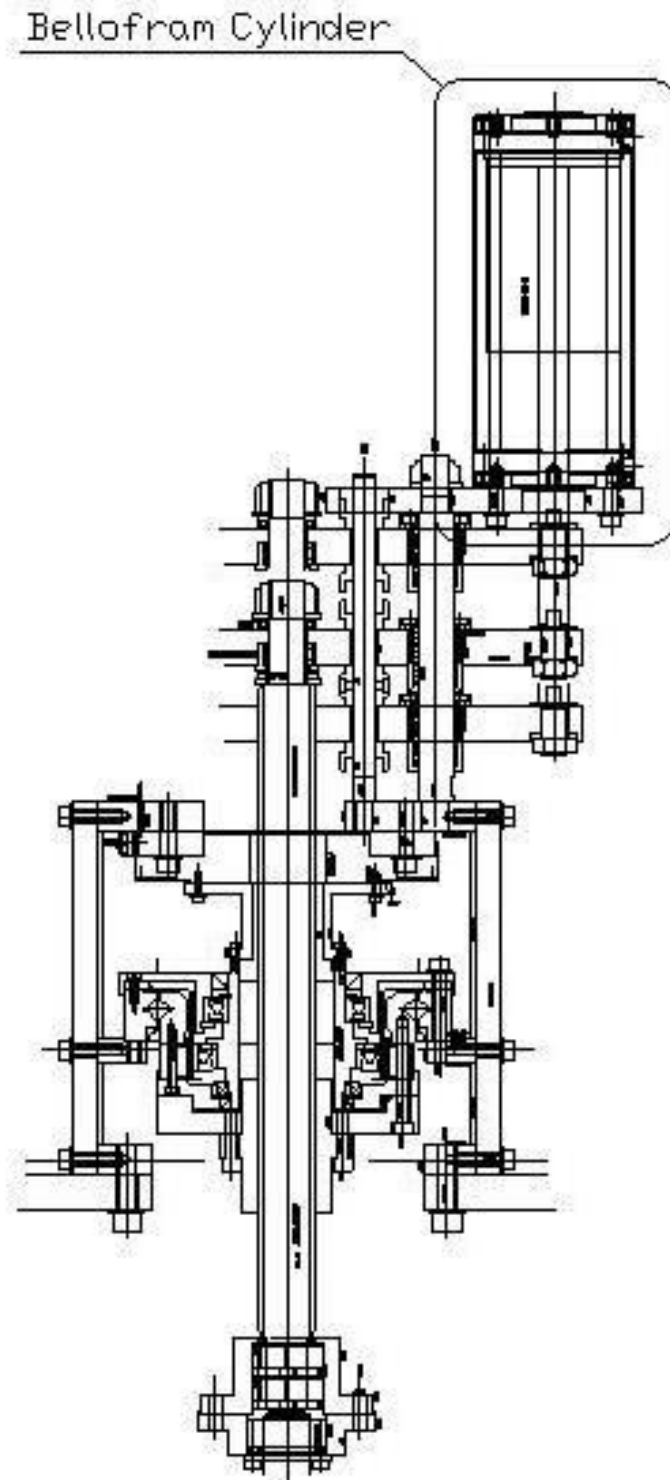
Fig. 2.3: Schematic figure of loading shaft and bellofram cylinder of axial loading system

Stacked-ring shear appratus
Scale 1/3

1. Acrylic cylinder
2. Acrylic cylinder cap (top)
3. Acrylic cylinder cap (bottom)
4. Cylinder cap fixing bolt
5. Tie rod
6. Triaxial cell footwall
7. Triaxial cell upper plate
8. Triaxial cell base
9. Triaxial cell spacer
10. Bearing
11. Clamp support plate
12. Clamp
13. Loading rods
14. Loading shaft seal
15. Bi-directional load cell
16. Load cell attachment
17. Loading axis attachment
18. Footwall mounting bolt w/ washer
19. Cell cylinder studs
20. Cell water supply hole
21. Valve mounting bracket A
22. Valve mounting bracket B
23. Displacement gauge
24. BPcylinder fixture A
25. BPcylinder mounting device B
26. BPcylinder,
    ball bearing joint connection
27. BPcylinder load receiver,
    displacement measurement ring A
28. BPcylinder load receiver,
    displacement measurement ring B

Fig. 2.4: Schematic figure of overall overview stacked-ring shear apparatus

Inner and outer ring section detail
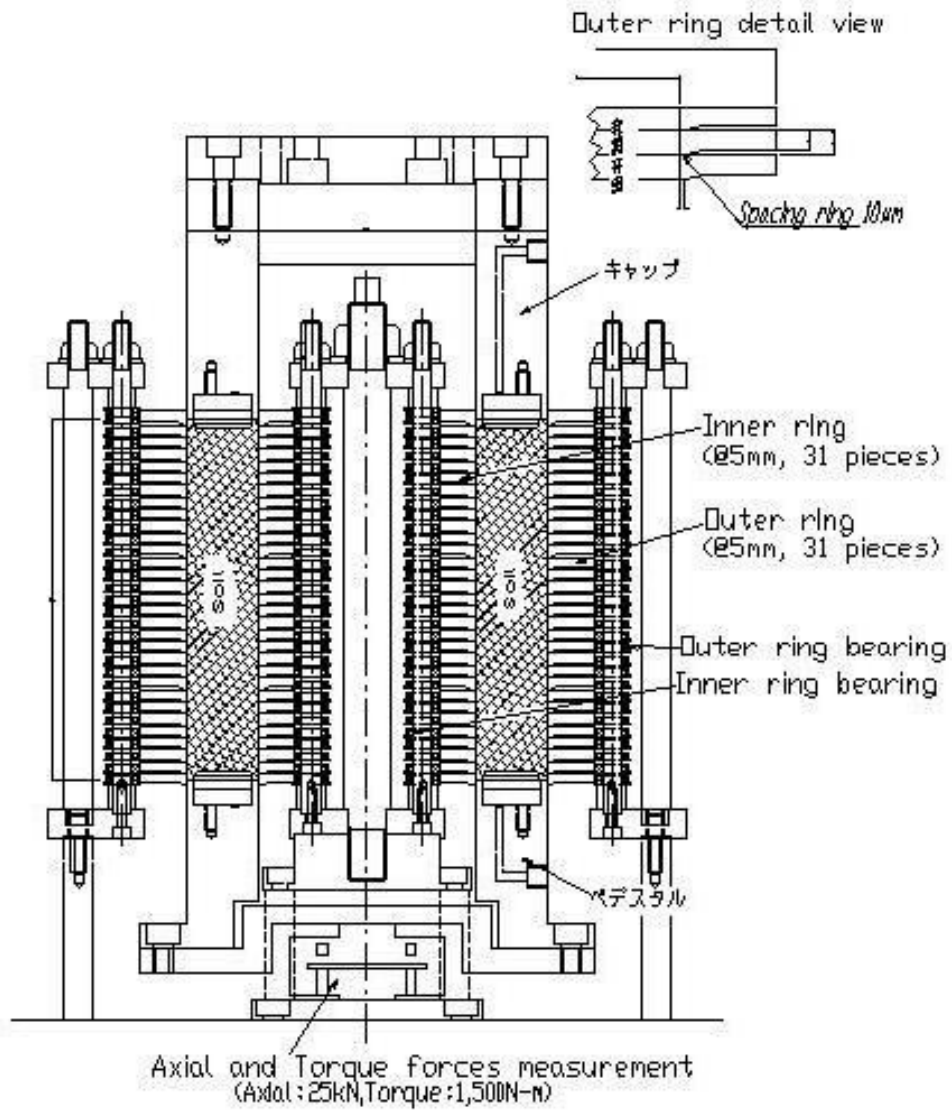
Fig. 2.5: Schematic figure of 31 stacked-ring shear type
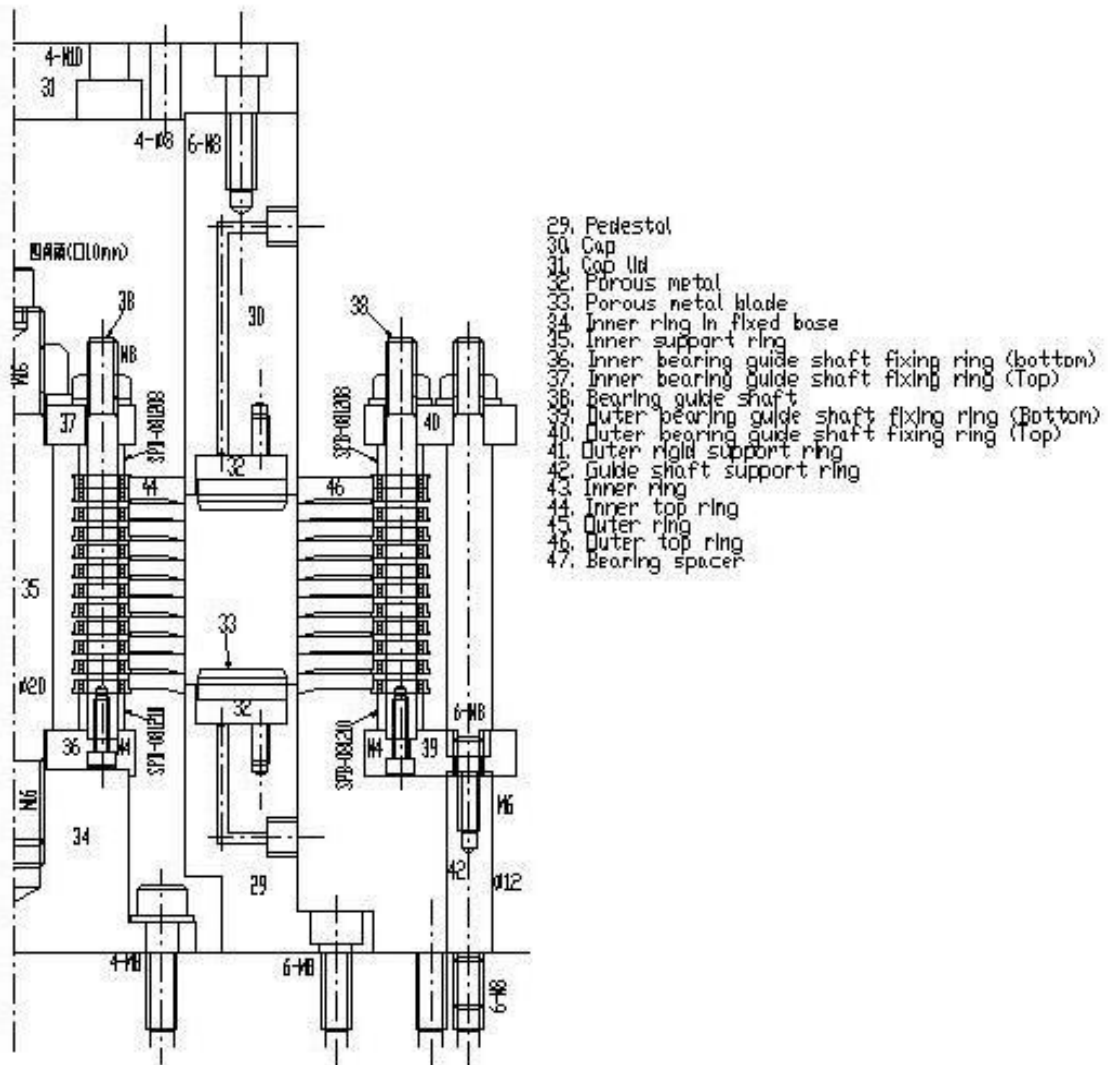
Fig. 2.6: Schematic figure of 11 stacked-ring shear type

8 stacked-ring shear type
Scale:1/1

29. Pedestal
30. Cap
31. Cap lid
32. Porous metal
33. Porous metal blade
34. Inner ring fixed base
35. Inner rigid support ring
36. Inner bearing guide shaft fixing ring (Bottom)
37. Inner bearing guide shaft fixing ring (top)
38. Bearing guide shaft
39. Outer bearing guide shaft fixing ring (Bottom)
40. Outer bearing guide shaft fixing ring (top)
41. Outer rigid support ring
42. Guide shaft fixing ring support
43. Inner ring
44. Inner top ring
45. Outer ring
46. Outer top ring
47. Bearing spacer

Fig. 2.7: Schematic figure of 8 stacked-ring shear type

5 stacked-ring shear type
Scale1/1

29. Pedestal
30. Cap
31. Cap lid
32. Porous metal
33. Porous metal blade
34. Inner ring fixed base
35. Inner rigid support ring
36. Inner bearing guide shaft fixing ring (bottom)
37. Inner bearing guide shaft fixing ring (top)
38. Bearing guide shaft
39. Outer bearing guide shaft fixing ring (bottom)
40. Inner bearing guide shaft fixing ring (top)
41. Outer rigid support ring
42. Guide shaft fixing ring with rigid support
43. Inner ring
44. Inner top ring
45. Outer ring
46. Outer top ring
47. Bearing spacer

Fig. 2.8: Schematic figure of 5 stacked-ring shear type
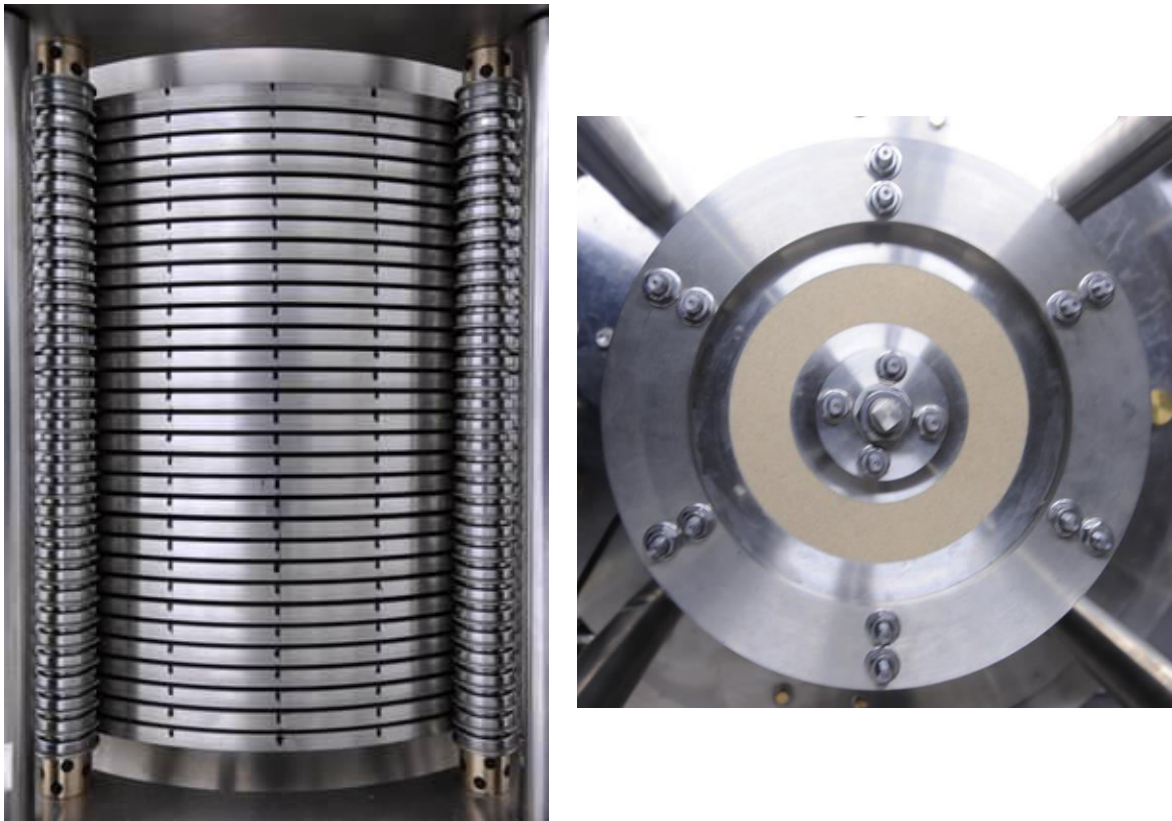
Fig. 2.9: Pictures of the front and plan views of the 31 non-coated stacked-ring shear type
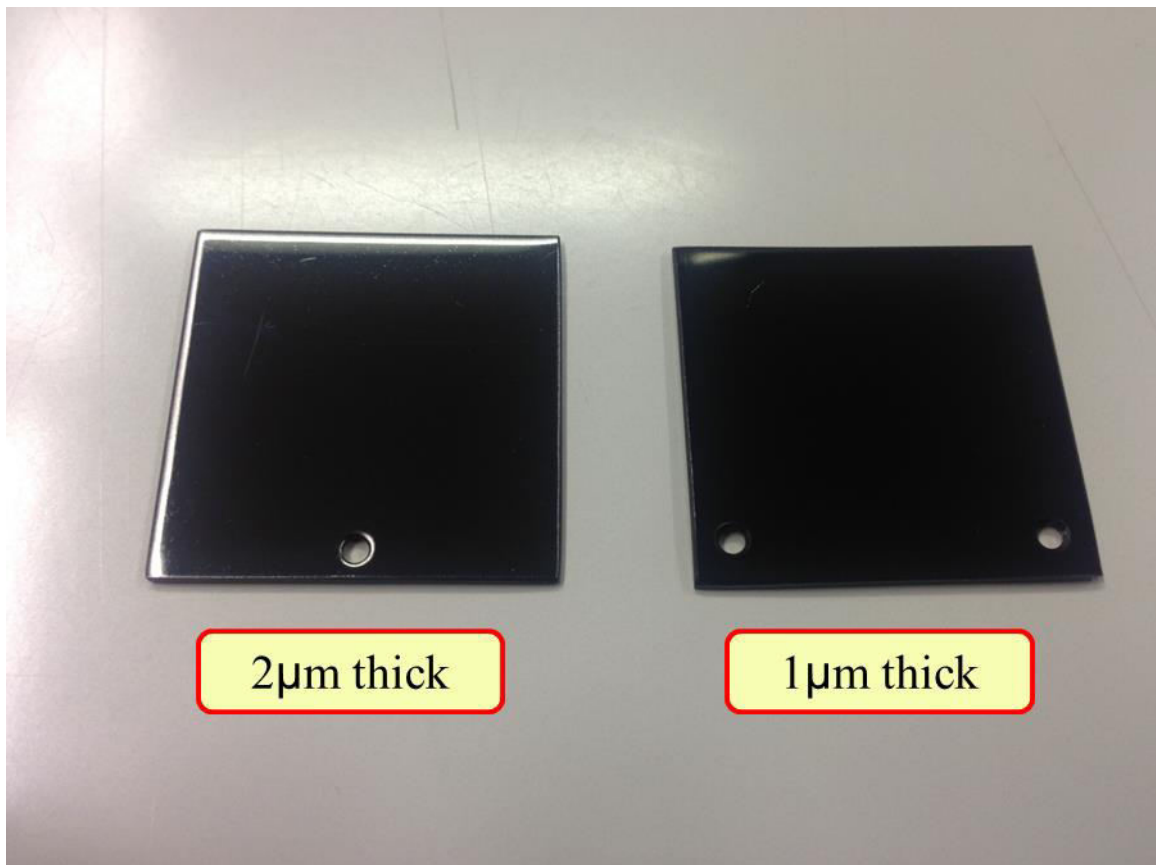
Fig. 2.10: Diamond-like coating prototype with 1.0µm and 2.0µm thick
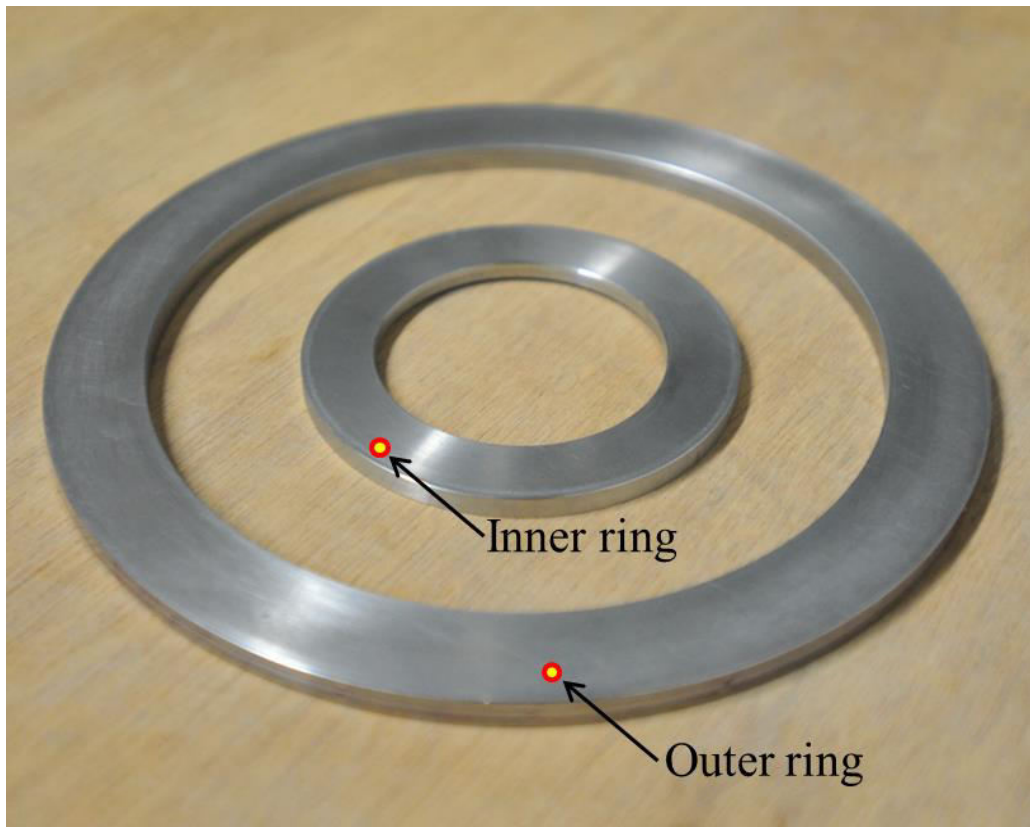
Fig. 2.11: Inner and outer rings with 5mm thick each
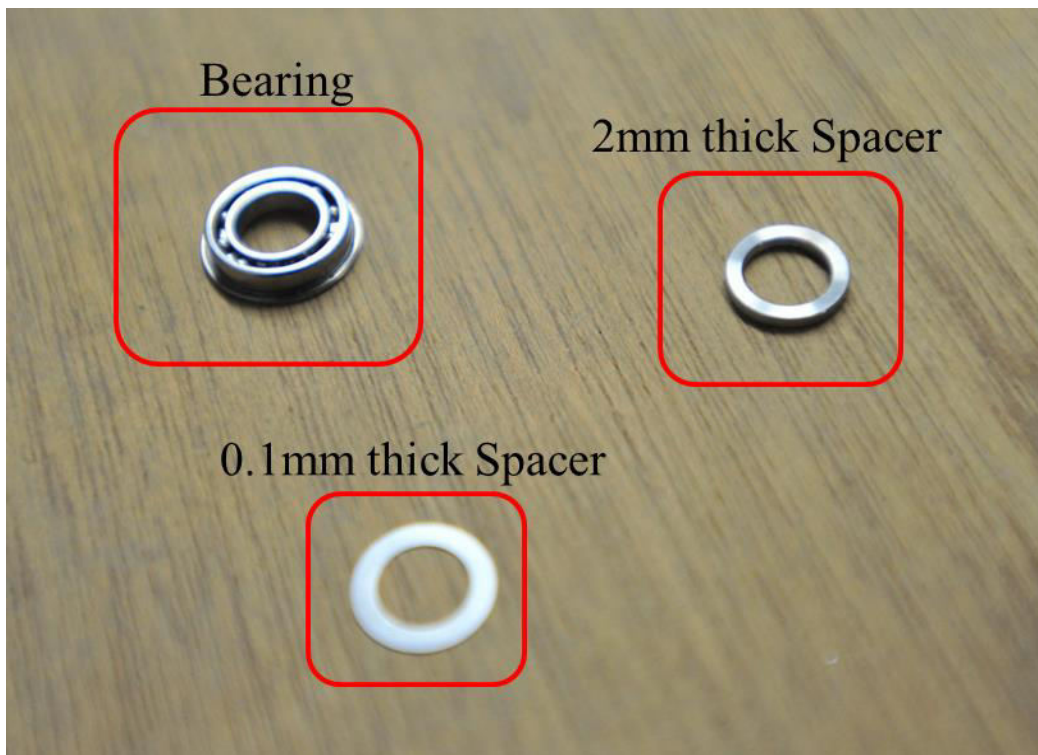
Fig. 2.12: Bearing and spacers in the stacked-ring shear apparatus
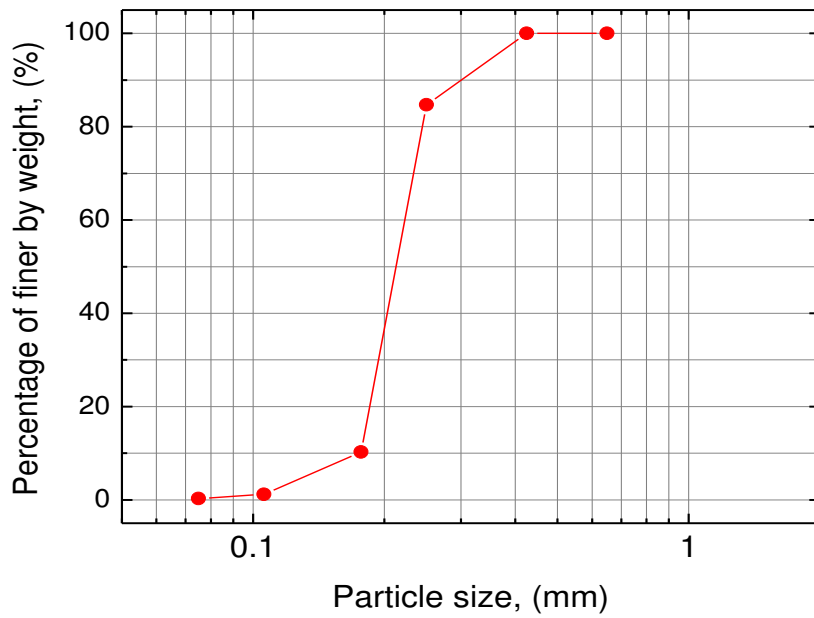
Fig. 2.13: Particle gradation curve of batch J Toyoura sand
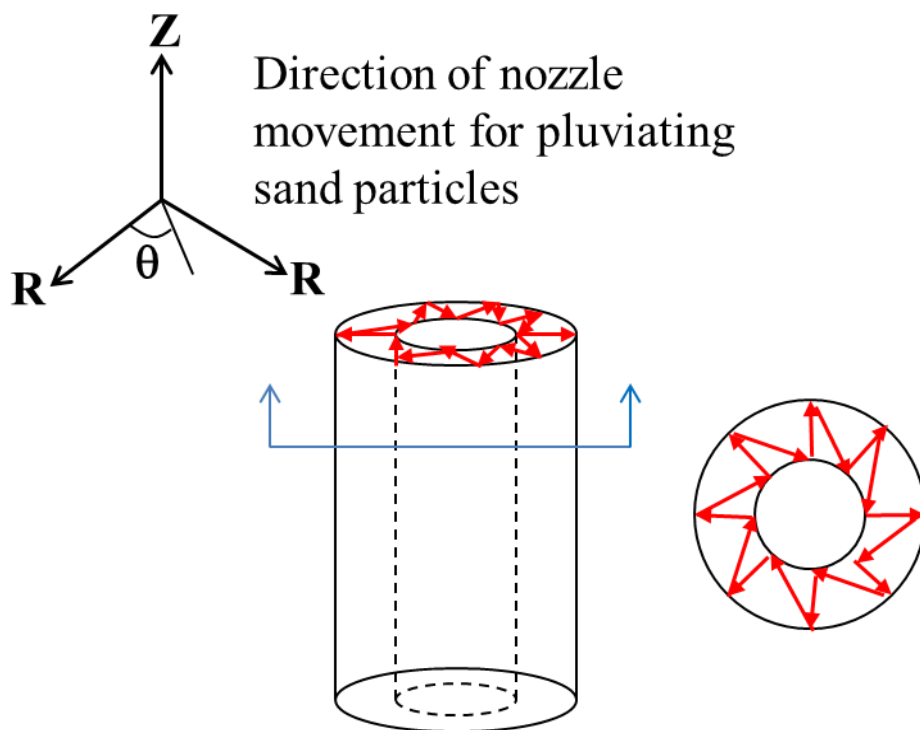
Fig. 2.14: Schematic diagram of pluviation technique (after De Silva et al., 2006)
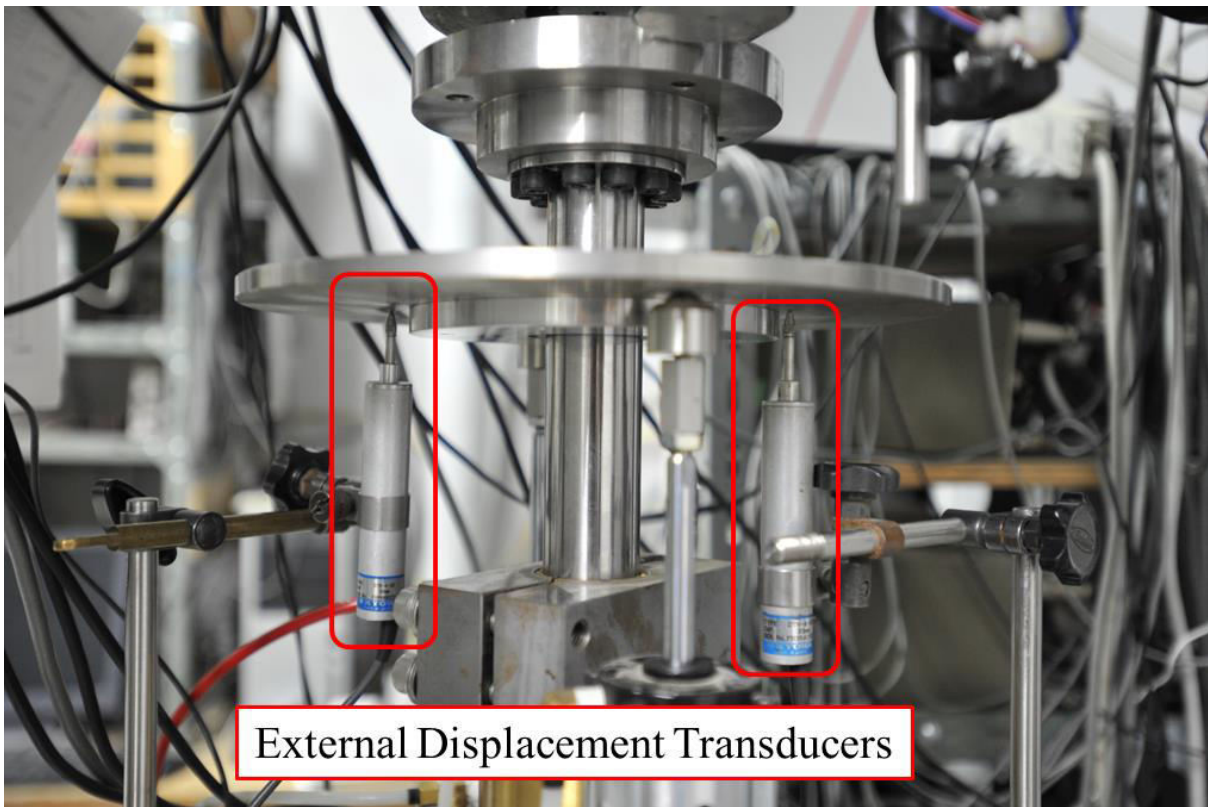
Fig. 2.15: EDTs (EDT-1 & EDT-2) to measure vertical displacement
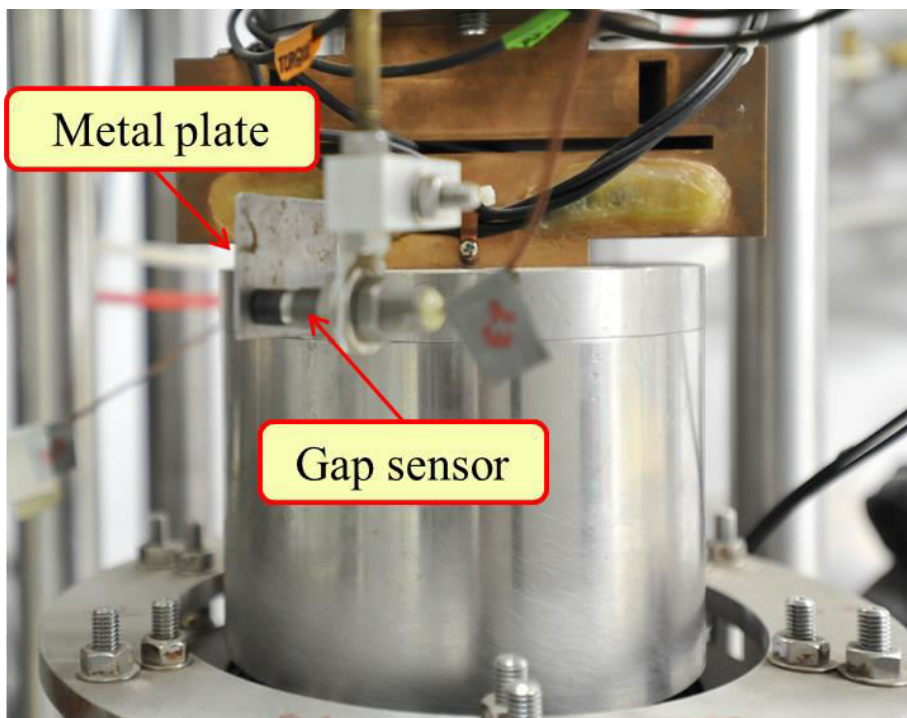
Fig. 2.16: Gap sensors (GS1 & GS-2) to measure lateral displacement
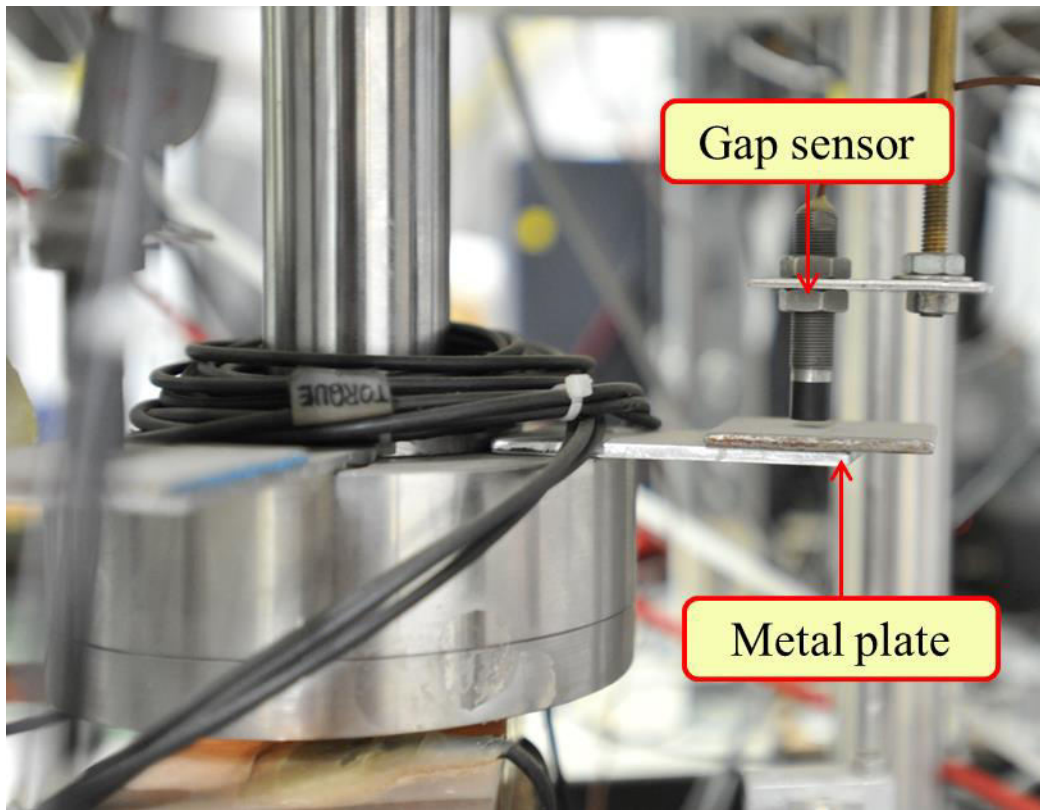
Fig. 2.17: Gap sensors (GS-3 & GS-4) to measure vertical displacement
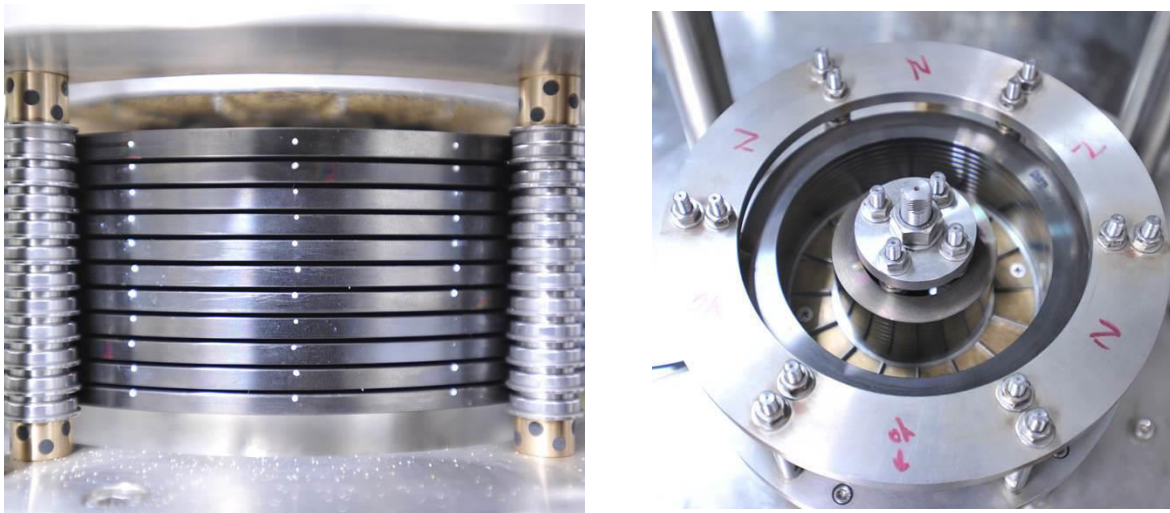
Fig. 2.18: Front and plan views of the 11 coated stacked-ring shear type
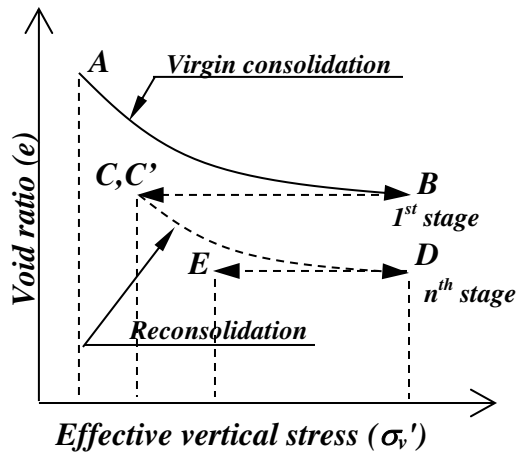
Fig. 2.19a: Typical void ratio and vertical stress relationship in re-liquefaction test
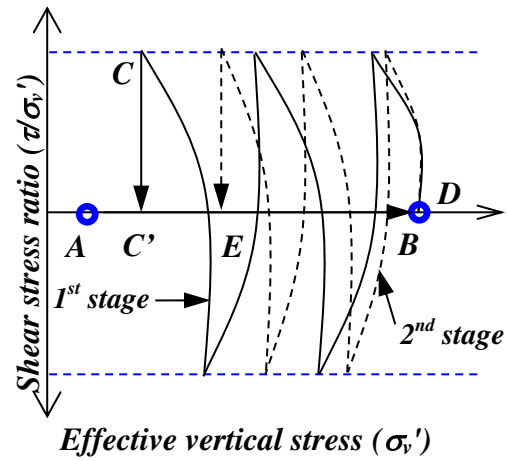
Fig. 2.19b: Typical shear stress ratio and vertical stress relationship in re-liquefaction test
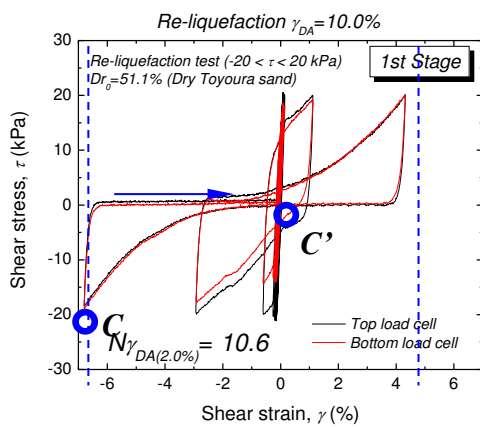
Fig. 2.19c: Typical shear stress and shear strain relationship in one stage of re-liquefaction test
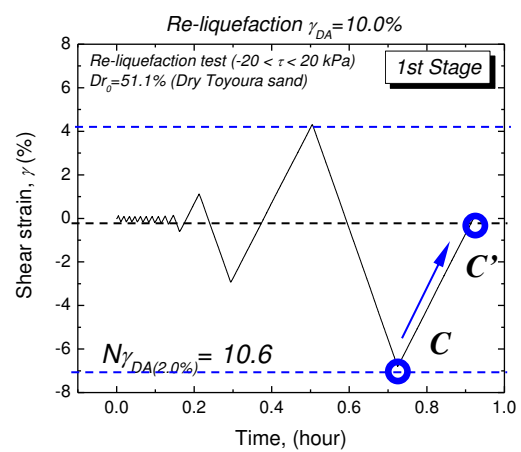
Fig. 2.19d: Typical shear strain and time relationship in one stage of re-liquefaction test
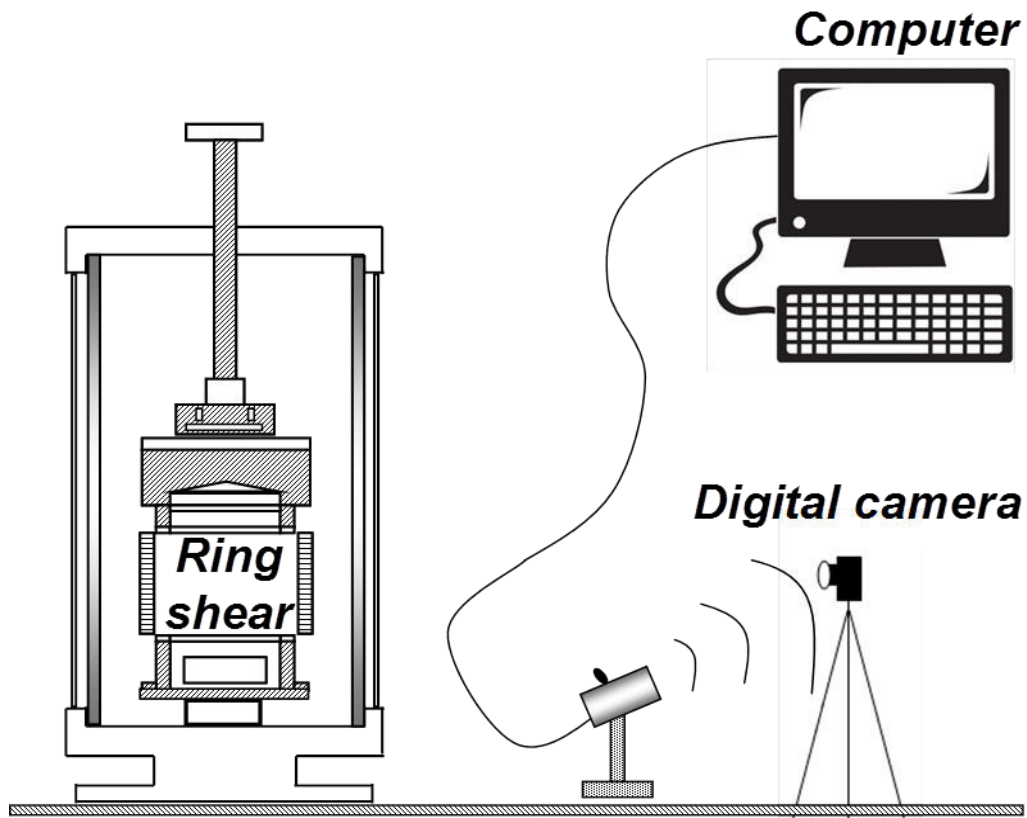
Fig. 2.20: Camera setting for image analysis process
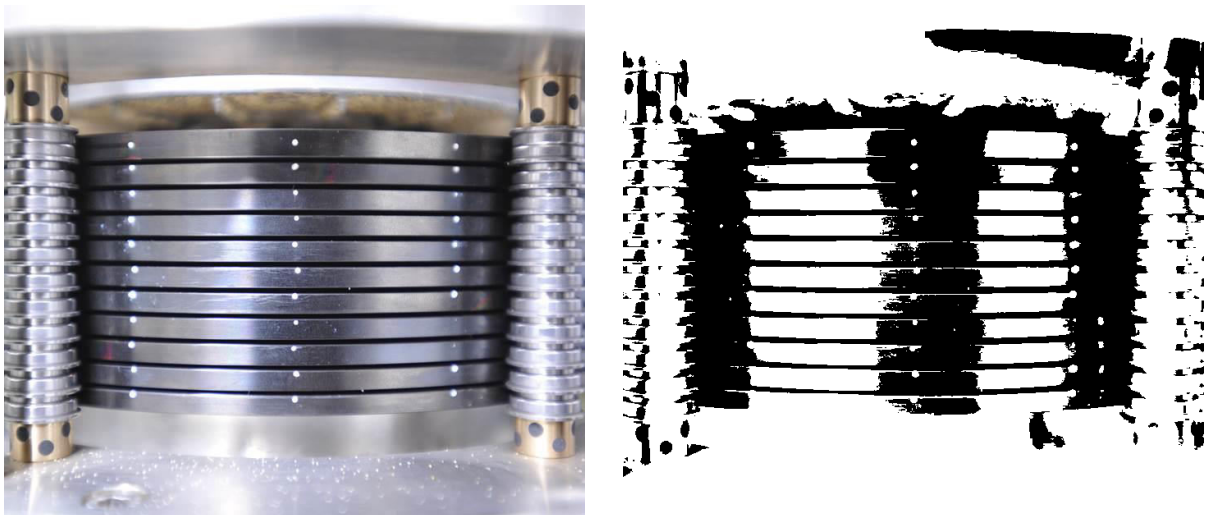
Fig. 2.21: Tracking process by Tr-2D software
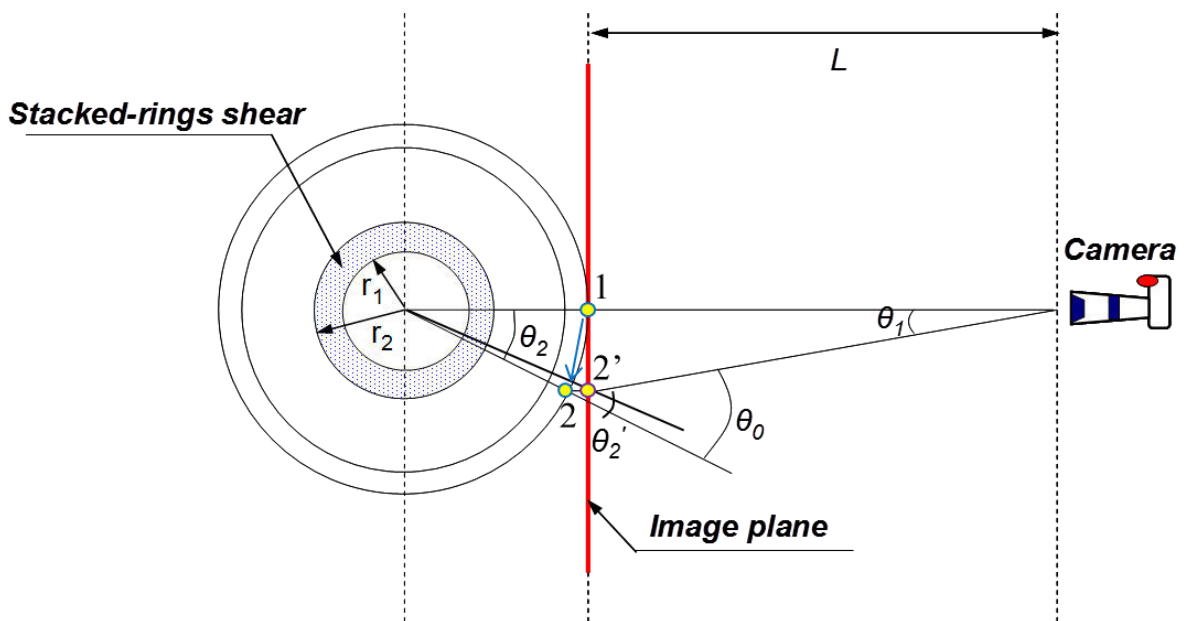
Fig. 2.22: Deformation of the cylindrical shape specimen in the stacked-ring shear apparatus

(a) Apparent coordinate plane

$(x', y') = f_1(x, y)$

(b) Real coordinate plan
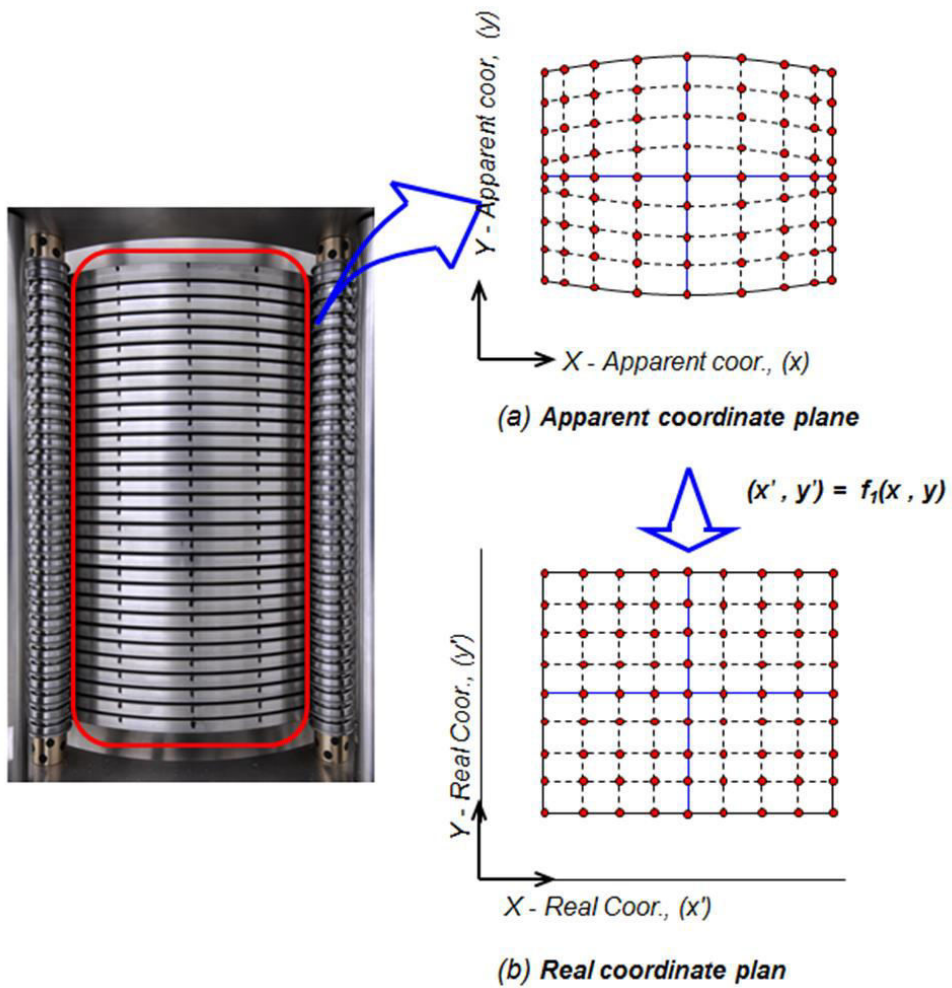
Fig. 2.23: Image distortion in the stacked-ring shear apparatus
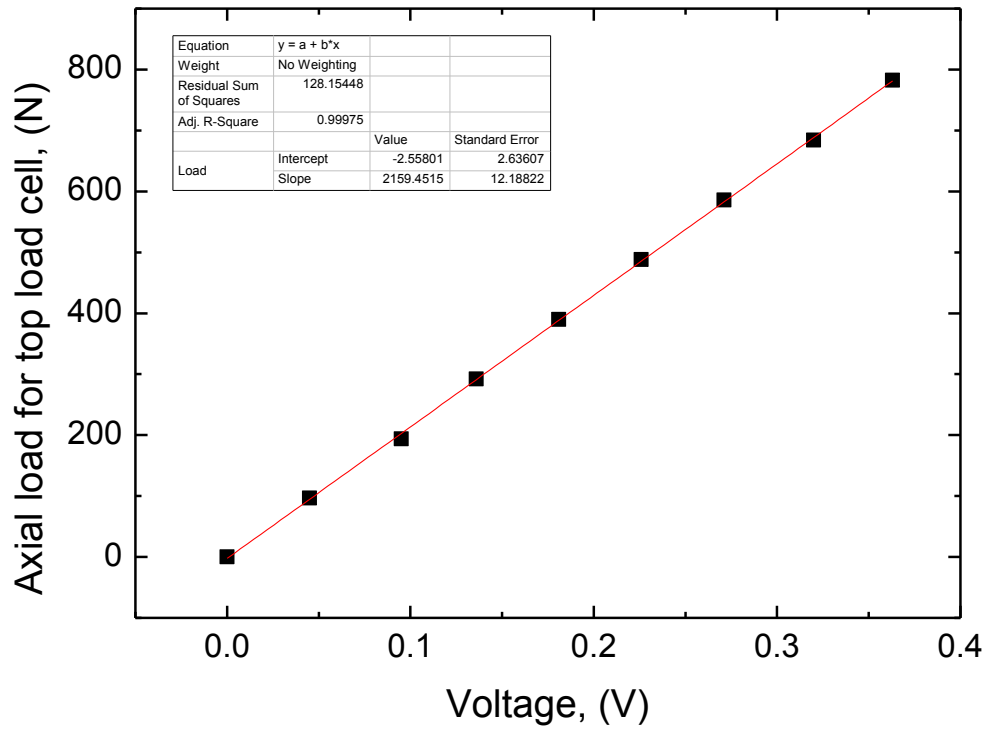
Fig. 2.24: Calibration of axial load for top load cell
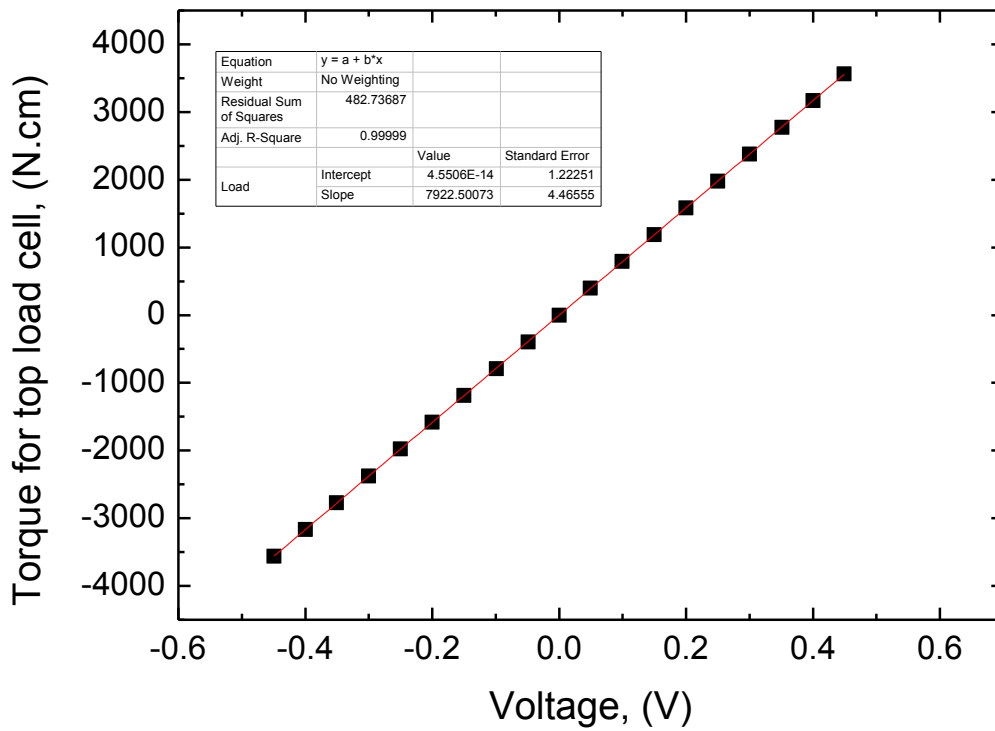
Fig. 2.25: Calibration of torque for top load cell

Equation	y = a + b*x		
Weight	No Weighting		
Residual Sum of Squares	53.92741		
Adj. R-Square	0.99984		
		Value	Standard Error
Load	Intercept	4.42664	1.91318
	Slope	842.24659	3.98306
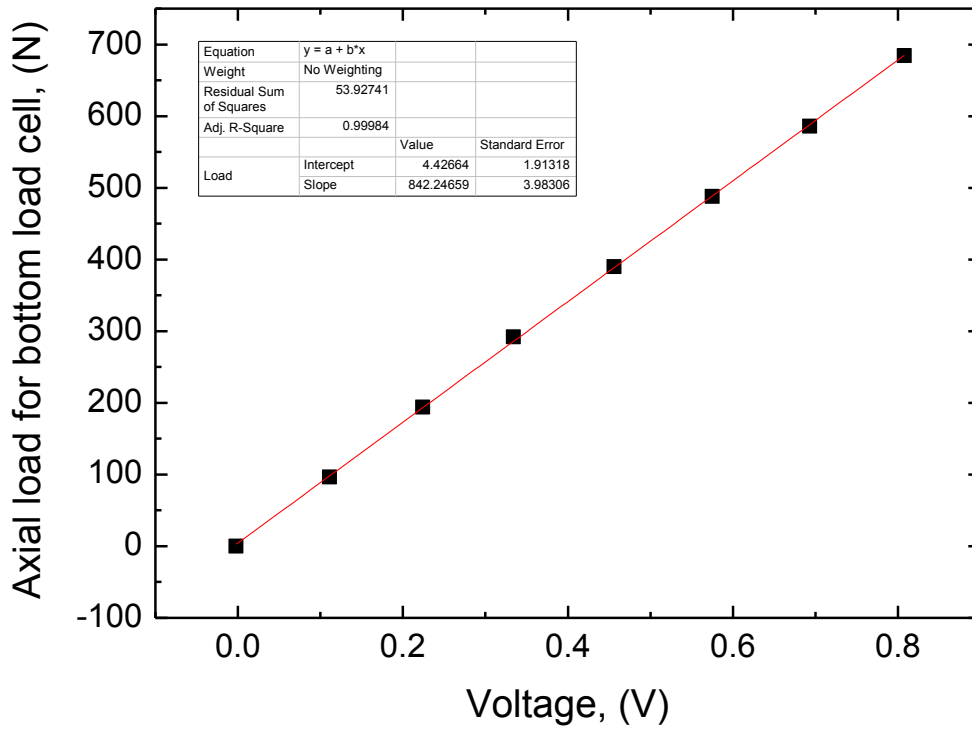
Fig. 2.26: Calibration of axial load for bottom load cell

Equation	y = a + b*x		
Weight	No Weighting		
Residual Sum of Squares	65.87007		
Adj. R-Square	0.99999		
		Value	Standard Error
Load	Intercept	-2.07862	1.88723
	Slope	4581.04767	4.58004
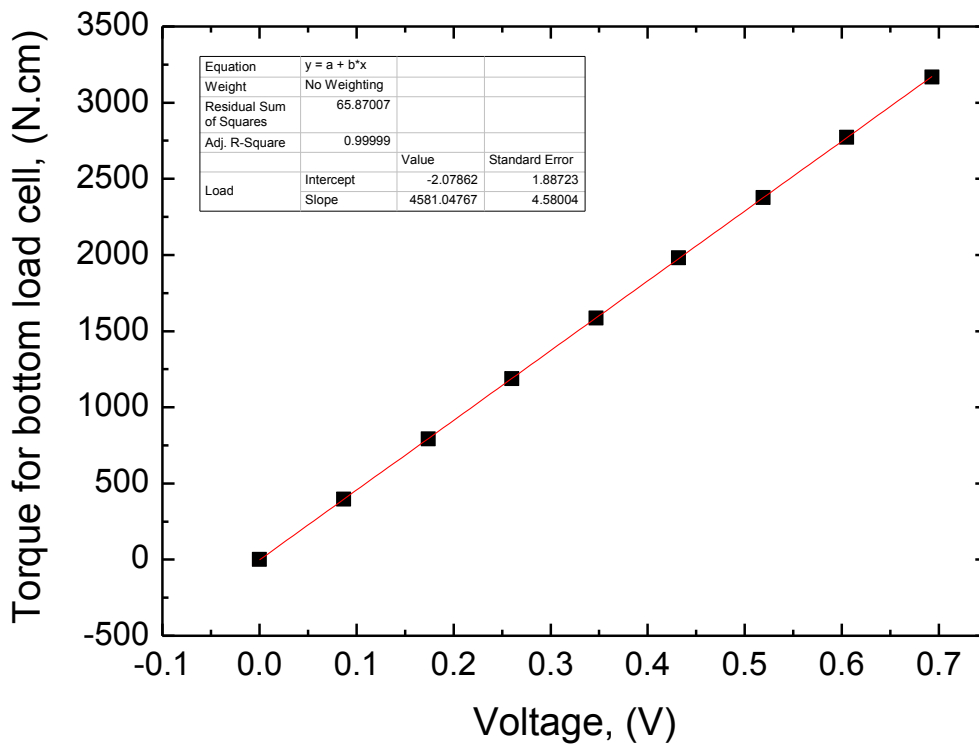
Fig. 2.27: Calibration of torque for bottom load cell

Equation	y = a + b*x		
Weight	No Weighting		
Residual Sum of Squares	2.99829E-30		
Adj. R-Square	1		
		Value	Standard Error
rad.	Intercept	6.66134E-16	3.25577E-16
	Slope	0.7795	1.10065E-16
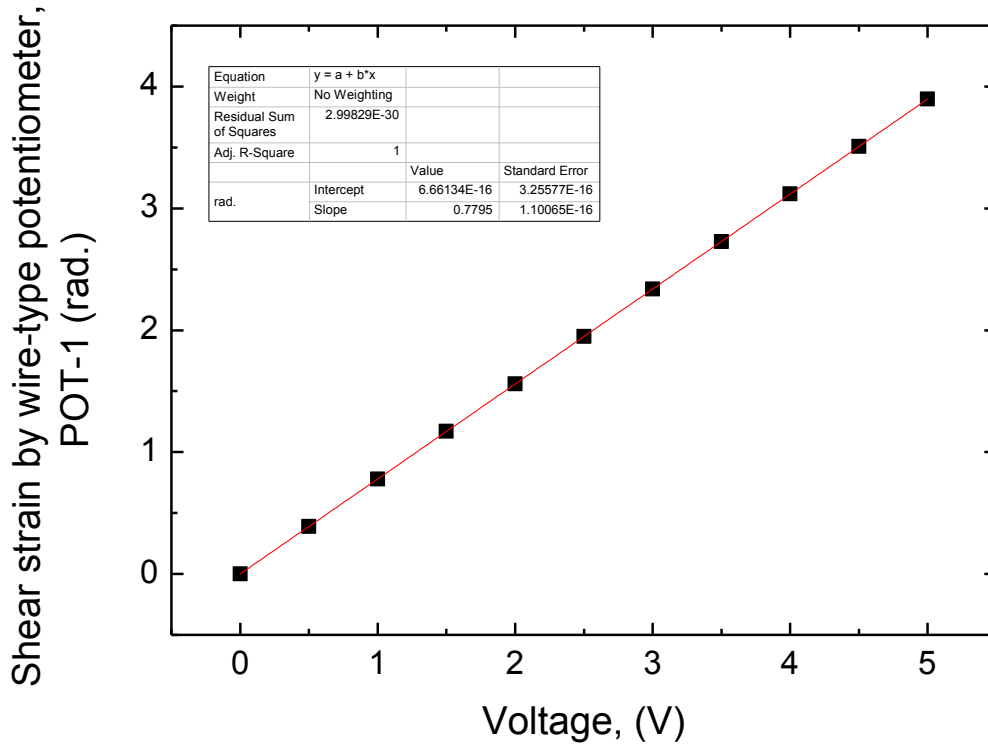
Fig. 2.28: Calibration of wire-type potentiometer (POT1)

Equation	y = a + b*x		
Weight	No Weighting		
Residual Sum of Squares	2.38261E-6		
Adj. R-Square	0.9999		
		Value	Standard Error
rad	Intercept	8.35809E-4	1.77356E-4
	Slope	0.07797	2.03021E-4
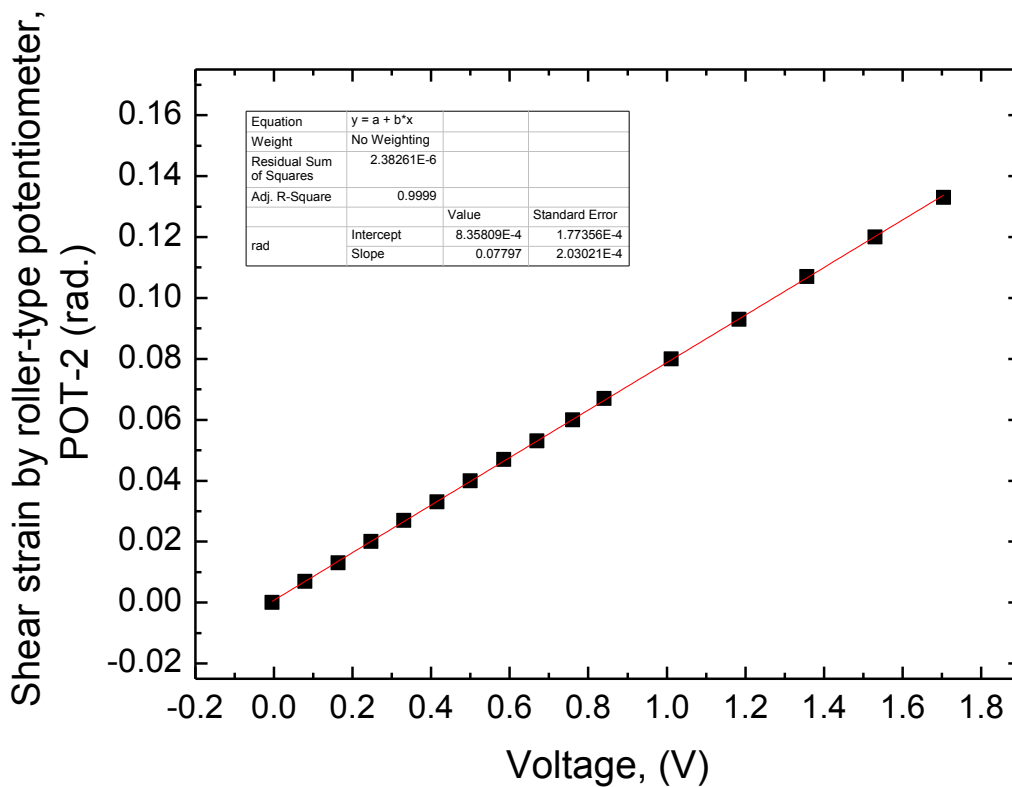
Fig. 2.29: Calibration of roller-type potentiometer (POT2)
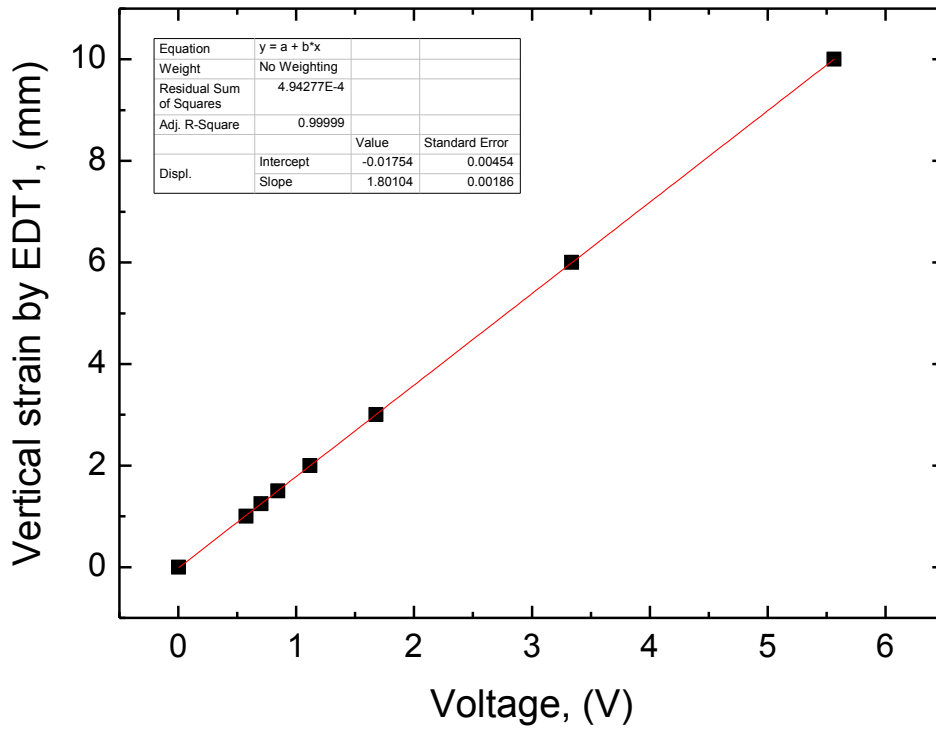
Fig. 2.30: Calibration of 1st External Displacement Transducer (EDT1)
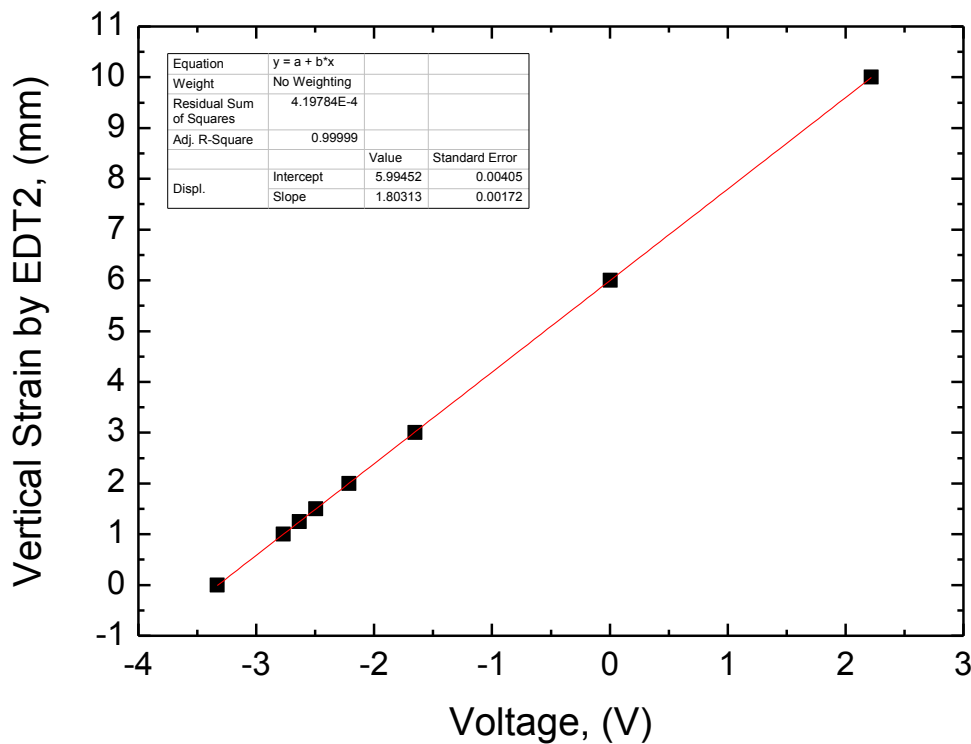
Fig. 2.31: Calibration of 2nd External Displacement Transducer (EDT2)

Equation	y = Intercept + B1*x^1 + B2*x^2	
Weight	No Weighting	
Residual Sum of Squares	0.00201	
Adj. R-Square	0.99982	
	Value	Standard Error
Displ. Intercept	2.00007	0.00936
B1	-0.4208	0.00199
B2	2.95801E-5	7.54086E-4
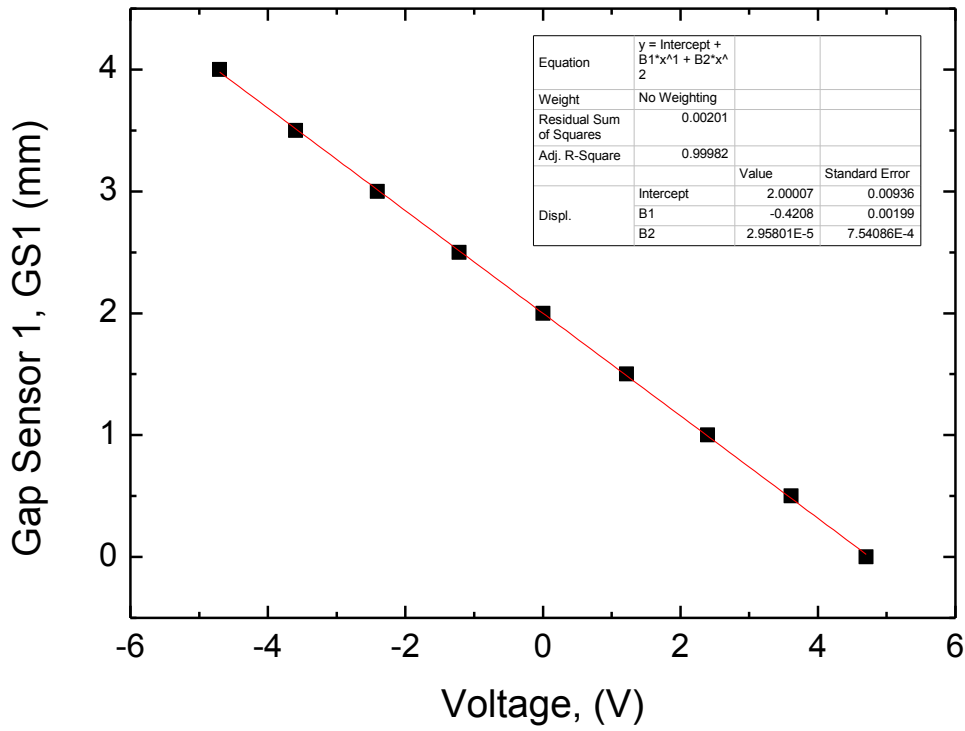
Fig. 2.32: Calibration of 1st Gap Sensor (GS1)

Equation	y = Intercept + B1*x^1 + B2*x^2	
Weight	No Weighting	
Residual Sum of Squares	0.00174	
Adj. R-Square	0.99985	
	Value	Standard Error
Displ. Intercept	2.0016	0.0087
B1	-0.42099	0.00185
B2	-2.72576E-5	7.01366E-4
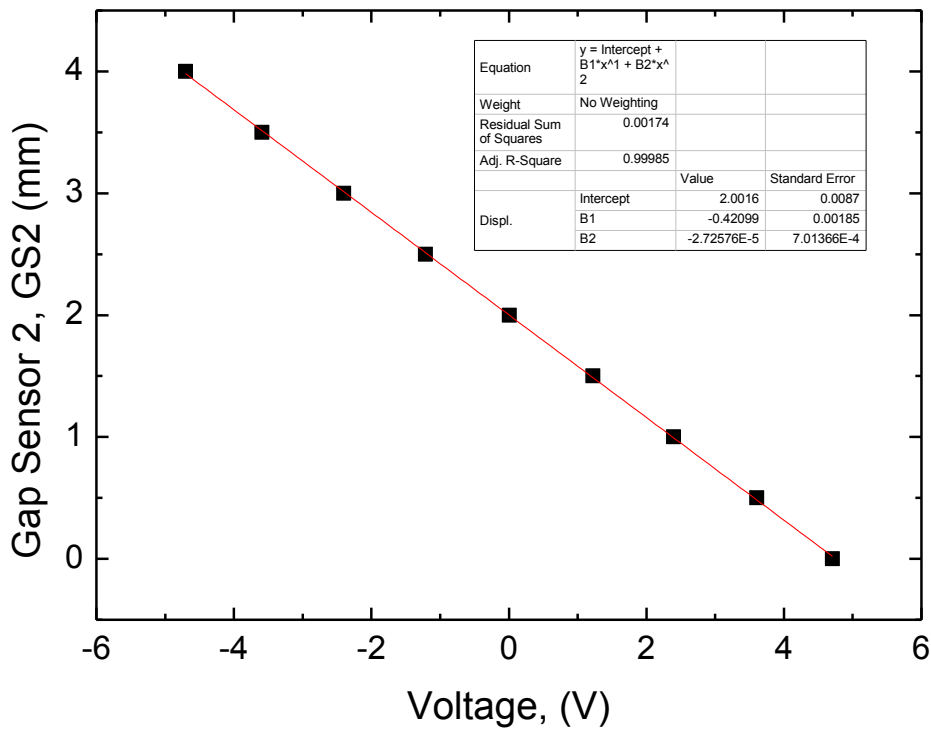
Fig. 2.33: Calibration of 2nd Gap Sensor (GS2)
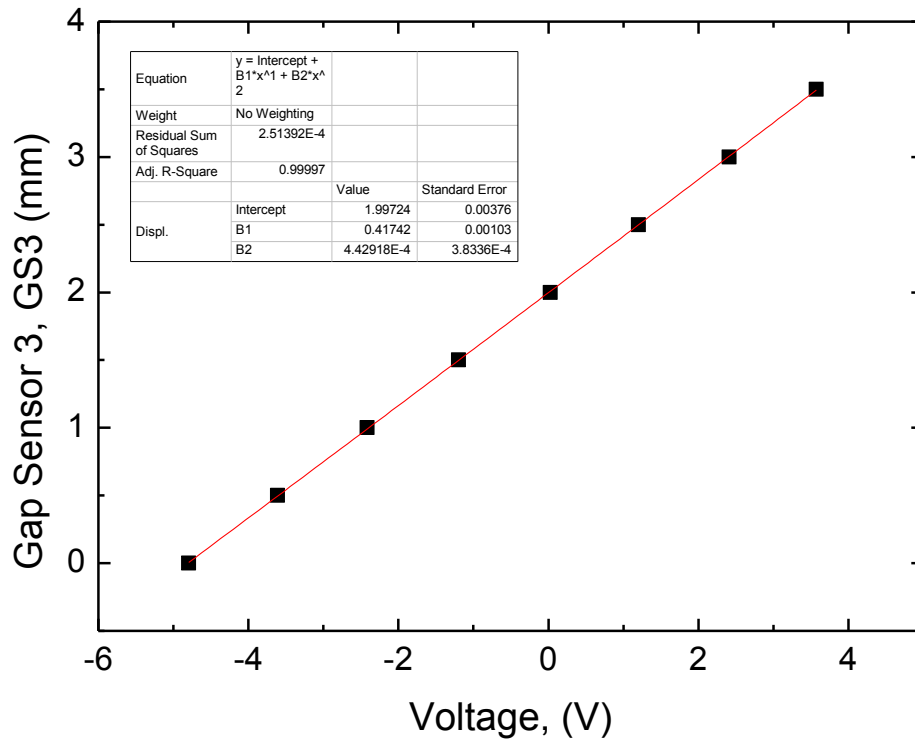
Fig. 2.34: Calibration of 3rd Gap Sensor (GS3)
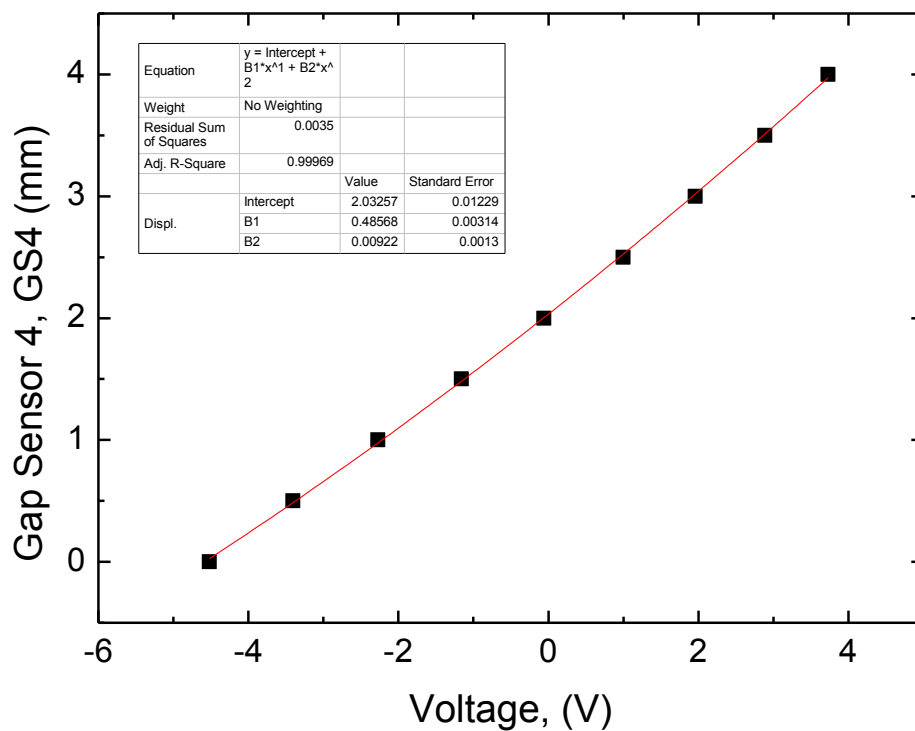
Fig. 2.35: Calibration of 4th Gap Sensor (GS4)

3 FORMULATION OF STRESSES AND STRAINS

3.1   Introduction

The stacked-ring shear apparatus is an effective tool capable of performing multi-stage liquefaction tests as well as conducting tests up to extremely large (virtually unlimited) shear deformation. Due to technical limitations, such sophisticated tests cannot be performed in conventional soil testing devices such as triaxial cell and hollow cylinder torsional shear apparatus. Previously, in the Institute of Industrial Science, The University of Tokyo, a large-size and a medium-size hollow cylinder torsional shear apparatuses were developed to simulate liquefaction response of isotropically and anisotropically consolidated specimens under various testing conditions including rotation of principal stresses. However, in the hollow cylinder torsional apparatus, only limited number of successive liquefaction stages could be performed, although largeshear strain double amplitudeup to 40% could be achieved in the large-size hollow cylinder torsional shear apparatus (De Silva, 2008) and up to 100% in the medium-size one (Kiyota, 2007 and Chiaro, 2010). In hollow cylinder torsional shear apparatus, the sheared specimen becomes non-uniform (stain localization)up to some levels of strain amplitude.

The newly developed stacked-ring shear apparatus itself is designed to have similar performance as hollow cylinder torsional shear apparatus. In fact, the loading conditions are in both apparatuses are the same,while the major difference is given by the specimen boundary conditions. Instead of using flexible membrane, the specimen in the stacked-ring shear apparatus is constrained by two rigid walls, composed of the inner and the outer vertically-stacked rings.

Since the basic features of the stacked-ring shear apparatus are similar to those of the hollow cylinder torsional shear apparatus, formulation of stresses and strains in the stacked-ring shear apparatus follows the one in hollow cylinder torsional shear apparatus, except for some modifications which are introduced by rigid boundary conditions.

In the hollow cylinder torsional apparatus, the formulations of the average stresses and strains are assumed to be linear elastic when calculating radial and circumferentialstresses (σ_r and σ_θ) and perfectly plastic when calculating shear stresses (Hight et al, 1983; Saada, 1988). In the current setting of the stacked-ring shear apparatus, there is no probing sensor installed to measure the radial and circumferential stresses due to technical difficulties. Therefore, the magnitudes of these stresses are unknown at this point.

Due to the rigid boundary, the radial and circumferential stresses are likely to be always different than the one applied vertically. In the current study, it is assumed that these stresses

are equal to the vertical stress multiplied by the earth pressure coefficient at rest (Ko), though, it is worth to note that this assumption may not be completely true due to the friction developed between soil and rings.

In the stacked-ring shear apparatus, there are two non-zero strain components, which are vertical strain and shear strain, while both of the radial and circumferential strains are kept zero. The evaluation of the axial strain is done by measuring the vertical movement of the top cap using two types of devices, which are EDT and gap sensor. It is assumed that the axial deformation of the specimen is uniformly distributed along the height of the specimen, which once again may not be entirely true due to the friction developed between soil and rings. The axial strain in the stacked-ring shear apparatus is equal to the volumetric strain of the specimen.

As mentioned in the earlier chapters, there are two types of shear strain measurements in the current study, which are the global and local shear strains measurement. Each of these measurements has its own purpose and analyzed with different methods. The analyses of both these two types will be discussed again later in detail.

The evaluations of material properties, stresses acted to the specimen, as well as the global and local strain measurements will be discussed in detail as follows.

3.2   Void ratio and relative density

In conducting the test, all the specimens need to be prepared with the certain initial relative density (Dr_{ini}).To do so, the basic concept of the soil element needs to be understood beforehand. In principal, the soil body can be divided into three phases, which are the air, water, and the soil itself as can be seen in the illustrated Fig. 3.1. The air and water account to the void part of the soil body, while the soil particles accounts to the solid part.To evaluate the specimen's relative density (Dr), the maximum and minimum void ratios (e_{max} and e_{min}) need to be evaluated beforehand. Maximum void ratio (e_{max}) corresponds to the loosest state possible of the soil material in a unit volume, while minimum void ratio (e_{min}) corresponds to the densest state. These two parameters can be only obtained by evaluating their specific gravity (G_s) beforehand, where specific gravity is defined asthe unit weight ratio of thematerial with thepure water (=1 Ton/m^3).

The evaluation of the specimen's relative density is given as follows.
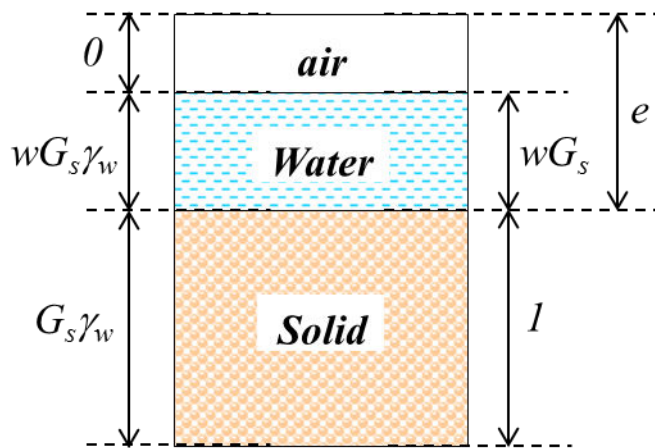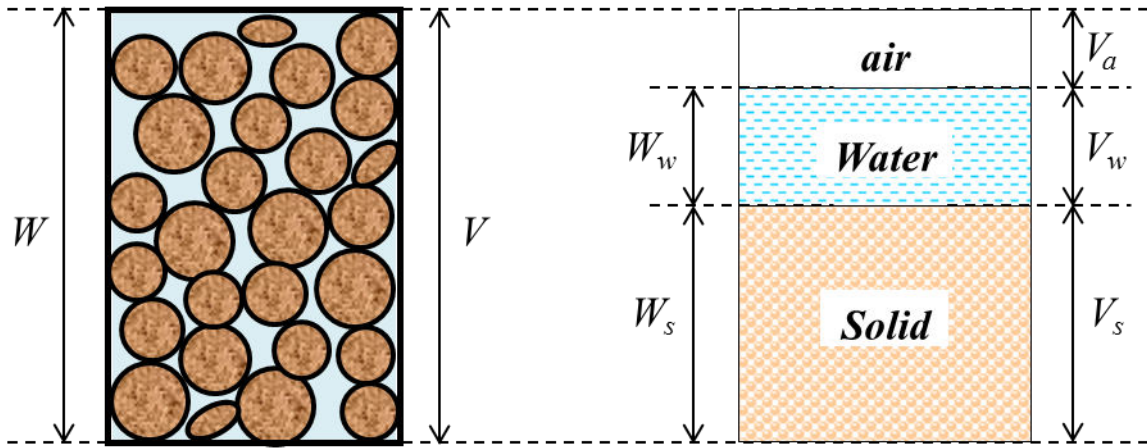
Fig. 3.1 Soil's phase diagram

Void ratio (e) is defined as,

$$e = \frac{V_V}{V_S} = \frac{V - V_S}{V_S} \qquad (3\text{-}1)$$

where, V_V is the volume of voids, V_S is the volume of solids and V is the total volume of the specimen. From Eq. 3-1:

$$\Rightarrow \frac{V}{V_S} = 1 + e \qquad (3\text{-}2)$$

and by taking the derivative while defining the positive volumetric strain ε_{vol} in compression,

$$de = \frac{dV}{V_S} \qquad (3\text{-}3)$$

$$de = \frac{dV}{V_S} = \frac{(1+e)}{V} dV = -(1+e)d\varepsilon_{vol} \qquad (3\text{-}4)$$

By integrating both side of Eq. 3-4 yields

$$\int_{e_0}^{e} -\frac{de}{(1+e)} = \int_{0}^{e_{vol}} d\varepsilon_{vol}$$

$$\Rightarrow \varepsilon_{vol} = \ln\frac{(1+e_0)}{(1+e)} \qquad (3\text{-}5)$$

$$\Rightarrow e = \frac{(1+e_0)}{\exp(\varepsilon_{vol})} - 1$$

In case of dry soil where there is no water,

$$M = M_S \text{ (assuming weight of air is negligible)}$$

where, M is the total mass of soil and M_S isthe weight of solids.

Substituting this in Eq. (3-2) gives,

$$\frac{V}{V_S} = 1+e \Rightarrow \frac{M}{V_S} \times \frac{V}{M} = 1+e \Rightarrow \frac{M_S}{V_S} \times \frac{V}{M} = 1+e \text{ (M}_S = M \text{ for dry soil)}$$

By definition,

$$\frac{M_S}{V_S} = G_S \text{ (Specific gravity of soil)} \quad \text{and} \quad \frac{M}{V} = \rho \text{ (Dry density of soil)}$$

$$\Rightarrow \frac{G_S}{\rho} = 1+e \quad \Rightarrow \quad e = \frac{G_S}{\rho} - 1 \qquad (3\text{-}6)$$

Relative density (D_r) of soil is defined as,

$$D_r = \frac{(e_{max} - e)}{(e_{max} - e_{min})} \times 100\,(\%) \qquad (3\text{-}7)$$

where,

e_{max} is the maximum void ratio (the loosest state possible)

e_{min} is the minimum void ratio (the densest state possible)

3.3   Formulation of stresses

Before describing the formulation of stresses in the stacked-ring shear apparatus, it is important to recall the stress conditions in a non-rigid hollow cylindrical specimen as in conventional torsional shear tests.

External loads acting on the cylindrical specimen are the axial load (F_z), the torque (T), the inner cell pressure (P_i),and the outer cell pressure (P_o) as shown in Fig. 3.2. From a loading point of view, the stresses acted on the hollow cylinder torsional shear apparatus are four degrees of freedom. The four surface tractions induce four stress components in a soil element and therefore four corresponding strain components. The four stresses are radial stress (σ_r), circumferential stress (σ_θ), axial stress (σ_z) and shear stress (τ_z)$_\theta$. Corresponding strain components are ε_r, ε_θ, ε_z, $\gamma_{z\theta}$, respectively.

In the stacked-ring shear apparatus, external loads acting on the cylindrical specimen are axial load F_z,torque T, while lateral pressures P_i and P_o are generated by the applied axial and torque loads and transferred to the soil element by the rigid boundary as shown in Fig. 3.3. Therefore, the cylindrical specimen in the stacked-ring shear apparatus has two degrees of freedom from a loading point of view. These two degrees of freedom correspond to two strain components only, which are axial strain and shear strain.
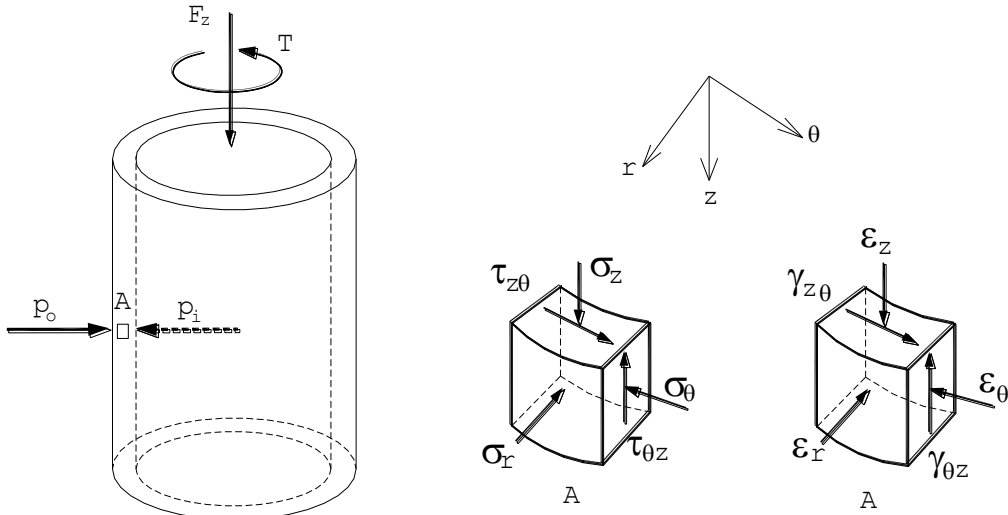
Fig. 3.2 Stresses and strains on a soil element inthe hollow cylinder torsional shear apparatus
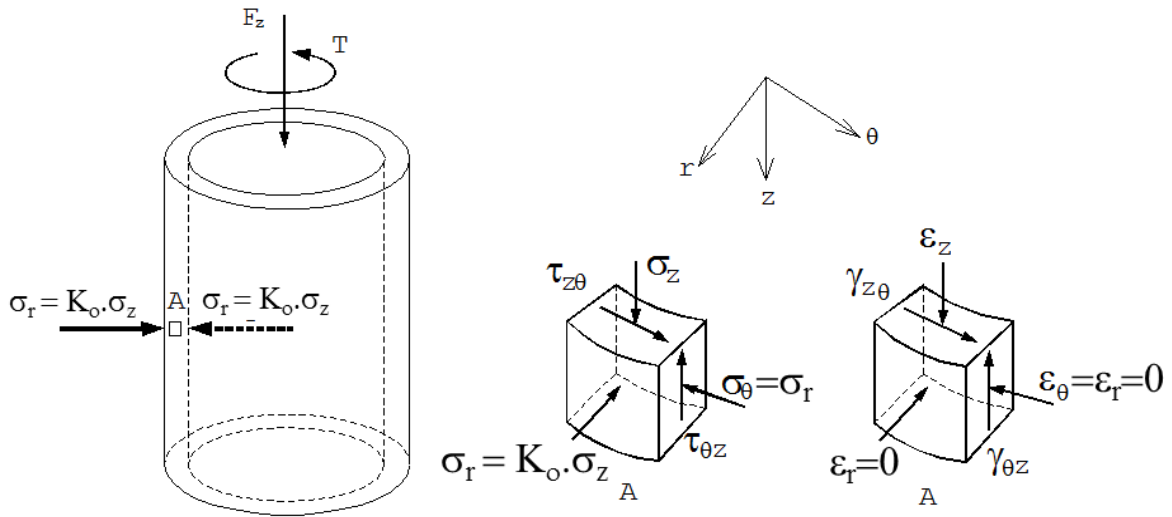
Fig. 3.3 Stresses and strains on a soil element in the stacked-ring shear apparatus

3.3.1 Radial and circumferential stresses (σ_r and σ_θ)

It should be noted that the actual distribution of stresses in a specimen is very complex due to the end restraint effect and bedding error. Timoshenko and Goodier (1970) gave a solution to the problem for hollow cylinder specimen on torsional shear apparatus subjected to uniform

inner (p_i) and outer pressures (p_o). To begin with, the stress distribution is assumed to be symmetrical with respect to the axis z of the hollow cylinder and the stress components do not depend on radial angle (θ) and are a function of radius (r) only. As a result, the shear stress ($\tau_r)_\theta$ is equal to 0. The equation of equilibrium in the radial direction yields,

$$\frac{\partial \sigma_r}{\partial r} + \frac{\sigma_r - \sigma_\theta}{r} + \omega = 0 \quad (3\text{-}8)$$

in which, ω is the body force. When ω equals to zero, Eq. (3-8) is satisfied as follows,

$$\sigma_r = \frac{B}{r^2} + 2C \quad (3\text{-}9)$$

$$\sigma_\theta = -\frac{B}{r^2} + 2C \quad (3\text{-}10)$$

where, B and C are two constants, which can be obtained from the following boundary conditions.

$$\sigma_r \big|_{r=R_i} = p_i \quad (3\text{-}11)$$

$$\sigma_r \big|_{r=R_o} = p_o \quad (3\text{-}12)$$

where, R_o and R_i denote current outer and inner radii of the specimen, respectively. By substituting Eq. (3-11) and Eq. (3-12) into Eq. (3-9) and Eq. (3-8), one gets,

$$\sigma_r = \frac{p_o R_o^2 - p_i R_i^2}{R_o^2 - R_i^2} - \frac{R_i^2 R_o^2 (p_o - p_i)}{R_o^2 - R_i^2} \frac{1}{r^2} \quad (3\text{-}13)$$

$$\sigma_\theta = \frac{p_o R_o^2 - p_i R_i^2}{R_o^2 - R_i^2} + \frac{R_i^2 R_o^2 (p_o - p_i)}{R_o^2 - R_i^2} \frac{1}{r^2} \quad (3\text{-}14)$$

Average stress components are computed with weighting and without weighting (Ampadu, 1991) as follows.

Averaging without weighting

$$\overline{\sigma}_r = \frac{\int_{R_i}^{R_o} \sigma_r\, dr}{\int_{R_i}^{R_o} dr} \quad (3\text{-}15) \qquad\qquad \overline{\sigma}_\theta = \frac{\int_{R_i}^{R_o} \sigma_\theta\, dr}{\int_{R_i}^{R_o} dr} \quad (3\text{-}16)$$

By substituting Eq. (3-13) into Eq. (3-15) and Eq. (3-14) into Eq. (3-16), one gets,

$$\overline{\sigma}_r = \frac{p_o R_o + p_i R_i}{R_o + R_i} \quad (3\text{-}17)$$

$$\overline{\sigma}_\theta = \frac{p_o R_o - p_i R_i}{R_o - R_i} \quad (3\text{-}18)$$

These equations were used by a number of researchers such as Hight et al. (1983) and Saada (1988).

Averaging with weighting

$$\int_{R_i}^{R_o} \sigma_r\, r\, dr = \int_{R_i}^{R_o} \overline{\sigma}_r\, r\, dr \quad (3\text{-}19) \qquad\qquad \int_{R_i}^{R_o} \sigma_\theta\, r\, dr = \int_{R_i}^{R_o} \overline{\sigma}_\theta\, r\, dr \quad (3\text{-}20)$$

$$\overline{\sigma}_r = \frac{\int_{R_i}^{R_o} \sigma_r\, r\, dr}{\int_{R_i}^{R_o} r\, dr} \quad (3\text{-}21) \qquad \overline{\sigma}_\theta = \frac{\int_{R_i}^{R_o} \sigma_\theta\, r\, dr}{\int_{R_i}^{R_o} r\, dr} \quad (3\text{-}22)$$

By substituting Eq. (3-13) into Eq. (3-21) and Eq. (3-14) into Eq. (3-22), one gets

$$\bar{\sigma}_r = \frac{p_o R^2{}_o - p_i R^2{}_i}{R^2{}_o - R^2{}_i} - \frac{2R^2{}_i R^2{}_o (p_o - p_i)}{(R^2{}_o - R^2{}_i)^2} \ln\left(\frac{R_o}{R_i}\right) \qquad (3\text{-}23)$$

$$\bar{\sigma}_\theta = \frac{p_o R^2{}_o - p_i R^2{}_i}{R^2{}_o - R^2{}_i} + \frac{2R^2{}_i R^2{}_o (p_o - p_i)}{(R^2{}_o - R^2{}_i)^2} \ln\left(\frac{R_o}{R_i}\right) \qquad (3\text{-}24)$$

Eqs. 3-17 up to 3-24 assume that both inner and outer radial pressures (p_o and p_i) are known. However, in the current setting of the stacked-ring shear apparatus, there are no probing sensors installed to measure these stress components. Therefore, the radial and circumferential stresses are obtained by multiplying the vertical stress with the earth pressure coefficient at rest (Ko).

$$\bar{\sigma}_r = \bar{\sigma}_z.Ko \qquad (3\text{-}25)$$

$$\bar{\sigma}_\theta = \bar{\sigma}_r = \bar{\sigma}_z.Ko$$

For simplicity reason, Ko value in the cyclic shear constant volume test using stacked-ring shear apparatus is assumed to be constant at 0.5 (in case of normally consolidated Toyoura sand). Okochi and Tatsuoka,(1984) and Tatsuoka et al. (1989)measured the change of Ko value in the Triaxial Simple Shear Test (TSST). It was found thatthe Ko valuemay increase within the range of 0.5 to 1.0 as the specimen's effective stress (σ_v') decreases.

3.3.2   Vertical stress σ_z

In the hollow cylinder torsional shear apparatus, the average vertical stress evaluated at the middle height of the specimen can be computed as follows:

$$\bar{\sigma}_z = \frac{LC}{A} + \sigma_h + \sigma_g + \sigma_{mem} \qquad (3\text{-}26)$$

where,

LC : Deviatoric load detected by the load cell,

A: Cross-sectional area of the specimen ($= \pi(R_o{}^2 - R_i{}^2)$),

σ_h: Horizontal stress (= σ_r= σ_θ), where both radial and circumferential stresses are assumed to be equal to one another.

σ_{mem}: Correction for the membrane stress (Tatsuoka et al., 1986)

if $\varepsilon_z > 0$, $\sigma_{mem} = 0$

if $\varepsilon_z > 0$, $\sigma_{mem} = -\dfrac{3}{8} \times \varepsilon_z \times t_{mem} \times \dfrac{E_{mem}}{\left(R_o - R_i\right)}$

where,

ε_z is the axial strain

t_{mem} is the membrane thickness

E_{mem} is the membrane Young's Modulus

σ_g is the overburden stress increment of the specimen due to its self-weight at its middle height,

$\sigma_g = \gamma'H/2$

$\gamma' = (G_s-1)/(1+e) \times \rho_w \times g$

where,

G_s is the specific gravity,

e is the void ratio,

g is the gravitational acceleration (9.80665 m/s^2)

ρ_w is the density of water (1 g/cm^3)

In the stacked-ring shear apparatus, the distribution of the vertical stress along the height of the specimen is not uniform due to the friction between the soil particle and the stacked rings. In addition, there is no membrane in the stacked-ring shear apparatus. Thus, Eq. 3-26 can be modified as follows

$$\overline{\sigma_{z \cdot Top}} = \frac{LC_{Top}}{A} \qquad \text{(3-27a)}$$

$$\overline{\sigma_{z \cdot Bottom}} = \frac{LC_{Bo}}{A} + \sigma_g \qquad \text{(3-27b)}$$

where,

LC_{Top} is the axial force measured by the top load cell.

LC_{Bot} is the axial force measured by the bottom load cell.

The overburden stress (σ_g) needs to be addedas well in the measured shear stress at bottom of the specimen sincethe output voltage was set to zero after putting the specimen on it.

3.3.3   Shear stress ($\tau_{z\theta}$)

In the hollow cylinder torsional shear apparatus, the shear stress $\tau_{z\theta}$ acting on a soil element with the area $dA = r\,d\theta\,dr$ can be integrated into the torque T as follows.

$$dT = \tau_{z\theta}r^2 d\theta dr \qquad (3\text{-}28)$$

$$T = \int_{R_i}^{R_o}\int_0^{2\pi} \tau_{z\theta}r^2 d\theta dr$$

$$T = 2\pi \int_{R_i}^{R_o} \tau_{z\theta}r^2 dr$$

If the material is perfectly plastic, then the distribution of shear stress is uniform and constant. Thus, one gets

$$T = 2\pi\tau_{z\theta} \int_{R_i}^{R_o} r^2 dr$$

$$T = \frac{2}{3}\pi\tau_{z\theta}\left(R_o^{\,3} - R_i^{\,3}\right) \qquad (3\text{-}29)$$

$$\tau_{z\theta} = \frac{3T}{2\pi\left(R_o^{\,3} - R_i^{\,3}\right)} \qquad (3\text{-}30)$$

If the material is linear elastic, then the distribution of shear stress is linear along the radial direction. In this case, by defining τ_{max} as the shear stress at $r = R_o$, the shear stress at any distance can be computed by the following equation:

$$\tau_{z\theta} = \left(\frac{\tau_{max}}{R_o}\right) r \qquad (3\text{-}31)$$

The average shear stress $\overline{\tau^*}_{z\theta}$ can be computed by the following equation.

$$\overline{\tau^*}_{z\theta} \int_{R_i}^{R_o} r^2 dr = \int_{R_i}^{R_o} \frac{\tau_{max}}{R_o} r^3 dr$$

$$\overline{\tau^*}_{z\theta} = \frac{3}{4} \frac{\tau_{max}}{R_o} \left(\frac{R_o^4 - R_i^4}{R_o^3 - R_i^3}\right) \qquad (3\text{-}32)$$

On the other hand, if an equivalent shear stress (that gives the same shear force as the linearly distributed shear stress) is considered, then the average shear stress $\overline{\tau^{**}}_{z\theta}$ can be computed as follows.

$$\overline{\tau^{**}}_{z\theta} = \frac{1}{2} \frac{\tau_{max}}{R_o}(R_o + R_i) \qquad (3\text{-}33)$$

By equating Eqs. (3-30) and (3-32) to get τ_{max} and substituting it into the Eq. (3-33), one gets

$$\overline{\tau^{**}}_{z\theta} = \frac{T}{\pi(R_o - R_i)(R_o^2 + R_i^2)} \qquad (3\text{-}34)$$

In this study, the shear stress is averaged from Eqs. (3-26) and (3-29) as shown below

$$\overline{\tau}_{z\theta} = \frac{1}{2}\left[\frac{3T}{2\pi(R_o^3 - R_i^3)} + \frac{T}{\pi(R_o - R_i)(R_o^2 + R_i^2)}\right] \qquad (3\text{-}35)$$

$$T = T_{LC} + T_{mem}$$

Since, the membrane is not used in the stacked-ring shear apparatus, thus:

$$T = T_{LC}$$

where,

T_{LC} = Torque detected by the inner load cell

In the stacked ring shear apparatus, the shear stresses measured at the top and bottom load cells are different. Therefore, Eq. 3-30 yields:

$$\bar{\tau}_{z\theta.Top} = \frac{1}{2}\left[\frac{3T_{Top}}{2\pi\left(R_o^{\ 3} - R_i^{\ 3}\right)} + \frac{T_{Top}}{\pi\left(R_o - R_i\right)\left(R_o^{\ 2} + R_i^{\ 2}\right)} \right] \quad (3\text{-}36a)$$

$$\bar{\tau}_{z\theta.Bo} = \frac{1}{2}\left[\frac{3T_{Bo}}{2\pi\left(R_o^{\ 3} - R_i^{\ 3}\right)} + \frac{T_{Bo}}{\pi\left(R_o - R_i\right)\left(R_o^{\ 2} + R_i^{\ 2}\right)} \right] \quad (3\text{-}36a)$$

3.3.4   Evaluation of soil-ring friction angle ($\sigma_{z\theta}$) in vertical direction

In the stacked-ring shear apparatus, the amount of generated friction in the vertical direction can be computed as the difference in the stress values measured by the top and bottom load cells. Therefore, the soil-ringfriction angle ($\delta_{z\theta}$) mobilized in the verticaldirectioncan be calculated as follows

From Eq. 3-27a and 3-27b,

$$P_{Top} = \left(\bar{\sigma}_{z.Top} \times A\right) \quad\quad\quad (3\text{-}39a)$$

$$P_{Bo} = \left(\bar{\sigma}_{z.Bo} \times A\right) \quad\quad\quad (3\text{-}39b)$$

The forces equilibrium within the specimen can be re-written as:

$$P_{Top} - P_{Bo} - F_{z\theta} + \left(\sigma_g \times A\right) = 0 \quad\quad (3\text{-}40)$$

$$F_{z\theta} = P_{Top} - P_{Bo} + \left(\sigma_g \times A\right)$$

where,

$F_{z\theta}$ is the generated friction between the soil particles and stacked rings.

The generated friction inside the specimen can be written as:

$$F_{z\theta} = f_{z\theta}\left(\int_0^{2\pi} R_i.d\theta + \int_0^{2\pi} R_o.d\theta\right) \qquad (3\text{-}41)$$

where,

$f_{z\theta}$ is frictional stress between the soil and metal rings in the vertical direction.

thus, the Eq. 3-40 becomes

$$P_{Top} - P_{Bo} + \left(\sigma_g \times A\right) = f_{z\theta}\left(2\pi.R_i + 2\pi.R_o\right)$$

$$f_{z\theta} = \frac{\left(P_{Top} - P_{Bo} + \sigma_g.A\right)}{2\pi\left(R_i + R_o\right)} \qquad (3\text{-}42)$$

From Eq. 3-42, the final formulation of soil-ring friction angle in the vertical direction ($\delta_{z\theta}$)becomes:

$$\delta_{z\theta} = \frac{f_{z\theta}}{\sigma_r}.\left(\frac{180}{\pi}\right)\text{deg.} \qquad (3\text{-}43)$$

3.3.5 Evaluation of soil-ringfriction angle($\delta_{\theta\theta}$) in the circumferential direction

Similar to the evaluation of friction in the vertical direction, the evaluation of the amount of generated friction in the circumferential direction can be computed based on the difference in shear stresses measured by the top and bottom load cells. Therefore, soil-ring friction angle in the circumferential direction ($\delta_{\theta\theta}$) can be formulated as follows:

from Eq. 3-35,

$$\bar{\tau}_{z\theta} = \frac{1}{2}\left[\frac{3T}{2\pi\left(R_o^{\;3} - R_i^{\;3}\right)} + \frac{T}{\pi\left(R_o - R_i\right)\left(R_o^{\;2} + R_i^{\;2}\right)}\right]$$

thus,

$$\bar{\tau}_{z\theta} = \frac{T}{2}\left[\frac{3}{2\pi\left(R_o^{\;3} - R_i^{\;3}\right)} + \frac{1}{\pi\left(R_o - R_i\right)\left(R_o^{\;2} + R_i^{\;2}\right)}\right]$$

$$\bar{\tau}_{z\theta} = \frac{T}{2}\left[\frac{3\pi\left(R_o - R_i\right)\left(R_o^{\;2} + R_i^{\;2}\right) + 2\pi\left(R_o^{\;3} - R_i^{\;3}\right)}{2\pi^2\left(R_o^{\;3} - R_i^{\;3}\right)\left(R_o - R_i\right)\left(R_o^{\;2} + R_i^{\;2}\right)}\right]$$

$$T = 2.\bar{\tau}_{z\theta}\left[\frac{2\pi^2\left(R_o^{\;3} - R_i^{\;3}\right)\left(R_o - R_i\right)\left(R_o^{\;2} + R_i^{\;2}\right)}{3\pi\left(R_o - R_i\right)\left(R_o^{\;2} + R_i^{\;2}\right) + 2\pi\left(R_o^{\;3} - R_i^{\;3}\right)}\right]$$

$$T_{Top} = 2.\bar{\tau}_{z\theta.Top}\left[\frac{2\pi^2\left(R_o^{\;3} - R_i^{\;3}\right)\left(R_o - R_i\right)\left(R_o^{\;2} + R_i^{\;2}\right)}{3\pi\left(R_o - R_i\right)\left(R_o^{\;2} + R_i^{\;2}\right) + 2\pi\left(R_o^{\;3} - R_i^{\;3}\right)}\right] \quad \text{(3-44a)}$$

$$T_{Bo} = 2.\bar{\tau}_{z\theta.Bo}\left[\frac{2\pi^2\left(R_o^{\;3} - R_i^{\;3}\right)\left(R_o - R_i\right)\left(R_o^{\;2} + R_i^{\;2}\right)}{3\pi\left(R_o - R_i\right)\left(R_o^{\;2} + R_i^{\;2}\right) + 2\pi\left(R_o^{\;3} - R_i^{\;3}\right)}\right] \quad \text{(3-44b)}$$

From Eq. 3-44a and Eq. 3-44b, the frictional force in the circumferential direction ($F_{\theta\theta}$) can be calculated as:

$$T_{Top} - T_{Top} - F_\theta = 0$$

$$F_{\theta\theta} = 2\left(\bar{\tau}_{z\theta.Top} - \bar{\tau}_{z\theta.Bo}\right)\left[\frac{2\pi^2\left(R_o^{\;3} - R_i^{\;3}\right)\left(R_o - R_i\right)\left(R_o^{\;2} + R_i^{\;2}\right)}{3\pi\left(R_o - R_i\right)\left(R_o^{\;2} + R_i^{\;2}\right) + 2\pi\left(R_o^{\;3} - R_i^{\;3}\right)}\right] \quad \text{(3-45)}$$

where,

$$F_{\theta\theta} = f_{\theta\theta}\left(\int_0^{2\pi} R_i.d\theta + \int_0^{2\pi} R_o.d\theta\right) \quad \text{(3-46)}$$

thus, the soil-wall frictional stress ($f_{\theta\theta}$) in the circumferential direction can be calculated as

$$f_{\theta\theta} = \frac{2\left(\bar{\tau}_{z\theta.Top} - \bar{\tau}_{z\theta.Bo}\right)\left[\dfrac{2\pi^2\left(R_o^3 - R_i^3\right)\left(R_o - R_i\right)\left(R_o^2 + R_i^2\right)}{3\pi\left(R_o - R_i\right)\left(R_o^2 + R_i^2\right) + 2\pi\left(R_o^3 - R_i^3\right)}\right]}{\left(\displaystyle\int_0^{2\pi} R_i.d\theta + \int_0^{2\pi} R_o.d\theta\right)} \qquad (3\text{-}47)$$

and the soil-ring friction angle in the circumferential direction ($\delta_{\theta\theta}$)is:

$$\delta_{\theta\theta} = \frac{f_{\theta\theta}}{\sigma_h}.\left(\frac{180}{\pi}\right) \text{ deg.} \qquad (3\text{-}48)$$
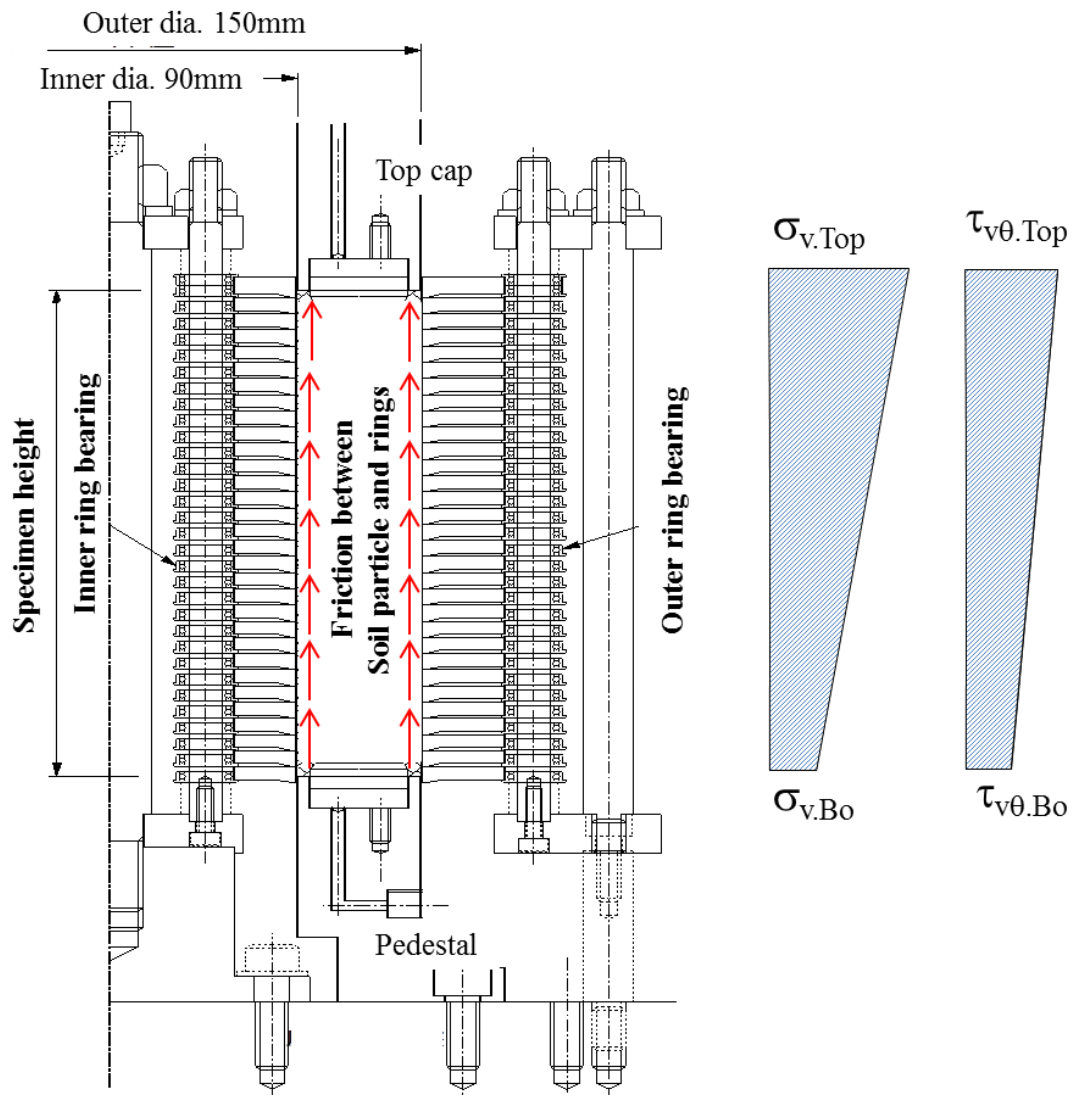
Fig. 3.4: Generated friction between the soil particles and stacked-rings
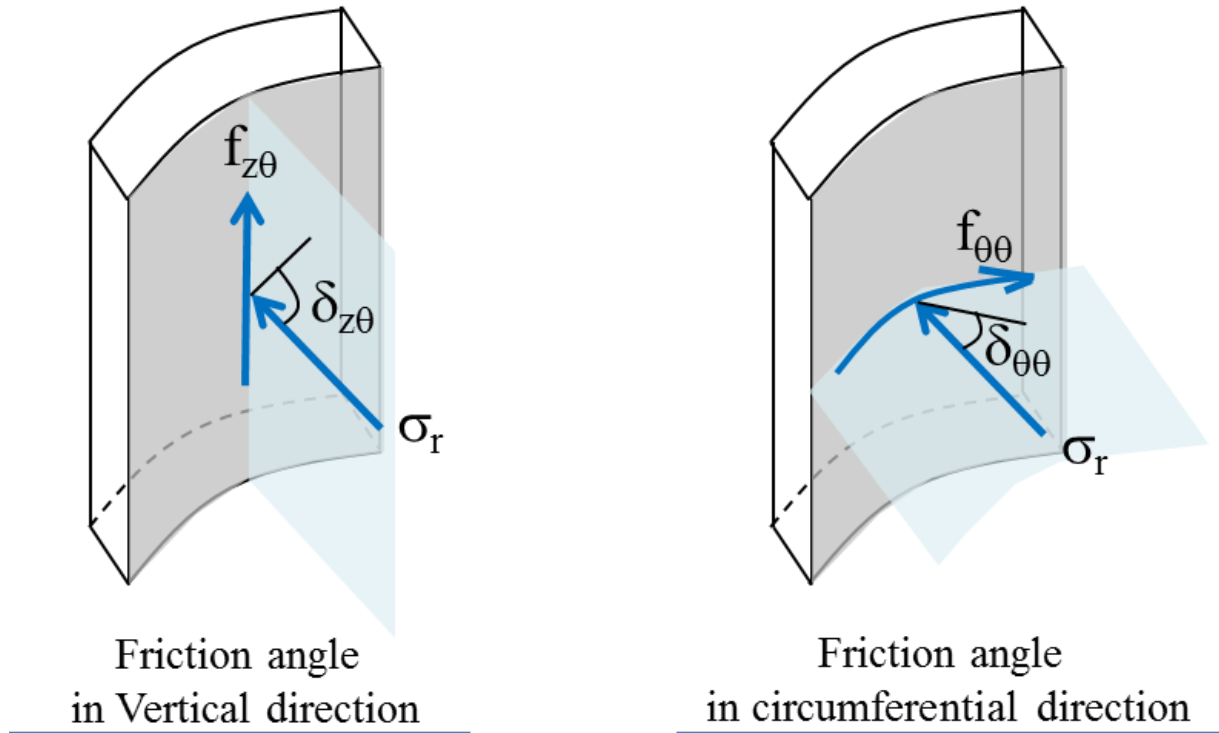
Fig. 3.5 Friction angles in vertical and circumferential direction

3.3.6 Principal stresses (σ_1 and σ_3)

Principal stresses can be computed from the four stress components as follows

$$\sigma_1 = \frac{\sigma_z + \sigma_\theta}{2} + \sqrt{\left(\frac{\sigma_z - \sigma_\theta}{2}\right)^2 + (\tau_{z\theta})^2} \qquad (3\text{-}49)$$

$$\sigma_2 = \sigma_r \qquad (3\text{-}50)$$

$$\sigma_3 = \frac{\sigma_z + \sigma_\theta}{2} - \sqrt{\left(\frac{\sigma_z - \sigma_\theta}{2}\right)^2 + (\tau_{z\theta})^2} \qquad (3\text{-}51)$$

3.4 Strain formulation

3.4.1 Global strain measurement

There are four strain components in the hollow cylinder torsional shear apparatus, which are the axial strain ε_z, the radial strain ε_r, the circumferential strain ε_θ, and the shear strain $\gamma_{z\theta}$ as shown in Fig. 3.6. The radial (ε_r) and circumferential (ε_θ) strains of a soil element can be calculated as,

$$\varepsilon_r = -\frac{u + (\delta u / \delta r)dr - u}{dr} = -\frac{du}{dr} \qquad (3\text{-}52)$$

$$\varepsilon_\theta = -\frac{(u + r)d\theta - rd\theta}{rd\theta} = -\frac{u}{r} \qquad (3\text{-}53)$$

where,

u is the deformation of a soil element in radial direction

r is the distance to the center of soil element from the center of the specimen
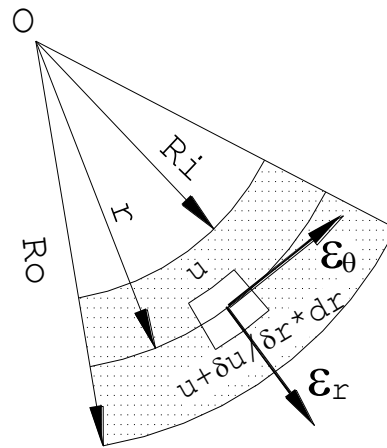
Fig. 3.6 Radial and circumferential strains of a soil element

Combining Eqs. (3-52) and (3-53) yields

$$\frac{d\varepsilon_\theta}{dr} + \frac{1}{r}\left(\varepsilon_\theta - \varepsilon_r\right) = 0 \quad (3\text{-}54)$$

If it is assumed that the distribution of u is linear in the radial direction, then

$$u = \frac{u_o - u_i}{R_o - R_i} r + \frac{u_i R_o - u_o R_i}{R_o - R_i} \qquad (3\text{-}55)$$

Therefore ε_r is given by,

$$\overline{\varepsilon}_r = -\frac{u_o - u_i}{R_o - R_i} \qquad (3\text{-}56)$$

and $\overline{\varepsilon}_\theta$ can be calculated by

$$\overline{\varepsilon}_\theta \int_{R_i}^{R_o} r\,dr = \int_{R_i}^{R_o} \varepsilon_\theta\, r\,dr = -\int_{R_i}^{R_o} \frac{u}{r} r\,dr$$

$$\overline{\varepsilon}_\theta = -\frac{u_o + u_i}{R_o + R_i} \qquad (3\text{-}57)$$

Since no lateral deformation is allowed in the lateral direction in the stacked-ring shear apparatus,

$$\overline{\varepsilon}_r = \overline{\varepsilon}_\theta = 0$$

while ε_z and $\gamma_{z\theta}$ can be calculated as

$$\varepsilon_z = - \, dw \, / dz \qquad (3\text{-}58)$$

$$\overline{\varepsilon}_z = -\frac{\Delta H}{H} \qquad (3\text{-}59)$$

$$\gamma_{z\theta} = r\, d\theta / \, dz \qquad (3\text{-}60)$$

$$\overline{\gamma}_{z\theta} = \frac{(R_o + R_i)}{2} \frac{\Delta\theta}{H} \qquad (3\text{-}61)$$

where,

$\bar{\varepsilon}_z$, $\bar{\varepsilon}_r$, $\bar{\varepsilon}_\theta$, $\bar{\gamma}_{z\theta}$ is theaverage axial, radial, circumferential, and shear strains of the specimen, respectively

u_o, u_i, w : Displacements in the radial direction at outer and inner radii, and vertical directionsof the specimen, respectively

$\Delta\theta$ is therotation angle.

3.4.2 Local shear strain measurement usingimage analysis in stacked-ring shear apparatus

It is well understood that the global deformation characteristics of soil are occasionally different from their local ones. The difference is more pronounced on a specimen that had undergone large deformation. The global deformation of soil measured by the potentiometer and gap sensor only represents the average deformation of soil specimen, while the local deformation will provide accurate details of the deformation characteristics of the specimen during a multiple-liquefaction test. These local deformation characteristics are closely related to the change of soil fabric (structure) in the post liquefaction state as well as possible strain localization. A specimen that undergoes large shear deformation is expected to have larger extent of non-uniformity along the height of the specimen (Kiyota et al., 2008; Chiaro et al., 2013). Some part of the specimen deform more than the others. The degree of non-uniform shear deformations within the specimens may create two major effects, which are the non-uniform void ratios distribution within the specimen as well as induced anisotropy. These two effects have significant impact to the soil behaviors during multiple liquefactions (Oda et al., 2001; Towhata and Ishihara, 1985; Suzuki and Toki, 1984; among others). The impacts of these two effects will be discussed further in detail on Chapter 5 and 6, respectively.

In this study, image analysis was used to measure the local deformations of the specimen. Image analysis has been widely used in the geotechnical engineering field due to need of accurate local measurements. Currently, there are various methods/means specifically developed by many researchers to conduct image analysis. Scarpelly and Wood (1982) and Han and Vardoulakis (1991) used X-ray radiograph method to investigate the void distributions in the sheared specimen. Tatsuoka et al. (1990) and Mokni (1992) used laser technique. Stereo photogrammetry was used by Desrues et al. (1985), Yoshida et al. (1994), and Harris et al. (1995) to investigate the shear band evolution, particle velocimetry technique (Sadrekarimi and Olson,2010, among others) uses a method to track single particle movements through a transparent media, among others.

In the current study, animage analysis method similar to the one used by Yoshida and Tatsuoka (1997), and Wahyudi et al.(2012) is employed to observe specimen shear deformation. This techniqueworks by tracking the movement of the particular object that has color contrast as compared to their surroundings. To do so, a series of imagesare taken during the entire test atconstant time interval. Full details of the employed image analysis technique have been described in Chapter 2.

Despite its great benefits, conducting image analysis in stacked-ring shear apparatus has some limitations, primarily due to the cylindrical shape of the specimen. Unlike the image analysis conducted on prismatic specimens such as those in plane strain compression test or sand box model test, the movement captured in the cylindrical specimen is not the real ones but the distorted ones. As one can easily understand, the digital camera works by transforming a three-dimensional object (horizontal, vertical, and depth) into a two-dimensional image (horizontal and vertical) as projected on the image plane as shown in points 2 and 2' in illustrated Fig. 3.7. Since the stacked-ring itself has a cylindrical shape, the deformation of soil is not just along the vertical and horizontal directions, but also in the depth. In the image analysis research field, this phenomenon is called barrel distortion and is schematically illustrated in Fig. 3.8.
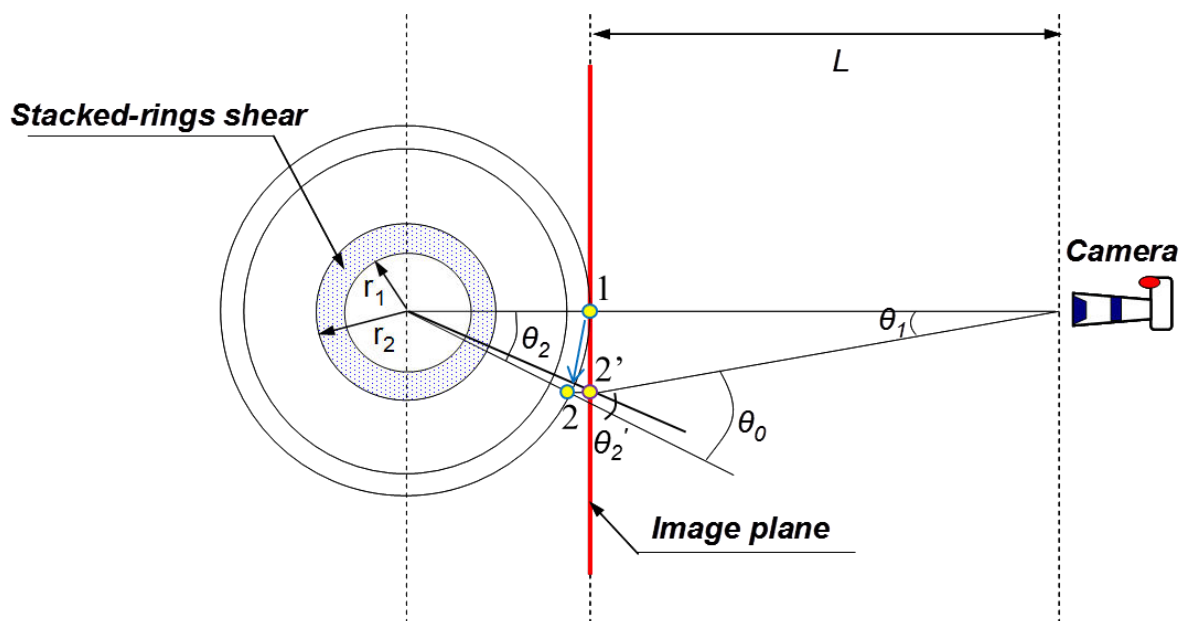
Fig. 3.7: Illustration of photo taking setting of the stacked-ring shear apparatus
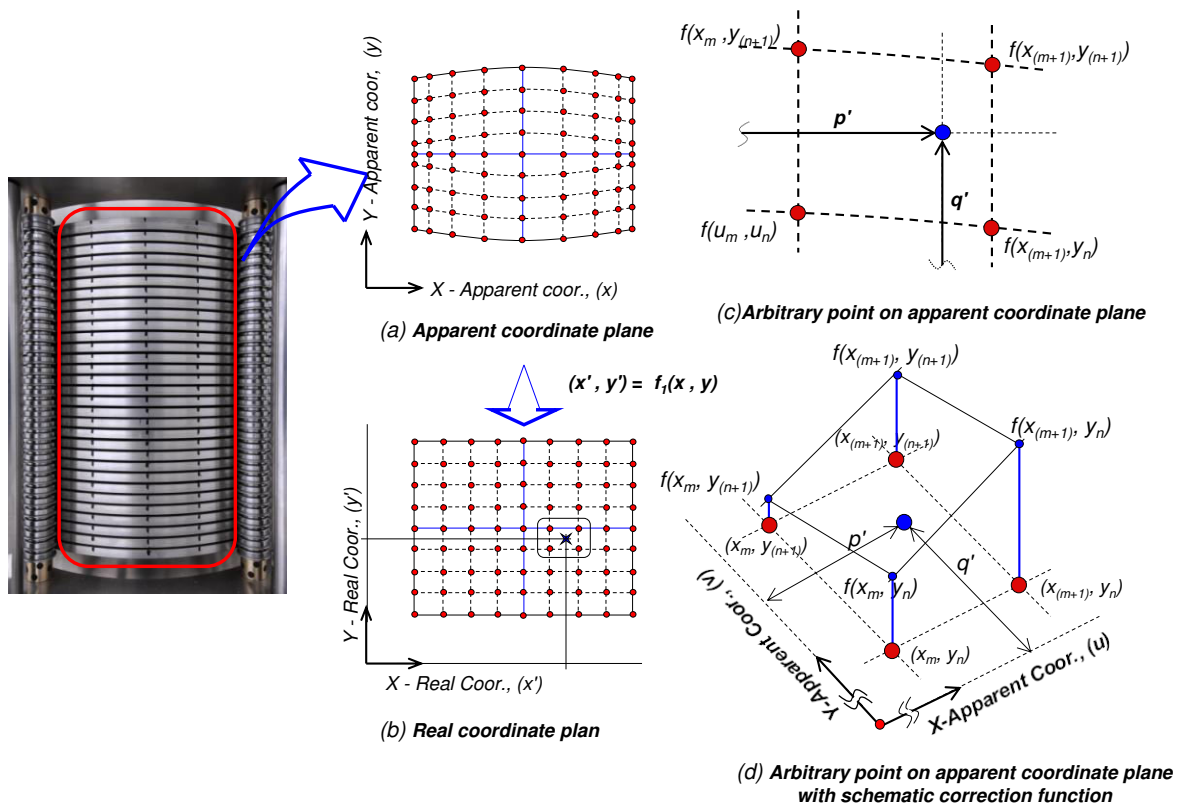
Fig. 3.8: Correction on image analysis by using bilinear interpolation method

To obtain the real deformation of soil from the distorted one, a mathematical solution is needed. Wahyudi et al. (2011) proposed simple mathematical solution to obtain the real coordinates (x', y') from the distorted ones (x, y) that can be written as follows:

$$(x', y') = f_1(x, y)$$
$$x'_{(m)} = a_{0(m)}.1 + a_{1(m)}.x_{(m)} + a_{2(m)}.y_{(m)} + a_{3(m)}.x^2_{(m)} + a_{4(m)}.x_{(m)}.y_{(m)} + a_{5(m)}.y^2_{(m)}$$
$$y'_{(n)} = b_{0(n)}.1 + b_{1(n)}.x_{(n)} + b_{2(n)}.y_{(n)} + b_{3(n)}.x^2_{(n)} + b_{4(n)}.x_{(n)}.y_{(n)} + b_{5(n)}.y^2_{(n)}$$

(3-62)

where, *x'* and *y'* are the real coordinates in the horizontal and vertical directions, respectively; *x* and *y* are the apparent coordinates in horizontal and vertical directions, respectively. The coefficients a_0 through a_5 and b_0 through b_5 are assigned based on calibration results by means of least square error method. *m* and *n* are the number of column and row, respectively.

Since the vertical movement is not allowed in the stacked-ring shear apparatus, Eq. 3.62 can be simplified as follows:

$$(x', y') = f_1(x, y)$$
$$x'_{(m)} = a_{0(m)}.1 + a_{1(m)}.x_{(m)} + a_{2(m)}.y_{(m)} + a_{3(m)}.x^2_{(m)} + a_{4(m)}.x_{(m)}.y_{(m)} + a_{5(m)}.y^2_{(m)}$$

(3-63)

The coefficients a_0 to a_5 can be obtained by least square error method

Eq. 3-63 can be re-written as

$$
\begin{pmatrix} x_0 \\ x_1 \\ x_2 \\ \vdots \\ x_n \end{pmatrix}^T = \begin{pmatrix} a_{0(m)} & a_{1(m)} & a_{2(m)} & \dots & a_{5(m)} \end{pmatrix} \begin{bmatrix} 1 & 1 & 1 & \dots & 1 \\ x_{0(m)} & x_{1(m)} & x_{2(m)} & \dots & x_{5(m)} \\ y_{0(m)} & y_{1(m)} & y_{2(m)} & \dots & y_{5(m)} \\ x_{0(m)}^2 & x_{1(m)}^2 & x_{2(m)}^2 & \dots & x_{5(m)}^2 \\ x_0 y_{0(m)} & x_1 y_{1(m)} & x_2 y_{2(m)} & \dots & x_5 y_{5(m)} \\ y_{0(m)}^2 & y_{1(m)}^2 & y_{2(m)}^2 & \dots & y_{5(m)}^2 \end{bmatrix}
$$

where the observation space coordinate is,

$$
x'_{(m)} = [x_{0(m)} \; x_{1(m)} x_{2(m)} \; \dots \; x_{i(m)}]
$$

and the coefficients of polynomial n-order can be expressed by,

$$
a = [a_{0(m)} a_{1(m)} a_{2(m)} a_{3(m)} a_{4(m)} \; a_{5(m)}]
$$

then,

$$
A = \begin{bmatrix} 1 & 1 & 1 & \dots & 1 \\ x_{0(m)} & x_{1(m)} & x_{2(m)} & \dots & x_{5(m)} \\ y_{0(m)} & y_{1(m)} & y_{2(m)} & \dots & y_{5(m)} \\ x_{0(m)}^2 & x_{1(m)}^2 & x_{2(m)}^2 & \dots & x_{5(m)}^2 \\ x_{0(m)} y_{0(m)} & x_{1(m)} y_{1(m)} & x_{2(m)} y_{2(m)} & \dots & x_{5(m)} y_{5(m)} \\ y_{0(m)}^2 & y_{1(m)}^2 & y_{2(m)}^2 & \dots & y_{5(m)}^2 \end{bmatrix}
$$

Eq. 3.63can be simplified as,

$$
x'_{(m)}{}^T = a \cdot A \qquad (3\text{-}64)
$$

The least mean square error can be written as

$$
\epsilon = (x'_{(m)} - a.A)^T . \, (x'_{(m)} - a.A) \qquad (3\text{-}65)
$$

Then, by multiplying each side of Eq. (3-64) with A^T yields

$$x'_{(m)}{}^T . A^T = a . A . A^T \qquad (3\text{-}66)$$

Finally the solution is,

$$a = [(A \times A^T)^{-1} \times A^T] . x'_{(m)}{}^T \qquad (3\text{-}67)$$

The local shear strain of the specimen is calculated based on the relative displacement in between two neighborhood rings. Fig. 3.9 shows the general concept of shear strain on a single elementthat deforms along X and Y directions, while Fig. 3.10 shows the case of shear strain on single element in stacked-ring shear apparatus.
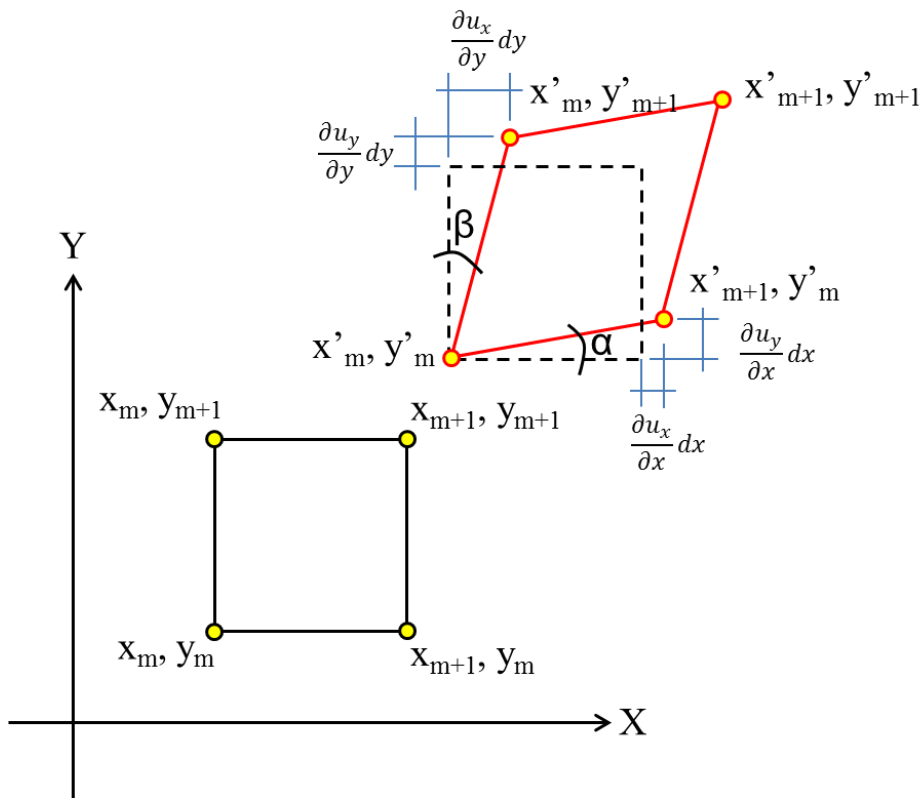
Fig. 3.9: General shear strain concept on two dimensional element of rigid body
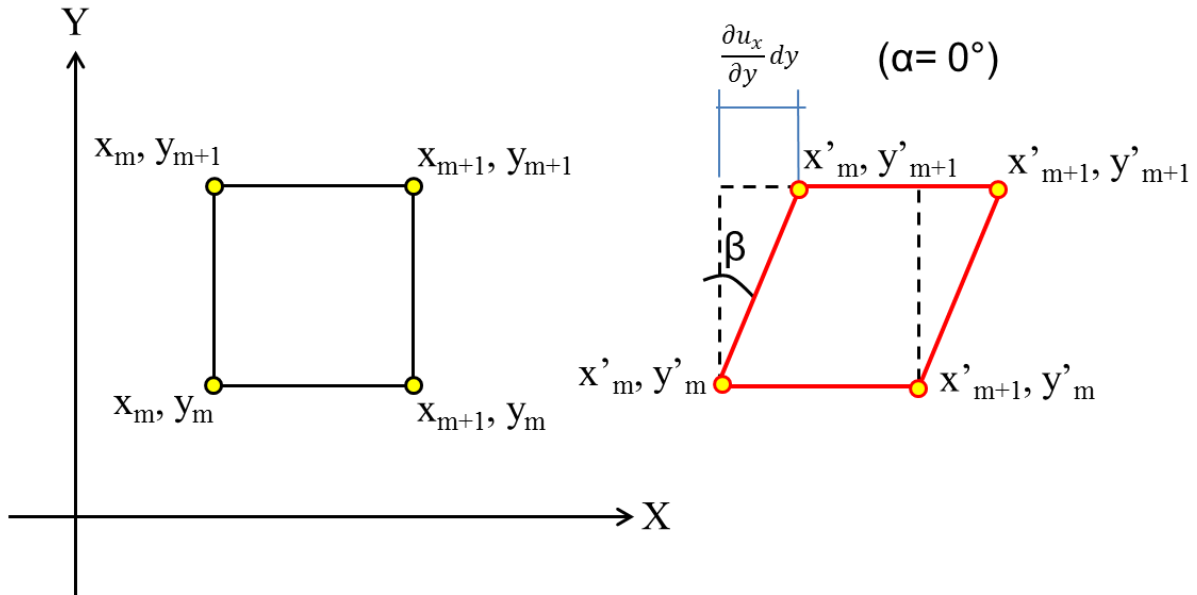
Fig. 3.10: Shear strain concepts in the stacked-ring shear apparatus

Based on Fig. 3.9, the general equation of single element shear strain can be written as follows

$$\gamma_{Loc.} = \alpha + \beta \qquad (3\text{-}68)$$

$$\alpha = \tan\left(\frac{\dfrac{\partial u_y}{\partial x}dx}{\dfrac{\partial u_x}{\partial x}dx + (\Delta X)}\right) \qquad (3\text{-}69)$$

$$\beta = \tan\left(\frac{\dfrac{\partial u_x}{\partial y}dy}{\dfrac{\partial u_y}{\partial y}dy + (\Delta Y)}\right) \qquad (3\text{-}70)$$

where,

β is the deformation angle in the vertical direction.

α is the deformation angle in the circumferential direction. In the stacked-ring shear apparatus, α is zero, since no vertical deformation allowed.

$\gamma_{Loc.}$ is the local shear strain of each section.

and

$$\Delta X = \left(x_{m+1} - x_m \right)$$

$$\Delta Y = \left(y_{m+1} - y_m \right)$$

Then Eq. 3-68 can be re-written as,

$$\gamma_{Loc.} = \alpha + \beta = \left\{ \tan\left(\frac{\dfrac{\partial u_y}{\partial x} dx}{\dfrac{\partial u_x}{\partial x} dx + \left(\Delta X \right)} \right) + \tan\left(\frac{\dfrac{\partial u_x}{\partial y} dy}{\dfrac{\partial u_y}{\partial y} dy + \left(\Delta Y \right)} \right) \right\} \qquad (3\text{-}71)$$

Since, there is no circumferential strain and vertical strain in the stacked-ring shear apparatus, the shear strain equation written in Eq. 3-71 can be simplified as described below:

Since

$$\alpha = 0$$

and

$$\frac{\partial u_y}{\partial y} dy = 0$$

$$\beta = \tan\left(\frac{\dfrac{\partial u_x}{\partial y} dy}{\left(\Delta Y \right)} \right)$$

thus, the final equation of shear strain in the stacked-ring shear apparatus becomes

$$\gamma_{Loc.} = \beta = \tan\left(\frac{\dfrac{\partial u_x}{\partial y} dy}{\left(\Delta Y \right)} \right) \qquad (3\text{-}72)$$

3.5   References

1. Ampadu, S. I. K. (1991). Undrained behaviour of kaolin in torsional simple shear. *Doctor of engineering thesis*, Department of civil engineering, The University of Tokyo, Japan.

2. Chiaro, G. (2010) "Deformation properties of sand with initial static shear in undrained cyclic torsional shear tests and their modelling," *Doctor of Engineering Dissertation*, Department of Civil Engineering, The University of Tokyo, Japan.

3. De Silva, L. I. N. (2008). "Deformation characteristics of sand subjected to cyclic drained and undrained torsional loadings and their modelling", *Doctor of Engineering Dissertation*, Department of civil engineering, The University of Tokyo, Japan.

4. Desrues, J., Lanier, J., and Stutz, P. (1985) "Localization of the deformation in tests on sand sample." *Engrg. Fracture Mech.*, 21(4), pp. 909-921.

5. Han, C. and Vardoulakis, I. G. (1991) "Plane strain compression experiments on water-saturated fine-grained sand." *Geotechnique*, 41(1), pp. 49-78.

6. Harris, W. W., Viggiani, G., Mooney, M. A. and Finno, R. J. (1995). "Use of stereophotogrammetry to analyze the development of shear bands in sand". *Geotechnical Testing Journal* 18 (4). pp. 405 – 420.

7. Hight, D. W., Gens, A. and Symes, M. J. (1983). "The development of a new hollow cylinder apparatus for investigating the effects of principal stress rotation in soils", *Geotechnique*, Vol. 33, No. 4, pp. 255-383.

8. Mokni, M. (1992) "Relations entre deformations en masse et deformations localisees dans les materiaux granulaires." *PhD Thesis*, Universite J. Fourier de Grenoble, France.

9. Oda, M., Kawamoto, K., Suzuki, K., Fujimori, H. and Sato, J. (2001): "Microstructural interpretation on reliquefaction of saturated granular soils under cyclic loding." *Geotechnical and Geo-environmental Engineering*, Vol. 127, no. 5.

10. Okuchi, Y. and Tatsuoka, F. (1984) "Some factors affecting Ko-values of sand measured at triaxial cell." *Soils and Foundations*, 24(3), pp. 52-68.

11. Pratt, W. K. (2007) "Digital Image Processing," 4th Ed, John Willey and Sons.

12. Saada, A. S. (1988). "Hollow cylinder torsional devices: Their advantages and limitations", State of the art paper. *In Advanced triaxial testing of soil and rock, ASTM STP 977*, Donaghe, R. T., Chaney, R. C. and Silver, M. L. (eds.), ASTM, Philadelphia, pp. 766-795.

13. Sadrekarimi, A. and Olson, S. A. (2010). "Shear band formation observed in ring shear tests on sandy soils". *Journal of Geotechnical and Geoenvironmental Engineering*, ASCE.

14. Scarpelli, G. and Wood, D. M. (1982) "Experimental observations of shear band patterns in direct shear tests." *Proc., IUTAM Conf. on Deformation and Failure of Granular Materials*, Balkema, Rotterdam, Netherland, pp. 473-484.

15. Tatsuoka, F., Pradhan, T. B. S., and Yoshi-ie, H. (1989) "A cyclic undrained simple shear testing method for soils." *Geotech. Testing J.*, 12(4), pp. 269-280.

16. Timoshenko, S. P. and Goodier, J. N. (1970). *Theory of Elasticity*. Third edition, McGraw-Hill Book company, Inc., N.Y., pp. 65-71.

17. Viggiani, G. and Atkinson, J. (1995) "Interpretation of bender element tests." *Geotechnique*, 45(1), pp. 149-154.

18. Wahyudi, S., Miyashita, Y. and Koseki, J. (2012) "Shear band behavior of sand in torsional shear tests by means of image analysis." *Proc. ISSMGE Conf. of Advances in Multiphisical Tesing of Soils and Shale*s, Lausanne, Switzerland.

19. Wahyudi, S., Koseki, J. and Sato, T. (2014) "The characteristics of re-liquefied behaviors of sand by means of image analysis in the stacked-ring shear apparatus." *Bulletin of ERS*, Institute of Industrial Science-University of Tokyo.

20. Yoshida, T., Tatsuoka, F., Siddique, M. S. A., Kamegai, Y. and Park, C. S. (1994) "Shear banding in sands observed in plane strain compression," *Proc. Symp. On Localization and Bifurcation Theory for Soils and Rocks*, R. cambou, J. Desrues, and I. Vardoulakis, eds., Balkema, Rotterdam, The Netherlands, pp. 165-179.

21. Yoshida, T. and Tatsuoka, F. (1997) "Deformation property of shear band subjected to the plane strain compression and its relation to particle characteristics." *Proc. of 14th Intl. Conf. on Soil Mech. and Found. Engrg.*, 1, pp. 237-240.

4 DEVELOPMENT OF STACKED-RING SHEAR APPARATUS

4.1   Introduction

In geotechnical engineering practice, several types of testing apparatuses such as direct shear, triaxial, hollow cylinder torsional shear and ring shear apparatusesare commonly used to investigate the soil behaviors under various testing conditions. Certainly, each of these apparatus has its own advantages and disadvantages in terms of specimen preparations, capability to simulate various testing conditions among others.

Direct shear – it is one of the simplest soil testing apparatus. Some of its advantages are: 1) its capacity to test undisturbed and reconstitute samples; 2) a well-established testing procedures and easy specimen preparation; 3) it is capable of simulating drained and undrained tests; 4) it is capable of simulating the rotation of principal stresses, though not continuous; 5) it is capable of maintaining cross-sectional area of the specimen to remain constant during shear deformation. Silver et al., 1980, Tatsuoka and Silver, 1981 among others conducted drained and undrained tests, while Finn and Vaid, 1977 conducted constant volume test using direct shear apparatus. Despite these advantageous, there are major drawbacks in using direct shear apparatus. The specimen tested in direct shear apparatus can achieve only limited level of shear deformation. Kramer et al. (2002) found possibility of pinching effects to the specimen if it was sheared with large shear deformation. In addition, direct shear apparatus also induces large friction between the soil particles and the shear wall. Therefore, the applied stress within the specimen is not uniform.

Triaxial - the triaxial apparatus is probably the most well-known and widely-used soil testing apparatus due to their numerous advantages: 1) the capacity to test undisturbed and re-constituted samples; 2) well-established testing procedures; 3) capable of conducting stress controlled and strain controlled tests; 4) the capacity to simulate various stress paths (e.g.. constant confining pressure; constant deviator stress, etc (Modoni et al., 2011); 5) the capacity to conduct drained and undrained tests; 6.) capable to control the rotation of principal stress, though limited, among others. The major disadvantages of the triaxial apparatus are as follows; it is only capable of testing the soil sample under limited shear deformation; and excessive deformation in the triaxial apparatus creates bulging effects, which increases the cross sectional area of the specimen, thus, the stress distributions is not uniform along the height of the specimen (Kramer et al. 1999). The triaxial apparatus is also not capable to evaluate the effect of intermediate stress to specimen (σ_2). Other disadvantage of this apparatus is unequal shear resistances in compression and extension sides during cyclic shear loading.

Torsional shear apparatus – it is the apparatus that has almost complete capabilities as compare to the two previous apparatuses. Some of the advantages are: 1.) capacity to perform tests on various combinations of stress conditions (e.g. controlled isotropic, anisotropic, and etc) 2.) capacity to perform stress controlled and strain controlled tests; 3.) capableof continuously simulating the rotation of principal stress; 4.) capableof performing drained and undrained tests, 5) capable to investigate the effect of intermediate stress (σ_2), among others. However, it has also some disadvantages, such as the difficulties to conduct the test using undisturbed sample and limitation to maintain the geometry of the specimen at very large shear strain levels (Kiyota, 2007; De Silva, 2008; and Chiaro, 2010).

Ring shear – the advantages of the ring shear apparatus are: 1.) simple specimen preparation; 2.) the capacity to conduct constant stress and constant volume tests; 3.) the capacity to perform stress controlled and strain controlled tests; 4.) the capacity to simulate continuously the rotation of principal stresses, though uncontrolled; 5.) capacity to apply from very large to virtually unlimited shear deformation. The major disadvantage of the ring-shear apparatus is the excessive friction generated between the soil particle and the rigid wall of the rings itself. As a result, the stress distributions are not uniform throughout the specimen.

From the above descriptions, it can be understood that none of these apparatuses are perfect. Each of them has its own advantages and disadvantages depending on the purpose of the test to be conducted. The major difference between direct shear, triaxial and hollow cylinder torsional shear apparatuses as compared to the ring shear apparatus is given by the extent of shear deformation that can be achieved. In fact, the earlier apparatuses are only capable of achieving limited shear deformation. Alternatively, the ring shear apparatus can apply from very large to virtually unlimited shear deformation while still maintaining the geometry of the specimen constant. This aspect is essential in the simulation of multiple-liquefaction tests.

Typicalring shear apparatus,also known as split ring shear, consists of two parts, which are the fixed ring and rotating ring. The first version of ring shear apparatus was developed by Hvorslev (1939). Such ring shear device was only capable of shearing the soil sample on a predetermined failure surface corresponding to the separation plane between the upper and lower rings. Since then, the ring shear apparatus has been continuously developed by various researchers such as La Gatta (1970), Bishop et al, (1971), Bromhead (1979), Hungr and Morgenstern (1984), Tika (1989), Garga and Sendano (2002), Sassa (1984), Sassa (2004), Sadrekarimi and Olson (2007), and Wahyudiet al. (2013). However, until now, the most commonly used ring shear device is that developed by Bishop et al. (1971). That is, Bishop's ring shear device has the advantage to measure the generated friction within the specimen e

the wall by two pairs of load cells (i.e. axial and torque) in both the rotating and fixed parts of the rings.Significantly, in the split ring shear apparatus, the specimen is confined between rigid boundaries along the radial direction. This feature allows the specimen to be sheared under very large deformation while maintaining the cross sectional area and thus its volume. Due to this capability, most of the studies conducted by using ring shear were meant to investigate the residual strength and liquefied shear strength of soil (Hvorslev, 1939, Bishop et al, 1971, Sassa et al. 2003, Sadrekarimi and Olson, 2011, among others).

However in the Bishop's ring shear type, two major problems, namely non-uniformity of stresses and of strains throughout the specimen as well as soil extrusion, commonly arise.

<u>Stresses and strains non-uniformity</u> – these problems appear as direct consequence of an absence of flexible membrane in the ring shear apparatus. Since the split ring shear device is composed by two rigid rings (upper and lower rings), the stresses and strains non-uniformity are pronounced. In addition, due to generation of excessive friction, the major shear forces are applied in the area where the two rings are separated, as shown in schematically in Fig. 4.1. As a result, like the direct shear tests, large deformation is essentially concentrated around the shear failure plane, while elsewhere only very small shear deformation is developed.

<u>Soil extrusion</u> – it is a critical problem in the split ring shear apparatus (Bishop, 1971; Tika et al, 1996; Iverson et al, 1998). The soil particle may extrude in the same area where large shear deformation occurs. The extruded soil generates additional friction that reduces the applied stresses. As a result, the apparent stresses measured by the load cells are much larger than those actually applied on the specimen. In many cases, the loading process cannot be continued if the soil particles keep extruding from the ring shear.

In 2011, in the Institute of Industrial Science, The University of Tokyo, a new type of ring shear apparatus, so called stacked-ring shear apparatus, was developed. This apparatus could provide the solution to the shortcomings of conventional split ring shear devices. The main purpose of the stacked-ring shear apparatus is to combine the advantages of hollow cylinder torsional shear apparatus and ring shear into a unique device. The stacked-ring shear is composed by thin pieces of vertically stacked donut-shape rings as schematically shown in Fig. 3.2. The stacked rings, made of hardened stainless steel having a thickness of 5mm, are separated each other by a 0.1mm spacer that prevents any contact between subsequent rings. Thus, each ring is free to move independently in the circumferential direction. Such 0.1mm space in between rings also will minimize extrusion of soil particle larger than 0.1mm during shearing.

To prevent as much as possible soil extrusion, Toyoura sand having mean particle diameter (D_{50}) of about 0.200mm, and fines content (F_c) of about 0.1%, was used as a testing material. Need to be noted that in the constant stress tests, there is the possibility that soil particles may extrude during shearing due to the particle crushing (i.e., after crushing particles might become very small and thus slides out form the 0.1mm gap). However, it was confirmed by visual observation conducted during multiple-liquefaction tests under constant volume condition, that the occurrence of particle crushing was negligible.

A sequence of 5mm-thick individual rings (as used in this study) ensures a substantial reduction of the degree of stresses and strains non-uniformity along the specimen height, compared to conventional split ring shear apparatus. Bishop et al. (1971), Hungr and Morgenstern (1984), Tika (1989), Garga and Sendano (2002), among others have used short-size ring shear apparatuses with specimen height less than 20mm. In the short-size ring shear device the amount of generated friction in the vertical direction can be reduced as much as possible. However, end restraint effects became predominant. On the other hand, tall-size ring shear device (Sassa et al., 2204; Sadrekarimi and Olsen, 2007) are expected to generate larger friction in both vertical and circumferential directions, thus, stresses and strains non-uniformity becomes predominant.

The generated friction in the ring shear apparatuses reduces both the vertical and shear stresses applied to the specimen. As a result, the apparent stresses are higher than those actually applied on the specimen. The generated friction in the circumferential direction can be greatly reduced in the stacked-ring shear apparatus, while the generated friction in the vertical direction remains to be the main challenge. A complete elimination of generated friction may not be possible. However, reducing the amount of generated friction in the stacked-ring shear apparatus is crucial in performing the liquefaction tests and becomes one of the main objectives of this research.

In principle, there are four possible modifications that can be made for reducing the excessive friction generated in stacked-ring shear apparatus:

1. The height of the stacked-ring shear can be reduced by simply removing some of the rings. By reducing the height of the stacked rings, obviously the friction will decrease due to smaller contact forces between the soil particles and the stacked-rings itself. However, this method will not eliminate the generated friction completely.

2. Moreover, the surface of the stacked-rings can be coated with frictionless material. Similar to the previous method, this method may only reduce the generated friction but not eliminate it completely.

3. Also, the diameter of the stacked-rings can be increased. In fact, a larger diameter of the specimenmeans a larger contact forces between the load cell and the specimen. This eventually may decrease the proportion of friction applied to the specimen. However, this method also may not fully eliminate the generated friction and also is difficult to employ in the current stacked-ring shear apparatus. In addition, changing the diameter of the specimen means major modifications on the apparatus, which is a very time consuming process.

4. The use of a pedestal connected to elastic springs may help to reduce the friction. However, similar to the third method, this method may take a long time to be realized. By using a pedestal connected to elastic springs, both the specimen and the stacked-ring shear will move together during consolidation, hence, the friction can be drastically reduced. However, this friction can be eliminated only during consolidation or re-consolidation process, but the friction will be generated during application of shear loading.

All the aforementioned options were considered during early development of the stacked-ring shear apparatus. Yet, due to the lack of time, only points 1 and 2 were possible to be made during this study. Further improvement is therefore expected in the future.

The series of liquefaction tests were carried out in the stacked ring shear apparatus on dry sand specimens under constant volume condition. It is assumed that the reduction of effective stress (vertical stress in ring shear apparatus) in dry sample during constant volume tests is equivalent to the increase of pore water pressure generation in undrained fully saturated tests. The first investigation to prove this assumption was conducted by Taylor (1952). Later Bjerrum and Landva (1966) and Dyvik et al. (1987) verified this theory in direct simple shear tests, while Berre (1982) and Sasitharan et al. (1994) verified it using triaxial apparatus.
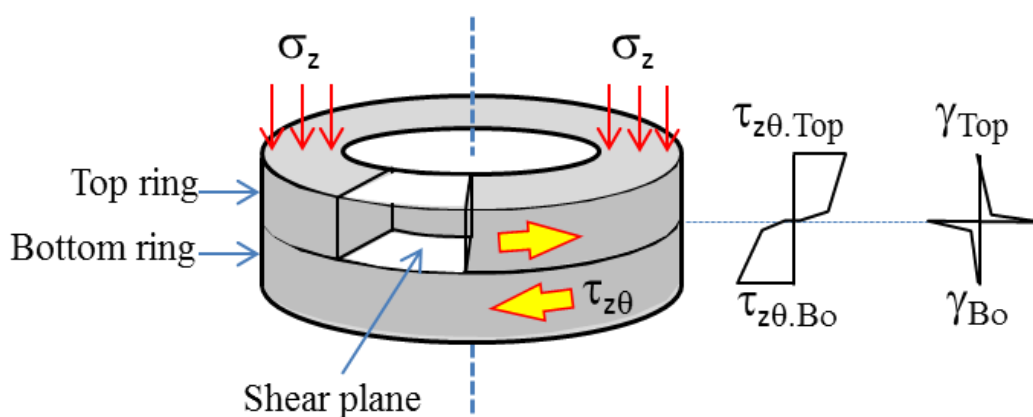
Fig. 4.1: Common split ring shear apparatus (Sadrekarimi and Olson, 2007)
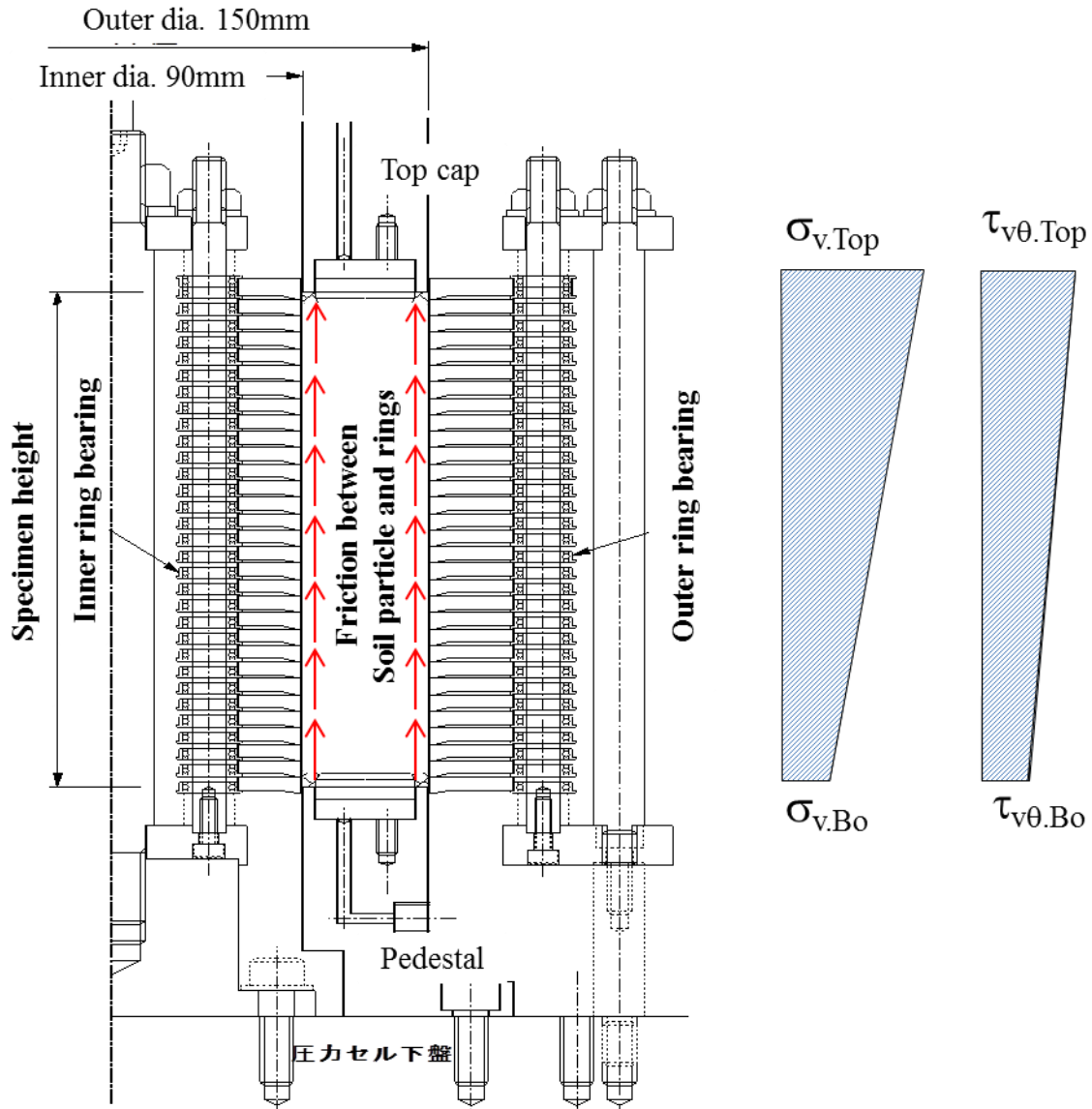
Fig. 4.2: Configuration of stacked-ring shear apparatus

4.2   Experiment program

Full details of newly developed stacked-ring shear were provided in Chapter 2. In the original design, the stacked-ring shear apparatus is composed by 31 pieces (155mm-high) of vertically stacked rings (Wahyudi et al. 2013). As well, a single bi-component load cell was installed at the rotating top cap to measure and control the applied stresses on the specimen. Preliminary tests were conducted in order to understand the characteristics and workability of the stacked-ring shear apparatus, including a series of monotonic loading tests under constant stress condition (i.e. by keeping vertical stress constant) and a series of multiple-liquefaction and single-stage liquefaction tests under constant volume conditions. It was understood that large

friction would be generated in the 155mm-high stacked-ring shear. Therefore, before conducting modification of the stacked-ring shear apparatus, the amount of generated friction needed to be measured in the first place. The basic principle to measure the amount of generated friction between the soil particles and the stacked-ring shear apparatus is based on the stress differences measured at the top and the bottom of the specimen. To do so, a second bi-component load cell was installed. At that point, two additional tests were conducted, which are a monotonic loading test under constant stress condition and a liquefaction test under constant volume condition.The tested specimens were prepared to have similar initial relative densities as those in previous tests to confirm the generated friction in the 31 pieces of stacked rings type.

After conducting measurements of the generated friction in the 31 rings type, a second modification was made by gradually reducing the number of the stacked rings to 11 rings (55mm), 8 rings (40mm) and 5 rings (25mm). To compare the amount of friction generated using these three different configurations, three specimens having similar initial relative density of about 50-55% were prepared and consolidated to a vertical stress of 200 kPa. Then, knowing the vertical stress applied at the top of the specimen (i.e. 200kPa) and measuring the transferred load at the bottom load cell, the generated friction could be evaluated.

To further reduce the generated friction, following a reduction in the height of the specimen, another modification was made by coating the surface of the ring with a frictionless material. In the process of choosing which type of material to be used as a coating, two types of prototypes were provided by the manufacturer. They correspond to different coating thicknesses made of the same material so-called Diamond-Like Coating (DLC). A stainless steel specimen withPrototype-A coating has the thickness of 1 μm while the other one with prototype-B coating has the thickness of 2 μm. Each specimen has the size of 5cm x 5cm and 5mm thick as shown in Fig. 4.3. The DLC material has a frictional coefficient of 0.2 (μ=0.2) while the original stainless steel stacked ring has the frictional coefficient of 0.8 (μ=0.8). Thus, it is expected that the use of DLC material will substantially reduce the amount of generated friction by about 75%.

Though, the two types were made of the same material, the manufacturing cost of the 2 μm-thick coating is much higher than 1μm-thick coating. The selection of the prototype to be used was also based on the material durability against loading. To do so, both types were tested under several different loading conditions, as described hereafter:

1. Before testing the two prototypes, the surface of each coating was analyzed by microscope. The used microscope has a resolution of 1μm. The purpose of this observation is to detect any initial defects (scratch) of coating surface before testing the prototypes.

2. To carry out durability tests, both prototypes were embedded at the same time in the sand specimen as described in detail in Chapter 2.

3. The two prototypes were tested under the following different loading conditions:

    3.1 Consolidation and re-consolidation up to a vertical stress of 50 kPa ($\sigma_{v.cy}$= 50 kPa) for 10 cycles, namely (CP1 test).

    3.2 Consolidation and re-consolidation up to a $\sigma_{v.cy}$= 100 kPa for 10 cycles, namely (CP2 test).

    3.3 Consolidation and re-consolidation up to a $\sigma_{v.cy}$= 150 kPa for 10 cycles, namely (CP3 test).

    3.4 Consolidation and re-consolidation up to a $\sigma_{v.cy}$= 200 kPa for 10 cycles, namely (CP4 test).

    3.5 Consolidation and re-consolidation up to a$\sigma_{v.cy}$= 300 kPa for 10 cycles, namely (CP5 test).

    3.6 Monotonic shear stress loading up to 90 kPa (τ= 90 kPa) under constant vertical stress of 200 kPa (σ_v= 200 kPa), namely (CP6 test).

    3.7 Monotonic shear stress loading under constant vertical stress of 200 kPa (σ_v= 200 kPa), namely (CP7 test).

    3.8 Monotonic shear stress loading under constant vertical stress of 300 kPa (σ_v= 300 kPa), namely (CP8 test).

    3.9 Cyclic shear stress loading of 200 kPa (τ_{cy}= 200 kPa) under constant vertical stress test of 300 kPa (σ_v= 300 kPa) for 10 cycles, namely (CP9 test).

    3.10 Cyclic shear stress loading of 250 kPa (τ_{cy}= 250 kPa) under constant stress test of 400 kPa (σ_v= 400 kPa) for 10 cycles, namely (CP10 test).

Each time a test was completed, the two prototypes were pulled out and checked with the microscope, to identify whether or not the applied stresses caused additional damage (scratches) on the surface of the coated prototypes. Any newly detected damage was recorded before the next text was conducted. See details in the section 4.3.4
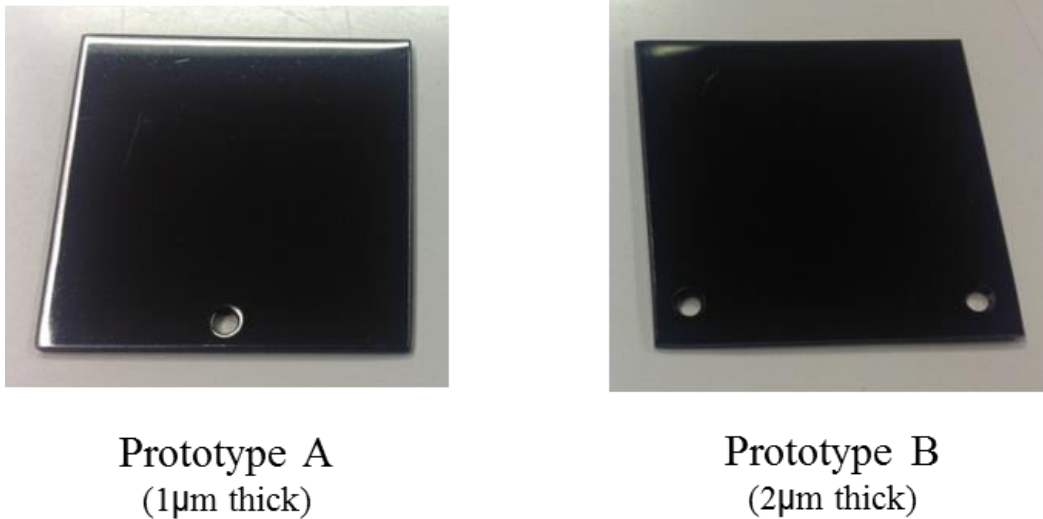
Prototype A
(1μm thick)

Prototype B
(2μm thick)

Fig. 4.3: Prototype-A and prototype-B stainless steel specimens with Diamond-Like Coating

4.3   Test results and discussion

4.3.1   Test results from 31 stacked-ring shear apparatus

4.3.1.1   Constant-stress monotonic shear test

To understand the characteristic of the stacked-ring shear apparatus, a series of monotonic constant stress tests were conducted. Three specimens (MCS-1, MCCS-2, and MCS-3) were prepared with an initial relative density of 83.2%, 73.7%, and 68.3%, respectively. Each of the specimens was one-dimensionally consolidated up to 200 kPa of vertical stress ($\sigma_{v.Top}$= 200 kPa). Then, the specimen was sheared with monotonic torsional loading under constant stress condition ($\sigma_{v.Top}$= 200 kPa). The shear deformation was measured by wire-type potentiometer with capacity up to 1000% shear strain. The overall shear stress and shear strain relationships of MCS1, MCS2, and MCS3 tests are shown in Fig. 4.4a. In general, denser specimens show higher peak shear strength as compared to the looser specimens. In addition, the residual shear stress was nearly constant for all the three tests up to shear stress of 160%. In addition, in the zoom up of the stress-strain relationships shown in Fig. 4.4b, it can be seen clearly that denser specimens also have stiffer pre-peak shear resistance as compared to the looser ones.

The overall volumetric strain and shear strain relationship is shown in Fig. 4.5a, while the volumetric strain and shear strain relationship in the range of 40% shear strain deformation is shown in Fig. 4.5b. At the beginning of the test, all specimens behaved contractive ($d\varepsilon_{Vol<0}$)

and then became dilative ($d\varepsilon_{Vol>0}$) as the shear deformation continued. Denser specimens showed smaller contraction and looser specimens showed the opposite.
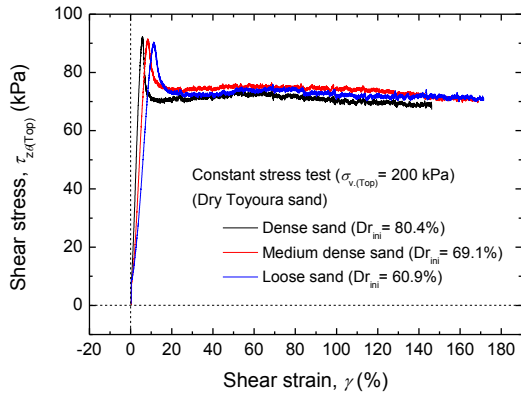

Fig.4.4a: Shear stress - shear strain relationships in 31 stacked-ring shear tests (MCS1 to MCS3 tests)
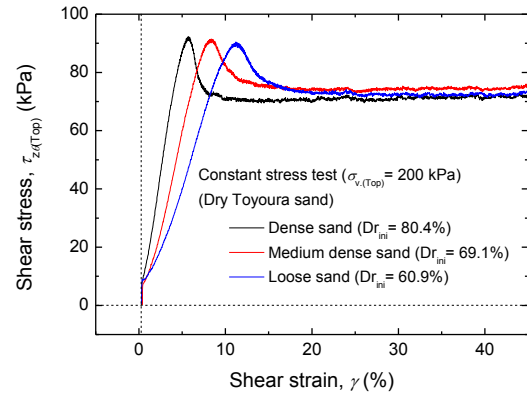
Fig. 4.4b: Close-up of stress -strain relationships shown in Fig. 4a
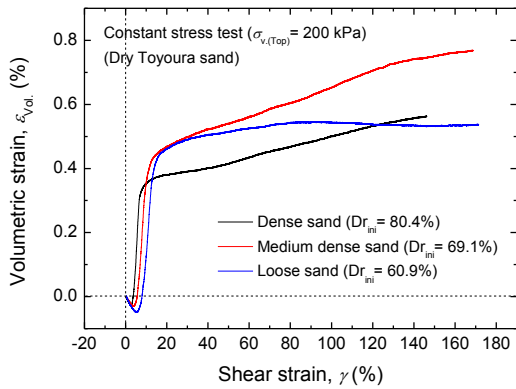

Fig. 4.5a: Volumetric strain - shear strain relationships in 31 stacked-ring shear tests (MCS1 to MCS3 tests)
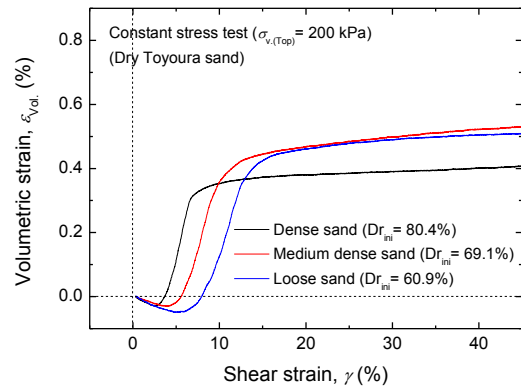
Fig.4.5b: Close-up of volumetric strain- shear strain relationships shown in Fig. 4.5a

4.3.1.2 Constant-volume cyclic shear test

Using the 31 stacked-ring shear type, four series of liquefaction tests were conducted. Two of them are multiple-liquefaction tests on dense and loose sand specimens. The other two series are single stage liquefaction tests under various initial relative densities and cyclic shear stress ($\tau_{cy.}$) of ±10 kPa and of ±20 kPa.

In this chapter only typical results of stacked-ring shear tests under constant volume condition are reported. The comparison between the single stage liquefaction and multiple liquefaction tests will be discussed in detail in Chapter 5.

First, four tests were conducted (ML1 to ML4 tests) in looseToyoura sand specimen subjected to τ_{cy} of10 kPa. The typical results on this series of test can be seen in Fig. 4.6 to Fig.4.8. Typical shear stress vs. vertical stress relationship is shown in Fig. 4.6, while the stress-strain behavior is shown in Fig. 4.7. For completeness, the time history of shear strain is shown in Fig. 4.8. From these figures, it can be seen that a sudden large decrease of vertical stress happened after a few cycles. As a result, large shear strain started to accumulate as indicated by the arrow in the inset in Fig. 4.8.

Second, five tests were conducted (ML5 to ML9 tests) in the dense Toyoura sand specimen subjected to τ_{cy} of 20 kPa. The typical results from this series of testare shown in Fig. 4.9 to Fig. 4.11. Figure 4.9 shows typical sshear stress vs. vertical stress relationship, while Fig. 4.10 shows typical the stress-strain behavior relationship. For completeness, the time history of shear strain is shown in Fig. 4.11. From these figures, it can be seen that the initial liquefaction (i.e. $\sigma_{v,top}$=0kPa) required only 1 cycle to take place. In fact, the vertical stress decreased very rapidly from the first-quarter cycle of loading as can be seen in Fig. 4.10.
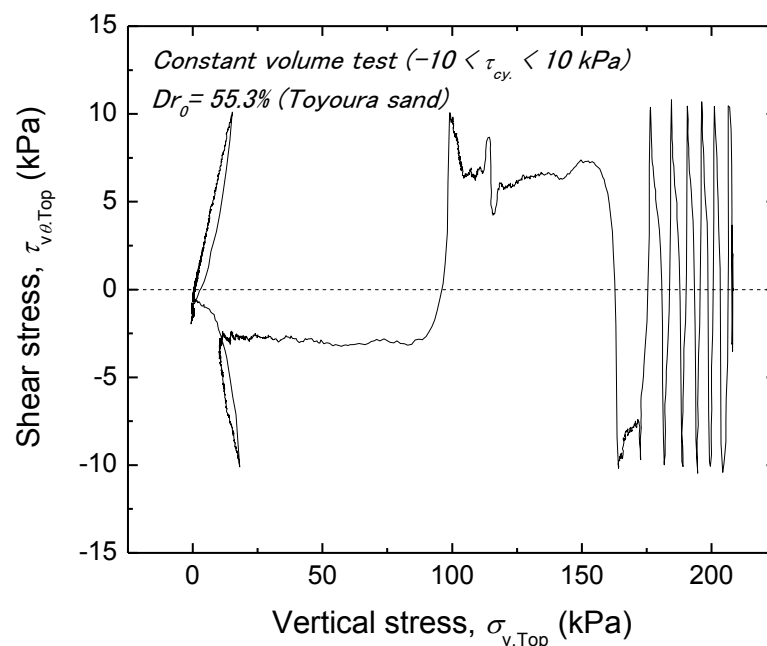

Fig. 4.6: Typical shear stress - vertical stress relationship in constant-volume cyclic ring shear tests ($\sigma_{v.Top.ini}$= 200kPa; $\tau_{cy.}$= ±10 kPa; 31 stacked rings)

Fig. 4.7: Typical shear stress - shear strain relationship in constant-volume cyclic ring shear tests ($\sigma_{v.Top.ini}$= 200kPa; τ_{cyclic}= ±10 kPa; 31 stacked rings)

Fig. 4.8: Time history of shear strain in constant-volume cyclic ring shear tests ($\sigma_{v.Top.ini}$= 200kPa; $\tau_{cy.}$= ±10 kPa; 31 stacked rings)

Fig. 4.9: Typical shear stress and volumetric relationship in constant-volume cyclic ring shear tests ($\sigma_{v.Top.ini}$= 200kPa; $\tau_{cy.}$= ±20 kPa; 31 stacked rings)
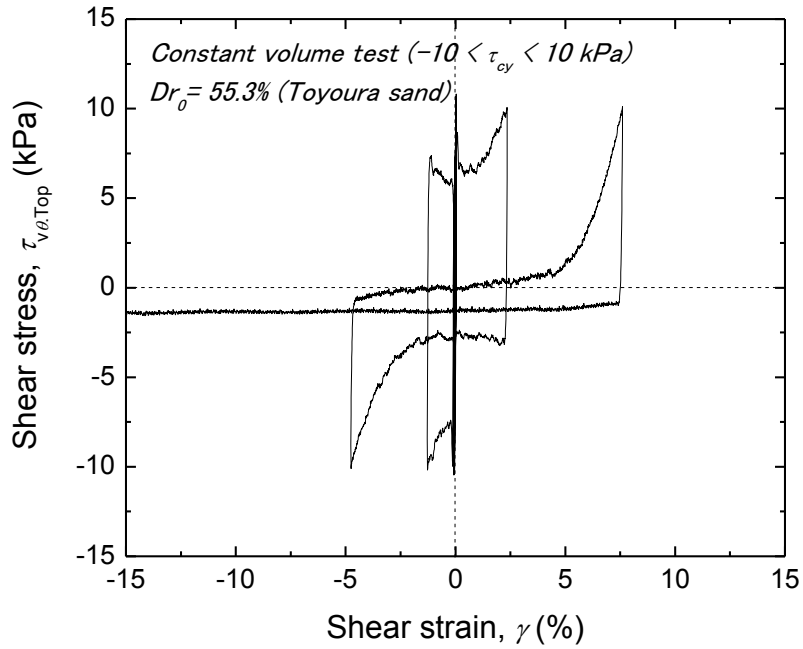

Fig. 4.10: Typical shear stress and shear strain relationship in constant-volume cyclic ring shear tests ($\sigma_{v.Top.ini}$= 200kPa; $\tau_{cy.}$= ±20 kPa; 31 stacked rings)
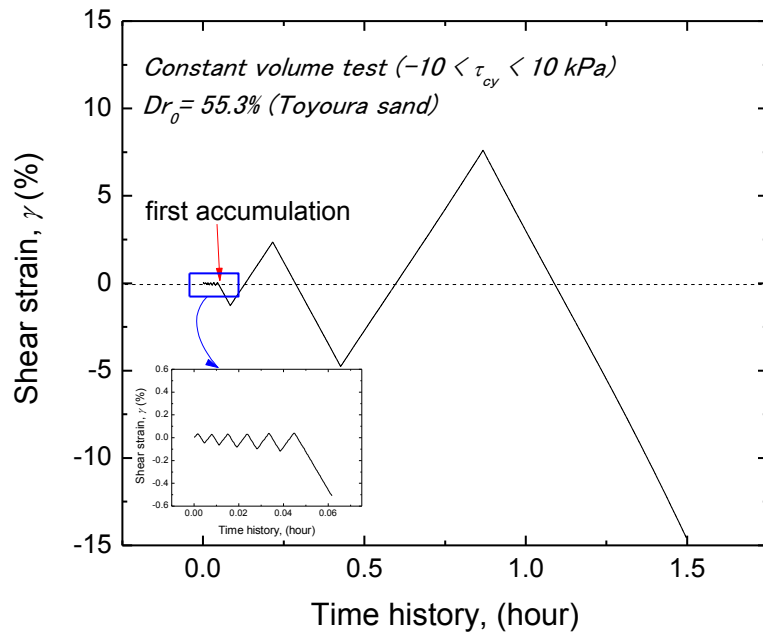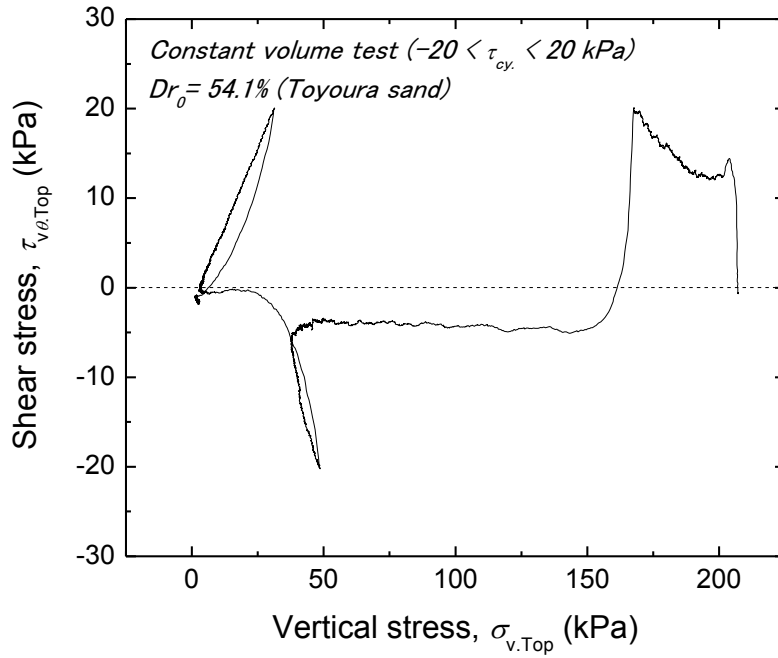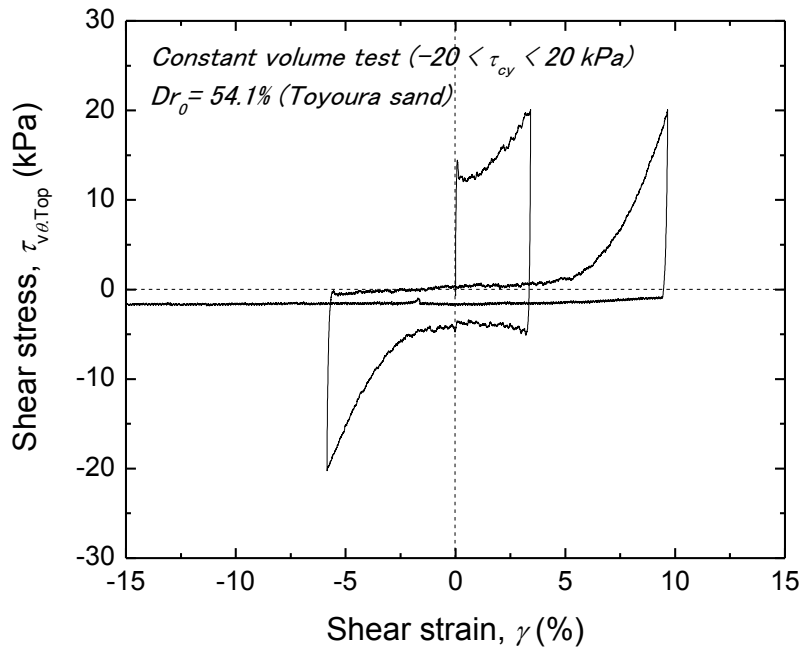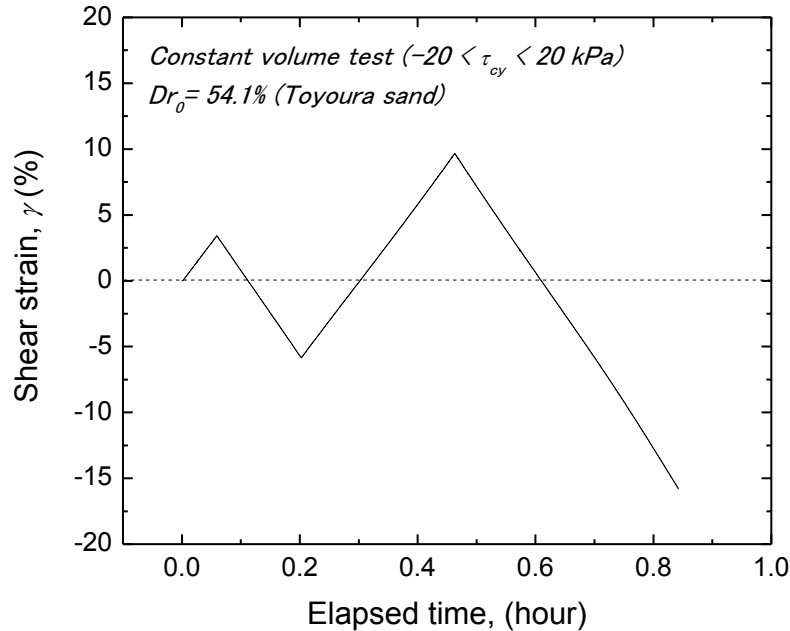
Fig. 4.11: Time history of shear strain in constant-volume cyclic ring shear tests ($\sigma_{v.Top.ini}$= 200kPa; $\tau_{cy.}$= ±20 kPa; 31 stacked rings)

Since on the specimens is applied an initial vertical stress of 200 kPa, these results showed remarkably low liquefaction resistances of Toyoura sand in the 31 stacked-ring shear type. This unexpected behavior may be associated with large extent of friction generated between the soil particles and the ring itself using the current setting of the apparatus. To address this issue, a bottom load cell was installed to measure the generated friction.

4.3.2   Test results from 31 stacked-ring shear apparatus with bottom load cell

The previous results showed remarkably low liquefaction resistance for the specimens subjected to a vertical stress ($\sigma_{v.Top}$) of 200 kPa. This low resistance must be affected by the generated friction within the specimen. In fact, due to excessive friction, the apparent stresses measured by the load cell were higher than the actual stresses applied to the specimen. In order to evaluate the amount of generated friction, an additional bi-component load cell was installed to measure the transferred stresses applied to the specimen. The new load cell was installed below the bottom pedestal. The amount of friction that was generated within the specimen was then calculated as the difference of measured stresses between top and bottom load cells.

After the installationof the new load cell, two tests were conducted to investigate the generated friction withthe 31 stacked-ring shear type apparatus. For comparison purpose, the tests were prepared at similar conditions as the tests before installation of the new load cell. Both specimens having initial relative density of about 51 - 55% were one-dimensionally consolidated up to a $\sigma_{v.Top}$ of 200 kPa. Then, one specimen was subjected to monotonic constant stress loading while the other one was subjected to constant volume cyclic loading with $\tau_{cy.}$of±10 kPa. The formulations to evaluate the friction angle in vertical and circumferential directions are provided in Chapter 3.

4.3.2.1   Constant-stress monotonic shear test

The results of the constant-volume monotonic shear test (MCS4 test) with friction measurement are reported in Fig. 4.12 through Fig. 4.15. Figure 4.12 shows the typical volumetric strain vs. vertical stress relationships during consolidation. This test confirmed that significant amount of friction is generated in the 31 stacked-ring shear type. As the specimen was consolidated to $\sigma_{v.Top}$ of 200 kPa, the measured vertical stress on the bottom load cell was about 8 kPa. It means about 95% of the vertical stress was drastically reduced at the bottom of the specimen due to friction. Based on the measurement of bottom load cell, both the vertical and circumferential soil-ring friction angles were evaluated. Fig. 4.13 shows the time history of soil-ring friction angles in vertical ($\delta_{z\theta}$) and circumferential ($\delta_{\theta\theta}$) directions during consolidation. It can be seen that both $\delta_{z\theta}$ and $\delta_{\theta\theta}$ were relatively constant throughout the test. However, $\delta_{z\theta}$ ($\approx 20°$) is much larger than $\delta_{\theta\theta}$($<0.5°$). This can be attributed to the fact that in the stacked-ring shear each of 5mm-thick rings is capable of moving independently in circumferential direction. This feature is unique as compared to the common split ring shear, in which large circumferential stress and strain non-uniformity may take place.

Figure 4.14 shows a typical shear stress and shear strain relationship. It can be seen that the difference in shear stress (τ) measurement between the top and bottom load cells were relatively constant throughout the shearing process. Figure 4.15 shows typical vertical stress and shear strain relationship. As the vertical stress was controlled based on the top load cell measurement it ($\sigma_{v.Top}$) remained constant at 200 kPa. Alternatively, the measured values of$\sigma_{v.Bot}$ kept changing until the peak stress state (τ_{peak}) was reached. The measured values of$\sigma_{v.Bot}$ increased from 8 kPa at the beginning of shearing up to 245 kPa at τ_{peak}. Then, in the post-peak stress state although the shear deformation continued, $\sigma_{v.Bot}$ remained constant at 245 kPa.
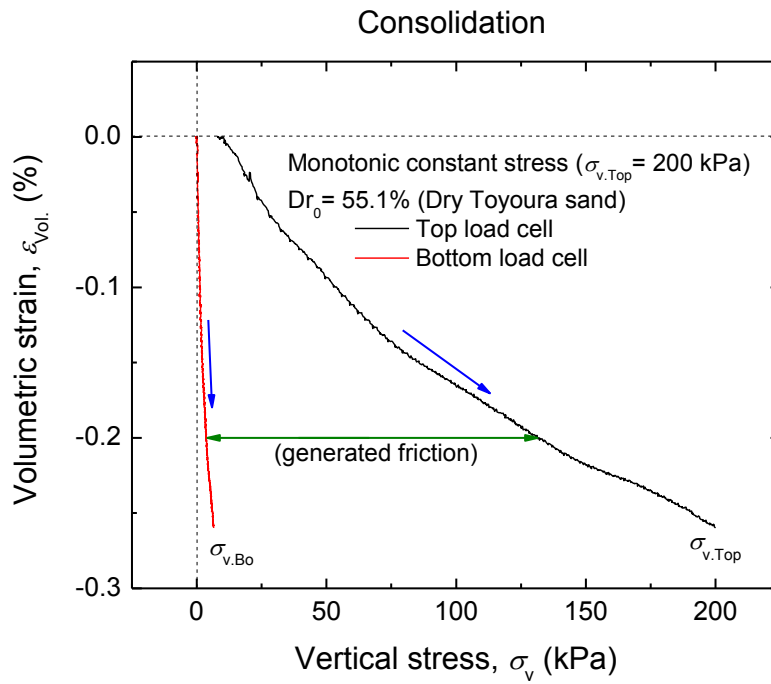
Consolidation

Fig. 4.12: Typical volumetric strain- vertical stress relationships during consolidation process in the 31 stacked-ring shear test (e.g. MCS4 test)
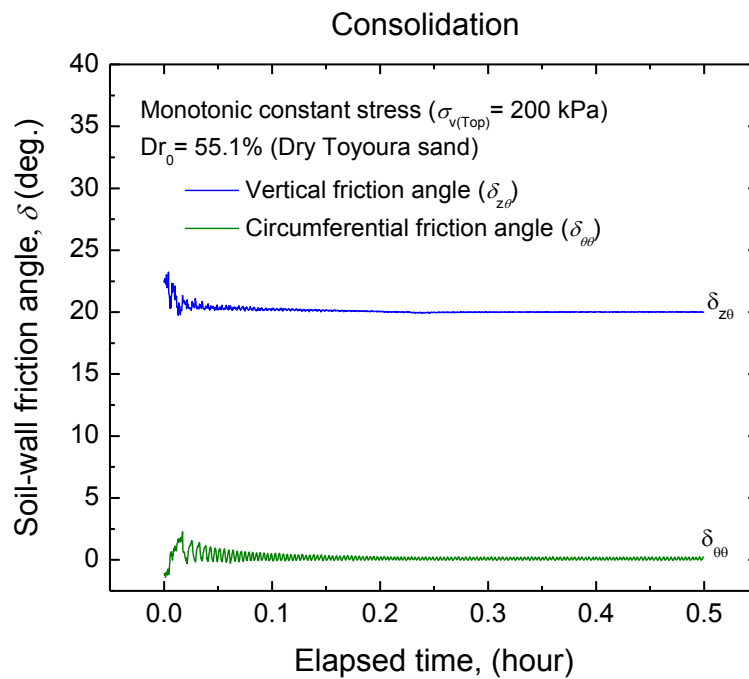
Consolidation

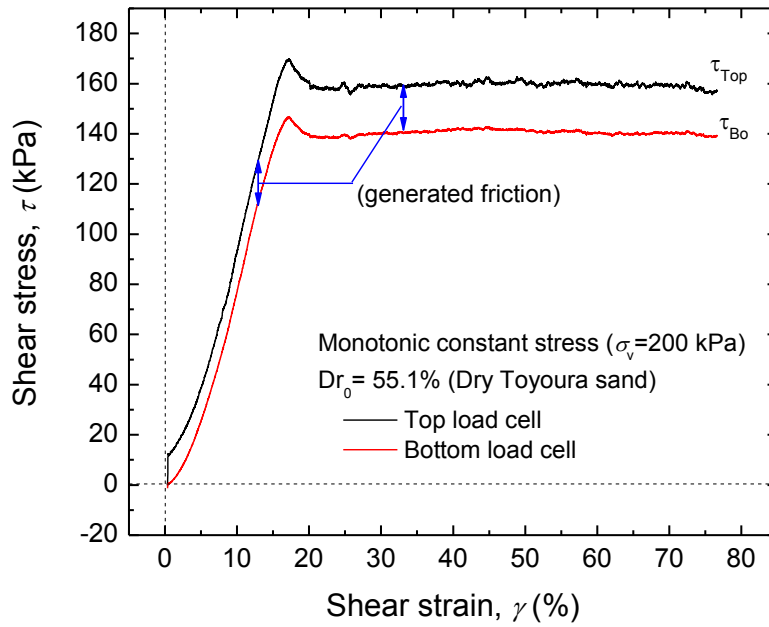Fig. 4.13: The soil-wall friction angles during consolidation in the 31 stacked-ring shear test (e.g. MCS4 test)

Fig. 4.14: Typical shear stress - shear strain relationships in the constant-stress monotonic stacked-ring shear test ($\sigma_{v(Top)}$ = 200kPa; 31 rings) (e.g. MCS4 test)
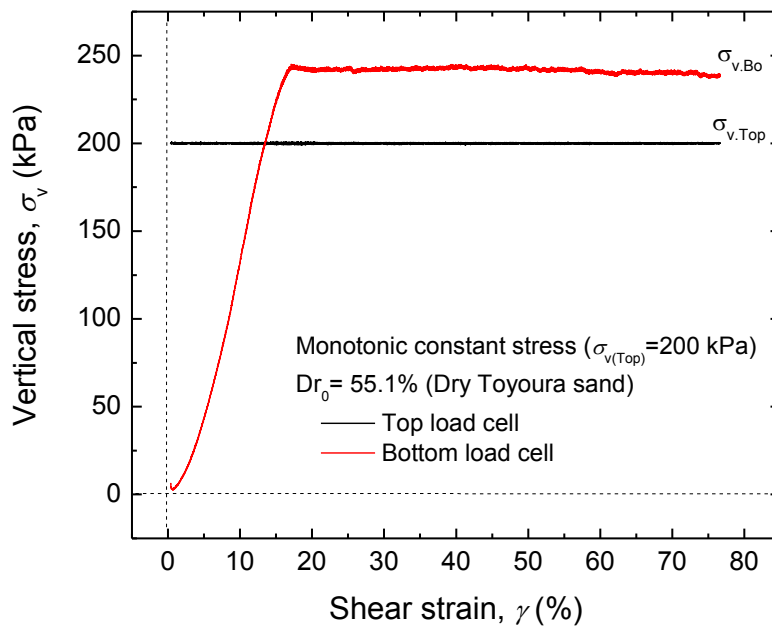

Fig. 4.15: Typical vertical stress - shear strain relationships in the constant-stress monotonic stacked-ring shear test ($\sigma_{v(Top)}$ = 200kPa; 31 rings) (e.g. MCS4 test)

4.3.2.2   Constant-volume cyclic shear test

The results of the constant-volume cyclic shear test (SL40 test) with friction measurement are reported in Fig. 4.16 through Fig. 4.19. Figure 4.16 shows the typical volumetric strain vs. vertical stress relationships during consolidation. Similar to the monotonic test results, about 95% of the applied vertical stress was lost due to friction. This result confirmed again the friction measurement obtained by theprevious constant-stress monotonic shear test. Figure 4.17 shows the time history of friction angles in vertical ($\delta_{z\theta}$) and circumferential ($\delta_{\theta\theta}$) directions during consolidation. It can be seen that both $\delta_{z\theta}$ and $\delta_{\theta\theta}$ were nearly constant during consolidation process and were about 20° and 0-0.5°, respectively. These results are similar to the onesobtained in constant stress monotonic shear test.

Figure 4.18 shows shear stress vs. vertical stress relationship, while Fig. 4.19 shows shear stress vs. shear strain relationship. It can be seen that the shear stress differences between the top and bottom of the specimen were significant. This can be associated with a significantly smaller vertical stress on the bottom parts of the specimen as compared to the top one. Thus, the lower sections of the specimen were expected to liquefy (i.e. σ_v=0kPa) much earlier than the upper sections of the specimen. Thus, the liquefaction state was not reached uniformly throughout the specimen.
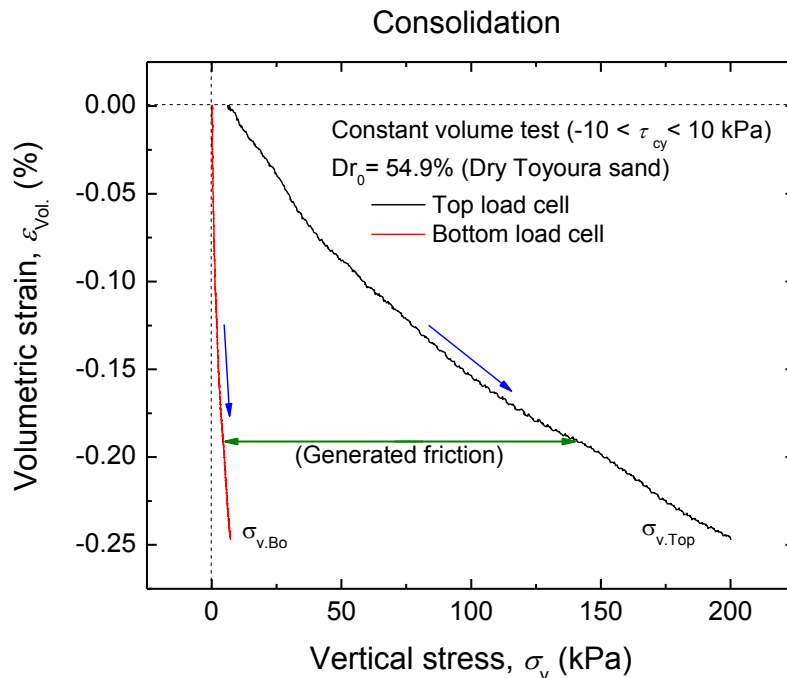

Fig. 4.16: Typical volumetric strain - vertical stress relationships during consolidation up to $\sigma_{v.Top}$= 200kPa (31 stacked rings) (e.g. SL40 test)
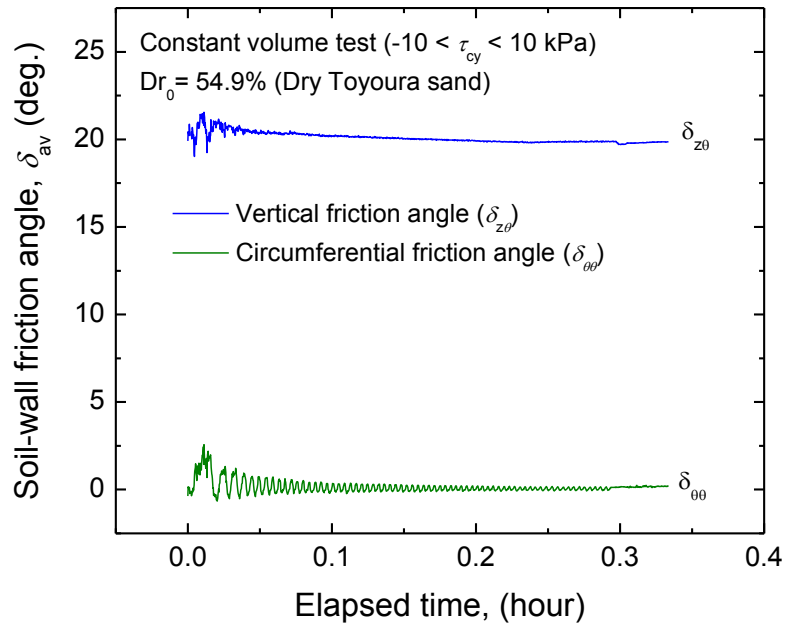
Fig. 4.17: Typical friction angles measurement during consolidation (31 stacked rings) (e.g. SL40 test)

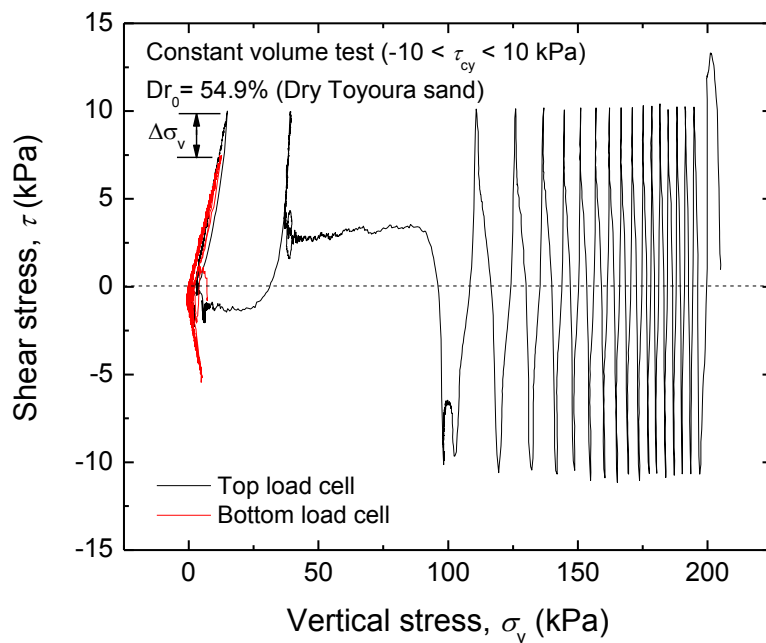Fig. 14.18: Typical shear stress - vertical stress relationships in constant-volume cyclic ring shear tests ($\sigma_{v.Top.ini}$= 200kPa; $\tau_{cy.}$= ±10 kPa; 31 stacked rings) (e.g. SL40 test)
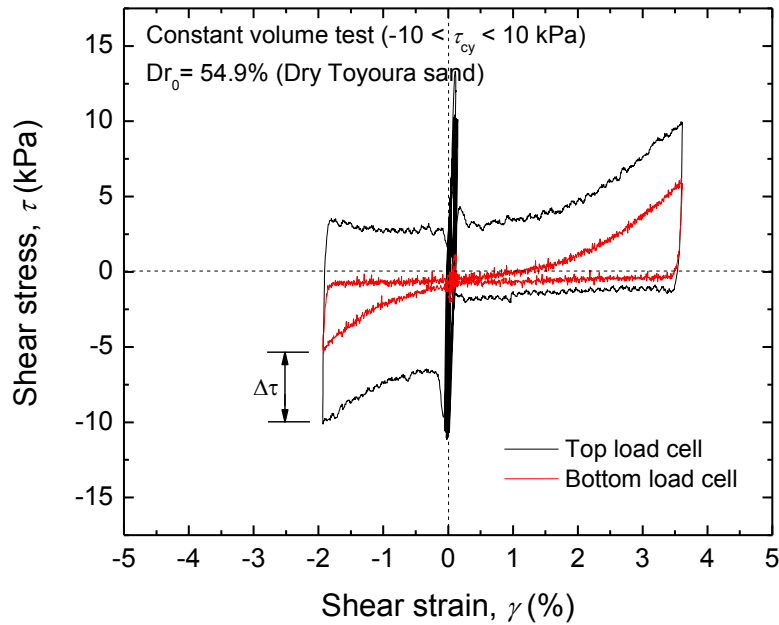
Fig. 4.19: Typical shear stress -vertical stress relationships in constant-volume cyclic ring shear tests ($\sigma_{v.Top.ini}$= 200kPa; $\tau_{cy.}$= ±10 kPa; 31 stacked rings) (e.g. SL40 test)

From this result, it was understood that the 31 stacked-ring shear type apparatus generates large friction in vertical direction. Therefore, with the expectation to reduce the generated friction, the height of the stacked-ring shear apparatus needs to be reduced. Therefore, a modification was made by reducing two-third of the current height of the stacked-ring shear specimen into 11 stacked rings.

4.3.3 Test results from 11 stacked-ring shear apparatus

To investigate the generated friction in the 11 stacked-ring shear apparatus, a test (ML11 test) was conducted on a specimen with initial relative density of 56.1% and consolidated at $\sigma_{v.Top}$ of 200 kPa. Then, the specimen was cyclically subjected to a $\tau_{cy.}$= ±20 kPa under constant volume condition. The results on this test are reported in Fig. 4.20 through Fig. 4.23.

Figure 4.20 shows the volumetric strain - vertical stress relationship during consolidation. It can be seen that of the 200 kPa of vertical stress applied at the top of the specimen, about 95 kPa was transferred to the bottom of the specimen. It means that around 52% of the applied vertical stress still vanished due to friction. This shows about 45% of improvement as compare to the 31 stacked rings case. The time history of friction angles during consolidation is shown in Fig. 4.21. During the entire consolidation process, the friction angles in both

vertical ($\delta_{z\theta}$) and circumferential ($\delta_{\theta\theta}$) directions were relatively constant at 22° and 0-0.5°, respectively. These results indicate that the friction angles in the 11 stacked-ring shear and 31 stacked-ring shear types were rather similar to each other.

The shear stress - vertical stress relationship is shown in Fig. 4.22. Though, $\sigma_{v.bot}$ was about half of $\sigma_{v.Top}$, the shear stress was rather uniformly distributed throughout the specimen height as can be seen in the shear stress - shear strain relationship in Fig. 4.23.

Comparing Figs. 4.18 and 4.19 with Figs. 4.22 and 4.23, it can be seen that the cyclic response of Toyoura sand observed in stacked-ring shear tests is very different when using 11 or 31 rings.
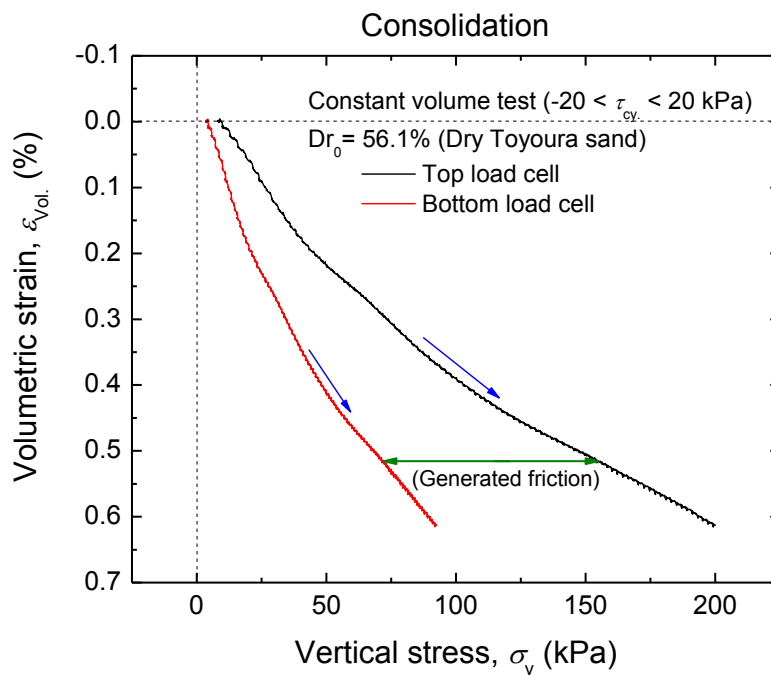

Fig. 4.20: Volumetric strain -vertical stress relationship during consolidation up to $\sigma_{v.Top}$= 200kPa (11 stacked rings) (e.g. ML11 test)
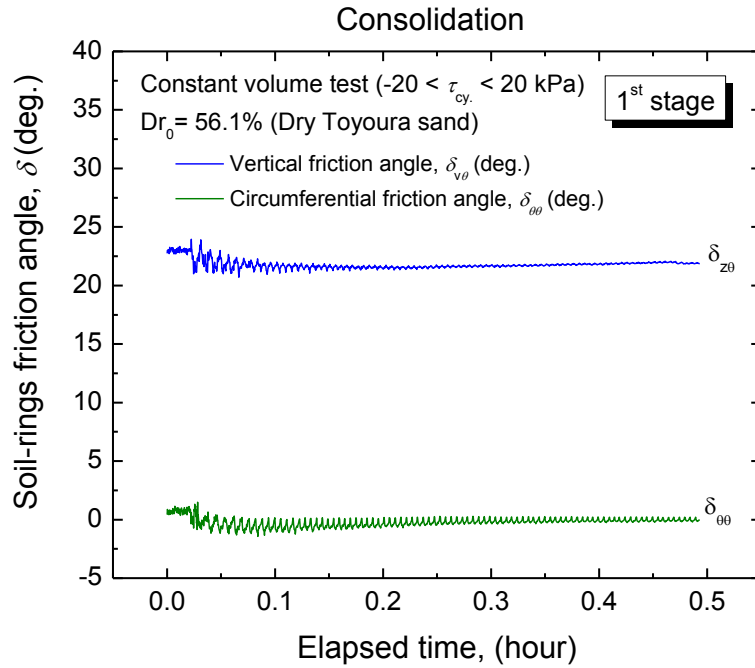
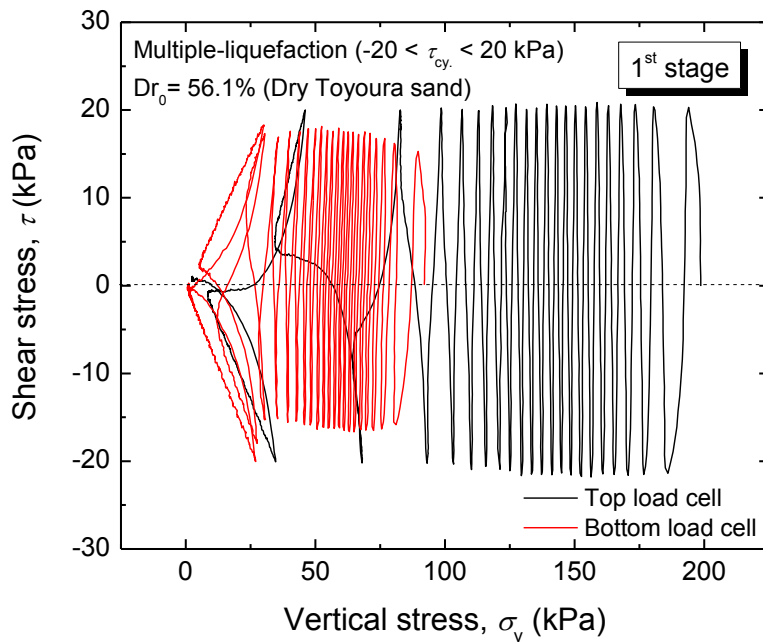Fig. 4.21: Time history of friction angle during consolidation (11 stacked rings) (e.g. ML11 test)

Fig. 4.22: Shear stress - vertical stress relationships in constant-volume cyclic ring shear tests ($\sigma_{v.Top.ini}$= 200kPa; $\tau_{cy.}$= ±20 kPa; 11 stacked rings) (e.g. ML11 test)

Fig. 4.23: Shear stress - shear strain relationships in constant-volume cyclic ring shear tests ($\sigma_{v.Top.ini}$= 200kPa; $\tau_{cy.}$= ±20 kPa; 11 stacked rings) (e.g. ML11 test)

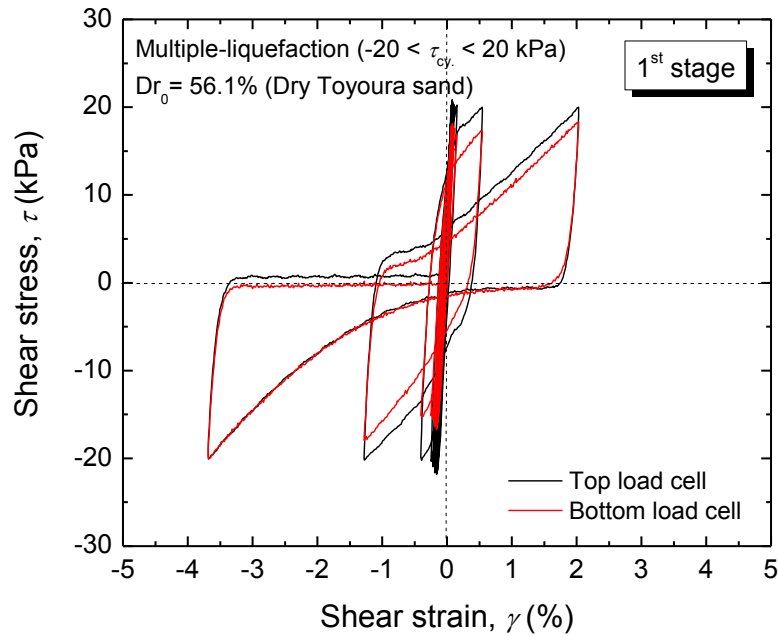Although a drastic reduction ofthe generated friction (45%) was obtained by using 11 stacked rings as compared to the original 31 rings setting, still a further improvement was required.Therefore, two additional steps were taken to address this issue, such as a further reductionof specimen height (i.e. 8 stacked rings or 40 mm height and 5 stacked rings or 20 mm height) as well as the coating the wall surface of the stacked rings by frictionless material. Typical tests results obtained after this major improvement will be presented later in the chapter.

4.3.4   The durability tests of the coating prototypes

As aforementioned, one of the major improvements made to improve performance of the stacked-ring shear apparatus was to use a frictionless coating material. To determine the optimum coating thickness, two factors,namely durability and manufacturing cost,can be considered. Although, as expected, the manufacturing cost can be reduced by reducing the coating thickness, experimental evidences revealed that actualdurability was the key selecting factor.

Ten tests were conducted (CP1 to CP10 tests) to investigate the durability of both prototypesA (1 μm thickness) and B (2 μm thickness) stainless steel specimens according to

the experiment program mentioned earlier in Section 2. After each test, the surfaces of the two prototypes were analyzed by using a high resolution microscope. The full details and results of durability tests on prototype A and prototype B specimenswill be provided in the APPENDIX.

For the visual observation analysis by microscope, the surface of each specimen was divided into four sections as shown in Fig. 4.24 (sections 1, 2, 3, and 4 correspond to the upper-left, upper-right, lower-left, and lower-right sections of the specimen, respectively). Before conducting a test, the surface of each specimen needs to be analyzed to identify their initial defects/scratches (Fig. 4.25 and Fig. 4.26). The initial defects must not be confused with the damages occurring due to the applied stress in the series of durability tests. Several initial defects were found on both the specimens provided by the manufacturer, as shown by numbers 1 and 2 in Figs. 4.25 and 4.26.

On the prototype A specimen, a hair-like scratch began to appear in the 4th test when the specimen was subjected to the cyclic axial loading ($5 < \sigma_{v.Top} < 200$ kPa) as can be seen in the lower left section on Fig. 4.27. However, in the following tests, there were no additional scratches/damages found. On the prototype B specimen, there was no damage found in all 10 series of tests. As expected, the prototype B with thicker coating showed a better performance than the prototype A. Therefore, the prototype B, having the coating thickness of 2μm, was selected for the subsequentimprovement of the stacked-ring shear.

Prototype A
(1μm thick)
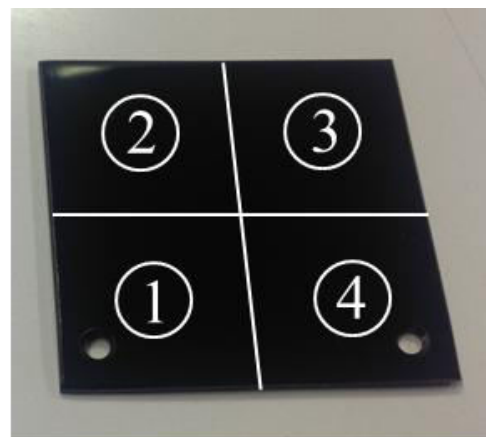
Prototype B
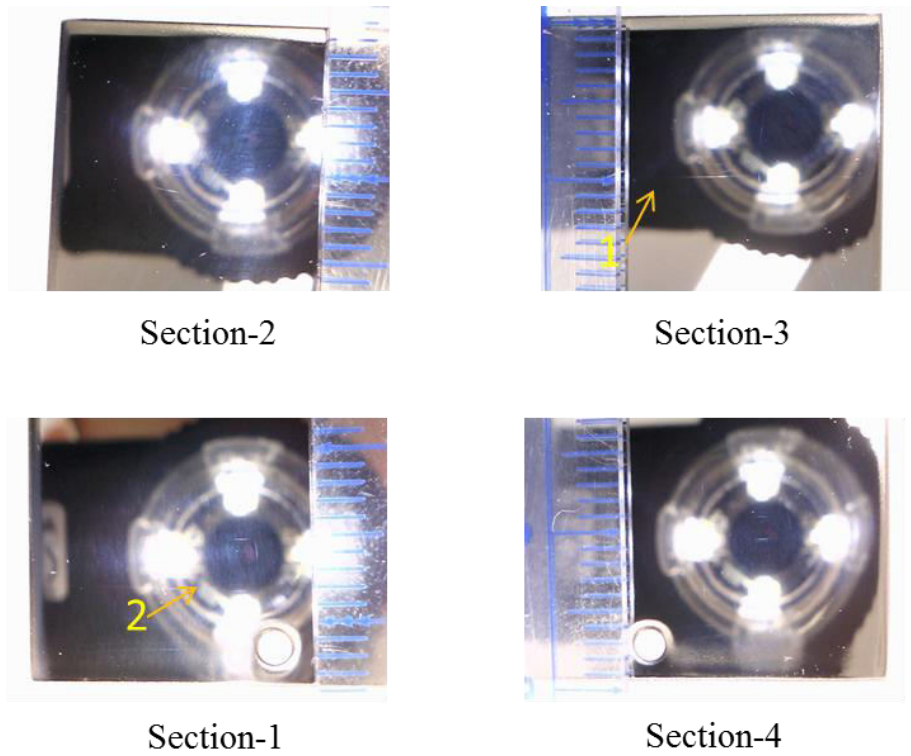(2μm thick)

Fig. 4.24: Photo of DLC prototype A and prototype B

Section-2

Section-3

Section-1

Section-4

Fig. 4.25: Initial defect of DLC prototype A

Section-2

Section-3
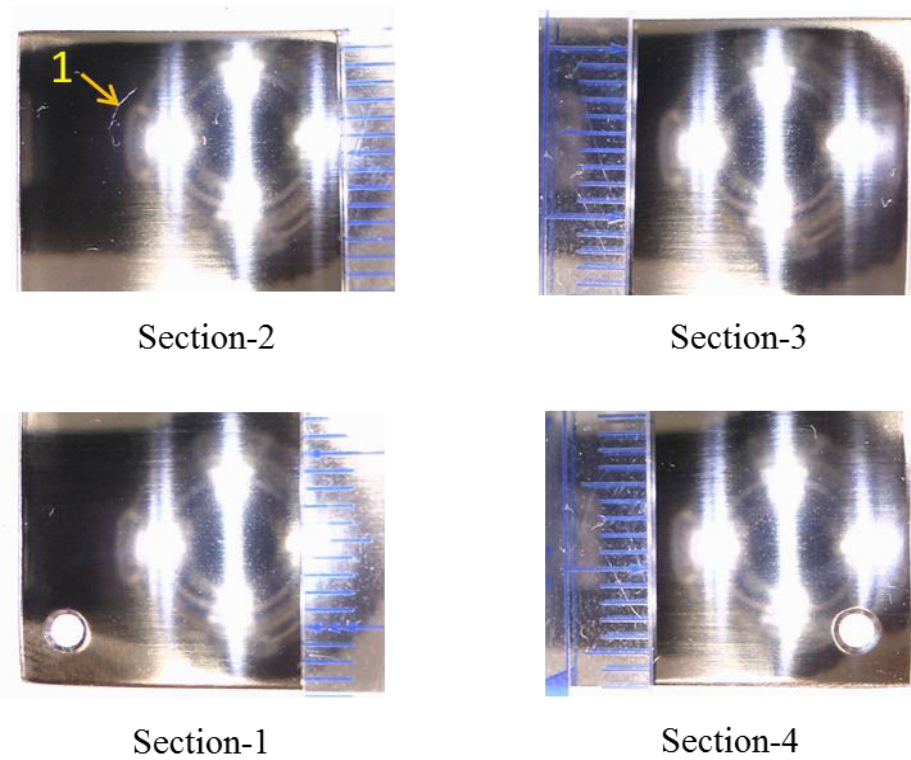
Section-1

Section-4

Fig. 4.26: Initial defect of DLC prototype B

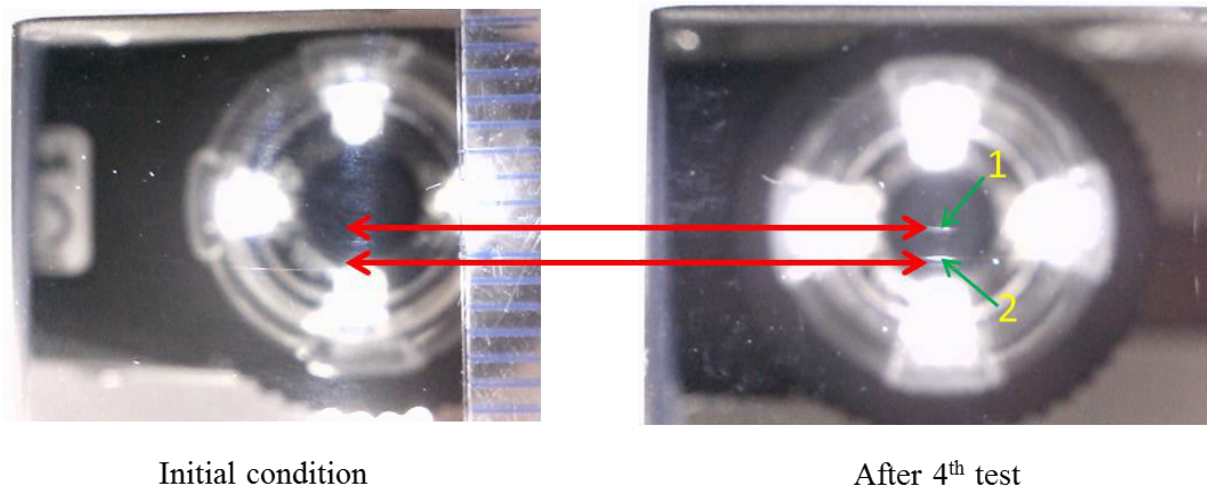Initial condition   After 4th test

Fig. 4.27: Damage on prototype A (section-2)

4.3.5   Generated friction on11coated stackedrings

After coated stacked-ring was manufactured, a multiple-liquefaction test was conducted using 11 stacked-ring shear type apparatus. A specimen (ML22 test) was prepared with an initial relative density of 51.6% andone-dimensionally consolidated up to $\sigma_{v.Top}$= 200 kPa. On each liquefaction stage, the specimen was sheared under a $\tau_{cy}$of±25 kPa.

Figure 4.28 shows the volumetric strain - vertical stress relationships during consolidation before the 1st liquefaction stage. Even though,a 200 kPa($\sigma_{v.Top}$) of vertical stress was applied to the top of the specimen, the vertical stress measured by the bottom load cell still remained to be about the half (=105 kPa). Therefore, the use of coating did not have significant impact in reducing the amount of generated friction. In using the 11 coated and 11 non-coated stacked-ring type apparatuses, the measured axial stress transferred at the bottom load cell was 95 kPa and 105 kPa, respectively. This means that only about 10 kPa in loss of vertical stress can be recovered. The time history of friction angles during consolidation is shown in Fig. 4.29. The friction angles in the vertical and circumferential directions remained constant throughout consolidation process of about 20° and 0-0.5°, respectively. These values are similar to the friction angles of 31 non-coated stacked-ring shear apparatus.

The shear stress - vertical stress relationships during 1st liquefaction-stageare shown in Fig. 4.30, while the corresponding shear stress- shear strain relationshipsare shown in Fig. 4.31. Both of these results appear to be very similar to those obtained using 11 non-coated stackedrings.
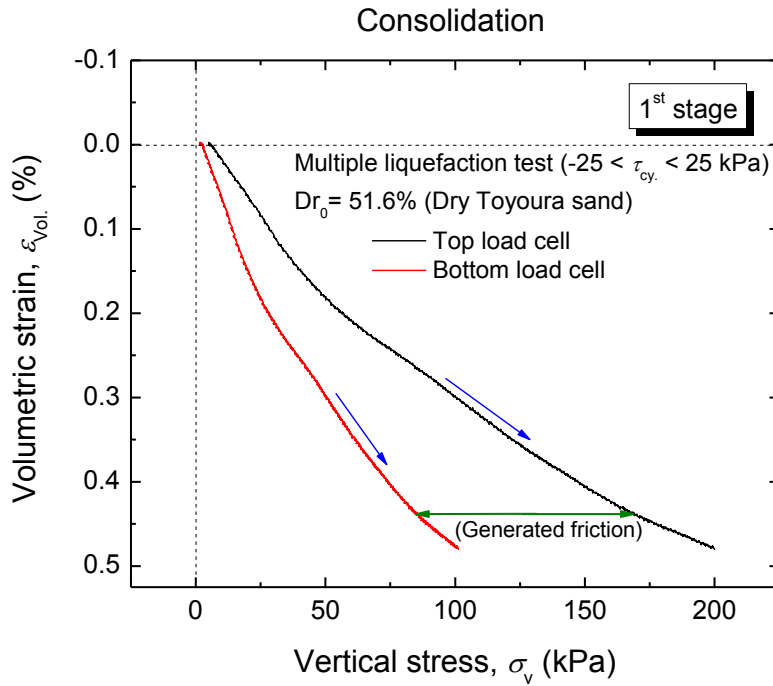
Fig. 4.28: Volumetric strain - vertical stress relationships during consolidation using 11 coated stacked rings (e.g. ML22 test)
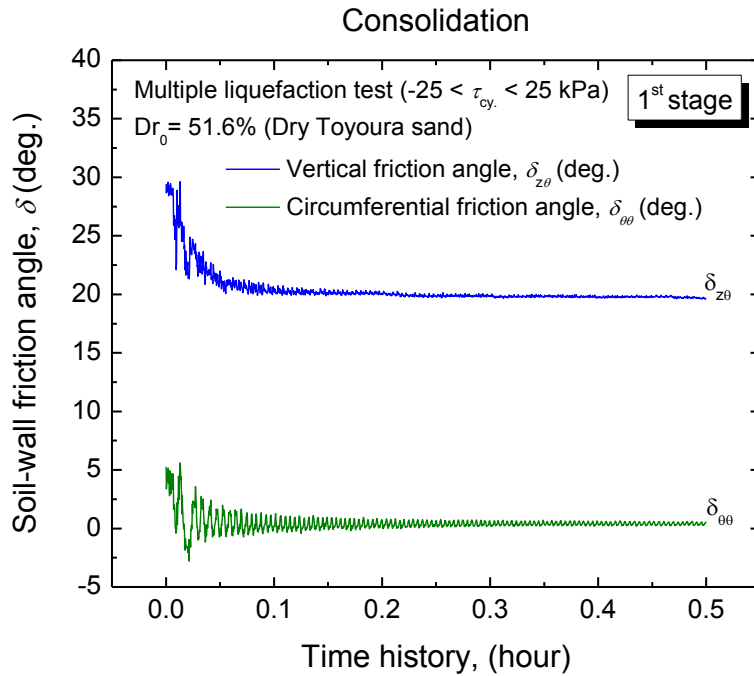

Fig. 4.29: Time history of friction angle during consolidation using 11 coated stacked rings (e.g. ML22 test)
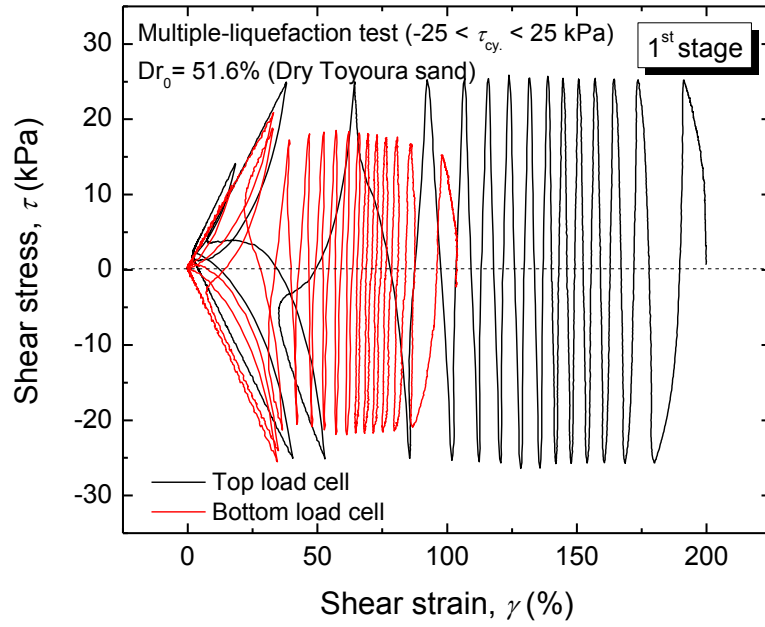
Fig. 4.30: Shear stress - vertical stress relationship using 11 coated stacked-ring (e.g. ML22 test)
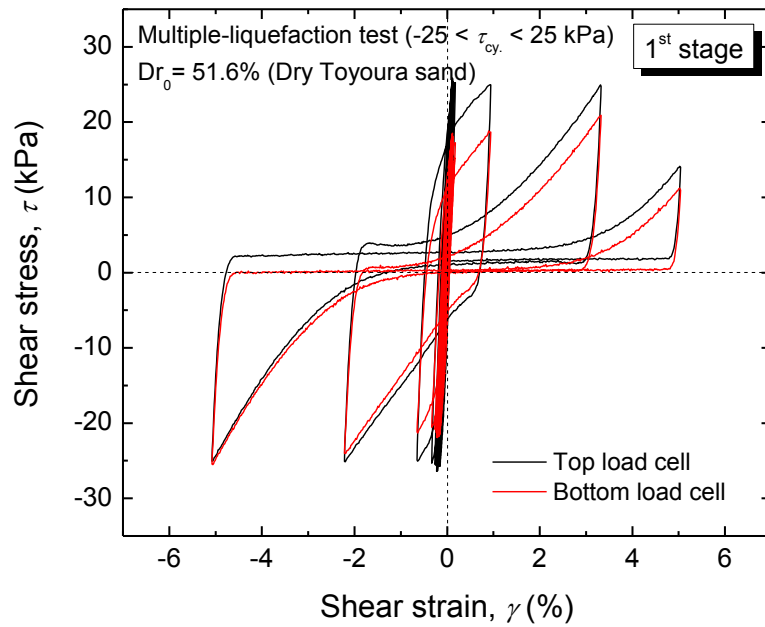

Fig. 4.31: Shear stress - shear strain relationship using 11 coated stacked-ring (e.g. ML22 test)

4.3.6   Generated friction on8coated stackedrings

A multiple-liquefaction test (MLRing8 test) was conducted using 8 coated rings in the stacked-ring shear apparatus. A specimen was prepared with initial relative density of 62.4% and one-dimensionally consolidated up to $\sigma_{v.Top}$= 200 kPa. In each liquefaction stage, the specimen was cyclically sheared by applying a $\tau_{cy.}$of30 kPa.

Figure4.32 shows the volumetric strain - vertical stress relationship during consolidation before the 1ststage of liquefaction. It can be seen that of the 200 kPa of vertical stress applied at the top of the specimen, about 140 kPa was transferred to the bottom of the specimen. This means that about 30% of the applied vertical stress was lost due to friction. The time history of friction angle in the vertical and circumferential directions during the consolidation process is shown in Fig. 4.33. The friction angle in the vertical direction slightly increased from about 12.5° to 15° at the end of consolidation, while the friction angle in the circumferential direction remained almost constant (0-0.5°) throughout the consolidation process. For completeness, the observed shear stress - vertical stress relationshipsare shown in Fig. 4.34, while the corresponding shear stress - shear strain behaviors are shown in Fig. 4.35.
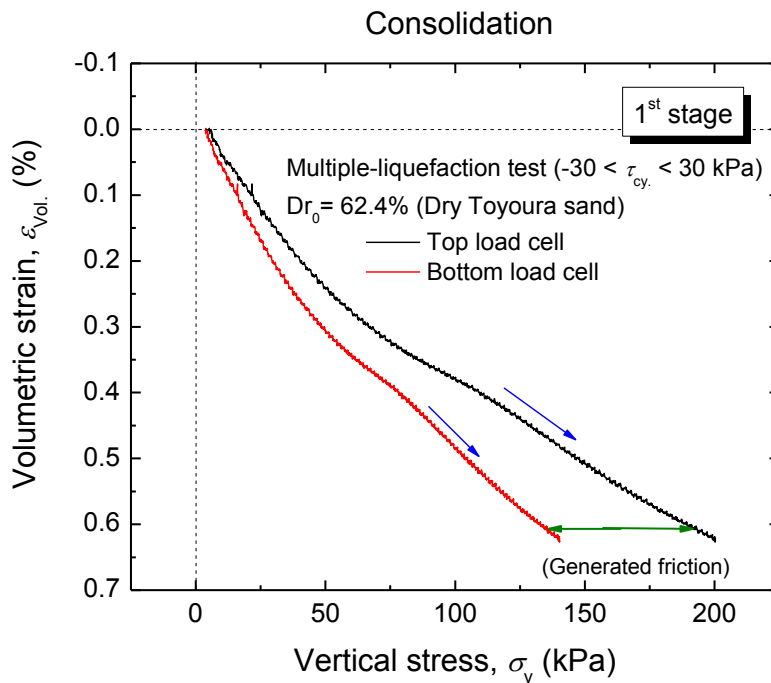

Fig. 4.32: Volumetric strain - vertical stress relationships during consolidation using 8 coated stacked rings (e.g. MLRing8 test)
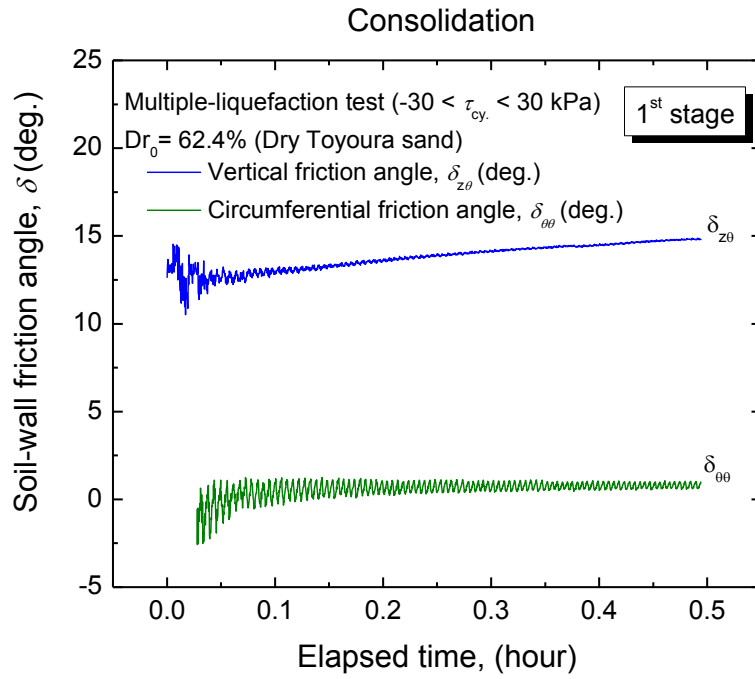
Fig. 4.33: Time history of friction angle during consolidation using 8 coated stacked rings (e.g. MLRing8 test)
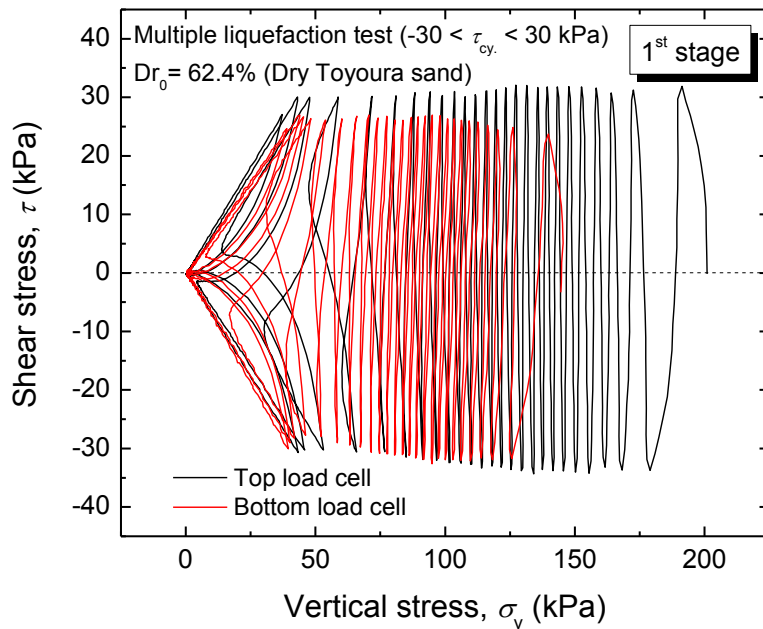
Fig. 4.34: Shear stress - vertical stress relationships using 8 coated stacked rings (e.g. MLRing8 test)
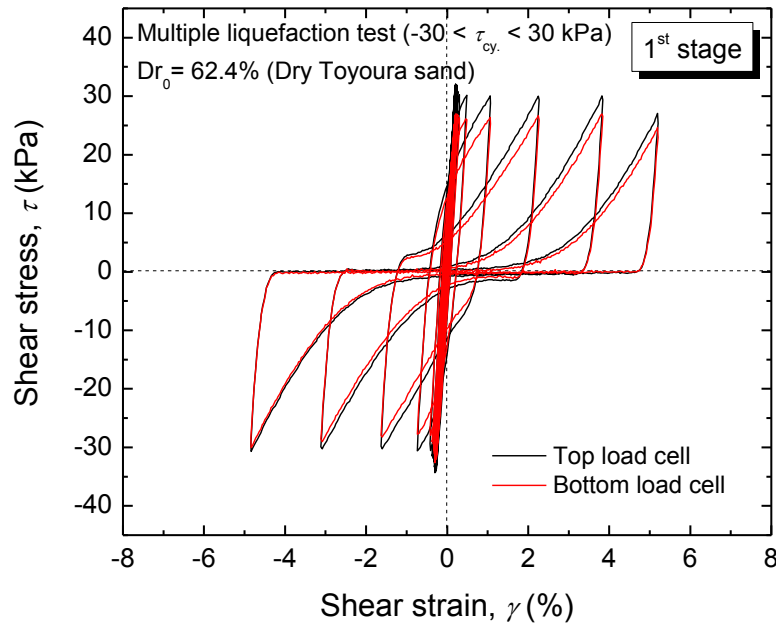
Fig. 4.35: Shear stress - shear strain relationships using 8 coated stacked rings (e.g. MLRing8 test)

4.3.7 Generated friction on5 coated stackedrings

In order to define the optimum height of the specimen (i.e. number of stacked rings) a multiple-liquefaction test (MLRing5 test) was conducted also using 5 coated rings in the stacked-ring shear apparatus. A specimen, having initial relative density of 51.1% and consolidated up to $\sigma_{v.Top}$= 200 kPa, was subjected to a cyclic shear stress amplitude of 40 kPa in each liquefaction stage. Figure 4.36 shows the volumetric strain - vertical stress relationships during consolidation before the 1st liquefaction stage. It can be seen that though a vertical stress of 200 kPa was applied at the top of the specimen, about 178 kPa was transferred to the bottom of the specimen. This means that about 11% of the applied vertical stress was lost due to friction. The time history of friction angle in the vertical and circumferential directions during consolidation is shown in Fig. 4.37. The friction angle in the vertical direction during consolidation process slightly increased from about -0.5° to 8°. In contrast, the friction angle in the circumferential direction also changed from -20° to -0.6° at the end of consolidation. Negative friction angles mean the frictional force is on the opposite direction. In other words, the stress measured at the bottom load cell is higher than the one measured by the top load cell. However, it can be noticed that these negative values rapidly changed into positive during an early stage of consolidation process. This is essentially

because at the beginning of consolidation, the difference between the stress measured at the bottom and the top of the specimen are very small. However, as the applied stress continuously increases, the vertical stress on top part of the specimen becomes higher than that measured at the bottom load cell. Therefore, the friction angle valuesin both vertical and circumferential directions become stable.

The shear stress - vertical stress relationshipsduring the 1st liquefaction stage using 5 coated rings in the stacked-ring shear apparatus are shown in Fig. 4.38, while the corresponding shear stress - shear strain behaviors are shown in Fig. 4.39.
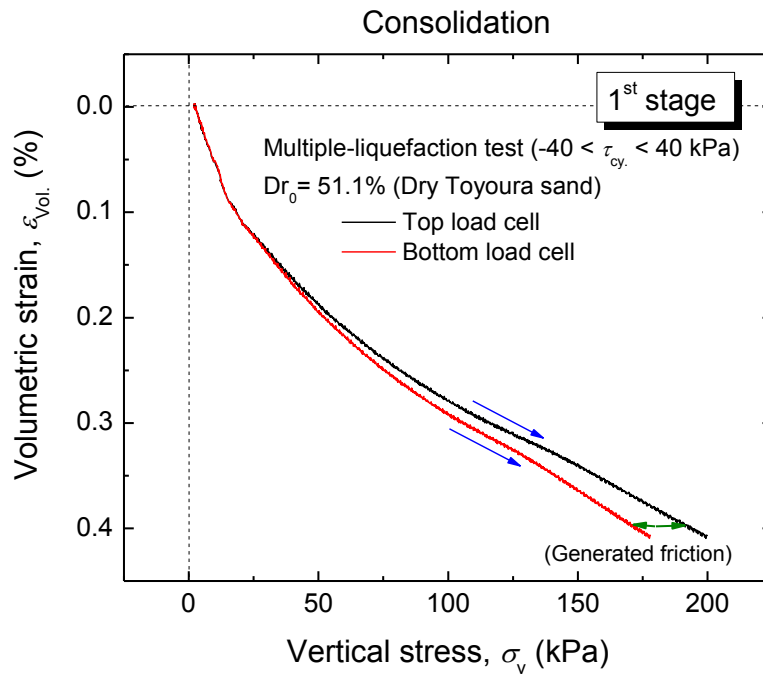

Fig. 4.36: Volumetric strain -vertical stress relationships during consolidation using 5 coated stacked rings (e.g. MLRing5 test)
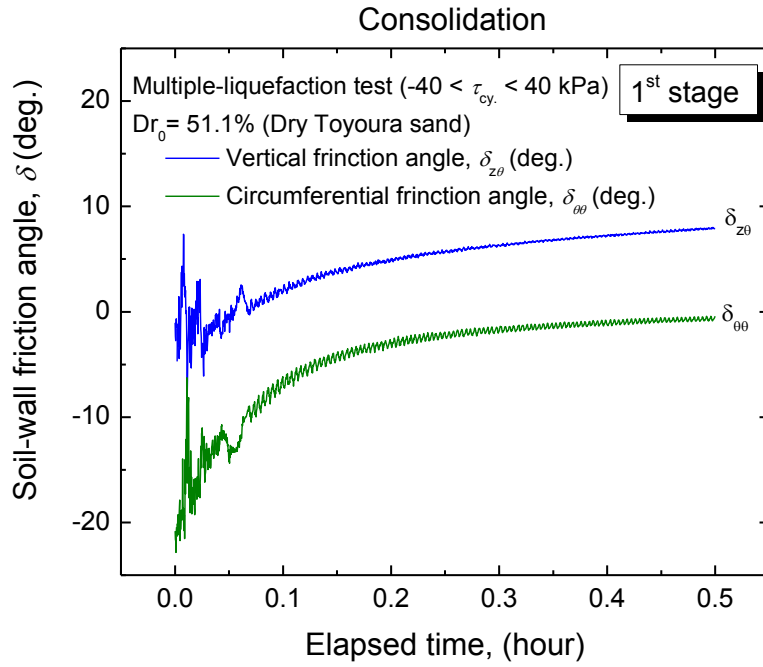
Consolidation

Fig. 4.37: Time history of friction angle during consolidation using 5 coated stacked rings (e.g. MLRing5 test)
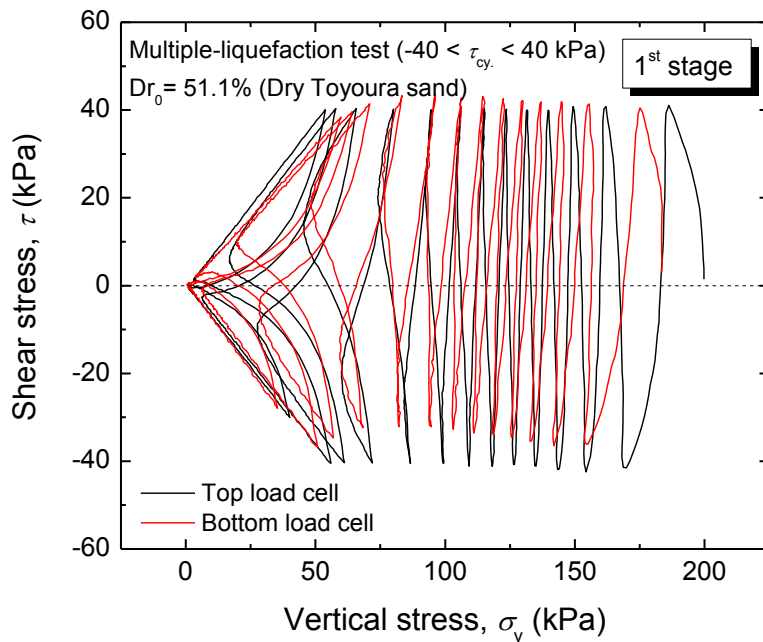

Fig. 4.38: Shear stress and vertical stress relationship on 5 coated stacked-ring (e.g. MLRing5 test)
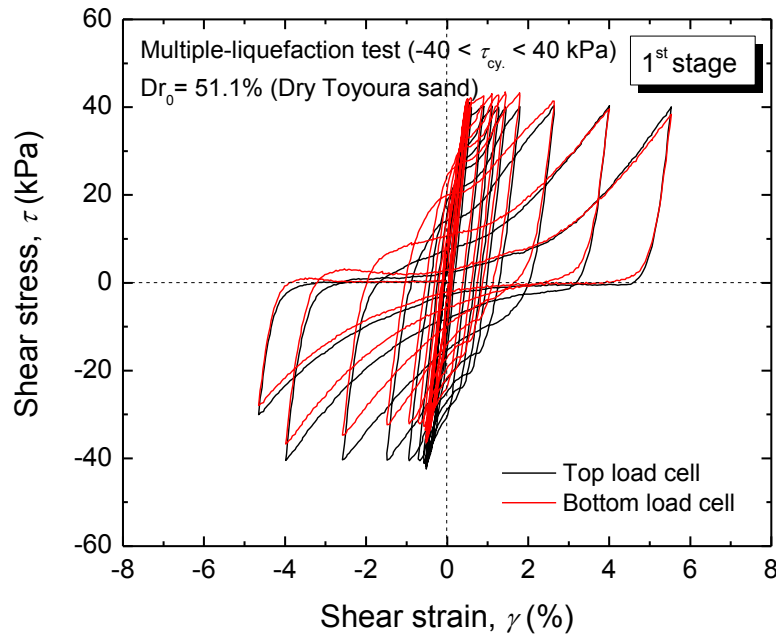
Fig. 4.39: Shear stress and shear strain relationship on 5 coated stacked-ring (e.g. MLRing5 test)

4.3.8 Generated friction from all types of stacked-ring shearsin multiple-liquefaction test

The results of the constant-volume shear tests clearly indicate that the generated friction in the stacked-ring shear apparatus highly depends on the specimen height/number of rings utilized. The higher the number of stackedrings is, the larger the contact surface between the soil particle and the stackedring wall isand thus the generated friction. Nevertheless, the use of a very shortspecimen in the stacked-ring apparatus should be avoided due to excessive end restraint effects on the shear resistance of soil. To further address this issue and find the optimum specimen height/number of rings, a series of multiple-liquefaction tests were conducted on different specimen heights using coated rings.

Figures 4.40 through 4.42summarizetheresults from various tests in terms of the vertical stress measured by the bottom load cell and generated frictions during various consolidation/re-consolidation stages. The following trends of behavior can be seen:

Non-coated 31 rings - the vertical stress measured by the bottom load cell ($\sigma_{v.bot}$) between the 1st and 8th liquefaction stages was almost constant and very low (i.e. 5 - 10 kPa). This means that about 95 – 97.5% of the applied vertical stress was lost due to friction during

virgin consolidation and re-consolidation stages. The vertical friction angles waskept nearly constant at about 20°in each liquefaction stage.

Non-coated 11 rings–the value of $\sigma_{v.bot}$during virgin consolidation (i.e. before 1st liquefaction stage)was about 90 kPa, which corresponds to a loss of 55% of the applied stress. The vertical friction angle was about 22.5°. During the 2nd re-consolidation stage, the measured $\sigma_{v.bot}$was about 75 kPa, corresponding to a loss of 62.5%. In the 3rd stage, the measured $\sigma_{v.bot}$increasedup to 90 kPa with the vertical friction angle of about 23°. After re-consolidation on 3rd stage, these values remained nearly constant for the remaining stages.

Coated 11 rings test –The values of $\sigma_{v.bot}$ during consolidation and re-consolidation stages between the 1stand the 3rd stages slightly fluctuatedwithin the range of 91 kPa to 104 kPa (54% - 47% reduction of $\sigma_{v.bot}$) corresponding to a vertical friction angle between 22°and 19°. However, after the 3rd stage,the value of $\sigma_{v.bot}$during re-consolidation was nearly constant to 100 kPa. This value corresponds to the loss of the applied $\sigma_{v.bot}$of about 50% and a friction angle of about 20°.

Quantitatively, the generated vertical friction could be reduced by using the coated rings by about 10 kPa. From a qualitative point of view, however, both types of rings showed similar behaviors (i.e. similar order of friction angle). In both tests, $\sigma_{v.bot}$first fluctuated slightlybetween the 1stand 3rd stages and then become relatively constant.

Coated 8 stacked rings – to verify the repeatability of test results, two identical tests were performed.During the virgin consolidation in both tests, the value of $\sigma_{v.bot}$was about140 kPa. In the 2ndand 3rdre-consolidation stages, the value of$\sigma_{v.bot}$drastically decreased to 118 kPa and 95 kPa, respectively. However, during the 4th re-consolidation stage, the values of $\sigma_{v.bot}$suddenly increasedup to its original values of about 130-135 kPa. Then, the $\sigma_{v.bot}$value remained unchanged during the subsequent stages of re-consolidation.

Coated 5 stacked rings–the value of $\sigma_{v.bot}$during the virgin consolidation stage was about 178 kPa. This value corresponds to only 11% loss of the applied vertical stress and a friction angle of 7.9°. Yet, during subsequent three re-consolidation stages, $\sigma_{v.bot}$continuously decreaseddown to111 kPa. Alternatively, the friction angles increased from 15°up to34°.
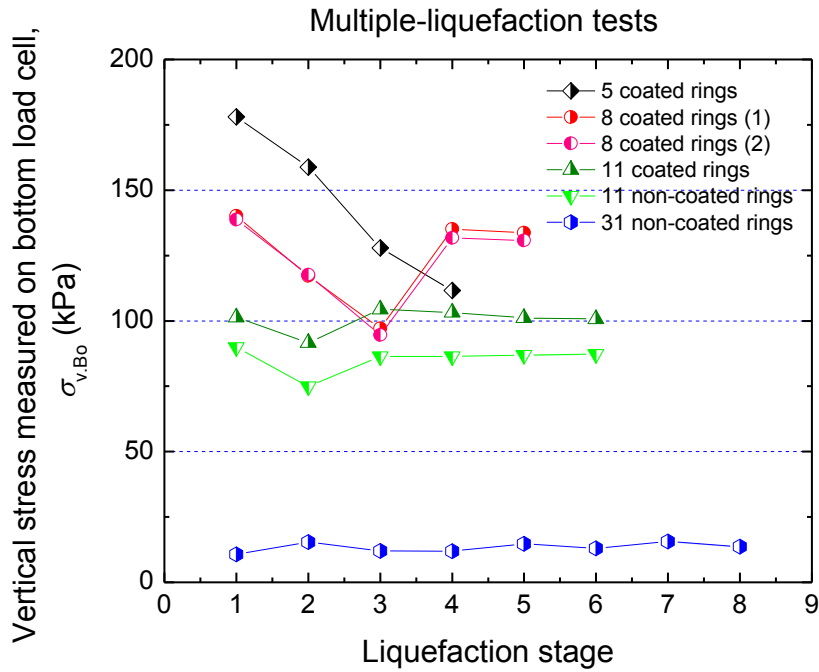
Fig. 4.40: Vertical stress measured by the bottom load cell during virgin consolidation and subsequent re-consolidations stages
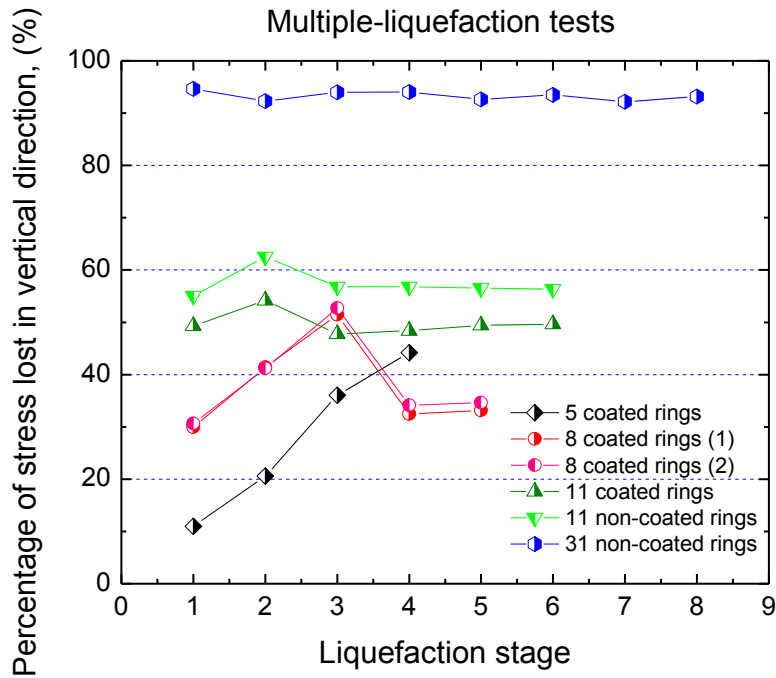

Fig. 4.41: Percentage of vertical stress lost during virgin consolidation and subsequent re-consolidations stages
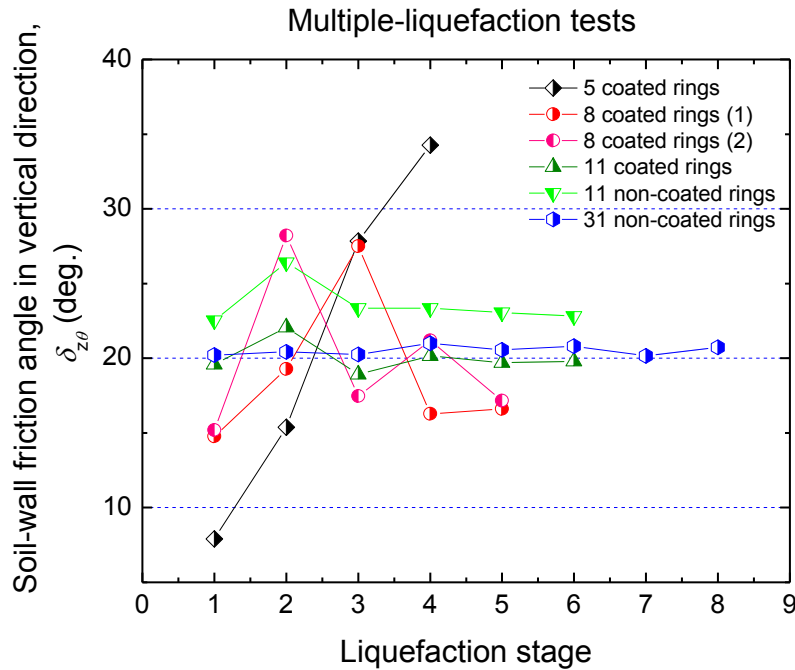
Fig. 4.42: Friction angle in the vertical direction during virgin consolidation and subsequent re-consolidations stages

These test results clearly show that,using 5 and 8 stacked rings, the amount of generated friction is not constant for successive liquefaction stages. Alternatively, using 11 and 31 stacked rings, the generated friction value remainsalmost constant during subsequent liquefaction stages. This behavior is not fully understood yet. However, a drastic change of generatedfriction is not desirablein performing multiple-liquefaction tests. The initial conditions of stress applied on the specimen aftereach stage of re-consolidation prior to the application of the cyclic shear loading need to be the same. It appears that only 11 and 31 rings satisfy such requirement. For these reasons, 11 coated rings were chosen as the optimum setting of the stacked-ring shear apparatus in conducting multi-liquefaction tests, which will be presented in chapter 5.

4.4   Summary

Based on the development process previously described, three major steps wereundertaken to define the optimum setting of the stacked-ring shear apparatus, as summarized hereafter:

1. Preliminary results of constant-volume shear test conducted using original 31 non-coated stackedringsrevealed an unexpected and very limited liquefaction resistance of Toyoura

sand specimen under the application of vertical stress of 200 kPa. This was associated with excessive friction generation.

2. The installation of the bottom load cell confirmed that large friction was generated using 31 non-coated stacked rings. Therefore, an attempt was made to reduce such high generated friction by reducing the number of stacked ringsdown to 11. Such improvement permitted to recover about 45% of vertical stresses.

3. Further improvement to reduce the excessive generated friction was made by coating the surface of the stacked-ring with frictionless material. The frictionless coating used in this study is called Diamond-Like Coating material (DLC). The DLC has 75% less friction (μ=0.2) than the original stainless steel ring (μ=0.8). Two prototypes were provided by the manufacturer with a thickness of 1μm and 2μm.A series of durability tests proved that while the 1.0μm-thick prototype suffered several hair-like scratches on its surface, no appreciable damage was found on the 2μm-thick prototype surface. Therefore, the 2μm-thick prototype was finally used to coat the stacked rings.

4. Nevertheless, to further reduce the generated friction, the number of stackedrings was reduced to 8 coated stacked rings (40 mm height) and 5 coated stacked rings (25 mm height). The results of multiple-liquefaction tests showed that using 11 coated stacked rings, the average of 46% loss of vertical stress during consolidation/re-consolidation between subsequent liquefaction stages. The use of 8 and 5 coated stacked rings generated smaller friction compare to the 11 rings, however, the loss of vertical stress was not constant in subsequent liquefaction stages. If friction cannot be completely removed, then a constant amount of friction during subsequent liquefaction stages is desirable in performing multiple-liquefaction tests. Consequently, 11 coated stacked rings wereselected as the optimum setting of the stacked-ring shear apparatus developed in this study.

4.5   References

1. Berre, T. (1982) "Triaxial testing at Norwegian Geotechnical Institute," Geotechnical Testing Journal, 5(1/2), pp. 3-17.

2. Bishop, A. W., Green, G. E., Garga, V. K., Andersen, A., and Browns J. D. (1971) "A new ring shear apparatus and its application to the measurement of residual strength," Geotechnique, 21, 4, pp. 273-328.

3. Bjerrum, L. and Landva, A. (1966) "Direct simple shear tests on a Norwegian quick clay," Geotechnique, 16, 1, pp. 1-20.

4. Bromhead, E. N. (1979) "A simple ring shear apparatus," Ground Eng., Vol. 12, No. 5, pp. 40-44.

5. Chiaro, G. (2010) "Deformation properties of sand with initial static shear in undrained cyclic torsional shear tests and their modelling," *Doctor of Engineering Dissertation*, Department of Civil Engineering, The University of Tokyo, Japan.

6. De Silva, L. I. N. (2008). "Deformation characteristics of sand subjected to cyclic drained and undrained torsional loadings and their modelling," *Doctor of Engineering Dissertation*, Department of civil engineering, The University of Tokyo, Japan.

7. Dyvik, R., Berre, T., Lacasse, S., and Raadim, B. (1987) "Comparison of truly undrained and constant volume direct simple shear tests," Geotechnique, Vol. 37, No. 1, pp. 3-10.3.

8. Finn, W. D. L. and Vaid, Y. P. (1977) "Liquefaction potential from drained constant volume cyclic simple shear tests," Proceeding of the 6th World Conference on Earthquake Engineering, New Delhi, Vol. 6, pp. 7-12.

9. Garga, V. K. and Sendano, J. I. (2002) "Steady state strength of sands in constant volume ring shear apparatus," Geotech Testing Journal, 25(4), pp. 414-421.

10. Hungr, O. and Morgenstern, N. R. (1984) "High velocity ring shear tests on sand," Vol. 34, No. 3, pp. 415-421.

11. Hvorslev, M. J. (1939) "Torsion shear tests and their place in the determination of shearing resistance of soils," Proc. of the American Society of Testing and Materials, 39, pp. 999 – 1022.

12. Iverson, N. R., Hooyer, T. S., and Baker R. W. (1998) "Ring shear studies of till deformation: Coulomb-plastic behavior and distributed strain in glacier beds," Journal of Glaciology, 22, pp. 167 – 175.

13. Kramer, S. L., Bennet, B. A., and Wang, C. H. (2002) "Sand behavior at large strain in ring simple shear," US-Japan Seminar on Seismic Disaster Mitigationin Urban Area by Geotechnical engineering, pp. 291 – 303.

14. Kramer, S. L., Wang, C. H. and Byers, M. B., (1999) "Experimental measurements of the residual strength of particular materials," Proc. of the Int'l workshop on the Physics and Mechanics of Soil Liquefaction, Baltimore Maryland, Balkeme, pp. 249 – 259.

15. Kiyota, T. (2007) "Liquefaction strength and small strain properties of in-situ frozen and reconstituted sandy soils," *Doctor of Engineering Dissertation*, Department of Civil Engineering, The University of Tokyo, Japan.

16. La Gatta, D. P. (1970) "Residual strength of clay and clay-shales by rotation of shear stress," Harvard Soil Mechanics Series, Cambridge, Massachussets, 86.

17. Modoni A., D'Amico A., Dallapiccola B., Mereu M.L., Merlini L., Pagliarani S., Pisaneschi E., Silvestri G., Torrente I., Valente E.M., Lo Monaco M. (2011) "Low-rate repetitive nerve stimulation protocol in an Italian cohort of patients affected by recessive myotoniacongenita." *J. Clin. Neurophysiol*, 28, pp. 39–44.

18. Sadrekarimi, A. and Olsen, S. M. (2007) "Development of an improved ring shear device to measure liquefied shear strength of sandy soils," 4th Int'l Conf. on Earthquake Geotechnical Eng. 1330.

19. Sasitharan, S., Robertson, P. K., Sego, D. C., and Morgenstern, N. R. (1994) "State boundary surface for very loose sand and its practical implications," Canadian Geotechnical Journal, 31, pp. 321 – 334.

20. Sassa, K. (1984) "The mechanism starting liquefied landslides and debris flows," Proc. of 4th Int'l Symp. On Landslides, Toronto, 2, pp. 349-354.

21. Sassa, K., Fukuoka, H., Wang, G., and Ishikawa, N. (2004) "Undrained dynamic loading ring shear apparatus and its application to landslides dynamics,"

22. Silver, M. L., Tasuoka, F., Phukunnhaphan, A. and Avramidis, A. (1980) "Cyclic undrained strength of sand by triaxial test and simple shear test," Proc. of the world Conf. on Earthquake Engineering, 3, pp. 281 – 288.

23. Tatsuoka, F. and Silver, M. L. (1981) "Undrained stress-strains behavior of sand under irregular loading," Soils and Foundations, 21(1), pp. 51-66.

24. Tika, T. E., Vaughan, P. R., and Lemos, L. J. (1996) "Fast shearing of pre-existing shear zones in soil," Geotechnique, 46(2), pp. 197 – 233.

25. Wahyudi, S., Koseki, J., and Sato, T. (2013) "Effects of pre-shearing history on repeated liquefaction behaviors of sand using stacked-ring shear apparatus," Proc. of Earthquake Resistance Structure Research, IIS-University of Tokyo, 46.

5 EFFECTS OF SHEAR STRAIN AMPLITUDE ON THE SOIL BEHAVIORSUBJECTED WITH MULTIPLE LIQUEFACTIONS

5.1   Introduction

As mentioned in Chapter 1, there are several factors that have major influence in determining the soil behaviors during liquefactions, which are the level of stain amplitude, anisotropy, and among others. This chapter is primarily discussing the effects of strain amplitudes to the behaviors of soil during multiple liquefactions.

Finn et al. (1970) and Seed et al. (1977)pioneered the investigation on the soil behaviors subjected with re-liquefaction. From their studies, it wasrecognized that the soil behaviors during multiple liquefactionsareaffected by several key factors related to pre-shearing history (strain and stress histories on previous liquefaction). Finn et al. (1970) conducted the 2-stage liquefaction test (re-liquefaction) using triaxial apparatus and found that the liquefaction resistance in the 2nd liquefaction is lower than the liquefaction resistance in the 1st liquefaction. In the other hand, Seed et al. (1977) conducted similar kind of test using soil chamber and found that the liquefaction resistance in the 2nd liquefaction is very much higher than the one in 1st liquefaction. The latter behavior seems more natural than the former one, because the densification is likely to take place at each liquefaction. Ishihara and Okada (1978 and 1982) found that this assumption is not completely true. It was confirmed that the tests conducted by Finn et al. (1970) and Seed et al. (1977) were conducted with different levels of strain amplitude. The former experiment was conducted with large shear strain amplitude, while the latter experiment was conducted with smaller shear strain amplitude. Furthermore, Ishihara and Okada (1978 and 1982) confirmed two conditions, in which the soil will have higher or lower resistances in the future liquefaction. The specimen that experience large pre-shearing in the 1st liquefaction should expect lower resistance in the 2nd liquefaction. Similarly, the specimen that experience small pre-shearing in the 1st liquefaction, should expect smaller resistance in the future liquefaction. Large pre-shearing is defined whenever the stress path of the sheared specimen passing the phase transformation line (PTL), while smaller pre-shearing is divined as the opposite. Suzuki and Toki (1984) also found a strain limit, so-called threshold strain, in which the specimen would show smaller liquefaction resistance if it is sheared beyond this limit.

Depending of the level of applied strain amplitudes, the applied strainmay cause the change in soil structure. It is possible to expect that smaller shear strain amplitude causesmaller change to the initial soil fabric.Niemunis (2003) conducted experimental study with the aim to observe the movements of soil particles in the specimen pre-sheared with small cyclic loading. The movements of the soil particles were tracked by using particle image velocimetry technique (PIV). Unfortunately, the results of his study could not reveal

the impact of the pre-shearing. In the opposite side, larger strain amplitude could destroy the fabric of the soil structures. Therefore, it is also possible to expect that the specimen sheared with larger strain amplitudes could cause soil non-uniformity, shear banding among others. Oda et al. (2001) conducted several types of test, in which one series of the tests was aimed to investigate the liquefaction resistance of the non-uniform sample. It was found that the non-uniform specimens have smaller liquefaction resistance as compare to the uniform specimens.

Based on the findings of the previous studies, additional investigation is needed to observe the local behaviors of the specimen as compare to their global behaviors during multiple liquefactions.

5.2   Experimental program

Several series of tests were conducted to investigate the effects of strain amplitudes to the soil behaviors during multiple liquefactions. To do so, each of the specimens was sheared with pre-fixed shear strain double amplitude ($\gamma_{DA.max}$), and typical test results and their comparison are presentedhereafter. The investigation on the effects of strain amplitudes can be broadly divided into three parts as follows:

1. The first part of the multiple-liquefaction tests wasconducted using the original version of the stacked-ring shear apparatus employing 31 stacked rings (155mm specimen height)withonly one load cell at the top of the specimen. Note that, the generated friction between the soil particles and the rings was not measured yet.

    A preliminary series of single stage liquefaction tests (virgin liquefaction) was conducted on specimens with different initial relative densities. Consequently, a reference liquefaction resistance curve was obtained. Such a curve is essential to evaluate and compare the results to the specimens subjected with multiple liquefactions.

    On the other hand, to comprehensively investigate the effects of the strain amplitude on the soil behaviors during multiple liquefactions, specimens were prepared at two different states of initial relative densities.

    The first set of multiple-liquefaction testswas conducted on loosespecimens having aninitial relative densityof 50–55% (ML1 to ML4 tests).The specimens were one-dimensionally consolidated up to a vertical stress of 200 kPa ($\sigma_{v.Top}$= 200 kPa) andthen subjected to ±10 kPa of cyclic shear stress($\tau_{cy.}$) under constant volume condition.

    The second series of multiple-liquefaction tests were conducted on dense specimen having an initial relative density of 80-82% (ML5 to ML9 tests). The specimenswere one-

dimensionally consolidated up to 200 kPa of vertical stress and then subjectedto ±20 kPa of cyclic shear stress amplitude($\tau_{cy.}$) under constant volume conditions.

In both of these series of test, each specimenwasshearedup to pre-fixedmaximum strain double amplitude ($\gamma_{DA.max}$).

2. The second part of multiple-liquefaction tests was carried out after installing an additional bi-component load cell at the bottom of the specimen. In addition, the number of rings was reduced to 11 in order to reduce excessive friction generated between soil particles and stacked rings.

Using this testing configuration, a series of multiple-liquefaction tests was conducted on loose sand specimens with an initial relative density of 50-55% (ML10 to ML12 tests).For comparison purpose, a series of single stage liquefaction tests were conducted on the specimens with various relative densities.Each specimen was one-dimensionally consolidated up to 200 kPaof vertical stress ($\sigma_{v.Top}$= 200 kPa) and then subjected to a $\tau_{cy.}$ of ±20 kPa.Each specimen is subjected withpre-determined maximum value of γ_{DA}. In this series of test, image analysis was conducted to evaluate the local deformation behaviors of soil during multiple liquefactions.

3. The third part ofthe multiple-liquefaction tests was carried out after coating the stacked rings with a frictionless material.Hence, using 11 coated stackedrings, a series of liquefaction testswas conducted on loose specimens with an initial relative density of 50-55% (ML13 to ML22 tests).All specimenswere one-dimensionally consolidatedup to 200 kPa of vertical stress ($\sigma_{v.Top}$= 200 kPa) and then subjected to$\tau_{cy.}$of ±25 kPa under constant volume condition. Each specimen was sheared under differentpre-fixed$\gamma_{DA.max}$. For comparison purpose, three 2-stage liquefaction tests were conducted under different initial relative densities.In these tests, specimenswere sheared up to $\gamma_{DA.max}$=10%in each liquefaction stage. Similar to the case of 11 non-coated stackedrings, the image analysis was also conducted to evaluate the local deformation behavior of soil during multiple liquefactions.

5.3   Results and discussion

5.3.1   Multiple-liquefaction tests using 31 non-coated stacked rings

5.3.1.1   Soil behaviors in loose specimen

In the case of loose sand, four tests (ML1 to ML4 tests) were subjected withdifferent $\gamma_{DA.max}$ of 2%, 4%, 7% and 10%, respectively.Typical shear stress - shear strain relationshipsfor subsequent multiple-liquefaction stages are shown in Fig. 5.1, while the corresponding shear stress - vertical stress relationshipsare presented in Fig. 5.2.Note that, in this study, the liquefaction resistance was defined as the number of uniform shear stress cycles required to cause a γ_{DA}value of 2% ($N\gamma_{DA(2\%)}$). Therefore, at each liquefaction stage, the variation of liquefaction resistance was obtained and its dependence on the change (increment) in specimen density was evaluated.

Thechange in specimen densityat each liquefaction stageis reported in Fig. 5.3.It can be seen that the density of each specimen increased almost linearly during subsequent liquefaction stages.In particular, the larger the applied shear strain was, the larger the increment of the specimen densitywas. On the other hand, the smaller the applied shear strainwas, the smaller the increment of the specimen density during re-consolidationin each liquefaction stage.In the real situation, large soilsettlement always occursin the postliquefaction of large magnitude of earthquake. Tokimatsu and Seed (1987)conducted a site investigation to evaluate the amount of post-liquefaction settlement and found larger soil settlement occurred in the larger magnitude of earthquake, while Nagase and Ishihara (1988) and Ishihara and Yoshimine (1992) found that the post-liquefaction settlement/volumetric strainincreases linearly with the applied shear strain amplitude up to some limit, beyond which the volumetric strain was nearly constant ($d\varepsilon_{Vol}=0$) at given shear strain amplitude.

The soil resistance on each stage of liquefaction is shown in Fig. 5.4.It can be seen that the smaller the applied shear strain was, the larger the soil resistances in the subsequent liquefaction stages. The specimen subjected with$\gamma_{DA.max}=$ 2% appeared to have the highest liquefaction resistance among the all tested specimens, followed by the specimens sheared at $\gamma_{DA.max}=$ 4%, 7% and 10%. By combining Figs. 5.3 and 5.4, the relationshipbetween liquefaction resistance and relative density is obtained, as shown in Fig. 5.5. From this figure,the effects of shear strain amplitude to the soil behaviors subjected with multiple liquefactions can be clearly seen. Despite havinga similar initial relative density, the four specimens that were undergonemultipleliquefaction stages show very different liquefaction resistance depending on the applied strain amplitudes. This figure also shows that the liquefaction resistances on the all the specimens subjected with multiple liquefactions arehigher than soil subjected with only single liquefaction. This may imply that the history of previous liquefaction has an impact in determining the behavior on the future liquefactions.
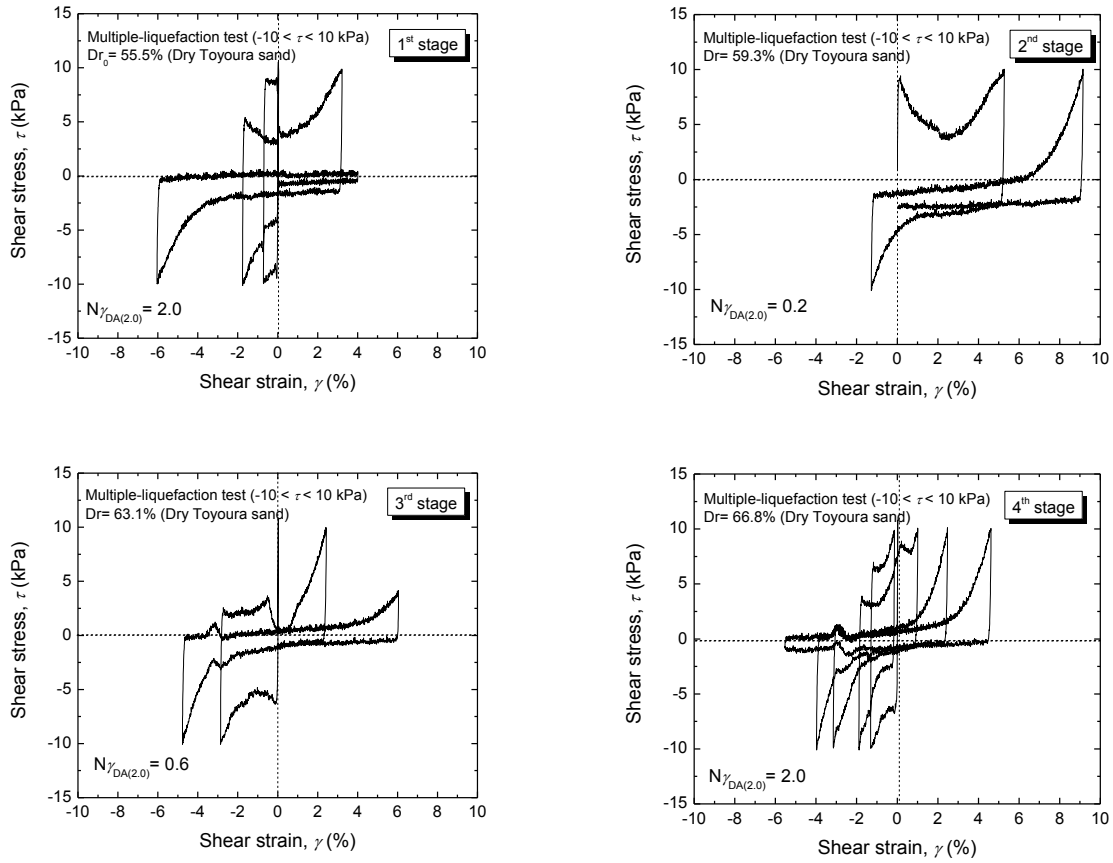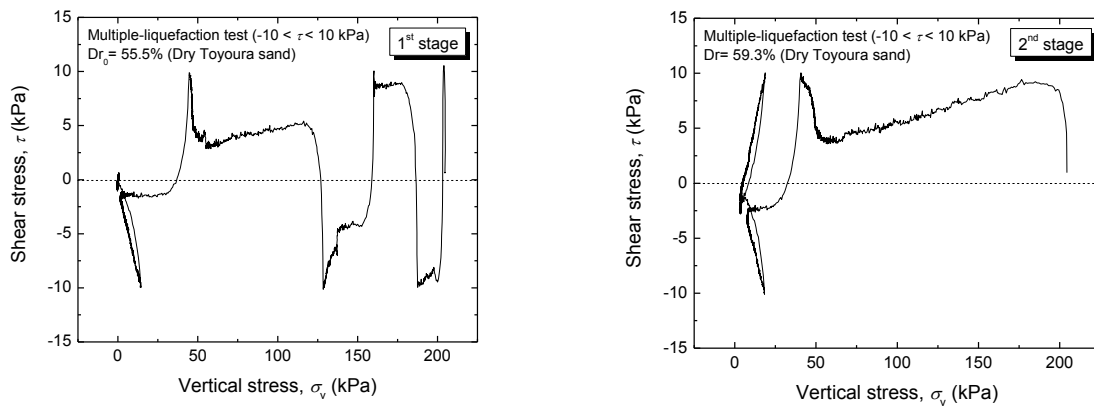
Fig. 5.1: Typical shear stress - shear strain relationships of loose sand in multiple-liquefaction tests using 31 non-coated stacked rings (e.g. ML4 test)
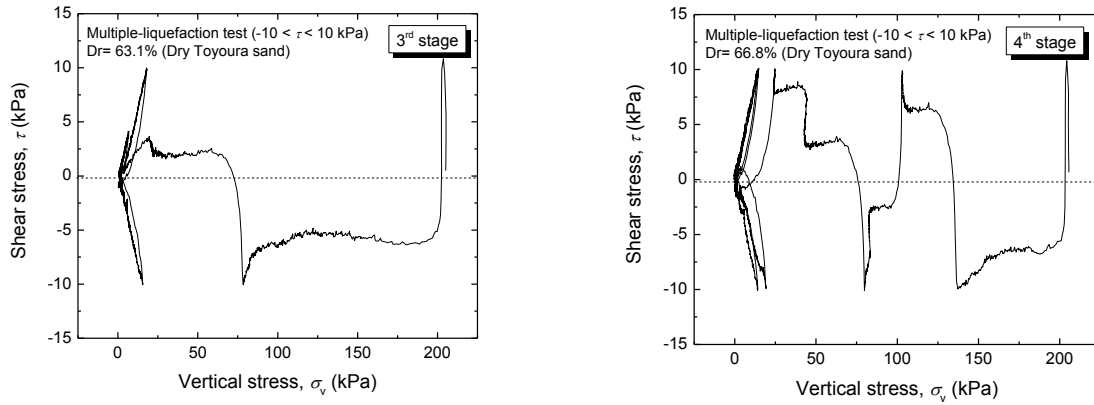
Fig. 5.2: Typical shear stress - vertical stress relationshipsof loose sand in multiple-liquefaction testsusing 31 non-coated stacked rings(e.g. ML4 test)
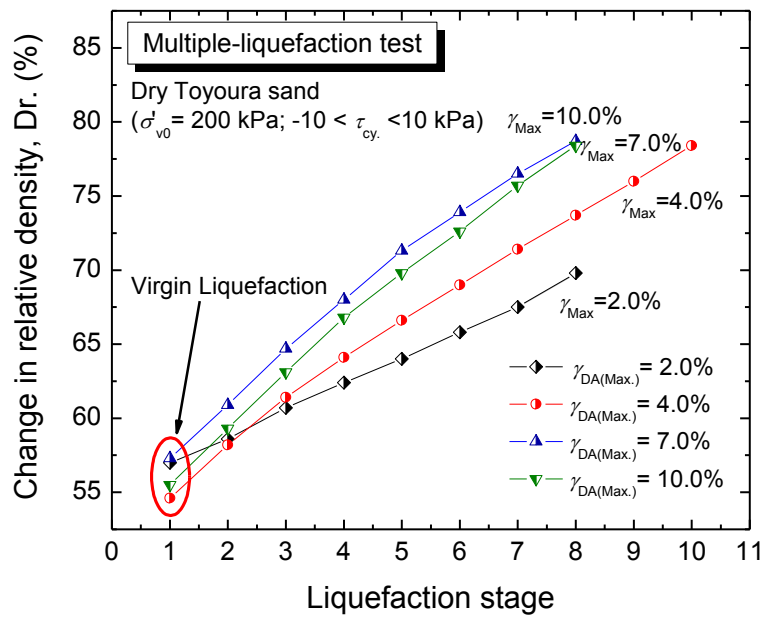

.

Fig. 5.3: Change in relative density of loose sand in multiple-liquefaction tests using 31 non-coated stacked rings
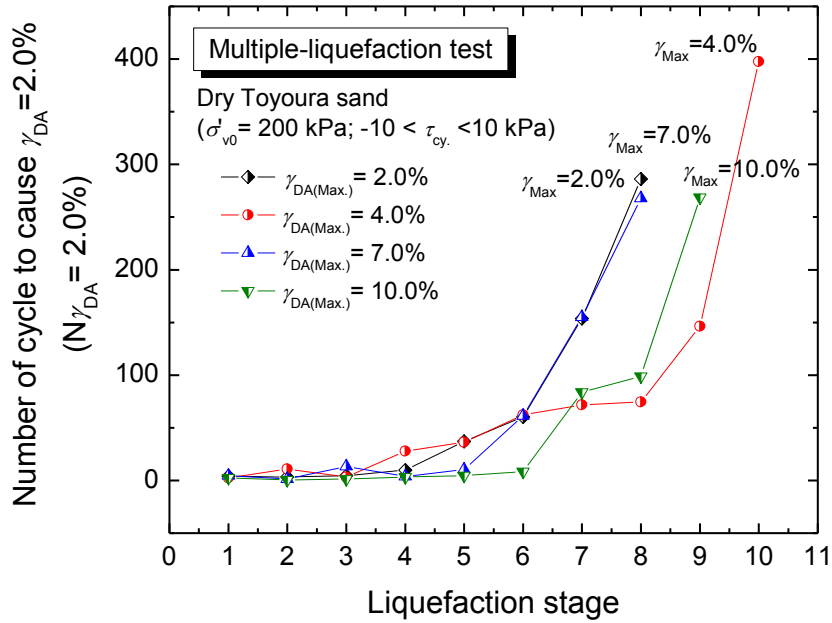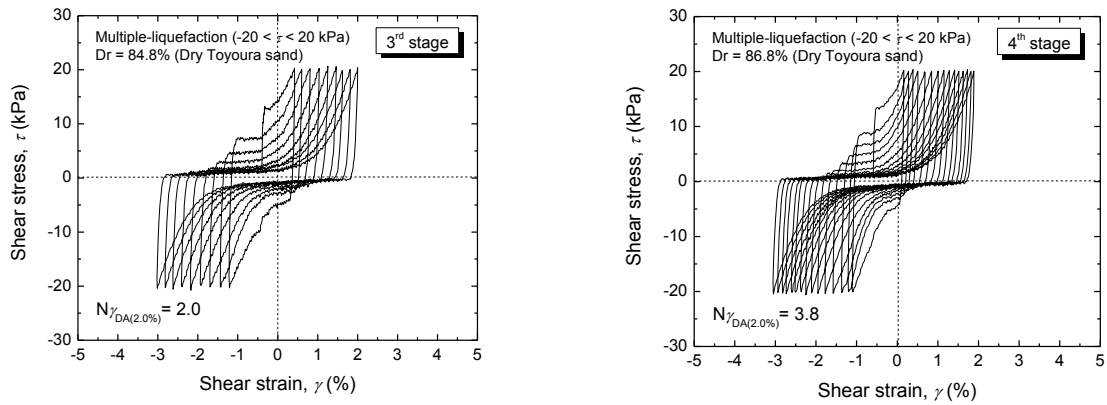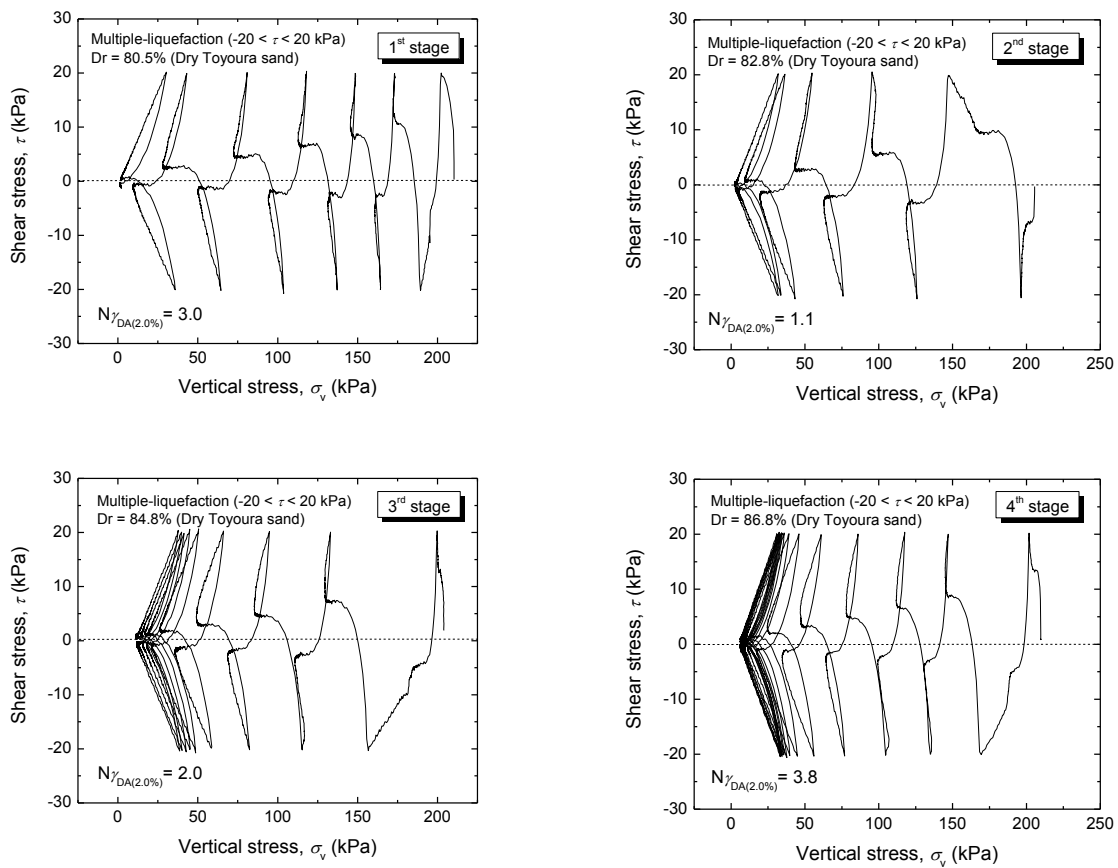
Fig. 5.4: Variation inliquefaction resistanceof loose sand in multiple-liquefaction tests using 31 non-coated stacked rings
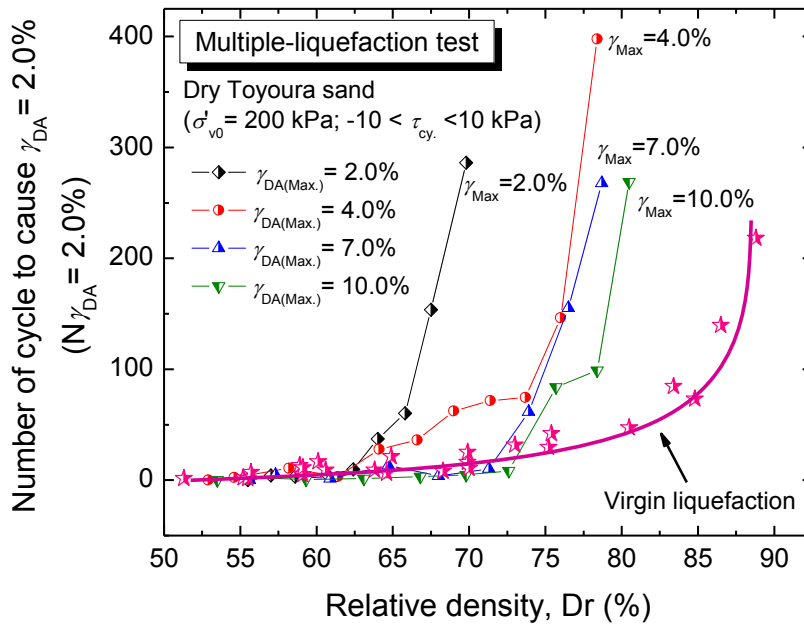
Fig. 5.5: Relationships between liquefaction resistance and relative density for loose sand in multiple-liquefaction tests using 31 non-coated stacked rings

5.3.1.2 Soil behaviors in dense specimen

In the series of multiple-liquefaction tests carried out on dense Toyoura sand, five tests (ML5 to ML9 tests) were conducted on specimens with initial relative density of 80–82%. Eachof the five specimenswassubjected to the pre-fixed $\gamma_{DA.max}$ of 2%, 3%, 4%, 5% and 10%.Typical shear stress - shear strain relationshipsare shown in Fig. 5.6, while corresponding shear stress - vertical stress relationshipsare shown in Fig. 5.7. Furthermore,the relationships between the change in specimen relative density with the number of liquefaction stages are shown in Fig. 5.8, while the relationships between theliquefaction resistanceand the number of liquefaction stages is shown in Fig. 5.9. The trend of behavior observed for the dense sand was similar to that seen for loose sands. The larger the applied shear strain was, the larger the increase in soil density was and the lower the resistance of soil subjected with multiple liquefactions.By combining Figs. 5.8 and 5.9, the relationships between the liquefaction resistance and relative density was during multiple liquefaction tests were obtained, as shown in Fig. 5.10. Similar to the case of loose sand, the liquefaction resistances of dense sand werehigher for the specimens sheared up to a smallervalue of $\gamma_{DA.max}$. Interestingly, this figure also shows that, the specimens sheared up to $\gamma_{DA.max}= 4\%$ - 10% have a lower liquefaction resistance than those undergoing a single (virgin) liquefaction stage. This finding is important, because it shows that the liquefaction resistance of multiple-liquefied sand may be higher or lower than the virgin liquefaction resistance depending on the strain history that soil experienced during previous liquefaction stages.
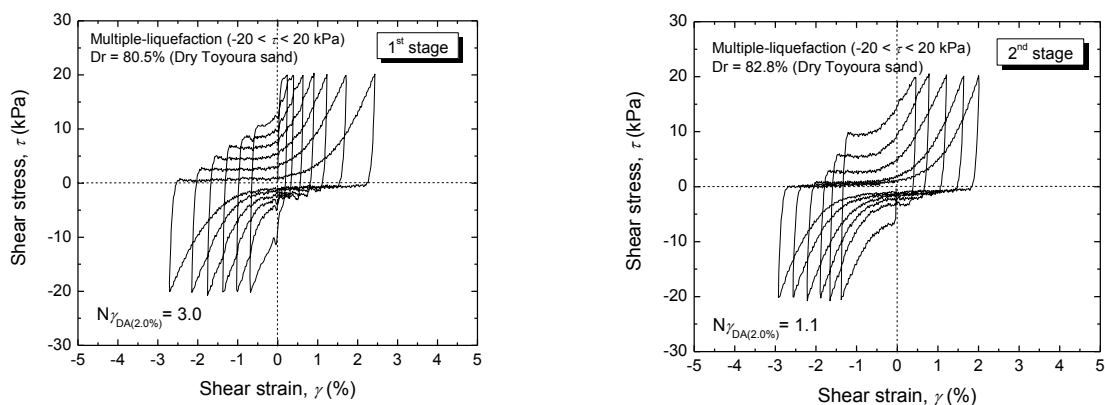
Fig. 5.6: Typical shear stress - shear strain relationshipsof dense sand in multiple-liquefaction tests using 31 non-coated stacked rings (e.g. ML8 test)

Fig. 5.7: Typical shear stress - vertical stress relationshipsof dense sand in multiple-liquefaction tests using 31 non-coated stacked rings (e.g. ML8 test)
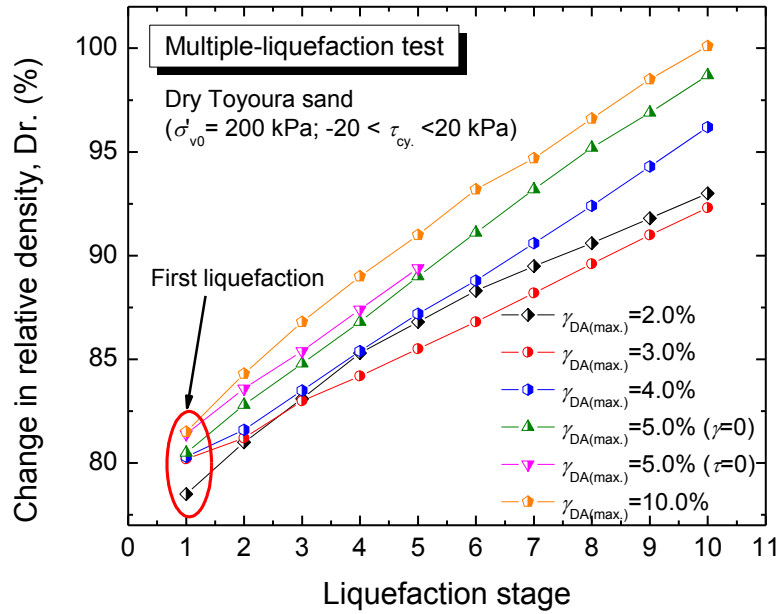
Fig. 5.8: Change in relative density of dense sand in multiple-liquefaction tests using 31 non-coated stacked rings
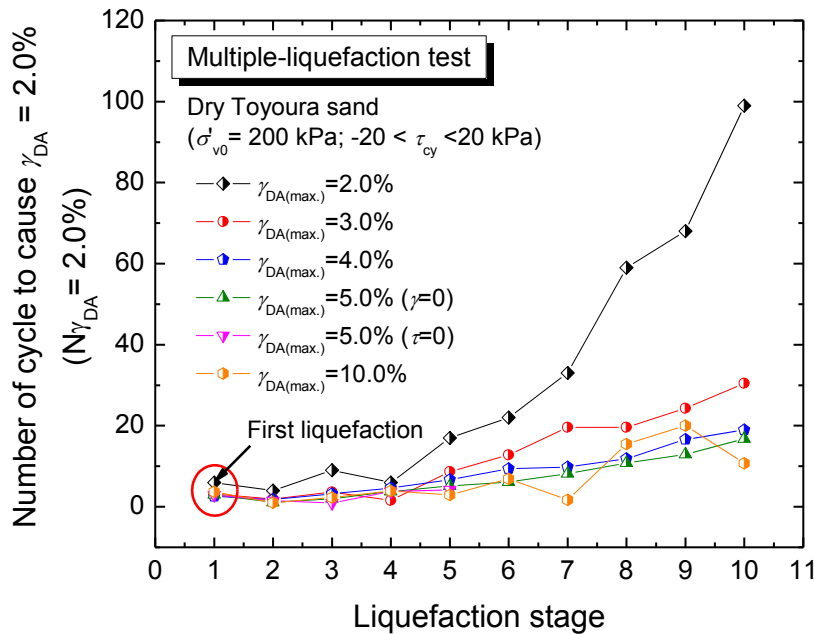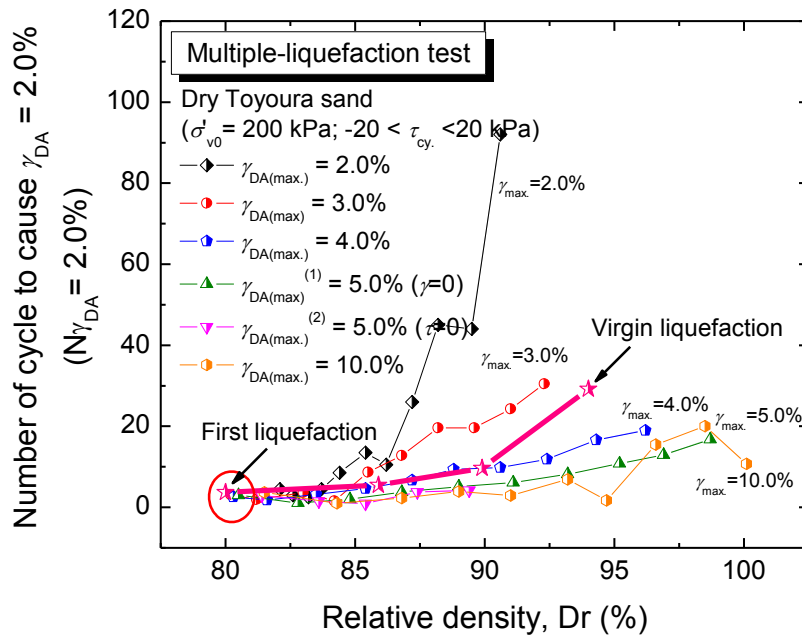
Fig. 5.9: Variation in liquefaction resistanceof dense sand in multiple-liquefaction tests using 31 non-coated stacked rings
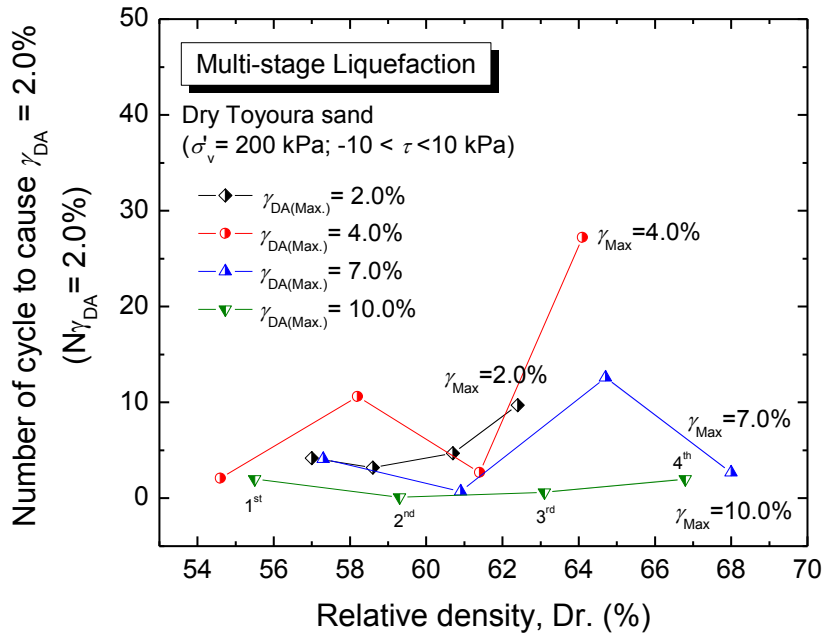
Fig. 5.10: Relationships between liquefaction resistance and relative density for dense sand in multiple-liquefaction tests using 31 non-coated stacked rings

From these two series of test, the general behaviorsof sand subjected with multiple liquefactions are partly revealed. It seems that the trends of liquefaction resistance during multiple liquefactions can be divided in two parts, which are the behavior during several few early stages of liquefaction and that during the latter stages. During a few early stages, the liquefaction resistancesshowed very small increase in their liquefaction resistance, while it increases exponentially during the latter stages. The details of the liquefaction resistance in the early stages for both loose and dense sands are reported in Fig. 5.11 and Fig. 5.12, respectively. It can be seen that the majority of the specimens,either loose or dense, have the lowest liquefaction resistance in the 2nd liquefaction stage. In the 3rd stage, the liquefaction resistance usually tends to slightly recover. This finding is also important, because it means that thedamage caused during2^{nd} liquefaction stage can be more severe(detrimental) than both the previous (virgin liquefaction stage) and future liquefaction stages.

Fig. 5.11: Relationships between liquefaction resistance and relative density during early stages of multiple-liquefaction tests on loose sand using 31 non-coated stacked rings
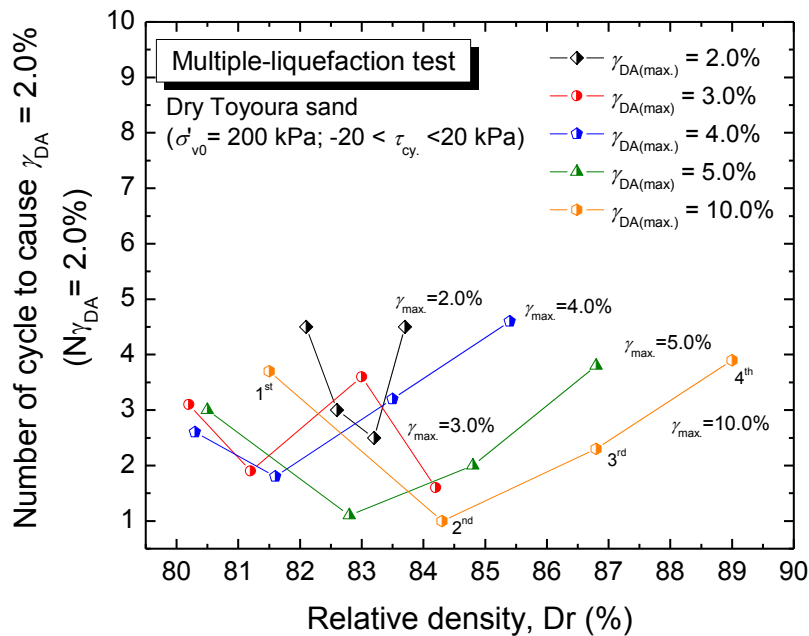
Fig. 5.12: Relationships between liquefaction resistance and relative density during early stages of multiple-liquefaction tests on dense sand using 31 non-coated stacked rings

5.3.2   Multiple-liquefaction testsusing 11 non-coated stacked rings

After the installment of the bottom load cell, the lossof applied vertical stress through the specimen height could be evaluated. It was confirmed in the previous chapter that substantial amount of friction was generated at the contact area between the soil particles and the 31 stacked rings, particularly in the vertical direction.

To reduce the amount of generated friction between soil particles and the stacked rings, the first initiation was to reduce the number of rings composing the stacked-ring itself. About two-third of the rings composing the 31 stacked-ring shear were removed to become 11 stacked rings shear type.

In this type of apparatus, three multiple-liquefaction tests (ML10 to ML12 tests) were conducted on loose specimens having theinitial relative densities of 50-55%. Each of the three specimens was subjected with pre-fixed $\gamma_{DA.max}$of 2%, 5% and 10%, respectively. For comparison purpose, a series of single stage liquefaction tests was conducted on six specimens at different relative density levels.

Typical shear stress - shear strain relationships of loose sand specimens, in multiple-liquefaction tests using 11 non-coated stacked rings, are shown in Fig. 5.13; while the corresponding vertical stress - shear stress relationships are shown in Fig. 5.14.

The changes in specimen density with the number of liquefaction stagesis shown in Fig. 5.15, while the variation inliquefaction resistance with the number liquefaction stagesis shown in Fig. 5.16.

The results of multiple-liquefaction tests using 11 non-coated stackedringsare similar to those using 31 non-coated stackedrings, in the sense that specimens subjected withlargervalue of $\gamma_{DA.max}$show significant increase in density besides a reduction in liquefaction resistance. By combining Figs. 5.15 and 5.16,the relationships between liquefaction resistanceand relative density in multiple liquefaction tests was obtained, as shown in in Fig. 5.17. A quantitative comparison between tests results obtained using 31 and 11 non-coated stacked rings cannot be made, since the amount of generated frictions is very different between the two testing conditions. However, qualitatively, it can be said that Toyoura sand showed similar behaviors under both testing conditions.

Fig. 5.17 also comparesthe soil behaviorssubjected with multiple liquefactionsand the ones subjected withsingle stage liquefaction.It can beseen that the Toyoura sand specimens subjected to multiple liquefaction may have a lower liquefaction resistance thanthose undergoing only single (virgin) liquefaction. In all stages, the specimen sheared up to $\gamma_{DA.max}$= 2% has higher liquefaction resistancesthan the one that liquefied once. Alternatively, in the case of the specimen sheared up to $\gamma_{DA.max}$= 5%, the liquefaction resistance was first lower than the reference virgin liquefaction resistance curve (i.e. during 1st, 2nd, and 3rd

stages)andthen dramatically increasedat the 4th stages. On the other hand, the specimen sheared up to $\gamma_{DA.max}$= 10% showed always a lower liquefaction resistance compared to the reference virgin liquefaction resistance curve.
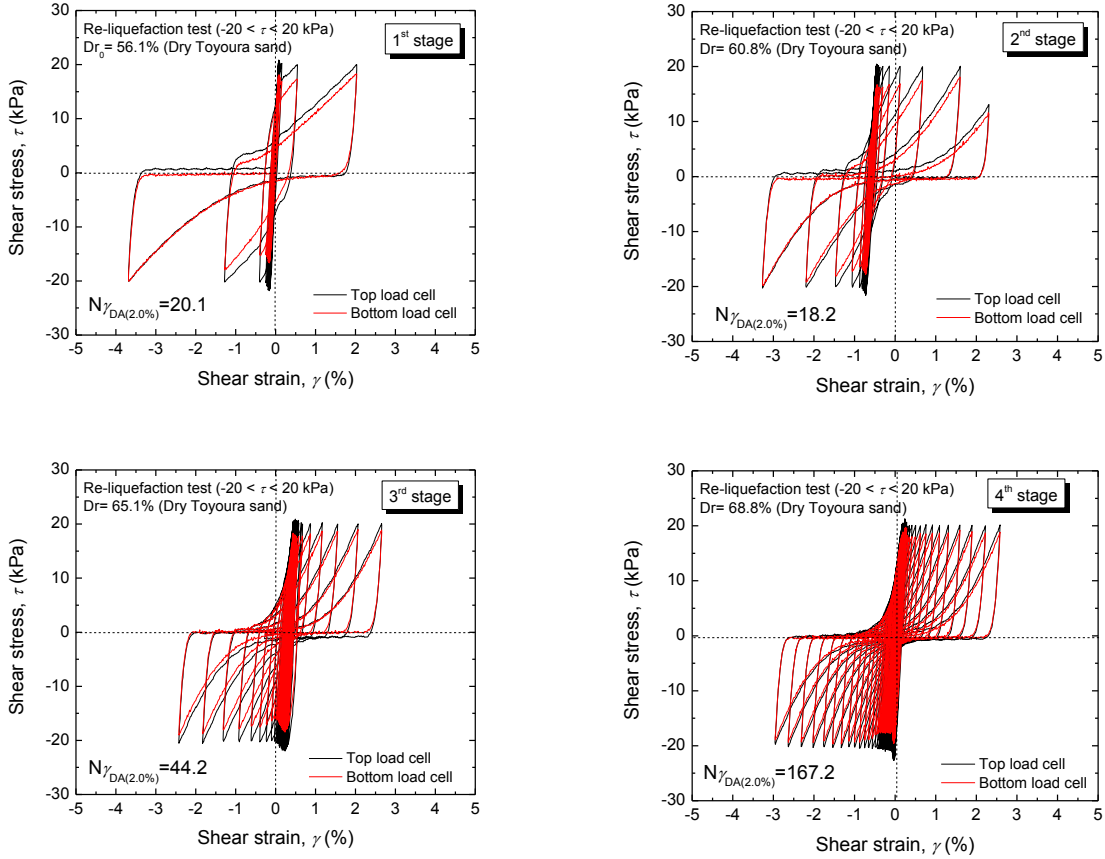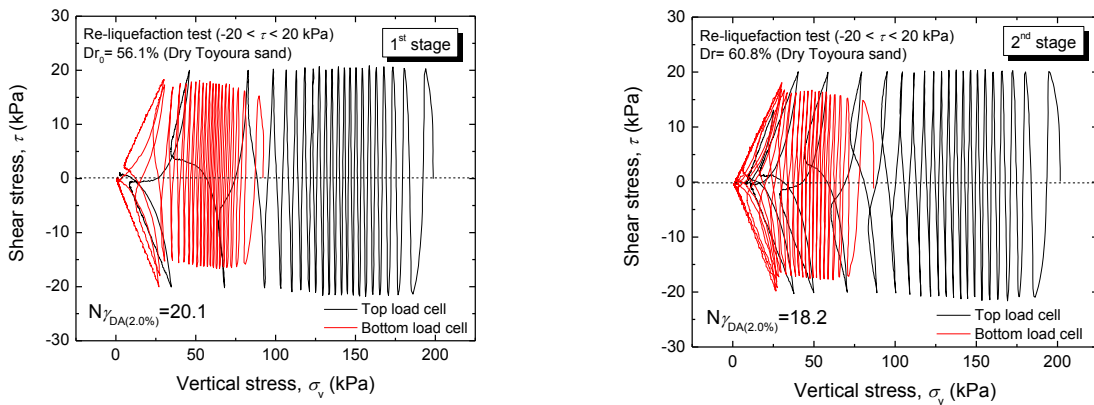

Fig. 5.13: Typical shear stress - shear strain relationships in the multiple-liquefaction testusing 11 non-coated stacked rings (e.g. ML11 test)
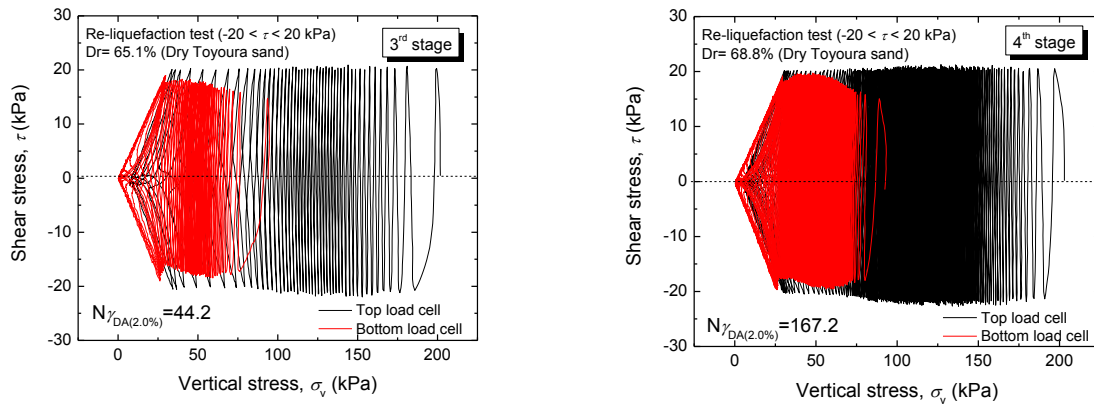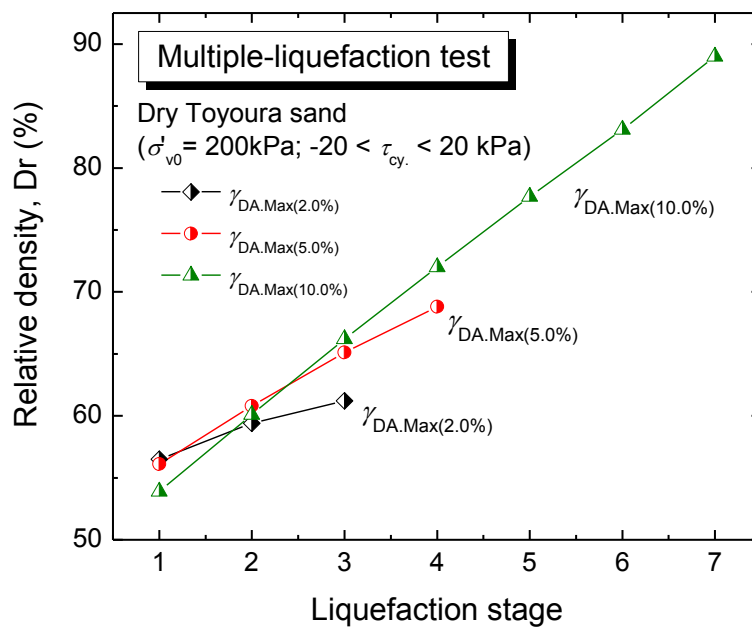
Fig. 5.14: Typical shear stress -vertical stress relationships in the multiple-liquefaction testusing 11 non-coated stacked rings (e.g. ML11 test)

Fig. 5.15: Change in relative density in each stage of multiple-liquefaction tests using 11 non-coated stacked rings
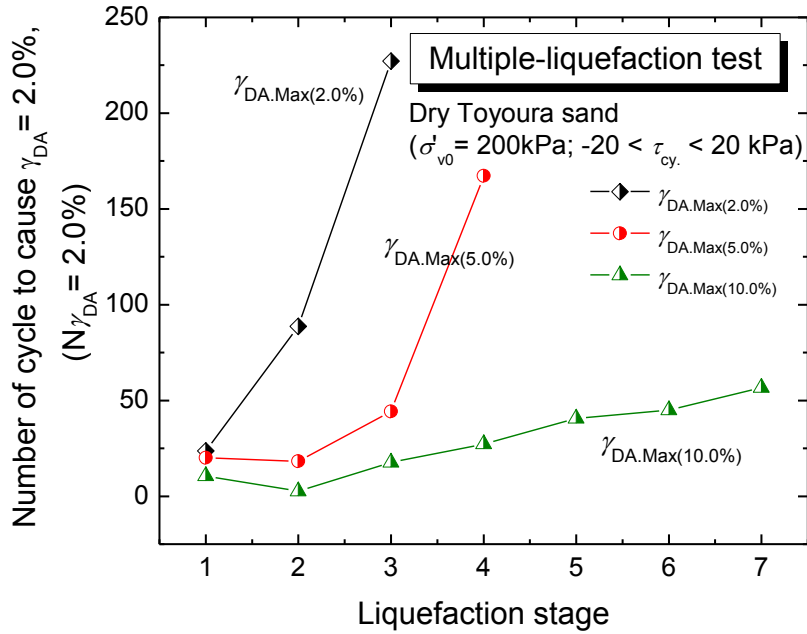
Fig. 5.16: Variation in liquefaction resistance with the number of liquefaction stages in multiple-liquefaction tests using 11 non-coated stacked rings
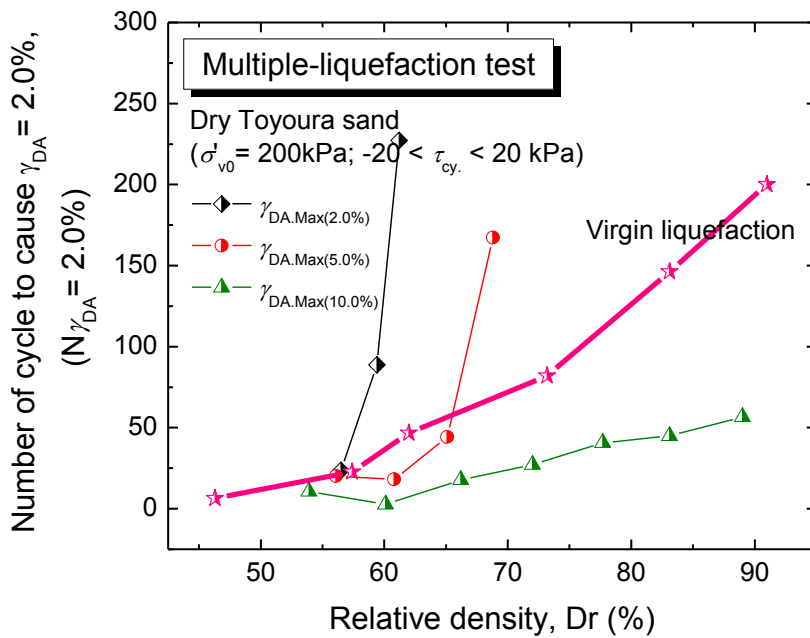
Fig. 5.17: Relationships between liquefaction resistance and relative density in multiple-liquefaction tests using 11 non-coated stacked rings

5.3.3　Multiple-liquefaction testsusing 11 coated stackedrings

An additional modification to further reduce the excessive frictiongenerated in using stacked-ring shear apparatus was madeby coating the stacked rings bya frictionless material, so called DLC coating. As mentioned in the previous chapter, the DLC coating has a much smaller coefficient of friction (μ=0.2) than the original stainless steel material (μ=0.8). Nevertheless, contrarily tothe expectations, the use of 11 DLC-coated stackedringsdid not produce a significantly reduction of the generated friction as reported in the previous chapter.

To investigate the soil behaviorsduring multiple liquefactions in the11 coated stacked-ring, ten tests (ML13 to ML22 tests) were conducted on loose specimens having initial relative densities of 52-55%. Each of ten specimenswassubjected with pre-fixed $\gamma_{DA.max}$of 0.2%, 0.25%, 0.3%, 0.4%, 0.5%, 1%, 2%, 5%, 7%, and 10%, respectively.Note that,the tests on specimens sheared up to γ_{DA} = 2-10% were carried out to investigate the effects of strain amplitudes on the cyclic behavior of multiple-liquefied sand.Alternatively, the tests on specimens sheared at smaller than γ_{DA} = 2% were performedlater to investigate the effects of dissipated energy on the soil behaviors during multiple liquefactions (refer to chapter 7 for details).

Fig.5.18 shows typical shear stress - shear strain relationshipsobserved in multiple-liquefaction test using 11 coated stackedrings, while Fig. 5.19 shows the corresponding shear stress - vertical stress relationships. The changein specimen density during subsequent re-consolidation stages on each liquefaction stage is shown in Fig. 5.20. The specimen sheared up to $\gamma_{DA.max}$= 2% showed the smallest increase indensity duringsubsequentre-consolidationstages, followed by the specimens sheared up to $\gamma_{DA.max}$= 5%, 7% and 10%. The variationin liquefaction resistance with the number of liquefaction stages is shown in Fig. 5.21. The specimen sheared up to $\gamma_{DA.max}$= 2% showed the highest liquefaction resistance ateach liquefaction stage, followed by the specimens sheared up to $\gamma_{DA.max}$=5%, 7%, and 10%. By combining Figs. 5.20and 5.21, the relationship between multiple-liquefaction resistance and relative density is obtained as shown in Fig. 5.22. Although prepared at a similar initial relative density, the specimen sheared up to $\gamma_{DA.max}$= 2% showed the highest multiple-liquefaction resistance when compared at similar values of current relative density, followed by the specimens sheared up to$\gamma_{DA.max}$= 5%, 7%, and 10%. The overall behavior of Toyoura sand investigated using 11 coted stacked rings was found to be similar to those observed in previous multi-liquefaction tests using either 31 or11 non-coated stackedrings.
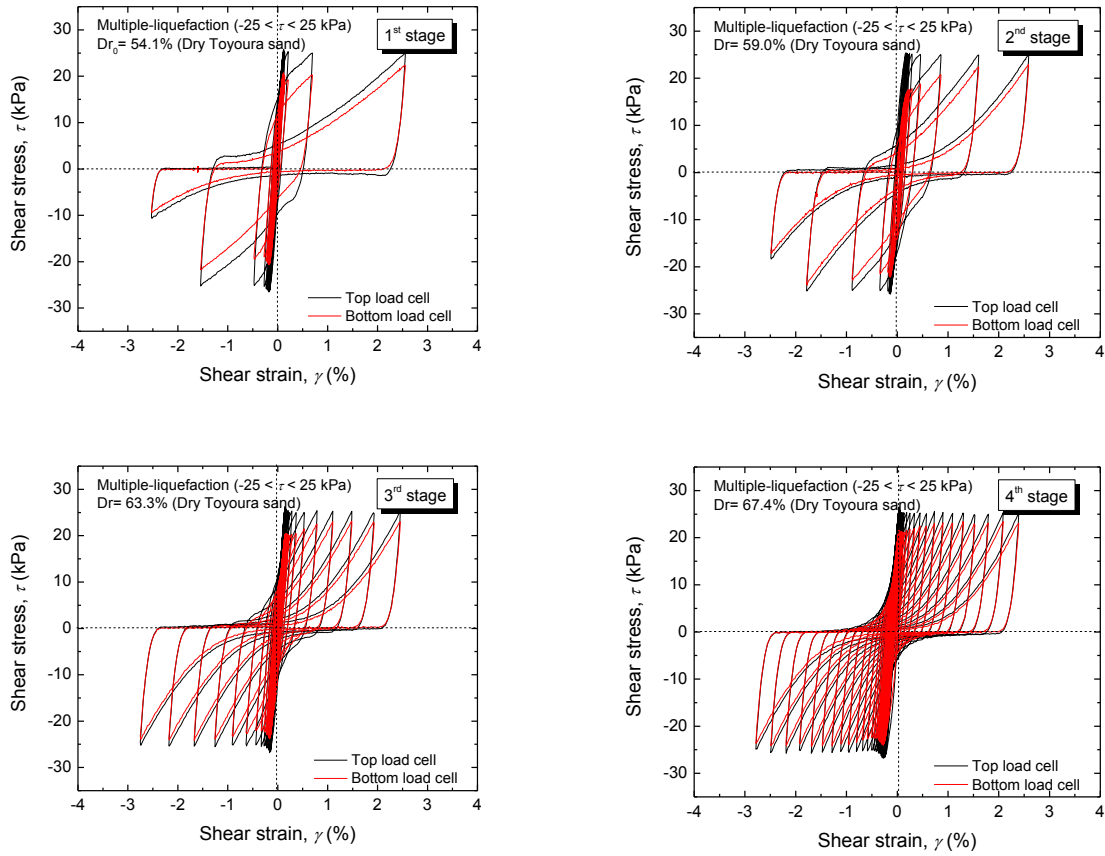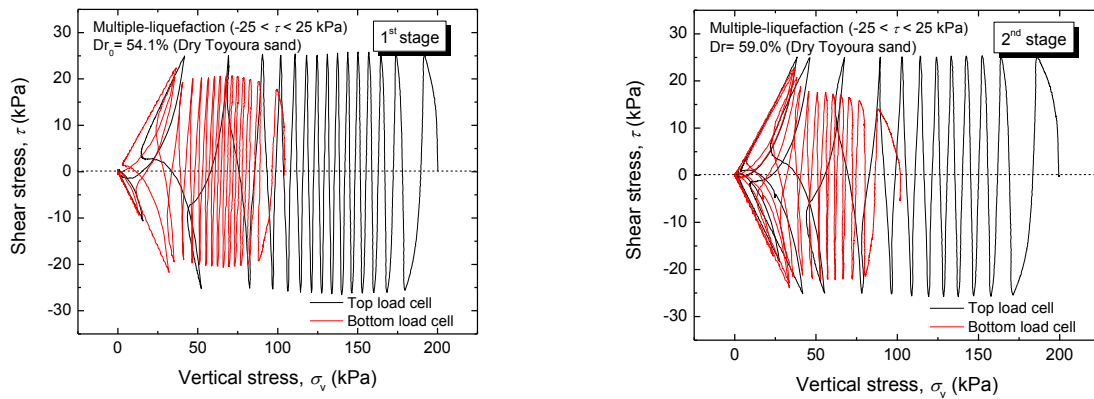
Fig. 5.18: Typical shear stress - shear strain relationships in multiple-liquefaction test using 11 coated stacked rings (e.g. ML20 test)
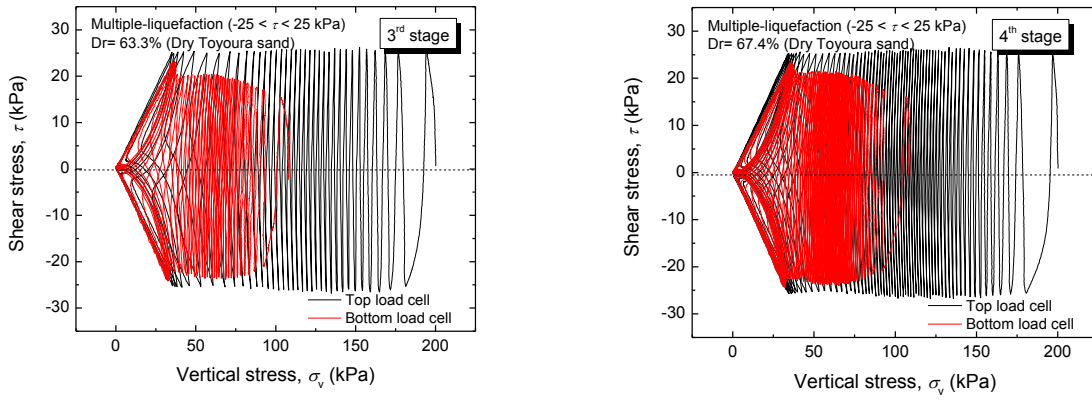
Fig. 5.19: Typical shear stress - vertical stress relationships in multiple-liquefaction testusing 11 coated stacked rings (e.g. ML20 test)
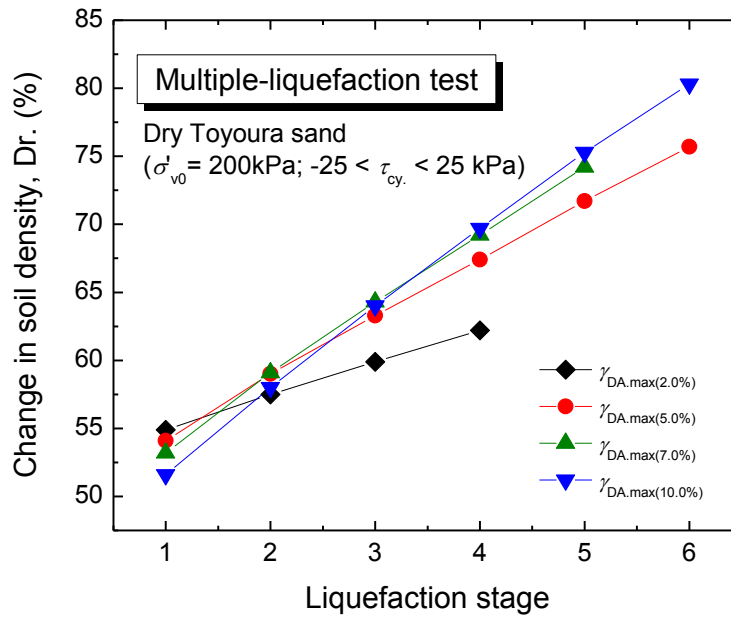

Fig. 5.20: Change in relative densitywith number of liquefaction stages in multiple-liquefaction tests using 11 coated stacked rings
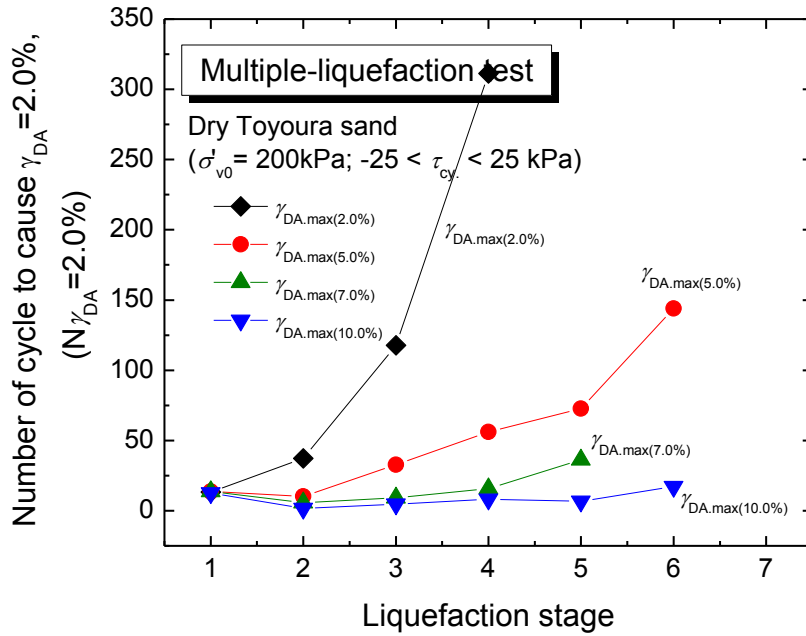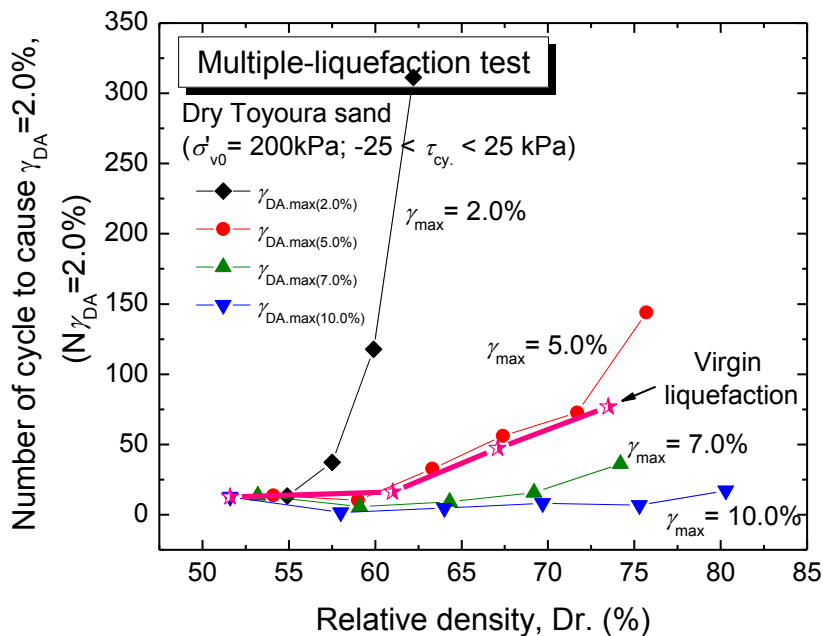
Fig. 5.21: Variation in liquefaction resistancewith number of liquefaction stagesin multiple-liquefaction tests using 11 coated stacked rings
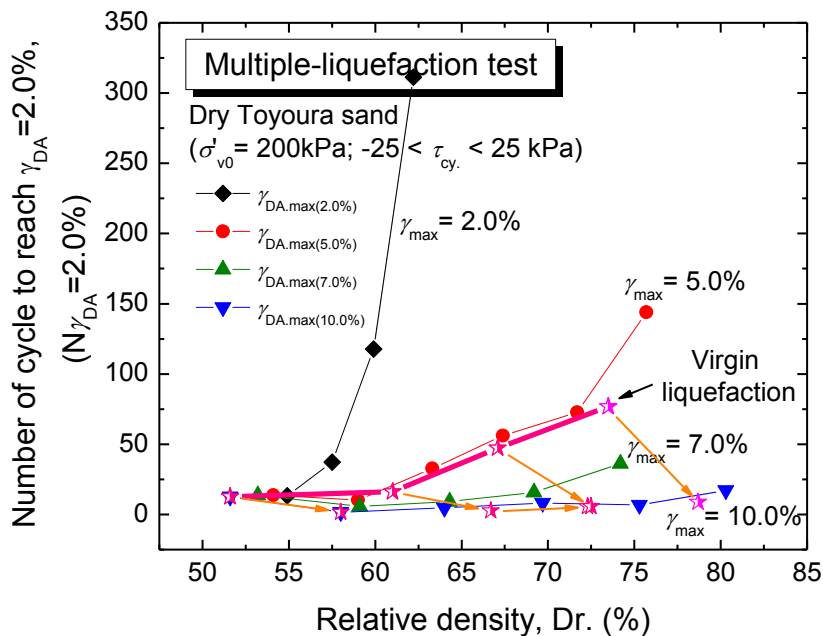

Fig. 5.22: Relationships between liquefaction resistance and relative density in multiple-liquefactionusing 11 coated stacked rings

For the sake of comparison, three re-liquefaction tests (2 stages of liquefaction) were conducted on specimens having initial relative density of 61.0%, 67.1% and 73.5%.Each specimen was sheared up to $\gamma_{DA.max}$= 10% during the 1st stage of liquefaction. Note that in multi-liquefaction tests, the 1st stage of liquefaction corresponds to the single-liquefaction

tests. Therefore, it could be used to define a reference virgin liquefaction resistance curve for Toyoura sand specimens sheared up to $\gamma_{DA.max}= 10\%$.

In Fig. 5.23 and Fig. 5.24, the liquefaction resistance in multiple-liquefaction tests is compared to the reference virgin liquefaction curve. It can be seen that the specimen sheared up to $\gamma_{DA.max}= 2\%$ showed a liquefaction resistance higher than the reference curve from single-liquefaction tests. The specimen sheared up to $\gamma_{DA.max}= 5\%$ showed smaller liquefaction resistance than reference curve in the 2nd liquefaction stage, but higher in the subsequent re-liquefaction stages. Alternatively, specimens sheared up to $\gamma_{DA.max}=7\%$ and 10% showed always smaller liquefaction resistance than the reference curve for any given density.

The results on two-stage liquefaction tests offer new evidence on the effects of shear strain amplitude on the cyclic behavior of multiple-liquefied sands. After the specimens were sheared up to $\gamma_{DA.max}= 10\%$ in the 1st stage of liquefaction, the liquefaction resistance of specimens in the 2nd liquefaction stage dropped in a similar way observed from multiple liquefactions test on Toyoura sand sheared up to $\gamma_{DA.max}$ of 10%.

Fig. 5.23: Relationships between liquefaction resistance and specimen relative density in multiple-liquefaction using 11 coated stacked rings
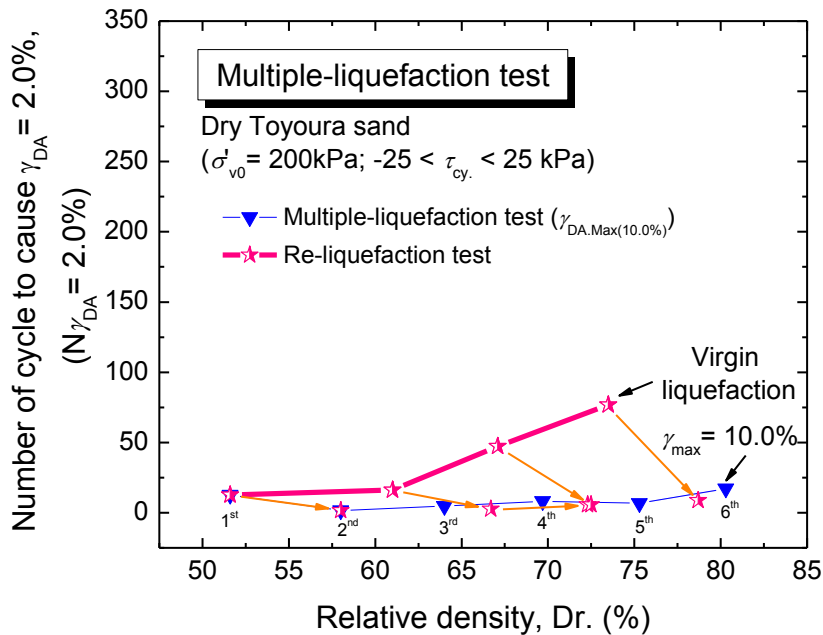
Fig. 5.24: Comparison between liquefaction resistance observed forrepeated liquefied sand and that observed in multiple liquefaction tests on specimens sheared up to $\gamma_{DA.max} = 10\%$

As mentioned earlier, additionalseries of test was conducted to investigate the effectsof strain amplitude history duringmultiple liquefactions on the specimens shearedat $\gamma_{DA.max}$less than 2%. In brief, the specimens in this series of test were subjected to the 3 stages of liquefactions. Specifically, in the 1st liquefaction stage, each specimen was sheared up toa specific $\gamma_{DA.max}$of 0.2%, 0.25%, 0.3%, 0.4%, 0.5% and 1%. Then, in the 2nd liquefaction stage, allthe specimens were sheared up to $\gamma_{DA.max} = 2\%$. Finally, all the specimens were sheared up to $\gamma_{DA.max} = 2\%$ in the 3rd liquefaction stage. The results of this series oftests wascompared to the results of previous multiple-liquefaction testson specimen sheared up to $\gamma_{DA.max} = 2\%$.

The results on this series of tests is reported inFigs. 5.25through5.30. Figure 5.25 shows the change inrelative densitywith the number of liquefaction stages. It can be seen that the specimens became denser-and-denser ateach liquefaction stages. Despite the small variation in the initial relative density (55-56.7%), theeffects of the strain amplitude on the change of soil density in the post-liquefaction re-consolidation stages can be clearly seen, as summarized in Fig. 5.26. As all the specimens were sheared with $\gamma_{DA.max} = 2\%$ in the 2nd liquefaction stage, the density increaseslarger in post liquefaction during 3rd re-consolidation as compare to the 2nd re-consolidation in first post liquefaction.

Fig.5.27 shows the variation of liquefaction resistance with the number of liquefaction stages. Interestingly, these results did not follow the cyclic sand behavior observedin all theprevious multiple-liquefaction tests. In fact, in the previous tests, the specimens sheared up

to $\gamma_{DA.max}$> 2% showed smaller multiple-liquefaction resistances as the $\gamma_{DA.max}$ level increased. The results on the specimens sheared using $\gamma_{DA.max}$<2% showedthe opposite tendency. The specimen sheared up to $\gamma_{DA.max}$= 0.2% has smaller liquefaction resistance than that sheared up to $\gamma_{DA.max}$= 0.25%. Moreover, the specimen sheared up to $\gamma_{DA.max}$= 0.25% has smaller liquefaction resistance than that sheared up to $\gamma_{DA.max}$= 0.30%, and so on up to $\gamma_{DA.max}$ = 0.5%. However, the specimen sheared up to $\gamma_{DA.max}$=0.5% showed the highest liquefaction resistance among alltested specimens, even larger than that sheared up to $\gamma_{DA.max}$= 1%. This implies that the applied strain amplitude may not be the single parameter that determines the soil resistance during multiple liquefactions. It is revealed later in Chapter 7 that instead of strain amplitude, the amount of dissipated energy during liquefaction is the real parameter that defines the soil behaviors during multiple liquefactions.

A summary of the cyclic resistance vs. relative density relationships observed in multiple-liquefaction tests for all specimens is given in Fig. 5.28. A close up of Fig. 5.28 showing only the data for loose sand specimen sheared $\gamma_{DA.max}$< 2% is shown in Fig. 5.29. From the latter figure, it can be seen that the liquefaction resistance decreases with the increase of$\gamma_{DA.max}$applied to the specimen in the 2nd liquefaction stage. For the sake of comparison, test results shown in Fig. 5.23 areplotted in Fig. 5.30 against those obtained bymultiple-liquefaction teston specimens sheared up to $\gamma_{DA.max}$= 2%. The liquefaction resistancesof all specimensin the 3rd liquefaction stage seems to approach the resistances of the specimen sheared with $\gamma_{DA.max}$= 2%.
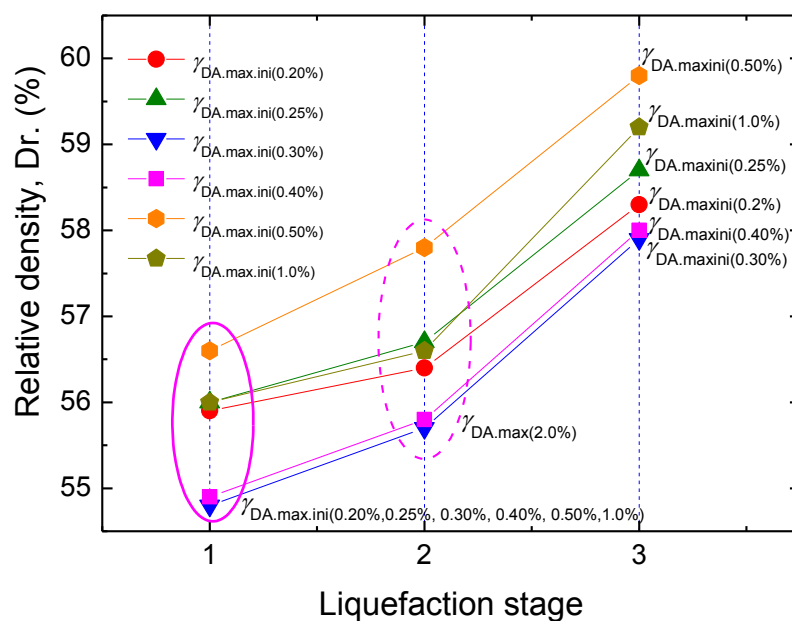
Fig. 5.25:Change in relative density with the number of liquefaction stages in multiple-

liquefaction tests on specimens sheared using $\gamma_{DA.max} < 2\%$ in the 1st liquefaction stage
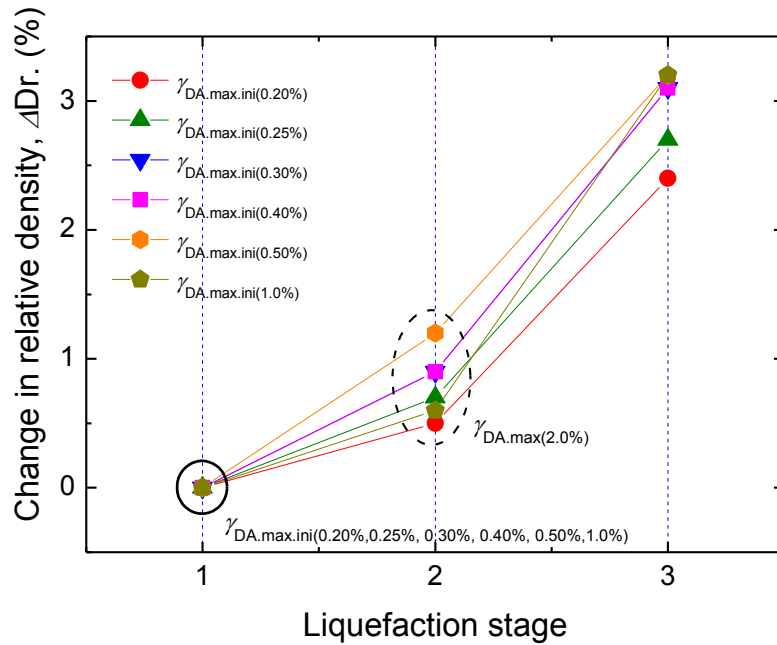

Fig. 5.26: Change in relative density increment with the number of liquefaction stages in multiple-liquefaction tests on specimens sheared using $\gamma_{DA.max} < 2\%$ in the 1st liquefaction stage
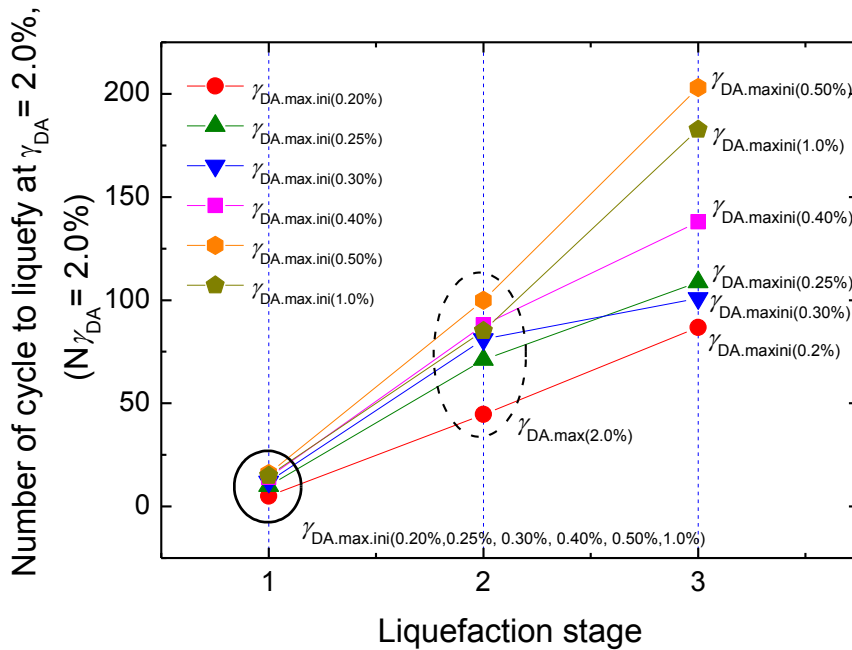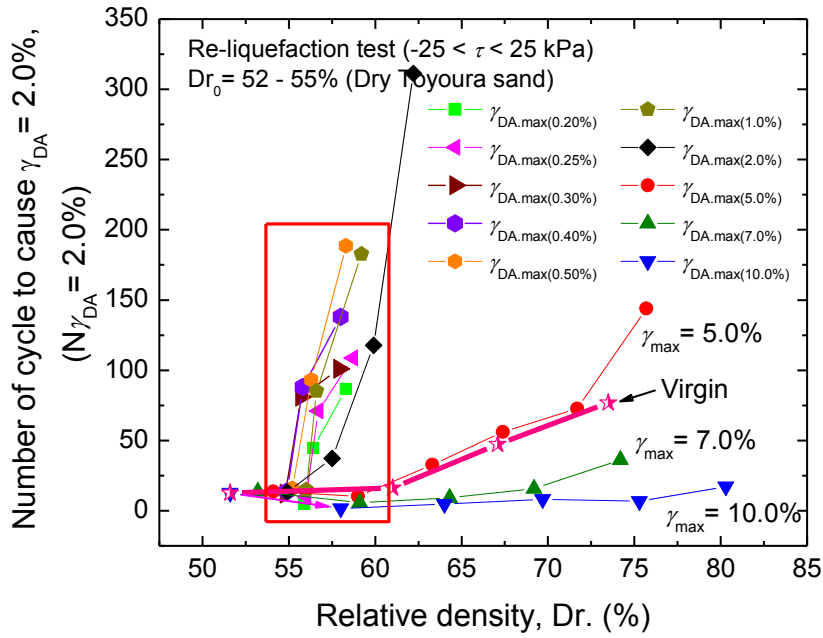

Fig. 5.27: Variation of liquefaction resistancewith the number of liquefaction stages in multiple-liquefaction tests on specimens sheared using $\gamma_{DA.max} < 2\%$ in the 1st liquefaction stage

Fig. 5.28: Liquefaction resistance vs. relative density relationshipsobserved in all multiple-liquefaction tests using 11 coated stackedrings
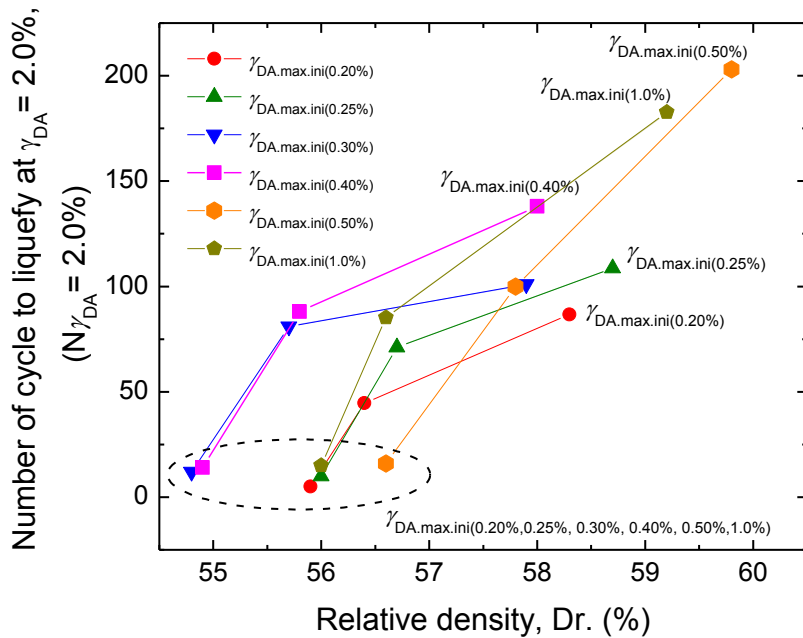
Fig. 5.29: Liquefaction resistance vs. relative density relationshipsof specimens sheared using $\gamma_{DA.max}$< 2% in the 1st liquefaction stage
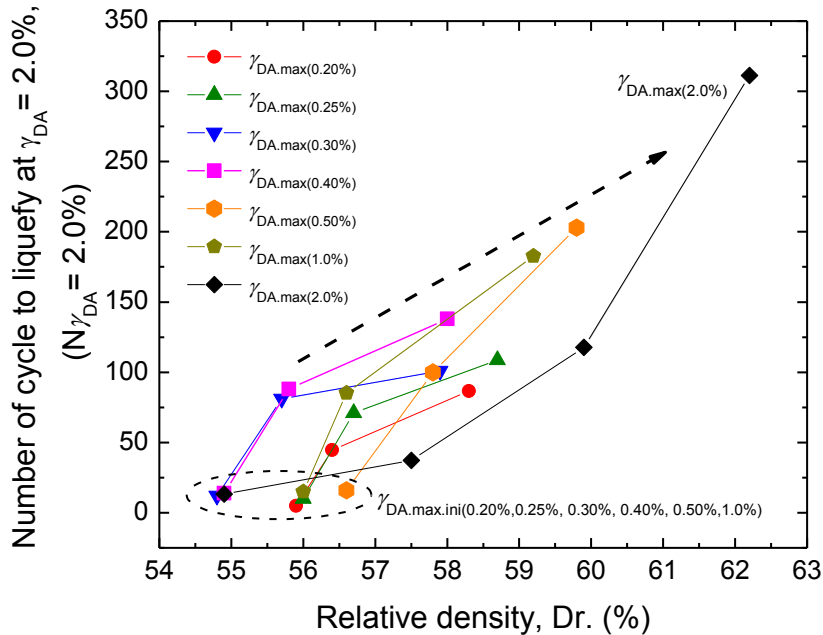
Fig. 5.30: Comparison between the liquefaction resistance of specimens sheared using $\gamma_{DA.max} < 2\%$ in the 1st liquefaction stage and those sheared up to $\gamma_{DA.max} = 2\%$

In summary, based on a number of multiple-liquefaction tests conducted by newly developed stacked-ring shear apparatus using 31 and 11 non-coated rings as well as 11 coated rings, it is clear that the liquefaction resistance of sandin multi-liquefaction stages is highly affected by thestrain history,i.e. strain amplitude, applied in previous liquefaction stages.

In particular, the series of tests carried out on specimens sheared using $\gamma_{DA.max} > 2\%$ showed that the larger the shear strain amplitude applied in the previous liquefaction stages is, the lowerthe liquefaction resistance in the next liquefaction stage is.

In contrast, tests conducted on specimens sheared using $\gamma_{DA.max} < 2\%$ showed the opposite tendency, since the larger the shear strain applied is, the higher the liquefaction resistance of the multiple-liquefied soil is.

However, it was found later that the reason beyond these two different behaviors may be the effect of dissipated energy in the previous liquefactionstages, as discussed in detail in Chapter 7.

In an attempt to better understand these behaviorsand to evaluate the local deformation behavior of the specimens as compared to their global response, image analysis technique was employed in several series of tests. Specifically, the image analysis was carried out in the tests employing the 11 non-coated and 11 coated stakedrings.

The procedure to conduct image analysis was explained in details in Chapter 3. Therefore, the current chapter will only discuss about the results of the image analysis.

5.3.4 Image analysis results in multiple-liquefaction test using 11 non-coated stacked-ring shear type

In using 11 stackedrings, the local deformationsof a specimen can be measuredin10 distinct sections, which arelocated between two adjacentrings as shown in Fig. 5.31. Yetfor simplicity, in this study the 10 sections were reduced into 5 sections by averaging a pair of neighboring sections. From the bottom to the top, these sections correspond to the lowest, middle-lower, center, middle-upper, and upper-most sections. Each ring was marked with 18 dots at equal spacing of 38.3mm,i.e. every 30° in circumferential direction.

Figure 5.32comparestypical local shear strain (γ_{Loc})measurements in the 1st liquefaction stage obtained by image analysis and the corresponding results detected by external potentiometer. On the other hand, Fig. 5.33 shows similar measurements at the 2nd liquefaction stage for the specimen shearedγ_{DA}> 5%. It can be seenthat,the values of γ_{Loc} were very similar to the global one for γ_{DA}< 1%. However, afterγ_{DA}exceeds 1%, some deviationbetween the local and global shear strain measurements was observed. Such initial deviation started when the vertical stress reachedapproximately 80 kPa as can be seen by looking at the shear stress - vertical stress relationshipsshown in Figs. 5.34 and 5.35.For completeness, thecorresponding typical shear stress - shear strain relationshipsare shown in Fig. 5.36 and Fig. 5.37.

It is important to mention that, in the current configuration of stacked-ring shear apparatus, both shear stress (τv_{θ}) and vertical stress (σ_v) are measured only at the upper-most and lowest sections of the specimen, whileforother sections such stress components cannot be directly measured. Nevertheless, it would be reasonable to assume that the variationof both the shear stress and vertical stress from the top to the bottom is linear (Fig. 5.38). Therefore, the unknown shear stress and the vertical stress for the intermediatesections can beapproximated by using the linear interpolationshown in Eqs. 5.1 and 5.2.

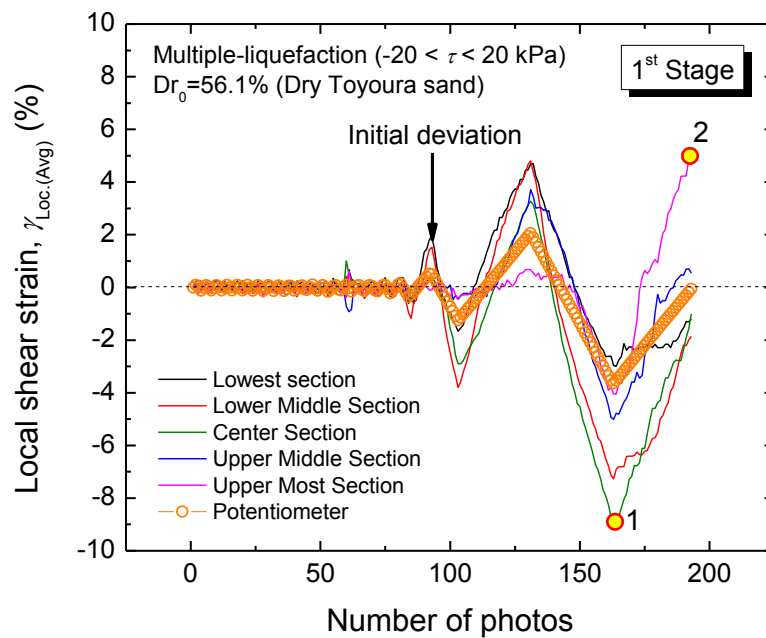Fig. 5.31: Sections of the 11 non-coated stackedrings used for image analysis

Fig. 5.32: Comparison between local shear strain measurement in the 1st liquefaction stage by image analysis and external potentiometerfor aspecimen sheared at maximum $\gamma_{DA.max} = 5\%$ (e.g. ML11 test)

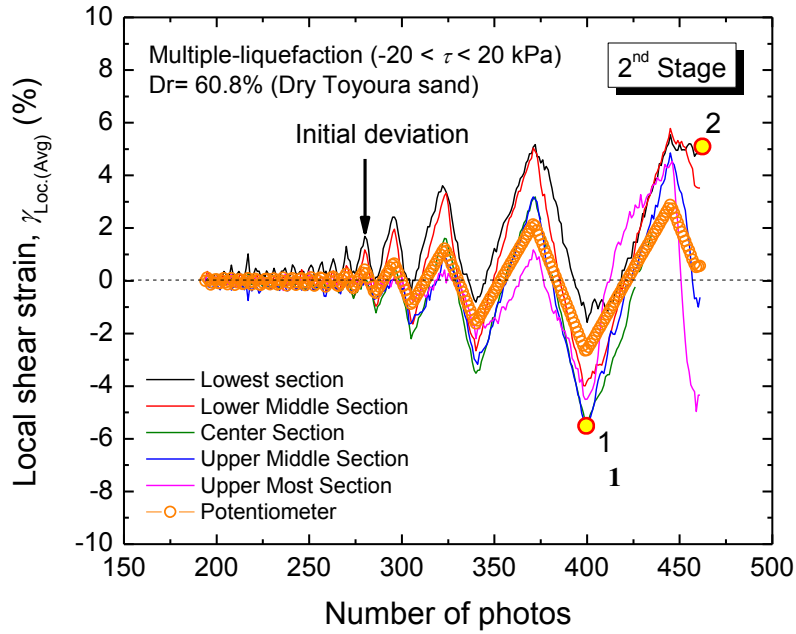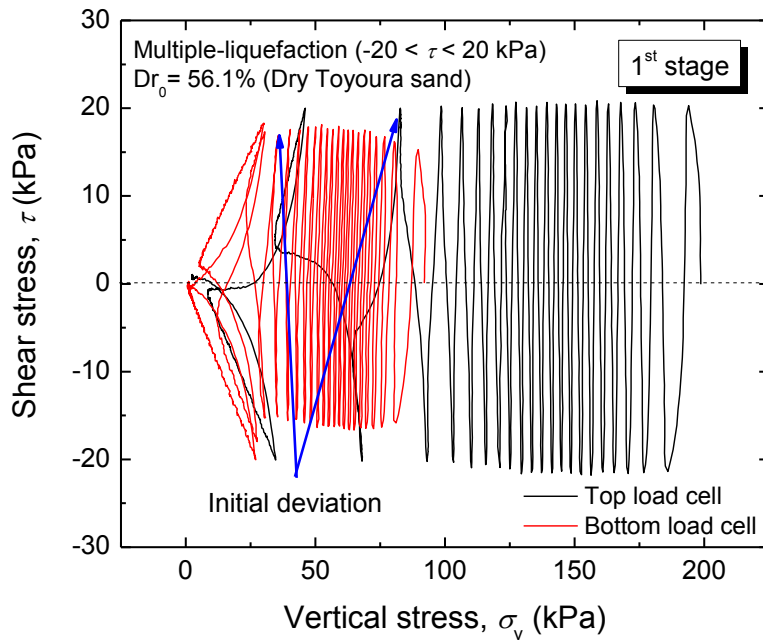Fig. 5.33: Comparison between local shear strain measurement in the 2nd liquefaction stage by image analysis and external potentiometer for a specimen sheared at maximum $\gamma_{DA.max}= 5\%$ (e.g. ML11 test)

Fig. 5.34: Shear stress - vertical stress relationshipsin the 1st liquefaction stagefor a specimen sheared at maximum $\gamma_{DA.max}= 5\%$ (e.g. ML11 test)
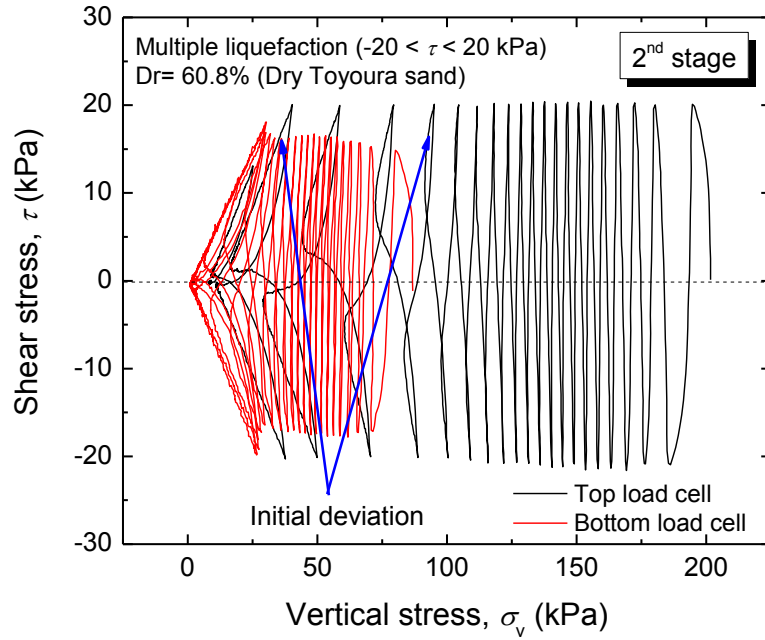
Fig. 5.35: Shear stress - vertical stress relationships in the 2nd liquefaction stage for a specimen sheared at maximum $\gamma_{DA.max}$= 5% (e.g. ML11 test)
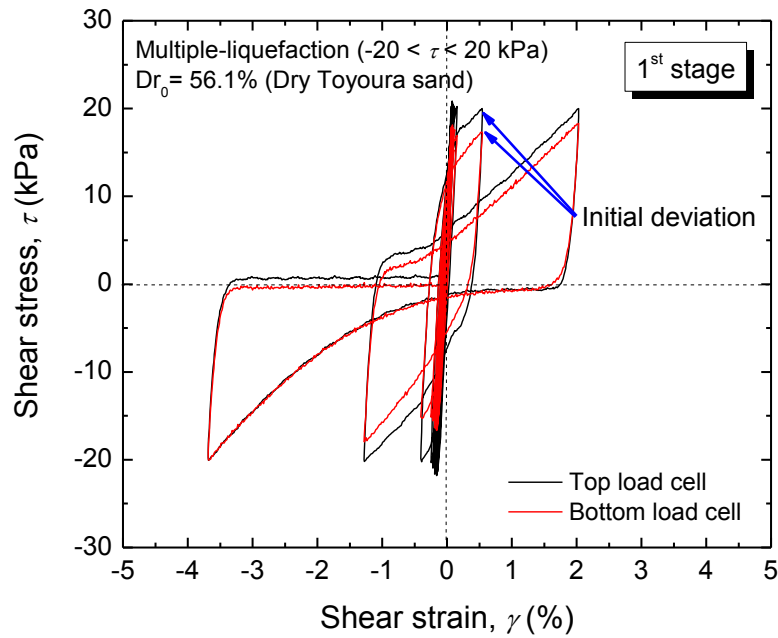
Fig. 5.36: Shear stress - shear strain relationships in the 1st liquefaction stage for a specimen sheared at maximum $\gamma_{DA.max}$= 5% (e.g. ML11 test)
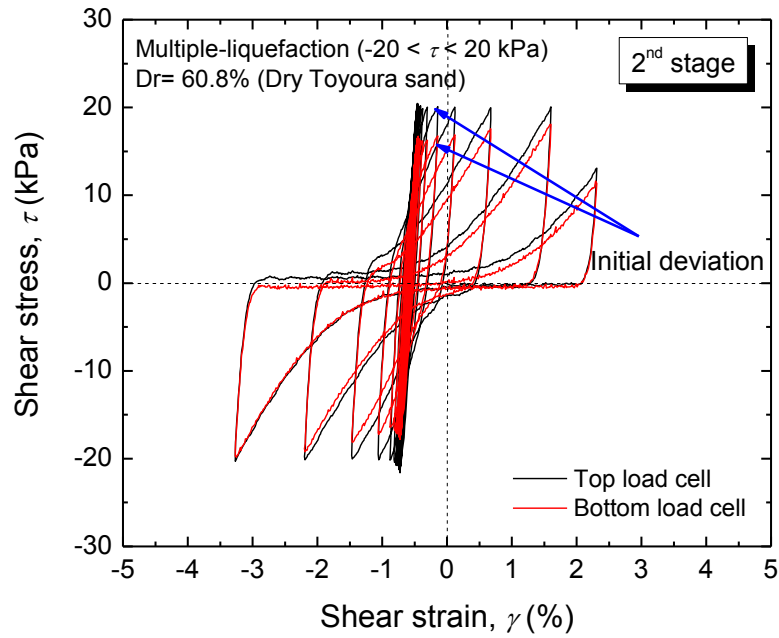
Fig. 5.37: Shear stress - shear strain relationships in the 2nd liquefaction stage for on a specimen sheared at maximum $\gamma_{DA.max}$= 5% (e.g. ML11 test)
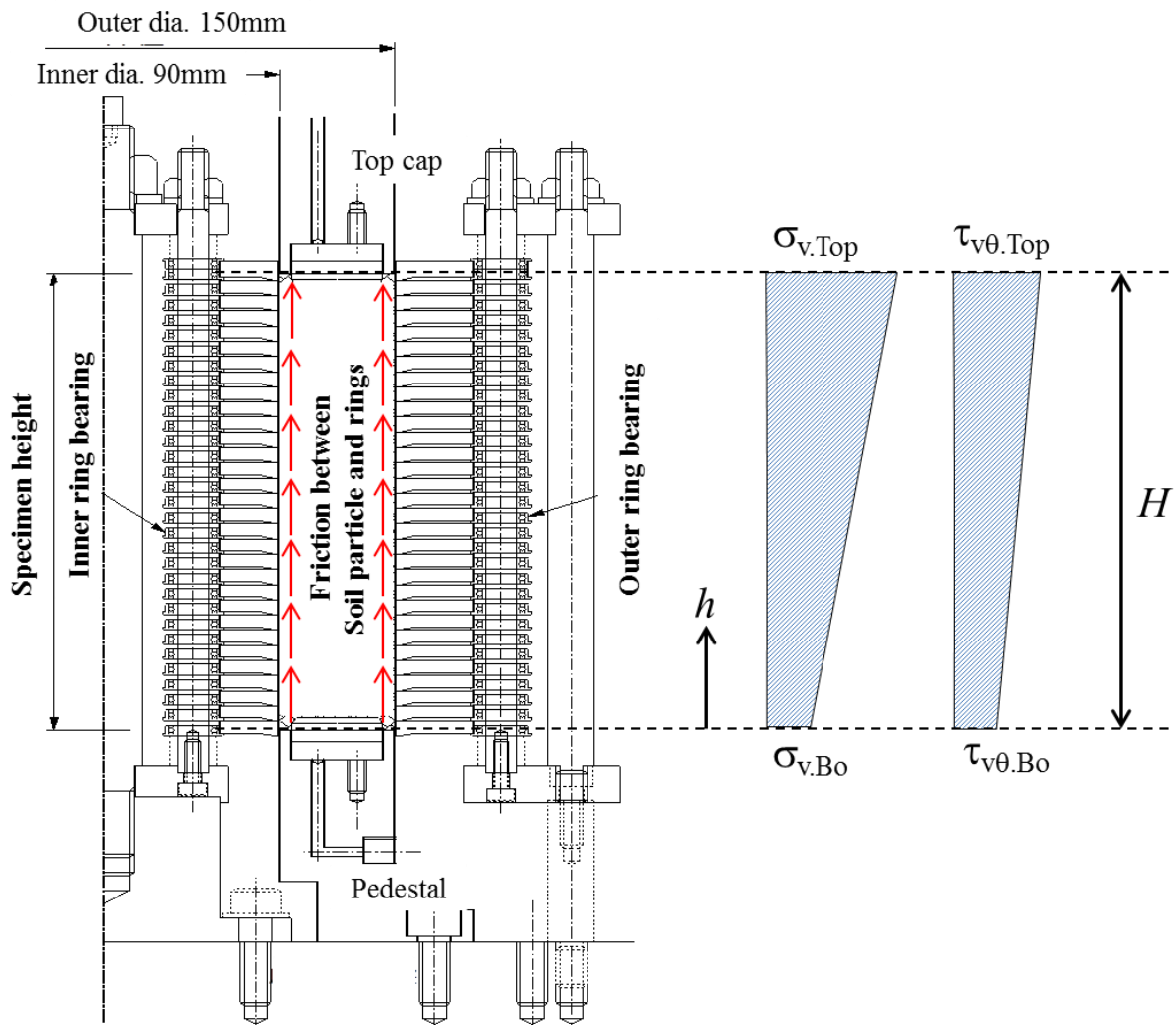
Fig. 5.38: Assumed linear distribution of local shear stress (τ_{Loc})and local vertical stress ($\sigma_{\text{v.Loc}}$)in the stacked ring shear apparatus

Based on Fig. 5.38, the local shear stress and local vertical stress at each section of the specimen can be calculated as follows:

$$\tau_{\theta v}(h) = \frac{(\tau_{\theta v.Top} - \tau_{\theta v.Bo})}{H} h + \tau_{\theta v.Bo} \qquad (5.1)$$

$$\sigma_v(h) = \frac{(\sigma_{v.Top} - \sigma_{v.Bo})}{H} h + \sigma_{v.Bo} \qquad (5.2)$$

where, $\tau_{\theta v}(h)$ and $\sigma_v(h)$ are the unknown shear stress and vertical stress along the height of the specimen, respectively. $\tau_{\theta v.Top}$ and $\tau_{\theta v.Top}$ are the shear stress measured at the top and the bottom of the specimens, respectively. $\sigma_{v.Top}$ and $\sigma_{v.Bo}$ are the vertical stress measured at the top and the bottom of the specimen, respectively. *H* and *h* are the total height of the specimen and the distance from the bottom of the section examined, respectively.

Based on the results of local stress evaluations, typical local shear stress (τ_{Loc}) - local shear strain (γ_{Loc}) relationships obtained for each section are presented in Fig. 5.39 and Fig. 5.40. Points 1 and 2 in these figures mark the maximum local shear strain ($\gamma_{\text{Loc(max)}}$) and residual local shear strain ($\gamma_{\text{Loc(res)}}$) in each stage of the multiple-liquefaction test, respectively. Therefore, the center section has the largest shear strain of about 8.7% during the 1st liquefaction. However, the upper-most section has the largest residual shear strain of about 5.1% at the end of the 1st liquefaction stage. Alternatively, the lower-middle and center sections underwent a shear strain of about 5.4% on the 2nd liquefaction stage which was larger than that detected by potentiometer, while the lowest section has the largest residual strain of about 5.1% at the end of the 2nd liquefaction stage.
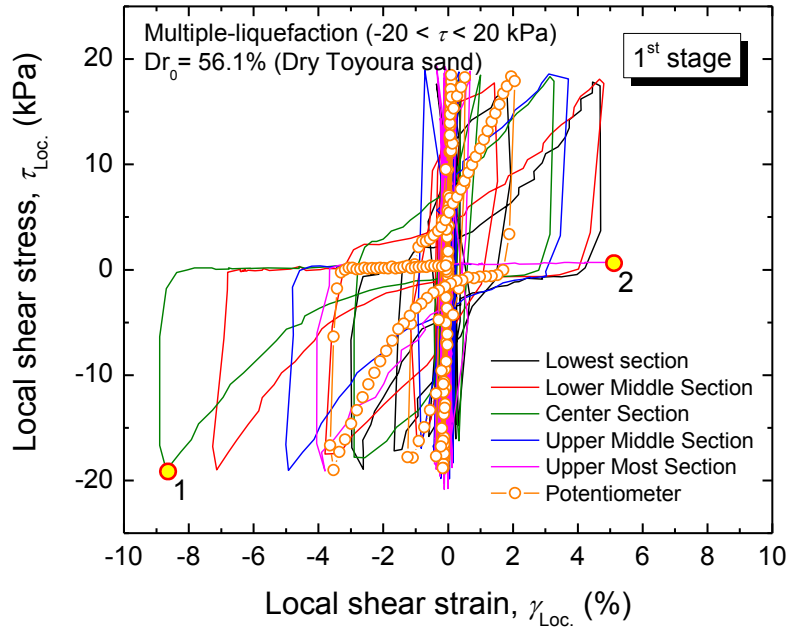
Fig. 5.39: Local shear stress - local shear strain relationships in the 1st stage for a specimen sheared at maximum $\gamma_{DA.max}=5\%$ (e.g. ML11 test)
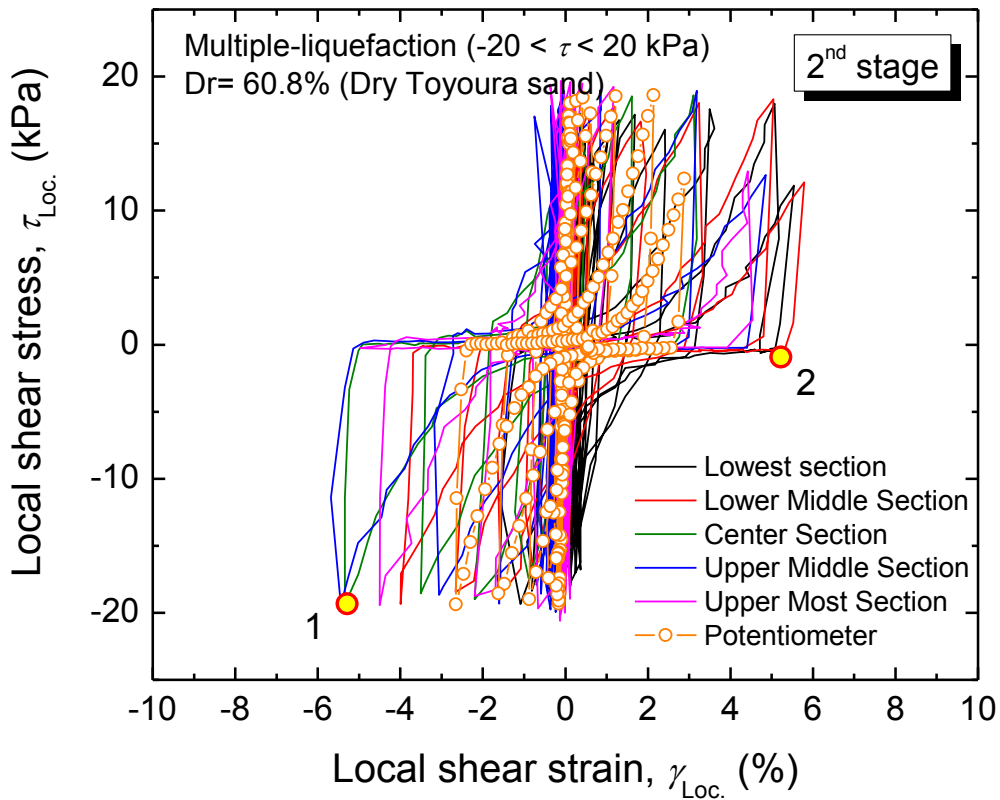

Fig.5.40: Local shear stress – local shear strain in the 2nd liquefaction stage for a specimen sheared at maximum $\gamma_{DA.max}=5\%$ (e.g. ML11 test)

Based on the image analysis results, two types of deviation of the local shear strain, namely the maximum local shear strain deviation (δ_{max}) and the residual local shear strain deviation (δ_{res}),are identified. Specifically, $\delta_{max}$is given by the difference between the largest local deformation experienced on each section andthe global shear strain deformation. In a similar way, $\delta_{res}$is given by the difference between the local deformation of each section and the global one at the end of each liquefaction stage.

Typical δ_{max}value evaluated for the specimens sheared up to γ_{DAmax}= 2%, 5% and 10% are shown in Fig. 5.41, Fig. 5.42, and Fig. 5.43, respectively. The largest δ_{max}occurred at the middle-lower, upper-most and middle-upper sections, respectively.

Typicalδ_{res}obtained for the specimens sheared up to $\gamma_{DA.max}$= 2%, 5% and 10% are shown in Fig. 5.44, Fig. 5.45, and Fig. 5.46, respectively. The largest δ_{res}occurred at the middle-lower, upper-most and middle-uppersections, respectively.

The comparison of δ_{max}andδ_{res}obtained in all the three tests can be seen in Fig. 5.47 and Fig. 5.48, respectively. In Fig. 5.47, the effects of shear strain amplitude can be seen clearly, since the larger the shear strain applied is, the larger theδ_{max} is. The range of δ_{max}in the specimen sheared up to$\gamma_{DA.max}$=2%, 5% and 10% are 0.5-2.0%,1.6-5.5%, and 2.1-32.8%,respectively.

In asimilar way, Fig. 5.48 shows that the larger the shear strain applied, the larger the δ_{res}. The range of δ_{res} in the specimen sheared up to $\gamma_{DA.max}$=2%, 5% and 10% are 0.0-1.3%, 0.5-5.2%, and 0.4-32.8%, respectively.
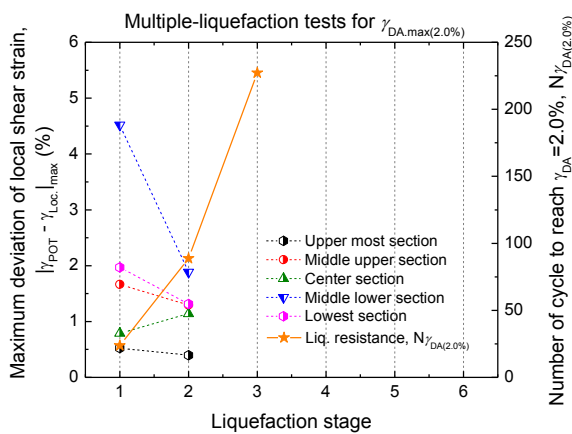
Fig. 5.41: Maximum deviation in the multiple-liquefaction test on specimen sheared up to $\gamma_{DA.max}$=2% (ML10 test)
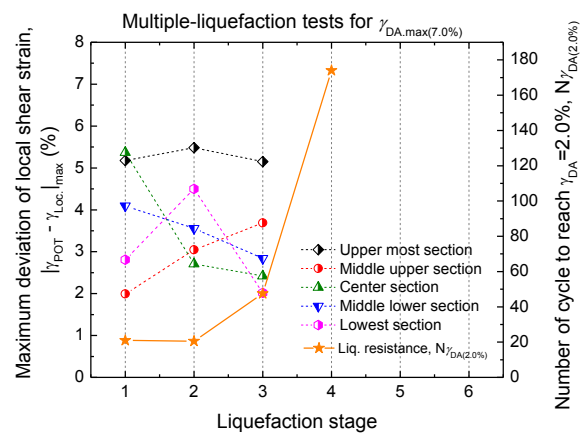
Fig. 5.42: Maximum deviation in the multiple-liquefaction test on specimen sheared up to $\gamma_{DA.max}$=5% (e.g. ML11 test)
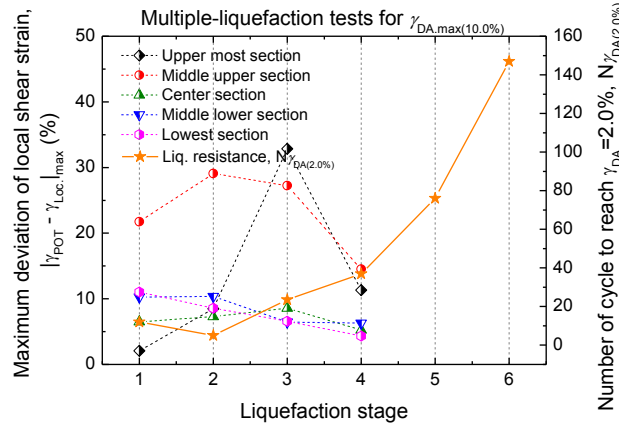
Fig. 5.43: Maximum deviation in the multiple-liquefaction test on specimen sheared up to $\gamma_{DA.max}$=10% (ML12 test)
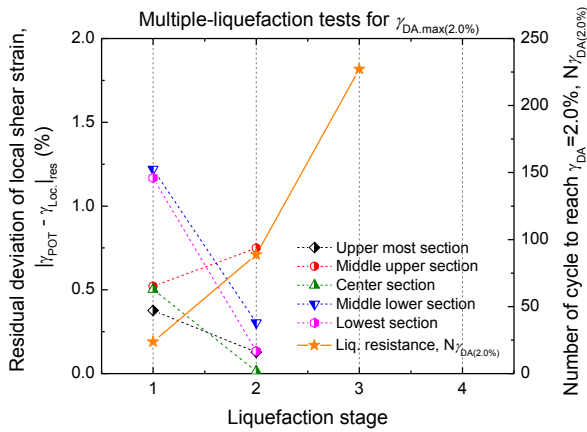

Fig. 5.44: Residual deviation in the multiple-liquefaction test on specimen sheared up to $\gamma_{DA.max}$=2%
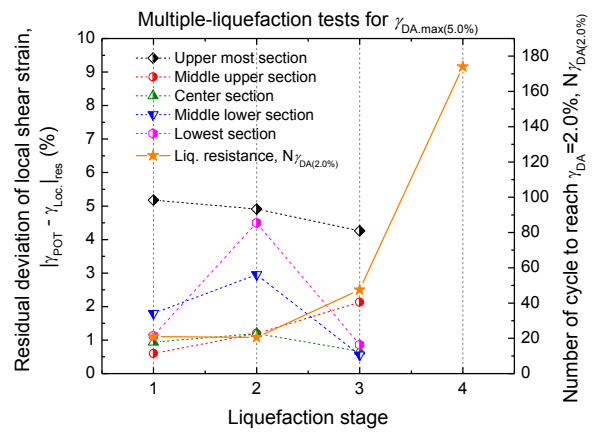

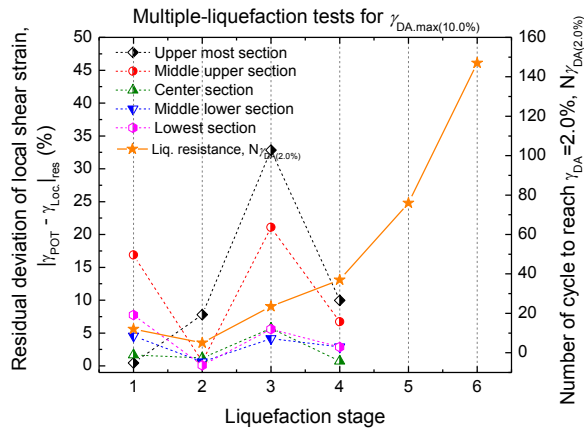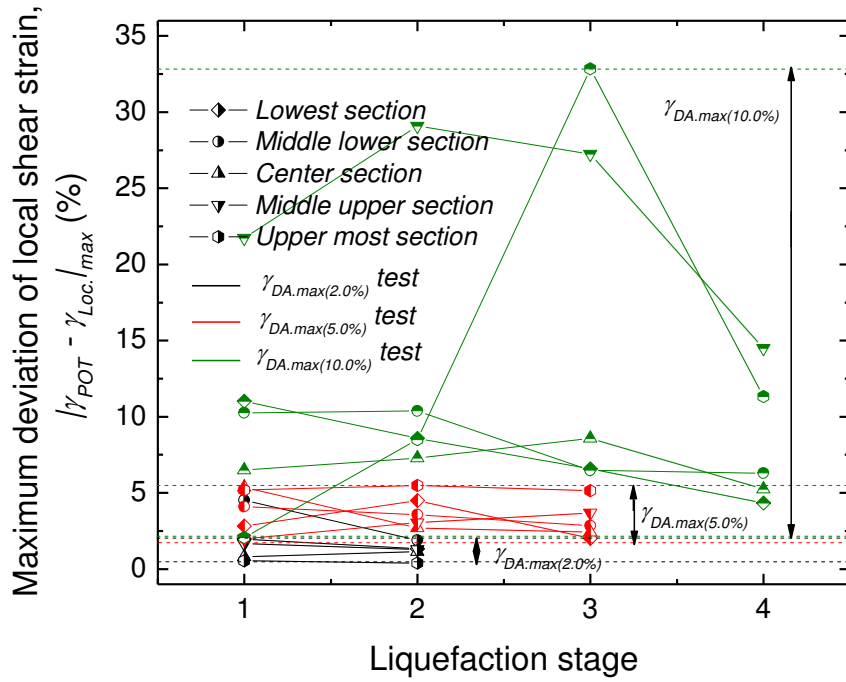Fig. 5.45: Residual deviation in the multiple-liquefaction test on specimen sheared up to $\gamma_{DA.max}$ =5%

Fig. 5.46: Residual deviation in the multiple-liquefaction test on specimen sheared up to $\gamma_{DA.max}$=10%

Fig. 5.47: Summary of maximum deviation of local shear strain in the multiple-liquefaction tests using 11 non-coated stackedrings
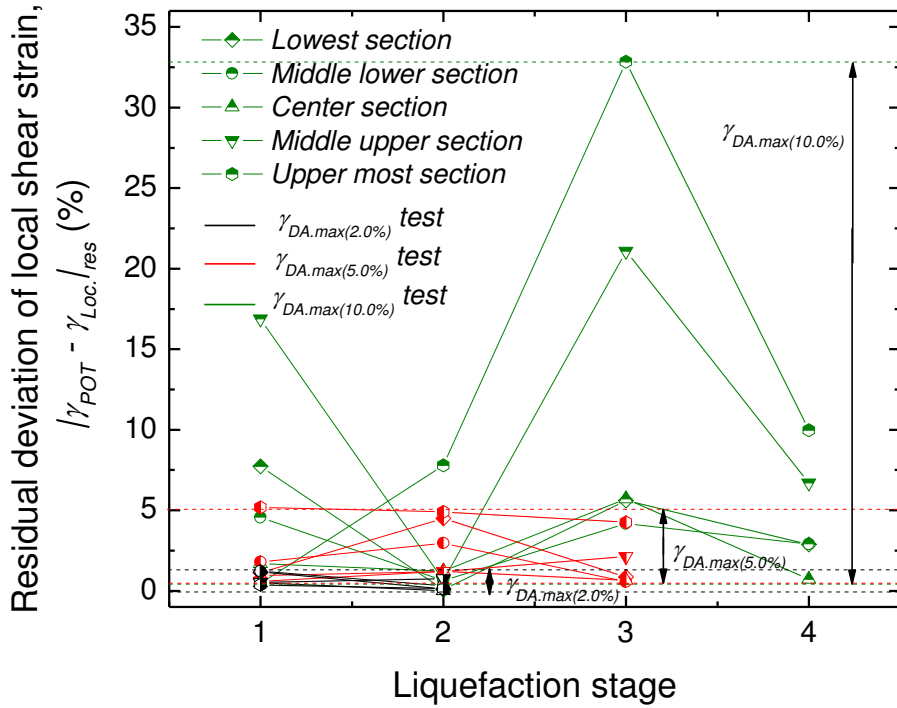
Fig.5.48:Summary of residual deviation of local shear strain in the multiple-liquefaction tests using 11 non-coated stacked rings

5.3.5   Image analysis results in multiple-liquefaction test using 11 coated stacked-ring shear type

Before conducting image analysis, the external surface of the 11 coated stackedringswas painted by black color, while the marking dots were painted by white color (Fig. 5.49). This modification was necessary to get better contrast between the marking dots and thedark background.

Comparison between typical γ_{Loc}measurement and global one (γ) during the 1st and 2ndliquefaction stagesare presented in Fig. 5.50 and Fig. 5.51, respectively. It can be seen that γ_{Loc}at each section started to deviate from the global one when the specimen was sheared up to γ_{DA} =1%. Similarly to the results of non-coated rings, the initiation of deviation started when the applied vertical stress reached 80 kPa ($\sigma_{v.Top}$= 80 kPa) asmarked by the arrows in Figs. 5.52 and 5.53, showing typical shear stress - vertical stress relationships.The corresponding shear stress - shear strain relationshipsare shownin Fig. 5.54 and Fig. 5.55.

Typical local shear stress - local shear strain relationships in the 1st and 2nd stage of liquefactions are presented in Fig. 5.56 and Fig. 5.57, respectively. Similar to the previous tests, the points 1 and 2 in these figures mark the location ofmaximum γ_{Loc}during the tests and maximum γ_{res}at the end of the test, respectively. It can be seen that, the maximum γ_{Loc}during the test in the 1stliquefactionwas-6.24%at the center section, while in the 2nd liquefaction it was 5.67% at the middle-upper section. The maximum γ_{res}at the end of the test in the 1st liquefaction was-2.93% at the center section, while in the 2nd liquefaction was -1.87% at the center section.

The values of $\delta_{max}$for the specimen sheared up to $\gamma_{DA.max}$=2%, 5%, 7% and 10%are shown in Fig. 5.58, Fig. 5.59, Fig. 5.60and Fig. 5.61, respectively. In the case of the specimen sheared up to $\gamma_{DA.max}$=2%, the middle-upper section showed the largest δ_{max}in all stages. For the specimen sheared up to $\gamma_{DA.max}$=5%, themiddle-upper and middle-lower sections showed the largest δ_{max}in the 1st and 2nd stages, while the upper-most section had the largest δ_{max}in the following stages. In case of the specimen sheared up to $\gamma_{DA.max}$=7%, the largest δ_{max}in each liquefaction stage appeared in the different sections. Finally, for the specimen sheared up to $\gamma_{DA.max}$=10%, the largest δ_{max}in the 1st and 2nd stages appeared on middle-upper and upper-mostsection, while the largest δ_{max}in the remaining e stages appeared again in the middle-upper section.

The values of δ_{res} for the specimen sheared up to $\gamma_{DA.max}$=2%, 5%, 7% and 10% are shown in Fig. 5.62, Fig. 5.63, Fig. 5.64, and Fig. 5.65, respectively. In all tests, it seems that the largest δ_{res} on each stage occurred randomly in different sections.

Fig. 5.66 shows the summary of the δ_{max} results during in each liquefaction stage, while Fig. 5.67 summarizes results of δ_{res} at the end of each liquefaction stage.

As shown in Fig. 5.66, similar tendency is found when using both non-coated and coated stacked rings. That is, the larger the applied shear strain is, the larger the value of δ_{max} is. The ranges of δ_{max} in the specimens sheared up to $\gamma_{DA.max}$= 2%, 5%, 7% and 10% are 0.34–1.43%, 1.72–9.31%, 2.37–6.94%, and 3.52–15.38%, respectively.

In a similar way, Fig. 5.67 shows that the larger the applied shear strain is, the larger the δ_{res} is. The ranges of δ_{res} in the specimen sheared up to $\gamma_{DA.max}$= 2%, 5%, 7% and 10% are 0–0.6%, 0.11–8.81%, 0.15–16.94%, and 0.11–15.3%, respectively. Interestingly, the specimen sheared up to $\gamma_{DA.max}$=7% exhibits larger values of δ_{max} and δ_{res}, as compared to the specimen sheared up to $\gamma_{DA.max}$=10%. However, this unexpected behavior only appears in the 2nd liquefaction stage. On the average, the values of δ_{max} and δ_{res} of the specimen sheared up to $\gamma_{DA.max}$=7% are still smaller than those of the specimen sheared up to $\gamma_{DA.max}$=10%.
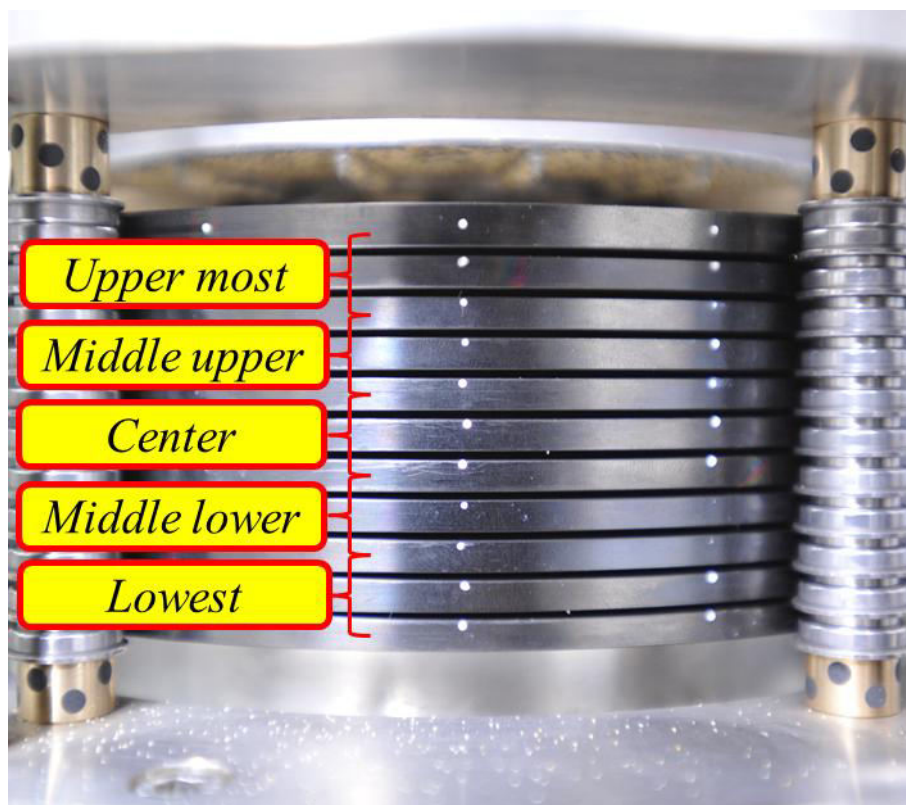
Fig. 5.49: Sections of the 11 coated stacked rings used for image analysis
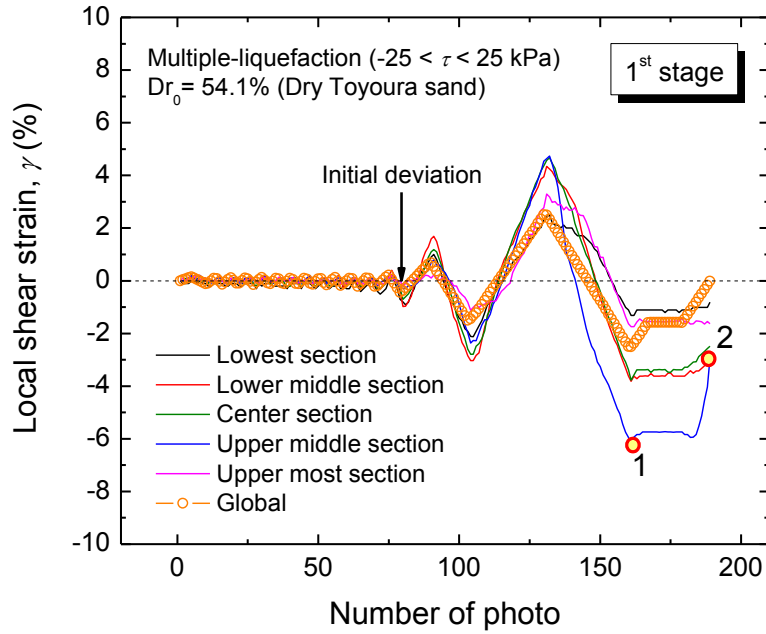
Fig. 5.50: Comparison between local shear strain measurement in the 1st liquefaction stage by image analysis and external potentiometer measurement for a specimen sheared at maximum $\gamma_{DA.max}= 5\%$ (e.g. ML20 test)
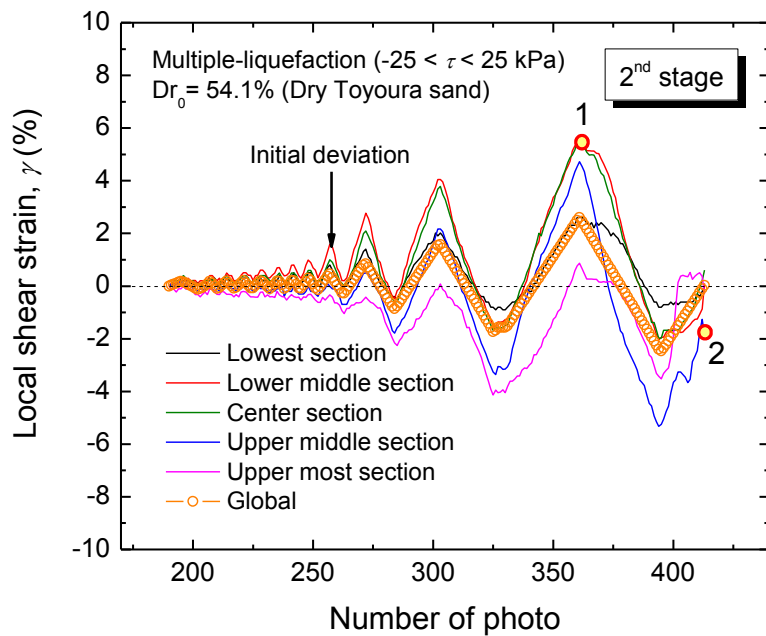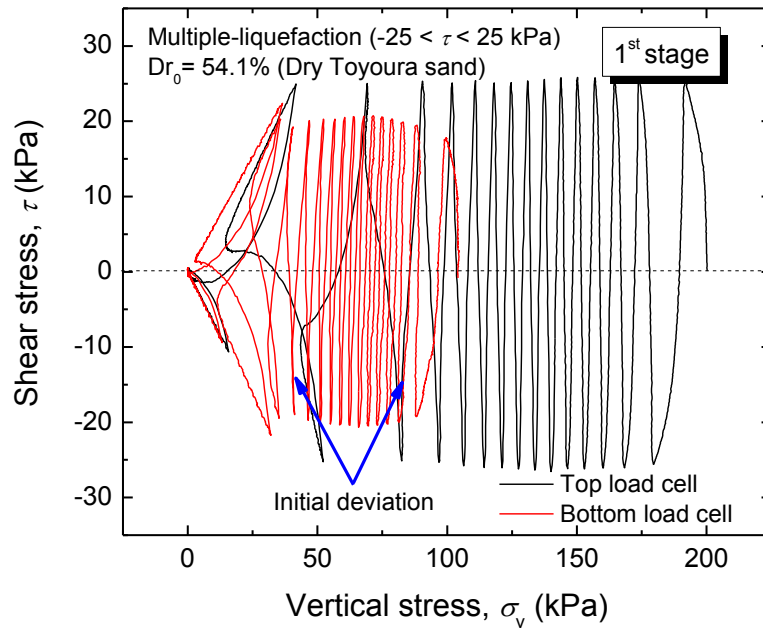

Fig. 5.51: Comparison between local shear strain measurement in the 2nd liquefaction stage by image analysis and external potentiometer measurement for a specimen sheared at maximum $\gamma_{DA.max}= 5\%$ (e.g. ML20 test)

Fig. 5.52: Shear stress - vertical stress relationshipsin the 1st liquefaction stage for a specimen sheared at maximum $\gamma_{DA.max} = 5\%$ (e.g. ML20 test)
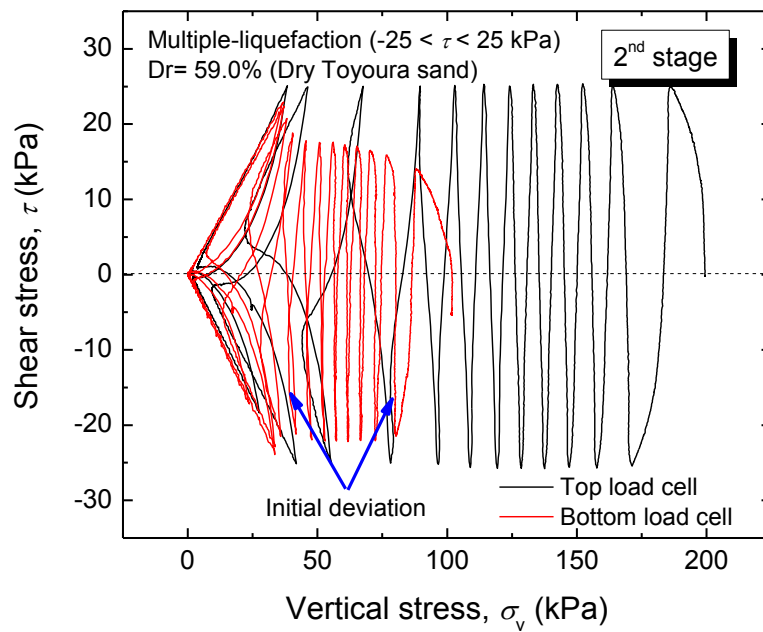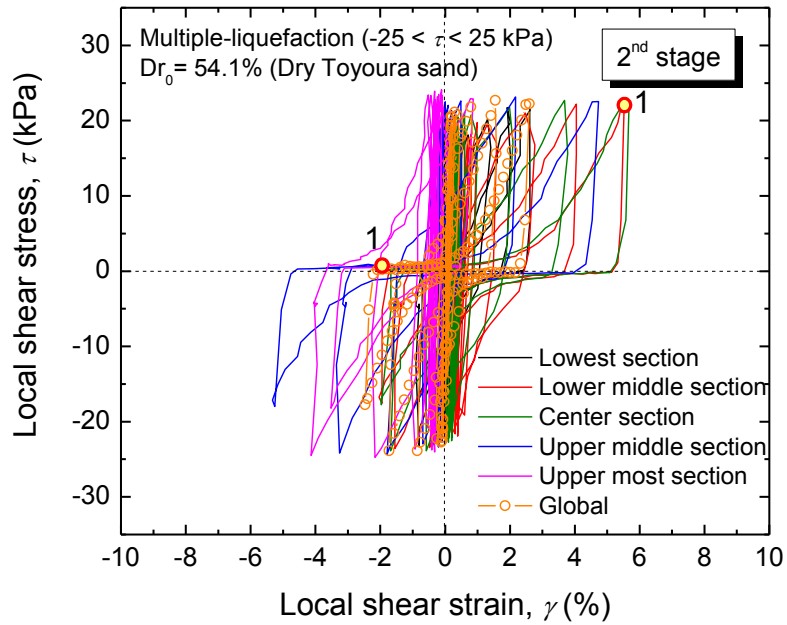

Fig. 5.53: Shear stress - vertical stress relationships on the 2nd liquefaction stage for a specimen sheared at maximum $\gamma_{DA.max} = 5\%$ (e.g. ML20 test)
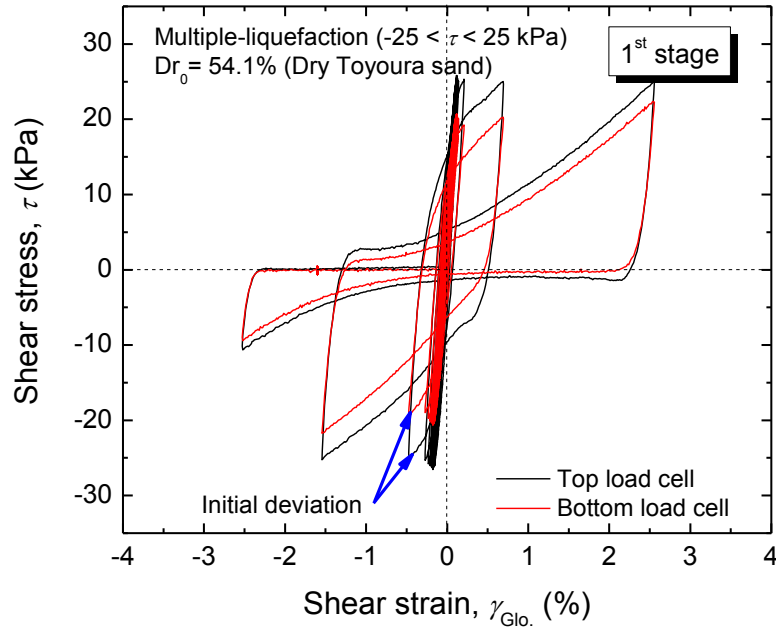
Fig. 5.54: Shear stress - shear strain relationships in the 1st liquefaction stage for a specimen sheared at maximum $\gamma_{DA.max}$ = 5% (e.g. ML20 test)
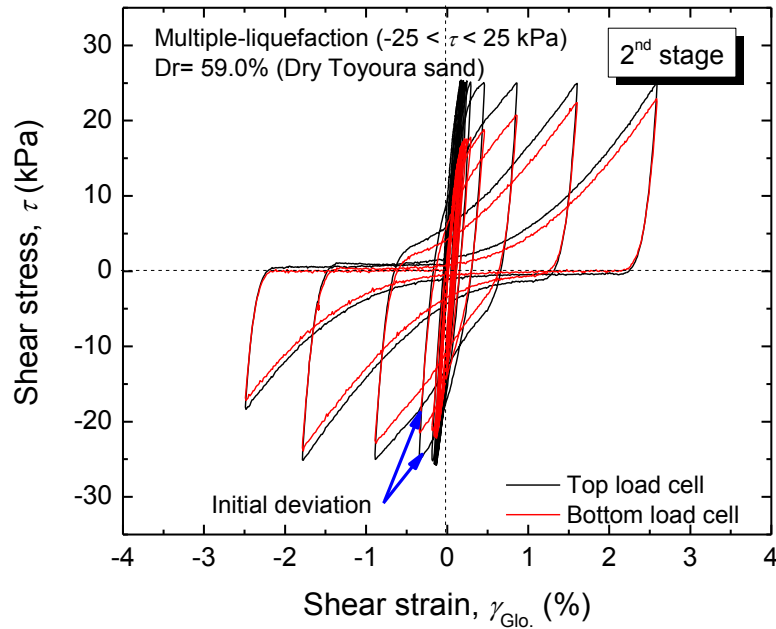
Fig. 5.55: Shear stress - shear strain relationships in the 2nd liquefaction stage for a specimen sheared at maximum $\gamma_{DA.max}$ = 5% (e.g. ML20 test)
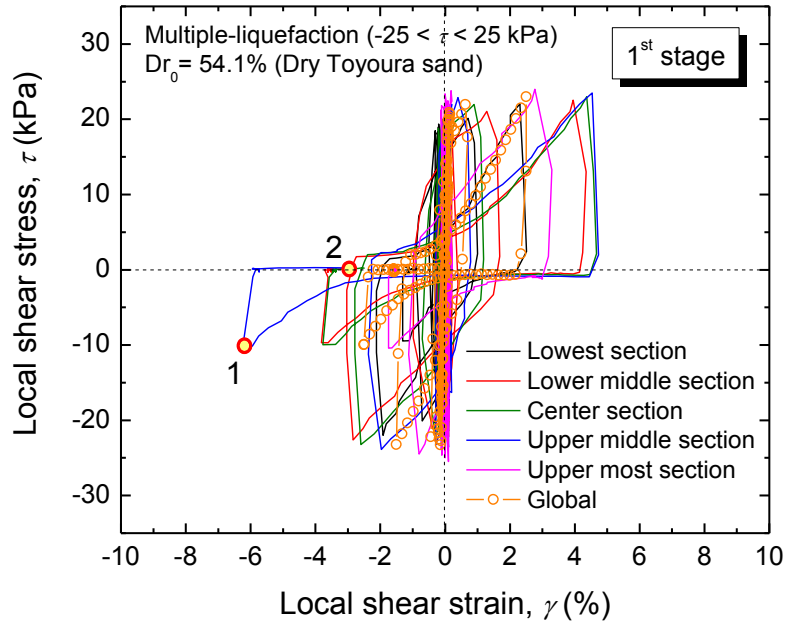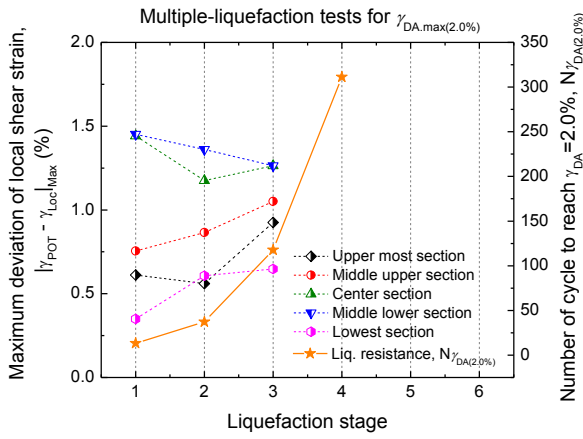
Fig. 5.56: Local shear stress - local shear strain relationships in the 1stliquefaction stage for a specimen sheared at maximum $\gamma_{DA.max} = 5\%$ (e.g. ML20 test)

Fig. 5.57: Local shear stress - local shear strain relationships in the 2nd liquefaction stage for a specimen sheared at maximum $\gamma_{DA.max} = 5\%$ (e.g. ML20 test)
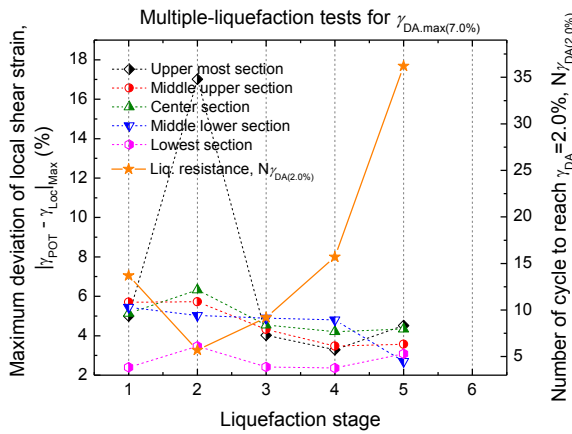
Fig. 5.58: Maximum deviation in multiple-liquefaction test on specimen sheared up to $\gamma_{DA.max}$=2%
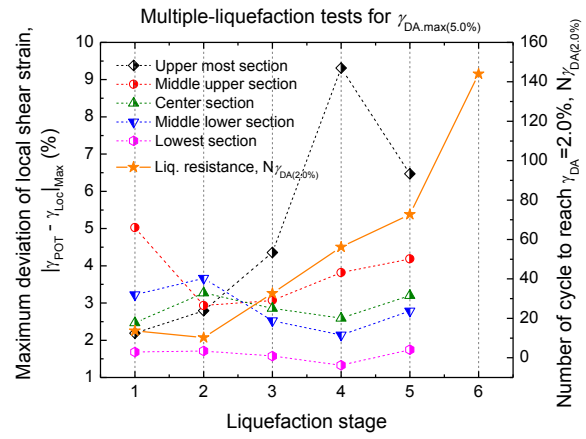
Fig. 5.59: Maximum deviation in multiple-liquefaction test on specimen sheared up to $\gamma_{DA.max}$=5% (ML20 test)

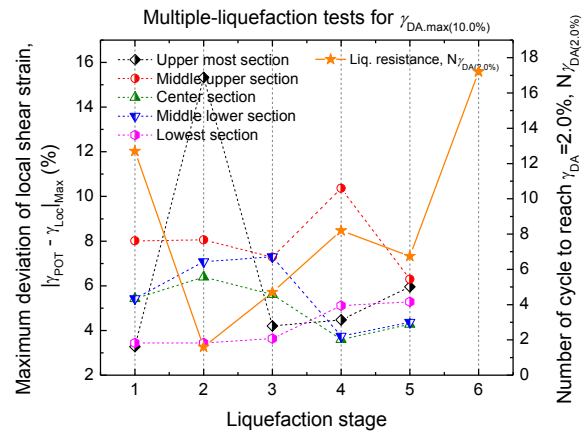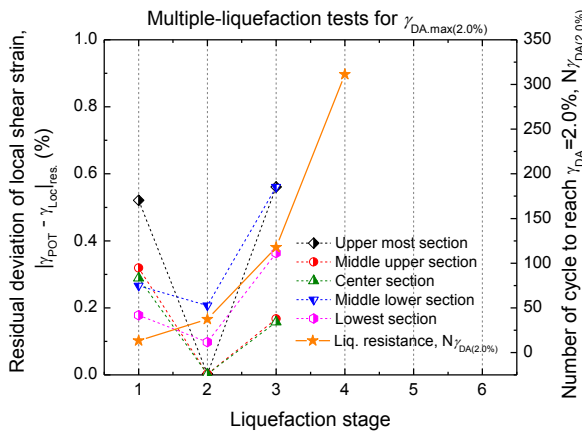Fig. 5.60: Maximum deviation in multiple-liquefaction test on specimen sheared up to $\gamma_{DA.max}$=7%

Fig. 5.61: Maximum deviation in multiple-liquefaction test on specimen sheared up to $\gamma_{DA.max}$=10%

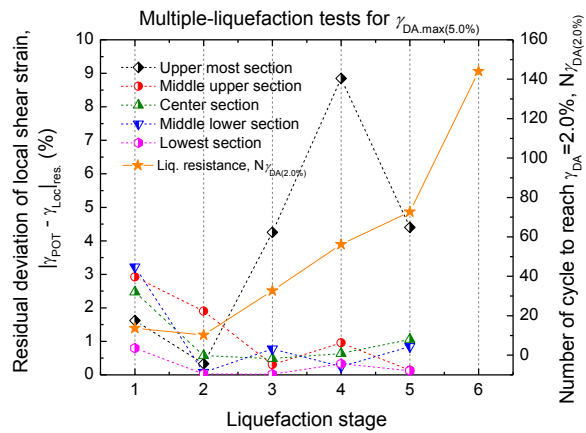Fig. 5.62: Residual deviation in multiple-liquefaction test on specimen sheared up to $\gamma_{DA.max}$=2%

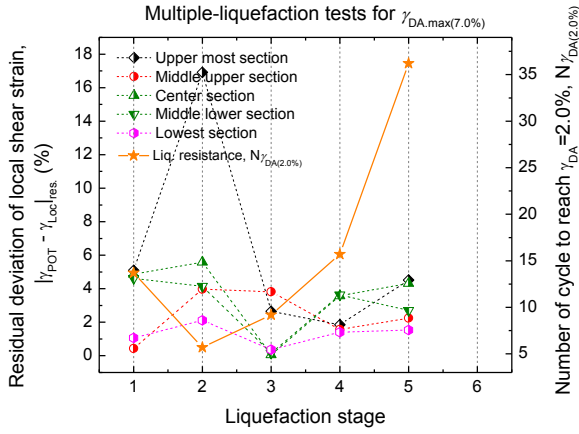Fig. 5.63: Residual deviation in multiple-liquefaction test on specimen sheared up to $\gamma_{DA.max}$=5%

Fig. 5.64: Residual deviation in multiple-liquefaction test on specimen sheared up to $\gamma_{DA.max}=7\%$
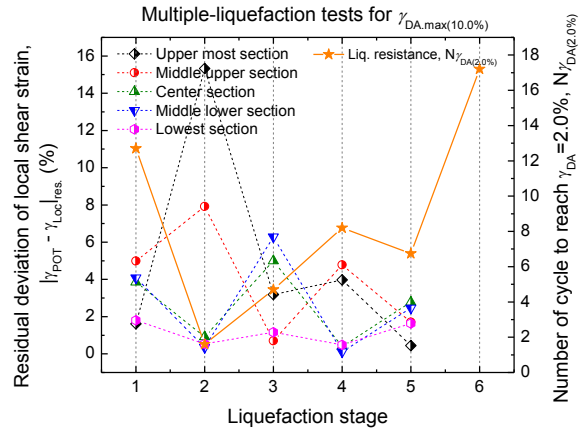

Fig. 5.65: Residual deviation in multiple-liquefaction test on specimen sheared up to $\gamma_{DA.max}=10\%$
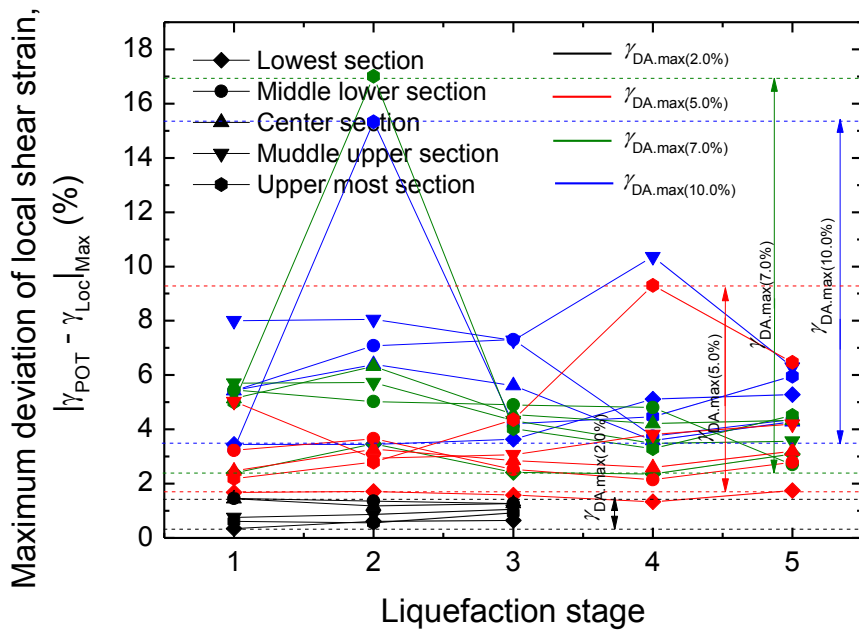

Fig. 5.66: Residual deviation in multiple-liquefaction test on specimen sheared up to $\gamma_{DA.max}<10\%$
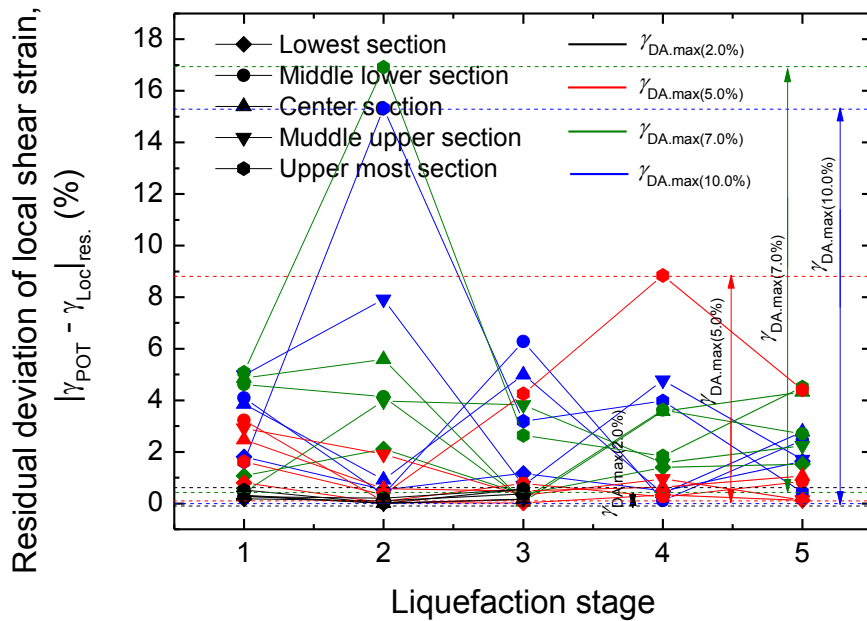
Fig. 5.67: Residual deviation in multiple-liquefaction test on specimen sheared up to $\gamma_{DA.max}$<10%

Based on the image analysis results, there are two observable effects of the strain history, i.e. shear strain amplitude, on the behavior of multiple-liquefied soil:

1. The specimens sheared up tolarger shear strain amplitudes always exhibit larger values of $\delta_{max}$and δ_{res}. Thesedeviations will have direct impactonthe extentof non-uniformity and fabric change throughout the specimen.Larger magnitudes of local shear strain deviation mean larger change in soil fabric.The change in soil fabric is closely related to the degree of induced-anisotropy within the specimen. Oda et al. (2001)and Yamada et al. (2010) reported that induced-anisotropy would cause un-equal liquefaction resistance on different loading directions.

2. The investigation onthe maximum local shear strain deviations in the multiple-liquefaction tests offer an interesting experimental evidence. In most of the tests, the section thatexperiencesthe largest deformation in 1stliquefaction stage is likely to exhibitalso the largest deformation in the following stages. This phenomenon may suggestthe occurrence ofstrain localization/formation of shear band in a specific section, which becomes the weak layer in the whole soil body.Thus, the next shear failure isexpected to happen in the previously formed shear band. Inthe localized sections, it is expected that ahigher distribution of voids would be createdasa result of soil expansion. Harris et al. (1995) reported similar finding that observedanincrease of void distributions within the shear band using stereophotogrammetry method. Yoshida et al. (1994), Viggiani et al. (1994) and Yoshida and Tatsuoka (1997) found large expansion was

created within the shear band by using image analysis in plane strain compression tests. Wahyudi et al. (2012) also confirmed these findings by using image analysis in the tests conducted usinga hollow cylinder torsional shear apparatus.

Sincethe specimen was re-consolidated prior to the next liquefaction stage, it was expected that re-consolidation process couldre-arrange the density distributions more uniformly throughout the specimens. However, the results showed that even after re-consolidating the specimen, the non-uniform distribution of the density created by the pre-shearing history did not vanish.

Since the local shear deformations were evaluated based on the external movement of the rings, it should to be reminded that there is also possibility that the deformation of the rings may not represent the actual deformation of the soil inside the stacked ring. This may happen when the specimen reachesthe state of initial liquefaction (zero vertical stress). After reaching this phase, the observed ring deformation may somehow underestimate the actual soil deformation inside the stacked rings. To investigate this problem using the stacked-ring shear apparatus may not be possible, since the soil particles are not visible through the ring. However, there is an ongoing research activity at the IIS, University of Tokyo, to address this problem by using transparent membrane with the hollow cylinder torsional shear apparatus.

5.4   Summary

From the investigation of the effects of strain amplitudes on the behavior of multiple-liquefied soil, the following conclusion can be drawn:

1. The magnitude of strain amplitude applied to the specimen has a direct impact in determining the increase of specimen relative density in each liquefaction stage. The larger the shear strain amplitude applied to the specimen is, the larger the increase of the specimen relative density is.

2. The magnitude of shear strain amplitude also has a direct impact in determining the cyclic resistance of multiple-liquefied sands as follows: 1) In the case of the specimen sheared by $\gamma_{DA.max}$>0.5%, the larger the appliedshear strain is, the lower the soil resistance in future liquefaction stage is; 2)in contrast, for the specimen sheared by $\gamma_{DA.max}$<0.5%, it was found that the smaller the applied shear strain is, the lower the liquefaction resistance in future liquefaction stage is. Such a behavior shows that the applied strain amplitude is not the single parameter to determine the behaviors of sand during multiple liquefactions. It was

found that the amount of energy dissipated during multiple liquefactions process is also one of the major parameters.

3. The comparison between the liquefaction resistance of multiple-liquefied soil and that of virgin liquefied soil revealed that the specimens sheared by large shear strain amplitude could havelower liquefaction resistance than the virgin liquefied soil havinga similar density. This means that the resistance of the multiple liquefied sands can be lower than the resistance of the original sand itself.

4. Based on local shear strain measurement, the effects of strain amplitude on the cyclic resistance of multiple liquefied sands can be summarized as follows: 1)The specimens sheared by larger strain amplitude show a significant deviation of local shear strain from theExternally measured global shear strain. These deviations include the maximum deviation during the test as well as the residual deviation at the end of the test. As a result, the strains are distributed non-uniformly throughout the specimen. In general, the larger the applied shear strain is, the larger the maximum and residual deviations of local shear strain from the global shear strain is; 2) for the specimens sheared by smaller shear strain amplitude show smaller local strain deformation compared to the global one. Thus, strains are distributed more uniformly throughout the specimen;3) larger non-uniformity of strain distribution mean some sections within the specimen were shared more than the others. As a result, the fabric in the multiple liquefied soil is destroyed; 4) Non-uniform strain distributions also mean non-uniform soil density distributions throughout the specimen, which the sections that experience very large shear deformation (localization) tends to have looser density. As a results, the localized section will become the weak layer on the next liquefaction.

5.5   References

1. Desrues, J., Lanier, J., and Stutz, P. (1985) "Localization of the deformation in tests on sand sample." *Engrg. Fracture Mech.*, 21(4), pp. 909-921.

2. Emery J., Finn, W. D., and Lee, K. W. (1973) "Uniformity of saturated sand specimens." *ASTM STP 523*, West Condhohocken, Pa.

3. Finn, W. D. L., Bransby, P. L., and Pickering, D. J. (1970) "Effects of strain history on liquefaction of sand." *J. Soil Mech. and Found. Div.,* ASCE, 96(6), pp. 1917-1934.

4. Finno, R. J. Harris, W. W., Mooney, M. A. and Viggiani, G. (1996) "Strain localization and undrained state of sand." *J. Geotech. Engrg.,* ASCE, 122(6), pp. 462-473.

5. Han, C. and Vardoulakis, I. G. (1991) "Plane strain compression experiments on water-saturated fine-grained sand." *Geotechnique*, 41(1), pp. 49-78.

6. Harris, W. W., Viggiani, G., Mooney, M. A., and Finno, R. J. (1995) "Use of stereophotogrammetry to analyze the development of shear bands in sand." *Geotech. Testing J.*, 18(4), pp. 405-420.

7. Ishihara, K. and Okada, S. (1978) "Effects of stress history on cyclic behavior of sand." *Soils and Foundations*, Tokyo, 18(4), pp. 31-35.

8. Ishihara, K. and Okada, S. (1982) "Effects of large preshearing on cyclic behavior of sand." *Soils and Foundations*, Tokyo, 22(3), pp. 109-125.

9. Ishihara, K. and Yoshimine, M. (1992) "Evaluation of settlements in sand deposits following liquefaction during earthquakes." *Soils and Foundations*, 32(1), pp. 172-188.

10. Koseki, J., Miyashita, Y., Deng, J., and Araki, H. (2012) "Liquefaction along Tone River basin in Japan caused by the 2011 Off the Pacific Coast of Tohoku Earthquake." *Proc. 2nd Intl. Conf. on Performance-based Design in Earthquake Geotechnical Engineering*, Taormina.

11. Kuribayashi, E. and Tatsuoka, F. (1975) "Brief review of soil liquefaction during earthquakes in Japan." *Soils and Foundations*, 15(4), pp. 81-92.

12. Mokni, M. (1992) "Relations entre deformations en masse et deformations localisees dans les materiaux granulaires." *PhD Thesis*, Universite J. Fourier de Grenoble, France.

13. Nagase, H. and Ishihara, K. (1988) "Liquefaction-induced compaction and settlement of sand during earthquakes." *Soils and Foundations*, 28(1), pp. 65-76.

14. Niemunis, A. (2003) "Extended hypoplastic models for soils" *Institute of Found. Engrg. and Soil Mech.*, Ruhr-university Bochum, Issue No. 34.

15. Oda, M. (1972a) "Initial fabrics and their relations to mechanical properties of granular material." *Soils and Foundations*, Tokyo, 12(1), pp. 17-36.

16. Oda, M. (1972b) "A mechanism of fabric changes during compressional deformation of sand." *Soils and Foundations*, Tokyo, 12(2), pp. 1-18.

17. Oda, M., Kawamoto, K., Suzuki, K, Fujimori, H., and Sato, M. (2001) "Microstructural interpretation on reliquefaction of saturated granular soils under cyclic loading." *J. Geotech. and Geoenvironmental Engrg*, 127(5), pp. 416-423.

18. Scarpelli, G. and Wood, D. M. (1982) "Experimental observations of shear band patterns in direct shear tests." *Proc., IUTAM Conf. on Deformation and Failure of Granular Materials*, Balkema, Rotterdam, The Netherland, pp. 473-484.

19. Seed, H. B., Chan, C. K., and Mori, K. (1977) "Influence of seismic history of liquefactions of sands," *J. Geotech. Engrg. Div., ASCE*, 103(4), pp. 257 – 270.

20. Suzuki, T. and Suzuki, T. (1988) "Effects of density and fabric change on re-liquefaction resistance of saturated sand." *J. Japanese Geotech. Soc.*, Tokyo, 28(2), pp. 187 - 195. (in Japanese)

21. Suzuki, T. and Toki, S. (1984) "Effect of preshearing on liquefaction characteristics of saturated sand subjected to cyclic loading." *Soils and Foundations*, Tokyo 24(2), pp. 16-28.

22. Toki, S., Miura, S. and Tanizawa, F. (1981) "A few remarks on the relationship between relative density and strength characteristics of sand." *Proc., Symp. On Relative Density and Engrg. Characteristics of Sand*, pp. 78-86. (in Japanese)

23. Tokimatsu, K. and Seed, H. B. (1987) "Evaluation of settlements in sands due to earthquake shaking," *J. of Geotech. Engrg.*, 113(8), pp. 861-878.

24. Towhata, I. and Ishihara, K. (1985) "Undrained strength of sand undergoing cyclic rotation of principal stress axes." *Soils and Foundations*, 25(2), pp. 135-147.

25. Viggiani, H. Finno, R. J. and Harris, W. W. (1994) "Experimental observations of strain lozalization in plane strain compression of a stiff clay." *Proc. 3rd Int'l Workshop on Localization and Bifurcation Theory for Soils and Rocks*, Balkema, Rotterdam, pp. 189-198.

26. Wahyudi, S., Miyashita, Y. and Koseki, J. (2012) "Shear band behavior of sand in torsional shear tests by means of image analysis." *Proc. ISSMGE Conf. of Advances in Multiphisical Tesing of Soils and Shale*s, Lausanne, Switzerland.

27. Yamada, S., Takamori, T., and Sato, K. (2010) "Effects on reliquefaction resistance produced by changes in isotropy during liquefaction." *Soils and Foundations*, 50(1), pp. 19-25.

28. Yamada, S., Kiyota, T., and Hosono, Y. (2011) "3rd big earthquake in Christchurch, New Zealand." *ISSMGE Bulletin*, 5(3), pp. 25-29.

29. Yasuda, S. and Tohno, I (1988) "Sites of reliquefaction caused by the 1983 Nihonkai-Chubu earthquake." *Soils and Foundations*, Tokyo, 28(2), 1-34, 61-72.

30. Youd, T. L. and Hoose, S. N. (1978) "Historic ground failure in Northern California triggered by earthquakes." *U.S. Geol. Surv. Profess*. Pap. 993.

31. Yoshida, T., Tatsuoka, F., Siddique, M. S. A., Kamegai, Y. and Park, C. S. (1994) "Shear banding in sands observed in plane strain compression," *Proc. Symp. On Localization and Bifurcation Theory for Soils and Rocks*, R. cambou, J. Desrues, and I. Vardoulakis, eds., Balkema, Rotterdam, The Netherlands, pp. 165-179.

32. Yoshida, T. and Tatsuoka, F. (1997) "Deformation property of shear band subjected to the plane strain compression and its relation to particle characteristics." *Proc. of 14th Intl. Conf. on Soil Mech. and Found. Engrg.*, 1, pp. 237-240.

33. Youd, T. L. and Weiczorek (1982) "Liquefaction and ground failure, in the Imperial Valley, California, Earthquake of October 15, 1979." *U.S. Geol. Surv. Profess. Pap. 1254*, pp. 223-246.

34. Wakamatsu, K. (2011) "Maps of historic liquefaction sites in Japan, 745 – 2008." *University of Tokyo Press* (In Japanese with English manual).

35. Wakamatsu, K. (2012) "Recurrence of liquefaction at the same site induced by 2011 Great East Japan Earthquake Compared with Previous Earthquakes." *Proc. of 15th Int'l World Conf. of Earthquake. Engrg.*

6 EFFECTS OF INDUCEDANISOTROPY ON THEBEHAVIORSOF SANDSUBJECTED WITH MULTIPLE LIQUEFACTIONS

6.1   Introduction

As mentioned in Chapter 1, the other parameter that also has significant impact in determining the behaviors of sand during multiple liquefactions is anisotropy. Anisotropy causes the soil to have different behavior in different directions.

Ingeotechnical engineering, anisotropy can be divided into two parts, namely inherent anisotropy and inducedanisotropy. Fundamentally, the inherentanisotropy is caused by the initial arrangementof soil particles during sedimentation process. In laboratory testing, the inherentanisotropy is caused by the direction and/or methodology employed to prepare a soil specimen.The initial arrangement of the soil particles affects the shear resistance of soil in different loading directions.Similar behavior was found in the case of soil resistance against liquefaction. Oda et al. (2011) conducted a series of triaxial testson specimens prepared by changing the direction of soil sedimentation. The results show that the specimen, in whichsoil particle was poured in parallel to the gravitational direction, has lower liquefaction resistance than that where soil particle was poured in parallel to the direction of the major principal stress (σ_1). The generation of pore water pressure was smaller for the specimen prepared in parallel to the major principal stress as compared to the specimen prepared in parallel to the gravitational force direction. The problem in inherent anisotropy becomes significant in the triaxial and direct shear apparatuses. In the torsional and ring shear apparatuses, such a problem is negligible.

Alternatively, induced anisotropy is caused by the re-arrangement of contact between the soil particles undergoing deformation. Induced anisotropy would have a great impact in determining the soil resistance against liquefaction or multiple liquefactions. Oda (1972), Ishihara and Okada (1978and 1982), Suzuki and Suzuki (1988), Towhata and Ishihara (1985), Oda et al. (2001), Yamada et al. (2011)among others found that the contribution of inducedanisotropy is significant to the reduction of liquefaction resistance. The specimen pre-sheared at larger shear deformation would have smaller re-liquefaction resistance. This reduction was also found to be a direct consequence of the large residual deformation during the previous liquefaction stages. In particular, the larger the residual deformation is, the greater the effects of inducedanisotropy are.

A recent study on the effects of inducedanisotropy on the re-liquefaction resistance of soil was conducted by Yamada et al. (2010). In this study,it was found that different loading direction may cause different resistance of soil during re-liquefaction (2-stage of liquefaction).The specimen will have higher liquefaction resistance in the next liquefaction, if

the liquefied specimenis sheared in the same direction as the direction of residual strain. In contrast, the specimen will have lower liquefaction resistance in the next liquefaction, if the liquefied specimen is sheared in the opposite direction to the direction of residual strain.

In the current study, it was originally attempted not to cause induced anisotropy by allowing no residual deformation in any of the post liquefaction stages.To do so, the deformation developed in the last cycle of loading was intentionally brought back to the origin ($\gamma = 0\%$). This was done to minimize theeffects of inducedanisotropy, while at the same time investigating the effects of strain amplitudes on the soil behaviorsduring multiple liquefactions.

In the current study, at least two methods can be used to investigate the effects of induced anisotropy to the soil behaviors during multiple liquefactions, which are the measurement of soil's stiffness in a particular direction and investigation of stress-dilatancy relation of the soil during multiple liquefactions.

For the first method, there are basically two types of measurement for evaluating the soil stiffness, which are dynamic and static measurements. Dynamic measurement has been widely developed in the soil testing laboratory and capableto accurately determine soil stiffness for a variety of soil, consolidated at different density state and confining pressure levels! Dynamic measurement can be conducted by using different techniques such asbender element (Schultheiss, 1981; DyvikandMadshus, 1985; Viggianiand Atkinson, 1995; Chaudhary et al., 2004; WicaksonoandKoseki, 2007), triggers and accelerometers (AnhDanandKoseki, 2002; Maqbool, 2005; Kiyota, 2008; WicaksonoandKoseki, 2007, Suwal, 2013), piezo-ceramic disk (Suwal 2013), among others.In dynamic measurement,soil stiffness is determined by measuring the time required by compression (P) and/or shear (S) wavesto travel from the trigger to the receiver along the height of the soil body.Therefore this method is best performed on specimen using latex membrane (e.g. triaxial tests). Consequently, in the stacked-ring shear apparatus, this method cannot be applied since a specimen is constrained by steel ring which are much stiffer than the soil.

Another method fordeterminingthe soil stiffness is the static measurement. For example, by applying a number of small cyclicloading and measuring the corresponding level of strain developed, one can evaluate the soils stiffness within the quasi-elastic region ($\gamma \approx 0.001\%$). Accurate probing tools are essential to measure such small strain levels. Recently, several high resolution transducers have been developed for this purpose, such as non-contact proximity transducer or gap sensor (Hird and Yung, 1987& 1989), inclinometer (Burland, 1989), LVDT (Cuccovillo and Coop, 1997),LDT (Goto et al., 1991), pin-typed LDT for hollow cylindrical specimens (Hong Nam, 2005; De Silva and Koseki, 2005) and etc.

As mentioned in earlier chapters, the stacked-ring shear apparatus is not capable ofcontrollingsmall cyclic shear loading within the quasi-elastic region ($\gamma \approx 0.001\%$), since itis aimed to conduct liquefaction test up to very large shear strain ($\gamma > 100\%$). To achieve such a large shear strain, a direct motor system was used instead of a gear system.Consequently, the smallest shear strain that can be measured was about 0.025%, well larger than the quasi-elastic strain region.

The second method to investigate theeffects of inducedanisotropy can be done by analyzing the specimen's dilatancy characteristics. Dilatancy describes the volumetric change characteristics of a soilinduced by shear deformation for any given stress states and directions. For the soil that is affected by the induced anisotropy, the dilatancy characteristics on each direction of the specimen would be different.

Rowe (1962, 1964, and 1969) originally derived the stress-dilatancy relations for triaxial compression, triaxial extension and plane strain conditions by assuming that a granular material can be represented by a regular packing of spheres or cylinders and that the ratio of the energy increment input to the output is a constant (K). Other researchers proposed different theoretical stress-dilatancy relations such as Taylor's energy dissipation equation (1948),Roscoe's energy dissipation equation (1963) and the sliding block theory (Tokue, 1978; Moroto, 1987, etc). Later, Pradhan (1990) found a unique relation between the shear stress ratio (τ/σ_v) and ratio between plastic volumetric strain increment over plastic shear strain increment ($-d\varepsilon_{vol}^p/d\gamma^p$) and modify the Rowe's stress-dilatancy relation based on experimental data result on cyclic constant stress test in torsional shear apparatus. Since then, other researchers have also investigated the soil stress-dilatancy relationship under different loading conditions, materials and apparatuses (Balakrishnaiyer, 2000; Shahnazari, 2001;Wahyudi, 2011; De Silva et al., 2014; andamong others).

The investigation of soil stress-dilatancy characteristics is conducted imposing drained conditions. However, volume change in drained shear tests can be considered as themirror image of pore water pressure build-up during undrained sheartests (i.e. liquefaction tests).Since the change of volume is restricted during liquefaction tests, a tendency of soil to contract will result in the generation of positive excess pore water pressure and thus a reduction in the effective stress. On the other hand, a tendency of soil to dilate will result in the build-up of negative excess pore water pressure and an effective stress increase.

6.2   Experimental program

6.2.1   Stiffness of soil measurement using static analysis

Since, the stacked-ring shear apparatus does not allow to conduct small cyclic loading within the quasi-elastic region (γ <0.001%). Therefore, soil stiffness wasanalyzed based on the stress-strain behavior during the first-quarter of the cyclic shear loading (i.e. virgin loading)in each liquefaction stage. Nevertheless, to accurately measure small shear strains, two gap sensors (GS-1 & GS-2) measuring the rotation of the top cap was installed. Before applying cyclic shear loading, the both gap sensors were positioned perpendicularly to the metal plate that was attached to the top cap. Each gap sensor enables to measure precise distance between two objects within the range of 0-4mm. Later, the measured displacement can be readily converted into the shear strain by simple equation similar to those described for the case of potentiometers in Chapter 2.

The measurement of soil stiffness is done to the multiple-liquefaction tests conducted in 11 non-coated stacked-ring (ML10 ML12 tests) and 11 coated stacked-ring (ML19 to ML22 tests) types. Typical shear stress - shear strain relationships during the first-quarter cyclic loading in the multiple-liquefactionare shown in Fig. 6.1, while the corresponding shear stress - vertical stress relationshipsare shown in Fig. 6.2. It can be seen that both shear stress and vertical stress within the specimen are not distributed uniformly as a result of the generated friction between the soil particles and the stacked-rings. Because of such stress non-uniformity, the average values of shear stresses and vertical stresses measured by the top and bottom load cells were used to evaluate the stiffness of multiple-liquefied soil. The average shear stress - shear strain – vertical stress relationshipsare shown in Figs. 6.3 and 6.4.

The GS-1 and GS-2 sensors are capable to measure strains within quasi-elastic region (i.e. γ < 0.001%), while the vertical stress ($\sigma_{v0.Top}$) applied to the specimen was maintained constant at 200 kPa. During the first-quarter of cyclic shear loading (virgin loading), the strain rate was set up to the lowest possible at the 0.12%/min, while the data point were recorded every 50 ms (=0.05 second).
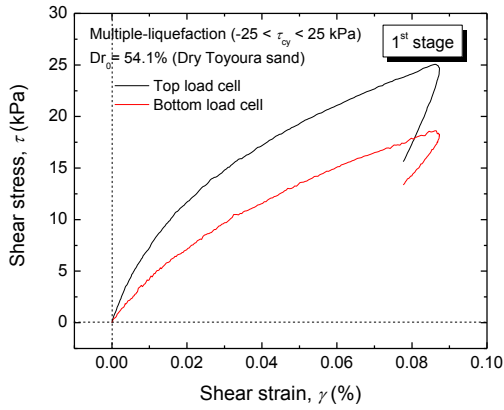
Fig. 6.1: Typical shear stress- shear strain relationships during first-quarter cyclicloading in a constant-volume shear test
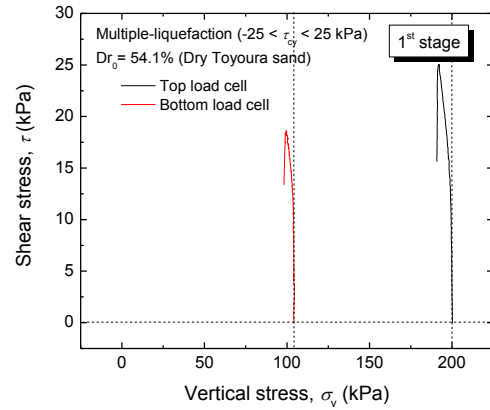
Fig. 6.2: Typical shear stress - vertical stress relationships during first-quarter cyclic loading in a constant-volume shear test
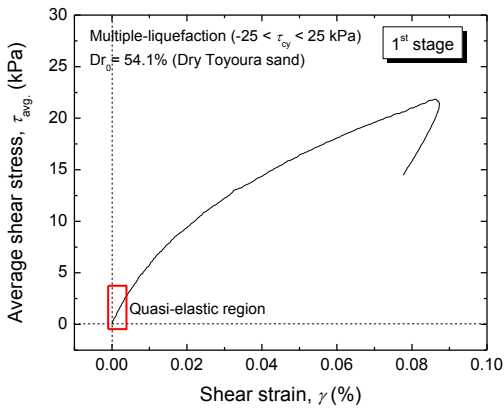
Fig. 6.3: Typical average shear stress - shear strain relationships during first-quarter cyclic loading in a constant-volume shear test
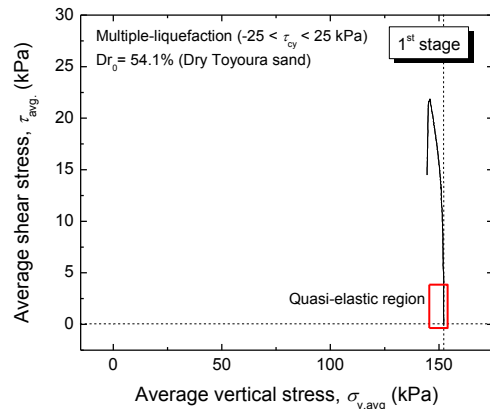

Fig. 6.4: Typical average shear stress - shear strain relationships during first-quarter cyclic loading in a constant-volume shear test

6.2.2   Stress-dilatancy relationship

A series of test that contains 7cyclic constant-stress tests (SDRL1 to SDRL7 tests) were conducted to investigate the dilatancy characteristic of liquefied soil. The list of tests and the stress path of each test was presented in Table 2.14 in Chapter 2.

In general, to examine the dilatancy characteristics of a soil subjected with multiple liquefactions, precise volumetric strain measurements are needed. Nevertheless, in the stacked-ring shear apparatus, the measurement of the volumetric strain is not difficult, since both radial and circumferential strains are constrained ($\varepsilon_r = \varepsilon_\theta = 0$).Therefore, the volumetric strain of the specimen coincideswith the axial strain ($\varepsilon_{vol} = \varepsilon_z$).

In the original setting of the apparatus, two EDTswere used to measure the volumetric strain of the specimen. However, this type of transducer does not have enoughresolution, which is required to accurately investigate the dilatancy characteristic of soil. To overcome this issue, two additional gap sensors (GS-3 and GS-4) were employed. They were positioned facing downward to the metal plate attached to the top cap. The GS-3 and GS-4 sensors enabled to measure accurately thevertical displacementup to4mm corresponding toan axial strain up to 7.5%.

Typical volumetric strain measurement obtained using EDTs and gap sensors can be seen in Fig. 6.5. Globally, the volumetric strain measurements by EDT and gap sensors showeda good agreement. However, significant differences in the volumetric strain measurement were observed during the reversal of loading as shown in Fig. 6.6. The largest amount of contraction usually takes place during the reversal of loading (Fig. 6.7); therefore, it is very important to accurately measure the stress-dilatancy characteristics in correspondence of the reversal of loading. From Fig. 6.7, it can be seen that the two types of sensors showed very different measurement during the reversal of loading. In particular, a hysteretic loop can be observed based on EDTsmeasurement, which is not shown by gap sensors measurement. This discrepancy is due mainly to the low accuracy of EDTs.

To analyze the dilatancy characteristics of soil during cyclic shear loading, the modified Rowe stress dilatancy relationship (Pradhan, 1990) is used.This relationship is illustrated in Fig. 6.8.The stress-dilatancy relationship is composed by the dilatancy ratio ($-d\varepsilon_{Vol.}^{p}/d\gamma^{p}$) and the shear stress ratio (τ/σ_v). In the case of cyclic constant stress test, the stress-dilatancy relationship is represented by two parallel lines as shown in the illustration of Fig. 6.8. These two lines represent different phases of loading as illustrated in the shear stress and shear strain relationship in Fig. 6.9 and the corresponding volume change in Fig. 6.10. During the reversal of cyclic shear loading, clockwise to anti-clockwise directions and vice-versa, the stress dilatancy relationship shift to theopposite side as marked by points 1-2 and 4-5. The dilatancy characteristicschange from contractive to dilative as it passes the zero dilatancy line ($-d\varepsilon_{Vol.}^{p}/d\gamma^{p}=0$).

A typical stress-dilatancy relationship obtained in the current study using stacked-ring shear apparatusdiffers from the theoretical one (Fig.6.11). The major difference can be seen at the time of reversal of cyclic loading. This happens due to the stacked-ring shear apparatus is not capable to control the direction of major and minor principal stresses (σ_1 and σ_3). If the direction of major principal stress (σ_1) is equal to the direction of the principal strain (ε_1), then the stress-dilatancy relationship will form a perfect parallel line as shown in previous Fig. 6.8. This term is called coaxial condition.
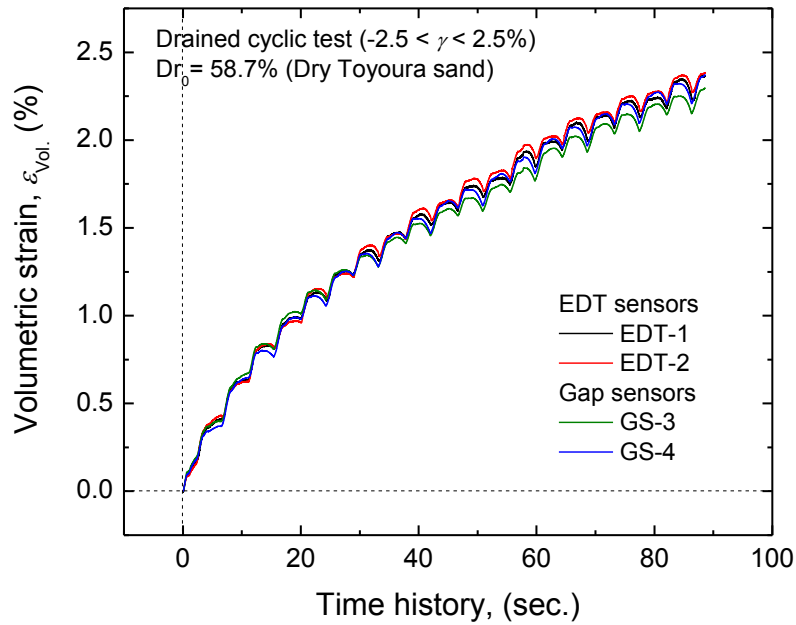
Fig. 6.5: Volumetric strain measurement during drained (constant-stress)cyclic shear tests by using EDTs and gap sensors
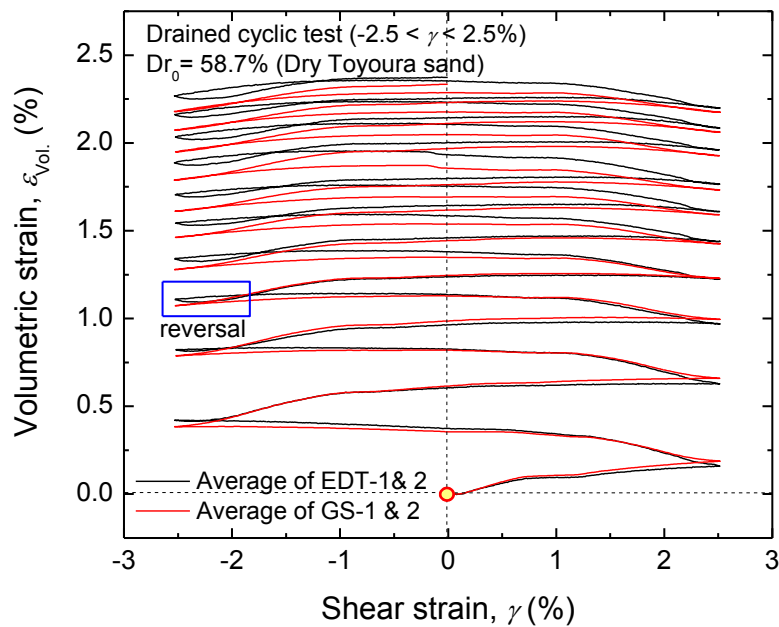

Fig. 6.6: Volumetric strain - shear strain relationships in drained (constant-stress) cyclic shear tests test by using EDTs and gap sensors
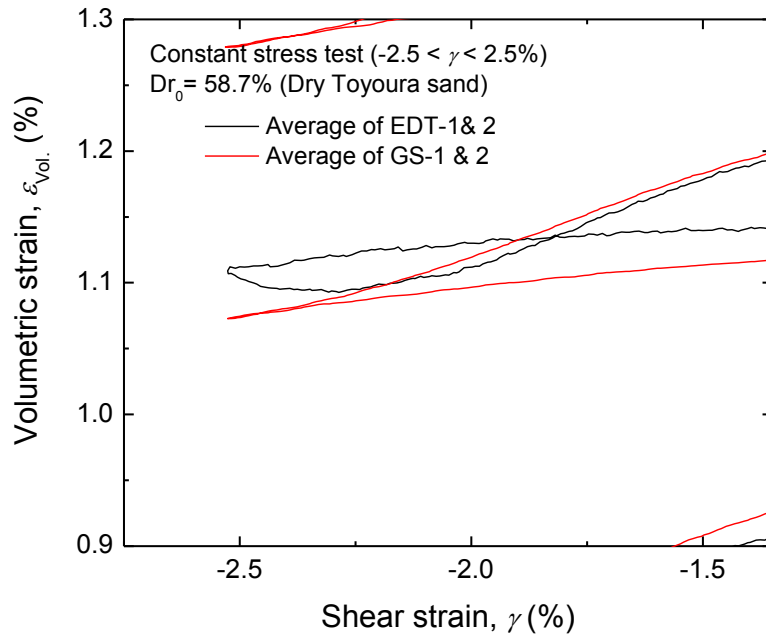
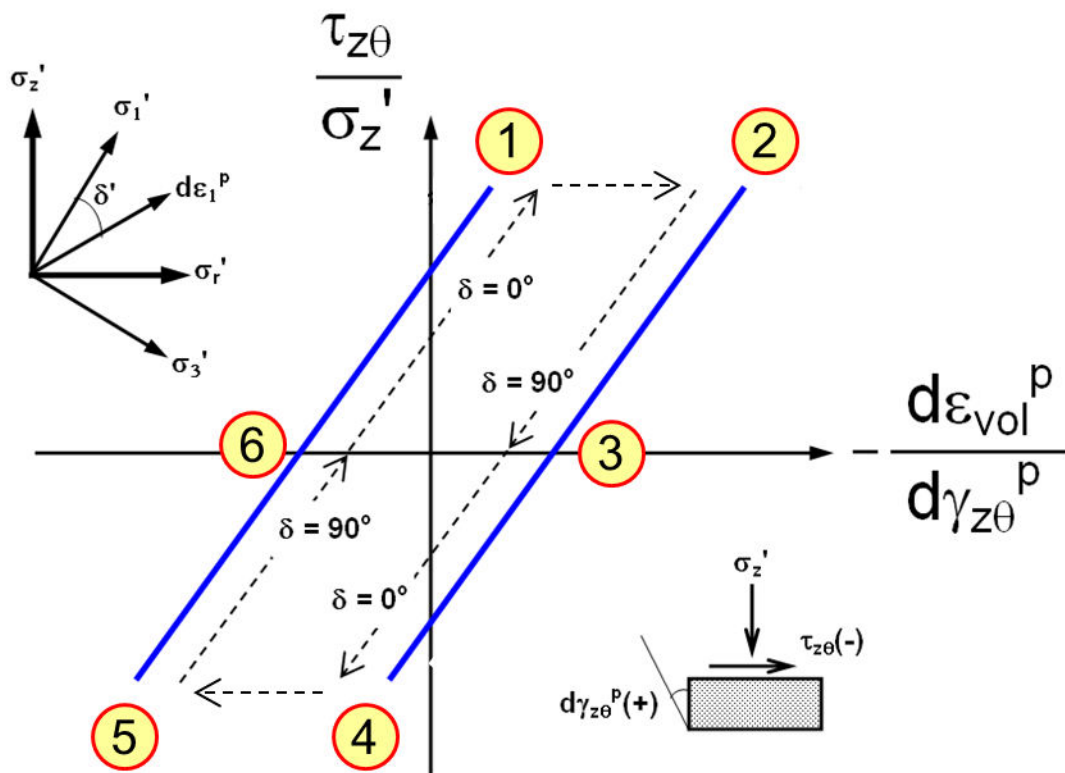Fig. 6.7: Close up of the volumetric strain - shear strain relationships shown in Fig 6.6

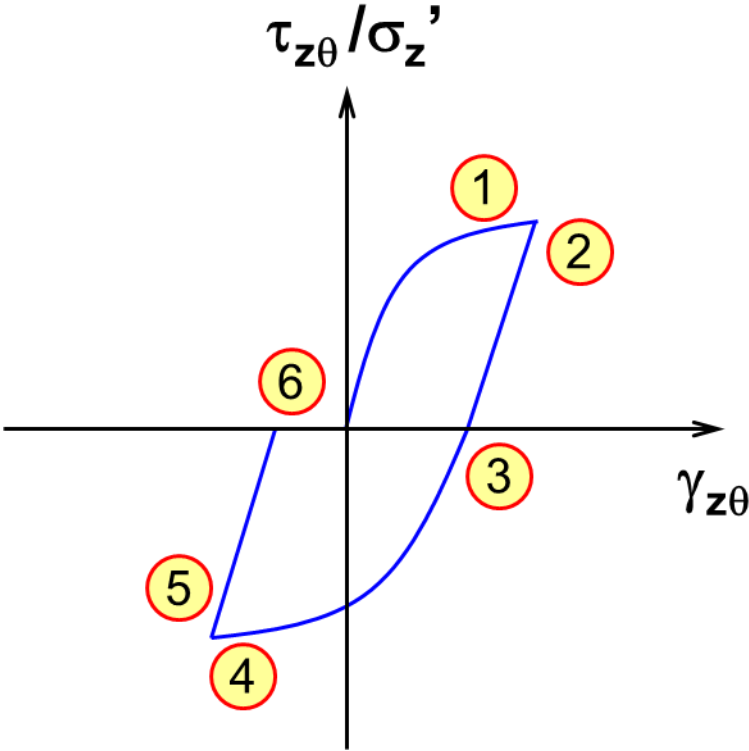Fig. 6.8: Modified Rowe's stress-dilatancy relationship (Pradhan, 1990)

Fig. 6.9: Schematic illustration of shear stress-shear strain relationship in the drained (constant-stress) cyclicshear tests
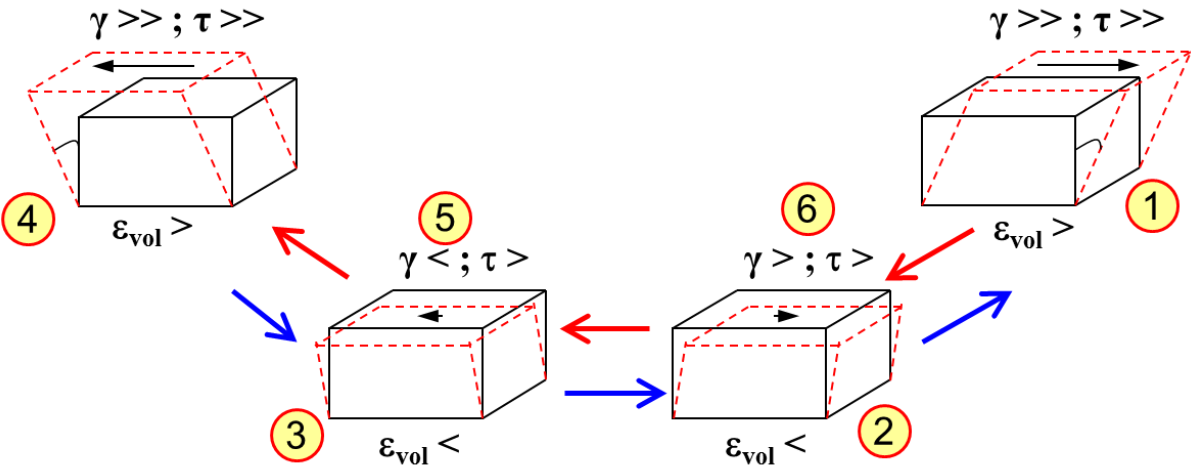
Fig. 6.10: Schematic illustration of soil element deformation while undergoing drained cyclic shear loading
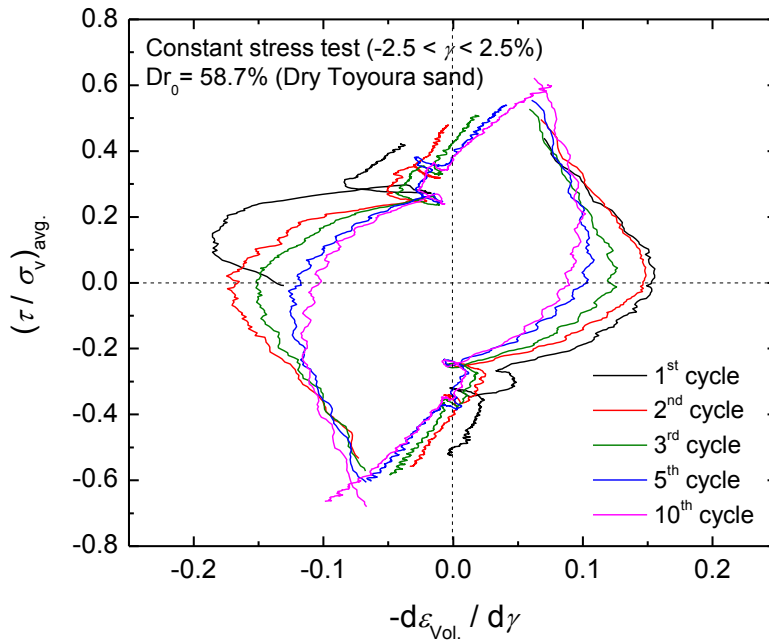
Fig. 6.11: Typical stress-dilatancy relationships in drained (constant-stress) cyclic stacked-ring shear tests

6.3 Results and discussions

6.3.1 Stiffness of soilduring multiple liquefactionsusing static measurement

Typical shear stress - shear strain relationships in different stages of multiple-liquefaction tests are shown the Fig. 6.12, while the corresponding shear stress - shear strain relationshipswithin quasi-elastic region are reported in the close up in Fig. 6.13.Though, gap sensors were employed to accurately measure the stress-strain relationships within quasi-elastic region, it can be seen that results are still scattering. However, this isdue to technical limitation of the employed apparatus. Specifically, the minimumstrain rate that could be used in conducting the tests was not small enough to measure smoothly the very small strains.Nevertheless, the results obtained still allow the evaluation of the maximum shear modulus (G_{max}), which was determined by using a linear interpolation method. For comparison purpose, the secant shear modulus (G_{sec}) of Toyoura sand within the range of γ= 0.0025%, 0.005%, and 0.010% was also calculated.

The comparison between$G_{max}$and G_{sec}obtained on the specimens sheared up to $\gamma_{DA.max}$= 2%, 5%, 7%, and 10% (ML19 to ML22 tests) are presented in Figs. 6.14 throughout 6.17,

respectively.The larger the range of strain amplitude is, the smaller the shear modulus is. Beyond the 0.002% range of shear strain, the initial vertical stress started to decrease, hence, the stress-strain relationship was no longer linear.

The comparison between liquefaction resistance (i.e. number of cycles to cause $\gamma_{DA}=2\%;N\gamma_{DA(2.0\%)}$) and G_{max}at each multiple-liquefaction stageis shownin Figs. 6.18through6.21. One may thinkthat a larger liquefaction resistance is a result of a higher soil stiffness or vice-versa.However, the current test results showed that thereis no such unique correlation between stiffness of soil measured at each liquefaction stageand the corresponding liquefaction resistances.

It is important to mention that,in these tests, the loading was always applied in clockwise direction. It was purposely done in order to have unified comparison at each liquefaction stage. Recently, Yamada et al. (2010) conducted series of 2 stages liquefaction test using triaxial apparatus, where they found that different loading directions may cause different liquefaction resistance. Such behaviorsare caused by the effects of inducedanisotropy. It should be noted that the re-liquefaction tests conducted by Yamada et al. (2010) were all stopped when reaching zero shear stress ($\tau_{z\theta}=$ 0 kPa) during unloading process. As a result, the liquefied specimen could have some of residual deformation in the post liquefaction stage. In contrast, in the current study, the shear strain at the last cycle of loading was brought back to the origin ($\gamma =0\%$) to avoid the effects of induced anisotropy in the future liquefaction. However, the tests results by Yamada et al. (2010) may imply that the effects of inducedanisotropy could be significant even in the multiple-liquefaction tests withno residual strain.

To investigate more about this phenomenon, a 2-stage liquefaction test (re-liquefaction), namely SDRL1 test, was conductedon a specimen having initial relative density of 54.2%. In the 1st liquefaction stage, cyclic shear loading was startedin the clockwise direction. The specimen was sheared under $\tau_{cy.}=\pm25$ kPa up to a maximum$\gamma_{DA.max}=$ 5%. After reaching the pre-determined$\gamma_{DA.max}$value, the shear strain was brought back to the origin ($\gamma =0\%$). In the 2nd liquefaction stage, the specimen was subjected with monotonic loading under constant volume. In this stage, the shear loading was applied anti-clockwise direction, which was opposite to the one applied in the 1ststage. The average shear stress - shear strain relationships in the 1stand 2nd liquefaction stagesare shown in Fig. 6.22, while the corresponding average shear stress - vertical stress relationshipsare shown in Fig. 6.23. For the sake of comparison, results of re-liquefaction test are plotted together with the first two liquefaction stages of a multiple-liquefaction tests conducted on a specimen sheared up to$\gamma_{DA.max}=$ 5% (ML20 test). The average shear stress - shear strain relationships in the multiple-liquefaction test during the

1st and 2nd stages are shown in Fig. 6.24, while the corresponding average shear stress - vertical stress are shown in Fig. 6.25. Inaddition, the stress-strain response of sand specimen sheared in both clockwise and anti-clockwise directions during the 1st stage in both tests are shown in Fig. 6.26. The single strain amplitude in the clockwise direction for theSDRL1 test was 2.22%, while for the ML20 test was 2.56%. On the other hand, the single strain amplitude in the anti-clockwise direction for the SDRL1test was 2.83% while in the ML20 test was 2.51%. In the SDRL1 test, the single strain amplitude on the anti-clockwise side (2.83%) was slightly larger than that in clock-wise direction (2.22%), the difference being 0.62%. In the ML20 test the single strain amplitude on both sides were similar.In the 2nd stage, the comparison of the average shear stress-shear strain relationships for the SDRL1 test and ML20test during first-quarter of cyclic loading are shown in Fig. 6.27. Because the shear loadings were applied in the opposite direction, the comparison between two test resultsisalso reported in terms of absolute shear strain ($|\gamma|$) as shown in Fig. 6.28. It clearly appears that the two curves almost coincide to each other. This imply that different loading directions have no significant impacts on the future liquefaction strength as long as the residual strain induced by the previous liquefaction stage is brought back to the origin ($\gamma = 0\%$).

These test results suggests that the effects of inducedanisotropy in multiple-liquefaction tests is negligible as long as liquefied soil is not subjected toany residual strain before the next liquefaction stage. To confirm this finding, two additional series of liquefaction tests were performed. The first series was conducted in order to investigate the effects of shear strain amplitudes on the dilatancy characteristics of soil subjected with multiple liquefactions. The second series was carried out to investigate the effects of residual strain on the dilatancy characteristics of soil subjected with multiple liquefactions.
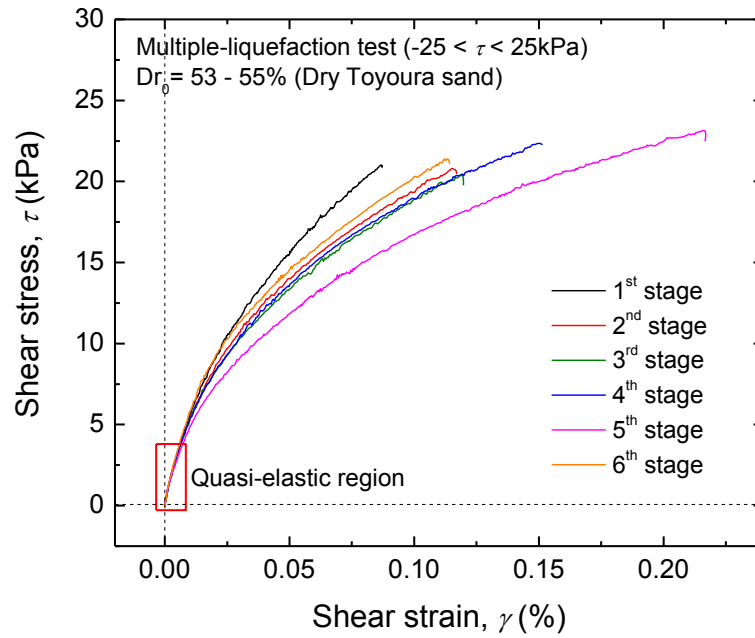
Fig. 6.12: Typical shear stress - shear strain relationshipsin the first-quarter of cyclic shear loading of multiple-liquefaction tests
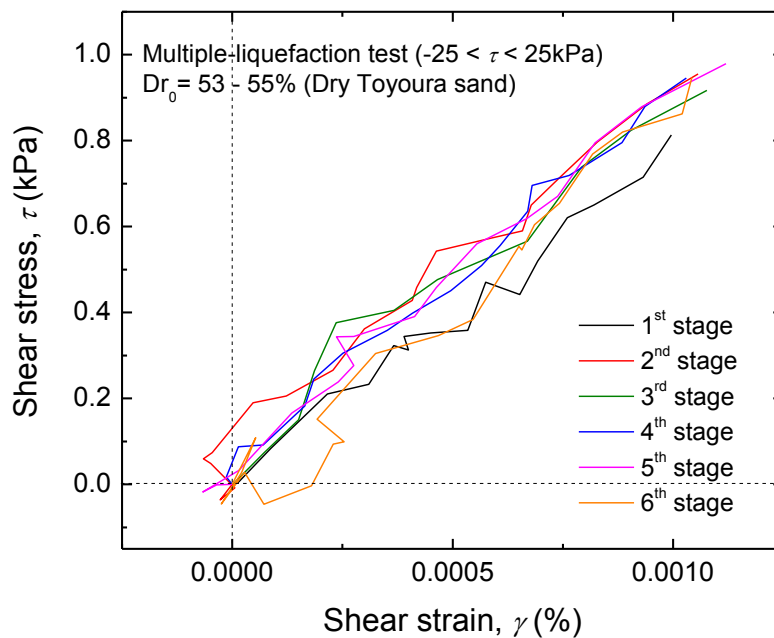
Fig. 6.13: Typical shear stress - shear strain relationships within the quasi-elastic region (i.e. γ < 0.001%)in multiple-liquefaction tests
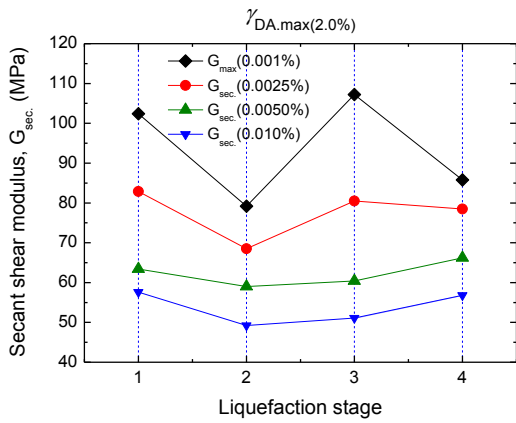
Fig. 6.14: Maximum and secant shear modulus in multiple-liquefaction testson specimen sheared up to $\gamma_{DA.max}= 2\%$ (e.g. ML19 test)
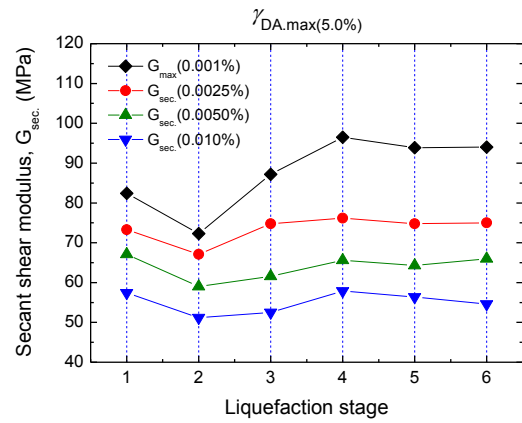
Fig. 6.15: Maximum and secant shear modulus in multiple-liquefaction tests on specimen sheared up to $\gamma_{DA.max}= 5\%$ (e.g. ML20 test)
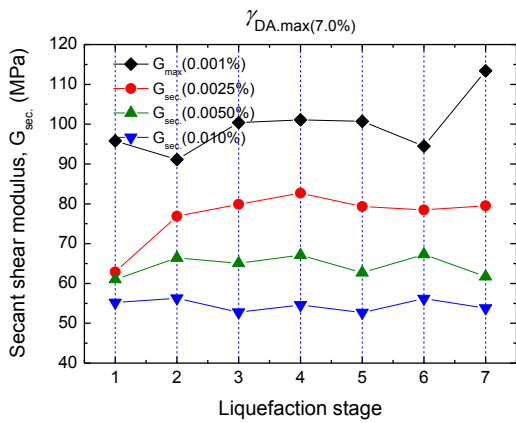
Fig. 6.16: Maximum and secant shear modulus in multiple-liquefaction tests on specimen sheared up to $\gamma_{DA.max}=7\%$ (e.g. ML21 test)
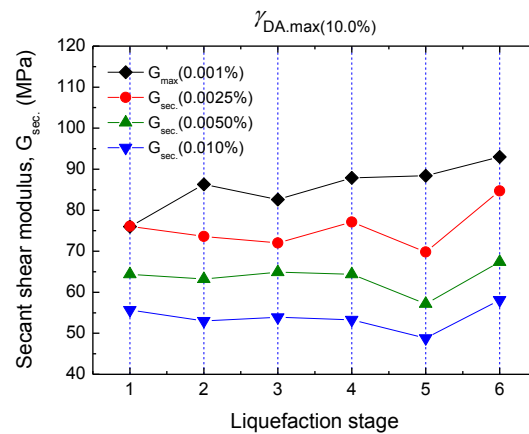
Fig. 6.17: Maximum and secant shear modulus in multiple-liquefaction tests on specimen sheared up to $\gamma_{DA.max}= 10\%$ (e.g. ML22 test)
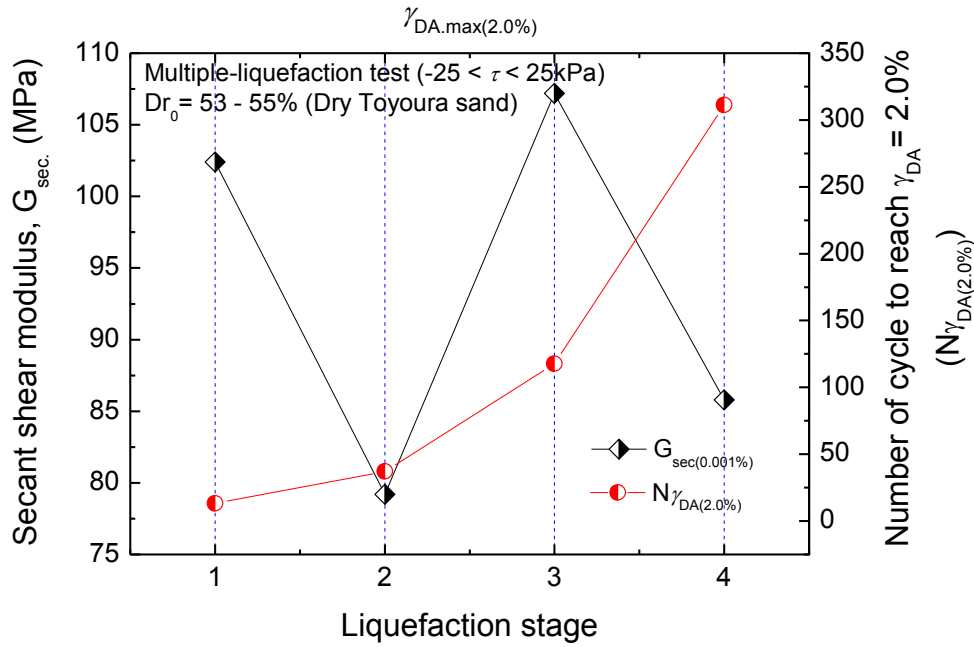
Fig. 6.18: Comparison between maximum shear modulus and liquefaction resistance in different liquefaction stage for specimen sheared up to $\gamma_{DA.max}$=2% (ML19 test)
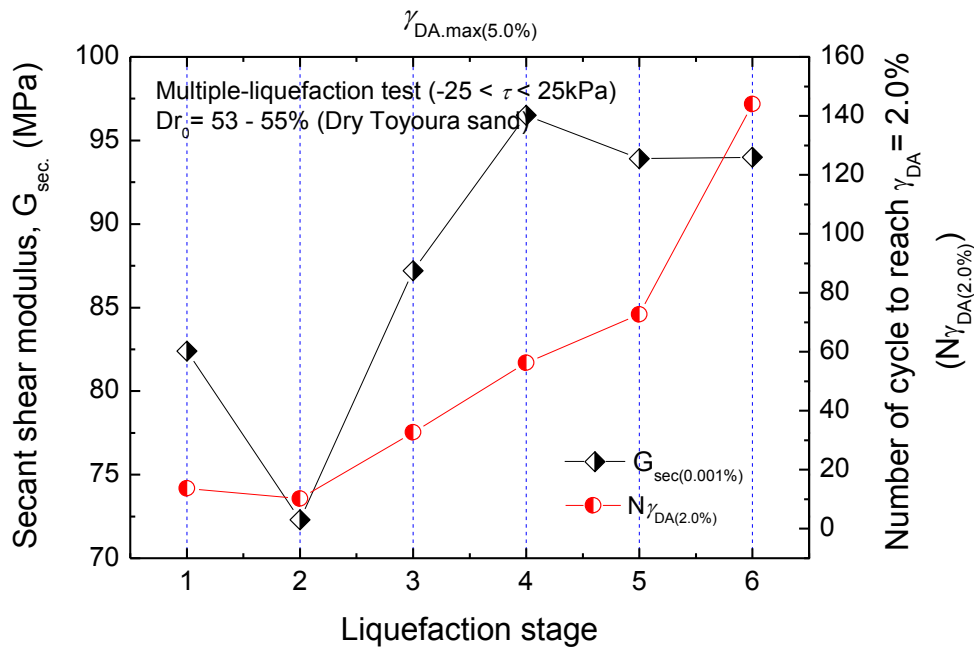
Fig. 6.19: Comparison between maximum shear modulus and liquefaction resistance in different liquefaction stage for specimen sheared up to $\gamma_{DA.max}$=5% (ML20 test)
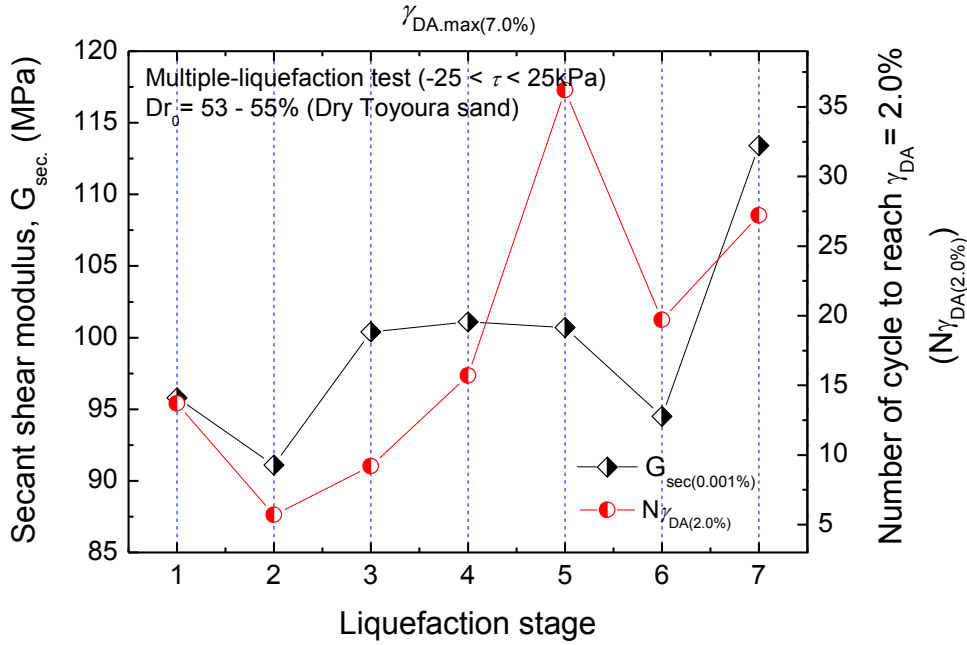
Fig. 6.20: Comparison between maximum shear modulus and liquefaction resistance in different liquefaction stage for specimen sheared up to $\gamma_{DA.max}$=7% (ML21 test)
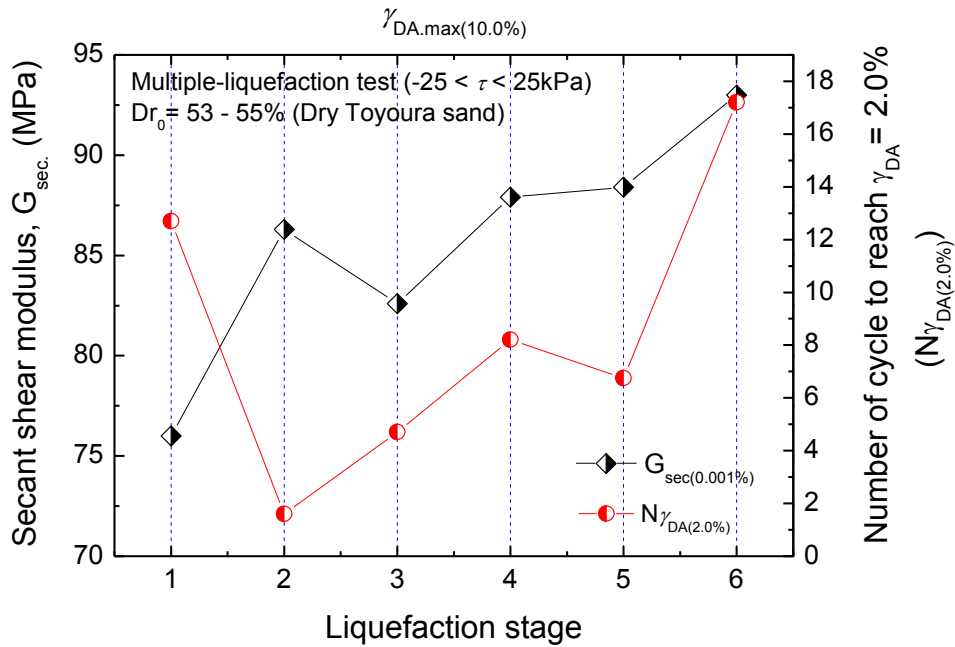
Fig. 6.21: Comparison between maximum shear modulus and liquefaction resistance in different liquefaction stage for specimen sheared up to $\gamma_{DA.max}$=10% (ML22 test)
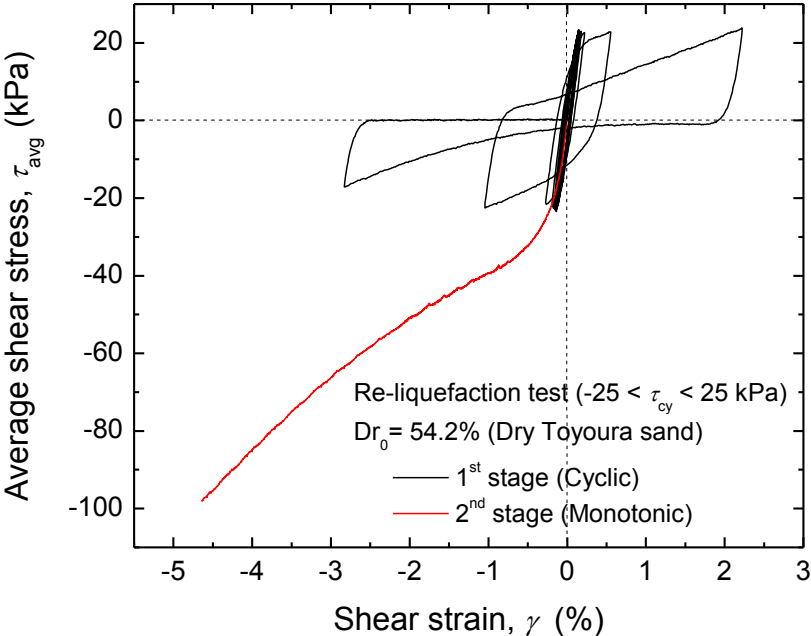
Fig. 6.22: Average shear stress - vertical stress relationships during the 1st and 2nd stages of SDRL1 test
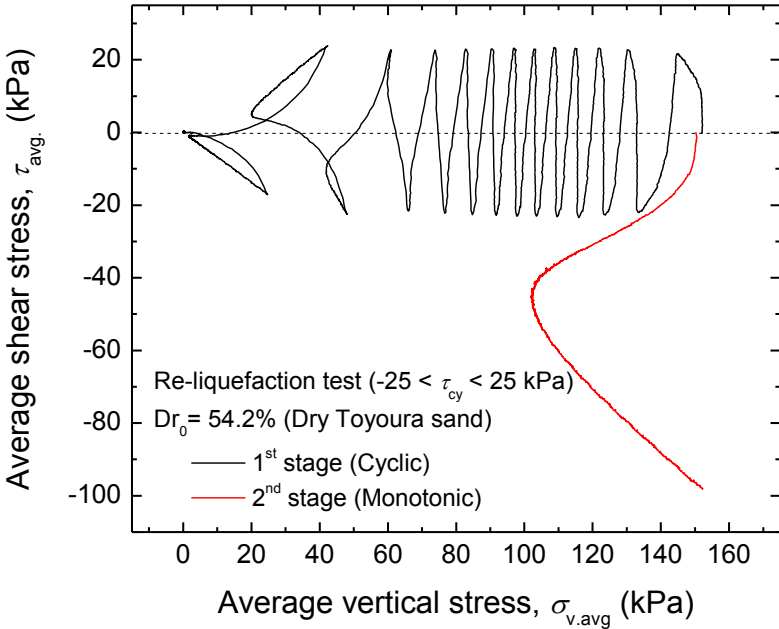
Fig. 6.23: Average shear stress - shear strain relationships during the 1st and 2nd stages of SDRL1 test
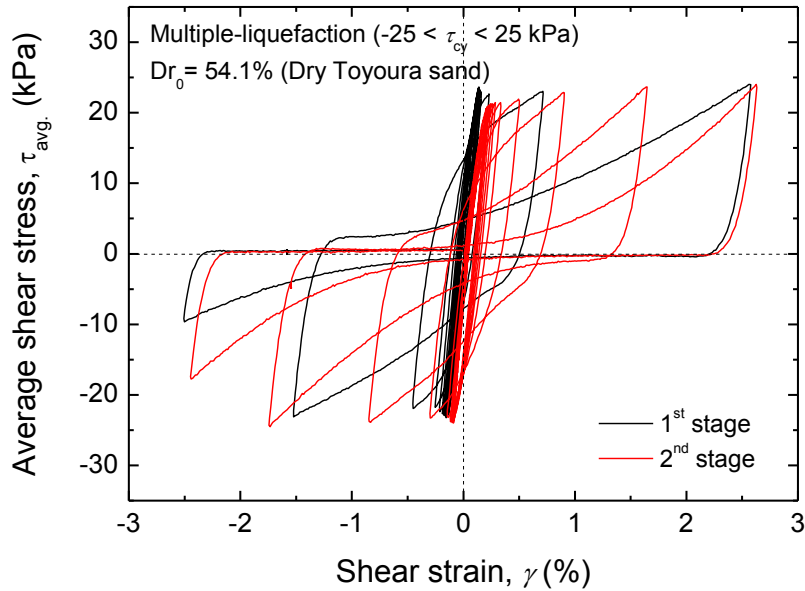
Fig. 6.24: Average shear stress -shear strain relationships during the 1st and 2nd stages of multiple-liquefaction tests on specimen sheared up to $\gamma_{DA.max}=5\%$ (ML20 test)
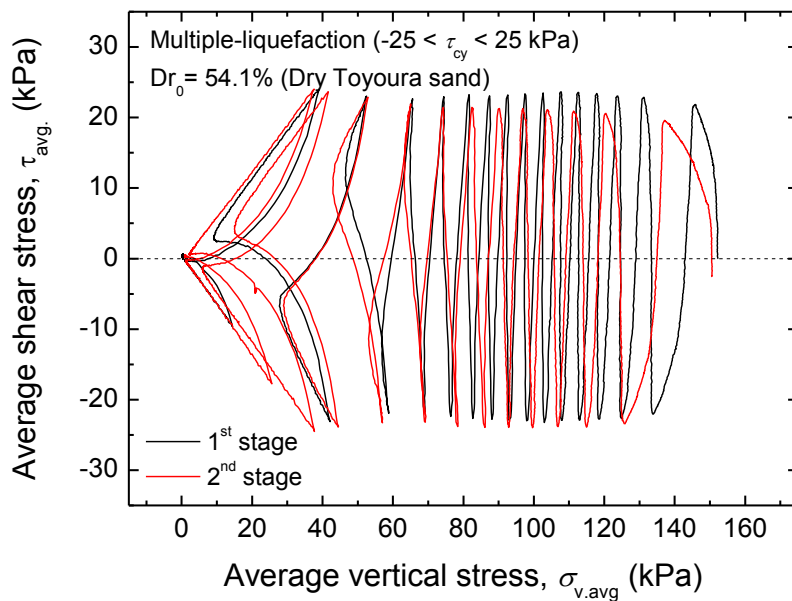
Fig. 6.25: Average shear stress -average vertical stress relationships during the 1st and 2nd stages of multiple-liquefaction tests on specimen sheared up to $\gamma_{DA.max}=5\%$ (ML20 test)
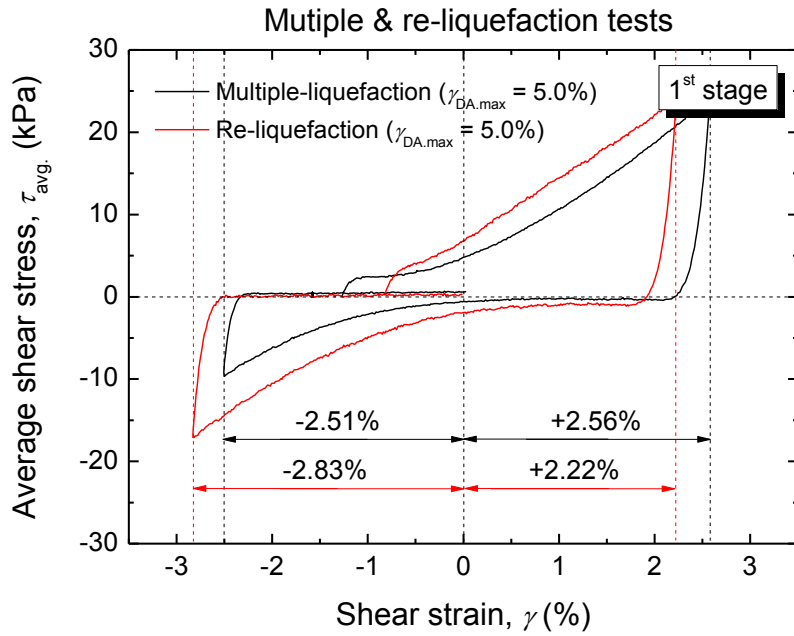
Fig. 6.26: Average shear stress -shear strain relationships during the 1st stage of SDRL1 and ML20 tests sheared up to $\gamma_{DA.max}$=5%
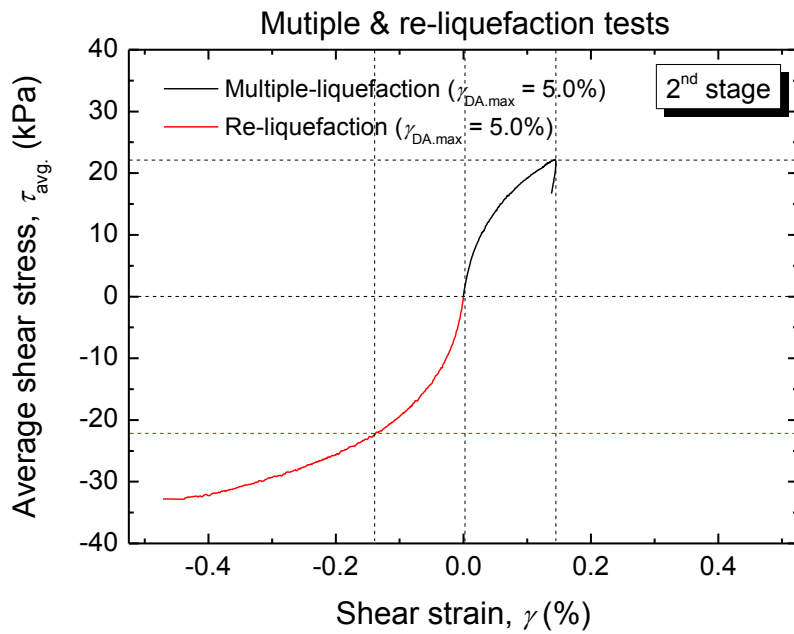
Fig. 6.27: Average shear stress -shear strain relationships during the 2nd stage of SDRL1 test and ML20 testsheared up to $\gamma_{DA.max}$=5%
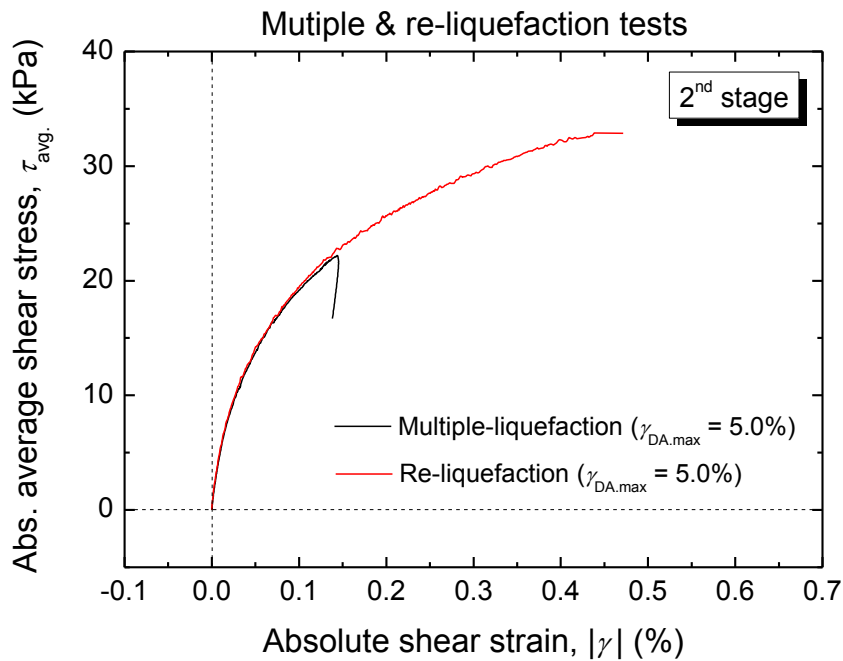
Fig. 6.28: Comparison of tests results in Fig. 6.27 in terms of absolute average shear stress –shear strain relationships

6.3.2 Stress-dilatancy relationshipsof soil during multiple liquefactions

6.3.2.1 Effects of strain amplitudes on the dilatancy characteristics of soilsubjected with multiple liquefactions

As mentioned above, additional series of tests was conducted to investigate the dilatancy characteristics of the multiple-liquefied soil. To do so, three multiple-liquefaction tests (SDRL2, SDRL3, and SDRL4 tests) were conducted on specimens sheared up to different$\gamma_{DA.max}$values of 2%, 5% and 10%. To avoid the effects on the variation of relative densities during subsequent liquefaction stages, each of multiple-liquefied specimens must be prepared carefully at similar relative densities. Therefore,initial relative density used to study the dilatancy characteristics of multiple-liquefied soil was 57-60%. This range of relative density was selected based on previous test results of multiple-liquefaction testsusing 11 coated stackedringsas shown in Figs. 6.29 and 6.30.Fig. 6.29 shows the relationship between liquefaction resistance and relative density, while Fig. 6.30 shows the change in relative density with the number of liquefaction stages.

6.3.2.1.1 Stress-dilatancy characteristics of soil during re-liquefaction test sheared up to $\gamma_{DA.max} = 2\%$

Amultiple-liquefaction test (SDRL2 tests)was carried out on a specimen sheared up to $\gamma_{DA.max}$= 2%. The specimen was prepared with an initial relative density of about 53%. To achieve the desired density of about 57-60%, the specimen was subjected to two stages of liquefaction with $\tau_{cy.}$=±25 kPa. The shear stress - shear strain relationships for the 1ststage are shown in Fig. 6.31, while the corresponding shear stress - vertical stress behaviors are shown in Fig. 6.32. For the 2nd liquefaction stage, the shear stress - shear strain curves are shown in Fig.6.33, while the shear stress - vertical stress relationships are shown in Fig. 6.34.It is important to mention that after each liquefaction stage, the residual shear strain was brought back to the origin. In the 1st liquefaction stage, the maximum shear strain single amplitude achieved in the clockwise and anti-clockwise directions were 0.89% and 1.21%, respectively, while in the 2nd liquefaction stage were 0.96% and 1.06%, respectively.

In the 3rd stage, the specimen was sheared under ±2.5% cyclic shear strain single amplitude under drained (constant-stress) conditions ($\sigma_{v.Top}$= 200kPa) for 10 cycles. The shear stress - shear strain relationshipsare reported in Fig. 6.35, while the vertical stress - shear stress relationshipsare shown in Fig. 6.36. Fig. 6.37 shows the corresponding volumetric strain - shear strain response. Finally, the stress-dilatancy relationshipis plottedin Fig. 6.38. From the last figure, it can be seen that the stress-dilatancy relationships in both directionsis not symmetric, particularly in the areaswhere the reversal of cyclic shear loading occurs. During subsequent cyclic loading, the amplitude of the maximum dilatancy ratio in the clockwise direction is higher (i.e. 0.25) than that in the anti-clockwise direction (i.e. 0.10). Therefore, the multiple-liquefied soil will exhibit a larger contraction when sheared in the clockwise direction rather than in the anti-clockwise direction in the future liquefaction.
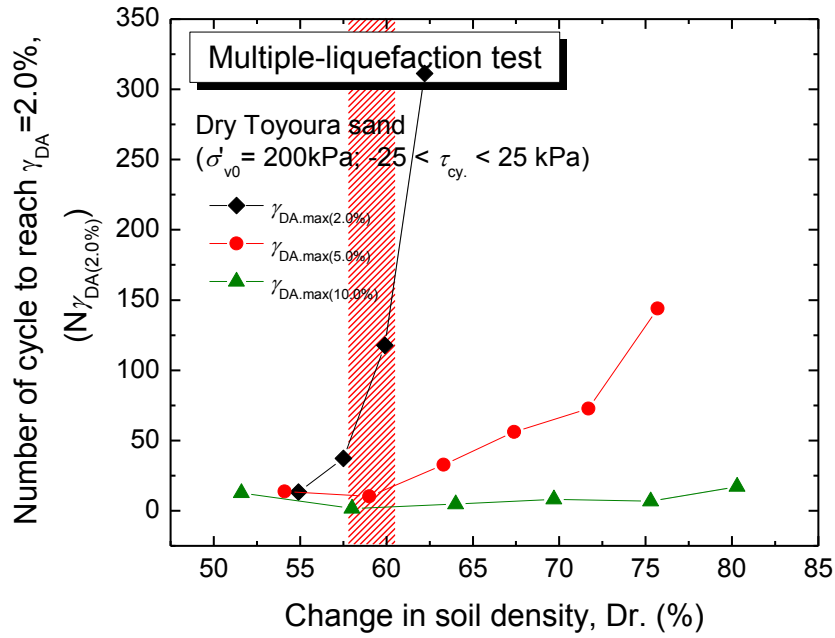
Fig. 6.29:Relationship between number of cycle to liquefy and relative density in multiple-liquefaction tests using11 coated stackedrings (ML10 to ML12 tests)
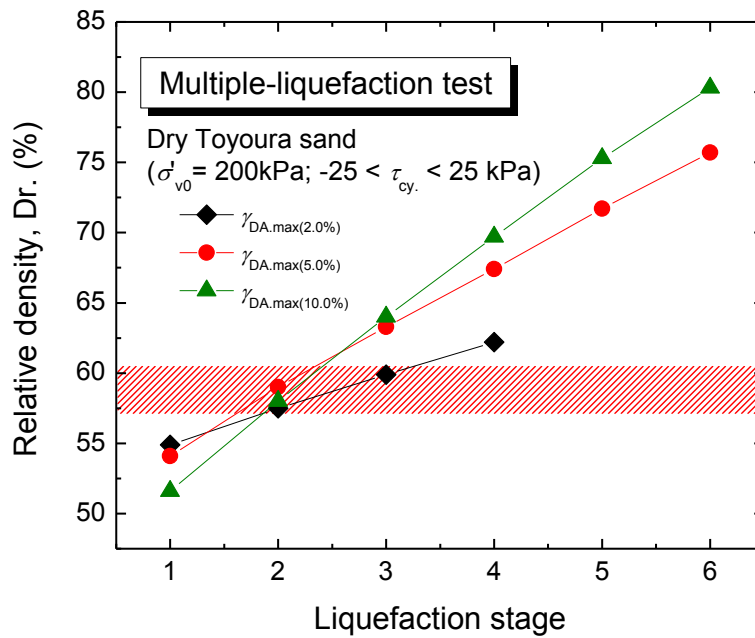
Fig. 6.30:Change in relative density with number of liquefaction stagesin multiple-liquefaction tests using11 coated stacked rings (ML10 to ML12 tests)
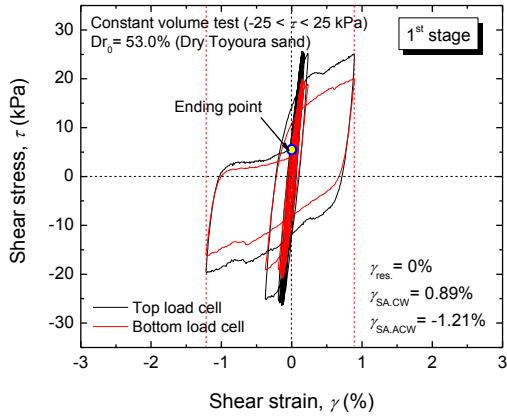
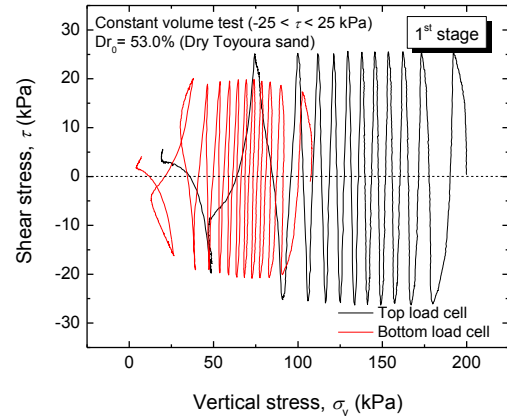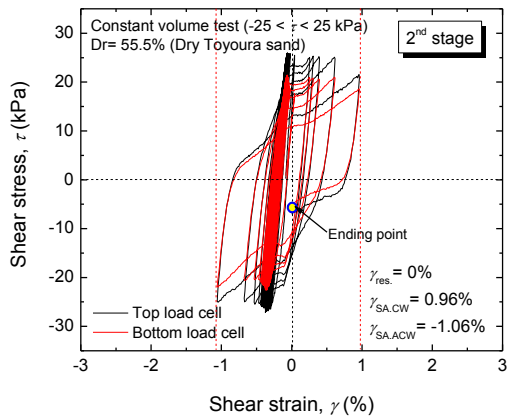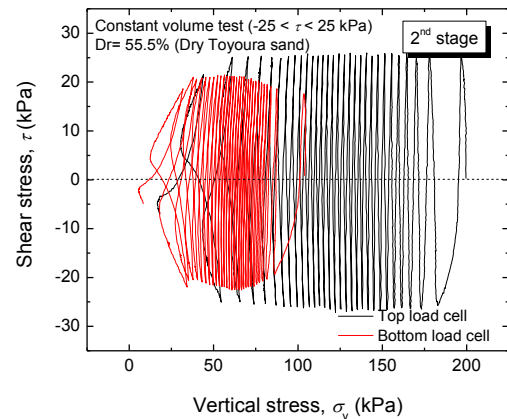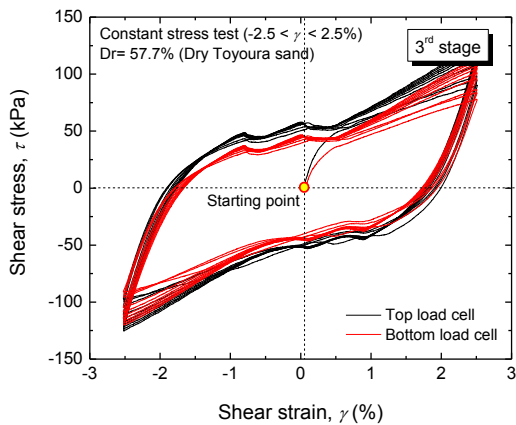Fig. 6.31: Shear stress - shear strain relationshipsin the 1st liquefaction stage (SDRL2 test)

Fig. 6.32: Shear stress- vertical stress relationshipsin the 1st liquefaction stage (SDRL2 test)

Fig. 6.33: Shear stress - shear strain relationshipsin the 2nd liquefaction stage (SDRL2 test)

Fig. 6.34: Shear stress -vertical stress relationships on the 2nd liquefaction test (SDRL2 test)

Fig. 6.35: Shear stress - vertical stress relationshipsin the 3rd drained stage (SDRL2 test)
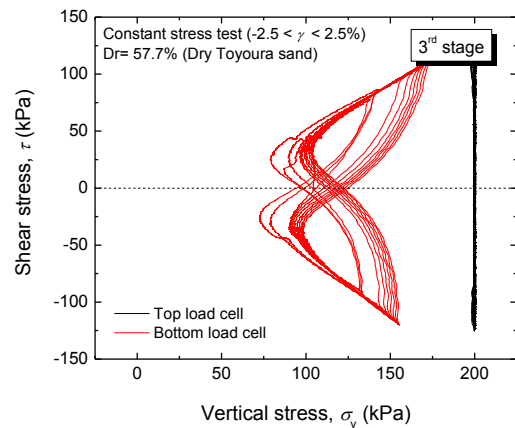
Fig. 6.36: Shear stress - vertical stress relationshipsin the 3rd drained stage (SDRL2 test)
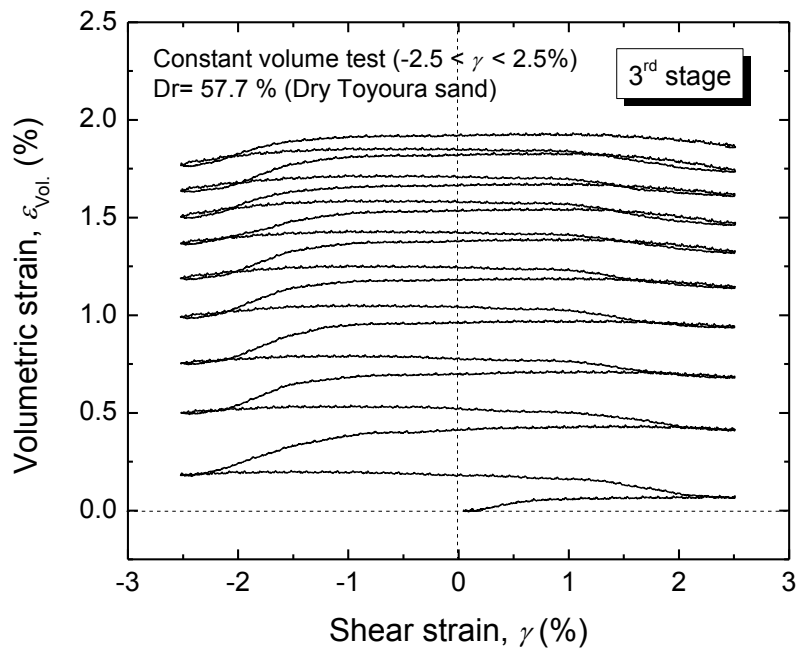
Fig. 6.37: Volumetric strain - shear strain relationshipsin the 3rddrained stage (SDRL2 test)
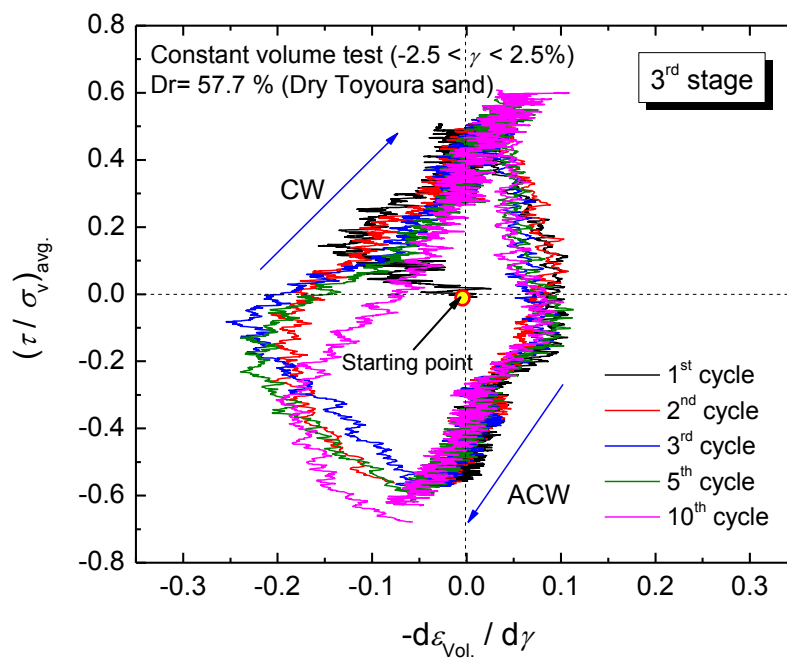
Fig. 6.38: Stress-dilatancy relationshipsin the 3rddrained stage (SDRL2 test)

6.3.2.1.2 *Stress-dilatancy characteristics of liquefied soil sheared up to $\gamma_{DA.max}= 5\%$*

A second multiple-liquefaction test (SDRL3 test)was conducted on a specimen sheared up to $\gamma_{DA.max}$= 5%. The specimen was prepared at an initial relative density of 54.5%. In the 1st stage, the specimen was subjected to $\tau_{cy.}$=±25 kPa under constant volume condition.The shear stress -shear strain relationships during this stageare shown in Fig. 6.39, while the shear stress - vertical stress relationships are reported in Fig. 6.40. The maximum shear strain single amplitude achieved on clockwise direction was about 2.28%, while in the anti-clockwise direction was about 2.75%. After the 1stliquefaction, the specimen was re-consolidated up to a vertical stress of 200 kPa and the relative density after the post re-consolidation was 59.2%, whichis still within the range of desired density to evaluate the dilatancy characteristic of multi-liquefied soil. In the 2nd stage, the re-consolidatedsoil was sheared within±2.5% shear strain single amplitude under drained (constant-stress) condition for 10 cycles. The shear stress - shear strain relationships for this stage are shown in Fig. 6.41, while the corresponding shear stress - vertical stress is given in Fig. 6.42. The volumetric strain - shear strain relationships is reported in Fig. 6.43. Finally, Fig. 6.44 shows the stress-dilatancy relationships. In this figure, the dilatancy characteristics during shearing in the clockwise and anti-clockwise directions are quite symmetrical with respect to the zero dilatancy axes. The amplitudes of dilatancy ratios on both directions are larger during the early cycles and then become smaller during subsequent drained cyclic loading. Since the dilatancy characteristics on both directions are very similar, there is no evidence that induced anisotropy may affect the resistance of liquefied soil. Therefore, it can be concluded that the resistance in the future liquefaction will be independent from the direction of loading.
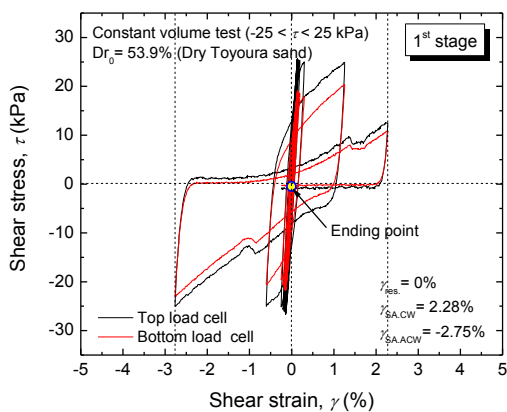

Fig. 6.39: Shear stress - shear strain relationshipsin the 1st liquefaction stage (SDRL3 test)
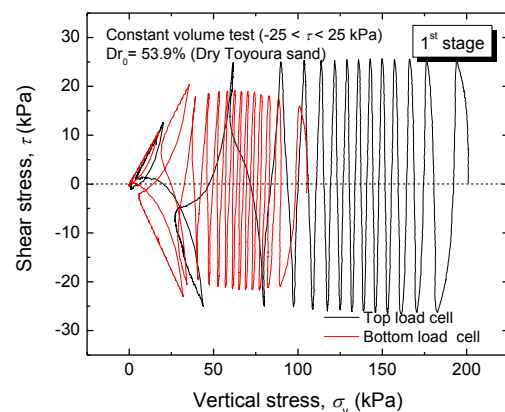

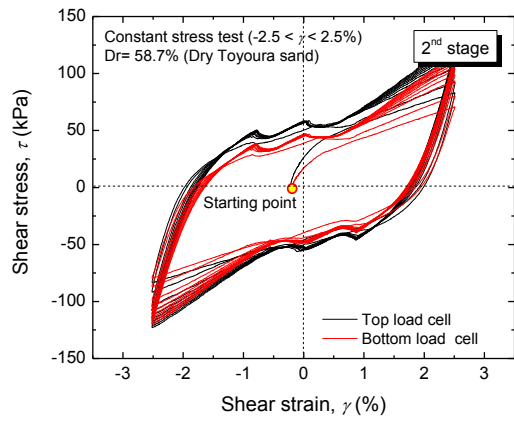Fig. 6.40: Shear stress - vertical stress relationships in the 1st liquefaction stage (SDRL3 test)

Fig. 6.41: Shear stress - shear strain relationshipsin the 2nd drained stage (SDRL3 test)

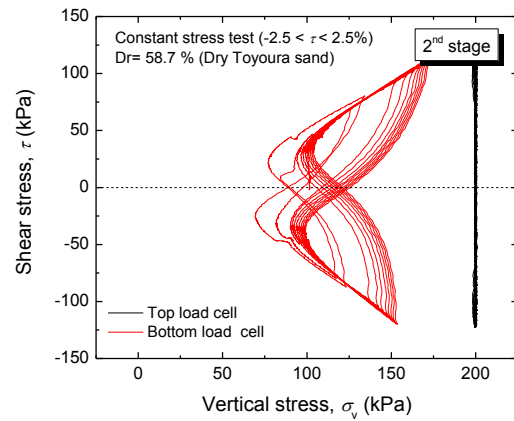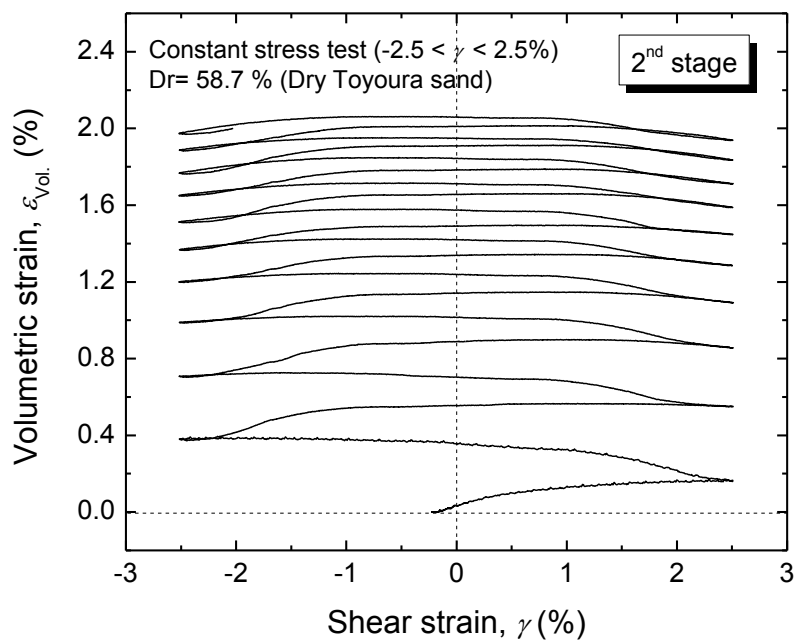Fig. 6.42: Shear stress - vertical stress relationshipsin the 2nd drained stage (SDRL3 test)

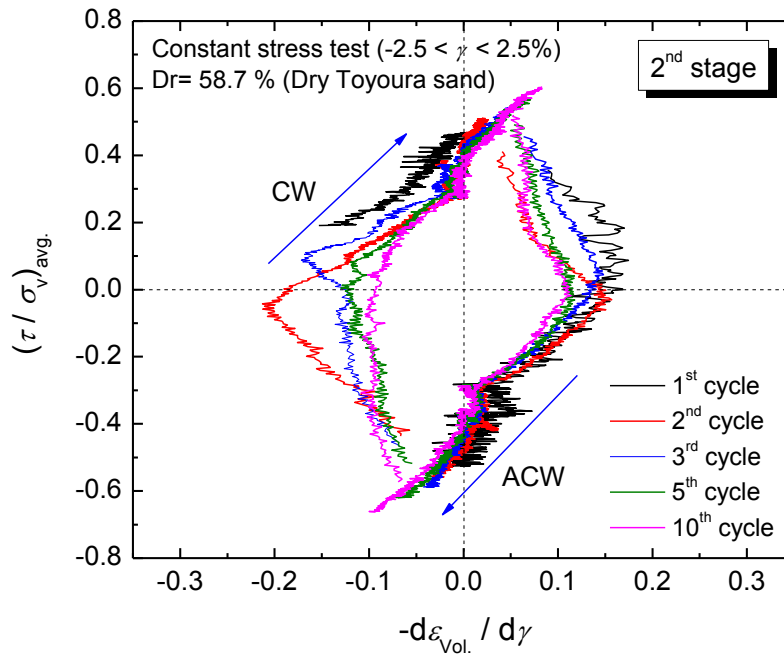Fig. 6.43: Volumetric strain - shear strain relationshipsin the 2nd drained stage (SDRL3 test)

Fig. 6.44: Stress-dilatancy relationshipsin the 2nddrained stage (SDRL3 test)

6.3.2.1.3 *Stress-dilatancy characteristics of liquefied soil sheared up to $\gamma_{DA.max}$= 10%*

Athirdmultiple-liquefaction test (SDRL4 test) was conducted on a specimen sheared up to $\gamma_{DA.max}$= 10%. The specimen was prepared withan initial relative density of 55.1%. In the 1st stage, the specimen was sheared by $\tau_{cy.}$=±25 kPa under constant-volume condition. The shear stress - shear strain relationshipsare shown in Fig. 6.45, while the shear stress - vertical stress relationshipsare reported in Fig. 6.46. The maximum shear strain single amplitude achieved on clockwise and anti-clockwise direction was 4.64% and 5.57%, respectively. After the 1st liquefaction, the specimen was re-consolidated up to a vertical stress of 200 kPa and therelative density after re-consolidation was61.8%. This density was slightly above the range of desired density (58% ≤ Dr ≤ 60%). In the 2nd stage, the specimen was sheared with ±2.5% shear strain single amplitude under drained (constant-stress) condition for 10 cycles. The shear stress - shear strain relationshipsfor this stage are shown in Fig. 6.47, while the corresponding shear stress - vertical stress is given in Fig. 6.48. The volumetric strain - shear strain relationships is reported in Fig. 6.49. The stress-dilatancy relationshipsare finally shown in Fig. 6.50. In this test, the dilatancy ratioson both directions were also nearly symmetrical with respect to the zero dilatancy axes, except during the 1st and 2nd cycles. Larger contraction took place during second-half of the 1st cycle and continued up to the first-half of the 2nd cycle. The specimen behaved less-and-less contractive in the subsequent cyclic loading.
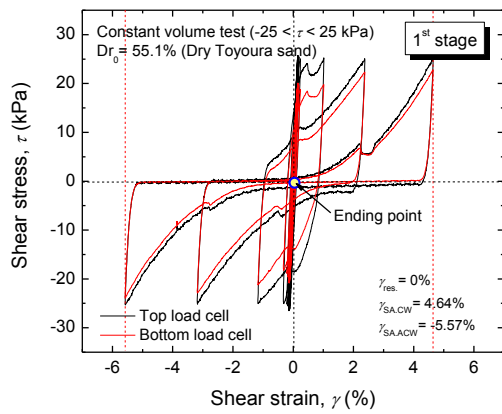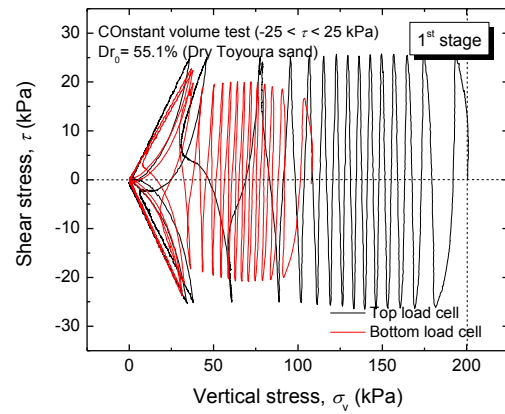
Fig. 6.45: Shear stress - shear strain relationshipsin the 1st liquefaction stage (SDRL4 test)

Fig. 6.46: Shear stress -vertical stress relationshipsin the 1st liquefaction stage (SDRL4 test)
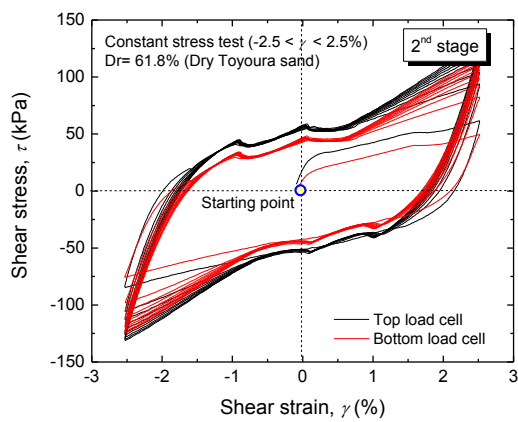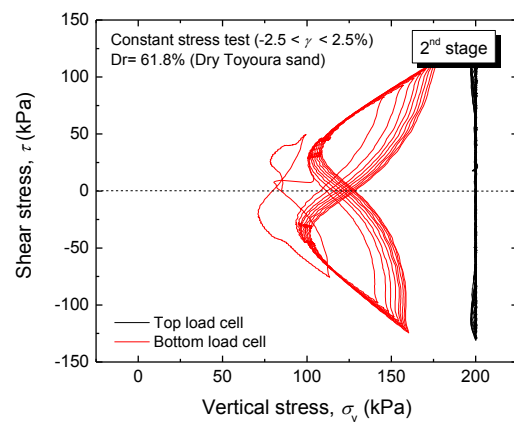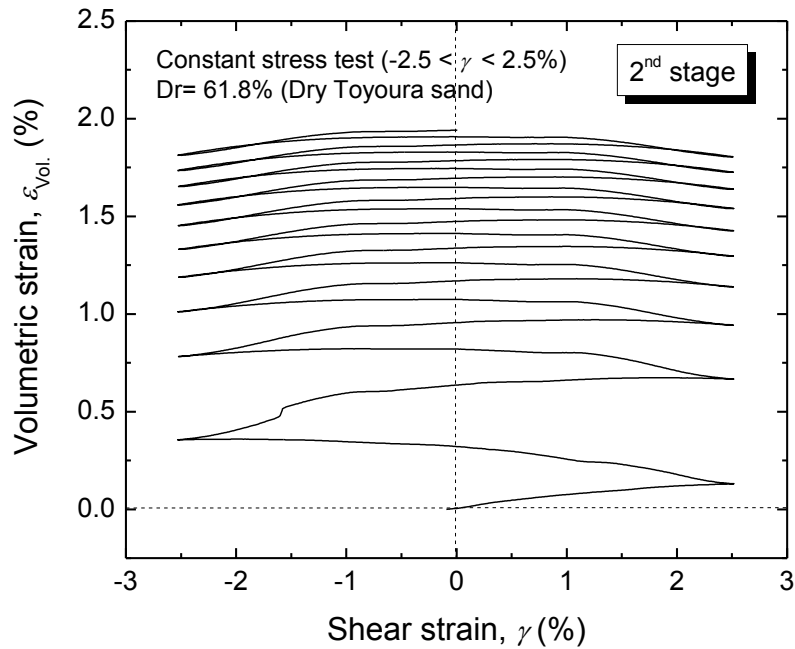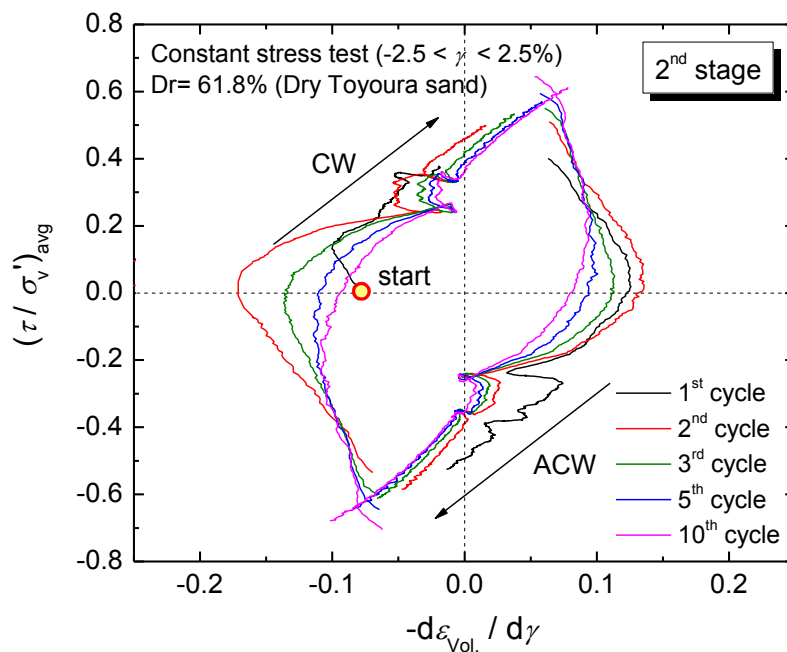

Fig. 6.47: Shear stress - shear strain relationshipsin the 2nddrained stage (SDRL4 test)

Fig. 6.48: Shear stress - vertical stress relationships in the 2nd drained stage (SDRL4 test)

Fig. 6.49: Volumetric strain - shear strain relationships in the 2nd drained stage (SDRL4 test)

Fig. 6.50: Stress-dilatancy relationships in the 2nd drained stage (SDRL4 test)

6.3.2.1.4 Stress-dilatancy characteristics of non-liquefied soil

For comparison purpose, the dilatancy characteristic of non-liquefied soil wasalso investigated. Without the history of liquefaction, the virgin specimen was expected to show

identical (symmetrical) dilatancy characteristics in bothclockwise and anti-clockwise loading directions. This also implies that there is no effect of inducedanisotropy on the behavior of non-liquefied soil. To do so, a specimen was prepared with aninitial relative density of 58.7% (SDCS1 test). Then, the specimen was sheared with ±2.5% shear strain single amplitudes for 10 cycles under drained (constant-stress) conditions. The shear stress - shear strain relationships of the virgin (non-liquefied) soil are shown in Fig. 6.51, while the shear stress - vertical stress relationshipsare reported in Fig. 6.52. The volumetric strain - shear strain relationshipsare given in Fig. 6.53 and the stress-dilatancy relationships is shown in Fig. 6.54. As expected, the dilatancy characteristics in both directions weresymmetrical with respect to the zero dilatancy axes.
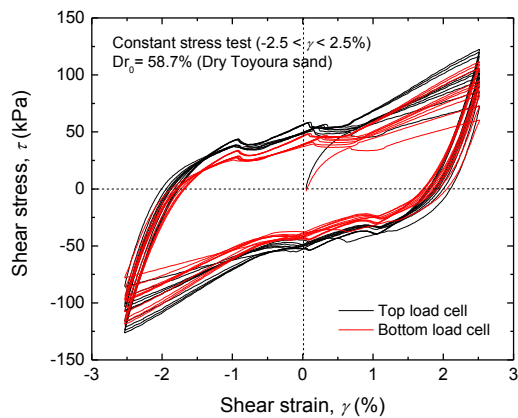

Fig. 6.51: Shear stress shear strain relationshipsin the drained cyclic test (SDCS1 test)
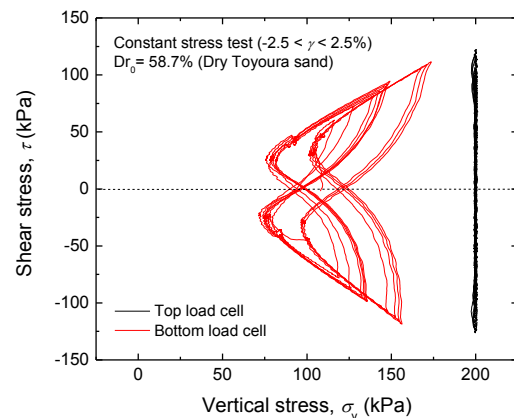

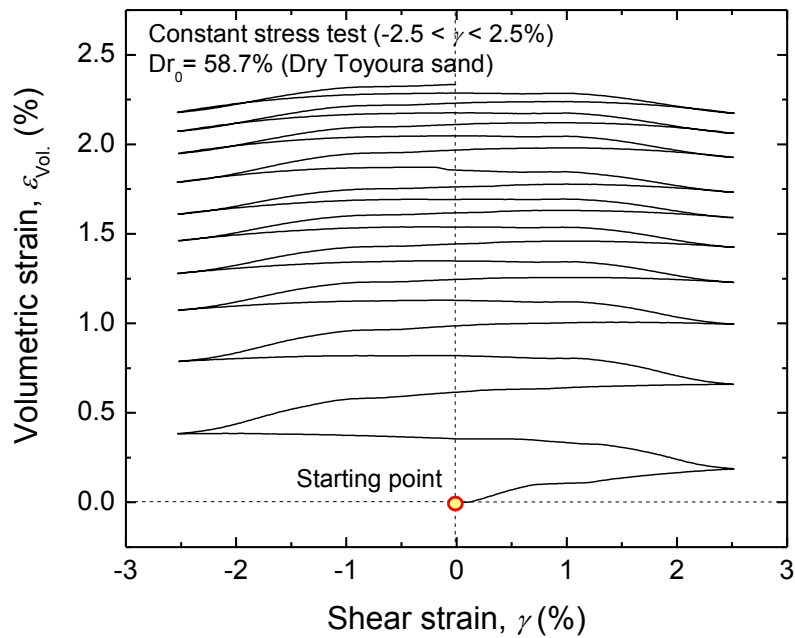Fig. 6.52: Shear stress vertical stress relationships in the drained cyclic test (SDCS1 test)

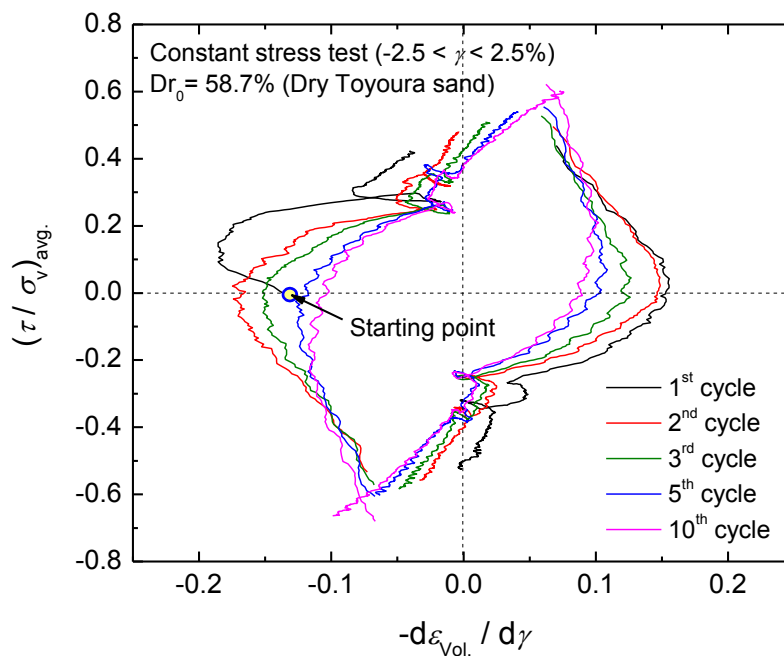Fig. 6.53: Volumetric strain - shear strain relationships in the drained cyclic test (SDCS1 test)

Fig. 6.54: Stress-dilatancy relationshipsin the drained cyclic test (SDCS1 test)

The results ofthese tests did not clarifythe impact of inducedanisotropy on the behavior of liquefied sand without residual strain. Among the three multiple-liquefaction tests, only in the multiple-liquefaction test carried out on the specimen sheared up to $\gamma_{DA.max} = 2\%$, the specimen with liquefaction historyshowed anon-symmetrical dilatancy characteristics in

clockwise and anti-clockwise directions after experiencing 2 stages of liquefaction.On the other hand, the dilatancy characteristics of soil specimens sheared up to $\gamma_{DA.max}$= 5% and 10% wasalmost symmetrical in both loading directions. These behaviors were also confirmed in the last cyclic drained test on the specimen with no previous history of liquefaction.

Based on these results, at least two observations can be drawn:1.) the effects of the induced anisotropy are negligiblein multiple-liquefied tests without residual strain. This was also confirmed by the fact that stress-dilatancy relationships of the specimens that underwent re-liquefaction (SDRL3and SDRL4 tests) and those without previous history of liquefaction (SDCS1 test)are symmetrical with respect to the zero dilatancy axes; 2.)itcan behowever expected that a specimen would behave differently in the different directions after experiencing several stages of liquefaction. This issue was investigatedby looking at the stress-dilatancy response of soil specimensheared up to $\gamma_{DA.max}$= 2%. Such a behavior may possibly happen because of the original fabric of soil is destroyed repeatedly during multiple-liquefaction stages.

6.3.2.2 Effects of residual shear strain on dilatancy characteristics of soil subjected with multiple liquefactions

Although, based on the previously-described test results, it appears that the effects of induced anisotropy are negligible in post-liquefaction stage if the residual strain is brought back to the origin, in reality, some extent of residual strain do always occur in post-liquefaction because the shear loading is always stopped at the zero shear stress (τ= 0 kPa). This is confirmed by previous studies done by Ishihara and Okada (1978 and 1982), Oda et al. (1972a), Towhata and Ishihara (1985), Suzuki and Toki (1984), Oda et al. (2001), Yamada et al. (2010) among others. In such studies, it is alsoshown that the residual strain would have major impacts on the soil behavior in future liquefaction.

To clarify this issue, three additional tests were conducted on specimen subjected to residual strain in different loading directions and subsequently sheared under drained (constant- stress) conditions in both directions. If the effect of induced anisotropy exists and it is significant, then the dilatancy characteristics on different loading directions should be non-symmetrical.

6.3.2.2.1 Stress-dilatancy characteristics of liquefied soil with residual shear strain applied in anti-clockwise direction

The first test(SDRL5 test)was conducted with the aim to investigate the dilatancy characteristics of a liquefied specimenshowing residual shear strain in anti-clockwise direction. The specimen was prepared with an initial relative density of 53.4%. Then, it was sheared by $\tau_{cy.}=\pm25$ kPa under undrained (constant-volume) condition. The 1^{st}liquefaction stage was intentionally stoppedat the time when a large residual shear strain was accumulated in anti-clockwise direction. The shear stress - shear strain relationshipsduring the 1st stage of liquefaction areshown in Fig. 6.55, while shear stress - vertical stress relationshipsare shown in Fig. 6.56. The maximum single strain amplitude in clockwise direction was 1.81%, while in anti-clockwise direction was 2.58%. The residual shear strain measured at zero shear stress ($\tau= 0$ kPa) was -2.27%.

In the 2nd stage, the specimen was sheared by applying 10 cycles under drained (constant stress) conditions. To evaluate the effects of induced anisotropy, the shear loading in the 2nd stage started in the clockwise direction.The shear stress - shear strain relationshipsin the 2nd stage are shown in Fig. 6.57, while the shear stress - vertical stress relationshipsare reported in Fig. 6.58. The volumetric strain - shear strain relationshipsare shown in Fig. 6.59. Based on these results, the stress-dilatancy characteristics of the liquefied soil were obtained as shown Fig. 6.60.Interestingly, the largest dilatancy ratio can be observed in clockwise direction during the virgin loading. A large dilatancy ratio observed in anti-clockwise direction during reversal of loading in the second half of 1st cycle. This means that large contractions only took place during the 1st cycle of cyclic loading, while in the subsequent cycles liquefied soil behaves less contractive.
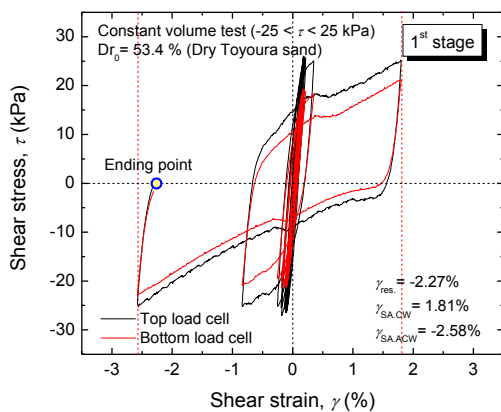

Fig. 6.55: Shear stress - shear strain relationshipsin the 1st liquefaction stage (SDRL5 test)
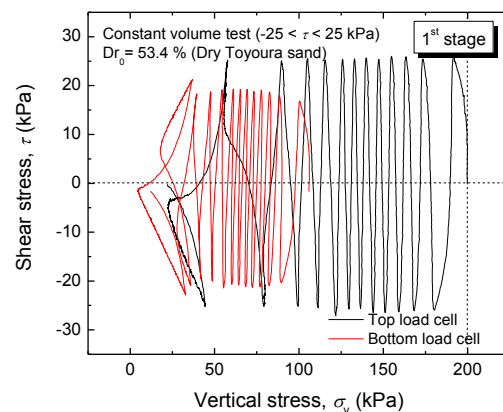
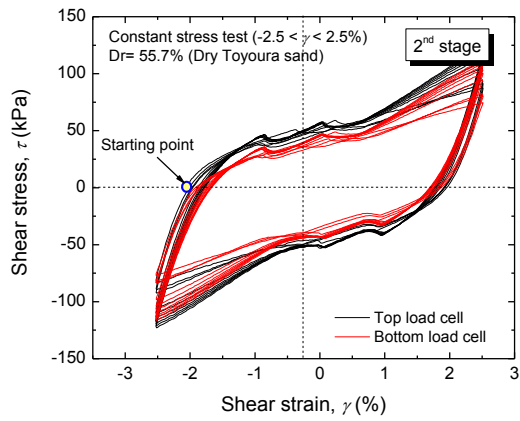Fig. 6.56: Shear stress - vertical stress relationshipsin the 1st liquefaction stage (SDRL5 test)

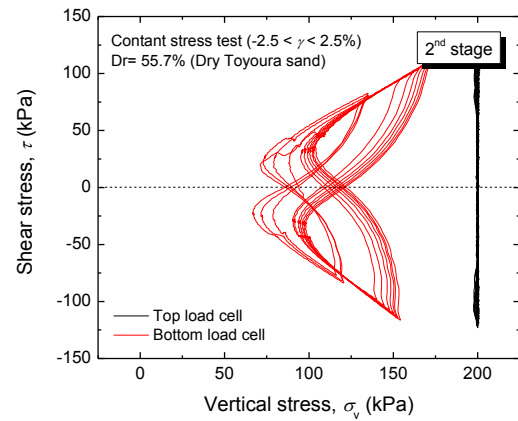Fig. 6.57: Shear stress - shear strain relationshipsin the 2nd drained stage (SDRL5 test)

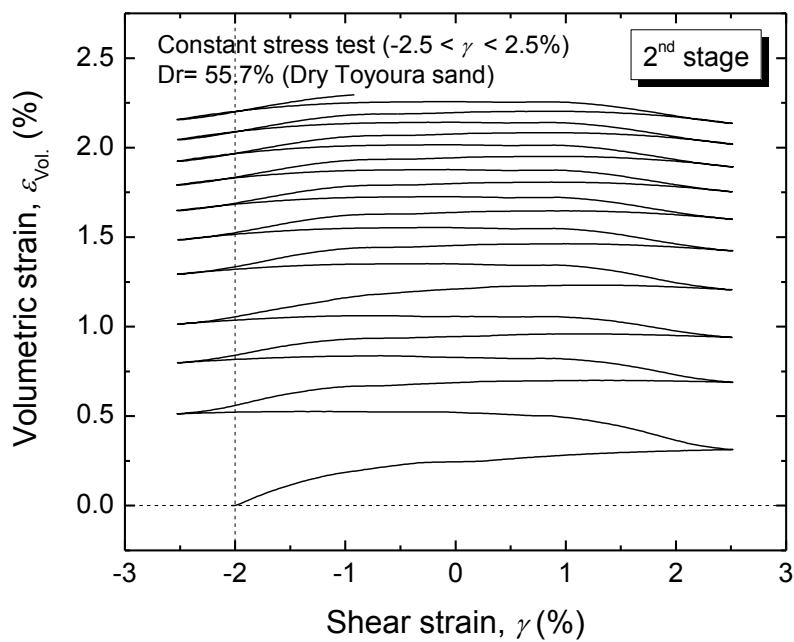Fig. 6.58: Shear stress - vertical stress relationshipsin the 2nd drained stage (SDRL5 test)

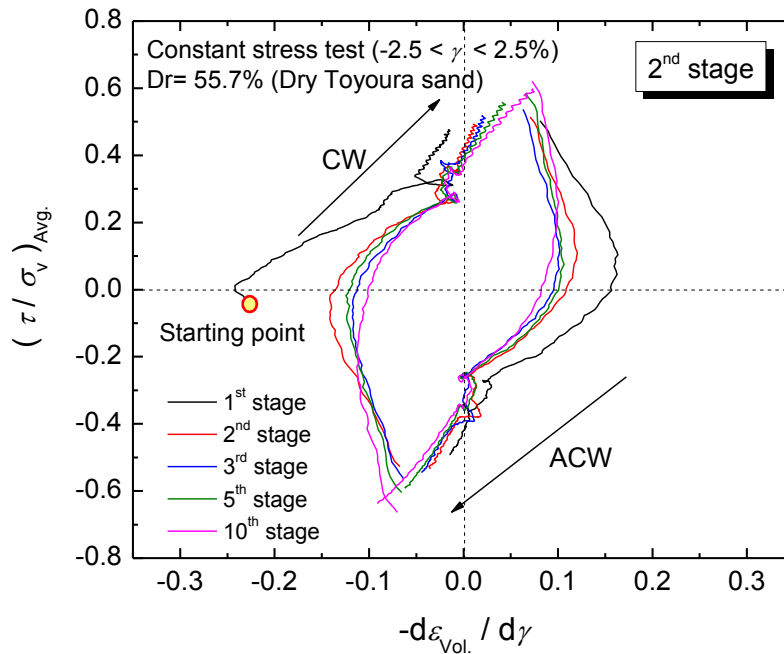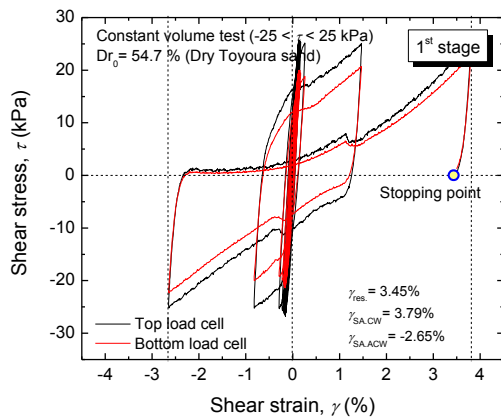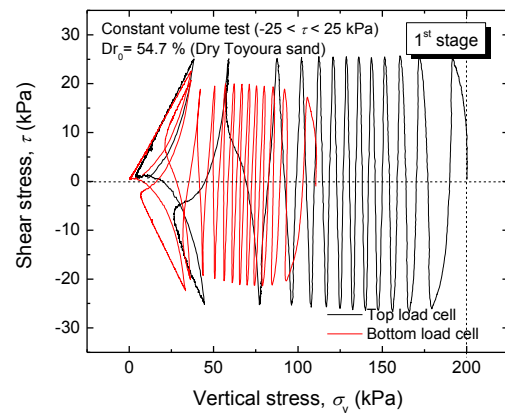Fig. 6.59: Volumetric strain - shear strain relationshipsin the 2nd drained stage (SDRL5 test)

Fig. 6.60: Stress-dilatancy relationshipsin the 2nd drained stage (SDRL5 test)

6.3.2.2.2 Stress-dilatancy characteristics of liquefied soil with residual shear strain applied in clockwise direction

The second test (SDRL6 test) was aimed to understand the dilatancy characteristic of a soil specimen showing residual shear strain in clockwise direction at the end of the 1st liquefaction stage. The specimen was prepared with an initial relative density of 54.7%. In the 1st liquefaction stage, the specimen was sheared by $\tau_{cy.}=\pm25$ kPa under undrained (constant-volume) conditions. The 1st stage was completed when residual shear strain was accumulated in clockwise direction. The shear stress - shear strain relationshipsare shown in Fig. 6.61, while the shear stress - vertical stress relationshipsare given in Fig. 6.62. The maximum shear strain single amplitude in clockwise direction was 3.79%, while in anti-clockwise direction was -2.65%. The residual shear strain after liquefaction was 3.46% in the clockwise direction. In the 2nd stage, the liquefied soil specimen was sheared cyclically under drained (constant-stress) conditions for 10 cycles. The liquefied specimen was first sheared in anti-clockwise direction in order to evaluate the effects of residual strain (i.e. induced anisotropy) on the dilatancy characteristics of liquefied soil. The shear stress - shear strain relationshipsin the 2nd stage are presented in Fig. 6.63, while the shear stress - vertical stress relationship is shown in Fig. 6.64. The volumetric strain - shear strain relationshipsare reported in Fig. 6.65. Finally, the stress-dilatancy relationship of the liquefied soil is plotted in Fig. 6.66. It can be seen that

the largest contraction took place during the first-quarter of the 1st cycle in anti-clockwise direction and continued after the reversal of loadingin clockwise direction.In the subsequent cyclic loading, the specimen behaves less-and-less contractive.

This behavior is very similar to thatobserved in the previous SDRL5 test on the specimen showingresidual shear strain in anti-clockwise direction. To confirm these findings, another test(SDRL7)was conducted, in which the residual shear strain was accumulated in clockwise direction, but drained cyclic shearing was conducted first in anti-clockwise direction during the 2nd stage.

Fig. 6.61: Shear stress - shear strain relationshipsin the 1st liquefaction stage (SDRL6 test)

Fig. 6.62: Shear stress and vertical stress relationshipsin the 1st liquefaction stage (SDRL6 test)
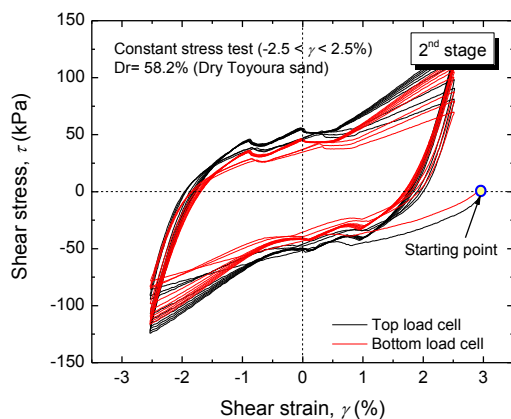

Fig. 6.63: Shear stress - shear strain relationshipsin 2^{nd}drained stage (SDRL6 test)
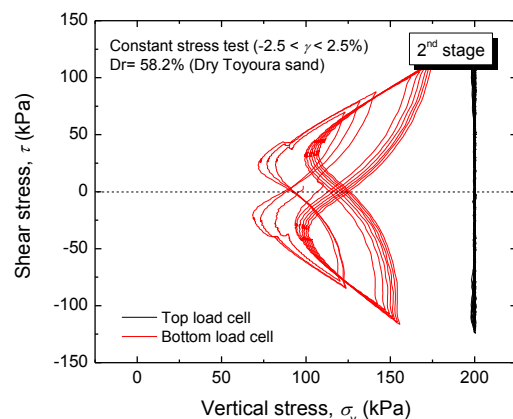

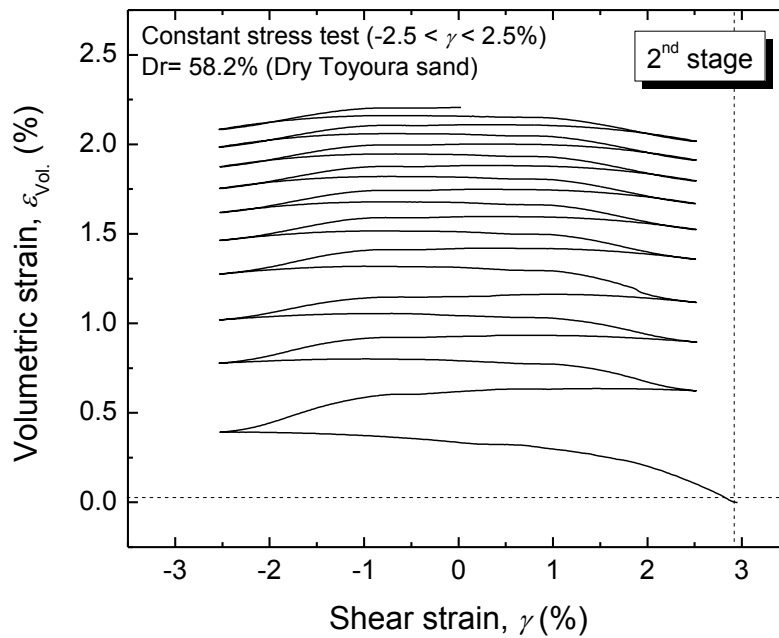Fig. 6.64: Shear stress - vertical stress relationships in 2nd drained stage (SDRL6 test)

Fig. 6.65: Volumetric strain - shear strain relationships in 2nd drained stage (SDRL6 test)
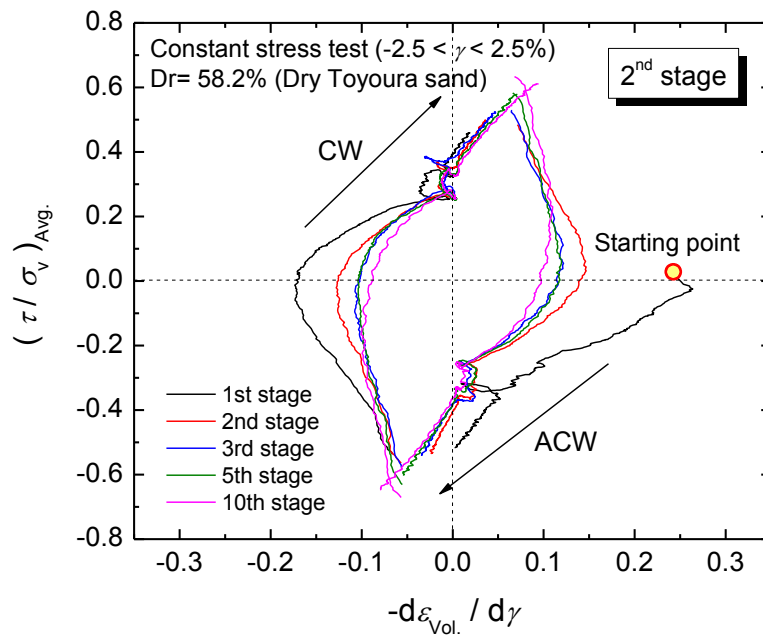

Fig. 6.66: Stress-dilatancy relationshipsin 2nd drained stage (SDRL6 test)

6.3.2.2.3 *Stress-dilatancy characteristics of liquefied soil with residual strain in clockwise directionand sheared in clockwise direction during 2^{nd}stage*

The third test (SDRL7) was carried out under similar conditions as the second one. However, the shear loading was applied in clockwise direction during 2nd drained stage. The specimen was prepared with an initial relative density of 53.9%. In the 1st liquefaction stage, the specimen was sheared by $\tau_{cy.}=\pm25$ kPa under constant-volume conditions. Under such imposed stress conditions, thelargest shear single amplitude was observed in anti-clockwise direction, while the residual shear strain was observed in clockwise direction. The shear stress - shear strain relationships during the 1st liquefaction stage are shown in Fig. 6.67, while the shear stress - vertical stress relationshipsare presented in Fig. 6.68. The maximum shear strain single amplitude in anti-clockwise direction was 5.87%, while in clockwise direction was 4.47%. The residual shear strain in this test was 4.28% in clockwise direction. In the 2nd stage, the soil specimen was sheared cyclically under constant-stress conditionsapplied first in clockwise direction. The shear stress - shear strain,the shear stress -vertical stress and the volumetric strain - shear strain relationshipsfor the 2nd drained stage are shown in Figs. 6.69 through 6.71. Alternatively, the stress-dilatancy relationship is shown in Fig. 6.72. It can be seen that only small contraction took place during the virgin loading. While, when the loading reversedfor the 1st time to anti-clockwise direction, the largest contraction took place. This large contraction still continued up to the first-half of the 2nd cycle, while in the following cycles, the specimen behaves less-and-less contractive.
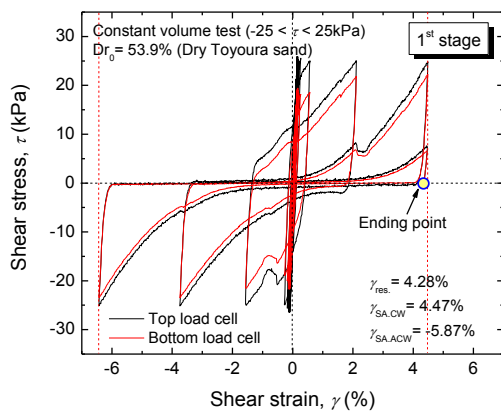

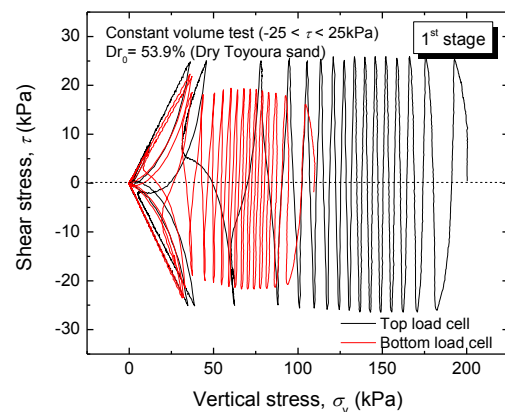Fig. 6.67: Shear stress - shear strain relationshipsin the 1st liquefaction stage (SDRL7 test)

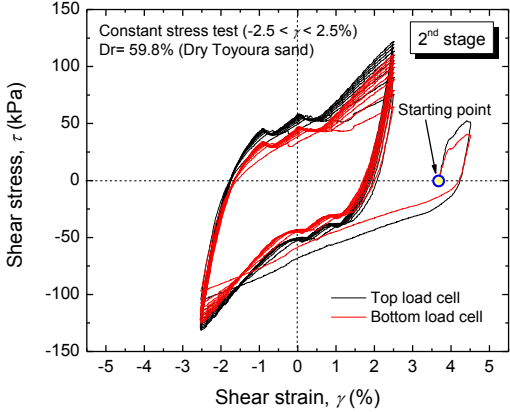Fig. 6.68: Shear stress - vertical stress relationships in the 1st liquefaction stage (SDRL7 test)

Fig. 6.69: Shear stress - shear strain relationshipsinthe 2nddrained stage (SDRL7 test)
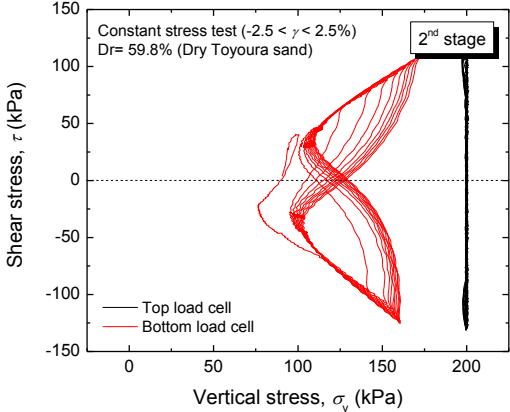
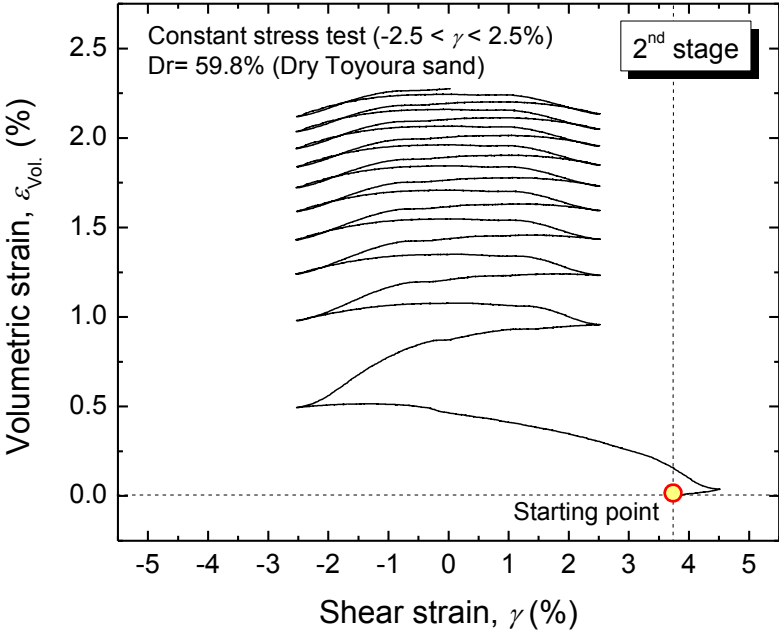Fig. 6.70: Shear stress - vertical stress relationships in the 2nd drained stage (SDRL7 test)

Fig. 6.71: Volumetric strain - shear strain relationships in the 2nd drained stage (SDRL7 test)
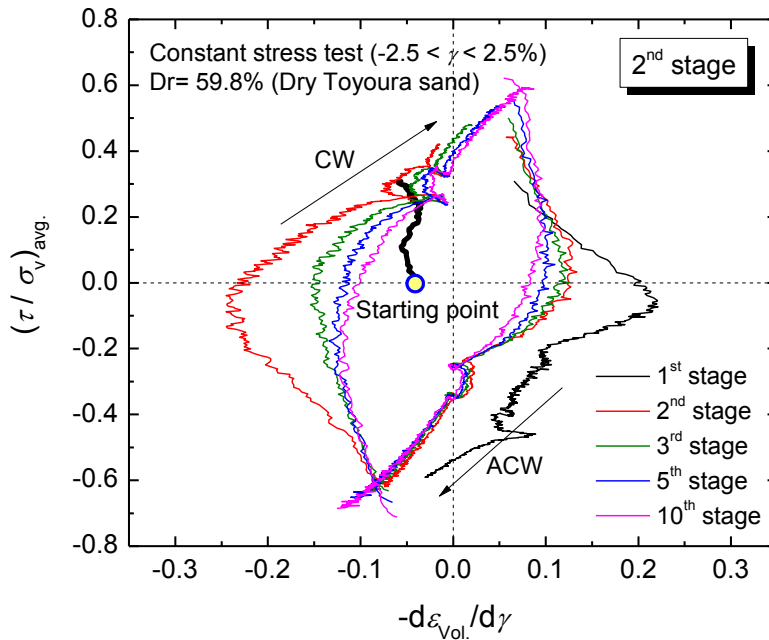
Fig. 6.72: Stress-dilatancy relationships in the 2nd drained stage (SDRL7 test)

6.3.2.2.4 Comparison between stress-dilatancy characteristics in the 1st and 2nd test

To have a comprehensive understanding on the impact of residual shear strain on the dilatancy characteristics of liquefied soil, the results on the three tests are compared.

First is the comparison between SDRL5 and SDRL6 tests. These two tests were intended to simulate mirror stress/strain conditions (i.e. residual strain in one direction and drained cyclic loading starting in the opposite one, and vice versa). The comparison between stress-dilatancy relationships in the two tests in the 1st and 2nd cycles of loading are shown in Fig. 6.73. It can be seen that the largest contraction took place during the virgin loading in both tests. Such a large contraction still continuedduring the reversal of the virgin loading. Then, the contraction continuously decreasedstarting fromthe 2nd cycle.

As the two tests conditions were symmetricalto each other, the stress-dilatancy on either test can be rotated as shown in Fig. 6.74. Interestingly, it appears that the dilatancy characteristics on both testsare very similar to each another.
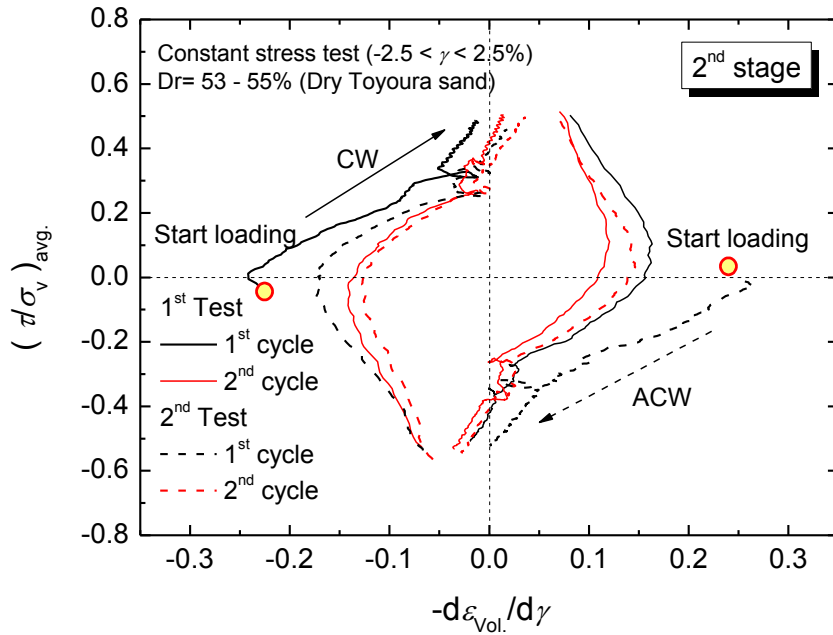
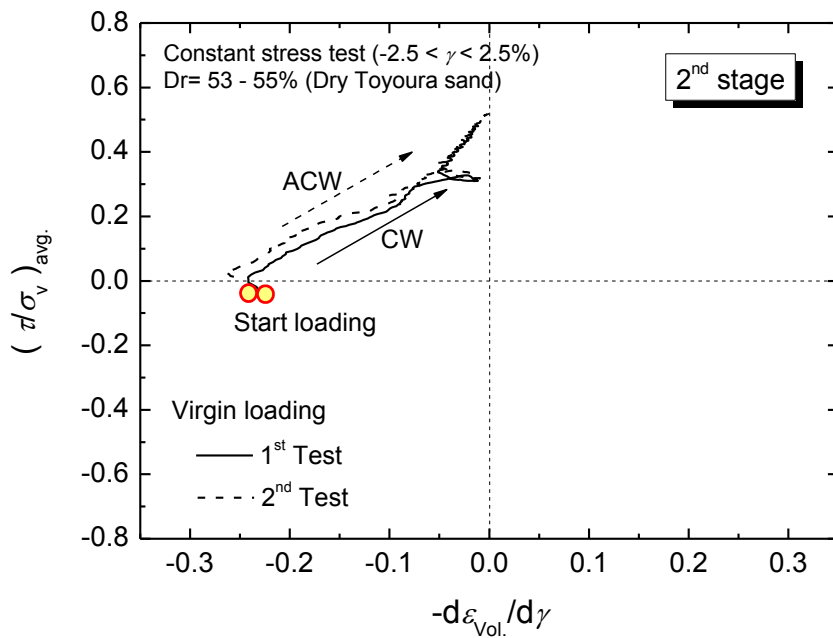Fig. 6.73: Comparison of dilatancy propertiesinSDRL5 and SDRL6tests for various cycles of loading

Fig. 6.74: Comparison of dilatancy properties in SDRL5 and SDRL6 tests for the 1st cycle of loading

6.3.2.2.5   Comparison between stress-dilatancy characteristics in the 1stand 3rd test

Hereafter, comparison between stress-dilatancy behaviors observed in SDRL5 and SDRL7 tests is presented inFig. 6.75. Note that in the first test, the residual shear strain wasapplied inanti-clockwise direction, while the in the 2nd stage, the drained cyclic shear loading started in clockwise direction. In contrast, in the third test, the residual shear strain was applied in clockwise direction, while in the 2nd stage, the drained cyclic shear loading also started in clockwise direction.Clearly the dilatancy characteristics are very different fromeach another. In fact, in the third test, small contraction appeared during the virgin loading, followed by very large contraction after the reversal of virgin loading in the anti-clockwise direction. For a better understanding, the comparison between dilatancy responses of soil during virgin loading in both tests is reported in Fig. 6.76. It can be seen that soil behavesin a very different way during virgin loading. A very large contraction took place in the first test, while a very small contraction is observed in the third test.
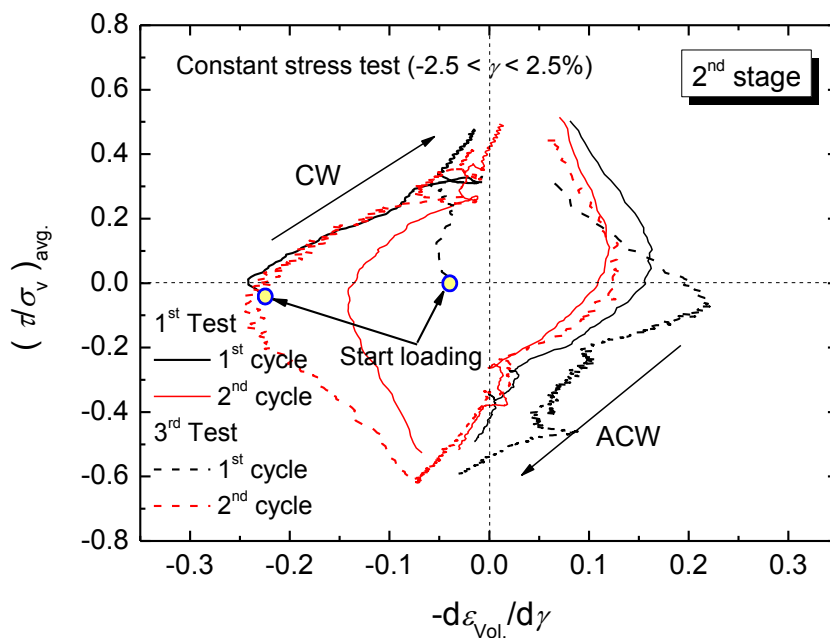

Fig. 6.75: Comparison of dilatancy properties in SDRL6 and SDRL7 tests for various cycles of loading
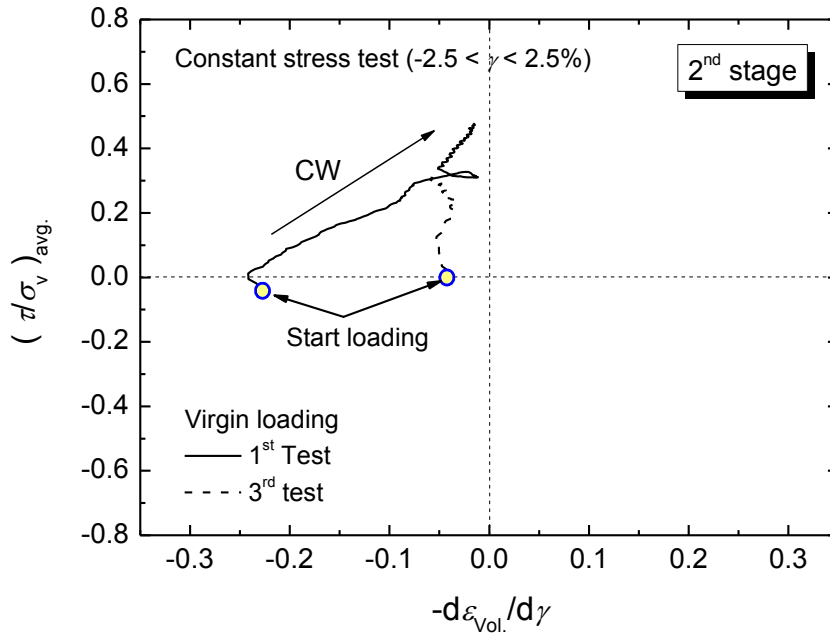
Fig. 6.76: Comparison of dilatancy properties in SDRL6 and SDRL7 for the 1st cycle of loading

The combination of residual shear strain and direction of the virgin loading has significant effects on the dilatancy characteristics of liquefied soil. This can be explained by referring to Figs. 6.77 and 6.78. Fig. 6.77 illustrates the conditions in the first and second tests, while Fig. 6.78 represents the conditions in the third test. Accordingly, large contraction can take place if the specimen is sheared in the same direction of the largest strain amplitude between the current loading positionsand the maximum shear strain achieved in the previous liquefaction stage $\left(\left| \gamma^{next} - \gamma_{SA.max}^{previous} \right| \right)$. On the other hand, small contraction will take place if the specimen is sheared in the same direction of the smallest strain amplitude between the current loading positionsand the maximum shear strain reached in the previous liquefaction stage. The larger the contractionin the constant-stress test is, the higher the reduction in effective stress in the constant-volume test and vice-versa.
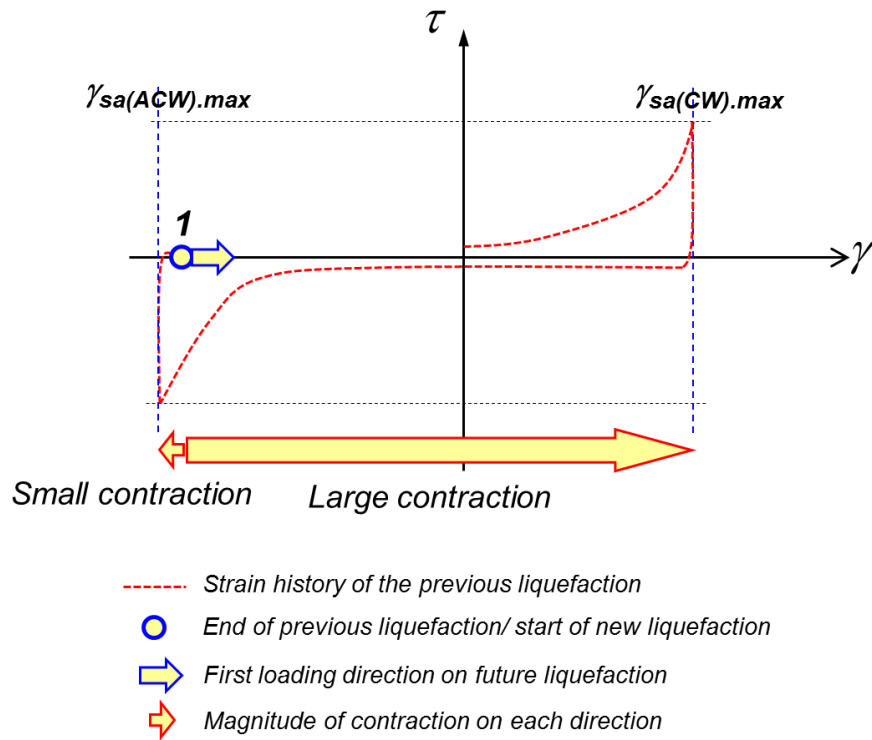
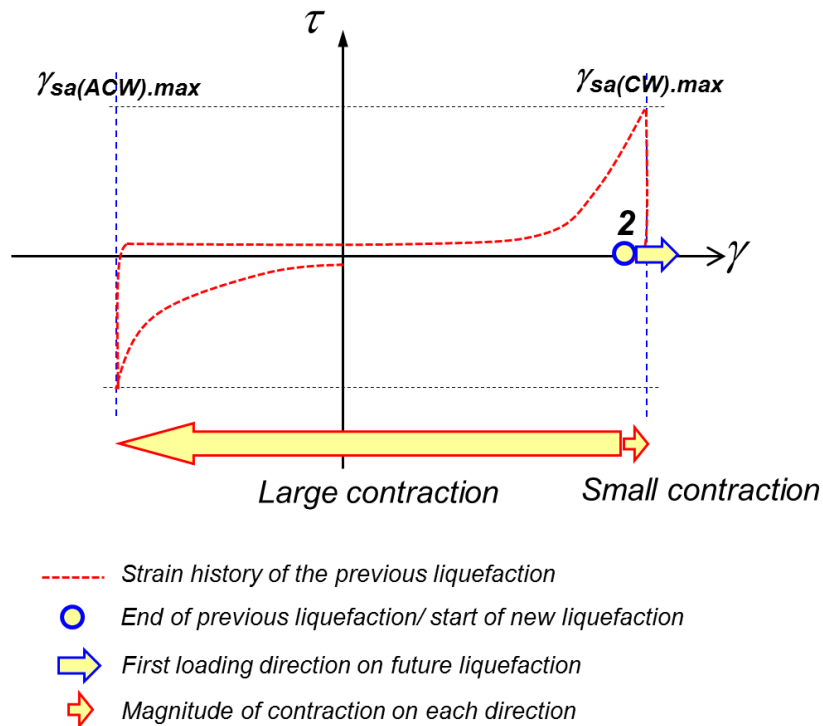Fig. 6.77:Schematic illustration of testing conditions in the first and second test

Fig. 6.78:Schematic illustration of testing conditions inthe third test

6.3.2.3   The impact of residualstrain on soil behaviors during multiple liquefactions

Twomultiple-liquefaction tests (MLRes1 and MLRes2 tests)with non-zeroresidual shear strain were conducted earlieron loose sand specimens having an initial relative density of 52-54% usingthe original 31 non-coated stackedrings. In one test soil was sheared up to $\gamma_{DA.max} = 2\%$ and the other up to $\gamma_{DA.max} = 4\%$.In each liquefaction stage, the loading was stopped when reaching zero shear stress ($\tau_{z\theta} = 0$ kPa) after it reached the pre-determined maximum $\gamma_{DA.max} = 2\%$ and 4%. Typical shear stress - shear strain relationshipsfor the 1ststage of liquefaction are shown in Fig. 6.79, while the corresponding shear stress - vertical stress relationshipsare shown in Fig. 6.80. For the sake of comparison, typical shear stress - shear strain and shear stress - vertical stress relationships for an theearlier test without residual strain ($\gamma = 0\%$)are shown in Figs. 6.81 and 6.82, respectively.

A summary of results of tests with and without residual strainsare givenin Figs. 6.83 through Fig. 6.85.By looking at the change in relative density with the number of liquefaction stages for both tests (Fig. 6.83), it can be seen that the increase in relative density for the tests with residual strain was smaller as compared to the case without residual strainat each liquefaction stage. Therefore, the application of last-quartercycle of loading has a significant impact on the change in soil density. The variation of liquefaction resistance with the number of liquefaction stages is reported in Fig. 6.84. It can be seen that in the tests with residual shear strain liquefaction resistance is smaller than that in the tests without residual shear strain. By combining those previous figures, the relationship between liquefaction resistance and relative density is obtained as shown in Fig. 6.85. For the completeness, the results of a series of single-stage liquefaction tests are also included in the figure. At the early liquefaction stages, the liquefaction resistance isalmost similarfor both series of tests. However, in the latter stages, the liquefaction resistance for the tests with residual shear strain is smaller than that for the tests without residual strain. These results clearly suggest that the effects of induced anisotropy have significantimpact to the behavior of soil during multiple liquefactions.
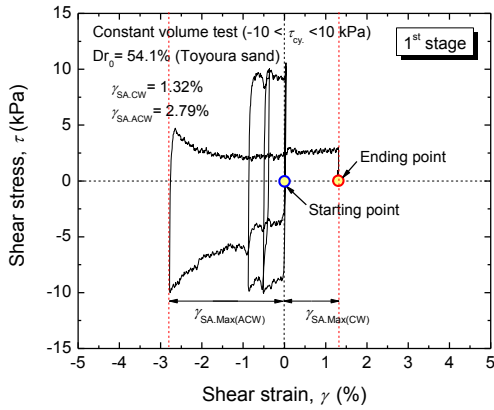
Fig. 6.79: Typical shear stress - shear strain relationshipsin a single-stage liquefaction test with residual shear strain (e.g. MLRes2 test)
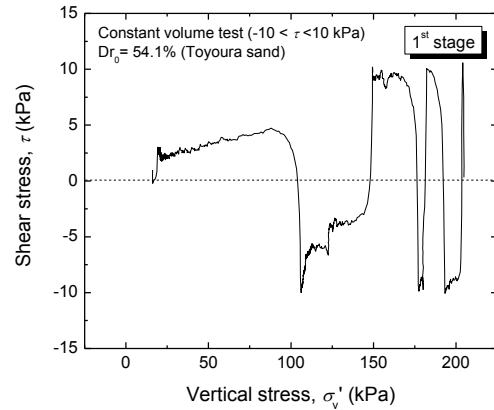
Fig. 6.80: Typical shear stress - vertical stress relationships in a single-stage liquefaction test with residual shear strain (e.g. MLRes2 test)
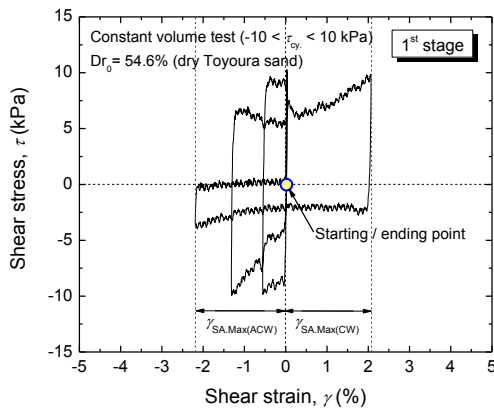
Fig. 6.81: Typical shear stress -shear strain relationships in a single-stage liquefaction test without residual shear strain (e.g. MLRes2 test)
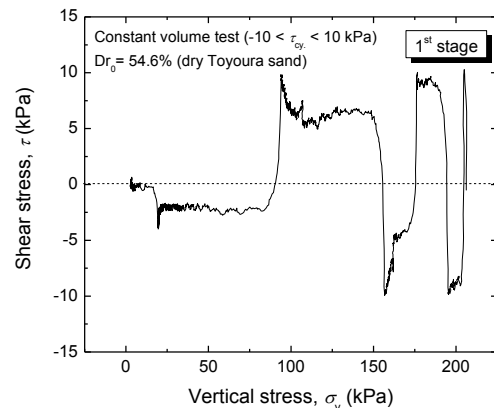
Fig. 6.82: Typical shear stress - vertical stress relationships in a single-stage liquefaction test without residual shear strain (e.g. MLRes2 test)
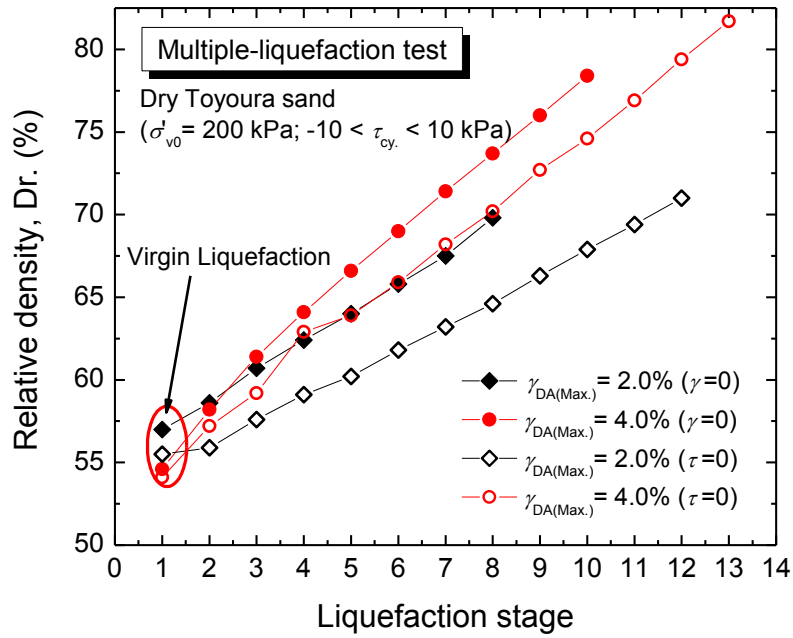
Fig. 6.83: Change in relative density with number of liquefaction stages in multi-stage liquefaction test with and without residual shear strain (MLRes1 and MLRes2 tests)
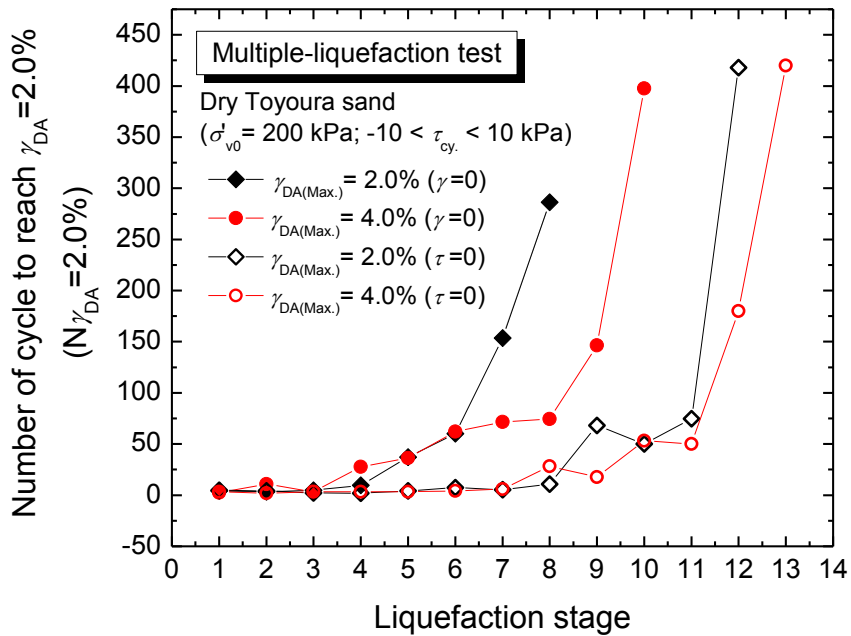

Fig. 6.84: Variation of liquefaction resistance with number of liquefaction stages in multi-stage liquefaction test with and without residual shear strain (MLRes1 and MLRes2 tests)
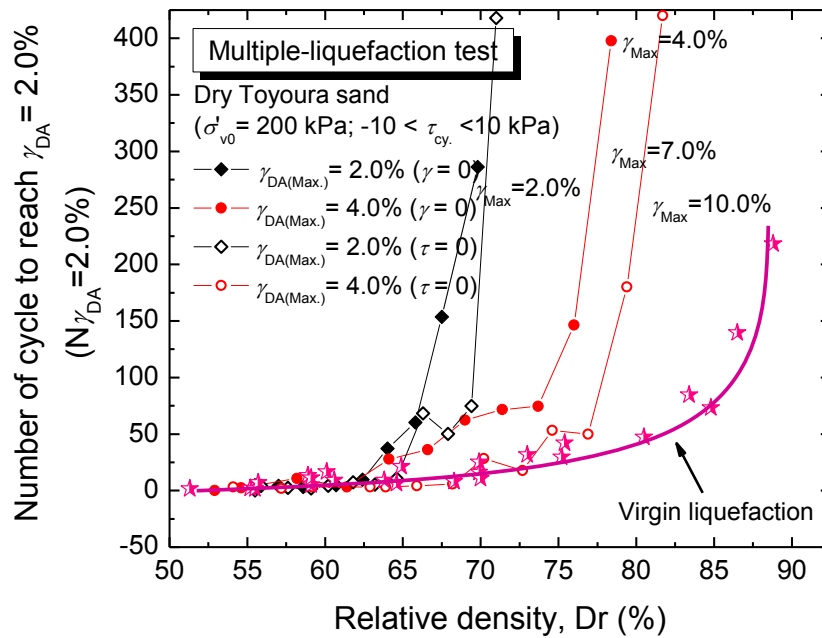
Fig. 6.85: Liquefaction resistance vs. relative density relationshipsin multi-stage liquefaction test with and without residual shear strain

As a result of the presence of residual shear strain, the liquefaction resistance in future liquefactionstages can be different in different loading directions. A large reduction of the vertical stress will occur if the specimen is sheared in the same direction to the largest amplitude between the starting loading position in the next liquefaction and the history of maximum strain amplitude in the previous liquefaction. As a result, the shear strain will tend to accumulate in this direction. This can be clearly seen by analyzing and comparing typical stress-strain relationships obtained in this study. For example, Fig.6.86and Fig 6.87 show the shear stress - shear strain relationships and shear stress − vertical stress relationships of multiple-liquefaction tests(MLRes2 test)on specimens sheared up to $\gamma_{DA.max}$= 4%, respectively.For each stage, the maximum absolute values of the single strain amplitude in clockwise and anti-clockwise directions as well as the residual shear strain after liquefaction stagesare evaluated and listed in Table 6.1. It can be seen that the shear strain is always accumulated in the direction wherethe largest amplitude between the starting point of loading in the subsequent liquefaction stage and the history of maximum shear strainin the previous liquefaction occurred.
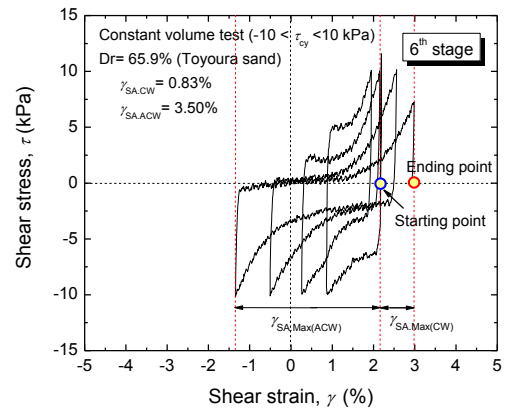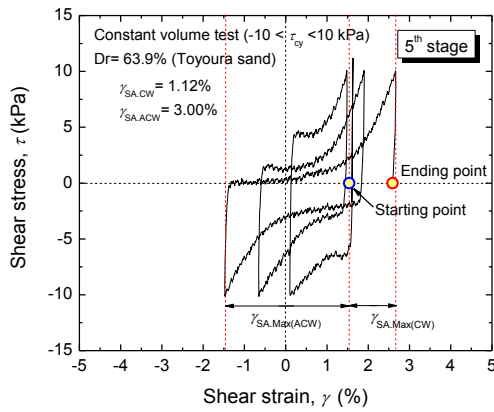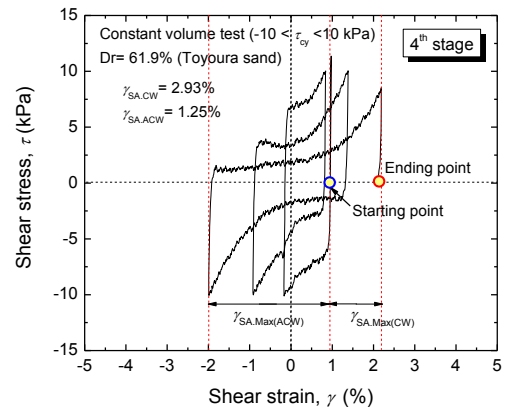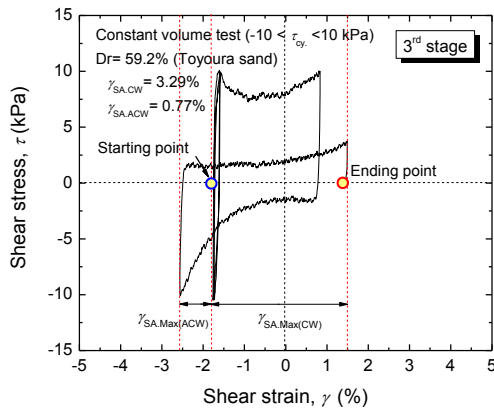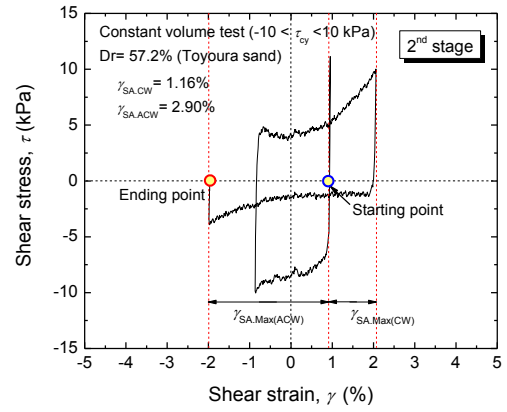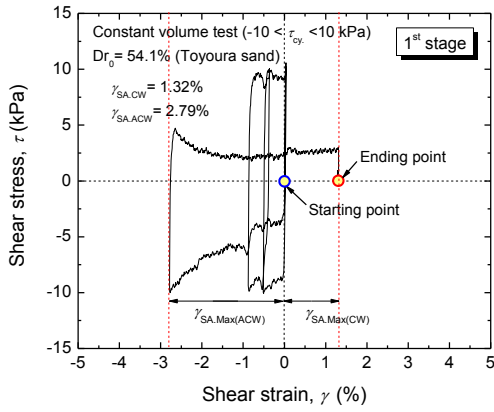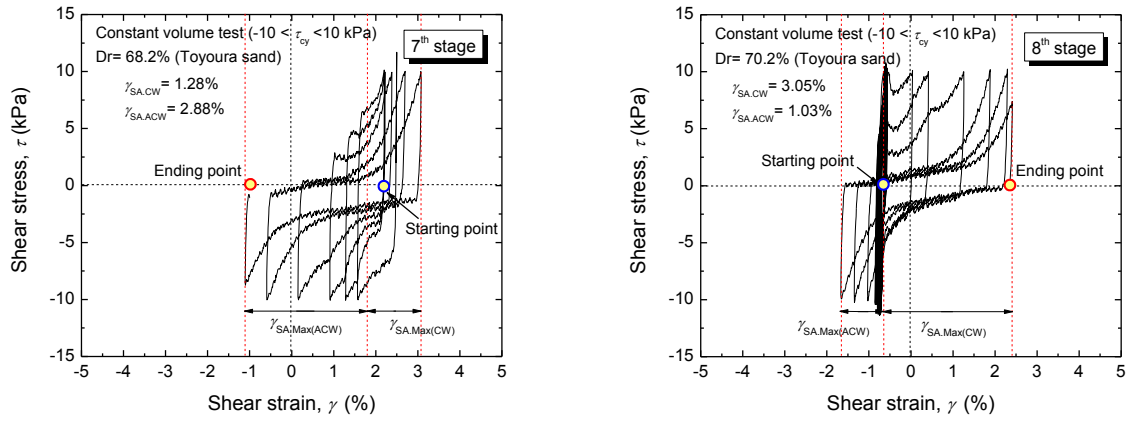
Fig. 6.86: Shear stress - shear strain relationship for the multiple-liquefied soil specimen sheared up to $\gamma_{DA.max}$= 4% (MLRes2 test)
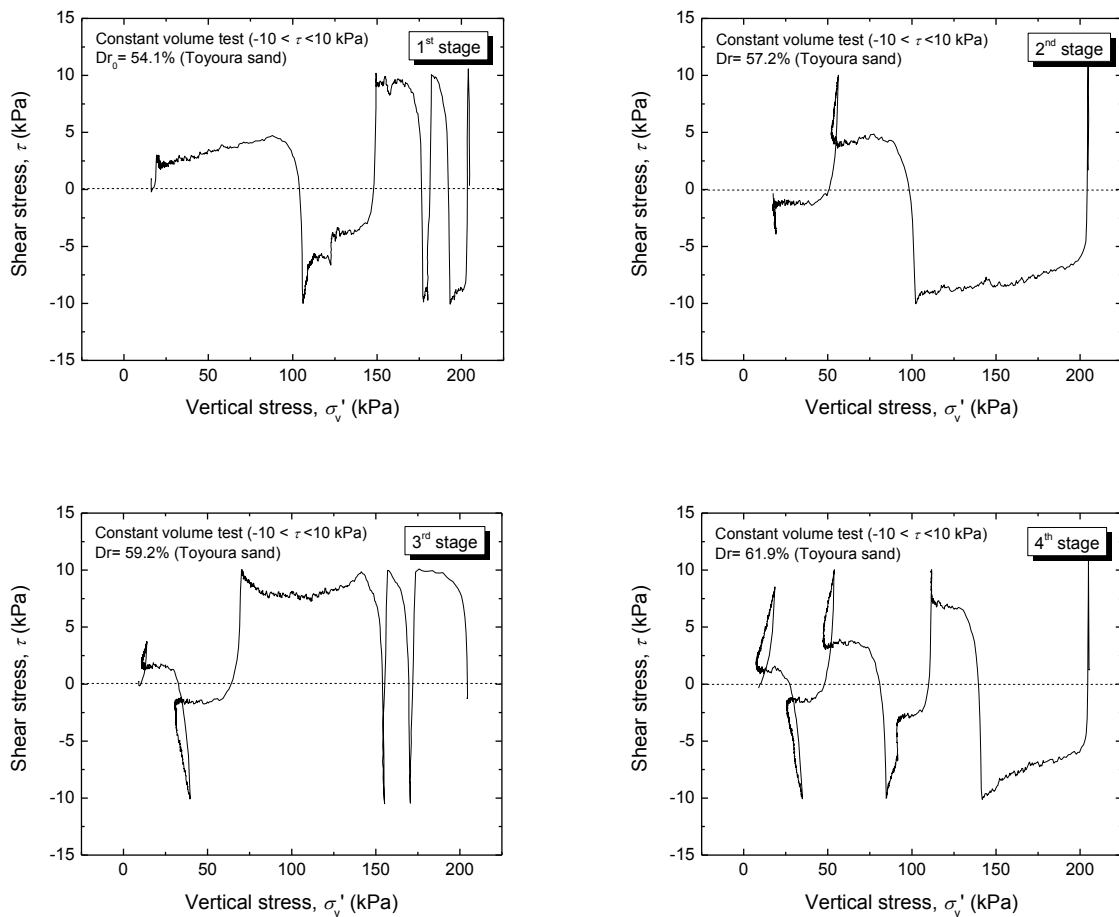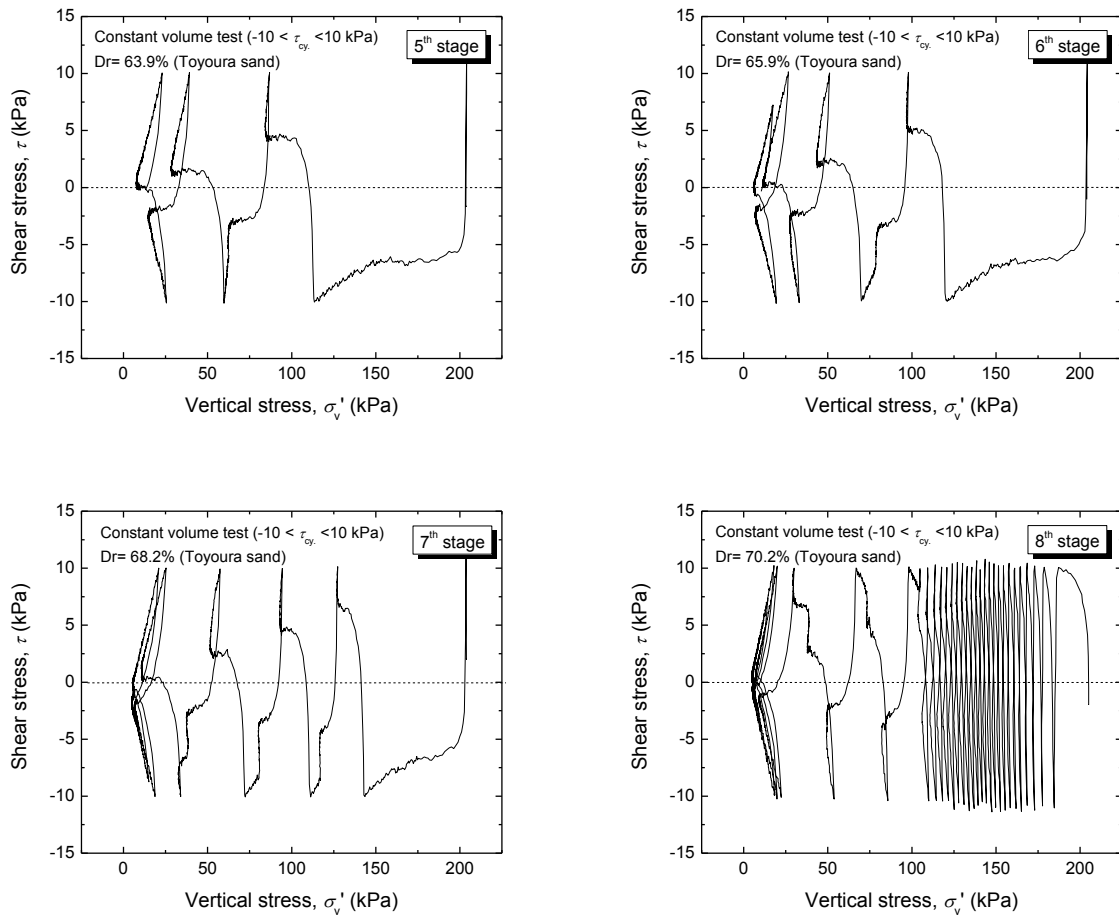
Fig. 6.87: Shear stress – vertical stress relationship for the multiple-liquefied soil specimen sheared up to $\gamma_{DA.max}= 4\%$ (MLRes2 test)

Table 6.1: Accumulation of shear strain in the multiple liquefaction test with residual strain (MLRes2 test)

Liquefaction stage	$|\gamma_{SA.max(ACW)}|$	γ_{Res}	$|\gamma_{SA.max(CW)}|$	Direction of accumulation
1st	2.79	1.30	1.32	n/a
2nd	2.90	-1.98	1.16	Anti-clockwise
3rd	0.77	1.39	3.29	Clockwise
4th	2.93	2.13	1.25	Anti-clockwise
5th	3.00	2.60	1.12	Anti-clockwise
6th	3.50	2.94	0.83	Anti-clockwise
7th	2.88	-0.98	1.28	Anti-clockwise
8th	1.03	2.35	3.05	Clockwise

6.4   SUMMARY

Results from the investigation on the dilatancy characteristics by multiple-liquefaction testswith and without residual shear strain can be summarized as follows:

1. The effect of inducedanisotropy in the subsequent liquefaction stage is negligible for a liquefied soil specimen without residual shear strain. The stress-dilatancy characteristics are almost identical (symmetric) in different loading directions. However, this finding cannot be applied to the case of multiple-liquefaction tests since the soil fabric may be repeatedly destroyed in each liquefaction stage. As a result, some form of induced anisotropy may affect significantly the behavior of soil in future liquefaction stages.

2. The magnitude of residual deformationachieved in previous liquefactionstages as well as thedirection of theapplication ofthe loading in the subsequent liquefaction stage will have a great impact on the soil behavior undergoing future liquefaction.The stress-dilatancy relation reveals that a large contraction in drained (constant-stress) test will take place if the liquefied soilis sheared in the direction where the magnitude between the starting point of loading in the next liquefaction stage and the max.strain amplitude in the previous liquefactionstage is the largest. In an undrained (constant-volume) test, this would correspondto a large reduction inthe effective stress along this loading direction. As a result,the strain in the future liquefaction stage will becertainly accumulated in this direction as well.

3. In general, in multiple-liquefaction test with residual shear strain,soil has lower liquefaction resistance than that soil tested in multiple-liquefaction test without residual shear strain. This happens due to the additional effects of induced anisotropy as mentioned earlier at point 2.

6.5   REFERENCES

1. AnhDan, L., Koseki, J. and Sato, T. (2002). "Comparison of Young's moduli of dense sand and gravel measured by dynamic and static methods", *Geotechnical Testing Journal*, ASTM, Vol. 25, No. 4, pp. 349-368.

2. Arthur, J. R. F. and Menzies, B. K. (1972). "Inherent anisotropy in a sand", *Geotechnique*, Vol. 22, No. 1, pp. 115-128.

3. Arthur, J. R. F., Chua, K. S. and Dunstan, T. (1977). "Induced anisotropy in a sand", *Geotechnique*, Vol. 27, No. 1, pp. 13-30.

4. Arthur, J.R.F., Chua, K.S., Dunstan, T. and Rodriguez del C, J.I. (1980). "Principal stress rotation: A missing parameter", Proceedings of ASCE, Vol.106, No.GT4, pp.419-433.

5. Balakrishnayer, K. (2000). "Modelling of deformation characteristics of gravel subjected to large cyclic loading", *Ph.D. thesis*, Department of civil engineering, The University of Tokyo, Japan.

6. Burland, J. B. (1989). "Small is beautiful- the stiffness of soil at small strains", Ninth LauritsBjerrum memorial lecture, *Canadian Geotechnical Journal*, Vol. 26, pp. 499-516.

7. Chaudhary, S. K., Kuwano, J. and Hayano, Y. (2004). "Measurement of Quasi-elastic Stiffness Parameters of Dense Toyoura Sand in Hollow Cylinder Apparatus and Triaxial Apparatus with Bender Elements", *Geotechnical Testing Journal*, ASTM, Vol. 27, No. 1, pp. 23-35.

8. Cuccovillo, T. and Coop, M. R. (1997). "The measurement of local axial strain in triaxial tests using LVDT's", *Geotechnique*, Vol. 47, No. 1, pp. 167-171.

9. De Silva, L. I. N. (2004). "Locally measured quasi-elastic deformation properties of geomaterials under torsional shear and triaxial loadings", *Master of Engineering thesis*, Department of Civil Engineering, The University of Tokyo, Japan.

10. De Silva, L. I. N. (2008). "Deformation characteristics of sand subjected to cyclic drained and undrained torsional loadings and their modelling," *Doctor of Engineering Dissertation*, Department of civil engineering, The University of Tokyo, Japan.

11. De Silva, L. I. N., Koseki, J., Sato, T. and Wang, L. (2005). "High capacity hollow cylinder apparatus with local strain measurements", *Proc. of the Second Japan-U.S. Workshop on Testing, Modeling and Simulation*, Geotechnical Special Publication, ASCE, Vol. 156, pp. 16-28.

12. Dyvik, R. and Madshus, S. (1985). "Laboratory measurement of G_{max} using bender elements", *Proceedings of ASCE convention*, Detroit, pp. 186-196.

13. Emery J., Finn, W. D., and Lee, K. W. (1973) "Uniformity of saturated sand specimens." *ASTM STP 523*, West Condhohocken, Pa.

14. Goto, S., Tatsuoka, F., Shibuya, S., Kim, Y. S. and Sato, T. (1991). "A simple gauge for local small strain measurements in the laboratory", *Soils and Foundations*, Vol. 31, No. 1, pp. 169-180.

15. Hardin, B. O. and Black, W. L. (1968). "Vibration modulus of normally consolidated clay", *Journal of soil mechanics and foundation division*, ASCE, Vol. 94, No. SM2, pp. 353-369.

16. Hardin, B. O. and Richart, F. E., Jr. (1963). "Elastic wave velocities in granular soils", *Journal of soil mechanics and foundation division*, ASCE, Vol. 89, No. 1, pp. 33-65.

17. Hird, C. C. and Yung, P.C.Y. (1989): The use of proximity transducers for local strain measurements in triaxial tests, *Geotechnical Testing journal*, 12(4), 292-296.

18. Hong Nam, N. and Koseki, J. (2005). "Quasi-elastic Deformation Properties of Toyoura Sand in Cyclic Triaxial and Torsional Loadings", *Soils and Foundations*, Vol. 45, No. 5,pp. 19-38.

19. HongNam, N. (2004). "Locally measured quasi-elastic properties of toyoura sand in cyclic triaxial and torsional loadings and their modelling", *PhD thesis*, Dept. of Civil Engineering, The University of Tokyo, Japan.

20. Ishihara, K. and Okada, S. (1978) "Effects of stress history on cyclic behavior of sand." *Soils and Foundations*, Tokyo, 18(4), pp. 31-35.

21. Ishihara, K. and Okada, S. (1982) "Effects of large preshearing on cyclic behavior of sand." *Soils and Foundations*, Tokyo, 22(3), pp. 109-125.

22. Kiyota, T. (2007). "Liquefaction strength and small strain properties of in-situ frozen and reconstituted sandy soils", *PhD thesis*, Dept. of Civil Engineering, The University of Tokyo, Japan (In Japanese).

23. Maqbool, S. (2005). "Effects of compaction on strength and deformation properties of gravel in triaxial and plain strain compression tests", *PhD thesis*, Dept. of Civil Engineering, The University of Tokyo, Japan.

24. Moroto, N. (1987). "On deformation of granular material in simple shear", *Soils and Foundations*, Vol.27, No.1, pp.77-85.

25. Oda, M. (1972a) "Initial fabrics and their relations to mechanical properties of granular material." *Soils and Foundations*, Tokyo, 12(1), pp. 17-36.

26. Oda, M. (1972b) "A mechanism of fabric changes during compressional deformation of sand." *Soils and Foundations*, Tokyo, 12(2), pp. 1-18.

27. Oda, M., Kawamoto, K., Suzuki, K, Fujimori, H., and Sato, M. (2001) "Microstructural interpretation on reliquefaction of saturated granular soils under cyclic loading." *J. Geotech. andGeoenvironmentalEngrg*, 127(5), pp. 416-423.

28. Pradhan, T.B.S., and Tatsuoka, F (1989). "On stress-dilatancy equations of sand subjected to cyclic loading", *Soils and Foundations*, Vol.29, No.1, pp.65-81.

29. Pradhan, T.B.S., and Tatsuoka, F. and Sato, Y. (1989). "Experimental stress-dilatancy relations of sand subjected to cyclic loading", *Soils and Foundations*, Vol.29, No.1, pp.45-64.

30. Roscoe, K.H., Schofield, A.N. and Thurairajah, A. (1963): "Yielding of clays in states wetter than critical,"*Geotechnique*, Vol.13, No.3, pp.211-240.

31. Rowe, P. W. (1969). "The relation between the shear strength of sands in triaxial compression, plane strain and direct shear", *Geotechnique*, Vol. 19, No. 1, pp. 75-86.

32. Rowe, P. W. Barden, L. and Lee, I.K. (1964). "Energy components during the triaxial tests and direct shear tests", *Geotechnique*, Vol. 14, No. 3, pp. 247-261.

33. Rowe, P.W. (1962). "The stress-dilatancy relation for static equilibrium of an assembly of particles in contact", *Proceedings of the Royal Society of London*, series A, Vol.269, pp.500-527.

34. Schultheiss, P. J. (1981). "Simultaneous measurement of P and S wave velocities during conventional soil testing procedures", *Marine Geotechnology*, Vol. 4, No. 4, pp. 343-367.

35. Shahnazari, H. (2001). "Experimental investigationon volume change and shear deformation characteristics of sand undergoing cyclic loading", *Ph.D. Thesis*, Department of civil engineering, The University of Tokyo, Japan.

36. Suwal, L. P. (2013) "Disk transducer for elastic wave measurement and its application to unsaturated sandy soils." *PhD thesis*, Dept. of Civil Engineering, The University of Tokyo, Japan.

37. Suzuki, T. and Suzuki, T. (1988) "Effects of density and fabric change on re-liquefaction resistance of saturated sand." *J. Japanese Geotech. Soc.*, Tokyo, 28(2), pp. 187 - 195. (in Japanese)

38. Suzuki, T. and Toki, S. (1984) "Effect of preshearing on liquefaction characteristics of saturated sand subjected to cyclic loading." *Soils and Foundations*, Tokyo 24(2), pp. 16-28.

39. Tatsuoka, F., Ishihara, M., Uchimura, T. and Gomes Correia, A. (1999). "Non-linear resilient behaviour of unbound granular materials predicted by the cross-anisotropic hypo-quasi-elasticity model", *Unbound Granular Materials*, Gomes Correia (ed.), Balkema, pp. 197-204.

40. Taylor, D. W. (1948), "Fundamentals of soil mechanics", John Wiley, New York.

41. Tokue, T. (1978). "A consideration about Rowe's minimum energy ratio principal and a new concept of shear mechanism", *Soils and Foundations*, Vol.18, No.1, pp.1-10.

42. Towhata, I. and Ishihara, K. (1985) "Undrained strength of sand undergoing cyclic rotation of principal stress axes." *Soils and Foundations*, 25(2), pp. 135-147.

43. Viggiani, G. and Atkinson, J. (1995). "Interpretation of bender element tests", *Geotechnique*, Vol. 45, No. 1, pp. 149-154.

44. Wahyudi, S. (2011) "Shear banding formation and stress-dilatancy of sand in the torsional shear apparatus." *Master thesis*, Dept. of Civil Engineering, The University of Tokyo, Japan.

45. Wicaksono, R. I., Tsutsumi, Y., Sato, T., Koseki, J. and Kuwano, R. (2007). "Small strain stiffness of clean sand and gravel based on dynamic and static measurements", *Proc. Of the 9th International Summer Symposium*, Yokohama, Japan.

46. Yamada, S., Takamori, T., and Sato, K. (2010) "Effects on reliquefaction resistance produced by changes in isotropy during liquefaction." Soils and Foundations, 50(1), pp. 19-25.

7 SOIL CHARACTERISTICS UNDERMULTIPLE LIQUEFACTIONS BASED ON ENERGY APPROACH

7.1   Introduction

In the previous chapters, it was revealed that the soil behaviorssubjected with multiple liquefactions are highly affected at least by two key factors, namely the amplitude of the applied shear strain and the degree of induced anisotropy. The effects of induced anisotropy are very difficult to predict, because it may involve a change in the micro-structures or fabricof the soil.Therefore, the current chapter mainly discusses the effects of strain amplitude to the soil behaviors during multiple liquefactions using energy approach.

Previous results on the multiple-liquefaction tests showed that a specimen subjected to a large shear strain amplitudewill have a lower liquefaction resistance in future liquefaction stages and vice-versa. This phenomenon was also confirmed in 2-stage liquefaction testsconducted by other researchers (e.g. Ishihara and Okada, 1978 and 1982; Suzuki and Suzuki, 1988, Oda et al. 2001; Wahyudi et al., 2013;and among others).However, this assumption was found to be not completely true.

In Chapter 5, the results on the multiple-liquefaction test also revealedanother fact that a specimen sheared withvery small shear strain may actually have a smaller resistance in future liquefaction stages than a specimen sheared with slightlylarger shear strains. This phenomenon is not fully understood yet. A possible reason is that the resistance in future liquefactionstages may not be solely influenced by the amplitude of shear strainin the previous liquefaction stages, but it may be also affected by the energy that is dissipated in previous liquefaction process.

Energy approachhas been widely used among researchers for predictingthe liquefaction potential of soils. A pioneer studywas done by Nemat-Nasser and Shookoh (1979). They found that the change in soil density in drained (constant-stress) testscan be correlated to the input energy, which can be mathematically expressed based onthe Newtonian energy preservation law.

By understanding soil behavior in drained (constant-stress) tests, the response of soil under undrained (constant-volume)conditions can be also formulated (e.g. volume change in drained tests can be considered as the mirror image of excess pore water pressure(PWP) generation or effective stress reduction in undrained tests).Davis and Berril (1982) and Berril and Davis (1985) proposed similarenergyapproach equations to simulate the generation of excess PWP. Figueroa (1990), Figueroa and Dahisaria (1991) and Figueroa et al. (1994) useda simpler method by calculating the area withinhysteretic loop in the cyclic shear loading to

link the relation between the dissipated energy per unit volume and the generation of excess PWP. In all of these methods, the amount of dissipated energy depends on several independent variables (e.g. initial density, initial confining stress, shear strain amplitude etc).Several other researchers (e.g. Towhata and Ishihara, 1985; Kokusho, 2013; among others) also developedsimilar methods to predict the generation of PWP during liquefaction.

All of experimental-based studies mentioned before were conducted using uniformnon-cohesive granular material. However, the real soil properties and the stress conditions are far more complex than the one simulated in the soil testing laboratory. Other researchers also attempted to investigate the liquefaction potential based on in-situ SPT tests data (Seed et al. (1971), Bieganuosky et al. (1976), Tatsuoka et al. (1980), Douglas et al. (1981), Tokimatsu and Yoshimi (1981),Seed et al. (1983), among many others). The SPT data are not just commonly used during construction, but also for practical reason to account all the parameters that could not be simulated in the soil testing laboratory.

Such experimental and field observations studies were conducted to obtain the liquefaction potential of the original soil without any history of previous liquefaction.The current studyattempts to use the energy approach for understanding the soil behavior not only in repeated (2-stage) liquefaction tests, but also in multi-stage liquefaction tests.

7.2   Experiment program

The main objective of this study is to investigate how the occurrence of previous liquefaction may affect the soil behavior during future liquefaction stages from an energy point of view. To do so, the dissipated energy on each liquefaction stage was evaluated.

The input energy applied to the soil specimen is separated into two parts, which are the reversible energy part and the irreversible (dissipated) energy part as illustrated in Fig. 7.1. The dissipated energy is mostly consumed through the friction between soil particles to induce rolling and sliding mechanisms during the shearing process. In drained test, the dissipated energy is responsible for causing the volumetric strain during shearing.Alternatively, in undrained tests, the dissipated energy governs the generation ofPWP or reduction in effective stress.

The dissipated energy duringcyclic shear loading is marked by the area within the hysteretic loop of the shear stress - shear strain relationship as illustrated in Fig. 7.2.To calculate this area,simple integration can be used, asshown in Fig. 7.3 and expressed by Eq. 7.1.
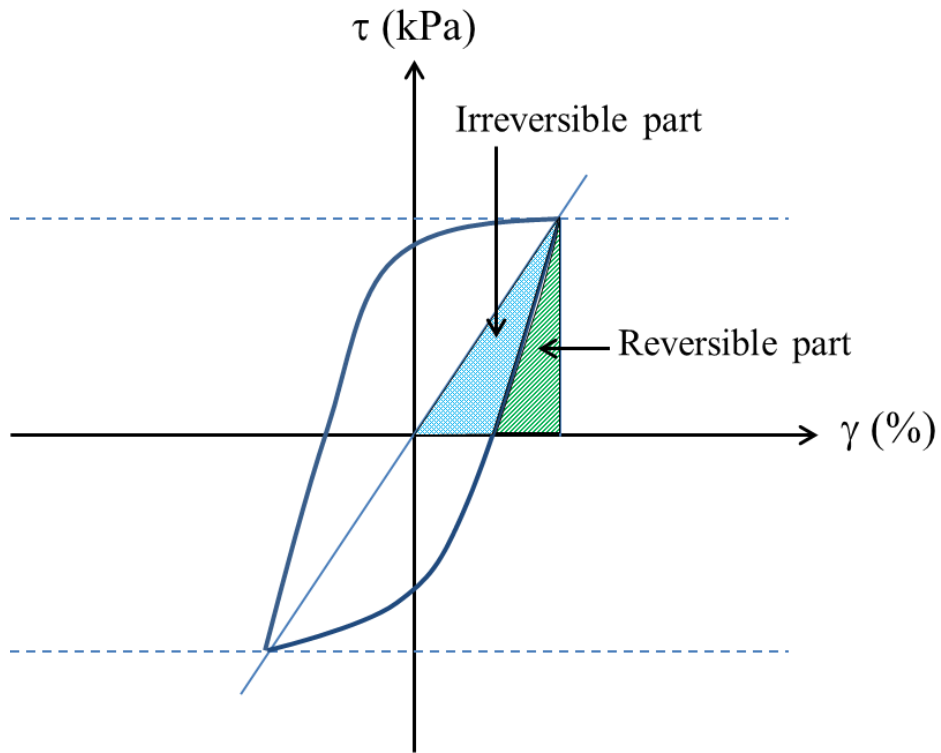
Fig. 7.1: Reversible and irreversible parts of input energy during cyclic shear loading
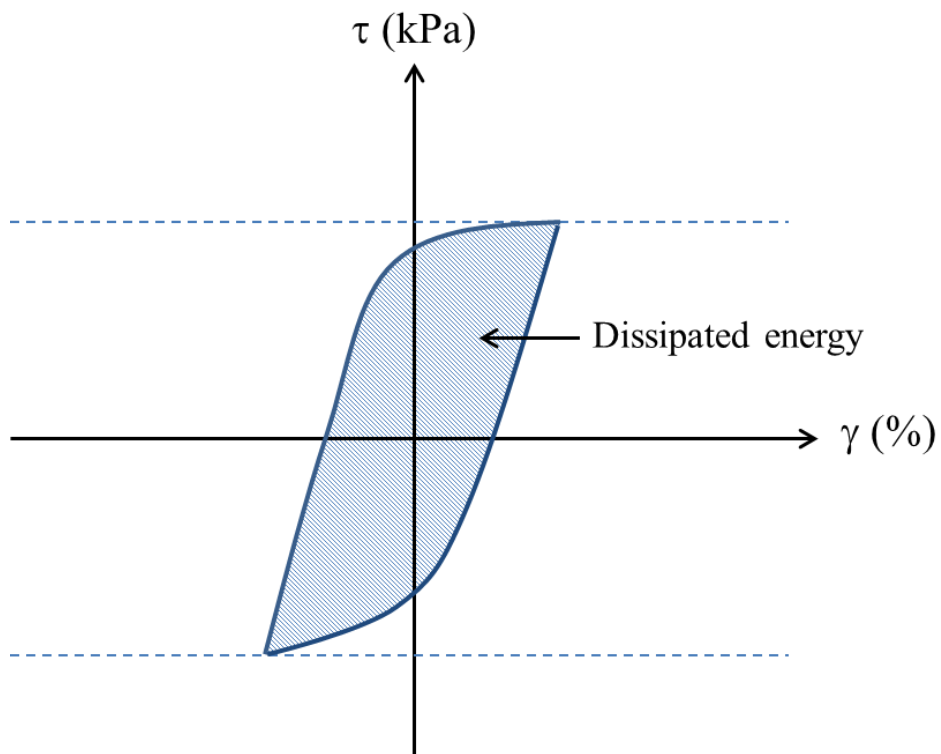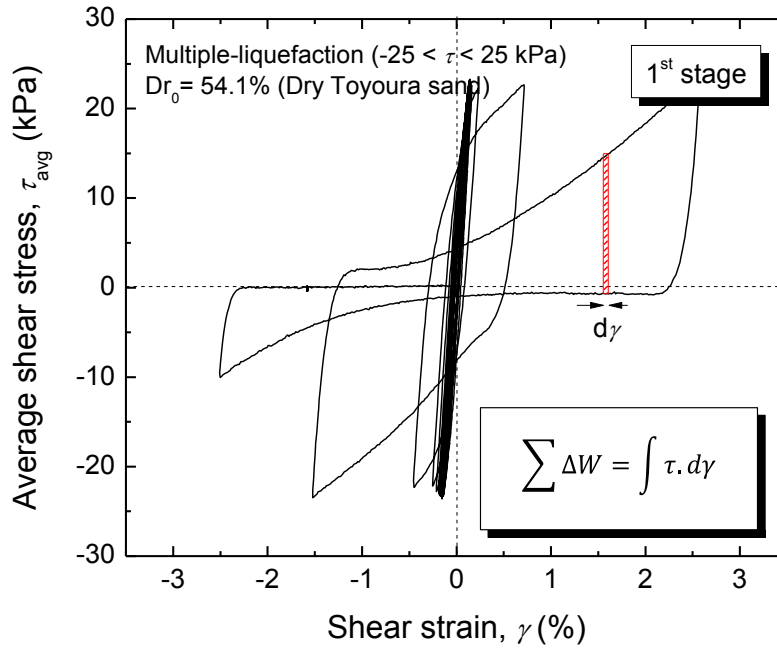

Fig. 7.2: Dissipated energy during cyclic shear loading

Fig. 7.3: Evaluation of dissipated energy in a stage of multiple-liquefaction test

$$\sum \Delta W = \int \tau . d\gamma \qquad \text{(Eq. 7.1)}$$

where, $\sum\Delta W$ is the amount of dissipated energy per unit volume (J/m^3); τ is the shear stress; and γ is the shear strain.

As mentioned in previous chapters, in using a staked-ring shear apparatus, the shear stress ($\tau_{v\theta}$) and vertical stress (σ_v) are not distributed uniformly throughout the specimenheight due to the friction generated between the soil particles and the stacked rings. Therefore, the evaluations of the dissipated energy in the current chapter are based on average stress values, which would correspond tothe stress components acting on a soil element located at the middle height of the specimen.

In relation to the dissipated energy, the accumulation of shear strain in a stage of multiple-liquefaction test is also calculated. The accumulated strain can be seen in a similar way to the total input energy applied in a stage of liquefaction test. The evaluation of shear strain is shown in Fig. 7.4 and calculated by Eq. 7.2.
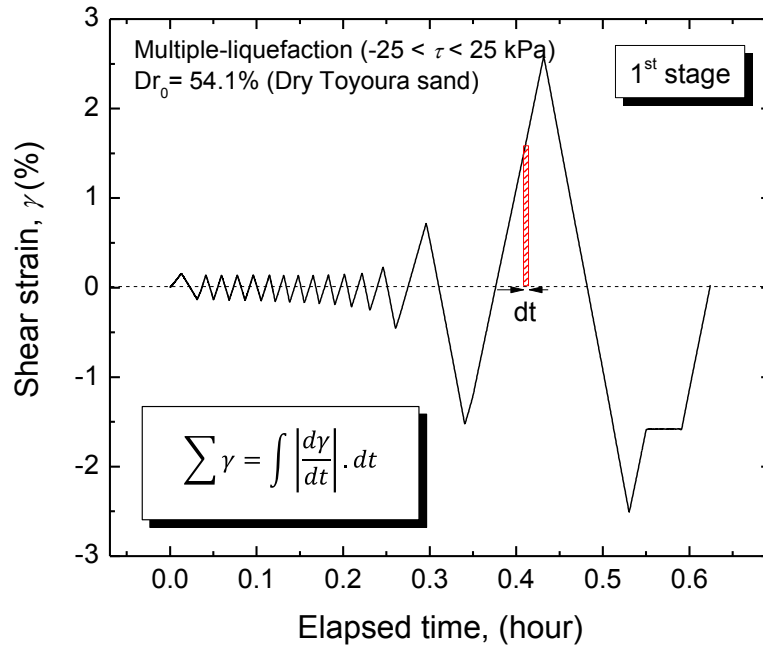
Fig. 7.4: Evaluation of accumulated shear strain in a stage of multiple-liquefaction test

$$\sum \gamma = \int \left| \frac{d\gamma}{dt} \right| . dt \qquad \text{(Eq. 7.2)}$$

where, $\sum\gamma$ is the accumulated strain; γ is the shear stress; and t is the elapsed time.

7.3   Results and discussions

7.3.1   Typical energy dissipation in the soil subjected with multiple liquefactions

Hereafter, the investigation on the soil behaviorsduring multiple liquefactionsby energy principle isdivided into two sections. The first part focuses on soil behavior during the firsttwo stages of liquefaction, while the second part of the analysis focuseson soil behavior during subsequent multi-liquefactionstages. All the analyses are conducted on the latest results of multiple-liquefaction tests using 11 coated stackedrings. However, to provide additional useful test data another series of testwas conducted. To do so, sixsand specimens (ML-13 to ML-18 tests) were prepared at a similar initial density and consolidation state described in Chapter 5. Each specimenwas then sheared up to pre-fixed $\gamma_{DA.max}$values of 0.2%,

0.25%, 0.3%, 0.4%, 0.5% and 1% in the 1st liquefaction stage.In the 2nd liquefaction stage,all the liquefied soil specimens were sheared up to $\gamma_{DA.max}$= 2%. This was done because the liquefaction resistance on the first series of tests was compared based on the number of cycles to cause γ_{DA}= 2% ($N\gamma_{DA(2.0\%)}$). The results of the supplementary multiple-liquefaction tests are shown in Fig. 7.5

Typical test results in terms ofshear stress - shear strain relationshipsat different stages in a multiple-liquefaction test are shown in Fig. 7.6. From these results, the corresponding dissipated energy and accumulated shear strain were calculated using Eq. 7.1 and Eq. 7.2. Typical time histories of dissipated energy and accumulated strainare shown in Figs. 7.7 and 7.8, respectively.By combining these two figures, the relationship between dissipated energy and accumulated strain in one stage of multiple-liquefaction tests is obtained, as shown in Fig. 7.9.Similarly, typical dissipated energy - accumulated strain relationships in different stages of a multiple-liquefaction test can be seen in Fig. 7.10. It can be seen that there is ageneral trend between the dissipated energy and accumulated strain. To investigate in detail the characteristics of this relation, the dissipated energy - accumulated strain relations during 1st liquefaction stage for all the tests(ML-13 to ML-22 tests) is reported in Fig. 7.11.Note that, all the specimens in the 1st stage of liquefaction did not have any pre-shearing history. From this figure, it can be seen that there isa uniquerelation, which can be divided into three steps as shown in Fig. 7.12. In the Step-I, dissipated energy linearly increases with accumulated strain at aconstant energy dissipation rate of 0.025 J/m3/% up to 0.2 J/m^3. Then, in the Step-II, the dissipation rate increases ($\approx$0.10 J/m3/%)up to 1 J/m^3. Finally, the rate of dissipated energy slightly decreases ($\approx$0.032 J/m3/%) in Step-III.Therefore, energy dissipation rates changethree times, as marked by the points 1, 2 and3 in Fig. 7.12.

Further investigations revealed that such changes well correspond to specificstress states during cyclic shear loading in undrained (constant-volume) tests as shown in Figs. 7.13 -7.15. At point1 the stress path passes the phase transformation line (PTL) for the first time (Fig. 7.13). At this point, the specimen is experiencing both zero dilation for the first time. After passing the PTL, large shear strains start to develop. As a result, the area of the hysteretic loop becomes larger and the increasing rate of dissipated energy becomes higher. At point 2 the stress path shows distinctive change in behavior from contractive to dilative (Fig 7.13). Until point 2,a small accumulation of shear strain can be seen by looking at the shear stress -shear strain relationship shown in Fig. 7.14. At point 3,the stress path reach almost zero vertical stress for the first time (Figs. 7.13 and 7.15). At this point, full liquefaction state is achieved and flow typefailure can be observed (Fig. 7.14).
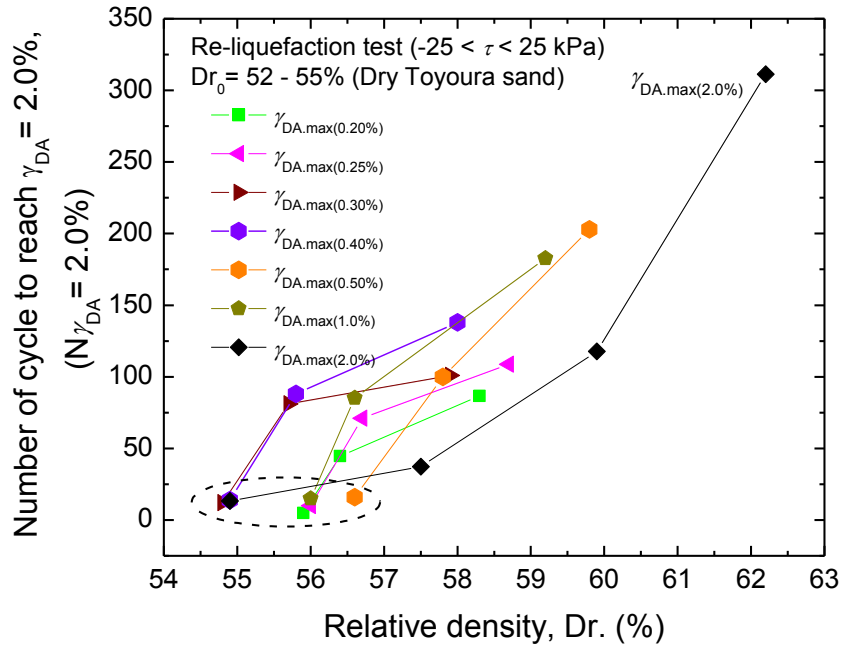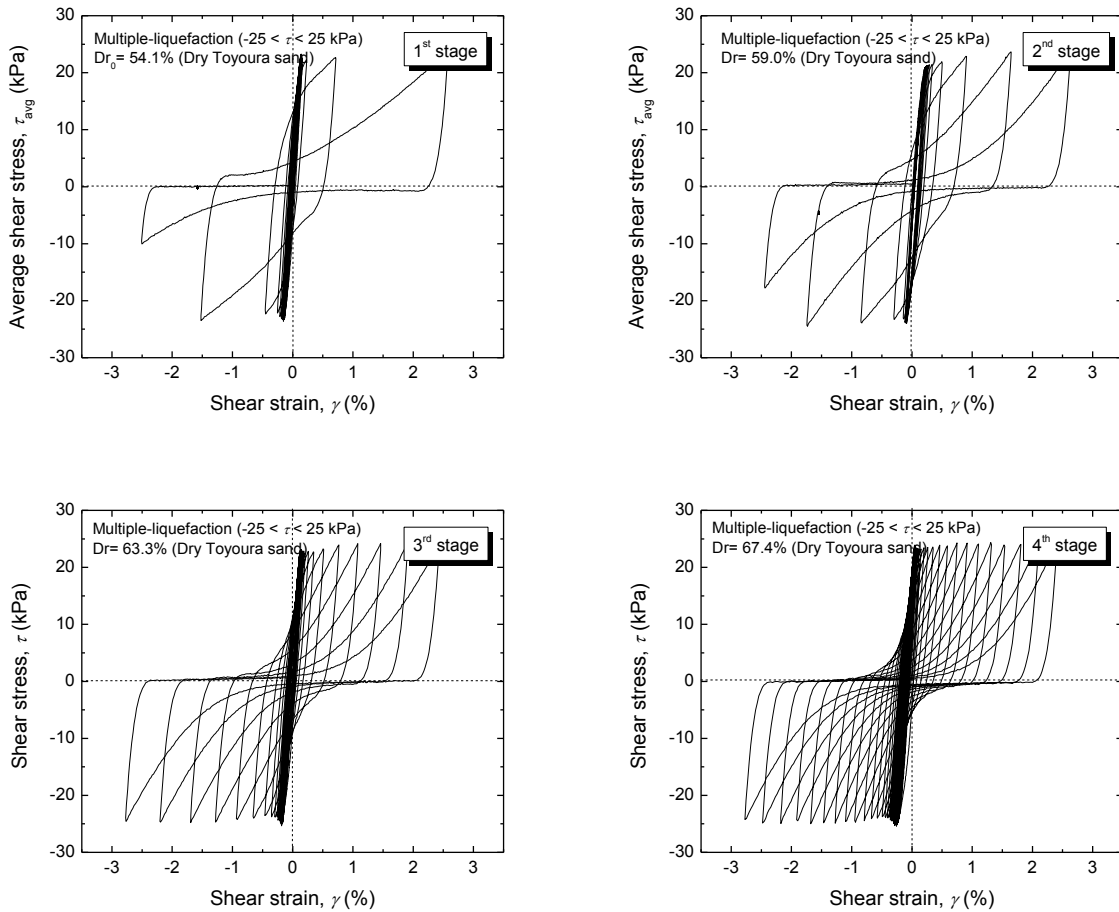
Fig. 7.5: Liquefaction resistance vs. relative density relationships of multiple-liquefied soil sheared at a $\gamma_{DA}< 2\%$ (ML13 to ML18 tests)
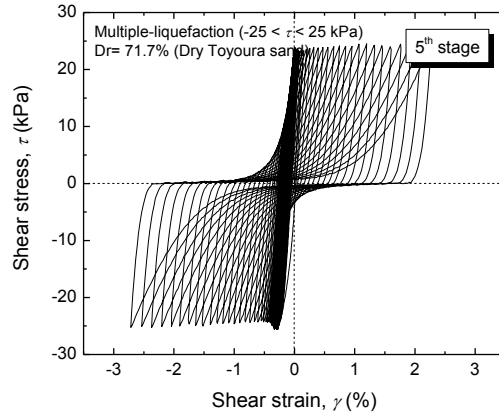
Fig. 7.6: Average shear stress - shear strain relationshipsfor a multi-liquefied soil specimen sheared up to $\gamma_{DA.max}$= 5% (e.g. ML20 test)
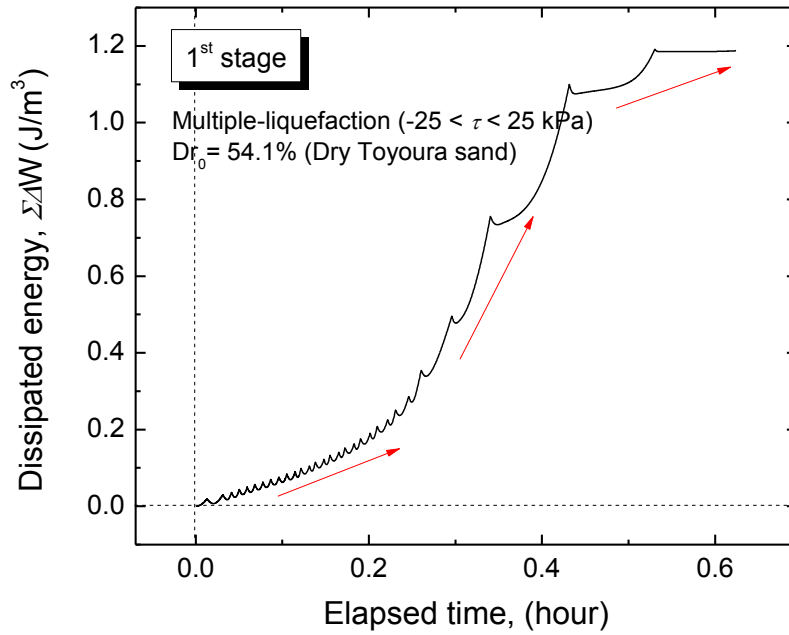

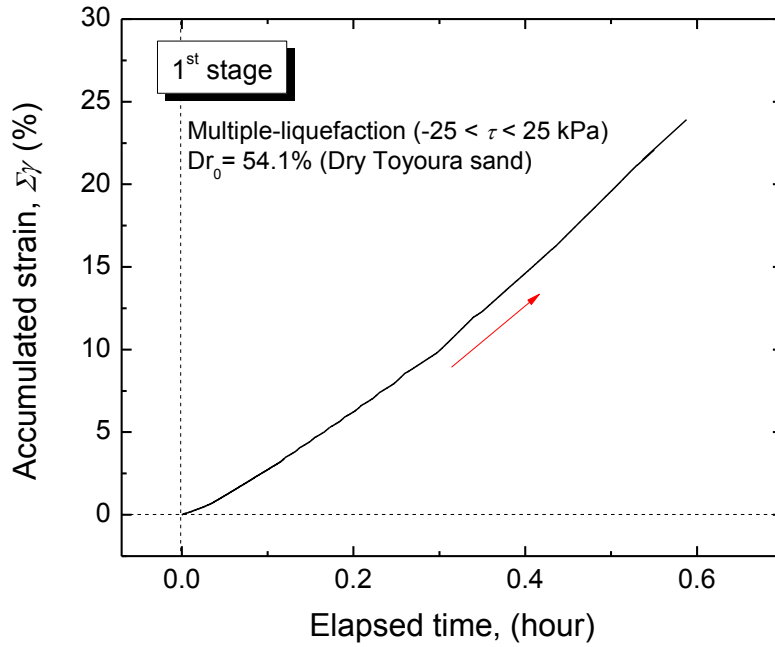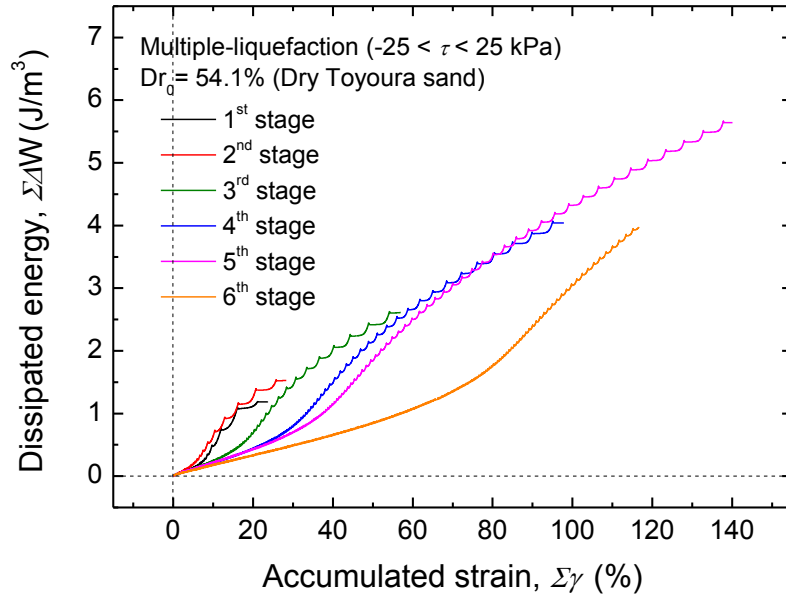Fig. 7.7: Typical time history of dissipated energy in a stage of multiple-liquefaction tests (e.g. ML20 test)

Fig. 7.8: Typical time history of accumulated strain in a stage of multiple-liquefaction tests (e.g. ML20 test)
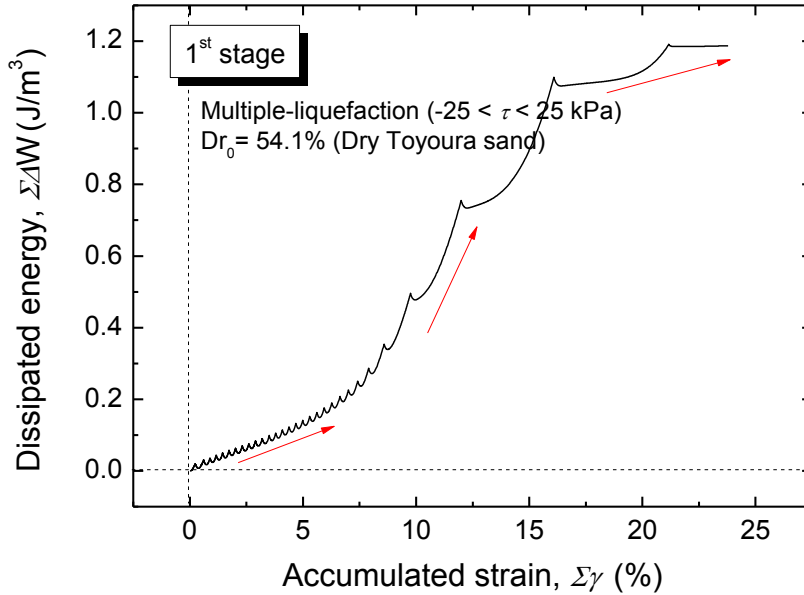
Fig. 7.9: Typical dissipated energy - accumulated strain relation in a stage of multiple-liquefaction test (e.g. ML20 test)

Fig. 7.10: Typical dissipated energy - accumulated strain relationships at different stages of multiple-liquefaction test (e.g. ML20 test)
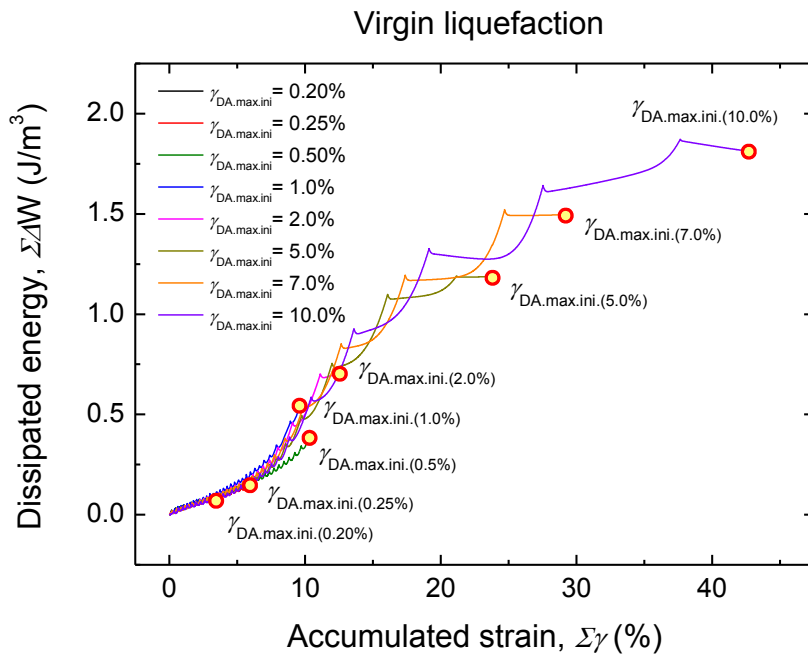
Fig. 7.11: Dissipated energy - accumulated strain relationships during the 1st stage of liquefaction test using 11 coated stackedrings (ML13 to ML22 tests)
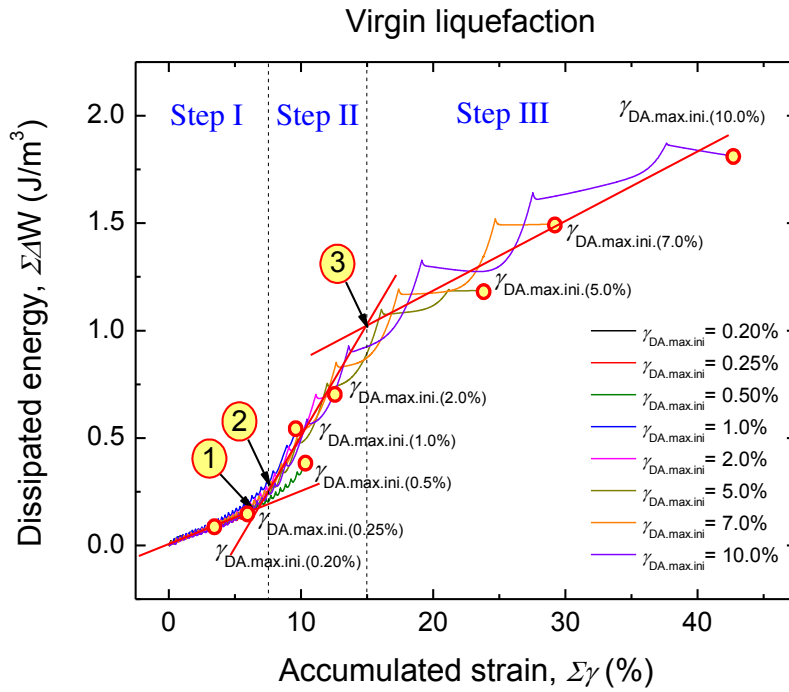
Fig. 7.12: Three-step dissipated energy - accumulated strain relationship
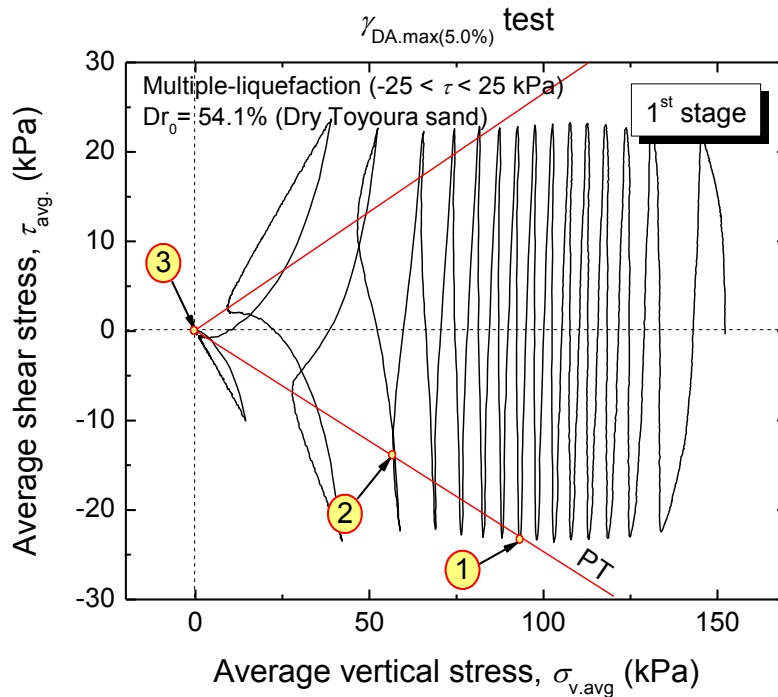
Fig. 7.13: Point-1, point-2, and point-3 in a typical shear stress - vertical stress relationship (e.g. ML20 test)
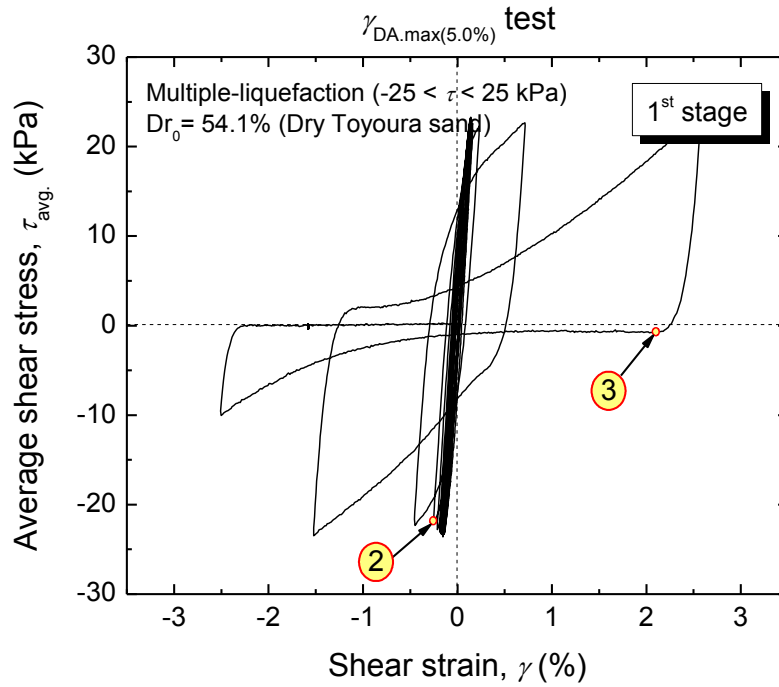
Fig. 7.14: Point-1, point-2, and point-3in a typical stress-strain relationship (e.g. ML20 test)
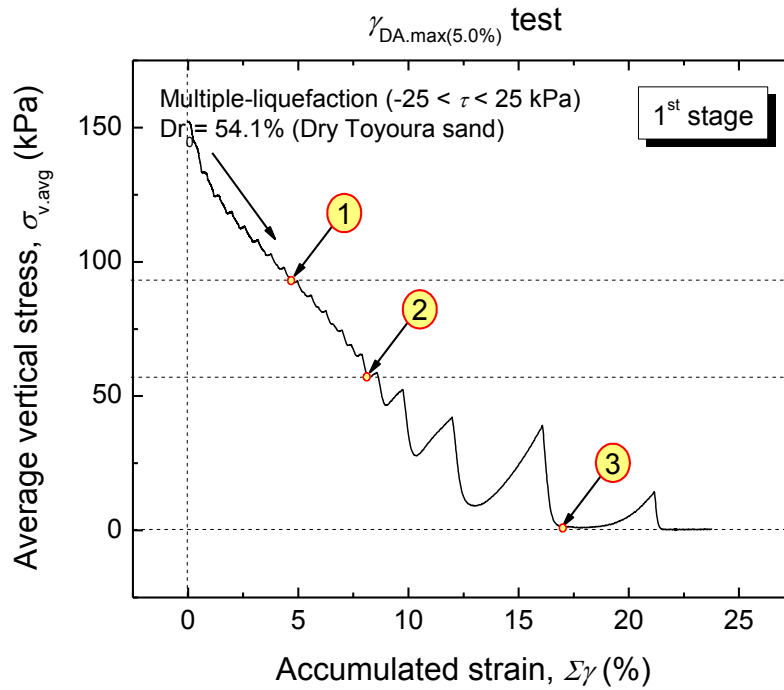
Fig. 7.15: Point-1, point-2, and point-3 in the typical average vertical stress and accumulated strain relationship (e.g. ML20 test)

7.3.2 Soil behaviorsin the first-two stages of multiple-liquefaction test based on energy approach

Inprevious studies (e.g. Nemat-Nasser and Shookoh, 1979; Davis and Berril, 1982; Figueroa, 1990; Towhata and Ishihara, 1985; Kokusho, 2013; among others), the liquefaction potential was evaluated for soils that did not have any history of previous liquefaction. However, in the case of2-stage of liquefaction of multi-stage of liquefaction, their behaviorin future liquefaction stages are highlyaffected by the history ofdissipated energy on the previous liquefaction, as discussed hereafter.

The total dissipated energy in the 1st liquefaction stage inboth series of tests (ML-13 to ML-22 tests) can be used toevaluate the liquefaction resistancesin the 2nd liquefaction stage, as shown in Fig. 7.16.In fact, it appears that the cyclic resistance in future liquefaction stageshas a unique relation with the amount of dissipated energy in the previous liquefaction stage. Specifically, the cyclic resistance in the 2nd liquefaction stage increases if the amount of dissipated energy during the 1st liquefaction does not exceed 0.41 J/m^3. This amount of energy well corresponds to that dissipated in a testwhere the soil specimen is sheared up to $\gamma_{DA.max}$= 0.5%.Next, for soil specimens sheared by 0.5% <$\gamma_{DA.max}$< 2%, a sharp decrease in cyclic resistance in their 2^{nd}liquefaction stage is observed. On the other hand, the cyclic resistance in the 2^{nd}liquefaction stage decrease only gradually forsoil specimen sheared by a 5% <$\gamma_{DA.max}$< 10%. Note that this behavior may not be completely true, since in the 2^{nd}liquefaction stage, cyclicresistance of soil specimen sheared by $\gamma_{DA.max}$> 5%was already small enough and only about 10.2 cycleswere necessary to cause to cause γ_{DA}= 2%, while at the same time, the liquefaction resistance cannot be smaller than zero.

Therefore the presence of dissipated energy in previous liquefaction stage can be advantageous (increase) or detrimental (decrease) for the cyclic resistance in future liquefaction stages. However, since the relationship between the dissipated energy and the cyclic resistance in future liquefaction is not linear from the beginning,it was not clear when the negative impact actually starts to take place.
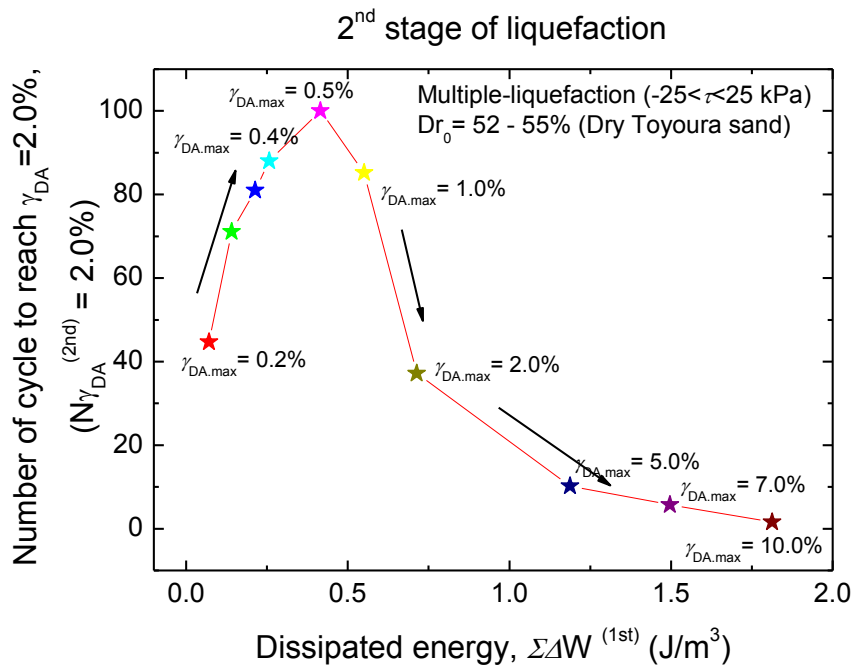
Fig. 7.16: The impact of dissipated energy in the 1st liquefaction to the soil cyclic resistance in 2nd stage of liquefaction

To address this issue, a series of four additional different tests was carried out on soil specimenssubjected to a different number of small cyclic shear loading under constant stress (drained) condition prior to the liquefaction stage.Consequently, the dissipated energy created during the application of small cyclic shear loading became the input energy for future analysis.

Four tests were conducted (SLPre1 to SLPre4 tests), in which all the specimens wereone-dimensionally consolidated up to 200 kPaof vertical stress ($\sigma_{v.Top}$= 200 kPa) and then sheared by applying 5, 10, 100 and 1000 cycles of small drained shear loadingup to γ_{DA} = 0.2%. Such γ_{DA}wassmall enough to prevent large increase of specimen relative density,so that obtained new data could be compared with those of previous multiple-liquefaction tests.The relation between accumulated strain and dissipated energy during small drained cyclic shear loading is reported in Fig. 7.17. The dissipated energy achieved after applying 5, 10, 100 and 1000 cycles was 0.029, 0.05, 0.24, and 1.06 J/m^3, respectively.From this figure, it can be seen that the increase of dissipated energy is not linear with the increase of accumulated strain. The dissipated energyrate was higher during the first few cycles, while it becamesmaller for the subsequentlarge numbers of cycles. This can be explained looking at typical average shear stress and shear strain relationshipsfor the 1st and 100th cycles as shown in Fig. 7.18. During early cycles, the dissipated energy was higher because of larger area of the hysteretic loop of shear stress - shear strain. At a large number of cycles, the dissipated energy became smaller

due to the reduced area of the hysteretic loop due mainly to hardening effects during cyclic drained loading.

The application of small drained cyclic shear loading has therefore a significant impacton the soil liquefaction resistance. This impact can be seen by comparing Figs. 7.19and 7.20. Figs.7.19(a) and 7.20(a) show the stress path and time history ofshear strain development for the non-pre-sheared specimen, respectively. Similarly, Figs. 7.20(a) and 7.20(b) show those for the pre-sheared specimen.By only applying 10 cycles of drained loading, the liquefaction resistance of the pre-sheared specimen (N=43.7) increased significantly as compared to that of the non-pre-sheared specimen (N=12.7).The variation of liquefaction resistance with dissipated energy during pre-shearing is shown in Fig. 7.21.

In Fig. 7.22, the liquefaction resistance from liquefaction tests with cyclic pre-shearing is compared with that evaluated for the firsttwo stages ofmultiple-liquefaction tests. Interestingly, a unique relationship is obtained up to 0.25 J/m^3. Then, it started to deviate from the relationship of pre-sheared specimen. Note that during small cyclic shear loading in the pre-sheared liquefaction tests, the soil behaved purely contractive. In the 1st stage of the multiple-liquefaction tests, the specimens also behaved purely contractive before passing the PTLat a dissipated energy level of about 0.25 J/m^3. Beyond this value, the stress path of the sheared specimen passed the PTL for the first time, thus, the specimen started to behave less contractive and more dilative. Therefore, it becomes clear that the negative impact of the dissipated energy in previous liquefaction stage starts when the stress path passes the PTL for the first time.

This finding is illustrated in Fig. 7.23, where a virtual boundary is plotted to identify the state at which the dissipated energy in the current/previous liquefaction will be advantageous (positive impact) or detrimental (negative impact) for the cyclic resistance in future liquefactionstages. From now on, the part of dissipated energy that create the positive impact to the next liquefaction stage will be called $\Sigma\Delta W^{(+)}$, while the amount of dissipated energy that create negative impact will be called $\Sigma\Delta W^{(-)}$. The$\Sigma\Delta W^{(+)}$will be seen if the dissipated energy is consumed solely by contraction. Alternatively, if the amount of dissipated energy exceeds this virtual boundary, the rest of the energy applied will induce a negative impact on the cyclic resistance in future liquefactionstages.
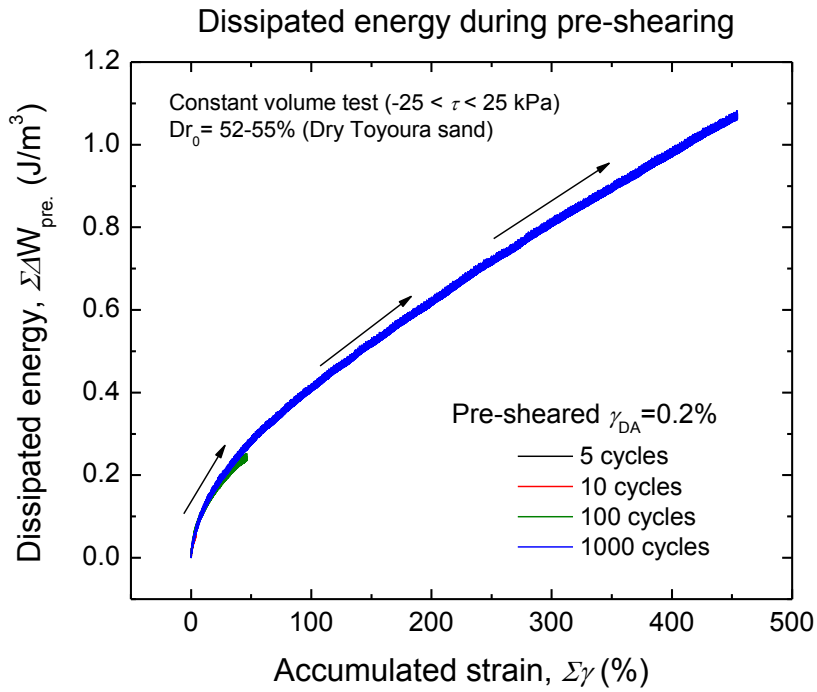
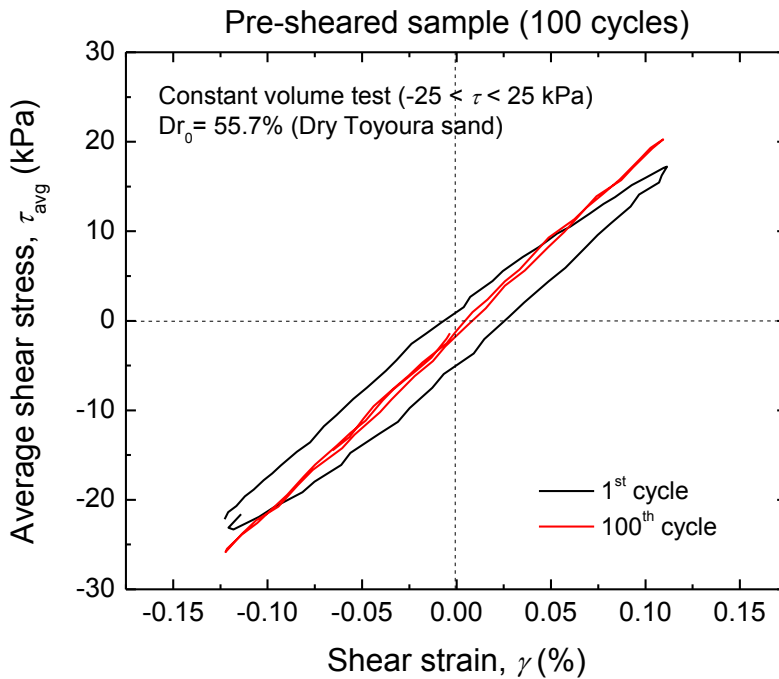Fig. 7.17: Dissipated energy - accumulated strain relationship during cyclic pre-shearing (SLPre1 to SLPre4 tests)

Fig. 7.18: Average shear stress - shear strain relationshipfor the 1st and 100th cycle of small drained shear loading (e.g. SLPre3 test)
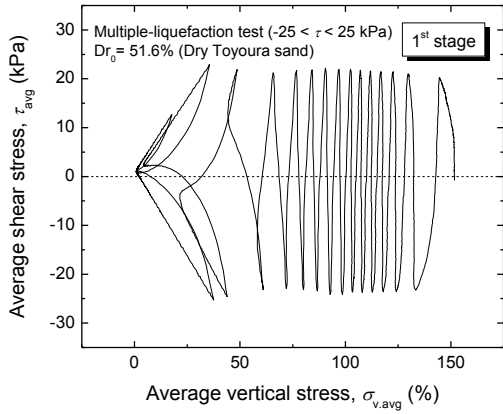
Fig. 7.19(a): Average shear stress - shear strain relationship in a constant volume test on non-pre-sheared specimen (e.g. ML22 test)
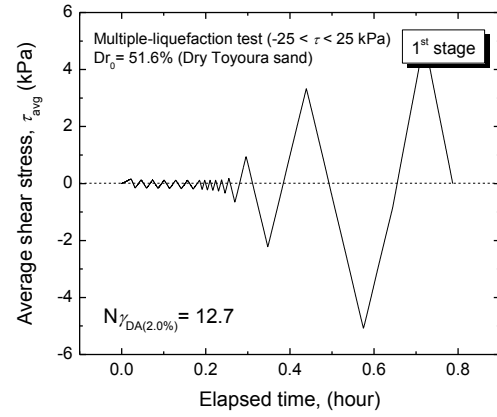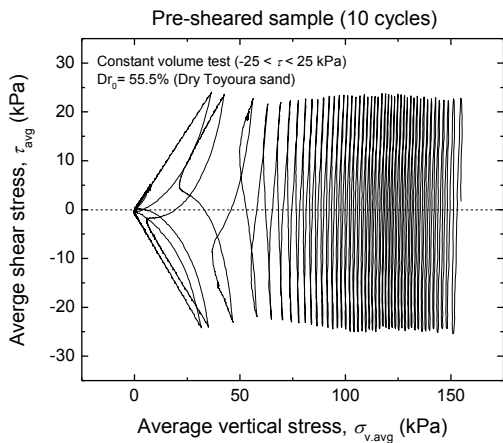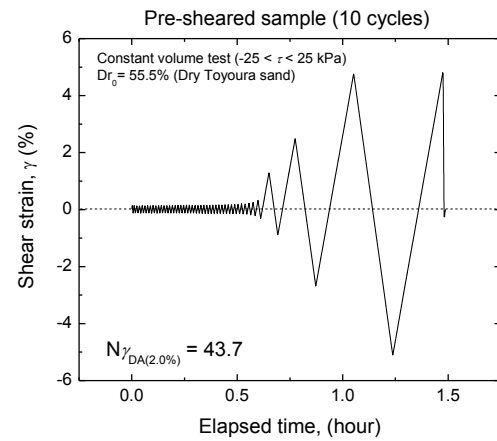

Fig. 7.19(b): Average vertical stress - average shear stress relationship in a constant volume test on non-pre-sheared specimen (e.g. ML22 test)

Fig. 7.20(a): Average shear stress - average shear strain relationship in a constant volume test on pre-sheared specimen(10 cycles) (e.g. SLPre2 test)

Fig. 7.20(b): Average vertical stress -average shear stress relationship in a constant volume test on pre-sheared specimen(10 cycles) (e.g. SLPre2 test)
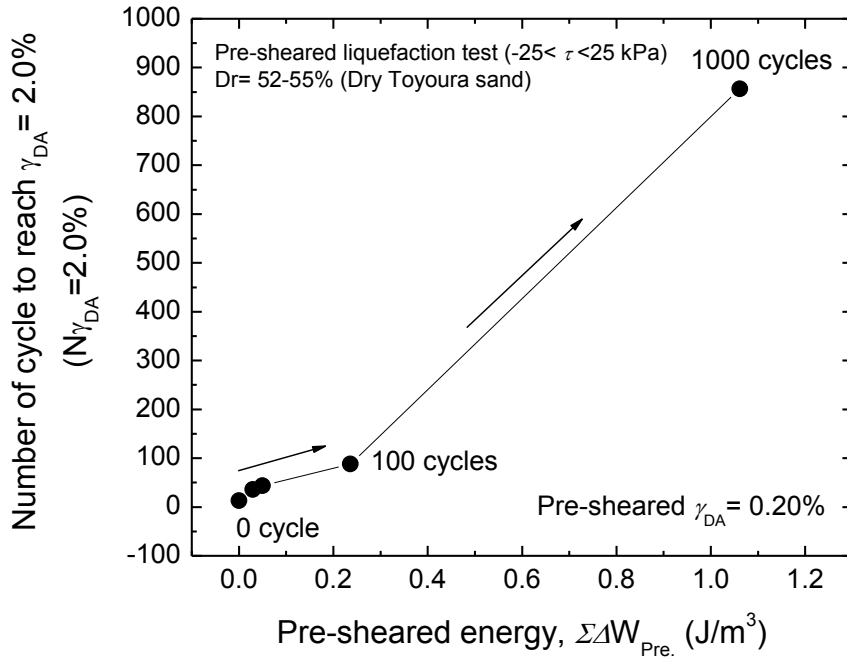
Fig. 7.21: Variation on liquefaction resistance due tocyclic drained pre-shearing (SLPre1 to SLPre4 tests)
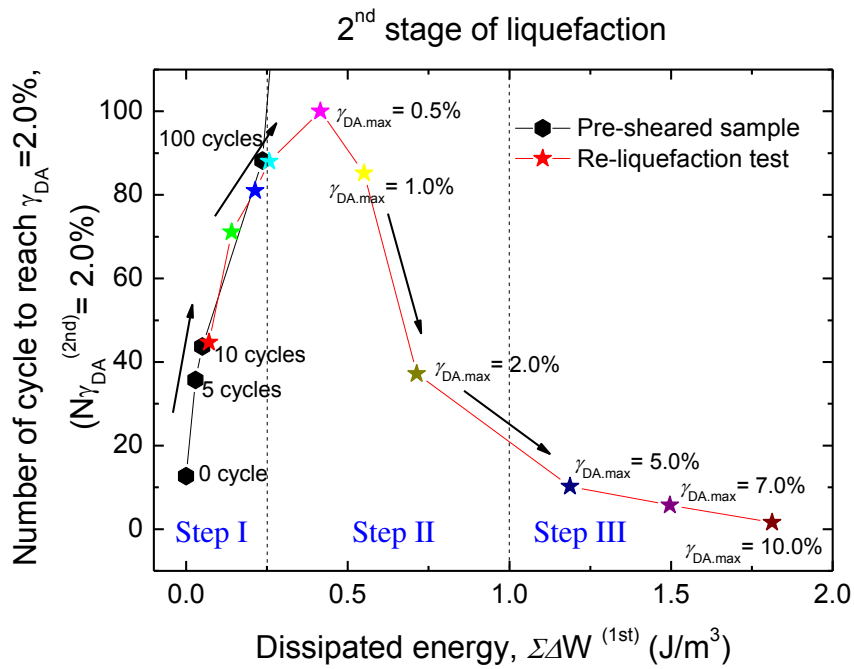
Fig. 7.22: Relationship between re-liquefaction resistance and the dissipated energy under various testing conditions
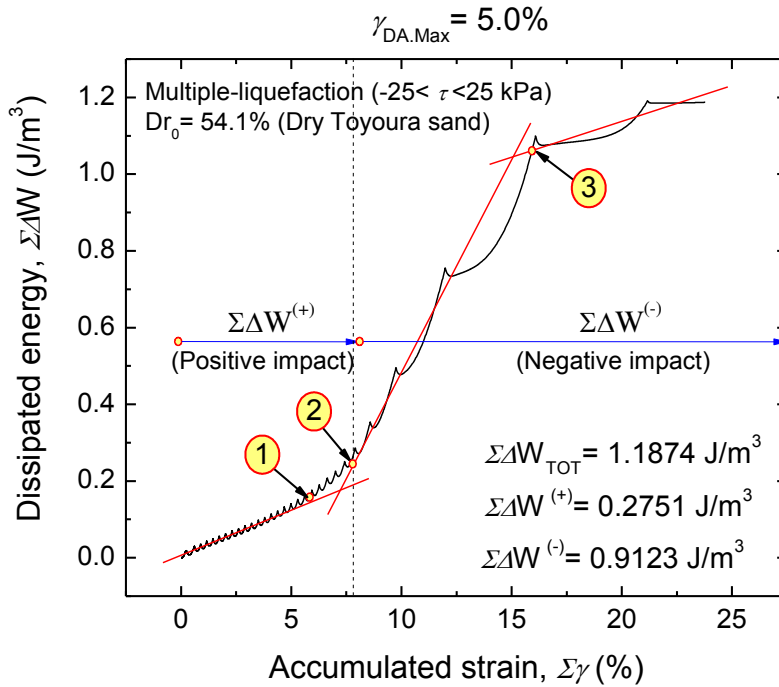
Fig. 7.23: Positive and negative impacts of dissipated energy on sand resistance during multiple liquefactions

7.3.3 Soil behaviorsduring multiple liquefactions using energy approach

Based on promising results obtained using dissipated energy approach to evaluate the liquefaction characteristic in the first two stages of multiple liquefaction tests, the same analysis is applied hereafter for the subsequent liquefaction stages. To do so, both $\Sigma\Delta W^{(+)}$ and $\Sigma\Delta W^{(-)}$in each stage of multiple-liquefaction tests were evaluated for the case of specimens shearedwith $\gamma_{DA.max}$up to 2%, 5%, 7% and 10% (ML19 to ML22 tests), as shown in Figs. 7.24 and 7.25, respectively. In Fig. 7.24, it was found that the $\Sigma\Delta W^{(+)}$ was very similar to the trend of liquefaction resistance of the multiple-liquefied soil as previously shown in Fig. 5.23 in Chapter 5. Interestingly, the $\Sigma\Delta W^{(+)}$decreases with the amount of $\gamma_{DA.max}$ applied but increases with the number of liquefaction stages. Contrarily, as shown in Fig. 7.26, the $\Sigma\Delta W^{(-)}$ during multiple-liquefaction tests increases with the amount of maximum γ_{DA} applied and with the number of liquefaction stages. From these two figures, the difference between $\Sigma\Delta W^{(+)}$ and $\Sigma\Delta W^{(+)}$(to be called hereafter as delta energy impact or simply $\Delta(\Sigma\Delta W)$) was evaluated at each liquefaction stage, as shown in Fig.7.27.From Fig 7.27, it can be seen that only in the case of a specimen sheared up to $\gamma_{DA.max}= 2\%$the $\Delta(\Sigma\Delta W)$ is positive. In general, the larger the

$\gamma_{DA.max}$ is, the larger $\Sigma\Delta W^{(-)}$ is and during subsequent liquefaction stages, thelarger the $\Delta(\Sigma\Delta W)$.

Fig.7.28 shows the contribution the two dissipatedenergy effects during the1st liquefaction stage on the cyclic resistance in the 2nd liquefaction stage. For the range of relative density investigated, the amount of dissipated energy to induce a positive impactin a future liquefaction stage is limitedto about 0.25 J/m^{3}andremains constant for any given $\gamma_{DA.max}$.Once the amount of dissipated energy exceeds this limit, the negative impactwill take place.Larger shear strain amplitude willgenerate a larger negative impact of the dissipated energy.

Fig. 7.29 shows the contribution of the two dissipatedenergy effectsduring the 2nd liquefaction stage on the cyclic resistance in the 3rd liquefaction stage.Unlike from the 1st liquefaction stage, the $\Sigma\Delta W^{(+)}$in the 2nd liquefaction stage is no longer constant and decreases with applied $\gamma_{DA.max}$. This is due to the effect of the pre-shearing history in previous liquefaction stage. A larger amount of $\Sigma\Delta W^{(-)}$in the 1st liquefactionwill reducethe amount of $\Sigma\Delta W^{(+)}$in the 2ndliquefaction.

By understanding the proportion and the change of $\Sigma\Delta W^{(+)}$and $\Sigma\Delta W^{(-)}$ in a stage of liquefaction, the impact on both of these parameters of can be traced in the future liquefaction $N\gamma_{DA(2.0\%).next}$. Fig. 7.29 shows the relation between $\Sigma\Delta W^{(+)}$and $\Sigma\Delta W^{(-)}$during 1st stage of multiple-liquefaction test. In different way of plotting, Fig. 7.30 shows the 3-D relationsof $\Sigma\Delta W^{(+)}$and $\Sigma\Delta W^{(-)}$created during 1ststage of liquefaction to the cyclic resistance of soilin the 2nd stage of liquefaction ($N\gamma_{DA(2.0\%)}^{2nd}$). From this figure, it can be seen clearly that the soil cyclic resistance in the 2nd stage of liquefaction was kept increasing as the amount of dissipated energy in the 1st stage of liquefaction within 0.25 J/m^3. Beyond this value, the excess of dissipated energy decreased the cyclic resistance of soil in the 2nd stage of liquefaction.

After knowing the relations in the first-two stages of multiple-liquefaction test, the relations on the rest of liquefaction stages can be drawn. Fig. 7.31 shows the impact of $\Sigma\Delta W^{(+)}$and $\Sigma\Delta W^{(-)}$that were created during previous stage of liquefaction to the cyclic resistance of soil in the next liquefaction stagein the multiple-liquefaction test. It can be seen that the soil resistances in the next liquefaction increase exponentially as the amount of $\Sigma\Delta W^{(+)}$increases, while the soil resistances in the next liquefaction decrease sharply as the amount of $\Sigma\Delta W^{(-)}$ increases.From these results, several virtual lines were drawn (marked by orange line in Fig. 7.31 and 7.32) to mark the boundaries where the amount of $\Sigma\Delta W^{(+)}$and $\Sigma\Delta W^{(-)}$in the previous liquefaction will resulting in specific $N\gamma_{DA(2.0\%).next}$.

In the simpler way, Fig. 7.31is re-plotted in 2-D manner as shown in Fig. 7.32. To confirm the validity of these relations, the values of $\Sigma\Delta W^{(+)}$, $\Sigma\Delta W^{(-)}$, and $N\gamma_{DA(2.0\%).next}$ of three independent testof pre-sheared specimen (SLPre1 to SLPre3 tests)were inserted. The results showed that all the three tests were located correctly within the predicted boundary.
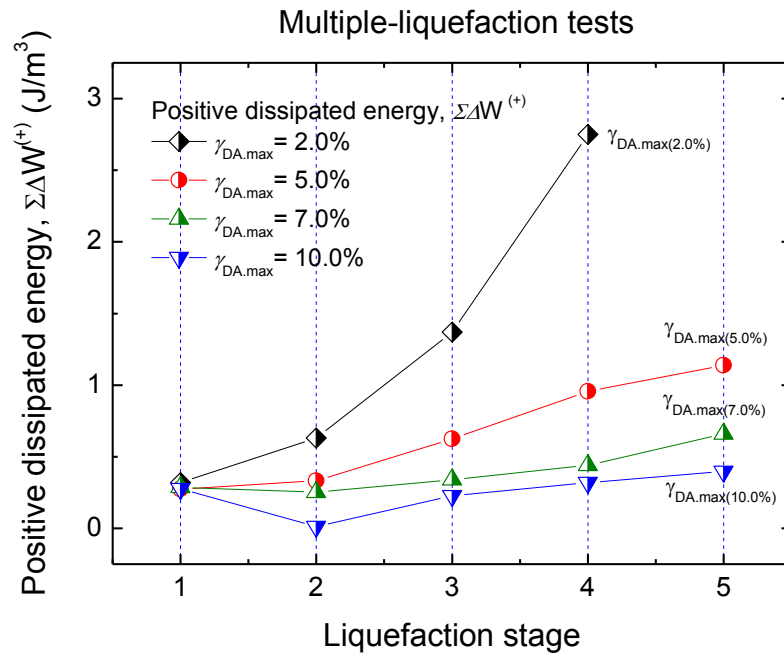

Fig. 7.24: Positive impact of dissipated energy in different stagesof the multiple-liquefaction tests (ML19 to ML22 tests)
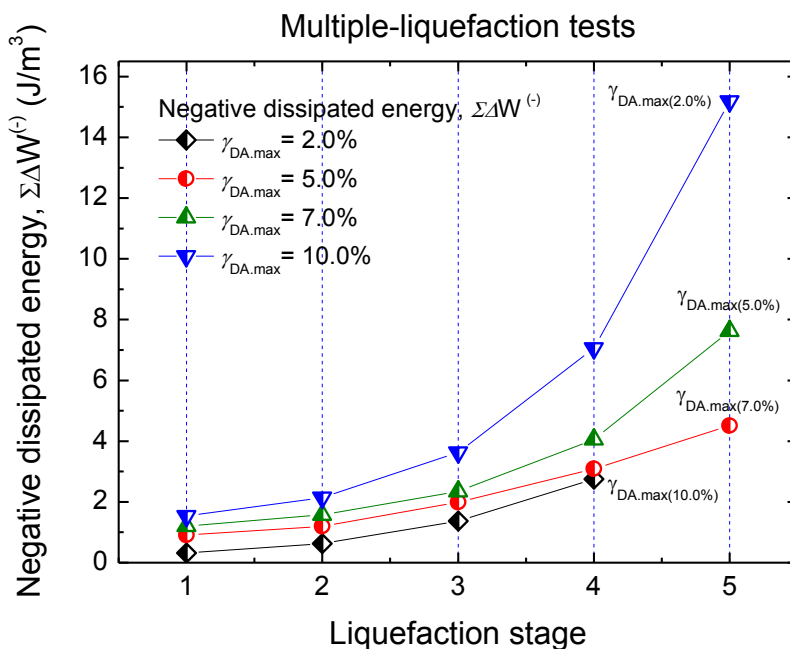
Fig. 7.25: Negative impact of dissipated energy in different stages of the multiple-liquefaction
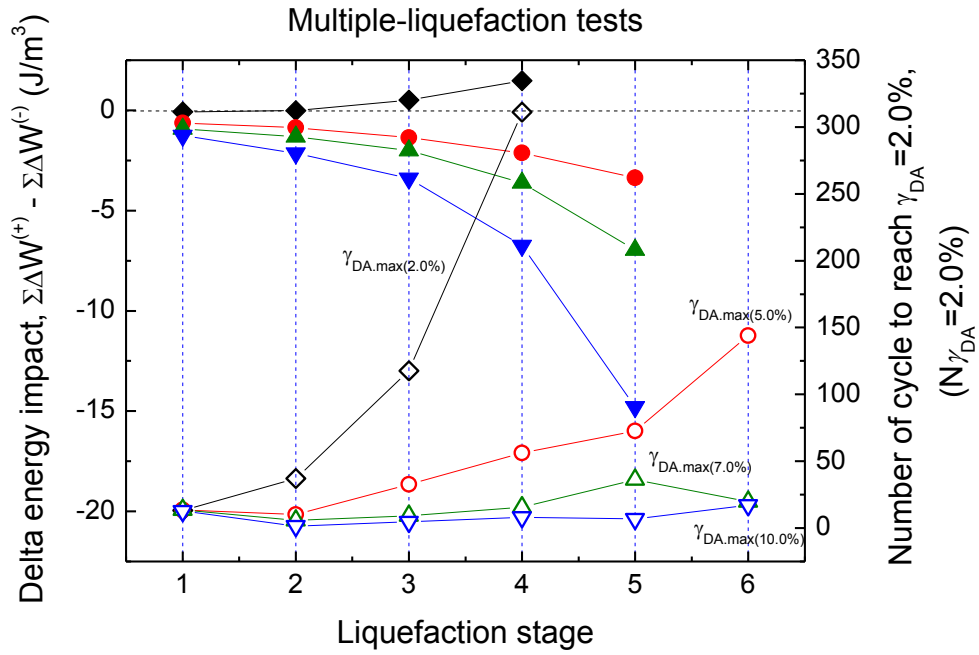
Fig. 7.26: Difference on the amount of positive and negative impact of dissipated energy in different stages of the multiple-liquefaction tests (ML19 to ML22 tests)
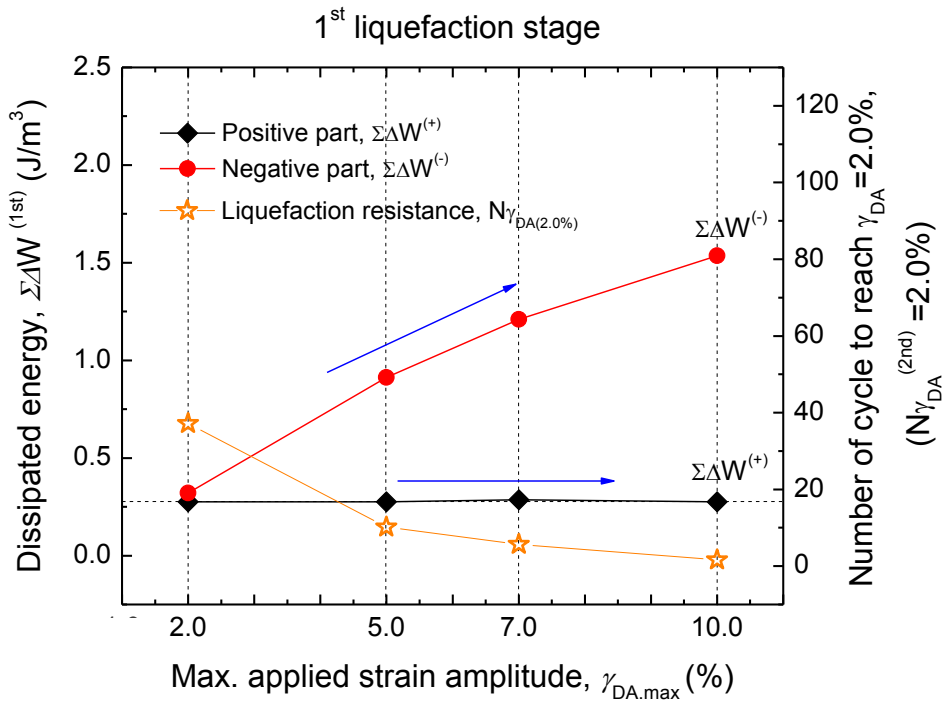
Fig. 7.27: Positive and negative dissipated energy in the 1st liquefaction stage and their impact on the cyclic resistance in the 2nd liquefaction stage (ML19 to ML22 tests)

2nd liquefaction stage
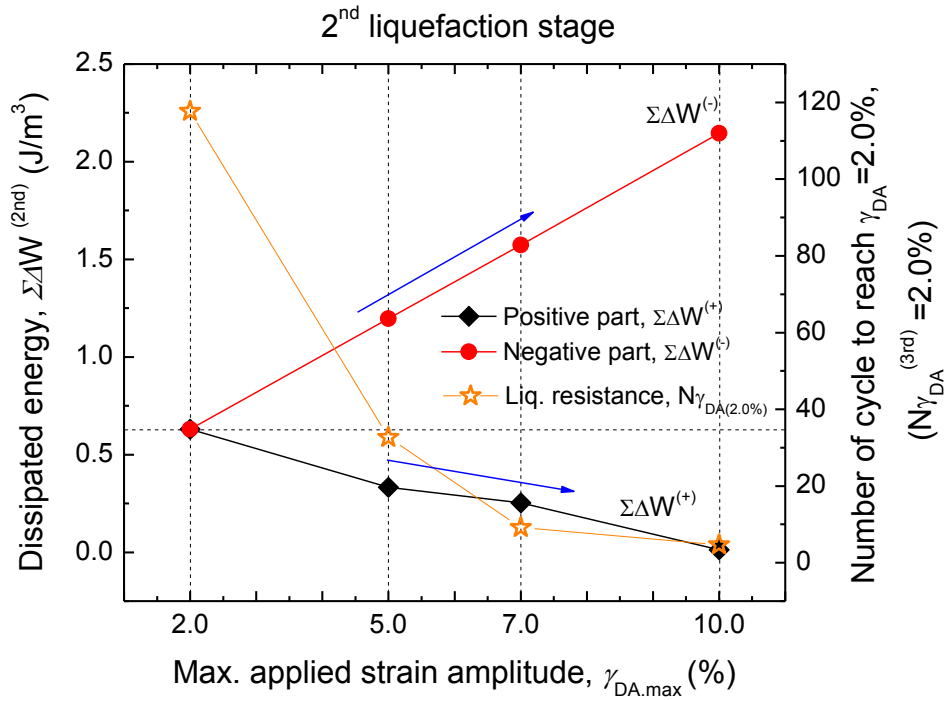
Fig. 7.28: Positive and negative dissipated energy in the 2nd liquefaction stage and their impact on the cyclic resistance in the 3rd liquefaction stage (ML19 to ML22 tests)

1st stage of multiple-liquefaction tests
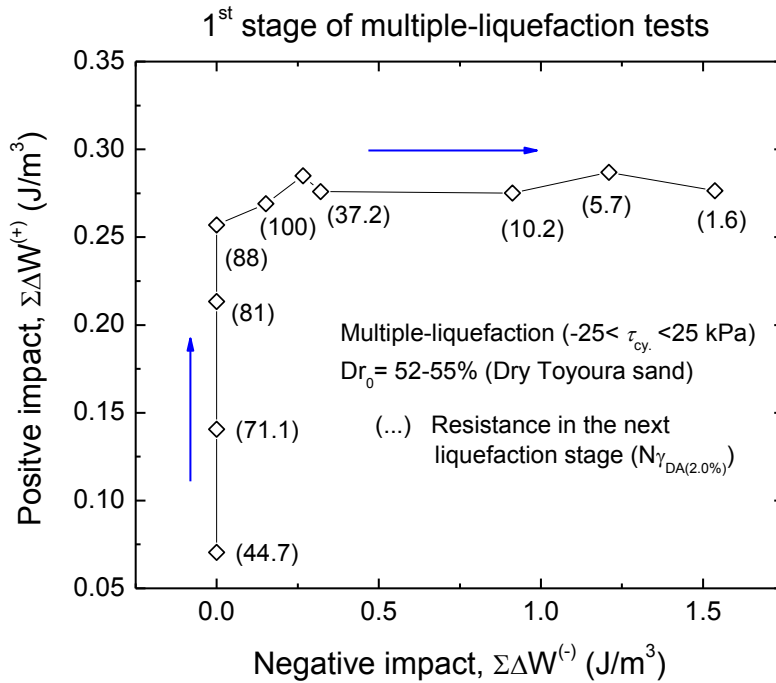
Fig. 7.29: Parts of dissipated energy that create positive and negative impacts during 1st stage of multiple-liquefaction tests (ML13 to ML22 tests)
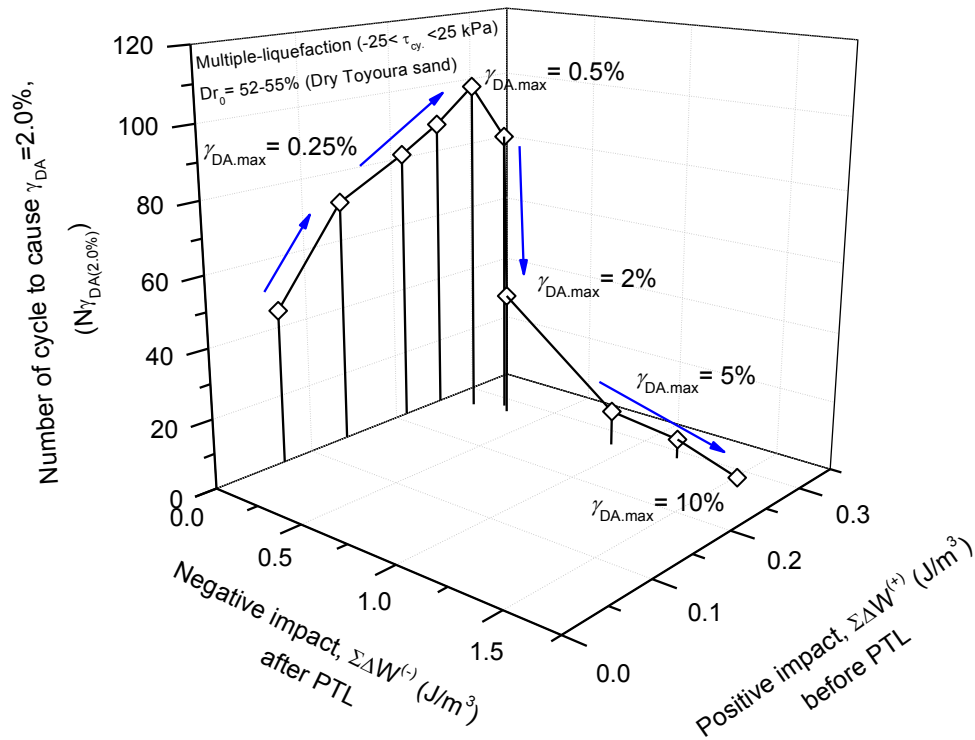
Fig. 7.30: The impacts of dissipated energy $(\Sigma\Delta W^{(+)} \& \Sigma\Delta W^{(-)})$ during 1st stage of liquefaction to the soil resistance in the 2nd stage of liquefaction (ML13 to ML22 tests)
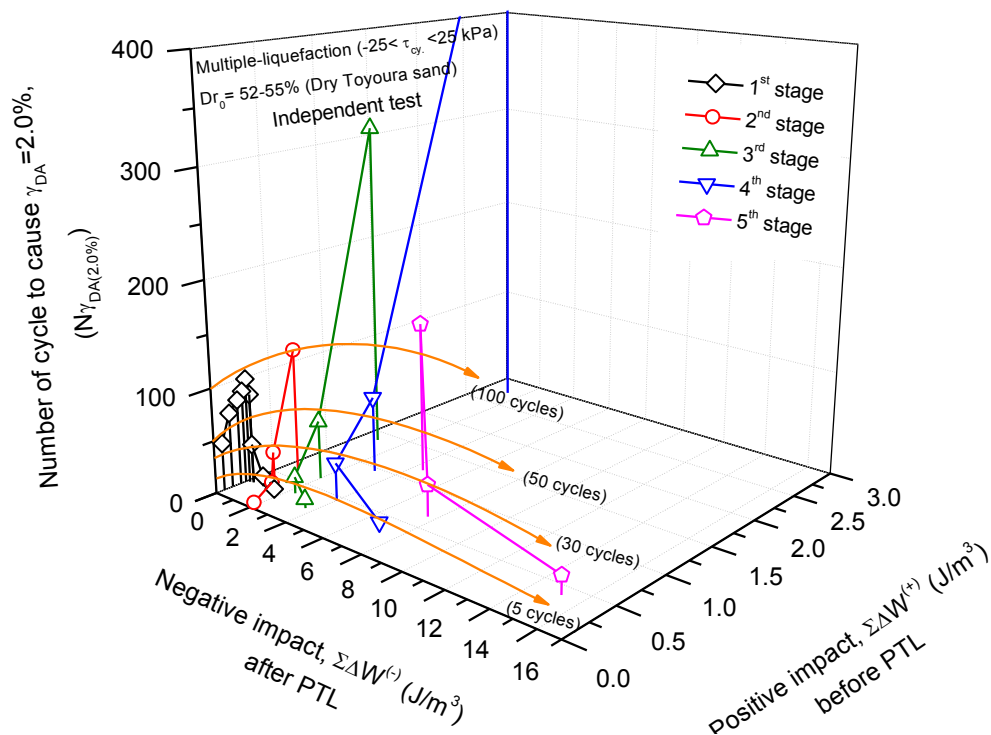
Fig. 7.31: Impacts of dissipated energy $(\Sigma\Delta W^{(+)} \& \Sigma\Delta W^{(-)})_{pre}$ in the previous liquefaction stage to the soil resistance next liquefaction stage during $(N\gamma_{DA(2.0\%)})_{next}$ during multiple liquefactions in 3D perspective (ML13 to ML22 tests)
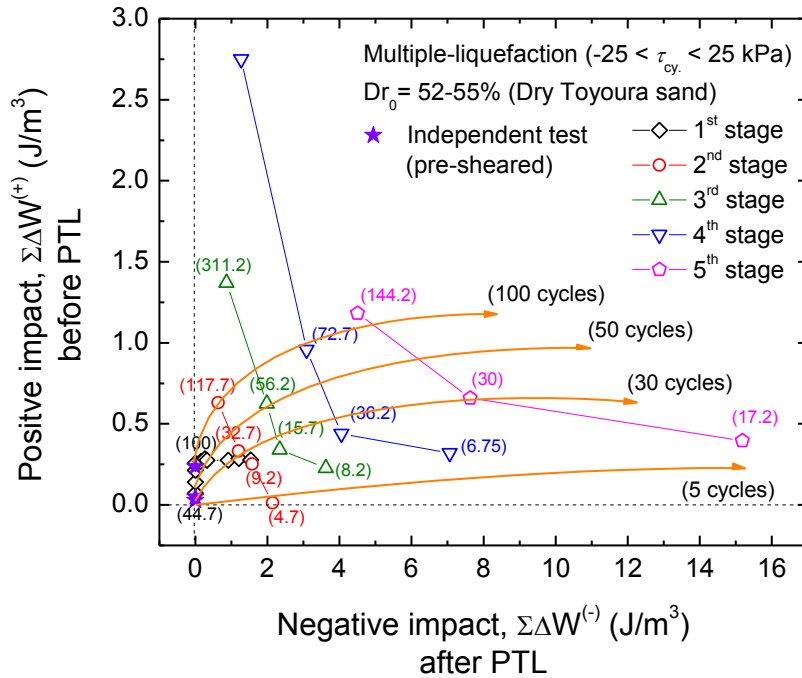
Fig. 7.32: Impacts of dissipated energy $(\Sigma\Delta W^{(+)}\&\Sigma\Delta W^{(-)})_{pre}$ in the previous liquefaction stage to the soil resistance next liquefaction stage during $(N\gamma_{DA(2.0\%)})_{next}$ during multiple liquefactions in 2D perspective (ML13 to ML22 tests)

7.4   Summary

From the analysis of sand behavior in multiple-liquefaction tests based on energy principle, several observations are drawn:

1. In a liquefaction test, the time history of dissipated energy can be divided into three steps corresponding to specific stress condition. In the Step-I, the stress path has not passed yet the PTL during cyclic undrainedshearing. Within this step, only pure contraction takes place. In the Step-II, the stress passed the PTL for the first time and dilation take place. In the Step-III, stress path reaches almost zero vertical stress (full liquefaction state) and consequently large shear strain is easily developed.

2. The amount of dissipated energy in previous liquefaction stages significantly affects the behavior of soil in the next liquefaction stage. In principle the total dissipated energy can be divided into two parts, namely positive and negative effects. The positive effect of the dissipated energy happens before the stress path passes the PTL. After this point, negative effect of the dissipated energy takes place. A larger positive effect will result in a higher liquefaction resistance in the future liquefaction stage, while a larger negative effect will have opposite impact.

3. During virgin (1-stage only) liquefaction tests, the positive effect of the dissipated energy is independent from the applied shear strain and remains constant for any appliedmaximum γ_{DA}.Note that, the amount of positive dissipated energy depends on the initial relative density, initial confining stress among others. Under testing condition used in this study, the positive effect is constant; therefore, the rest of the dissipated energy will producea negative effect. The larger the shear strain applied is, the larger the negative effect of the dissipated energy is. In the 2nd liquefaction, the positive effect of the dissipated energy is no longer constant. This is due to the history of previous liquefaction.

4. The results from all multiple-liquefaction tests analyzed using energy approach reveal that specific combination of $\Sigma\Delta W^{(+)}$ and$\Sigma\Delta W^{(-)}$in the previous liquefactions will produce specific liquefaction resistance in the future liquefaction.

7.5   References

1. Berril, J. B. and Davis, R. O. (1985) "Energy dissipation and seismic liquefaction of sands: revised model." *Soils and Foundations*, 25(2), pp. 106-118.

2. Bieganuosky, W. A. and Marcuson, W. F. (1976) "Liquefaction potential of dams and foundations-Report 1: Laboratory Standard Pene4tration tests on Reid Bedford Model and Ottawa Sand." Report S-76-2, Water ways experimental station.

3. Davis, R. O. and Berril, J. B. (1982) "Energy dissipation and seismic liquefaction of sands." *Earthq. Engrg. Struct. Dyn.*, 10, pp. 59-68.

4. *Douglas, B. J., Olsen, R. S. Richard, S., and Martin, G. R. (1981) "Evaluation on cone penetration tests for SPT liquefaction assessment." In Situ Testing to Evaluate Liquefaction Susceptibility, ASCE.*

5. Figeroa, J. L., Saada, A. S., Liang, L., and Dahisaria, N. M. (1994) "Evaluation of soil liquefaction by energy principles." *J. of Geotech. Engrg.*, ASCE, 120(9), pp. 1554-1569.

6. Figueroa, J. L. (1990) "A method for evaluating soil liquefaction by energy principles." *Proc. 4th Nat'l. Conf. on Earthquake Engrg.*, Earthquake Engineering Research Institute.

7. Figueroa, J. L. and Dahisaria, M. N. (1991) "An energy approach in defining soil liquefaction." *Proc. 2nd Int'l. Conf. on Recent Advances in Geotech. Earthquake Engrg. and Soil Dyn.*, University of Missouri, Mo.

8. Figueroa, J. L., Saada, A. S., Liang, L., and Dahisaria, N. M. (1994) "Evaluation of soil liquefaction by energy principles." *J. Geotech. Engrg.*, 120, pp. 1554-1569.

9. Ishihara, K. and Okada, S. (1982) "Effects of large preshearing on cyclic behavior of sand." *Soils and Foundations*, Tokyo, 22(3), pp. 109-125.

10. Ishihara, K. and Okada, S. (1978) "Effects of stress history on cyclic behavior of sand." *Soils and Foundations*, Tokyo, 18(4), pp. 31-35.

11. Kokusho, T. (2013) "Applicability of energy-based liquefaction potential evaluation method compared with FL-method." *Proc. Japanese Geotech. Society Conf.* 8(3), pp. 463-475.

12. Nemat-Nasser, S. and Shookoh, A. (1979) "A unified approach to densification and liquefaction of cohesionless sand in cyclic shearing." *Can. Geotech. J.*, 16, pp. 659-678.

13. Oda, M., Kawamoto, K., Suzuki, K, Fujimori, H., and Sato, M. (2001) "Microstructural interpretation on reliquefaction of saturated granular soils under cyclic loading." *J. Geotech. and Geoenvironmental Engrg*, 127(5), pp. 416-423.

14. Seed, H. B. and Idriss, I. M. (1971) "Simplified procedure for evaluating soil liquefaction potential."J. of Soil Mech. and Found. Div., ASCE, 107, pp. 501-518.

15. Seed, H. B. and Peacock, W. H. (1971) "Test procedures for measuring soil liquefaction characteristics." *J. of Soil Mech. and Found. Div.*, ASCE, 97, pp. 1099-1119.

16. Seed, H. B., Idriss, I. M., and Arango, I. (1983) "Evaluation of liquefaction potential using field performance data." *J. of Geotech. Engrg.,* 109, pp. 458-482.

17. Suzuki, T. and Suzuki, T. (1988) "Effects of density and fabric change on re-liquefaction resistance of saturated sand." *J. Japanese Geotech. Soc.*, Tokyo, 28(2), pp. 187 - 195. (in Japanese)

18. Tatsuoka, F., Iwasaki, T., Tokida, K., Yasuda, S., Hirose, M., Imai, M., and Kon-no, M. (1980) "Standard penetration tests and soil liquefaction potential evaluation." *Soils and Foundations*, 20(4).

19. Tokimatsu, K. and Yoshimi, H. (1981) "Field correlation of soil liquefaction with SPT and grain size." *Proc. of the Int'l. Conf. on Recent Advances in Geotech. Eartquake Engrg and Soil Dynamics*.

20. Tokimatsu, K. and Yoshimi, Y. (1983) "Empirical correlation of soil and liquefaction based on SPT N-value and fines content." Soils and Foundations, 23(4), pp. 56-74.

21. Towhata, I. and Ishihara, K. (1985) "Shear work and pore water pressure in undrained shear." *Soils and Foundations*, 25(3), pp. 73-84.

22. Wahyudi, S. and Koseki, J. (2013) "Effects of pre-shearing history on re-liquefaction behaviors of loose sand in stacked-ring shear apparatus." *Proc. 2ⁿᵈ Int'l. Symp. On Japan Assoc. of Earthquake Engrg.*, Tokyo, Japan.

8 CONCLUSIONS AND RECOMMENDATIONS

8.1   Conclusions

There are two major objectives in the current study, which are first is to investigate the soil behaviors during multiple liquefactions and second is to develop the new stacked-ring shear apparatus itself. Both objectives were conducted simultaneously during the period of this study.

8.1.1 The development of the stacked-ring shear apparatus

The stacked-ring shear apparatus representsthe state-of-the-art development of common ring shear apparatus. A ring shear apparatus, so called split ring shear, is generally composed by two rings. Alternatively, the stacked-ring shear apparatus is composed by a series of vertically stacked individual rings.

As usually happens in all type of ring shear apparatus, excessive friction is generated between the soil particles and the metal rings, which significantly affects the stress and strain distributions throughout the specimen in both vertical and circumferential directions.Therefore, the newly developed stacked-ring shear apparatus was designed to reduce as much as possible the generation of excessive friction. The use of vertically stacked 5mm-highindividual rings allows to have a more uniform shear strain and shear stress distribution along the height of the specimen. However, while friction in circumferential direction could be effectively reduced, the friction in vertical direction remains to be a major challenge in developing the stacked-ring shear apparatus. The amount of friction in the vertical direction highly depends on the number of stackedrings used (i.e. specimen height). In fact,in a taller specimen,a larger contact surface exists between the soil particles and the stacked rings. As a result, the extent of generated friction becomes very significant, since it induces larger non-uniformity of stresses and strains along the vertical direction(e.g. significant reduction in vertical stress along specimen height).

To address this issue and obtain an optimum setting for the new apparatus, several modifications were made, which are:

1. One additional bi-component load cell was installed at the bottom of the specimen to measure the transferred vertical and shear stresses applied at the top of the specimen. By doing so, it wasfound that an unexpectedlarge friction was generated when usingthe original set of 31 stacked ringsor 150 mm specimen height (i.e. about 95% of the applied vertical stress was lost due to friction). Such large generation of friction was also

responsible for a very low and unusual soil resistance against liquefaction in multiple-liquefaction tests as compared to torsional shear tests. Therefore, the original height of the specimen was reduced to 11 stacked rings (55 mm specimen height). The new test results revealed that still about 52% of the vertical stress applied to the specimen was lost due to friction. However, the improvement was that about 45% of the loss of the vertical stress could be recovered.

2. Further development to reduce the excessive friction was made by covering the surface of the stackedringsby a frictionless material,so called Diamond-Like Coating (DLC). The DLC coating has nominally 75% less friction (μ=0.2) than the original stainless steel ring (μ=0.8). Two prototypes were provided by the manufacturer with the thickness of 1.0µm and 2.0µm. Based on a series of durability tests, the 2.0 µm-thick DLC was finally selected to coat the new version of the stackedrings.Yet, the use of DLC coating could only improve about 6% of the loss of the vertical stress as comparedto the non-coated ring.

3. The effects of specimen height on the friction generation was further evaluated by reducing the number of coated rings to 8 (40 mm height) and 5 (25 mm height). The results of multi-stage liquefaction tests showed that,using8 and 5 coated stacked rings, the generated friction was smaller than that using 11 coated stacked rings.However, the generated friction was not constant in the subsequent liquefaction stages. A constant amount of friction during subsequent liquefaction stages is essential for comparing soil behavior undergoing multiple-liquefaction stages. Therefore, 11 coated stacked rings wereregarded as the optimum setting for conducting multi-liquefaction tests in the current study.

8.1.2 Soil behaviors during multiple liquefactions

The behaviors of soil subjected with multiple liquefactions were found to be significantly affected by at least two factors, which are first is the level of applied strain amplitude and second is anisotropy. In the current study, the effects of strain amplitude are investigated in three ways. First is by analyzing the output of experimental data on the series of tests where the soil specimens are subjected with different shear strain amplitudes. Second,toconductan additional measurementalong with the experimental tests mentioned earlier to investigate the local deformation behaviors of the specimen as compare to their global ones. This measurement is conducted by using so-called image analysis method. Third, conduct an additional analysis based on the experimental results using energy approach.

Another factor that have significant impact is anisotropy, in particular induced anisotropy. The effects of induced anisotropy is investigated by two methods, which are first by measuring the stiffness of soil in particular direction at each liquefaction stage, and second by analyzing the stress-dilatancy characteristics of the specimen.

The results on all of these measurements and analyses are reported as follows:

8.1.2.1 The effects of strain amplitude on the soil behaviors during multiple liquefactions

8.1.2.1.1 *Experimental results on the effects of different shear strain amplitudes*

1. The amplitude of shear strain applied to a specimen has a direct impact in the change (increase) of specimen relative density during re-consolidation in each stage of multiple-liquefaction tests. The larger the applied shear strain is, the larger the increase in relative densityis.

2. The comparison between results of multiple-liquefaction tests and those of single-liquefaction (virgin liquefaction) tests revealed that thespecimen sheared under large shear strain amplitude may have lower liquefaction resistance than the virgin liquefied soilfor a given similar density. This impliesthat the cyclic resistance of soil subjected with multiple liquefactions can be lower than that of the soil undergoing virgin liquefaction because of the histories of previous liquefactions.

3. The extent of shear strain amplitude also has a direct impact on thecyclic resistance of soil subjected with multiple liquefactions. From the series of tests conducted using 11 coated stacked-ring shear apparatus, two observations were obtained, which are: 1.)thespecimens sheared by larger maximum shear strain double amplitudes(in this case $\gamma_{DA.max}>0.5\%$) will showlower cyclic resistance in the future liquefaction stage. Alternatively, the specimens sheared with smaller shear strain double amplitude (in this case $\gamma_{DA.max}<0.5\%$) shows lower cyclic resistance in the future liquefactions.Suchbehaviorswere later found to be directly related to the amount of energy dissipated in each liquefaction stage. This means that the level of strain amplitude as well as the amount of dissipated energy during previous liquefaction will determine the soil resistance during multiple liquefactions.

8.1.2.1.2 *Image analysis results on the effects of different shear strain amplitudes*

Based on local shear strain measurement obtained by image analysis, further evidences regarding the impact of strain amplitude onthe cyclic resistance of multiple liquefied soil were also found: 1) in the case of specimens sheared by a larger strain, a larger deviation between the local shear strain and the global strain (externally measured) was observed. Such strain deviation include the maximum deviation throughout the test as well as the residual deviation at the end of the test. As a result, strains were distributed non-uniformly throughout the specimen. The larger the applied shear strain is, the larger the maximum and residual deviations are. Similarly, for the specimens sheared by smaller shear strain,a smallerdeviation between the local shear strain and the global strain was observed. Thus, strains are distributed more uniformly throughout the specimen; 2) larger non-uniformity of strain distributions implies that some sections within the specimen were shared more than others. Therefore, it is possible to assume that certain levels of soil fabric is destroyed with the application of larger strain amplitudes; 3) non-uniform strain distributions may also imply a non-uniform soil density distributions throughout the specimen, where the sections undergoing very large shear strains (inducing localization) may tend to have looser density. As a result, the localized section will become the weak layer in the next liquefaction stage.

8.1.2.1.3 *Energy approach to evaluate the effects of shear strain amplitude*

1. In a liquefaction test, the time history of dissipated energy can be divided into three steps, which correspond to a specific stress state during liquefaction. In the Step-I, the stress path has not passed yet the phase transformation line (PTL) during cyclic undrained (constant-volume) shearing. Within this step, only pure contraction takes place. In the Step-II, the stress path passes for the first time the PTL, therefore soil behaves in a more dilative manner. In the Step-III, the stress path reaches almost zero vertical stress (full liquefaction state) and development of large shear strain is observed.

2. In principle, the total dissipated energy can be advantageous (positive) or detrimental (negative) impacts for the cyclic resistance in the next liquefaction stage. The amount of dissipated energy during liquefaction is positive ($\Sigma \Delta W^{(+)}$) before the stress path passing the PTL. After passing the PTL, negative effect of the dissipated energy takes place ($\Sigma \Delta W^{(-)}$). Larger positive effect will result in a higher liquefaction resistance against future liquefaction, while larger negative effect will have an opposite impact.

3. During virgin liquefaction tests, the part of dissipated energy that creates positive impact ($\Sigma\Delta W^{(+)}$) in the future liquefaction is limited up to certain level of strain amplitude. This limit is determined by several initial factors such as the initial relative density, initial confining stress among other factors. As the specimens sheared larger and the amount of dissipated energy exceeds this limit, this excess of dissipated energy becomes creates negative impact to the cyclic resistance of soil in the next liquefaction. The larger the applied shear strain is, the larger the negative effect of the dissipated energy is.

4. In the subsequent liquefaction stages (other than 1st stage of liquefaction), the relationship as mentioned in the previous point is no longer the same. This happens due to the history of previous liquefaction.

5. The compilations from all multiple-liquefaction tests reveal specific relations between the combinations of parts of dissipated energy that create positive impact ($\Sigma\Delta W^{(+)}$) and negative impact ($\Sigma\Delta W^{(-)}$) to the cyclic resistance of soil during multiple liquefactions. The result show that certain combination of $\Sigma\Delta W^{(+)}$ and $\Sigma\Delta W^{(-)}$ in the previous liquefactions will produce certain cyclic resistance in the future liquefaction.

8.1.2.2   Effects of induced anisotropy on the soil behavior during multiple liquefactions

Another key factor that may significantly affect the soil behavior during multiple liquefactions is the induced anisotropy. In a multiple-liquefaction test, the induced anisotropy may induce different liquefaction resistance in different loading directions.

The investigation on the effects of induced anisotropy revealed that:

1. The effect of inducedanisotropy on the behavior of soil in the next liquefaction is negligible when the residual shear strain is zero (however this condition is very unlikely to happen in reality, since the cyclic loading would stop at the zero shear stress ($\tau = 0$ kPa), not at the zero shear strain). In such a case, the stress-dilatancy characteristics of the soil subjected with multiple liquefactions is almost identical in each loading direction.

2. The magnitude of residual deformation achieved in previous liquefaction stages as well as the direction of the starting of the loading in the subsequent liquefaction stage will have a great impact on the soil behavior in the future liquefaction stage. In particular, large contraction underdrained (constant-stress)conditions will take place if the liquefied soil is sheared in the direction where the magnitude between the starting point of loading in the next liquefaction and the max.strain amplitude in the previous liquefaction is the largest. In undrained test, this implies that a large reduction in the effective stress will take place

along this loading direction. As a result, the strain in the future liquefaction will be accumulated in this direction as well.

3. In general, under the same density and effective vertical stress conditions, multiple-liquefaction tests with non-zero residual shear strain provide a lower soil liquefaction resistance than those in the tests without residual shear strain. This is due possibly to additional effects of induced anisotropy as mentioned earlier in point 2.

8.2   Recommendations for future study

The recommendations for the future experiments and studies is divided into two parts, which are the future developments of the apparatus and the remaining works on investigating the soil behaviors during multiple liquefactions.

8.2.1   Future development of the stacked-ring shear apparatus

Recommendations for future study essentially reflect further improvements of the stacked-ring shear apparatus to reduce the excessive friction, particularly in the vertical directions. Note that to completely eliminate the generated friction is not possible. However, by reducing as much as possible the generated friction will ensure more uniform distribution of stresses and strains throughout the specimen.

Some of thepossible modifications of the stacked-ring shear apparatus that can be done in the future are as follows:

1. Increasing the surface area of the specimen while maintaining its height. The surface area can be increased by increasing the outer diameter of the specimen or decreasing the inner diameter ora combination of both. A larger diameter will potentially reduce the ratio between the generated friction and the increase of applied forces.

2. Installing elastic springsunderneaththe bottom plate. Currently, the position of the bottom plate is fixed. As a result, large friction is generated during consolidation. With a mobileplate, the compressed soil and plate are able to move together during consolidation process. Note that the free movement of the platemay be allowed only during the consolidation process. In conducting the liquefaction tests, the position of the bottom plate needs to be fixed to prevent anychange of volume during the application of shear loading under undrained (constant-volume) conditions.

8.2.2 Future experiments and studies

Several experiment programs are not able to deliver in the current study due to limited time frame. However, additional studies are also need to be investigated based on the findings in the current study.

1. Effect ofinduced anisotropy:

   Additional series of test need to be conducted to investigate the effects of induced anisotropy on soil behaviors during multiple liquefactions.Similar test has been conducted using the original version of 31 non-coated stacked-ring shear apparatus. However, it needs to be conducted in the latest version of 11 coated stacked-ring shear apparatus for several reasons. First is to prove the hypotheses that have been found in the investigation of stress-dilatancy relations in the series of 2 stages liquefaction tests as presented in the Chapter 6. Second is because the 11 coated stacked ring shear apparatus has the most complete data than other series of test conducted in the earlier version of the stacked-ring apparatuses.

2. Energy approach:

   - Related with point no 1, the series test that is affected by induced anisotropy need to be re-analyzed using energy approach. So that a complete comparison can be made on the multiple-liquefaction test with the effects of induced anisotropy and the series of test having negligible impact of induced anisotropy.

   - To conduct series of tests where a single specimen is subjected to different level of strain amplitudes on each liquefaction stage (e.g.$\gamma_{DA.max}$= 2% at the 1st stage, $\gamma_{DA.max}$= 10% at the 2nd stage, $\gamma_{DA.max}$= 5% at the 3rd stage, and etc.). Later, the experimental results of these tests need to be investigated using energy approach. These experiments aims to reveal whether or not the soil behaviors of the next liquefaction is only affected by the history of previous liquefaction (1 liquefaction earlier) or it is affected by the histories of all earlier liquefactions combined (history of 1st, 2nd, 3rd and so on).

3. Effects of relative density

   In the current study, the effects of strain amplitude are only known during single stage liquefaction tests, where the specimens do not have any history of previous liquefaction. In the multiple-liquefaction tests, the quantitative impact of the increase in soil's density has not been fully understood. Therefore, special tests need to be conducted to reveal the impacts of the soil's density during multiple liquefactions.

APPENDIX A

Fig. A1: Prototype A (1µm thick.)

Fig. A2: Initial condition of section 1

Fig. A3: Cyclic axial loading $\sigma_{v.cy}$= 0 − 50 kPa (10 cycles) (Section-1)

Fig. A4: Cyclic axial loading $\sigma_{v.cy}$= 0 − 100 kPa (10 cycles) (Section-1)

Fig. A5: Cyclic axial loading $\sigma_{v.cy}$= 0 − 150 kPa (10 cycles) (Section-1)
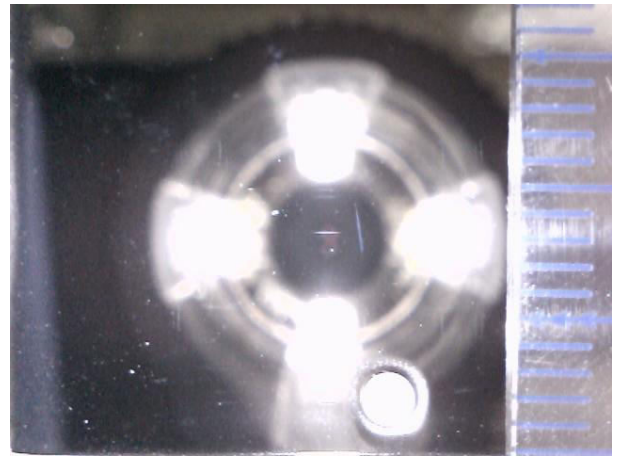
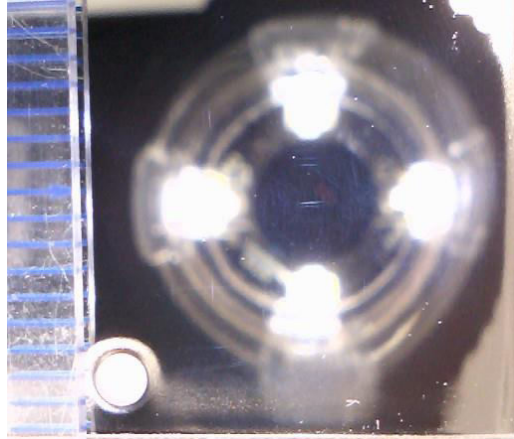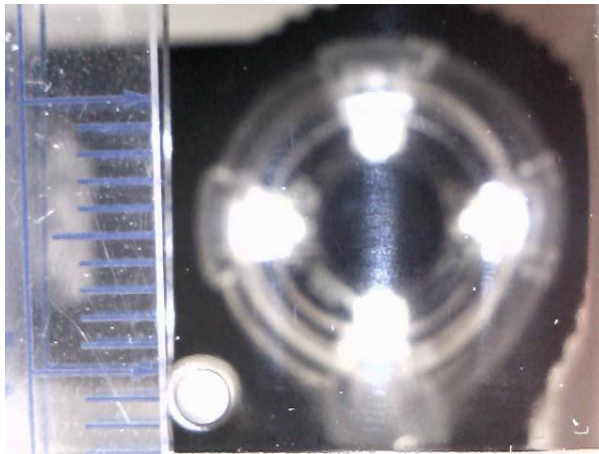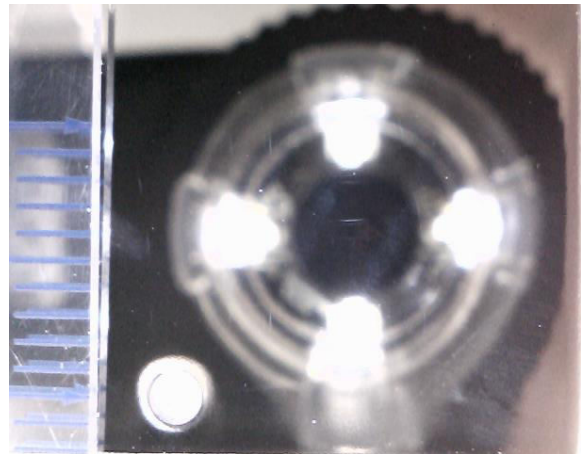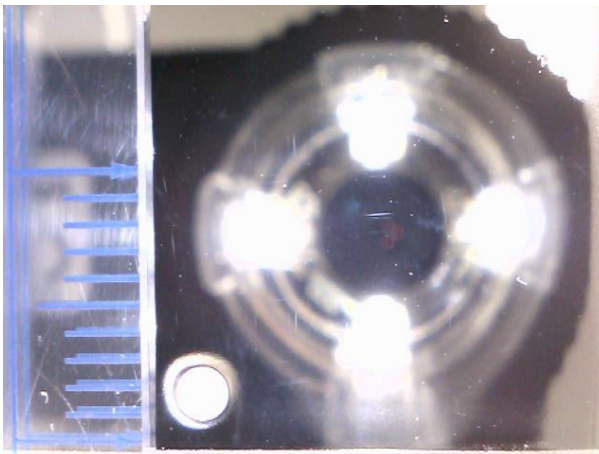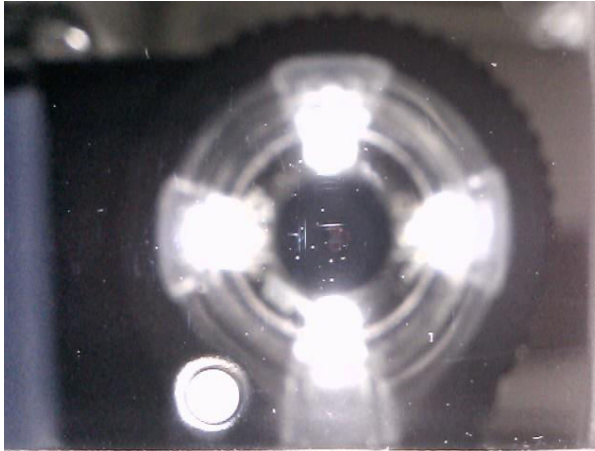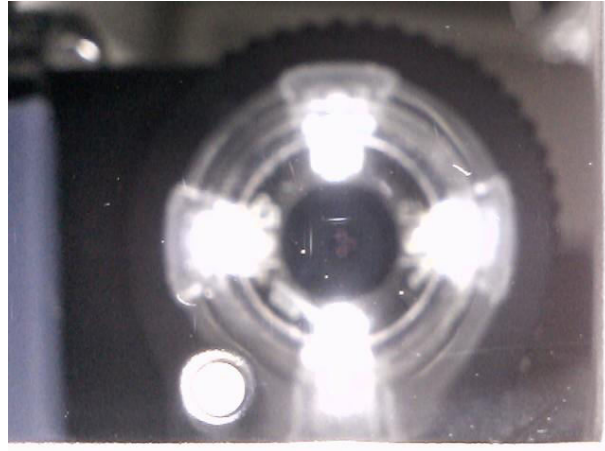Fig. A6: Cyclic axial loading $\sigma_{v.cy}$= 0 − 200 kPa (10 cycles) (Section-1)

Fig. A7: Constant stress monotonic loading test ($\sigma_{v.Top}$= 200 kPa & τ= 90 kPa) (Section-1)

Fig. A8: Constant stress monotonic shear loading test ($\sigma_{v.Top}$= 200 kPa & τ_{peak}) (Section-1)
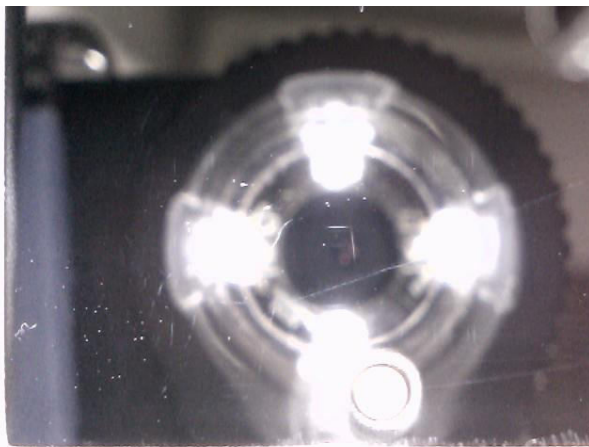
Fig. A9: Cyclic axial loading $\sigma_{v.cy}$= 0 – 300 kPa (10 cycles) (Section-1)
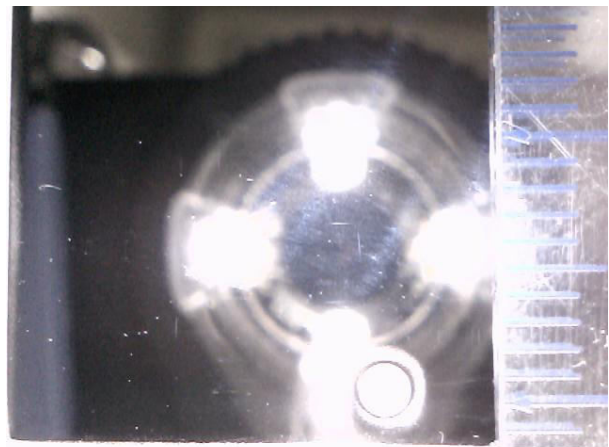
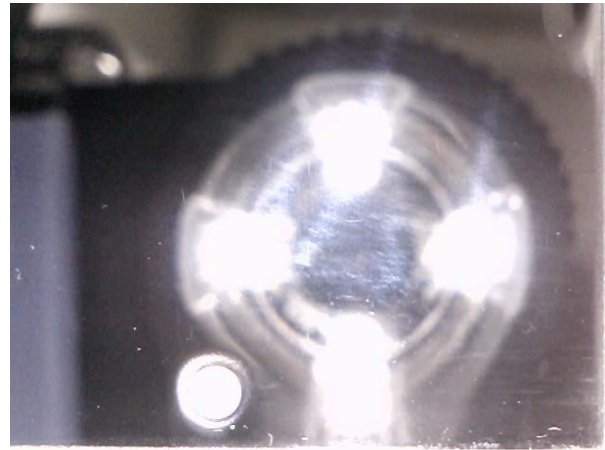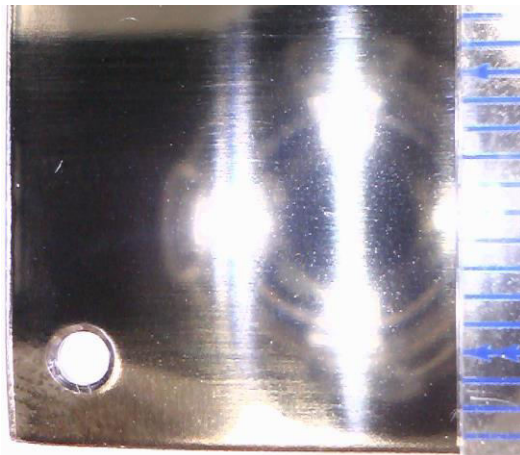Fig. A10: Constant stress monotonic shear loading test ($\sigma_{v.Top}$= 200 kPa) (Section-1)

Fig. A11: Constant stress monotonic shear loading test ($\sigma_{v.Top}$= 300 kPa) (Section-1)

Fig. A12: Constant stress cyclic shear loading test ($\sigma_{v.Top}$= 300 kPa & τ_{cy}= 200 kPa) (Section-1)
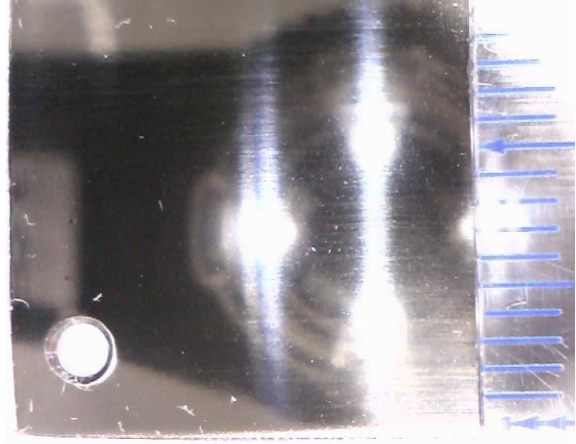

Fig. A13: Initial condition of section 2
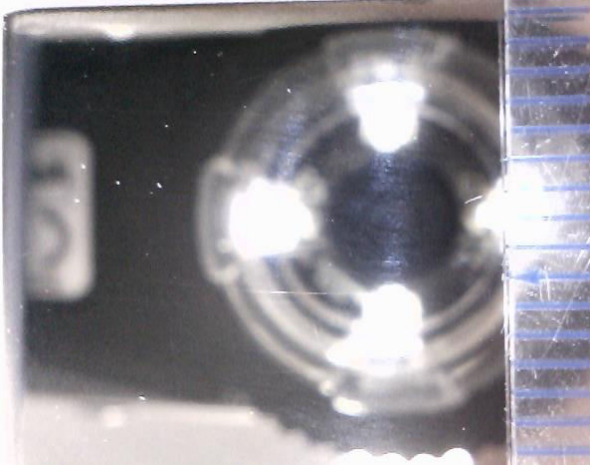
Fig. A14: Cyclic axial loading $\sigma_{v.cy}$= 0 – 50 kPa (10 cycles) (Section-2)
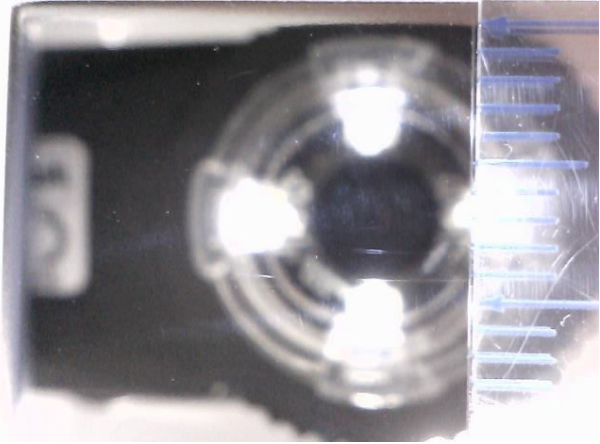
Fig. A15: Cyclic axial loading $\sigma_{v.cy}$= 0 – 100 kPa (10 cycles) (Section-2)

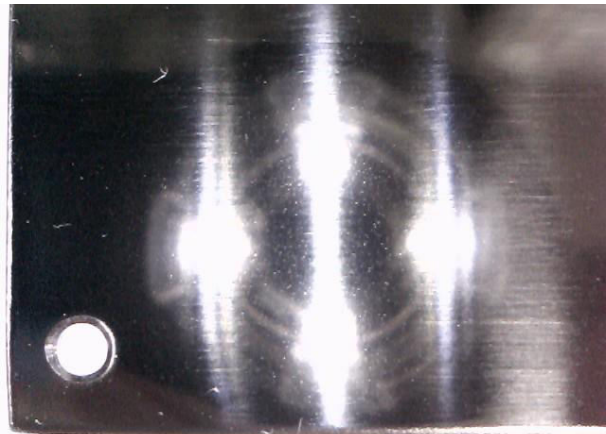Fig. A16: Cyclic axial loading $\sigma_{v.cy}$= 0 – 150 kPa (10 cycles) (Section-2)

Fig. A17: Cyclic axial loading $\sigma_{v.cy}$= 0 – 200 kPa (10 cycles) (Section-2)

Fig. A18: Constant stress monotonic loading test ($\sigma_{v.Top}$= 200 kPa & τ= 90 kPa) (Section-2)

Fig. A19: Constant stress monotonic shear loading test ($\sigma_{v.Top}$= 200 kPa & τ_{peak}) (Section-2)

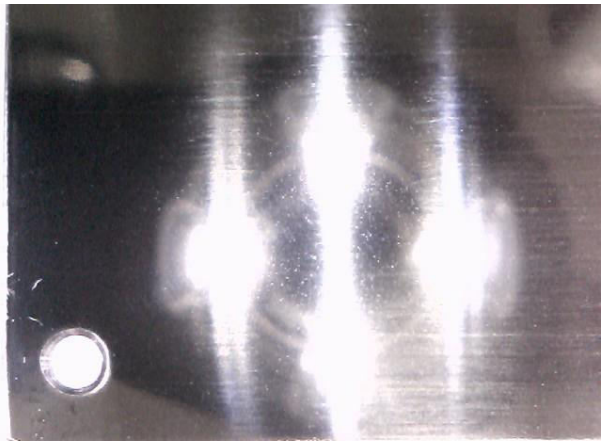Fig. A20: Cyclic axial loading $\sigma_{v.cy}$= 0 – 300 kPa (10 cycles) (Section-2)

Fig. A21: Constant stress monotonic shear loading test ($\sigma_{v.Top}$= 200 kPa) (Section-2)

Fig. A22: Constant stress monotonic shear loading test ($\sigma_{v.Top}$= 300 kPa) (Section-2)
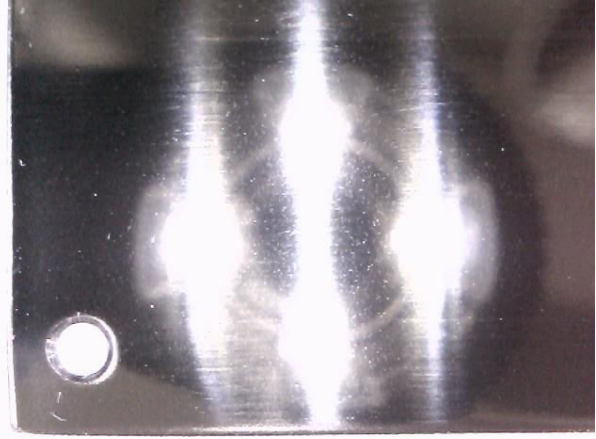

Fig. A23: Constant stress cyclic shear loading test ($\sigma_{v.Top}$= 300 kPa & τ_{cy}= 200 kPa) (Section-2)
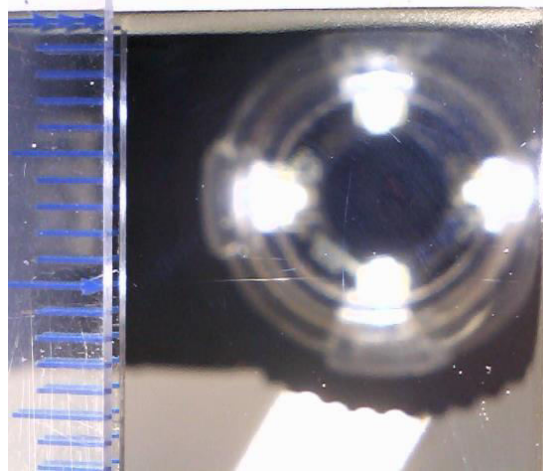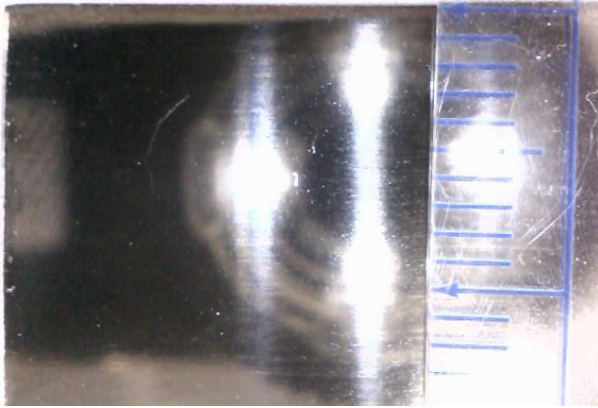
Fig. A24: Initial condition of section 3

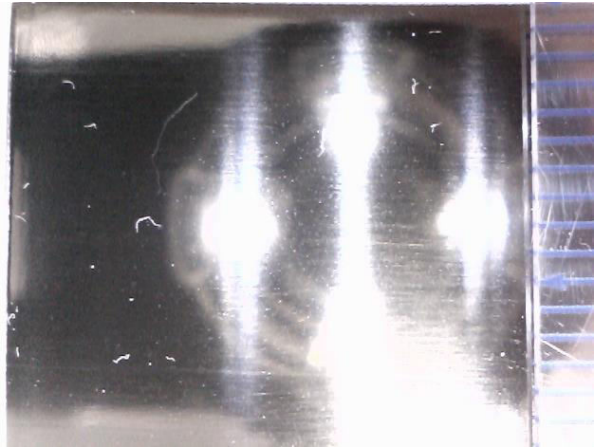Fig. A25: Cyclic axial loading $\sigma_{v.cy}$= 0 – 50 kPa (10 cycles) (Section-3)
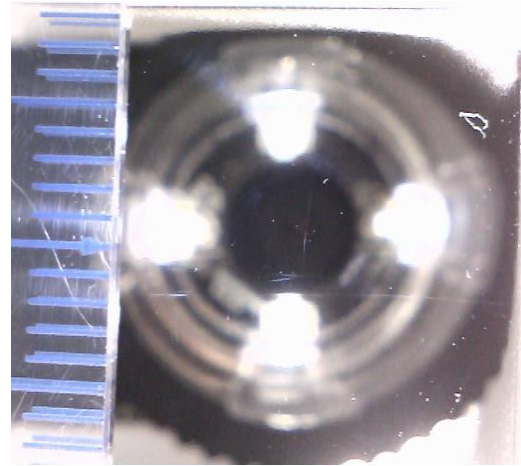
Fig. A26: Cyclic axial loading $\sigma_{v.cy}$= 0 – 100 kPa (10 cycles) (Section-3)

Fig. A27: Cyclic axial loading $\sigma_{v.cy}$= 0 – 150 kPa (10 cycles) (Section-3)

Fig. A28: Cyclic axial loading $\sigma_{v.cy}$= 0 – 200 kPa (10 cycles) (Section-3)

Fig. A29: Constant stress monotonic loading test ($\sigma_{v.Top}$= 200 kPa & τ= 90 kPa) (Section-3)

Fig. A30: Constant stress monotonic shear loading test ($\sigma_{v.Top}$= 200 kPa & τ_{peak}) (Section-3)
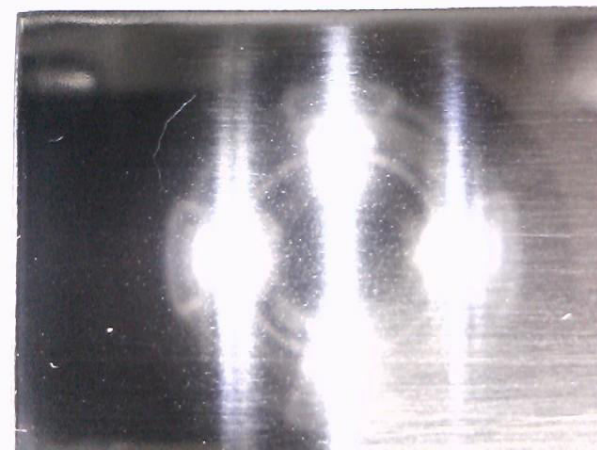

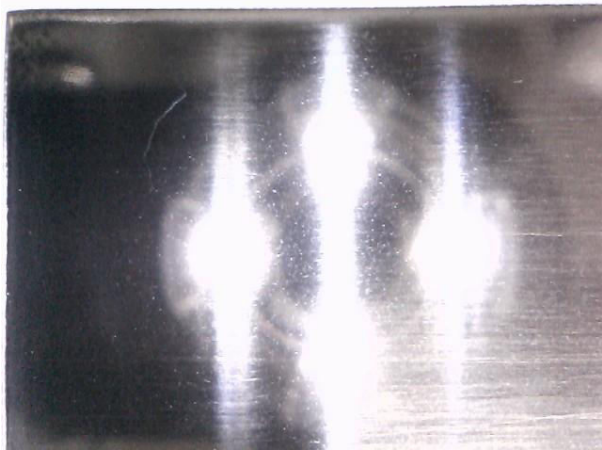Fig. A31: Cyclic axial loading $\sigma_{v.cy}$= 0 – 300 kPa (10 cycles) (Section-3)

Fig. A32: Constant stress monotonic shear loading test ($\sigma_{v.Top}$= 200 kPa) (Section-3)
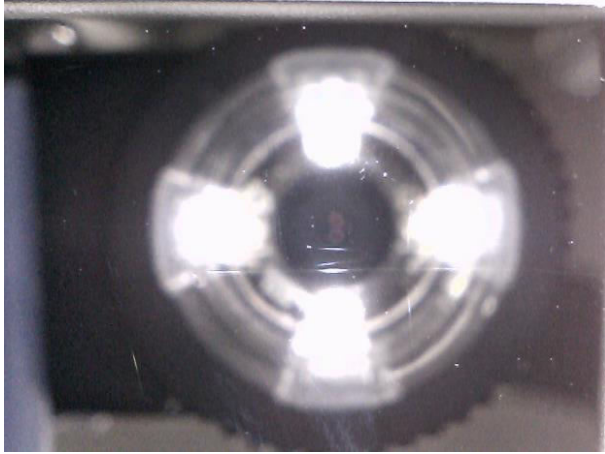
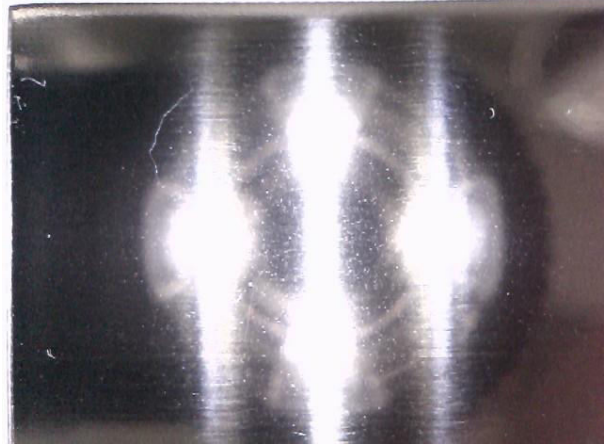Fig. A33: Constant stress monotonic shear loading test ($\sigma_{v.Top}$= 300 kPa) (Section-3)

Fig. A34: Constant stress cyclic shear loading test ($\sigma_{v.Top}$= 300 kPa & τ_{cy}= 200 kPa) (Section-3)

Fig. A35: Initial condition of section 4

Fig. A36: Cyclic axial loading $\sigma_{v.cy}$= 0 – 50 kPa (10 cycles) (Section-4)

Fig. A37: Cyclic axial loading $\sigma_{v.cy}$= 0 – 100 kPa (10 cycles) (Section-4)

Fig. A38: Cyclic axial loading $\sigma_{v.cy}$= 0 – 150 kPa (10 cycles) (Section-4)

Fig. A39: Cyclic axial loading $\sigma_{v.cy}$= 0 – 200 kPa (10 cycles) (Section-4)

Fig. A40: Constant stress monotonic loading test ($\sigma_{v.Top}$= 200 kPa & τ= 90 kPa) (Section-4)
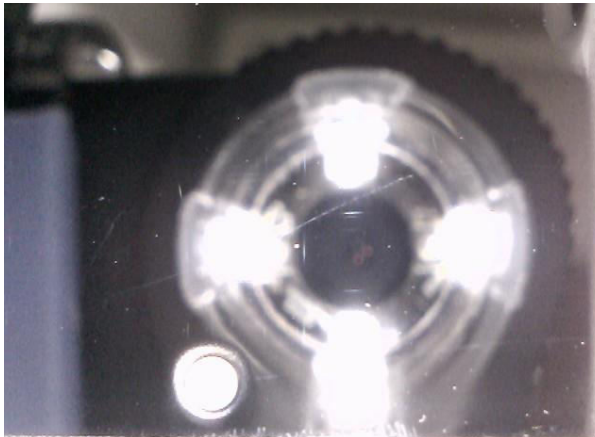
Fig. A41: Constant stress monotonic shear loading test ($\sigma_{v.Top}$= 200 kPa & τ_{peak}) (Section-4)
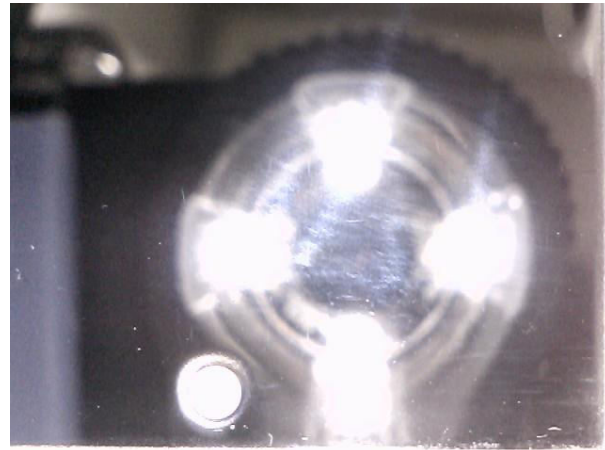
Fig. A42: Cyclic axial loading $\sigma_{v.cy}$= 0 – 300 kPa (10 cycles) (Section-4)
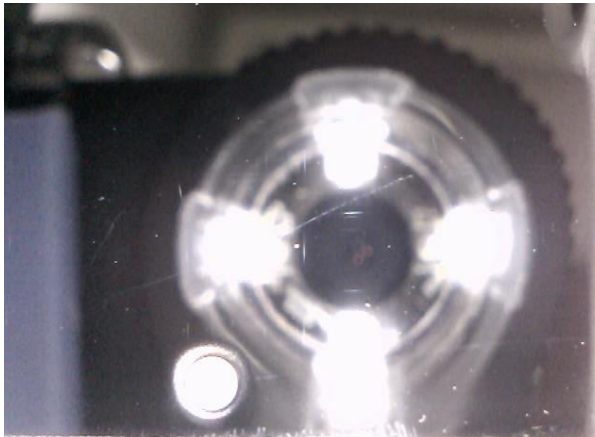
Fig. A43: Constant stress monotonic shear loading test ($\sigma_{v.Top}$= 200 kPa) (Section-4)

Fig. A44: Constant stress monotonic shear loading test ($\sigma_{v.Top}$= 300 kPa) (Section-4)

Fig. A45: Constant stress cyclic shear loading test ($\sigma_{v.Top}$= 300 kPa & τ_{cy}= 200 kPa) (Section-4)

Fig. A46: Prototype B (2μm thick.)

Fig. A47: Initial condition of section 1

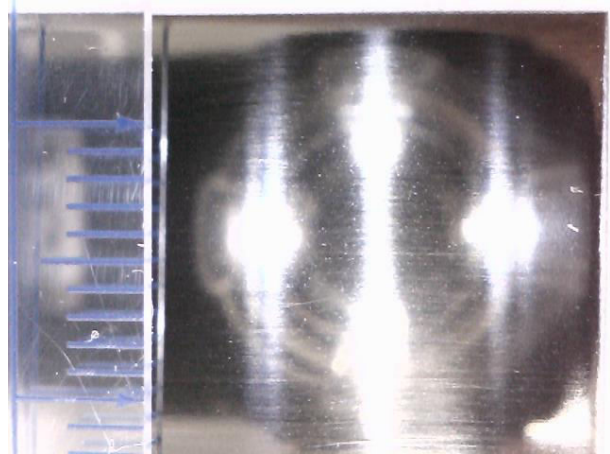Fig. A48: Cyclic axial loading $\sigma_{v.cy}$= 0 – 50 kPa (10 cycles) (Section-1)

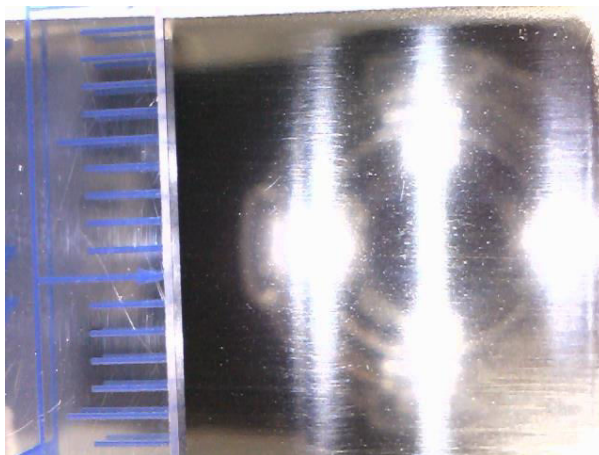Fig. A49: Cyclic axial loading $\sigma_{v.cy}$= 0 – 100 kPa (10 cycles) (Section-1)

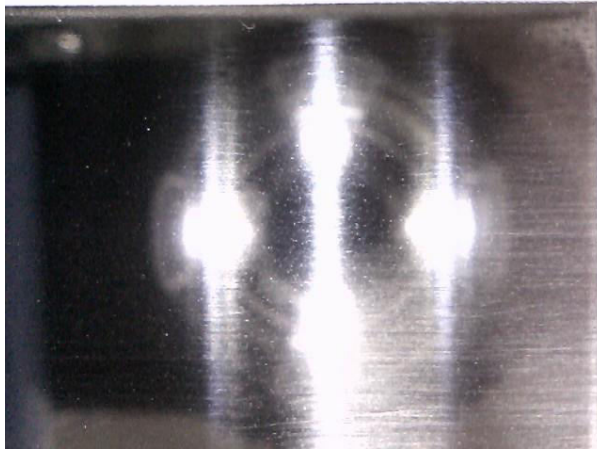Fig. A50: Cyclic axial loading $\sigma_{v.cy}$= 0 – 150 kPa (10 cycles) (Section-1)

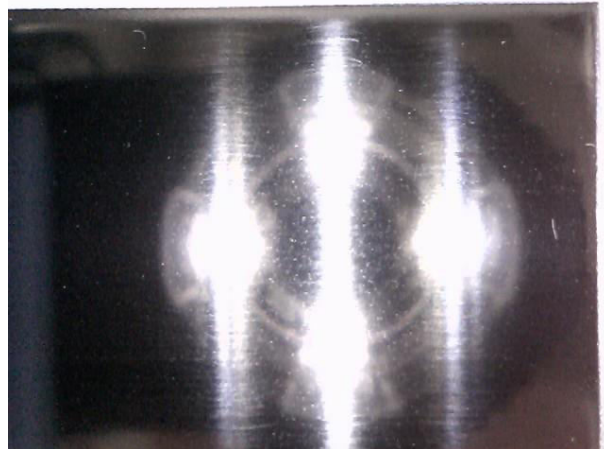Fig. A51: Cyclic axial loading $\sigma_{v.cy}$= 0 – 200 kPa (10 cycles) (Section-1)

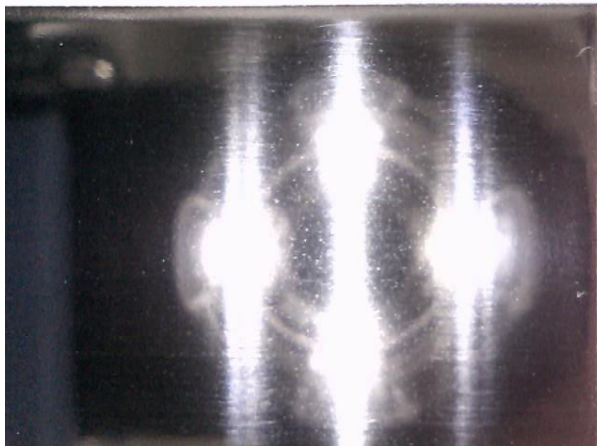Fig. A52: Constant stress monotonic loading test ($\sigma_{v.Top}$= 200 kPa & τ= 90 kPa) (Section-1)

Fig. A53: Constant stress monotonic shear loading test ($\sigma_{v.Top}$= 200 kPa & τ_{peak}) (Section-1)
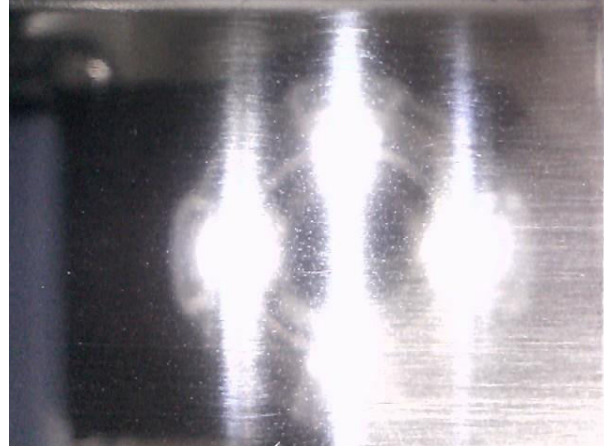

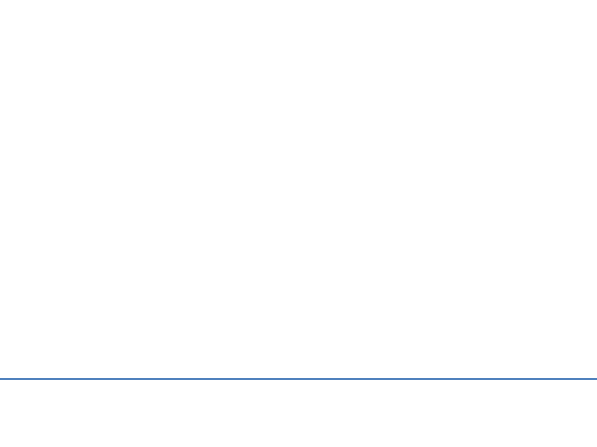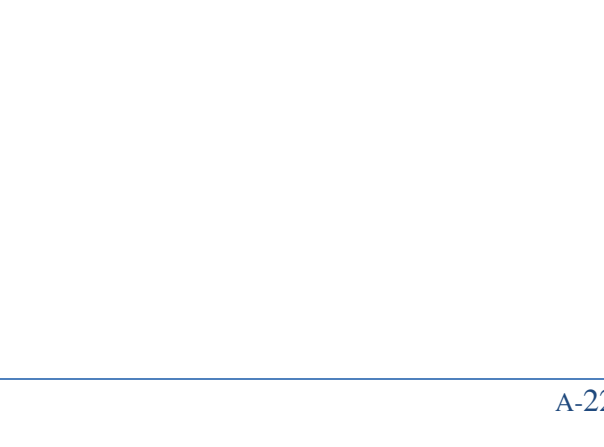Fig. A54: Cyclic axial loading $\sigma_{v.cy}$= 0 – 300 kPa (10 cycles) (Section-1)

Fig. A55: Constant stress monotonic shear loading test ($\sigma_{v.Top}$= 200 kPa) (Section-1)

Fig. A56: Constant stress monotonic shear loading test ($\sigma_{v.Top}$= 300 kPa) (Section-1)

Fig. A57: Constant stress cyclic shear loading test ($\sigma_{v.Top}$= 300 kPa & τ_{cy}= 200 kPa) (Section-1)

Fig. A58: Initial condition of section 2

Fig. A59: Cyclic axial loading $\sigma_{v.cy}$= 0 – 50 kPa (10 cycles) (Section-2)

Fig. A60: Cyclic axial loading $\sigma_{v.cy}$= 0 – 100 kPa (10 cycles) (Section-2)

Fig. A61: Cyclic axial loading $\sigma_{v.cy}$= 0 – 150 kPa

Fig. A62: Cyclic axial loading $\sigma_{v.cy}$= 0 – 200 kPa

(10 cycles) (Section-2)   (10 cycles) (Section-2)
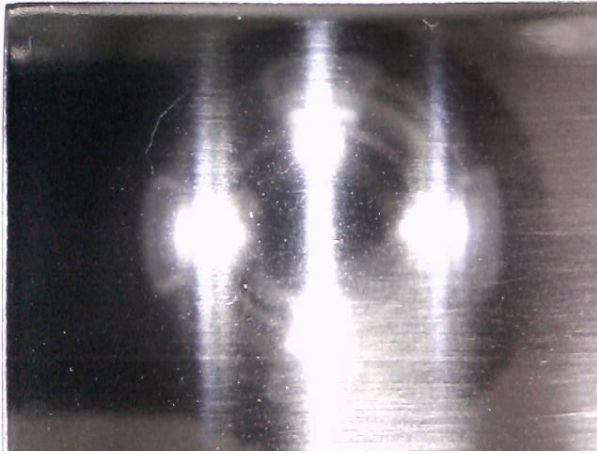
Fig. A63: Constant stress monotonic loading test ($\sigma_{v.Top}$= 200 kPa & τ= 90 kPa) (Section-2)

Fig. A64: Constant stress monotonic shear loading test ($\sigma_{v.Top}$= 200 kPa & τ_{peak}) (Section-2)

Fig. A65: Cyclic axial loading $\sigma_{v.cy}$= 0 – 300 kPa (10 cycles) (Section-2)

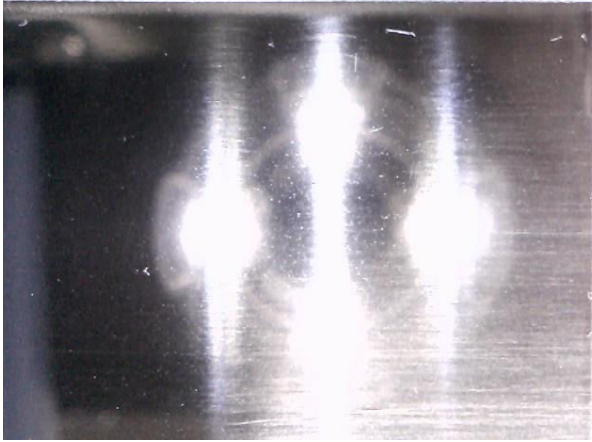Fig. A66: Constant stress monotonic shear loading test ($\sigma_{v.Top}$= 200 kPa) (Section-2)

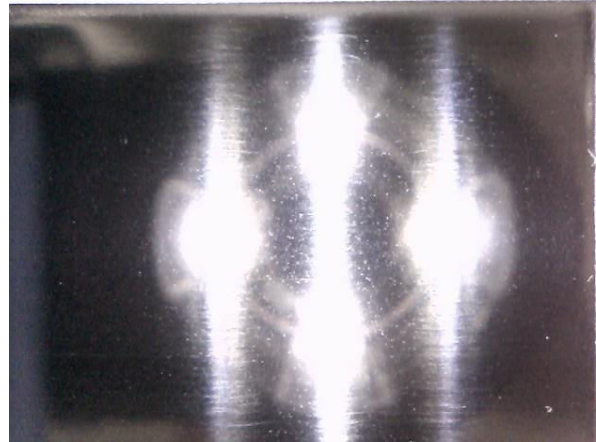Fig. A67: Constant stress monotonic shear loading test ($\sigma_{v.Top}$= 300 kPa) (Section-2)

Fig. A68: Constant stress cyclic shear loading test ($\sigma_{v.Top}$= 300 kPa & τ_{cy}= 200 kPa) (Section-2)
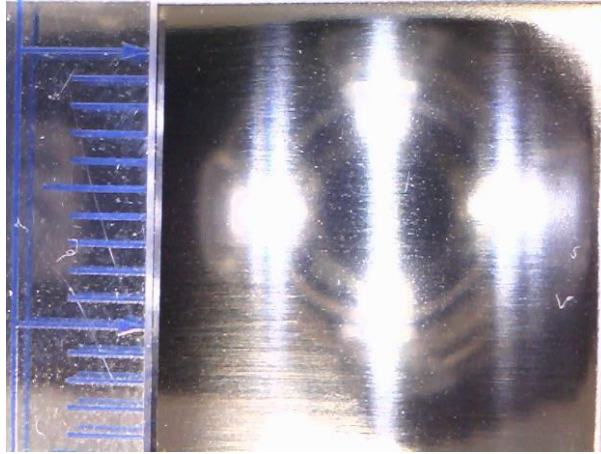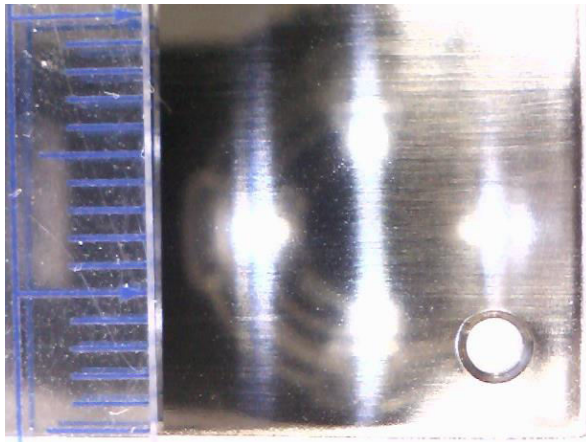
Fig. A69: Initial condition of section 3

Fig. A70: Cyclic axial loading $\sigma_{v.cy}$= 0 – 50 kPa (10 cycles) (Section-3)

Fig. A71: Cyclic axial loading $\sigma_{v.cy}$= 0 – 100 kPa (10 cycles) (Section-3)

Fig. A72: Cyclic axial loading $\sigma_{v.cy}$= 0 – 150 kPa (10 cycles) (Section-3)

Fig. A73: Cyclic axial loading $\sigma_{v.cy}$= 0 – 200 kPa (10 cycles) (Section-3)

Fig. A74: Constant stress monotonic loading test ($\sigma_{v.Top}$= 200 kPa & τ= 90 kPa) (Section-3)

Fig. A75: Constant stress monotonic shear loading test ($\sigma_{v.Top}$= 200 kPa & τ_{peak}) (Section-3)

Fig. A76: Cyclic axial loading $\sigma_{v.cy}$= 0 – 300 kPa (10 cycles) (Section-3)

Fig. A77: Constant stress monotonic shear loading test ($\sigma_{v.Top}$= 200 kPa) (Section-3)

Fig. A78: Constant stress monotonic shear loading test ($\sigma_{v.Top}$ = 300 kPa) (Section-3)

Fig. A79: Constant stress cyclic shear loading test ($\sigma_{v.Top}$ = 300 kPa & τ_{cy} = 200 kPa) (Section-3)
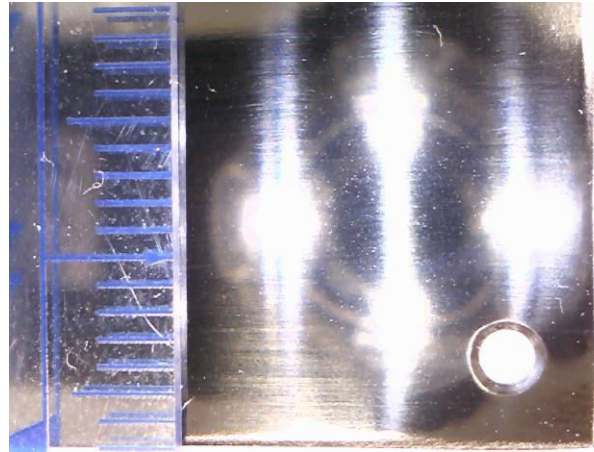
Fig. A80: Initial condition of section 4

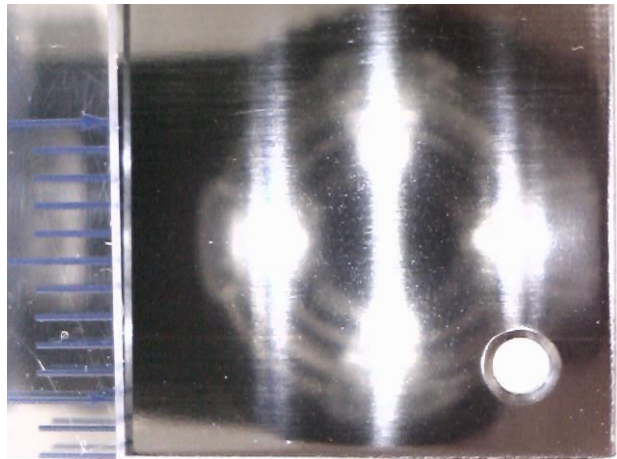Fig. A81: Cyclic axial loading $\sigma_{v.cy}$= 0 – 50 kPa
(10 cycles) (Section-4)

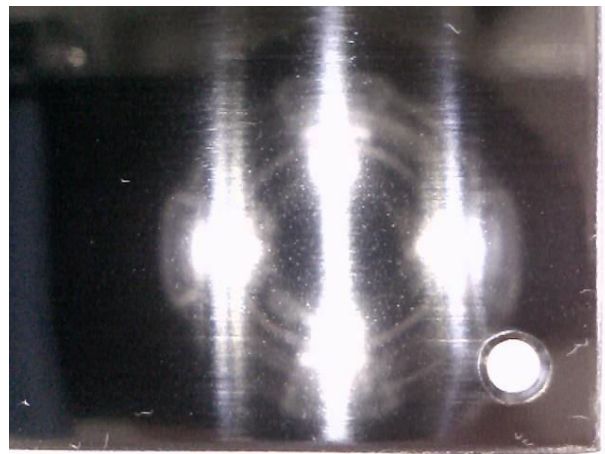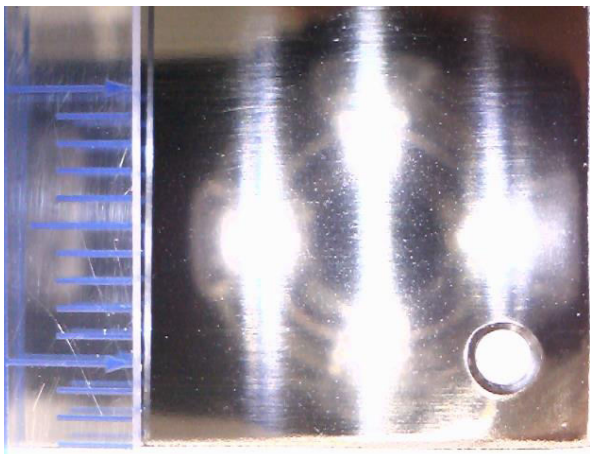Fig. A82: Cyclic axial loading $\sigma_{v.cy}$= 0 – 100 kPa
(10 cycles) (Section-4)

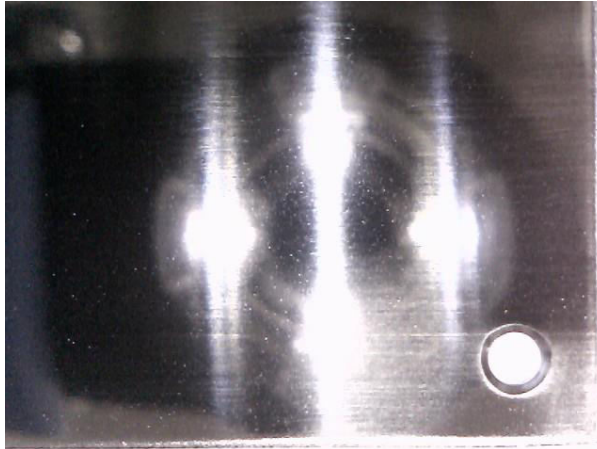Fig. A83: Cyclic axial loading $\sigma_{v.cy}$= 0 – 150 kPa (10 cycles) (Section-4)

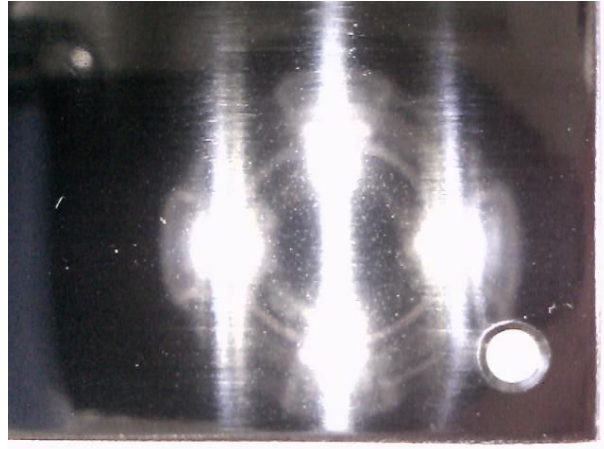Fig. A84: Cyclic axial loading $\sigma_{v.cy}$= 0 – 200 kPa (10 cycles) (Section-4)

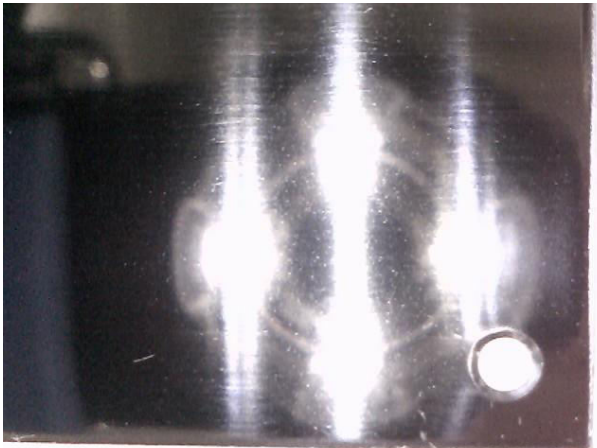Fig. A85: Constant stress monotonic loading test ($\sigma_{v.Top}$= 200 kPa & τ= 90 kPa) (Section-4)

Fig. A86: Constant stress monotonic shear loading test ($\sigma_{v.Top}$= 200 kPa & τ_{peak}) (Section-4)
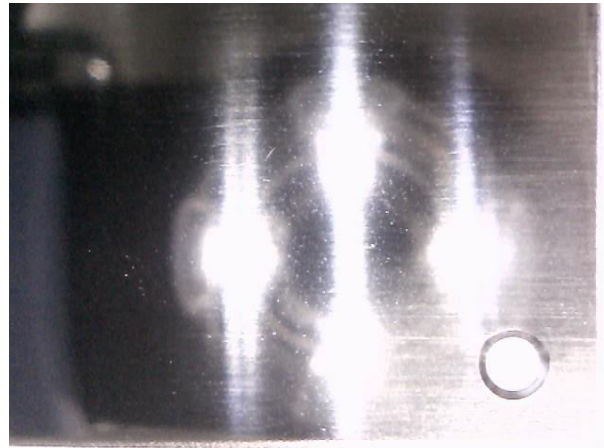

Fig. A87: Cyclic axial loading $\sigma_{v.cy}$= 0 – 300 kPa (10 cycles) (Section-4)

Fig. A88: Constant stress monotonic shear loading test ($\sigma_{v.Top}$= 200 kPa) (Section-4)

Fig. A89: Constant stress monotonic shear loading test ($\sigma_{v.Top}$= 300 kPa) (Section-4)

Fig. A90: Constant stress cyclic shear loading test ($\sigma_{v.Top}$= 300 kPa & τ_{cy}= 200 kPa) (Section-4)